

This work is protected by copyright and other intellectual property rights and duplication or sale of all or part is not permitted, except that material may be duplicated by you for research, private study, criticism/review or educational purposes. Electronic or print copies are for your own personal, non-commercial use and shall not be passed to any other individual. No quotation may be published without proper acknowledgement. For any other use, or to quote extensively from the work, permission must be obtained from the copyright holder/s.



Monitoring metabolism: improving  
the management of age related  
hearing loss using mass  
spectrometry and vibrational  
spectroscopy techniques

---

Thesis submitted for the degree of Doctor of Philosophy

**Amy Jayne Worrall**

June 2025

Faculty of Medicine and Health Sciences

**Keele University**



# Table of Contents

---

Acknowledgements.....	i
Abbreviations.....	iii
List of Figures.....	v
List of Tables.....	xiv
Abstract.....	xvi
1. Introduction.....	1
1.1. Motivations for the Study .....	1
1.2. Introduction to Hearing Loss .....	1
1.3. Age Related Hearing Loss – Condition and Diagnosis .....	4
1.3.1. Introduction to ARHL .....	4
1.3.2. The ARHL Diagnosis Process .....	5
1.4. Metabolic ARHL.....	7
1.4.1. Fibrocytes, Potassium Recycling, and the Endocochlear Potential .....	7
1.4.2. Cochlear Fibrocyte Pathology .....	8
1.5. Inflammation and the Cochlea .....	9
1.5.1. Inflammaging.....	9
1.5.2. Inflammation, Mitochondrial Dysfunction, and ARHL.....	10
1.6. Treatment of ARHL .....	11
1.6.1. Existing ARHL Treatments.....	11
1.6.2. Intervention Strategies Using Fibrocyte Manipulation.....	13
1.6.3. Fibrocytes and cell replacement therapies .....	16
1.7. Spectrometry and Spectroscopy for the Monitoring of Cochlear Fibrocytes- Introduction to Relevant Techniques .....	20

1.7.1.	Raman Spectroscopy .....	20
1.7.2.	ATR-FTIR Spectroscopy .....	23
1.7.3.	Synchrotron-based Analysis .....	26
1.7.4.	Vibrational Spectroscopy in Inflammation and Hearing Studies .....	28
1.7.5.	Selected Ion Flow Tube Mass Spectrometry (SIFT – MS) .....	31
1.8.	Mass spectrometry in diagnosis .....	32
1.9.	The present study- Aims and Objectives .....	34
2.	Materials and Methods .....	35
2.1.	Cell Culture Methods .....	35
2.1.1.	Dissection and Growth of Murine Cochlear Fibrocytes .....	35
2.1.2.	General Cell Culture Conditions .....	37
2.1.3.	Passage and Storage .....	38
2.1.4.	Cell Survival Assays .....	39
2.1.5.	Cochlear Fibrocyte Characterisation .....	39
2.2.	Raman Spectroscopy of Cochlear Fibrocytes .....	40
2.2.1.	Raman Sample Preparation and Sampling.....	40
2.2.2.	Raman Data Pre-processing .....	41
2.2.3.	Raman Data Analysis .....	44
2.3.	ATR-FTIR Spectroscopy of Cochlear Fibrocyte Supernatant .....	47
2.3.1.	The Dxcover Sampling System .....	47
2.3.2.	ATR-FTIR Sample Preparation and Sampling.....	48
2.3.3.	ATR-FTIR Data Processing and Analysis.....	49
2.4.	Synchrotron FTIR Spectroscopy (S-FTIR) and Hyperspectral Raman.....	52
2.4.1.	Synchrotron Instrumentation and Sample Preparation.....	52

2.4.2.	Synchrotron Data Processing and Analysis .....	52
2.5.	SIFT-MS of Cochlear Fibrocytes.....	53
2.5.1.	SIFT-MS Instrumentation .....	53
2.5.2.	SIFT-MS Vessel Selection for Cell Sampling.....	53
2.5.3.	SIFT-MS Low Cell Number Testing.....	55
2.5.4.	Fibrocyte Sample Preparation and SIFT- MS Sampling.....	55
2.5.5.	SIFT-MS Data Processing and Analysis .....	56
2.5.6.	Mann Whitney U Test and Kruskal Wallis H Test .....	57
2.6.	Cerumen Investigations .....	57
2.6.1.	Human Cerumen Samples .....	57
2.6.2.	Vibrational Spectroscopy of Cerumen .....	58
2.6.3.	Headspace Analysis of Cerumen .....	58
3.	Characterisation of Healthy and Inflamed Cochlear Fibrocyte Cultures by Raman Spectroscopy and ATR-FTIR .....	59
3.1.	Introduction .....	59
3.1.1.	The Healthy Cochlear Fibrocyte State .....	59
3.1.2.	Cochlear Fibrocyte Classification .....	59
3.1.3.	Traditional Methods of Cochlear Fibrocyte Observation .....	62
3.1.4.	Modelling Cochlear Fibrocyte Inflammation <i>In vitro</i> .....	62
3.1.5.	The Role of TNF- $\alpha$ in Cochlear Fibrocyte Inflammation .....	63
3.1.6.	IL-1 $\beta$ and the NLRP3 Inflammasome .....	64
3.1.7.	Anti-IL-1 Therapies Revisited .....	65
3.1.8.	Detection of Cochlear Fibrocyte Health via Raman and ATR-FTIR Spectroscopy.....	66
3.2.	Chapter Aims.....	66

3.3.	Materials and Methods .....	67
3.3.1.	Cochlear Fibrocyte Explantation, Growth and Maintenance .....	67
3.3.2.	Observation of Cell Outgrowth from the Spiral Ligament .....	67
3.3.3.	Characterisation of Cultured Cells by Immunocytochemistry .....	68
3.3.4.	Induction of Inflammation and Confirmation of the Inflammatory State .....	69
3.3.5.	Raman Spectroscopy of Healthy and Inflamed Cochlear Fibrocytes .....	69
3.3.6.	ATR-FTIR Spectroscopy of Healthy and Inflamed Cochlear Fibrocyte Supernatant ...	70
3.3.7.	Data Processing and Analysis .....	70
3.4.	Results and Interpretation .....	72
3.4.1.	Explantation, Growth and Characterisation of Explanted Cochlear Fibrocytes .....	72
3.4.2.	Raman Spectroscopy of Healthy Cochlear Fibrocytes.....	77
3.4.3.	ATR-FTIR Spectroscopy of Healthy Cochlear Fibrocyte Supernatant .....	79
3.4.4.	The Induction of Inflammation in Cochlear Fibrocyte Cultures by TNF- $\alpha$ Dosage .....	84
3.4.5.	Raman Spectroscopy of TNF- $\alpha$ -dosed Cochlear Fibrocytes.....	87
3.4.6.	ATR-FTIR of TNF- $\alpha$ -dosed Cochlear Fibrocyte Supernatant.....	111
3.4.7.	The Induction of Inflammation in Cochlear Fibrocyte Cultures by IL-1 $\beta$ Dosage.....	116
3.4.8.	Raman Spectroscopy of IL-1 $\beta$ -dosed Cochlear Fibrocytes .....	119
3.4.9.	ATR-FTIR of IL-1 $\beta$ -dosed Cochlear Fibrocyte Supernatant .....	148
3.5.	Discussion .....	154
3.6.	Conclusions .....	160
4.	Hyperspectral Raman Spectroscopy and Synchrotron micro-FTIR of Interleukin-1 $\beta$ Induced Inflammatory Changes in Cochlear Fibrocyte Cultures .....	162
4.1.	Introduction .....	162
4.1.1.	Infrared Spectroscopy- Synchrotron vs. Benchtop .....	163

4.1.2.	The Present Investigation – The Study of Biochemical Changes in Murine Cochlear Fibrocytes due to Inflammation using Synchrotron-based MicroFTIR (S-FTIR) .....	164
4.2.	Chapter Aims .....	165
4.3.	Materials and Methods .....	165
4.3.1.	Sample Preparation .....	165
4.3.2.	Synchrotron Facility at Diamond Light Source, UK.....	166
4.3.3.	S-FTIR Sampling.....	167
4.3.4.	Raman Sampling.....	167
4.3.5.	Data Processing.....	167
4.4.	Results and Interpretation .....	168
4.4.1.	Raman Spectroscopy .....	168
4.4.2.	S-FTIR – Spectral Analysis and PCA .....	230
4.4.3.	FTIR – Generation of the Non-linear Model.....	256
4.5.	Discussion .....	260
4.6.	Concluding Remarks .....	263
5.	Towards Translation- Exploring the Potential of SIFT-MS and Cerumen Sampling in Non-Invasive ARHL Diagnoses .....	264
5.1.	Introduction.....	264
5.1.1.	Headspace Analysis for Non-invasive Cell Profiling .....	264
5.1.2.	ARHL Investigation- Considering the Cerumen Approach .....	265
5.1.3.	Typical Production and Composition of Cerumen .....	266
5.1.4.	Factors Affecting Cerumen Production and Composition.....	268
5.2.	Chapter Aims .....	269
5.3.	Materials and methods .....	269

5.3.1.	Cochlear Fibrocyte Cultures .....	269
5.3.2.	Induction of Inflammation in Cochlear Fibrocytes.....	270
5.3.3.	Headspace Analysis of Cochlear Fibrocyte Cultures Using SIFT-MS .....	270
5.3.4.	Human Cerumen Samples .....	270
5.3.5.	Raman Spectroscopy of Cerumen .....	271
5.3.6.	ATR-FTIR Spectroscopy of Cerumen.....	271
5.3.7.	Headspace Analysis of Cerumen Using SIFT-MS.....	272
5.3.8.	Data Processing and Analysis .....	272
5.4.	Results and Interpretation .....	273
5.4.1.	SIFT-MS of Healthy Cochlear Fibrocytes.....	273
5.4.2.	SIFT-MS of TNF- $\alpha$ -dosed Cochlear Fibrocyte Culture Headspace .....	276
5.4.3.	SIFT-MS of IL-1 $\beta$ -dosed Cochlear Fibrocyte Culture Headspace.....	278
5.4.4.	Raman Spectroscopy of Human Cerumen .....	281
5.4.5.	ATR-FTIR Spectroscopy of Human Cerumen.....	282
5.4.6.	SIFT-MS of Cerumen Sample Headspace .....	284
5.5.	Discussion.....	285
5.6.	Concluding Remarks .....	289
6.	Conclusions and Future Work.....	291
6.1.	Addressing the Necessity- ARHL Revisited.....	291
6.2.	Study Findings.....	291
6.3.	Future Work .....	295
6.3.1.	Improving the Model.....	295
6.3.2.	Next Experimental Steps – Investigating the Citric Acid Cycle .....	296
6.3.3.	Towards Clinical Translation- Bioreactors and the Application of Automation .....	297

6.3.4. Towards Clinical Translation- Alternatives to Biofluids .....	298
6.4. Final Conclusions.....	299
References .....	301
Appendix A – Authorisation for Animal Use .....	329
Appendix B – Kinetic Library for SIFT-MS Analysis .....	330
Appendix C – FMHS FREC Approval for Cerumen Use.....	345



# Acknowledgements

---

Upon submission of this thesis, I would like to recognise the contributions which have enabled the continuation and completion of my research. First and foremost, I wish to thank Doctor Abigail Roberts who, throughout my studies, has empowered me to become the researcher that I am today. Dr Roberts has been a vast source of scientific knowledge, and has given me numerous opportunities for collaboration, travel, and development throughout the course of my research. I would like to thank her for ensuring an experience that I will remember for a lifetime.

I would also like to thank my co-supervisors, Dr Falko Drijfhout and Professor Nicholas Forsyth who have supported me throughout my doctoral studies. I thank Dr Falko Drijfhout for his tremendous technical expertise and for use of the facilities in his laboratory. I thank Professor Nicholas Forsyth for his invaluable insight throughout my studies.

In addition to my supervisory team, I wish to thank Professor David Furness, whose immeasurable knowledge of cochlear anatomy and wealth of hearing research has been indispensable, and who from my undergraduate degree, has inspired me to pursue the field which I am passionate about, however small.

I wish to express my gratitude, also, to those that have collaborated with me across the course of this research, particularly to Dr Gianfelice Cinque and his team at the Synchrotron Diamond Light Source MIRIAM B22 beamline.

Further thanks go to collaborators at Dxcover Ltd., Glasgow for their generous provision of a Dxcover® Sampling Unit and Dxcover® Sample Slides to enable ATR-FTIR liquid sampling in this research. In particular, I wish to thank Dr Holly Butler for her scientific input on the use of ATR-FTIR in biological sampling and overall assistance with the supernatant sampling setup.

I would also like to take this opportunity to thank the technical and administrative staff of Guy Hilton Research Centre, and Keele University as a whole, for assuring the smooth and safe operation of the laboratory facilities which enabled project to reach its goal.

I thank the sponsors of this research, the ESPRC and Keele University for generously providing the funds and facilities necessary for its conduction.

I wish to thank my friends for their unending encouragement and unwavering support throughout the best and worst of my PhD study. In particular, I wish to thank Adam for illuminating my life at its darkest.

Last, but by no means least, I thank my parents, Susan and Raymond, for ceaselessly nurturing my scientific spirit and for reminding me that the most important step of any journey is the first.

# Abbreviations

---

Age-related hearing loss (ARHL)

Attenuated total reflection (ATR)

Cochlear implant (CI)

C-reactive protein (CRP)

Dulbecco's modified eagle's medium (DMEM)

Dimethyl sulphoxide (DMSO)

Endocochlear potential (EP)

Faculty of medicine and health sciences (FMHS)

Faculty research ethics committee (FREC)

Foetal bovine serum (FBS)

Fourier transform infrared (FTIR)

Full scan (FS)

Gas chromatography mass spectrometry (GC-MS)

Hearing aid speech perception index (HASPI)

Hearing aid speech quality index (HASQI)

Hearing loss (HL)

Heat shock proteins (HSPs)

Induced pluripotent stem cells (iPSCs)

Industrial methylated spirit (IMS)

Infrared (IR)

Inner hair cells (IHCs)

Insulin-like growth factor (IGF)

Insulin transferrin selenium G (ITS-G)

Interleukin (IL)

Lateral wall (LW)

Mechanoelectrical transducer (MET)

Mesenchymal stem cells (MSCs)

Multi-ion monitor (MUI)

Non-essential amino acids (NEAA)

Nitric oxide (NO)

Outer hair cells (OHCs)

Phosphate buffered saline (PBS)

Principal component analysis (PCA)

Principal component (PC)

Reactive oxygen species (ROS)

Selected ion flow tube mass spectrometry (SIFT-MS)

Spiral ganglion neurons (SGNs)

Spiral ligament fibrocyte (SLF)

Transforming growth factor (TGF)

Tumour necrosis factor (TNF)

United Kingdom (UK)

World health organisation (WHO)

# List of Figures

---

Figure 1: The Organ of Corti and lateral wall. ....	3
Figure 2: Cross-section of the cochlea. ....	7
Figure 3: General intensity over time of the biochemical events associated with the onset and resolution of inflammation. ....	9
Figure 4: Anti-interleukin-1 therapeutic agents and their modes of action. ....	15
Figure 5: Vibrational modes of molecules. ....	22
Figure 6: Types of scattering in Raman spectroscopy. ....	23
Figure 7: The principal of ATR-FTIR – total internal reflection and evanescent wave generation. ....	25
Figure 8: A Simple Diagram of Typical Synchrotron Setup. ....	27
Figure 9: A simplified schematic of the SIFT-MS instrument. ....	31
Figure 10: Photographic images of the cochlea dissection procedure. ....	36
Figure 11: Fluorescence images of cochlear fibrocyte secondary cultures with and without collagen. ....	38
Figure 12: Average Raman spectra of cell samples vs blank CaF <sub>2</sub> slide. ....	41
Figure 13: Average Raman spectra of cell samples at each pre-processing stage. ....	43
Figure 14: Average second derivative Raman spectrum of cell samples. ....	44
Figure 15: Accessories employed in the ATR-FTIR setup. ....	47
Figure 16: A Dxcover® sample slide. ....	48
Figure 17: Average ATR-FTIR spectra of cell samples at each pre-processing stage. ....	50
Figure 18: Average second derivative ATR-FTIR spectrum of cell samples. ....	51
Figure 19: Fibrocyte regions within the spiral ligament. ....	60
Figure 20: 7-day overview of cells emerging from murine spiral ligament fragments. ....	73
Figure 21: Light microscopy images of cells emerging from tissue explants. ....	74
Figure 22: Light microscopy and fluorescence microscopy images of monolayer secondary cultures. ....	75
Figure 23: Fluorescence images of cultured cells stained for common fibrocyte markers. Scale bars= 100µm. ....	76

Figure 24: Fluorescence microscopy images of monolayer secondary cultures- SLF vs. MG63.....	77
Figure 25: Average Raman spectrum of healthy cochlear fibrocytes.....	78
Figure 26: ATR-FTIR spectra of cochlear fibrocyte supernatant and control media. ....	79
Figure 27: Second derivative ATR-FTIR fingerprint region spectra of cochlear fibrocyte supernatant and control media.....	80
Figure 28: PCA of the fingerprint region of cochlear fibrocyte supernatant vs control media. ....	82
Figure 29: PCA of the high wavenumber region of cochlear fibrocyte supernatant vs control media. ....	83
Figure 30: Fluorescence imaging of TNF- $\alpha$ -dosed cochlear fibrocytes labelled for IL-6. Scale bars= 100 $\mu$ m.....	85
Figure 31: Fluorescence imaging of TNF- $\alpha$ -dosed cochlear fibrocytes labelled for IL-6. Scale bars= 100 $\mu$ m.....	86
Figure 32: Average Raman spectra of murine cochlear fibrocytes following 24hrs incubation with TNF- $\alpha$ . ....	87
Figure 33: Average Raman spectra of healthy and 1ng/mL-dosed cochlear fibrocytes following 24hrs incubation with TNF- $\alpha$ (fingerprint region).....	88
Figure 34: Second derivative Raman fingerprint region spectra of 0ng/mL and 1ng/mL TNF-dosed cochlear fibrocytes. ....	91
Figure 35: Average Raman spectra of healthy and 1ng/mL-dosed cochlear fibrocytes following 24hrs incubation with TNF- $\alpha$ (high wavenumber region). ....	92
Figure 36: Second derivative Raman high wavenumber region spectra of 0ng/mL and 1ng/mL TNF-dosed cochlear fibrocytes. ....	93
Figure 37: Average Raman spectra of healthy and 5ng/mL-dosed cochlear fibrocytes following 24hrs incubation with TNF- $\alpha$ (fingerprint region).....	94
Figure 38: Second derivative Raman fingerprint region spectra of 0ng/mL and 5ng/mL TNF-dosed cochlear fibrocytes. ....	96
Figure 39: Average Raman spectra of healthy and 5ng/mL-dosed cochlear fibrocytes following 24hrs incubation with TNF- $\alpha$ (high wavenumber region). ....	97
Figure 40: Average Raman spectra of healthy and 10ng/mL-dosed cochlear fibrocytes following 24hrs incubation with TNF- $\alpha$ (fingerprint region). ....	98

Figure 41: Second derivative Raman high wavenumber region spectra of 0ng/mL and 5ng/mL TNF-dosed cochlear fibrocytes. ....	98
Figure 42: Second derivative Raman fingerprint region spectra of 0ng/mL and 10ng/mL TNF-dosed cochlear fibrocytes. ....	100
Figure 43: Average Raman spectra of healthy and 10ng/mL-dosed cochlear fibrocytes following 24hrs incubation with TNF- $\alpha$ (high wavenumber region). ....	101
Figure 44: Second derivative Raman high wavenumber region spectra of 0ng/mL and 10ng/mL TNF-dosed cochlear fibrocytes. ....	102
Figure 45: Average Raman spectra of healthy and 50ng/mL-dosed cochlear fibrocytes following 24hrs incubation with TNF- $\alpha$ (fingerprint region).....	103
Figure 46: Second derivative Raman fingerprint region spectra of 0ng/mL and 50ng/mL TNF-dosed cochlear fibrocytes. ....	105
Figure 47: Average Raman spectra of healthy and 50ng/mL-dosed cochlear fibrocytes following 24hrs incubation with TNF- $\alpha$ (high wavenumber region). ....	106
Figure 48: Second derivative Raman high wavenumber region spectra of 0ng/mL and 50ng/mL TNF-dosed cochlear fibrocytes. ....	107
Figure 49: PCA of the fingerprint region of undosed vs TNF-dosed cochlear fibrocytes. ....	108
Figure 50: PCA of the fingerprint region of undosed vs TNF-dosed cochlear fibrocytes. ....	109
Figure 51: Confidence tables for neural network modelling of Raman spectra of murine cochlear fibrocytes following 24hrs incubation with TNF- $\alpha$ . ....	110
Figure 52: ATR-FTIR spectra of TNF-dosed cochlear fibrocyte supernatant samples. ....	112
Figure 53: Second derivative ATR-FTIR fingerprint region spectra of TNF-dosed cochlear fibrocyte supernatants. ....	113
Figure 54: PCA of the fingerprint region of TNF-dosed cochlear fibrocyte supernatant. ....	114
Figure 55: PCA of the high wavenumber region of TNF-dosed cochlear fibrocyte supernatant. ....	115
Figure 56: Fluorescence imaging of IL-1 $\beta$ -dosed cochlear fibrocytes labelled for IL-6. Scale bars= 100 $\mu$ m.....	117
Figure 57: Fluorescence imaging of IL-1 $\beta$ -dosed cochlear fibrocytes labelled for IL-8. Scale bars= 100 $\mu$ m.....	118

Figure 58: Average Raman spectra of murine cochlear fibrocytes following 24hrs incubation with IL-1 $\beta$ .....	119
Figure 59: Average Raman spectra of healthy and 1ng/mL-dosed cochlear fibrocytes following 24hrs incubation with IL-1 $\beta$ (fingerprint region). ....	120
Figure 60: Second derivative Raman spectra of healthy and 1ng/mL-dosed cochlear fibrocytes following 24hrs incubation with IL-1 $\beta$ (fingerprint region).....	123
Figure 61: Average Raman spectra of healthy and 1ng/mL-dosed cochlear fibrocytes following 24hrs incubation with IL-1 $\beta$ (high wavenumber region). ....	124
Figure 62: Second derivative Raman spectra of healthy and 1ng/mL-dosed cochlear fibrocytes following 24hrs incubation with IL-1 $\beta$ (high wavenumber region). ....	125
Figure 63: Average Raman spectra of healthy and 5ng/mL-dosed cochlear fibrocytes following 24hrs incubation with IL-1 $\beta$ (fingerprint region). ....	126
Figure 64: Second derivative Raman spectra of healthy and 5ng/mL-dosed cochlear fibrocytes following 24hrs incubation with IL-1 $\beta$ (fingerprint region).....	127
Figure 65: Average Raman spectra of healthy and 5ng/mL-dosed cochlear fibrocytes following 24hrs incubation with IL-1 $\beta$ (high wavenumber region). ....	128
Figure 66: Second derivative Raman spectra of healthy and 5ng/mL-dosed cochlear fibrocytes following 24hrs incubation with IL-1 $\beta$ (high wavenumber region). ....	129
Figure 67: Average Raman spectra of healthy and 10ng/mL-dosed cochlear fibrocytes following 24hrs incubation with IL-1 $\beta$ (fingerprint region). ....	130
Figure 68: Second derivative Raman spectra of healthy and 10ng/mL-dosed cochlear fibrocytes following 24hrs incubation with IL-1 $\beta$ (fingerprint region).....	132
Figure 69: Average Raman spectra of healthy and 10ng/mL-dosed cochlear fibrocytes following 24hrs incubation with IL-1 $\beta$ (high wavenumber region). ....	133
Figure 70: Second derivative Raman spectra of healthy and 1ng/mL-dosed cochlear fibrocytes following 24hrs incubation with IL-1 $\beta$ (high wavenumber region). ....	134
Figure 71: Average Raman spectra of healthy and 25ng/mL-dosed cochlear fibrocytes following 24hrs incubation with IL-1 $\beta$ (fingerprint region). ....	135

Figure 72: Second derivative Raman spectra of healthy and 25ng/mL-dosed cochlear fibrocytes following 24hrs incubation with IL-1 $\beta$ (fingerprint region).....	137
Figure 73: Average Raman spectra of healthy and 25ng/mL-dosed cochlear fibrocytes following 24hrs incubation with IL-1 $\beta$ (high wavenumber region). ....	138
Figure 74: Second derivative Raman spectra of healthy and 25ng/mL-dosed cochlear fibrocytes following 24hrs incubation with IL-1 $\beta$ (high wavenumber region). ....	139
Figure 75: Average Raman spectra of healthy and 50ng/mL-dosed cochlear fibrocytes following 24hrs incubation with IL-1 $\beta$ (fingerprint region). ....	140
Figure 76: Second derivative Raman spectra of healthy and 50ng/mL-dosed cochlear fibrocytes following 24hrs incubation with IL-1 $\beta$ (fingerprint region).....	143
Figure 77: Second derivative Raman spectra of healthy and 50ng/mL-dosed cochlear fibrocytes following 24hrs incubation with IL-1 $\beta$ (high wavenumber region). ....	144
Figure 78: Average Raman spectra of healthy and 50ng/mL-dosed cochlear fibrocytes following 24hrs incubation with IL-1 $\beta$ (high wavenumber region). ....	144
Figure 79: PCA of the fingerprint region of undosed vs IL-dosed cochlear fibrocytes. ....	145
Figure 80: PCA of the high-wavenumber region of undosed vs IL-dosed cells. ....	146
Figure 81: Confidence tables for neural network modelling of Raman spectra of murine cochlear fibrocytes following 24hrs incubation with IL-1 $\beta$ . ....	147
Figure 82: ATR-FTIR spectra of IL-dosed cochlear fibrocyte supernatant samples.....	150
Figure 83: Second derivative ATR-FTIR fingerprint region spectra of IL-dosed cochlear fibrocyte supernatants. ....	151
Figure 84: PCA of the fingerprint region of IL-dosed cochlear fibrocyte supernatant.....	152
Figure 85: PCA of the high wavenumber region of TNF-dosed cochlear fibrocyte supernatant. ....	153
Figure 86: The end station of B22 (MIRIAM), Diamond Light Source, Oxford, UK. ....	166
Figure 87: Comparison of undosed cell spectra- a single undosed cell vs neighbouring undosed cells in contact. ....	169
Figure 88: Raman hyperspectral heat map of 0ng/mL dosed cell at 750cm <sup>-1</sup> .....	179
Figure 89: K-means clustering of hyperspectral Raman data – 0ng/mL dosed single cell. ....	184
Figure 90: K-means clustering of hyperspectral Raman data – 0ng/mL dosed cell pair. ....	198

Figure 91: Comparison of dosed and undosed cell spectra- a single undosed cell vs neighbouring undosed cells in contact vs 10ng/mL interleukin-1-dosed cells in contact. ....	200
Figure 92: Raman hyperspectral chemical maps of 0ng/mL dosed vs 10ng/mL dosed cell pairs below 600cm <sup>-1</sup> .....	208
Figure 93: Raman hyperspectral chemical maps of 0ng/mL dosed vs 10ng/mL dosed cell pairs at ~1650cm <sup>-1</sup> . ....	211
Figure 94: K-means clustering of hyperspectral Raman data – 10ng/mL dosed cell pair. ....	213
Figure 95: Comparison of dosed and undosed cell spectra via hyperspectral Raman spectroscopy. ....	214
Figure 96: K-means clustering of hyperspectral Raman data – 10ng/mL dosed granular cell. ....	226
Figure 97: PCA scatter plots of low vs high cell seeding density samples analysed by S-FTIR.....	230
Figure 98: Loadings plot of low vs high cell seeding density sample PCA. ....	231
Figure 99: Average S-FTIR spectra of dosed and undosed cochlear fibrocytes. ....	233
Figure 100: Offset average S-FTIR spectra of dosed and undosed cochlear fibrocytes. ....	234
Figure 101: Second derivative S-FTIR spectral fingerprint region of dosed and undosed cochlear fibrocytes. ....	235
Figure 102: Second derivative S-FTIR spectral high wavenumber region of dosed and undosed cochlear fibrocytes. ....	236
Figure 103: PCA of the fingerprint region of IL-dosed cochlear fibrocyte S-FTIR.....	237
Figure 104: PCA of the high wavenumber region of IL-dosed cochlear fibrocyte S-FTIR. ....	238
Figure 105: Average S-FTIR fingerprint region spectra of 0ng/mL and 1ng/mL IL-dosed cochlear fibrocytes. ....	239
Figure 106: Second derivative fingerprint region S-FTIR spectra of 0ng/mL and 1ng/mL IL-dosed cochlear fibrocytes. ....	240
Figure 107: PCA scatter plots of the fingerprint region of IL-dosed cochlear fibrocyte S-FTIR.....	240
Figure 108: PCA loadings plot of the fingerprint region of IL-dosed cochlear fibrocyte S-FTIR. ....	241
Figure 109: Second derivative S-FTIR high wavenumber region spectra of 0ng/mL and 1ng/mL IL-dosed cochlear fibrocytes. ....	242

Figure 110: Average S-FTIR high wavenumber region spectra of 0ng/mL and 1ng/mL IL-dosed cochlear fibrocytes. ....	242
Figure 111: PCA scatter plots of the high wavenumber region of 0ng/mL and 1ng/mL IL-dosed cochlear fibrocyte S-FTIR.....	243
Figure 112: PCA loadings plot of the high wavenumber region of 0ng/mL and 1ng/mL IL-dosed cochlear fibrocyte S-FTIR.....	243
Figure 113: Average S-FTIR fingerprint region spectra of 0ng/mL and 5ng/mL IL-dosed cochlear fibrocytes. ....	244
Figure 114: Second derivative S-FTIR fingerprint region spectra of 0ng/mL and 5ng/mL IL-dosed cochlear fibrocytes. ....	245
Figure 115: PCA loadings plot of the fingerprint region of 0ng/mL and 5ng/mL IL-dosed cochlear fibrocyte S-FTIR.....	246
Figure 116: PCA scatter plots of the fingerprint region of 0ng/mL and 5ng/mL IL-dosed cochlear fibrocyte S-FTIR.....	246
Figure 117: Average S-FTIR high wavenumber region spectra of 0ng/mL and 5ng/mL IL-dosed cochlear fibrocytes. ....	247
Figure 118: Second derivative S-FTIR high wavenumber region spectra of 0ng/mL and 5ng/mL IL-dosed cochlear fibrocytes. ....	248
Figure 119: PCA scatter plots of the high wavenumber region of 0ng/mL and 5ng/mL IL-dosed cochlear fibrocyte S-FTIR.....	248
Figure 120: PCA loadings plot of the high wavenumber region of 0ng/mL and 5ng/mL IL-dosed cochlear fibrocyte S-FTIR.....	249
Figure 121: Second derivative S-FTIR fingerprint region spectra of 0ng/mL and 10ng/mL IL-dosed cochlear fibrocytes. ....	251
Figure 122: Average S-FTIR fingerprint region spectra of 0ng/mL and 10ng/mL IL-dosed cochlear fibrocytes. ....	251
Figure 123: PCA scatter plots of the fingerprint region of 0ng/mL and 10ng/mL IL-dosed cochlear fibrocyte S-FTIR.....	252

Figure 124: PCA loadings plot of the fingerprint region of 0ng/mL and 10ng/mL IL-dosed cochlear fibrocyte S-FTIR.....	253
Figure 125: Average S-FTIR high wavenumber region spectra of 0ng/mL and 10ng/mL IL-dosed cochlear fibrocytes. ....	254
Figure 126: Second derivative S-FTIR high wavenumber region spectra of 0ng/mL and 10ng/mL IL-dosed cochlear fibrocytes. ....	254
Figure 127: PCA loadings plot of the high wavenumber region of 0ng/mL and 10ng/mL IL-dosed cochlear fibrocyte S-FTIR.....	255
Figure 128: PCA scatter plots of the high wavenumber region of 0ng/mL and 10ng/mL IL-dosed cochlear fibrocyte S-FTIR.....	255
Figure 129: Confidence tables from 50:50 train to test neural network model showing predicted condition as a proportion of actual condition. ....	257
Figure 130: Confidence tables from 70:30 train to test neural network model showing predicted condition as a proportion of actual condition. ....	258
Figure 131: Confidence table from dosed vs undosed neural network trial. ....	259
Figure 132: FS heat maps demonstrating compound visualisation across $\text{H}_3\text{O}^+$ and $\text{NO}^+$ conditions for cellular samples. ....	273
Figure 133: Full scan mode $\text{H}_3\text{O}^+$ data for cell culture media and cochlear fibrocyte samples. ....	274
Figure 134: MUI $\text{H}_3\text{O}^+$ data demonstrating statistically significant compound differences between cell culture media and cochlear fibrocyte samples. PPB = parts per billion. ....	275
Figure 135: FS heat maps demonstrating compound visualisation across $\text{H}_3\text{O}^+$ and $\text{NO}^+$ conditions for TNF-dosed cellular samples. ....	276
Figure 136: SIFT-MS MUI $\text{H}_3\text{O}^+$ data demonstrating significant differences across acetaldehyde levels in TNF-dosed cochlear fibrocytes. PPB = parts per billion. ....	277
Figure 137: SIFT-MS MUI $\text{H}_3\text{O}^+$ data demonstrating significant differences across pyruvic acid levels in TNF-dosed cochlear fibrocytes. PPB = parts per billion. ....	278
Figure 138: FS heat maps demonstrating compound visualisation across $\text{H}_3\text{O}^+$ and $\text{NO}^+$ conditions for IL-dosed cellular samples. ....	279

Figure 139: SIFT-MS MUI $\text{H}_3\text{O}^+$ data demonstrating significant differences across acetaldehyde levels in IL-dosed cochlear fibrocytes. PPB = parts per billion. ....	279
Figure 140: SIFT-MS MUI $\text{H}_3\text{O}^+$ data demonstrating significant differences across pyruvic acid levels in IL-dosed cochlear fibrocytes. PPB = parts per billion. ....	280
Figure 141: Average Raman spectrum of human cerumen samples from patients. ....	281
Figure 142: Raw ATR-FTIR spectra of human cerumen samples in dry and processed states. ....	282
Figure 143: Average ATR-FTIR spectra of human cerumen samples. ....	283
Figure 144: FS heat maps demonstrating compound visualisation across $\text{H}_3\text{O}^+$ and $\text{NO}^+$ conditions for human cerumen samples. ....	284

# List of Tables

---

Table 1: Comparison of Raman Spectroscopy and FTIR Spectroscopy (adapted from Kendall et al. (2009)).....	21
Table 2: Reaction mechanics of common SIFT-MS precursor ions. ....	32
Table 3: Raman band assignments.....	44
Table 4: ATR-FTIR band assignments.....	51
Table 5: Table of percentage viability for each potential SIFT-MS vessel. ....	54
Table 6: Fluorescence markers of cochlear fibrocytes (Adapted from Furness, 2019) .....	62
Table 7: Cytokines of interest in inflammation investigations (Adapted from Michaud <i>et al.</i> , 2013) ..	63
Table 8: Chemical maps, wavenumbers and localisations of molecules in the fingerprint region of a single undosed cochlear fibrocyte spectrum analysed by hyperspectral Raman spectroscopy. ....	171
Table 9: Chemical maps, wavenumbers and localisations of molecules in the high wavenumber region of a single undosed cochlear fibrocyte spectrum analysed by hyperspectral Raman spectroscopy.....	177
Table 10: Chemical maps, wavenumbers and localisations of molecules in the fingerprint region of a pair of undosed cochlear fibrocytes' spectrum analysed by hyperspectral Raman spectroscopy. .	186
Table 11: Chemical maps, wavenumbers and localisations of molecules in the high wavenumber region of a pair of undosed cochlear fibrocytes' spectrum analysed by hyperspectral Raman spectroscopy.....	191
Table 12: Chemical maps, wavenumbers and localisations of molecules in the fingerprint region of a pair of 10ng/mL dosed cochlear fibrocytes' spectrum analysed by hyperspectral Raman spectroscopy.....	201
Table 13: Chemical maps, wavenumbers and localisations of molecules in the high wavenumber region of a pair of 10ng/mL dosed cochlear fibrocytes' spectrum analysed by hyperspectral Raman spectroscopy.....	207
Table 14: Chemical maps, wavenumbers and localisations of molecules in the fingerprint region of granulated 10ng/mL dosed cochlear fibrocytes' spectrum analysed by hyperspectral Raman spectroscopy.....	216

Table 15: Chemical maps, wavenumbers and localisations of molecules in the high wavenumber region of granulated 10ng/mL dosed cochlear fibrocytes' spectrum analysed by hyperspectral Raman spectroscopy. ....	222
Table 16: Summary of Raman Spectral Changes in Cochlear Fibrocytes in Response to IL-1 $\beta$ Stimulation .....	228
Table 17: Confidence tables for 50:50 neural network modelling of low, high and mixed cell seeding densities.....	232
Table 18: Confidence tables for 70:30 neural network modelling of low, high and mixed cell seeding densities.....	232

# Abstract

---

Age-related hearing loss (ARHL) is the third most prevalent degenerative condition in the elderly, with cochlear fibrocyte inflammation preceding sensory cell loss. A deeper understanding of inflammatory mechanisms is essential for developing regenerative therapies.

In a novel multi-modal investigation, this study utilised Raman spectroscopy, FTIR spectroscopy (ATR-FTIR and Synchrotron S-FTIR), and SIFT-MS to analyse primary cochlear fibrocytes, their supernatant (culture media from cells), and headspace (culture vessel gas). Fibrocytes were stimulated with TNF- $\alpha$  and IL-1 $\beta$  (1–50 ng/mL) to assess dose-dependent inflammatory responses. Human cerumen was preliminarily examined for diagnostic potential.

Raman spectroscopy revealed inflammation-associated biochemical changes, including CoA depletion (927  $\text{cm}^{-1}$ , 950  $\text{cm}^{-1}$ ), lipid accumulation (1447  $\text{cm}^{-1}$ ), oxidative stress markers (962  $\text{cm}^{-1}$ ) and disrupted protein/lipid membrane assemblies (1658  $\text{cm}^{-1}$ ). S-FTIR further revealed alterations in proteins (1527  $\text{cm}^{-1}$ , 2800–3100  $\text{cm}^{-1}$ ), lipids (2800–3100  $\text{cm}^{-1}$ ), nucleic acids (<1100  $\text{cm}^{-1}$ , 1115–1130  $\text{cm}^{-1}$ ), phospholipids (<1100  $\text{cm}^{-1}$ ), and carbohydrates (<1100  $\text{cm}^{-1}$ ), suggesting membrane structural changes and metabolic dysregulation. S-FTIR data may warrant consideration of a fibrocyte activation state similar to that seen in macrophages. Neural network models classified cytokine dosages with >80% accuracy, reinforcing the diagnostic relevance of these findings.

ATR-FTIR analysis of supernatant identified cytokine-driven disruptions in protein secondary structure (amide I: ~1650  $\text{cm}^{-1}$ ) and lipid composition (~1740  $\text{cm}^{-1}$ ), indicative of metabolic dysregulation. Proposed histidine-related spectral variations in supernatant and headspace suggest cytokine-induced alterations in amino acid metabolism. SIFT-MS headspace data, through changes seen in acetaldehyde and pyruvate, support a hypothesis of citric acid cycle disruption in inflamed fibrocytes.

Overall, this research advances understanding of cochlear inflammation in ARHL. Raman and S-FTIR facilitated detailed cellular examination while ATR-FTIR provided critical insights into supernatant composition – potentially translatable to cochlear fluid analyses. Cerumen

demonstrated preliminary promise as a diagnostic biofluid. With further refinement, these findings could contribute to future ARHL detection and monitoring strategies.



# 1. Introduction

---

## 1.1. Motivations for the Study

As one of the three most seen degenerative conditions affecting the elderly, age related hearing loss (ARHL, also known as presbycusis) affects around a third of people over 65 and over half of all people over the age of 75 <sup>[1-5]</sup>. This gradually worsening hearing loss stems from damage or death of sensory and support cells within auditory circuitry and is not only debilitating but leads to additional social and cognitive impairments in patients <sup>[1,6-10]</sup>. As such, it is vital that detection and intervention in this condition occur in as accurate and expedient manner as possible- something which is of limited possibility with current time-intensive testing methods.

With a focus on the potential for early, quick, and patient-friendly detection of and intervention in age related hearing loss (ARHL), the primary purpose of this research is to highlight the diagnostic potential of spiral ligament fibrocytes- a largely under-investigated support cell type in hearing loss research, and to introduce a method by which this potential may be employed. Paired with non-invasive techniques such as selected ion flow tube mass spectrometry (SIFT-MS), which allow detection of trace levels of compounds in samples, and the employment of biofluid sampling, it is possible that fibrocyte degeneration may be detected early enough to allow intervention before hearing loss occurs to any great severity.

Such techniques may also be employed in the application of regenerative therapies (see section 1.6.3), enabling non-invasive monitoring of cultured cells for markers of health. Such monitoring facilitates the assessment of cultures for clinical suitability without the necessity for intervention or disruption beyond sampling of headspace and supernatant, potentially via automated means.

## 1.2. Introduction to Hearing Loss

Though the present research focuses on ARHL, it may be argued that the data gathered is relevant to hearing loss (HL) research as a whole, with advances in the facilitation of ARHL therapies potentially applicable to other hearing loss types. This is of great interest as, in general terms, HL

affects around five-hundred million people worldwide <sup>[11]</sup> and is the leading cause of years lived with disability in the UK <sup>[12]</sup>.

Hearing loss can occur at any age and originate from a range of pathologies affecting all points of the auditory system from outer to inner ear. It is commonly believed that there are two general types of hearing loss- with loss stemming from cochlear pathologies known as sensorineural hearing loss, and hearing loss caused by mechanical impairment to sound transmission known as conductive hearing loss <sup>[11,13]</sup>.

In general, conductive hearing loss types may originate in the external ear (pinna) and auditory canal, where issues which may affect hearing ability include impaction of cerumen, obstruction of the ear canal, abnormality of the ear canal, and otitis externa <sup>[14]</sup>. Treated via cerumen removal, surgical intervention, foreign body removal and antimicrobial/anti-inflammatory medication respectively, these conditions do not typically affect hearing long-term. However, where otitis infections are concerned, recurrence may lead to further complications.

Moving inwards, the tympanic membrane is often subject to issues which affect hearing capabilities. Typically, this is perforation, often stemming from manual ear trauma such as impacts to the head. Perforation of the eardrum can also occur via barotrauma (i.e. pressure shock) and frequent infection. Perforation risk may be increased by use of cotton buds in ear cleaning, as users often probe too deeply into the ear canal <sup>[15]</sup>. Use of cotton buds in this manner may also increase risk of infection, as highlighted in one case wherein a patient was found to have necrotising otitis externa due to the retention of part of a cotton bud in the ear canal <sup>[16]</sup>. Usually, perforations of the eardrum are able to heal naturally. Those that do not may require surgical intervention, with antibiotics often administered to treat existing or arising infections.

In the middle ear, conditions which affect hearing become more difficult to treat, with anatomical components less easily accessible. Still considered to be conductive hearing loss, issues which may affect the middle ear include disruption of the ossicular chain, otosclerosis and otitis media, typically managed using surgical interventions and antibiotic treatment respectively <sup>[13]</sup>.

The inner ear is where the more fine-tuned components of hearing occur and is the region responsible for around 90% of hearing loss cases. The main sensory organ of the auditory pathway, the cochlea, resides in the inner ear and contains the sensory, nerve and support cells necessary for signal transduction. The cochlea is composed of three fluid-filled compartments which enable the necessary ion gradient for depolarisation. To simplify an intricate process, upon the input of sound, vibrations from the oval membrane are transmitted to the fluids contained within these chambers, causing vibration of the basilar membrane. Upon this membrane, cochlear hair cells on the organ of Corti detect motion via deflection of stereocilia (small hair-like projections) (Fig. 1). There are two types of hair cell, outer hair cells (OHCs) and inner hair cells (IHCs) which amplify signals and transduce signals to the auditory nerve respectively. This deflection of stereocilia opens mechanoelectrical transducer (MET) channels, allowing conversion and transduction of signals to auditory spiral ganglion neurons (SGNs) <sup>[132]</sup>.

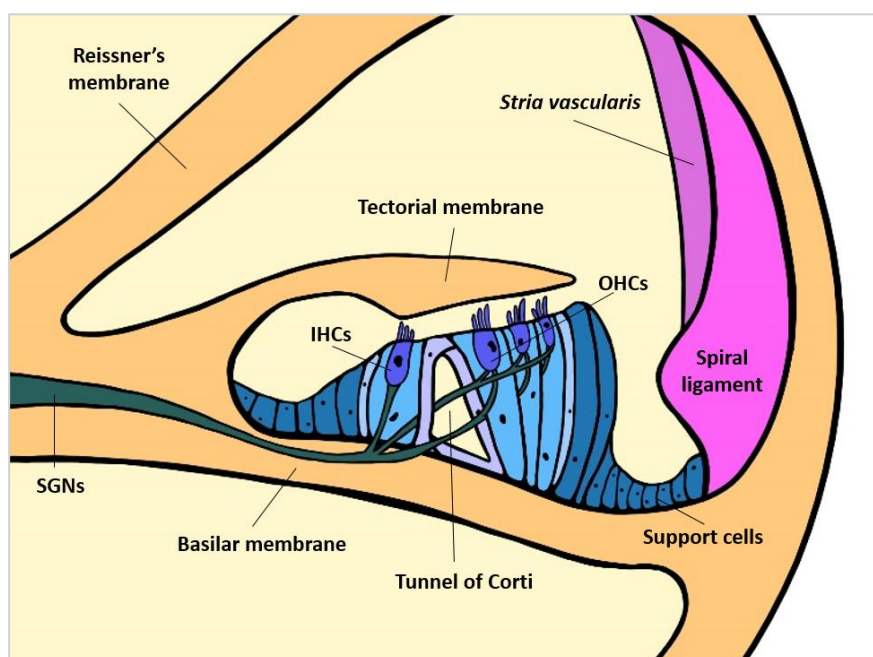


**Figure 1: The Organ of Corti and lateral wall.**

**A simple diagram highlighting the main components of the cochlea which contribute to auditory transduction. The Organ of Corti, consisting of hair cells and support cells, is indicated in blue. The lateral wall (LW), consisting of the stria vascularis and spiral ligament, is indicated in pink. (SGNs= Spiral ganglion neurones).**

Inner ear conditions, often sweepingly referred to as sensorineural hearing losses, are the most difficult to treat due to location and the delicate fluid and cell system of the cochlea. Inner ear-based

hearing losses typically stem from degradation of cells within the cochlea, whether this be hair cells, SGNs or support cells such as cochlear fibrocytes. Such degradation may be due to a range of factors including ageing, noise exposure, ototoxic drugs, and disease.

## 1.3. Age Related Hearing Loss – Condition and Diagnosis

### 1.3.1. Introduction to ARHL

As with most bodily functions, human hearing capabilities tend to decline with age. Alongside other sensory issues including visual deterioration and loss of balance, reductions in auditory acuity are unfortunately an inevitability of the ageing process, with age related hearing loss (ARHL, also known as presbycusis) noted as one of the three most seen degenerative conditions affecting the elderly [2,4,5]. As early as the 1990s, ARHL was identified as the third most common condition seen in the elderly, with arthritis and heart disease leading [17]. In fact, ARHL affects around a third of people over 65 and over half of all people over the age of 75, with a 2011 statistic presented via the WHO suggesting that 299million men and 239million women worldwide experience hearing loss [1,3].

Typically, ARHL arises between the ages of 55 and 65, beginning in high frequency hearing loss and progressing to more severe bilateral hearing loss with time, worsening as patients age [1,7,9]. Generally, this hearing loss stems from damage or death of sensory and support cells within auditory circuitry, though other contributory factors beyond the inner ear are noted. Such factors include arthritis of the ossicular chain, tympanic membrane stiffening and muscular degeneration [18].

Sensory losses like ARHL are not only physically debilitating to those who experience them, but lead to additional social and cognitive difficulties, with depression and isolation common among sufferers [6,8,10]. Additionally, hearing impairment in older patients is known to contribute to falls, apparent frailty, and is noted to even exacerbate dementia and cognitive decline [19-21,26].

In examination of ARHL, symptoms are classified into four sub-types based upon primary area of damage [1,9,22,23]. Though distinct in precise pathologies, ARHL can present with mixed phenotypes adding further difficulty to diagnosis and treatment. The types of ARHL, originally noted by Schuknecht

via temporal bone studies <sup>[24,25]</sup>, are sensory, neural, strial (metabolic), and cochlear conductive, with sensory and neural ARHL often combined under the title of sensorineural ARHL.

To briefly introduce the types- sensory ARHL occurs via the death of hair cells. Neural ARHL, as its name suggests, stems from damage to spiral ganglion neurones. Cochlear conductive ARHL is the result of alterations in the mechanical properties and conductive characteristics of the inner ear, not damage to a particular cells type. Finally, metabolic ARHL occurs via strial atrophy (implying the death of cochlear fibrocytes and strial cells) and the resultant shutdown of the EP <sup>[23-25]</sup>. Of these, metabolic ARHL is known to be the most prevalent and, by extension, is arguably the most clinically significant category of ARHL <sup>[23]</sup>.

### 1.3.2. The ARHL Diagnosis Process

Where diagnosis of ARHL is concerned, examination occurrence is heavily reliant upon patients being aware of and acknowledging their condition. If patients do not realise that they are experiencing reduced hearing capability, or are experiencing denial, they are unlikely to seek diagnosis and treatment without encouragement from family, friends, or clinicians. Research suggests that, without report from patients themselves, even clinicians may fail to notice the signs of age-related hearing loss in its early stages as it relies upon patient reports <sup>[13]</sup>. This regularly leads to late intervention and under-treatment, particularly in more severe cases where patients are highly aware of their issues yet are unwilling to seek treatment due to social stigma. It is, thus, not unfounded to suggest that alternative methods of hearing loss assessment, that do not lead to apprehension regarding complexity and social stigma, should be investigated.

Typically, once patients decide to attend a hearing test appointment, diagnosis of ARHL can be made by an audiologist (however, metabolic ARHL is often overlooked due to difficulty in detection, with sensorineural sub-types far more apparent during diagnosis <sup>[22]</sup>). Appointments typically begin with evaluation of patient medical history and conversation regarding auditory symptoms. Often, family or friends will accompany patients to provide assistance and support, and to weigh in on symptom evaluation by providing an external perspective of the patient's hearing issues. Symptoms

such as noise sensitivity, tinnitus, and vertigo may also be discussed as these are often indicators of hearing loss of some kind <sup>[27,28]</sup>. A particular notable feature of ARHL is a gradual loss of hearing, beginning particularly in high frequencies, with particular difficulty in discriminating speech from background noise <sup>[13]</sup>. In addition to auditory and balance-related symptoms, clinicians also aim to be aware of additional medical conditions which may experience comorbidity with hearing loss, such as diabetes mellitus, depression, and dementia <sup>[29-32]</sup>.

Following initial evaluation of patient history and discussion of symptoms, physical examination typically occurs, with general inspection of patient health and a focus on the ear (usually via otoscope). Typically, the ear is examined for abnormalities including ear wax (cerumen) impaction, signs of otitis media, retraction of or damage to the tympanic membrane, immobility in tympanic membrane, obstructions to the ear canal, inflammation, and visible injuries to the ear canal. Often, external auditory anatomy will appear normal in ARHL cases, as issues typically arise from inner ear degradation <sup>[13]</sup>. General patient examination beyond the ear focuses on detection of symptoms such as face and neck weakness, numbness, and stiffness, fever, nystagmus (involuntary eye movement), head and neck injuries, and hematoma <sup>[33]</sup>.

Where hearing loss of any kind is suspected and physical symptoms alone are not sufficient for diagnosis, pure tone audiometry testing is required to investigate further <sup>[28,34]</sup>. This method assigns severity of hearing loss by examination of the volume at which pure tones are detectable by the patient <sup>[13]</sup>. This is typically a referral process, wherein patients are sent to a specialist to undergo testing.

Based upon these parameters, diagnosis of ARHL may be made and intervention recommended. In recent years, advancements have been made in the distinction of metabolic and sensory components of ARHL via audiograms, though these methods do not appear to have been employed clinically to date <sup>[35]</sup>. Laboratory evaluation including imaging may also be conducted, but this is generally not required where ARHL is suspected <sup>[28]</sup>. Such investigations are primarily used in characterisation of cases such as asymmetrical hearing loss and sudden hearing loss <sup>[36]</sup>. Generally, even before referrals to specialists, the diagnosis process for hearing losses is time consuming and often off-putting to patients. Additionally, as mentioned, metabolic hearing loss is difficult to diagnose

and distinguish in comparison with sensorineural sub-types. Ideally, a faster, more routine approach to diagnosis, able to detect and distinguish hearing loss sub-types, should be developed.

## 1.4. Metabolic ARHL

### 1.4.1. Fibrocytes, Potassium Recycling, and the Endocochlear Potential

Though hair cells are arguably the main component of the cochlea, converting mechanical signals to electrical signals, they are primarily responsible for only one type of ARHL (sensory). An under-recognised subtype of arguably equal/greater prevalence metabolic ARHL, stems instead in part from damage to fibrocytes which aid in the regulation ion concentrations of cochlear fluids. As mentioned in section 1.2, the cochlea is divided into three fluid filled compartments. These compartments are the upper *scala vestibuli*, central *scala media* and lower *scala tympani*<sup>[1,131]</sup> (Fig. 2). The *scala tympani* and *scala vestibuli* are filled with perilymph, a fluid high in sodium and low in potassium. The *scala media*, contrastingly, contains high potassium and low sodium endolymph<sup>[1,37]</sup>. The fluid variations across the cochlear chambers allow generation and maintenance of the endocochlear potential (EP), an 80-90mV homeostatic trans-epithelial potential in the *scala media*<sup>[38]</sup>.

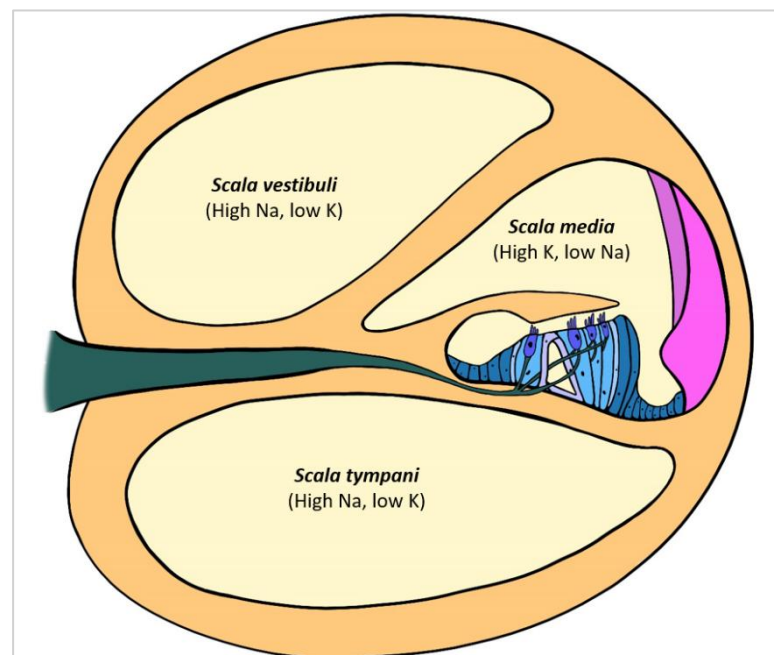


Figure 2: Cross-section of the cochlea.

A simple diagram indicating the three fluid chambers of the cochlea. High Na, low K denotes perilymph. High K, low Na denotes endolymph.

The endocochlear potential acts as a biological battery, maintaining homeostasis via secretion and recycling of potassium ions by support cells known as cochlear fibrocytes <sup>[39-42]</sup>. This function occurs via diffusion of potassium from the *scala media* via one of two routes (intracellular or extracellular) into the *stria vascularis* and back to the *scala media* via the spiral ligament, where fibrocytes reside. These fundamental support cells, surrounded by connective tissue and perilymph, contain cell junctions, ATPases, connexins, and channels necessary to perform potassium recycling <sup>[40,42,43]</sup>. Research additionally demonstrates structural specialisation of fibrocytes, with high mitochondrial density and numerous potassium channels indicative of their ion recycling function <sup>[44,45]</sup>.

Without the presence of fibrocytes, specialised for the role of potassium recycling, the recirculation of potassium into the *scala media* would not take place. Thus, generation of the endocochlear potential would not be properly maintained, preventing depolarisation and removal of potassium from the organ of Corti. Without such removal, cochlear hair cells are susceptible to potassium toxicity, which leads to cell damage and death and, subsequently, loss of auditory function <sup>[37]</sup>. As such, deterioration in metabolic ARHL is primarily attributed to damage to these fibrocytes. This vital function is well discussed in the highly comprehensive review by Furness <sup>[46]</sup>, who focused on fibrocytes to explore their properties and roles in great detail.

### 1.4.2. Cochlear Fibrocyte Pathology

As mentioned above, fibrocyte degeneration is one of the primary forms of damage in ARHL, particularly in the metabolic subtype and mixed subtypes. Studies have shown, that fibrocyte degeneration in HL cases generally occurs before degeneration of other cells (i.e. hair cells, neurones) with both types of damage contributing to the loss of hearing function <sup>[47,48]</sup>. Cochlear fibrocyte degradation, as such, may be taken as a precursor for further damage, making it the ideal indicator of metabolic ARHL in its early stages. From this, a breadth of treatment options may be made available to counteract fibrocyte, general spiral ligament, and *stria vascularis* damage (see section 1.6).

Furthermore, in addition to preceding downstream cell losses, fibrocyte damage may be contributory to further degeneration in the rest of the cochlea. Certainly, it is not beyond the realm of

possibility that the alterations in cochlear fluid composition caused by fibrocyte degradation would negatively affect the functions of hair and neural cells to the point of hearing loss. However, though research into fibrocyte damage often hints to this effect, researchers cannot confidently assign a causal link. This is due to the unfortunate lack of consensus regarding the mode of fibrocyte degeneration and its effect on other cochlear cells downstream. In literature, fibrocyte loss is typically attributed to factors known to arise/worsen with age, such as mitochondrial dysfunction, ROS (reactive oxygen species) accumulation, and general inflammation, though specific mechanisms of degradation within cells and how these affect functional properties are not well understood [4,5,48-52]. As such, cochlear fibrocytes are an ideal target for investigations into pathological mechanisms such as those conducted in this research.

## 1.5. Inflammation and the Cochlea

### 1.5.1. Inflammaging

The term inflammaging refers to the chronic low-grade inflammation often seen in age-related diseases [53]. ARHL is one such disease, wherein the lateral wall of the cochlea, home to the spiral ligament, is known to be a typical site of inflammation [54] with proximity to the fluid-blood barrier enabling signals to be met with the release of pro-inflammatory cytokines in the *stria vascularis*. As such, the pathology of ARHL has often been linked to the inflammaging process [1,5,55-57].

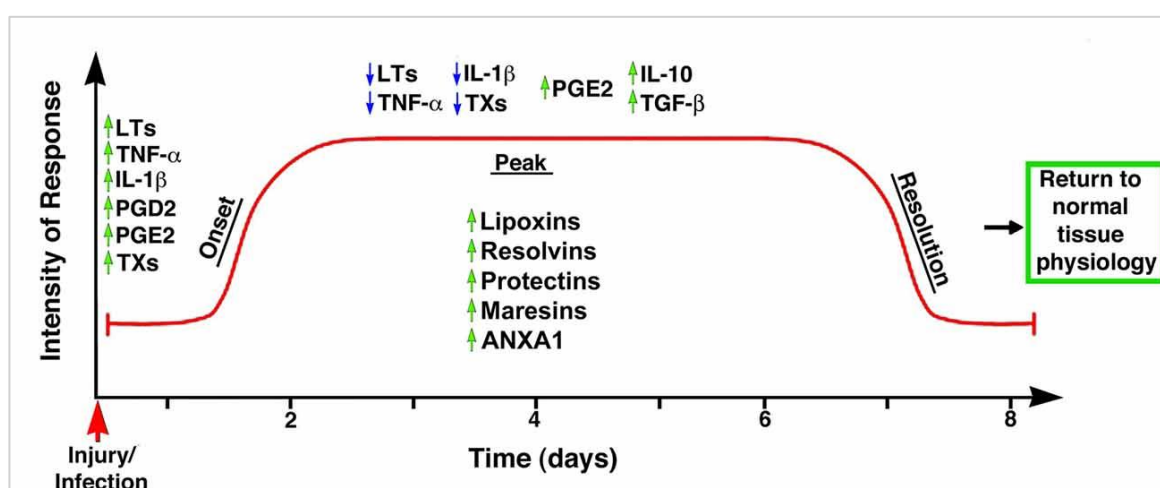


Figure 3: General intensity over time of the biochemical events associated with the onset and resolution of inflammation.

(From Kalnec *et al.*, 2017, Modified from Maderna and Godson, 2009.)

There are several hypotheses for the exact pathways of inflammaging, but research predominantly suggests two causes: pro-inflammatory protein build-up <sup>[57]</sup> and cell debris accumulation <sup>[53]</sup>. The suggested pathology of inflammatory build-up appears to be a simple one, in that rather than a return to normal pathology following inflammation (Fig. 3), the inflammatory state persists at a low level, gradually building over time. The cellular debris hypothesis is similarly simple in general theory, with poor clearance of cell waste resulting in the production of a continuous immune response and inflammatory state. Arguably, the pro-inflammatory protein build-up pathology is the more logical target of *in vitro* studies, as it may be better controlled than cellular debris clearance. The pro-inflammatory protein pathology is explored in this research due to the capacity for better controls than the cellular debris option.

### 1.5.2. Inflammation, Mitochondrial Dysfunction, and ARHL

Considering relevance to ARHL, as outlined in section 1.4.2 metabolic ARHL is becoming recognised as likely the most prevalent form of the condition, with fibrocyte damage and resultant reduction in endocochlear potential (enabling hair cell depolarisation) often preceding further damage <sup>[9,23,46-48,58]</sup>. As above, the cause of cochlear fibrocyte damage and general atrophy of the cochlear lateral wall is believed to be primarily caused by factors exacerbated with age such as inflammation, accumulation of reactive oxygen species, and mitochondrial dysfunction <sup>[4,5,48,49,51,52]</sup>.

In 2022, Seicol *et al.* <sup>[59]</sup> highlighted the presence of low-grade inflammation in animal models and deceased human subjects with early onset ARHL. Through their investigation, it is suggested that this inflammation is perpetuated through macrophage activation/accumulation and upregulation of pro-inflammatory signals. However, this research does not address cochlear fibrocytes or the tissues of the lateral wall thus, despite the presence of resident macrophages within the lateral wall that may behave similarly <sup>[60]</sup>, this pathology is not confirmed in the present context.

Considering mitochondrial damage, another of the highlighted pathologies in inflammaging and cochlear degeneration, the recent research by Miwa *et al.* <sup>[50]</sup> is of interest. In this research, a gradual dysfunction of respiratory complexes in cochlear fibrocytes with age was noted. Such dysfunction was shown to yield mitochondrial changes, cell senescence and EP reduction, leading to downstream

damage to sensory cells and neurons. Though this study, unlike the present research, focuses on the use of knockout mice, the results linking the accumulation of dysfunctional mitochondria in cochlear fibrocytes to the onset of ARHL are of undeniable relevance to the present research.

## 1.6. Treatment of ARHL

### 1.6.1. Existing ARHL Treatments

Though ARHL is a well-recognised and prevalent issue, there are relatively few treatments available for sufferers. Those who develop age related hearing loss are typically left with one option- hearing aids. Hearing aids are known to be effective in improving quality of life and auditory function in hearing loss sufferers, with improvements most apparent in speech recognition and prolonging good cognitive function <sup>[61]</sup>. Information such as this, outside the general device functionality of hearing aids, often arises from self-reports as testing using objective metrics such as the hearing aid speech perception and quality indexes (HASPI and HASQI) is relatively rare <sup>[62-64]</sup>. Though beneficial to patients on a fundamental level, hearing aids cannot recover the fine tuning of natural hearing and do not provide continued functional improvement as hearing loss progresses. Additionally, hearing aids lack the capacity to function completely independently, requiring tuning and maintenance (such as battery changes) which may prove difficult for ageing patients <sup>[65]</sup>. Such issues with use easily occur in elderly patients, despite training on the use of hearing aids and rehabilitative measures offered by practitioners <sup>[33]</sup>.

Though hearing aids are seemingly common among the elderly, usage rate is fairly low, with the administration of hearing aids to ARHL patients is often delayed by perceived lack of need, lack of prescription and high cost, leaving many hearing loss sufferers without relief <sup>[66]</sup>. In a longitudinal cohort study, <sup>[67]</sup> identified an average delay of 8.9 years between hearing aid candidacy (i.e. when a hearing aid may be required/of benefit) and hearing aid adoption. It would seem that many patients often refuse to acknowledge their auditory decline, or patients fail to notice hearing losses in the early stages of ARHL, as high frequency sounds are uncommon in everyday situations. Additionally, other factors may be at play including whether patients are able to see the mouths of conversation partners and adaptation of family and friends (i.e. speaking louder). In this manner, recognition and subsequent

treatment of ARHL may be delayed until greater hearing losses or declines in visual acuity occur. Within this time, hearing capability, cognitive function, and physical faculties are likely to decline, making eventual hearing aid adoption more difficult a task.

Generally, it would seem that elderly patients dislike hearing aids, with studies reporting complaints of feedback (e.g. whistling), the occlusion effect (wherein patients perceive distortions in their own voices) and general disturbances in sound processing <sup>[68]</sup>. Even when in possession of hearing aids, it would seem that elderly patients are reluctant to use them due to lack of comfort, difficulties with use, and social stigma <sup>[69]</sup>. Such stigmatization is often exacerbated by media representation of the elderly, with deafness associated with accelerated age and frailty that many patients do not wish to acknowledge <sup>[70]</sup>. Thus, denial of ageing frequently leads to denial of hearing loss and under-use of the therapeutic device, despite the improved quality of life that such use typically provides <sup>[71,72]</sup>.

Additionally, hearing aids, when administered, require a period of adjustment for patients to acclimatise to the new device, with greater cognitive processing than usual required during this time <sup>[73]</sup>. Coupled with the cognitive decline often associated with ARHL and ageing in general, the increased cognitive strain of hearing aid adjustment, as well as the necessity for regular tuning, renders hearing aids unsustainable in the treatment of an ageing population of ARHL patients <sup>[74]</sup>.

In more severe ARHL cases, where there is insufficient auditory function remaining for hearing aid use, or where patients experience poor word understanding with hearing aids, cochlear implants (CI) may be considered as a therapy for ARHL <sup>[75]</sup>. These are offered as an alternative when hearing aids no longer serve to provide distinction between speech and background noise <sup>[76]</sup>. CIs are surgically implanted and essentially replace the function of the cochlea, stimulating the spiral ganglion directly. An external component of the implants transduces sound signals in a similar way to that in which the cochlea performs this function, with auditory input converted to electrical signals which can be interpreted by the brain as sound. Such intervention appears to demonstrate success in older patients, increasing hearing capabilities and quality of life similarly to that seen in younger hearing loss sufferers <sup>[77,78]</sup>.

This is not to say, however, that cochlear implants are a faultless replacement for organic cochleae. In fact, such implants are not nearly well-developed enough to replicate the delicate fine tuning of the cochlea, thus auditory experiences of patients are often comparably inferior to those relying upon the natural cochlea. As such, for patients who have previously had no issue in hearing, cochlear implants are difficult to adjust to and provide little satisfaction, with greater successes seen in patients who have experienced deafness from birth or early childhood. In age related hearing loss cases, the additional facet of surgical complications must be considered, with ageing patients less likely to successfully undergo surgery without issue. Above the ages of 55, patients are at higher risk of infection, poor healing and even death.

With the faults of these treatments considered, it is undeniable that better alternatives should be strived for in research. Such interventions should be effective in restoration of hearing function with little requirement for maintenance. Ideally, these interventions would prevent or delay further decline of hearing capabilities. From these criteria, it is logical that early intervention in the form of cell-focused treatments should be investigated thoroughly.

### 1.6.2. Intervention Strategies Using Fibrocyte Manipulation

At present, no cure exists for ARHL. However, in the search for a starting point for such a cure (or at least for a more effective treatment than hearing aids/cochlear implants), the potential of a focus on fibrocytes must be considered. Due to the tendency of fibrocyte death to precede further cell death in ARHL, it is prudent to consider interventions focusing on this cell type a suitable starting point.

In terms of treatment, focusing on therapies for the lateral wall wherever possible is ideal, as its accessibility and relative toughness allow it to better withstand procedures than, for instance, the organ of Corti, which is far more easily damaged. Where such fibrocyte-based interventions are concerned, there are three main paths which may be taken: stimulation of repair, manipulation of fibrocyte physiology to prolong cell functions, and cell replacement therapies. It is important to note while considering such treatment paths, that the size and inaccessibility of the inner ear still pose issues in treatment provision and often dictate the nature of treatment that may be considered alongside patient factors such as age.

Concerning stimulation of regeneration, it is known that fibrocytes possess an innate capacity for proliferation due to their mesenchymal nature <sup>[79-81]</sup>. However, the nature of metabolic ARHL, in that hearing loss is progressive, highlights that this regenerative capacity is not sufficient to maintain the lateral wall (LW) without intervention.

However, application of treatments to the LW may have the potential to prolong the health of remaining cells and potentially prevent further death. Though focused on the inflammatory response seen following acute otitis media infection rather than ARHL, research by Moriyama *et al.* <sup>[82]</sup> noted that increased nitric oxide (NO) production plays a role in inflammatory cochlear pathology (suggested to be a contributing factor in metabolic ARHL <sup>[4,5,48,49,51,52]</sup>), and proposed application of corticosteroids as a potential solution. Using cultured murine spiral ligament fibrocytes (predominantly of type I), the research team found that TNF- $\alpha$ -induced production of NO could be significantly inhibited by dexamethasone (a clinically popular corticosteroid). From this, it is possible that application of corticosteroids, or other similarly acting drugs, in suitable dosages may limit the inflammation seen during metabolic ARHL and prolong the life and function of spiral ligament fibrocytes.

Additionally of interest in combating symptoms arising from inflammation is the application of anti-interleukin-1 therapies. These therapies rely on the application of antibodies against IL-1 (typically IL-1 $\beta$ ) such as Akinara, Rilonacept, and Canakinumab (Fig. 4) <sup>[83]</sup>. These antibodies work to prevent signal transduction of IL-1 $\beta$  and its receptors, alleviating downstream inflammatory effects. In the context of hearing loss, it is known that some HL forms can be improved through the application of these therapies <sup>[84]</sup>, though this does not appear to have been trialled to date in the context of ARHL and it is noted that younger patients tend to respond better to treatment of this kind. It is also valuable to note, particularly where elderly patients are concerned, that the application of anti-interleukin-1 therapies

may lead to lower cell density in the spiral ganglion <sup>[85]</sup>. With this in mind, the necessity for certainty in diagnosis and the development of additional treatment methods is made even clearer.

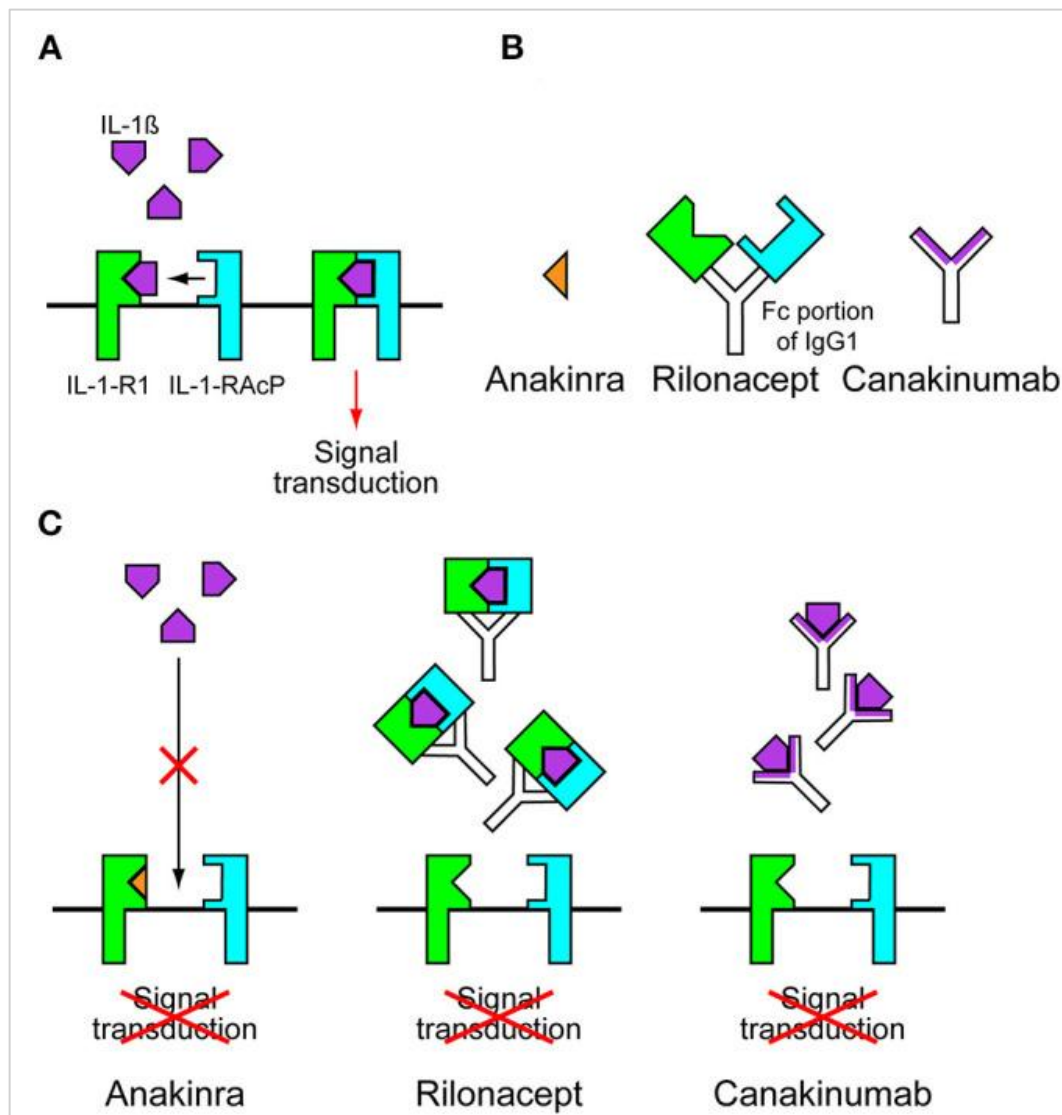


**Figure 4: Anti-interleukin-1 therapeutic agents and their modes of action.**

**A) Typical mode of IL-1 $\beta$  signal transduction. B) Therapeutic agents and their structures. C) Anakinra acts as a competitive inhibitor to IL-1 $\beta$  in binding to IL-1-R1. Rilonacept and Canakinumab bind IL-1 $\beta$  to prevent signal transduction (from Nakanashi *et al.*, 2022).**

Alteration of fibrocytes via methods such as genetic engineering is a further viable option in enhancing growth of fibrocytes *in vivo*. Genetic modification may focus on triggering the upregulation of growth factors to enhance cell growth and maintenance. In particular, insulin-like growth factor (IGF-1), which is involved in inner ear development, is known to improve survival of hair cells and is being investigated as a therapeutic agent for hearing loss in clinical trials <sup>[86]</sup>. These may be added to

the spiral ligament directly or, where cell replacement is concerned, cochlear fibrocytes may be genetically engineered to express these factors to maintain the LW as well as other cochlear cell types [87,88]. Though, it should be noted that the genetic engineering process is substantially more complex and time consuming than direct application of growth factors to the cochlea which may be preferred for ease.

### 1.6.3. Fibrocytes and cell replacement therapies

An additional therapy to counteract the effects of fibrocyte damage in metabolic ARHL is cell replacement. Ideally, autologous spiral ligament fibrocytes could be extracted, cultured *in vitro*, and re-implanted in greater numbers than harvested. However, this is largely unfeasible due to difficulties in extracting autologous fibrocytes without cochlear damage and does not appear to have been trialled to date. However, where non-autologous cochlear fibrocytes are concerned, replacement is possible as cochlear fibrocytes (due to their regenerative capacity) can be cultured *in vitro* when healthy, allowing scale up of small cultures for potential cell replacement [89,90].

One criticism of cochlear fibrocyte implantation is that, when cultured *in vitro*, it appears that it is rare for all sub-types of fibrocytes to be seen (with labelling often indicating type III fibrocytes as most common), thus threatening to leave areas of the spiral ligament essentially unfilled upon replacement if all subtypes are not present. Additionally, where re-implantation of fibrocytes is concerned, it is known that activated fibrocytes (cells expressing pro-inflammatory cytokines) encourage the persistence of inflammation in the spiral ligament [91]. Thus, re-implanted cells may be subject to the same inflammation as native tissue.

In considering alternative cell types, it is notable that iPSCs have been shown to effectively act as cochlear hair cells when implanted [2]. This regeneration is both morphological and functional, in contrast to MSC-derived hair cells, which have not been shown to functionally replace/regenerate hair cells to date. Use of iPSCs, however, is limited in application to the inner ear, particularly where ARHL patients are concerned. This is due to the high risk of rejection and tumour development noted with iPSC use [250], despite suggested immunomodulatory properties [251].

In contrast to iPSCs, whose applications seem to lie primarily in the recovery and replacement of hair cells <sup>[2]</sup>, MSCs appear to be more suited to the replacement of inner ear cells possessing mesenchymal properties (e.g. cochlear fibrocytes), though they may be suitable for hair cell replacement as well <sup>[252]</sup>. In the interest of the present research this is a desirable feature due to the fibrocyte death which initiates symptomatic metabolic ARHL. Furthermore, where seeking to treat ageing patients, it must be noted that MSCs possess immunomodulatory and anti-inflammatory properties which reduce the risk of rejection and may prove therapeutic to the site of implantation.

A particular benefit of potential MSC use lies in the application of MSCs in anti-inflammatory treatment. The review by Regmi *et al.* <sup>[92]</sup> noted the use of MSCs in this manner, citing several ongoing clinical trials employing MSCs to counteract inflammation. This anti-inflammatory property, alongside the potential of MSCs to differentiate and replicate fibrocytes when implanted <sup>[93, 94]</sup>, would potentially allow replacement of damaged fibrocytes and improvement of the native environment to discourage further damage simultaneously. This is further supported in studies wherein MSCs have been applied with less specificity and have shown evidence of migration to damage inner ear tissues spontaneously <sup>[95]</sup>.

Though MSC implantation in this context has not yet been performed in humans, several research groups have produced promising results in animal models. In perhaps the earliest successful study of its kind, Kamiya *et al.* <sup>[94]</sup> demonstrated the use of murine bone marrow derived MSCs in the improvement of ABR thresholds in treated animals. In this study implanted MSCs differentiated to show fibrocyte-like morphologies and functions *in vivo*, enabling functional recovery. Following transplantation of bone marrow derived mesenchymal stem cells into the lateral semi-circular canal, stem cells were discovered to have migrated to the lateral wall (wherein an injury had been induced via 3NP application). Transplanted stem cells in the lateral wall were shown to express connexin 26 and connexin 30 similarly to native cells, suggesting *in vivo* alterations based upon local environment. The singular query regarding this work in a translational context is that the damage from which animals recovered was chemically induced rather than as a result of natural degradation through the use of an accelerated age model for instance. Nonetheless, if the replacement technique could be refined and translated to humans, it may offer the first step to long-term functional recovery in ARHL.

Almost a decade later, Ma *et al.* <sup>[95]</sup> demonstrated similarly encouraging results in a congenitally deaf guinea pig species. In this study, human umbilical cord MSCs were applied to animals via the subarachnoid cavity, and successfully migrated to the *stria vascularis*, basal membrane and spiral ganglion. Migration was also seen to other bodily tissues such as the heart, brain and liver, but this does not appear to have caused any adverse effects- likely as MSCs are generally considered safe due to their immunomodulatory properties <sup>[96]</sup>. Reviewing the results of this study, ABR testing demonstrated new waveform generation in some treated animals, suggesting auditory function. However, despite the positive outcomes of this research, there is some concern as to the consistency of its effectiveness, with only 3 in 8 treated animals showing improvement. It is clear from this and other studies of the kind that there is still development to be made in cell replacement therapies for the inner ear <sup>[97]</sup>.

More recently still, Kada *et al.* (2020) <sup>[253]</sup> demonstrated via similar methods to Kamiya (3NP damage, semi-circular canal application) the migration of implanted MSCs to the spiral ligament, and the partial recovery of hearing function following implantation in mice. In inspection of repopulated cells, the cellular density in the spiral ligament was shown to be improved, with implanted cells shown to express relevant functional proteins. This is congruent with previous research in the field. Additionally, utilising methods from the group's earlier research <sup>[254]</sup>, this study measured the endocochlear potential both prior to and after MSC implantation, demonstrating its recovery following replacement therapy. Such recovery serves to verify the health of implanted cells and restoration of appropriate function in the spiral ligament facilitated by MSC implantation.

In a human study of MSC transplantation for sensorineural hearing loss, MSCs were verified as safe for use. However, no recovery of hearing function was seen in patients <sup>[255]</sup>. This casts doubt upon the ability to replicate animal study results in humans, though the lack of similar hearing function restoration may be due to several factors beyond species variation. These factors include but are not limited to a distinct difference in cell administration technique between studies. Whereas rodent models were administered cell therapy via semi-circular canal injection, human patients had cells administered via the subclavian line. This, as noted in the study, is unlikely to yield hearing status improvement as delivery directly to the inner ear environment is required in order for cells to bypass

the blood-labyrinth barrier. While local transplantation of cells into the patient cochlea is theoretically possible, this is likely to yield damage to the cochlear and does not yet appear to have been trailed in humans to date.

Though not verified in humans to date, it is undoubtable that, if successful, transplantation of MSCs into the injured inner ear may prove useful in reducing inner ear damage. In metabolic ARHL (the focus of the present research) MSC transplantation is likely to allow regeneration of fibrocytes (due to factors secreted by SLFs promoting transdifferentiation of MSCs) as well as functional recovery aided by the natural anti-inflammatory properties of MSCs <sup>[93]</sup>. Should a viable method by which to apply MSCs to human inner ears be developed, it is undoubtable that they may be of therapeutic benefit, particularly in the treatment of metabolic ARHL. Where this condition is concerned (as well as other hearing loss types wherein cochlear fibrocyte death precedes further damage), it may be reasonably stated that successful cell replacement therapy administered prior to hair cell damage/death may delay or even halt disease progress. However, this is dependent upon timely application, ideally before hair cell loss occurs (i.e. prior to symptomatic damage).

Though there are no clinically available biological interventions for hearing loss or fibrocyte damage currently, evidence from research implies there is growing potential for treatment development. Should such a treatment to repair or replace damaged fibrocytes become available, it is likely that hearing function may be restored as shown in animal-based studies and that progression to further hearing loss types may be limited or even prevented.

In pursuit of viable cell replacement therapies for the inner ear, present inability to reliably determine which cells remain in the patient cochlea must be addressed. Not only does this mean that researchers cannot accurately determine the nature of cell replacement required, but in cases of metabolic ARHL it may be reasonably stated that inability to assess the inner ear state may prevent the derivation of any benefit from treatment. As mentioned above, Kada *et al.* (2020) <sup>[253]</sup> recently demonstrated partial recovery of hearing function following MSC implantation in mice. Within the study, however, it was noted that recovery was only seen in the mild degeneration model, with researchers suggesting that improvement may only be feasible should sensory cells remain undamaged. As hearing loss is minimally symptomatic prior to sensory cell damage, without an

alternate insight into inner ear health of patients, MSC replacement of cochlear fibrocytes cannot offer functional recovery.

In aims to combat this issue, the present research suggests the use of non-invasive mass spectrometry technique SIFT-MS to detect patient inner ear health in a minimally invasive manner via biofluids. More specifically, the present research aims to conduct the first stage of investigations on the path to the establishment of distinguishable profiles of healthy and unhealthy murine cochlear cells, with a view to progressing towards profiling inner ear health in live animals via relevant biofluids. Eventually, it is hoped, this research will come to form the groundwork of clinically applicable research into inner ear health detection in human patients.

## 1.7. Spectrometry and Spectroscopy for the Monitoring of Cochlear Fibrocytes- Introduction to Relevant Techniques

In order to identify metabolic and mixed ARHL in the fibrocyte stage, and to monitor cells *in vitro* non-invasively, mass spectrometry and vibrational spectroscopy techniques may be of use. As metabolic and mixed phenotypes of HL are so difficult to determine and to distinguish from other subtypes, techniques capable of identifying small variations are vital to achieve the goal of detection and distinction of metabolic ARHL in a clinically translatable setting. Combining sensitive molecule detection methods with minimally invasive techniques such as gas sampling (or supernatant sampling for cell cultures) facilitates both the advancement of potential ARHL diagnostics and treatments. To this end, the techniques Raman spectroscopy, FTIR spectroscopy and SIFT-MS are explored in the present research.

### 1.7.1. Raman Spectroscopy

In the present research, cultured cells were first explored through vibrational spectroscopy to observe the cell endometabolome (metabolic environment within cells) for comparison with the exometabolome (metabolic environment outside of cells e.g. supernatant, gas headspace). Both

Raman spectroscopy and Synchrotron-FTIR spectroscopy were employed to this end (direct cellular analysis).

To briefly introduce vibrational spectroscopies – analytical techniques within this category provide insights into molecular structure, dynamics, and interactions through the examination of molecules' vibrations in response to light. Both Raman spectroscopy and FTIR spectroscopy are widely used across industry and academia in various fields including chemistry, materials science and even clinical biology. While both Raman and IR based techniques fundamentally rely on light interaction with molecules, they differ in their modes of action. Put simply, Raman spectroscopy relies on changes to molecule polarizability (ease of electron cloud distortion) of a molecule, while IR techniques (e.g. FTIR) rely on changes in a molecule's dipole moment (separation of opposing charges). As such, Raman and IR spectroscopies are considered complementary.

**Table 1: Comparison of Raman Spectroscopy and FTIR Spectroscopy (adapted from Kendall et al. (2009)).**

	<b>Raman Spectroscopy</b>	<b>FTIR Spectroscopy</b>
<b>Principle</b>	Scattering of light by vibrating molecules.	Absorption of light by vibrating molecules.
<b>Molecular Activity</b>	A molecule is Raman active if incident light causes a change in polarizability.	A molecule is IR active if incident light causes a change in dipole moment.
<b>Molecular Bond Sensitivities</b>	Non-polar bonds including C-C double and triple bonds.	Strong polar bonds including hydroxyl (OH), carbonyl (CO) and amide bonds.
<b>Spatial Resolution</b>	Higher spatial resolution (1 $\mu$ m) due to diffraction limit.	Lower spatial resolution (10 $\mu$ m) due to diffraction limit. Synchrotron sources (2-5 $\mu$ m).

To introduce further - Raman spectroscopy operates via the quantification of Raman scattering (inelastic scattering of incident photons) by molecules of interest. Dependent upon the nature of their bonds, molecules may possess various vibrational modes (Fig. 5) enabling the continuous movement of their atoms. Vibrational modes include symmetric and asymmetric stretching, symmetric bending in a plane (bending), asymmetric bending in a plane (rocking), symmetric bending out of a plane (twisting), and asymmetric bending out of a plane (wagging).

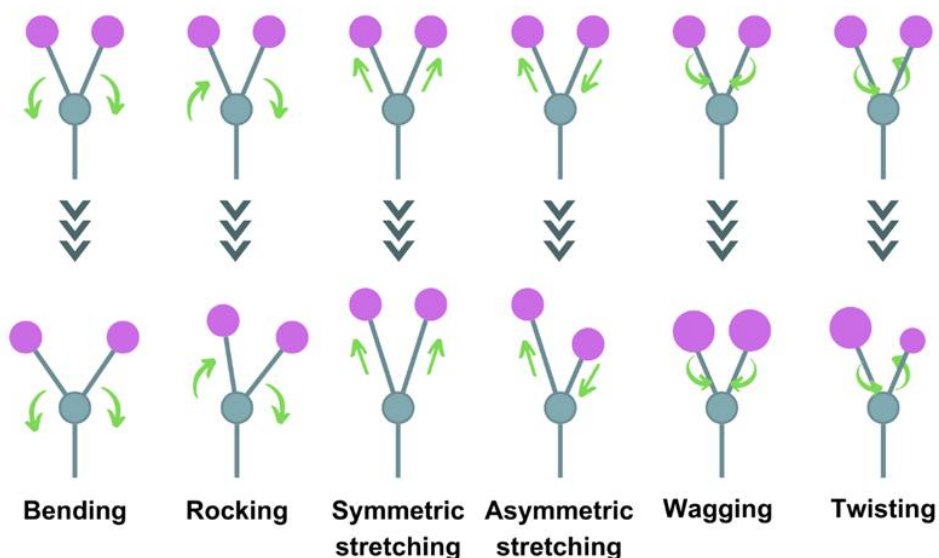


**Figure 5: Vibrational modes of molecules.**

**Fundamental vibrational modes of a triatomic non-linear molecule observed in infrared (IR) and Raman spectroscopy. Bending (Scissoring ( $\beta$ )): Atoms move toward and away from each other in the same plane, altering bond angles. Rocking ( $\rho$ ): Atoms oscillate side to side in parallel motion, maintaining bond lengths. Symmetric Stretching ( $\nu_1$ ): All bonds elongate and contract in-phase, maintaining molecular symmetry. Asymmetric Stretching ( $\nu_2$ ): Bonds stretch and compress in an out-of-phase manner, leading to dipole moment changes crucial for IR activity. Wagging ( $\omega$ ): Atoms move in and out of the plane in unison, resembling a "wagging" motion. Twisting ( $\tau$ ): Atoms rotate in opposite directions about the bond axis, introducing torsional strain.**

As such, when monochromatic light interacts with these molecules, photons are either absorbed or subject to scattering, with some absorption occurring when the incident energy is equal to that of the vibrational mode and scattering occurring in all other cases. Raman scattering can take three forms- Rayleigh, where scattered photons have the same energy as incident photons; Raman Stokes, where scattered photons have higher energy than incident photons; Raman anti-Stokes, where scattered photons have higher energy than absorbed photons (Fig. 6) <sup>[98]</sup>. From this, given that the incident energy is known, researchers may infer qualitative and quantitative information about samples of interest based upon their absorption/scattering.

Where the diagnosis and monitoring of disease is concerned, Raman spectroscopy has a range of applications depending upon the specifics of the methods used. It has been employed to date in the context of countless conditions including cancers <sup>[99]</sup>, Alzheimer's disease <sup>[100]</sup>, and Hepatitis C <sup>[101]</sup>, along with a notable potential for application in COVID-19 diagnosis (and the diagnosis of similar viral illnesses at pandemic scale) <sup>[102]</sup>.

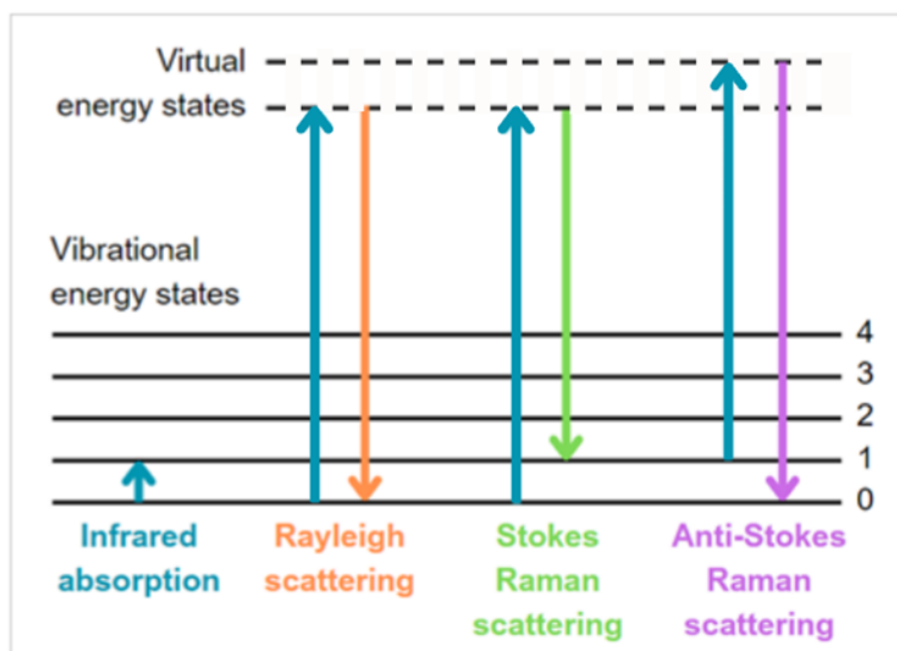


**Figure 6: Types of scattering in Raman spectroscopy.**

**Rayleigh scattering –  $\lambda_{\text{scatter}} = \lambda_{\text{laser}}$ . Stokes Raman scattering –  $\lambda_{\text{scatter}} > \lambda_{\text{laser}}$ . Anti-Stokes Raman scattering –  $\lambda_{\text{scatter}} < \lambda_{\text{laser}}$ .**

### 1.7.2. ATR-FTIR Spectroscopy

ATR-FTIR spectroscopy was employed in this research to examine supernatant samples of cochlear fibrocyte cultures to contribute to cell exometabolome understanding. ATR-FTIR (an enhanced form of FTIR spectroscopy), similarly to Raman spectroscopy, operates via measurement of the absorption and scattering of incident light to infer molecular features. Once again, this technique relies upon the vibrational modes of molecules noted in figure 5. As its name suggests, FTIR observations are conducted in the infrared spectrum, with infrared radiation typically produced via Globar (thermal light) source passed through a sample and the resulting absorbance and transmittance (passage of radiation through the sample) recorded to generate spectra via the Fourier

transform<sup>[103]</sup>. Absorbance occurs when the resonance frequency of analysed molecules matches the frequency of the IR radiation applied.

The Fourier transform, simply put, is employed in FTIR spectroscopy to arrange signal outputs into measures of frequency and amplitude which may be interpreted as spectra, essentially acting as a series of filters which separate signals into constituents. That is, given an output, the Fourier Transform works in reverse to calculate input components, generating spectra that allow molecules to be identified.

Through combining the fundamental technique of FTIR with the attenuated total reflection (ATR) sampling method, ATR-FTIR enables non-destructive, high sensitivity analysis of samples with minimal preparation requirements. In the context of cell culture media analysis, the technique is particularly applicable as it enables direct analysis of water-rich liquid samples. The ATR sampling method operates by IR absorption by a sample in contact with a high-refractive-index crystal (referred to as the ATR crystal e.g. diamond, germanium, zinc selenide). Total internal reflection (incident angle > critical angle) in the ATR crystal generates a phenomenon known as an evanescent wave (see Fig. 7). This evanescent wave penetrates the sample, interacting with its molecules to produce detectable IR absorption relative to vibrational modes.

ATR-FTIR, through use of total internal reflection to improve signal strength, enables the direct examination of solid and liquid samples without requirement for excessive preparation. This is of great

interest in the context of disease monitoring and diagnosis, where samples are likely to arise in solid and liquid form and timely results are vital in order to intervene.

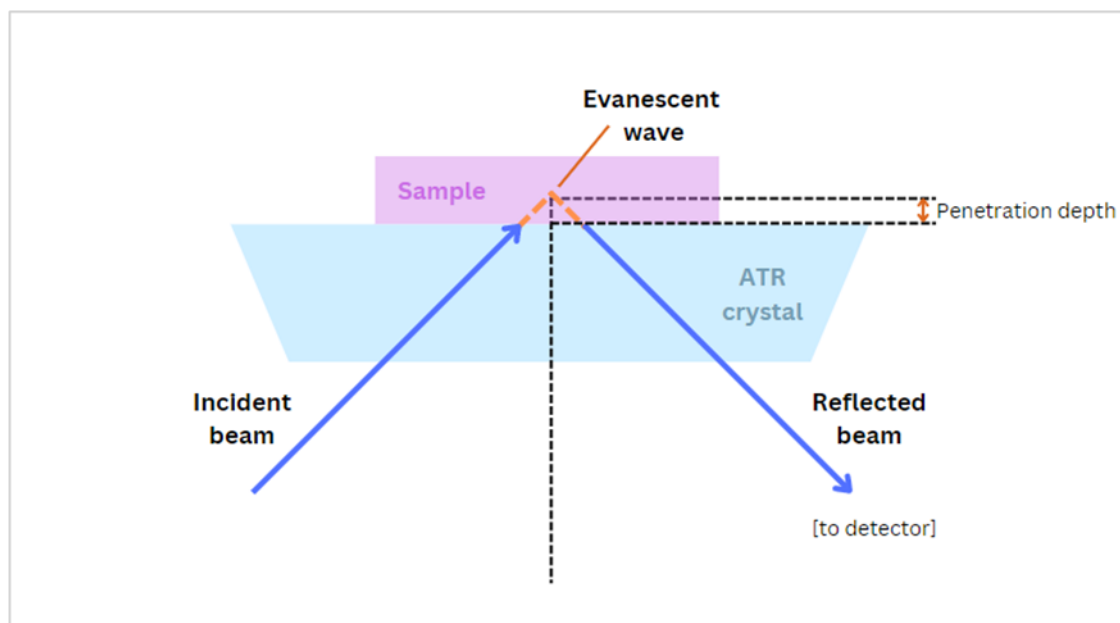


**Figure 7: The principal of ATR-FTIR – total internal reflection and evanescent wave generation.**

**Infrared light enters a high-refractive-index crystal at an angle exceeding the critical angle, undergoing total internal reflection at the crystal-sample interface. This creates an evanescent wave that extends a few micrometres into the sample, enabling interaction with molecular vibrations. Absorption of specific IR frequencies by the sample alters the reflected light, producing an IR spectrum characteristic of the sample's molecular composition. The depth of penetration depends on factors such as wavelength, refractive indices, and angle of incidence.**

As such, ATR-FTIR spectroscopy is employed across a wide range of applications including studying molecular structures, examining surface properties and monitoring chemical reactions. In the biological context, the technique has been employed in the diagnoses and monitoring of a range of conditions and their treatments including Hepatitis (B and C) <sup>[104]</sup>, chronic kidney disease <sup>[105]</sup> and ovarian cancer <sup>[106]</sup>. Such studies are typically targeted at the use of biofluids such as serum, saliva and urine, with a clear drive towards the development of minimally invasive, rapid detection and monitoring methods.

### 1.7.3. Synchrotron-based Analysis

In the course of this research, FTIR spectroscopy using a Synchrotron light source (Diamond Light Source, Oxford, UK) was conducted in order to further analyse subcellular alterations to cochlear fibrocytes. Compared to benchtop FTIR which uses global light, synchrotron light-based techniques offer higher resolution sampling and improved signal-to-noise ratio. This improvement is of considerable value when seeking to analyse changes at a subcellular and molecular level.

Synchrotron light is initiated via electron gun, in which a cathode produces free electrons which are then pulled into a stream via magnetic field. The produced electron stream travels through a linear accelerator where high energy microwaves and radio waves split the stream into pulses. The linear accelerator feeds into the booster ring wherein the electron stream is modulated to a circular path and accelerated to relativistic velocity by a series of particle accelerators. Once stable, the electron stream is fed into the storage ring, a vacuum-maintained tube wherein a magnetic lattice keeps the electron beam focused to a true circular path. Synchrotron light is produced when a bending magnet deflects the electron beam, with each bending magnet linked to a beam line wherein synchrotron-based analyses may be conducted using the emitted electromagnetic radiation. This is summarised in figure 8.

Though Synchrotron and benchtop spectroscopic methods differ in their mode of action, both may be analysed similarly. A crucial component of spectral data analysis is the conduction of multivariate data analysis (MVDA). MVDA methods such as principal component analysis (discussed in greater detail in section 2.2.3) enable researchers to handle the large volumes of highly variable

data typical of spectroscopic techniques, identifying patterns and relationships within data, reducing dimensionality, and providing ease in data visualization and interpretation.

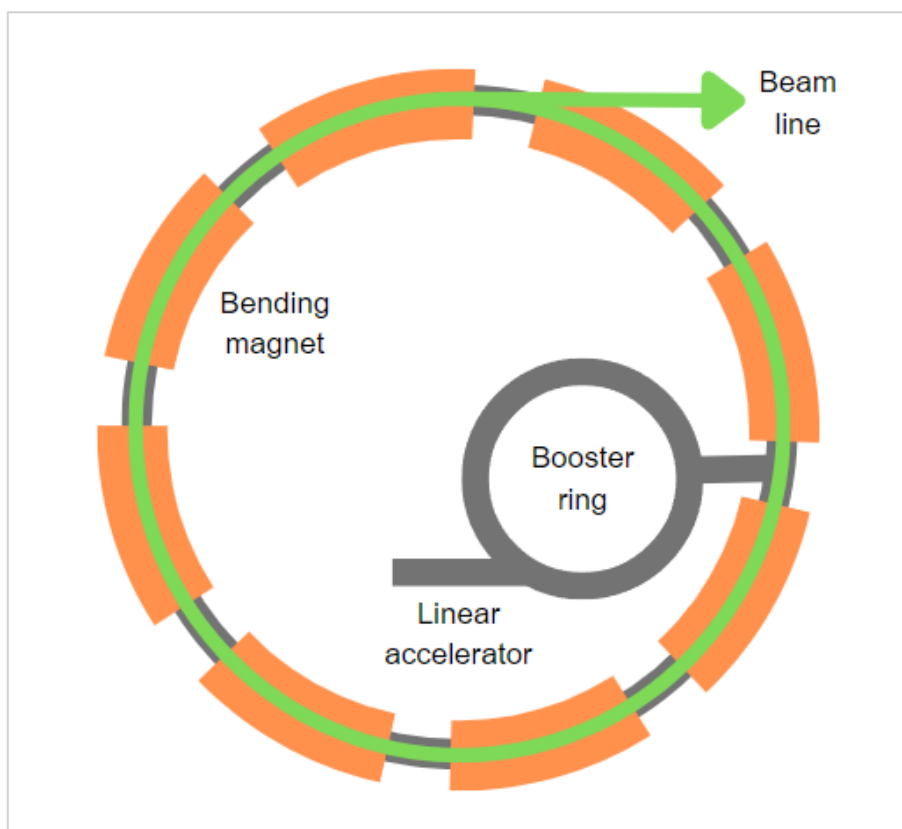


**Figure 8: A Simple Diagram of Typical Synchrotron Setup.**

**Electrons are initially accelerated in a linear accelerator (linac) before being injected into a booster synchrotron, where they gain energy through radiofrequency cavities. The electrons are then transferred to the storage ring, where they circulate at relativistic speeds, emitting synchrotron radiation as they are deflected by bending magnets or insertion devices such as wigglers and undulators. This radiation is directed into beamlines for various spectroscopic and imaging applications.**

Of particular interest in the present research is the capacity of MVDA methods to be used in the classification of samples. Should classification of cochlear fibrocyte samples by inflammation level be feasible, this may inform creation of a predictive model which, in theory, could distinguish inflamed cells from healthy and inform diagnostic/clinical applications. Such a model, if performance could be appropriately validated, could be employed in real-world settings to rapidly identify and categorise cell inflammation state in the hearing loss context and beyond.

### 1.7.4. Vibrational Spectroscopy in Inflammation and Hearing Studies

Techniques such as Raman spectroscopy and FTIR can be highly valuable tools in the study of inflammation-related metabolic changes in cells. These methods provide label-free, non-destructive analysis with high specificity, making them uniquely suited for detecting subtle biochemical alterations linked to inflammation, mitochondrial dysfunction, and metabolic pathway disruptions. As noted previously, Raman and FTIR are complementary techniques and, used together, enable molecular fingerprinting of samples revealing chemical and structural modifications in proteins, lipids, and other metabolites.

It should be noted that the label-free, non-invasive nature of vibrational spectroscopies in this context contrast with traditional biochemical validation methods for inflammation and inflammatory markers (such as western blot, ELISA, mitochondrial function assays etc.) which are time consuming and often considered invasive to cultures under study. FTIR in particular, when employing the media sampling methods used in the present research, presents a potentially highly effective non-invasive analysis method for cells in culture.

Though not conducted in the context of ARHL, both Raman and FTIR spectroscopies have been employed in numerous studies of cellular inflammation and related biomarkers. Concerning Raman spectroscopy, the paper by Borek-Dorosz et al. (2024) <sup>[265]</sup> is of particular interest as it explores the activation of glucose and lipid metabolism in endothelial cells by inflammation with TNF- $\alpha$ . This research suggested alteration in the ratio of lipid:protein/lipid bands in Raman spectra as a result of inflammation, as well as general accumulation of lipids – known to arise as a product of inflammation <sup>[266]</sup>. Such lipid alterations as a result of inflammation have been analysed by Raman spectroscopy across a variety of contexts including nervous system-focused research <sup>[267]</sup>. Though not strictly applicable to studies of ARHL, the versatility of Raman spectroscopy in inflammatory studies, particularly where lipid and protein analyses are concerned, lend it well to the present research. In particular, where lipids are concerned, Raman spectroscopy presents a label-free alternative to

perhaps more traditional immunocytochemical methods, enabling the preservation of potential inflammatory cellular features (e.g. lipid droplet accumulation in macrophage-like cells).

FTIR spectroscopy, similarly, has been employed across a range of studies surrounding inflammation and mitochondrial dysfunction, as well as more generally in diagnostics [268,269]. Though not directly linked to cochlear fibrocytes, the 2018 paper by Rodrigues et al. [270] provides general insight into the analysis of cell and tissue inflammation using FTIR. Researchers in this study demonstrated FTIR differentiation of several variations between normal and pathological mucosa samples, with differences arising in spectral regions including those attributed to DNA ( $\sim 970\text{cm}^{-1}$ ), proteins ( $1312\text{cm}^{-1}$ ) and lipids ( $1743\text{cm}^{-1}$ ). Of particular interest is the variation seen in glycogen ( $\sim 1080\text{cm}^{-1}$ ) between inflamed and normal tissue. Glycogen is a key molecule in energy production and is broken down during glycolysis to generate pyruvate and, subsequently, acetyl-CoA through the citric acid cycle. This is particularly interesting in the context of cochlear fibrocytes as they are, like macrophages, considered immunocompetent cells [271] and it is known that in macrophages, performance of the citric acid is affected by inflammation [272]. As such, the present research also serves to explore where cochlear fibrocyte inflammatory responses resemble those of macrophages and where they differ.

Concerning the diagnoses of ARHL, vibrational spectroscopy techniques such as Raman and FTIR spectroscopies are of great value. However, to date there have not been any studies which have employed these techniques specifically to monitor the health of cochlear fibrocytes.

Raman spectroscopic studies surrounding the ear typically appear more broadly focused, often concentrating on outer and middle ear health and adaptations to current treatment options (e.g. cochlear implants) [107-109]. However, though there do not appear to be any studies focused solely on cochlear fibrocytes and their health, Raman studies into the composition of perilymph and its diagnostic potential have been conducted.

In their 2016 study, Höhl et al. employed UV-resonance-enhanced Raman techniques to examine amino acids in aqueous solutions such as human perilymph [110]. In 2019, the group continued in this line of research, taking a first step towards their long-term goal of developing a fibre-based Raman endoscope for non-invasive perilymph measurements during cochlear implant surgeries [111]. In this

study, Höhl *et al.* (2019) presented a prototype fibre optic probe to acquire Raman spectra of heat shock proteins (HSPs) 70 and 90 in perilymph. These proteins are known to perform several functions including preventing stress-induced apoptosis in hair cells and, as such, form part of the inner ear ‘stress proteome’ – a potential target for drug-based interventions <sup>[112]</sup>. In the study, researchers employed the prototype probe to collect Raman spectra of purified HSP70 and HSP90 samples *ex vivo*, successfully identifying key spectral components and demonstrating the accuracy of their methods via PCA and predictive model. To date, this research group appears to still be working towards its long-term goal.

Though this research differs from the present study in the setup and nature of samples observed, it is still highly relevant to the present research with the actions of cochlear fibrocytes directly impacting the composition of perilymph *in vivo*. As such, the goals and findings of this research were considered when conducting the present study. However, it is arguable that the present study’s ATR-FTIR analyses are more relevant to the Höhl *et al.* research direction than Raman analyses, as these deal with cell supernatant rather than cells themselves.

As successful diagnosis of age-related hearing loss (ARHL) by the methods studied requires access to reliable and relevant biofluids from which to elucidate biomarker information, it is of value to consider perilymph in this context. Perilymph, due to its proximity to cochlear cells, reflects the physiological and biochemical state of the inner ear, making it a highly relevant fluid for investigating cochlear inflammation and metabolic changes. Certainly, if *in vitro* cell culture supernatant may be used as an analogue for perilymph in this proof of concept research, it serves to demonstrate how further spectroscopic techniques such as ATR-FTIR may be of value in analysing the ‘stress proteome’ (e.g. proteins such as HSP70 and HSP90) of the inner ear and cochlear fibrocytes. Should inflammation-based variation be detectable through culture media by ATR-FTIR, the present research encourages the techniques use as a further, complementary, biomarker analysis approach to the Raman analyses shown by Höhl *et al.* Success in these methods could enable earlier detection, improved monitoring, and personalized intervention strategies for ARHL.

ATR-FTIR, similarly to Raman spectroscopy, appears widely used in studies surrounding adaptations to HL treatment options (such as cochlear implants) <sup>[109]</sup>, with seemingly fewer studies

devoted to ear cell investigations. Most studies that do involve inner ear cells (e.g. hair cells/SGNs) appear to focus on biomaterial development for cell scaffolds, nanoparticles, and artificial cell-like structures, with FTIR employed to characterise these materials rather than cells themselves <sup>[126, 259]</sup>. To date, it does not appear that FTIR-based techniques have been used to examine cochlear fibrocytes or their surrounding fluids.

With this in mind, the investigations conducted in the present research are undoubtedly unique, with vibrational spectroscopy being used to characterise *in vitro* cochlear fibrocytes for the first time. Not only are fibrocytes analysed in their healthy state, but inflamed cells are also investigated. Furthermore, in addition to benchtop analyses, this research presents findings of S-FTIR fibrocyte analyses conducted at Diamond Light Source Synchrotron Facility (Oxford, UK) and marks the first occasion in which such cells have been scrutinised at a synchrotron facility.

### 1.7.5. Selected Ion Flow Tube Mass Spectrometry (SIFT – MS)

In pursuit of minimally invasive cell observation methods, and further to vibrational spectroscopy techniques, this research employed Selected Ion Flow Tube Mass Spectrometry (SIFT-MS) in examining the gas headspace of cochlear fibrocytes *in vitro*. This method allows real-time identification of compounds within gaseous samples, often requiring significantly less preparation than other gas analysis methods such as gas chromatography mass spectrometry (GC-MS). Compared with GC-MS, SIFT-MS is a newer, faster method for metabolomic study which has shown

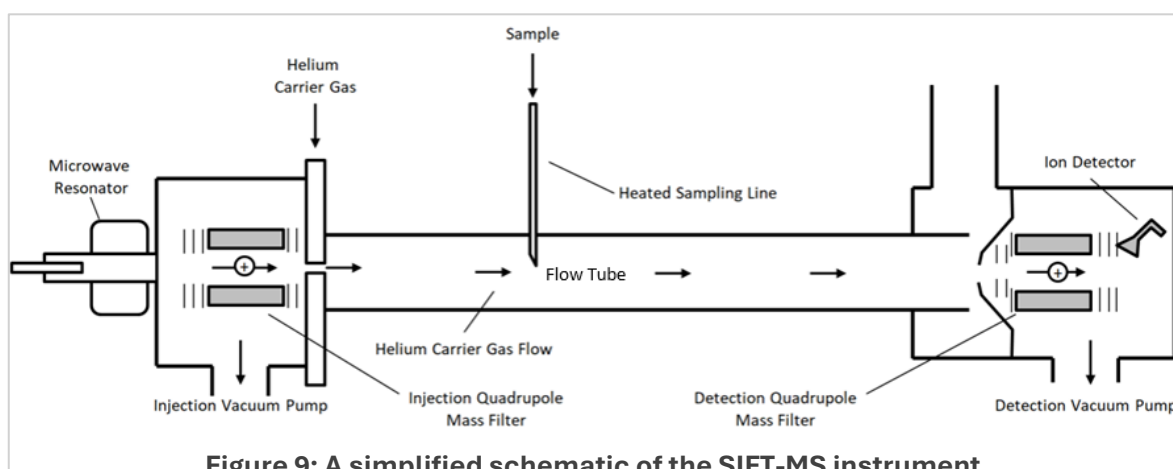


Figure 9: A simplified schematic of the SIFT-MS instrument.

**Schematic indicates the arrangements of SIFT-MS components including quadrupole filters, ion detector and microwave resonator. Helium carrier gas flow is indicated in the main flow tube (adapted from Smith & Španěl, 2005).**

extensive potential for diagnostic use. It is a radiation-free, analytical method that allows real-time analysis of gaseous sample composition, producing a profile of volatile organic compounds (VOCs) from samples.

SIFT-MS operates via soft chemical ionisation, wherein a sample vapour is reacted with known ions selected by a quadrupole mass filter (typically  $\text{H}_3\text{O}^+$ ,  $\text{NO}^+$  or  $\text{O}_2^+$  due to their lack of reactivity with major compounds in air) from a mixture of ions produced via microwave discharge through air <sup>[113]</sup>. The selected ion (one of  $\text{H}_3\text{O}^+$ ,  $\text{NO}^+$  or  $\text{O}_2^+$ ) is reacted with samples in an inert carrier gas (usually helium) at a controlled flow rate to generate analyte ions. These analyte ions are then sampled by a mass spectrometer which generates a measure of ion counts (Fig. 9).

Assignment of molecules to samples is made based upon ion reaction mechanics, according to the precursor ion employed.  $\text{H}_3\text{O}^+$  precursor ions react with sample molecules via proton transfer, with products often undergoing hydration due to sample humidity.  $\text{NO}^+$  precursor ions typically react via charge transfer, wherein an electron is drawn from the sample molecule to neutralise the  $\text{NO}^+$  ion to NO.  $\text{NO}^+$  precursors may also react via hydride ion transfer (due to sample humidity) or association.  $\text{O}_2^+$  precursors react similarly to  $\text{NO}^+$ , in that typical reactions with sample molecules occur in the form of charge transfer. These reaction mechanisms are summarised in Table 2 below.

**Table 2: Reaction mechanics of common SIFT-MS precursor ions.**

<i>Reaction Type</i>	<i>Reaction Equation</i>
<b><math>\text{H}_3\text{O}^+</math></b>	
Proton transfer	$\text{M} + \text{H}_3\text{O}^+ \rightarrow \text{MH}^+ + \text{H}_2\text{O}$
Product ion hydration	$\text{MH}^+ + \text{H}_2\text{O} \rightarrow \text{MH}^+(\text{H}_2\text{O})$
Reaction with hydrated precursor ions	$\text{M} + \text{H}_3\text{O}^+(\text{H}_2\text{O}) \rightarrow \text{MH}^+(\text{H}_2\text{O}) + \text{H}_3\text{O}^+$
<b><math>\text{NO}^+</math></b>	
Charge transfer	$\text{M} + \text{NO}^+ \rightarrow \text{M}^+ + \text{NO}$
Hydride ion transfer	$\text{MH} + \text{NO}^+ \rightarrow \text{M}^+ + \text{HNO}$
Association	$\text{M} + \text{NO}^+ \rightarrow \text{NO}^+\text{M}$
<b><math>\text{O}_2^+</math></b>	
Charge transfer	$\text{M} + \text{O}_2^+ \rightarrow \text{M}^+ + \text{O}_2$

## 1.8. Mass spectrometry in diagnosis

Concerning the diagnoses of ARHL as well as the distinction between subtypes and monitoring of cell health, non-invasive gas sampling techniques such as SIFT-MS are ideal, though liquid sampling

using vibrational spectroscopy is also feasible *in vitro*. SIFT-MS has previously been used in non-hearing-related studies focused upon diagnosis <sup>[114-120]</sup>, though clinical use in relation to ARHL has not yet occurred.

To date, SIFT-MS has been used to determine the profiles of and distinguish between a variety of human cell types, typically with little sample preparation and real-time analysis possible <sup>[113, 128]</sup>. This capacity is of great interest in seeking a non-invasive monitoring method for cochlear fibrocyte pathologies *in vitro* and may lend itself to *in vivo* investigations should an appropriate sample source be obtainable from patients.

Generally, clinical SIFT-MS research focuses on the use of breath as this is an accessible, patient-friendly sample type and the large gas-exchange surface of the lungs allows VOC profiles from blood to be carried into exhaled breath. Breath studies conducted using SIFT-MS are highly versatile, characterising ‘breathprints’ for a range of conditions including cancers, Crohn’s disease, cystic fibrosis, and renal failure <sup>[115-120, 129]</sup>.

Though most clinically relevant SIFT-MS studies focus on breath research, breath can be tricky capture and store and, as such, may not be the ideal approach to developing potential ARHL diagnostics. With such issues in mind, alternative sample types may be used provided that they have a gas headspace that can be collected for analysis. For example, though far less common than breath studies, research into plasma and blood headspace analysis via SIFT-MS has been conducted <sup>[121,122]</sup>. However, such sampling methods cannot be considered truly non-invasive, with blood tests and similar needle-based procedures (including the extraction of perilymph) off-putting to many patients <sup>[123]</sup>.

Based on these factors, cerumen is suggested as a biomarker of interest in this research. Though only the first stages of investigation are conducted alongside cell analyses presently, GC-MS based studies have demonstrated the biofluid’s diagnostic potential <sup>[127]</sup>. Cerumen, though external to the cochlea, offers a potential non-invasive alternative biofluid for biomarker analysis compared with blood sampling or perilymph extraction. Its composition includes a mixture of lipids and proteins which may reflect metabolic processes and indicate inflammation-related processes such as oxidative stress, and its properties as a wax offer potential for the entrapment of volatile organic

compounds from the ear which may offer further metabolic information. By complementing or replacing perilymph analysis, cerumen may provide a patient-friendly approach that aligns with the broader push toward non-invasive diagnostic strategies in precision medicine. This is explored in depth in chapter 5.

## 1.9. The present study- Aims and Objectives

In order to further the field of hearing loss research, the present thesis provides the first stage of investigation into the potential of Raman spectroscopy, FTIR spectroscopy and SIFT-MS in the assessment of cochlear fibrocyte damage by inflammation. Based upon the literature, inflammation was induced in this research via cytokine administration. This method was selected to enable dose-response-like analysis wherein inflammation may be observed at a range of levels. From this, it is hoped that distinct and detectable metabolic profiles of healthy and inflamed cells may be characterised with a view to future clinical translation following further study and the identification of appropriate patient sample sources such as perilymph and cerumen.

As such, the key aims of this thesis are:

1. To further understanding of cochlear fibrocyte inflammatory pathology via analysis of healthy and inflamed cell and supernatant profiles using Raman spectroscopy, S-FTIR spectroscopy and ATR-FTIR spectroscopy.
2. To investigate, via SIFT-MS, the headspace profiles of healthy and inflamed cochlear fibrocytes, providing insight into biomarkers of interest for potential clinical translation.
3. To conduct preliminary investigations into the use of cerumen as a non-invasive sample biofluid for Raman spectroscopy, ATR-FTIR spectroscopy and SIFT-MS analyses of cochlear fibrocyte health.

It is hoped that the findings from these studies will improve understanding of the metabolic mechanisms of cochlear fibrocytes in response to inflammation and contribute to the development of technologies intended to detect and inhibit the progression of ARHL.

## 2. Materials and Methods

---

### 2.1. Cell Culture Methods

#### 2.1.1. Dissection and Growth of Murine Cochlear Fibrocytes

Primary murine cochlear fibrocytes were retrieved from CD/1 mice using methods adapted from the gerbil dissection protocol of Gratton *et al.* <sup>[89]</sup>. Prior to their termination, mice were bred and maintained in the Biomedical Services Unit of the University of Keele according to the 1986 Animals (Scientific Procedures) Act under regulatory control of the UK Home Office and following appropriate project approval. All terminations were carried out under Schedule 1 of the act (see letter in Appendix A) by trained persons at the Biomedical Services Unit.

Mice at approximately postnatal day 10 were humanely euthanized via anaesthetic overdose using an injection of 0.05mL sodium pentobarbital (Vetalar). A toe pinch check was performed on each animal to ensure no motor response before proceeding with transportation and dissection. Once proper anaesthetization was achieved and animals confirmed to be deceased, they were safely transported to the Keele University Guy Hilton Research Centre site in a sealed, cooled container. Once at the Guy Hilton Research Centre site, animals were immediately transferred from the container to a biological safety cabinet prepared via cleaning with Virkon followed by 70% industrial methylated spirit (IMS), containing petri dishes, sterile scissors, sharp sterile tweezers, magnification equipment, a waste disposal container, a container of appropriate dissection buffer, and a container of appropriate culture media.

In the first stage of dissection, wherein otic capsules were removed, mouse heads were detached and bisected sagittally to expose the brain (Fig. 10, image 1). Brains were then removed to expose otic capsules (Fig. 10, image 2), the approximate locations of which can be ascertained by visually following the lower jawbone of the animal and identifying a characteristic protrusion from the skull. Once located, otic capsules were carefully detached from the skull whole using sharp, sterile tweezers (Fig. 10, images 3 and 4).

To extract spiral ligaments, the shell of each cochlea (made accessible by the removal of the otic capsule from the skull) was peeled away to access the lateral wall, residing immediately beneath the bone. From the lateral wall, tissue was removed (Fig. 10, image 5) and spiral ligaments isolated (Fig. 10, image 6). During this stage of dissection, tissue was handled in a petri dish containing dissection buffer composed of 90% sterile phosphate buffered saline (PBS) (Corning) and 1% penicillin-streptomycin- amphotericin B (Lonza). Isolated ligaments were individually placed in a 6 well plate and topped with a sterile, dry coverslip (sterilized via submersion in 70% IMS, with IMS allowed to evaporate off before use). Once plated, sufficient fibrocyte culture media (composed as listed in the general cell culture procedures (section 2.1.2)) to cover the ligament and coverslip was added to each well, before transferring the plate to an incubator set at 37°C and 5% CO<sub>2</sub>. Following dissection, all waste products and consumable items employed in the dissection process were disposed of via clinical waste and the safety cabinet thoroughly cleaned with Virkon and 70% IMS.

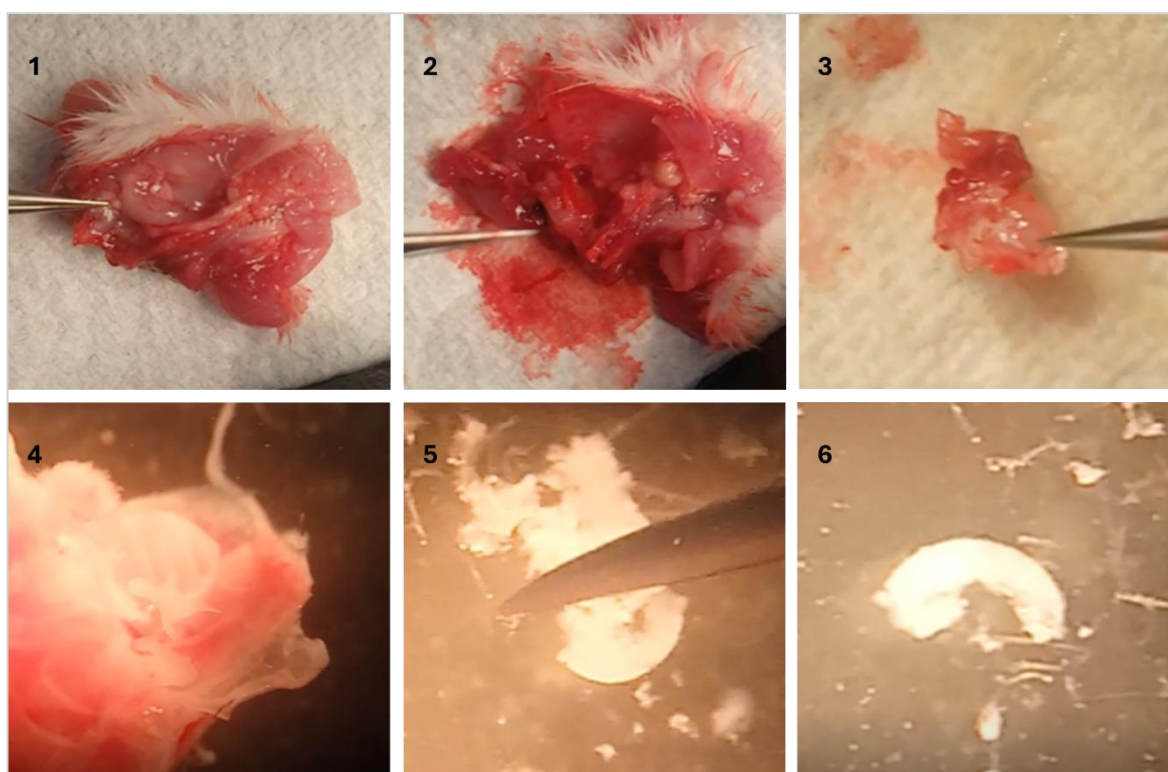


**Figure 10: Photographic images of the cochlea dissection procedure.**

**1) Sagittally bisected mouse head, brain indicated by tweezers. 2) Sagittally bisected mouse head with brain removed, otic capsule indicated by tweezers. 3) Explanted otic capsule, cochlea indicated by tweezers. 4) Close up image of the explanted otic capsule with cochlea clearly visible. 5) Explanted lateral wall tissue. 6) Isolated spiral ligament piece. (Furness, 2020, pers. comm.).**

Plates containing ligaments were cultured in a 37°C (5% CO<sub>2</sub>) incubator with media changes every other day. Coverslips were removed once ligaments had adhered to plates. Ligaments were removed and discarded after around 1-2 weeks depending upon the rate of cell proliferation from the explant. Cells were cultured until confluent patches formed in wells, then split for use in experiments or frozen for future use according to the protocols outlined in section 2.1.3.

### 2.1.2. General Cell Culture Conditions

Murine cochlear fibrocytes from tissue explants were cultured in a 37°C (5% CO<sub>2</sub>) incubator in media composed of 88% glucose-free culture medium (Sigma Aldrich) (powdered, diluted in sterile dH<sub>2</sub>O, D-glucose (Sigma Aldrich) added 1 g/L, pH balanced using sodium bicarbonate (Fisher Scientific)), 10% Foetal Bovine Serum (FBS) (Labtech), 1% L-glutamine (Lonza), 1% non-essential amino acids (NEAA) (Lonza), 1% penicillin-streptomycin-amphotericin B, and 1% insulin-transferrin-selenium-G (ITS-G) (Thermofisher). To minimize degradation of media components, glucose, FBS, and ITS-G were not added to media aliquots until the point immediately before use. Media 'base' without these components was made in large quantities and stored under refrigeration (2-8°C) to further minimize this degradation. Ahead of experiments, media was prepared in full a day before at maximum, with surplus experimental media used for general cell culture and housekeeping activities. All media changes and passages were conducted under sterile cell culture conditions.

Contrary to typical culture methods for cochlear fibrocytes, cell culture surfaces were not collagen coated. This revised method was used as quality and preparation of the collagen solution used for coating can significantly impact fluorescence imaging (as seen in Fig. 11). In initial attempts to incorporate collagen coating into the culture methods, it was observed that the presence of collagen interfered with the fluorescence staining of S100B, leading to increased background signal and potential misinterpretation of results. This interference could be due to non-specific binding of the S100B antibody to collagen fibres. With this in mind, culture without collagen coating was trialled,

with lack of collagen in culture demonstrating no apparent effect on overall cell morphology and marker expression (see chapter 3). As such, the revised collagen-free method was deemed acceptable for the present investigations.

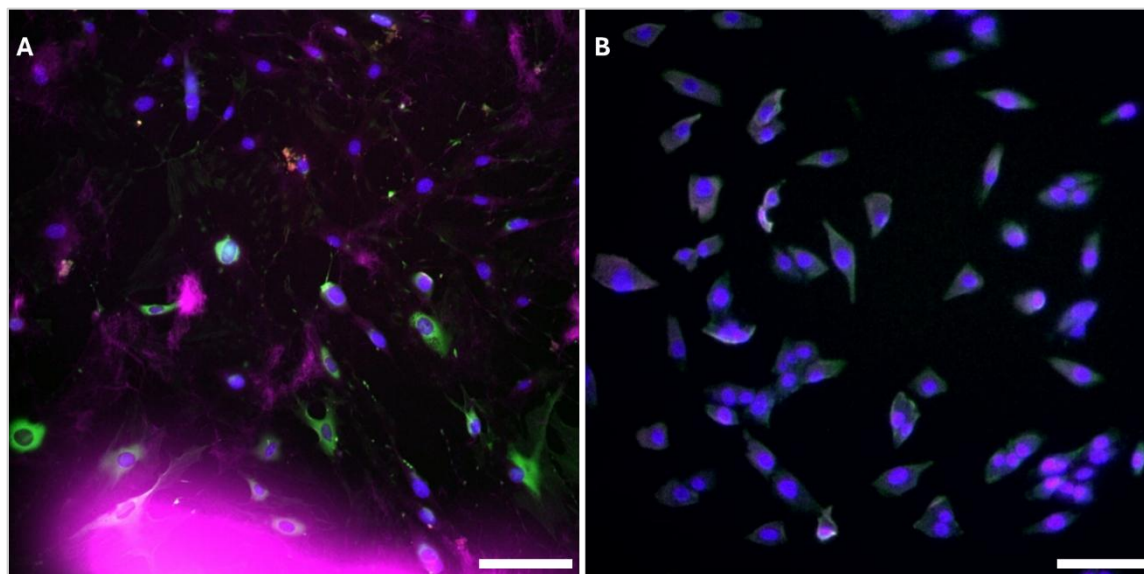


**Figure 11: Fluorescence images of cochlear fibrocyte secondary cultures with and without collagen.**

**Fluorescence images of cochlear fibrocyte staining for Na<sup>+</sup>/K<sup>+</sup>ATPase (green), S100B (magenta) and AQP1 (red) with DAPI nuclear stain. A) With rat tail collagen 1 coating- collagen fibres can be seen in the culture environment, making cells more difficult to visualize. B) Without collagen coating- cells may be seen clearly. Scale: 100µm.**

In vessel selection and cell number detection experiments, MG63 human osteosarcoma cells (cell line derived from the left femur of a 14-year-old Caucasian male), provided by Professor Ying Yang at Keele University, were cultured in a 37°C (5% CO<sub>2</sub>) incubator in media composed of 87% Dulbecco's Modified Eagle's Medium (DMEM) (Corning), 10% FBS, 1% L-glutamine, 1% NEAA, and 1% penicillin-streptomycin-amphotericin B. This cell line was employed to minimize unnecessary animal use in optimization stages.

### 2.1.3. Passage and Storage

Passages were performed once cultures reached approximately 80-90% confluence. To passage, cell culture media was removed and 8:6 trypsin (Corning): PBS added, followed by incubation for 5-10 minutes in a 37°C (5% CO<sub>2</sub>) incubator. Manual aggravation was applied following the incubation

period to ensure thorough cell detachment. Once cells were adequately detached, flasks were quenched with media and cell suspensions centrifuged at the appropriate rate (1000 rpm for 8 minutes for cochlear fibrocytes, 1200rpm for 5 minutes for MG63). Supernatants were discarded and pellets resuspended in 5mL media. 20µl of cell suspension was then combined with 20µl of 0.4% trypan blue solution (Lonza) to perform counts using a haemocytometer. Bright, unstained cells were counted as live and dark, stained cells were counted as dead/non-viable.

Where not immediately required and to avoid senescence (anticipated early into the culture process for primary (non-immortalised) cells), cells were frozen. Cells were trypsinised, centrifuged, resuspended, and counted as above. For every million cells, 1.8mL of freezing media was created- for MG63s this was 90% standard MG63 media, 10% Dimethyl Sulphoxide (DMSO (Fisher Scientific)); for cochlear fibrocytes this was 70% media, 20% FBS, and 10% DMSO. Cells were centrifuged again following counts, at the appropriate rate indicated above. Supernatants were discarded and pellets resuspended in the appropriate freezing media (at 1.8mL per million cells as stated). Each 1.8mL of cell suspension was added to a cryovial, placed in a thawed freezing container, and added to a -80°C freezer. Following approximately 24 hours in the freezer, cryovials were transferred to liquid nitrogen containment for long-term storage.

#### 2.1.4. Cell Survival Assays

Cell viability, whether for storage or experimental purposes, was determined using the trypan blue exclusion method. Trypan blue solution (0.4%) was mixed 1:1 with cell suspension, with stained cells counted via haemocytometer as noted above.

#### 2.1.5. Cochlear Fibrocyte Characterisation

Cochlear fibrocytes were characterised via immunocytochemistry, staining against NaK-ATPase, S-100, and aquaporin 1. Specifics of antibodies and methods employed are detailed in chapter 3.

## 2.2. Raman Spectroscopy of Cochlear Fibrocytes

### 2.2.1. Raman Sample Preparation and Sampling

In preparation for Raman spectroscopy, cells were detached from flasks via trypsin (similarly to the passage methods outlined in section 2.1.3.) and cytopun through a cytofunnel and filter card (Shandon, UK) at 900rpm for 3 minutes (medium setting) onto 0.5mm thickness IR/Raman-grade calcium fluoride ( $\text{CaF}_2$ ) slides (Crystran, UK) to form a monolayer of approximately 250,000 cells. Cytospinning was employed in preference to growing cells directly onto sample slides as it flattens cell bodies- a benefit in sampling techniques whose results may be affected by uneven topography. Cytospinning also mimics clinical cytological preparation and may be relevant to future translational steps. Cytospun samples on slides were placed in a petri dish and fixed using 4% paraformaldehyde in 0.9% NaCl for 15 minutes, followed by one wash using NaCl solution and three washes using  $\text{dH}_2\text{O}$ , and air dried at room temperature. Prior to air drying, excess liquid was carefully removed from slides using filter paper to minimise the formation of any artefacts (e.g. crystals).

In cerumen sample analysis, cerumen samples were not subject to any pre-processing. Cerumen was spread directly upon IR/Raman-grade calcium fluoride sample slides. In depth methods for this sample preparation may be found in section 2.7.

Raman spectroscopy measurement was conducted using a Thermofisher DXR 3 Raman spectrometer (532nm laser, full range 900lines/mm grating). For point maps, typically, 100-300 spectra were collected per condition (1 point per cell with sampling conducted around the nuclear region). A 120 second acquisition time was used for each sample point, with 3 scans per sample and 4 scans of background. Following every 25 cells sampled, a series of 'blank' spectra were taken from cell free substrate regions in order to facilitate baseline correction, identify potential sources of interference and ensure instrument calibration. Sample spectra were collected at 20x magnification. Laser power was 10mW, with a 50 $\mu\text{m}$  pinhole aperture employed. A spot size of approximately 2.5 $\mu\text{m}$  was achieved. Prior to sample spectrum collection, samples were photobleached for 30 seconds to mitigate sample fluorescence and improve the contrast of Raman bands in spectra. A high cosmic ray threshold was employed.

## 2.2.2. Raman Data Pre-processing

Following collection, point maps were split in Omnic software and individual spectra exported as .SPA files. All data processing and analysis was conducted in Orange (Quasar) software (versions 1.7.0 to 1.9.1) (<https://quasar.codes>).

Sample data were first compared with blanks collected at slide locations with no cells. This was done to check for artefacts arising from the instrument and to ensure that variations seen arose from sampled cells, not slides. A comparison of raw undosed cell sample data against blanks is presented in figure 12 below, with difference between sample and blank clearly visible.

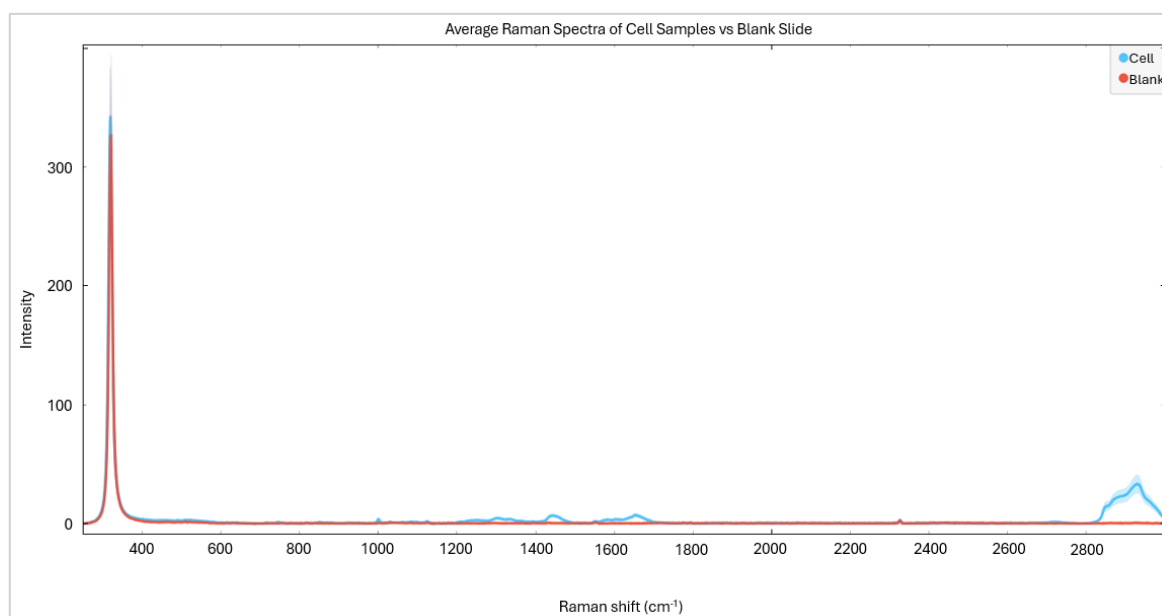


**Figure 12: Average Raman spectra of cell samples vs blank CaF<sub>2</sub> slide.**

**Representative samples of 100 cells and 12 blanks employed in the generation of averages. The characteristic CaF<sub>2</sub> peak at 321cm<sup>-1</sup> as well as a peak at 2325cm<sup>-1</sup> are noted in both blanks and cell samples.**

Following checks against blanks, data were pre-processed to reduce variations in samples not introduced through experimental means. Such variations may originate from environmental factors such as instrument drift, temperature and humidity. Spectra were first cut to remove noise (if necessary) and the large CaF<sub>2</sub> peak, followed by the application of a rubber band baseline correction. Following this, data were smoothed using Savitsky Golay (window 11, polynomial 2) and vector

normalised to reduce variation arising from sample thickness and to allow for comparison across instruments. Window and polynomial were selected to achieve optimum smoothing and signal to noise ratio without over-processing. Finally, data were cut to regions of interest (400-3600 $\text{cm}^{-1}$  general, 400-1800 $\text{cm}^{-1}$  fingerprint, 2800-3600 $\text{cm}^{-1}$  high wavenumber). Any clearly anomalous spectra were excluded from data prior to averaging and analysis. A comparison of raw and pre-processed Raman data is presented in figure 13 on overleaf.

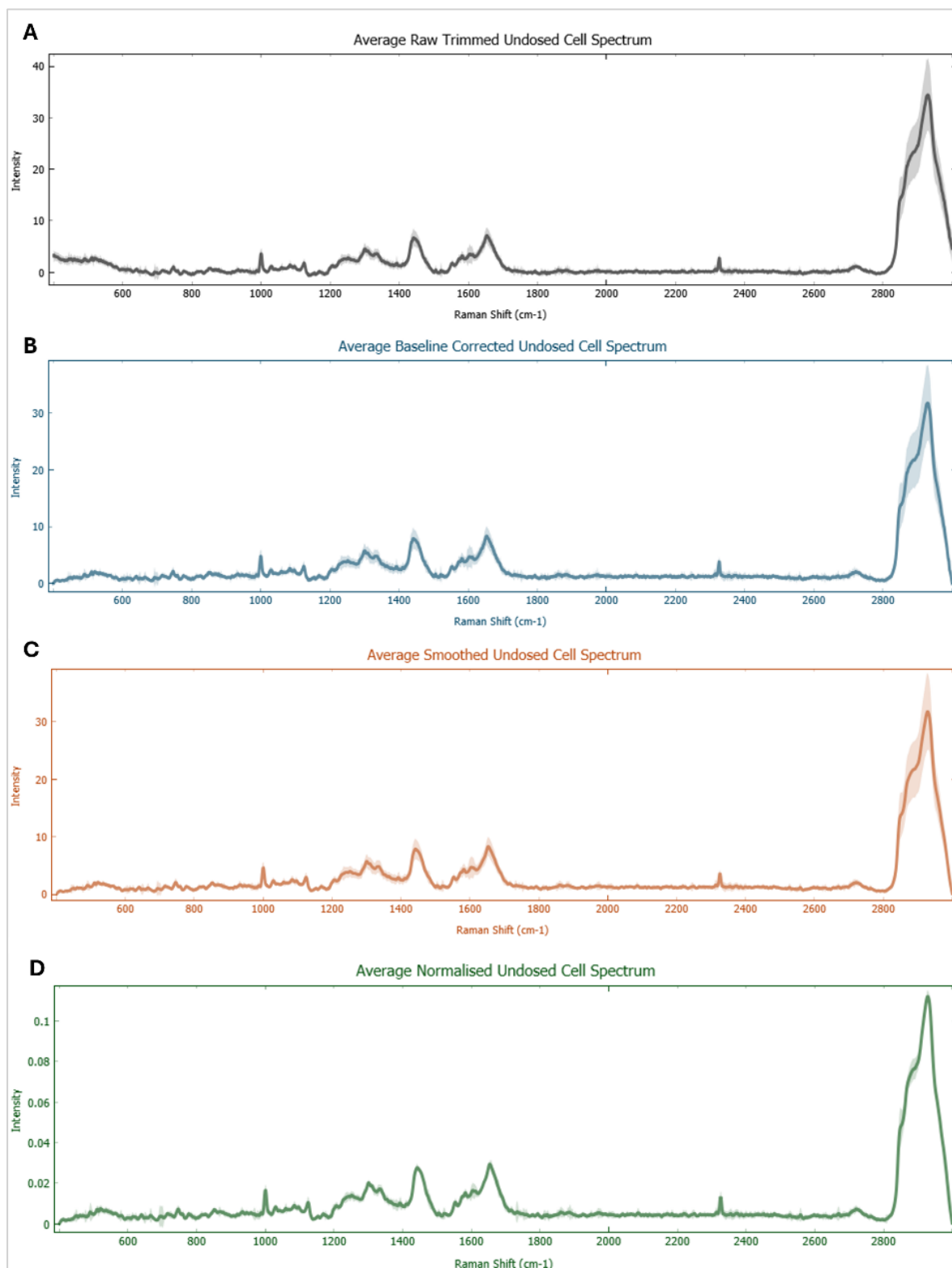


**Figure 13: Average Raman spectra of cell samples at each pre-processing stage.**

**A) Trimmed raw spectrum. B) Rubber band baseline correction applied. C) Savitsky Golay smoothing applied. D) Vector normalisation applied.**

Second derivative spectra were generated by increasing derivative order at the Savitsky-Golay smoothing stage. Generation of second derivative spectra enabled clearer visualisation of Raman bands by reducing background and interference. To reduce noise in second derivative spectra, Savitsky Golay filter window was increased to 27. An example second derivative plot of the undosed cell is shown in figure 14 below.

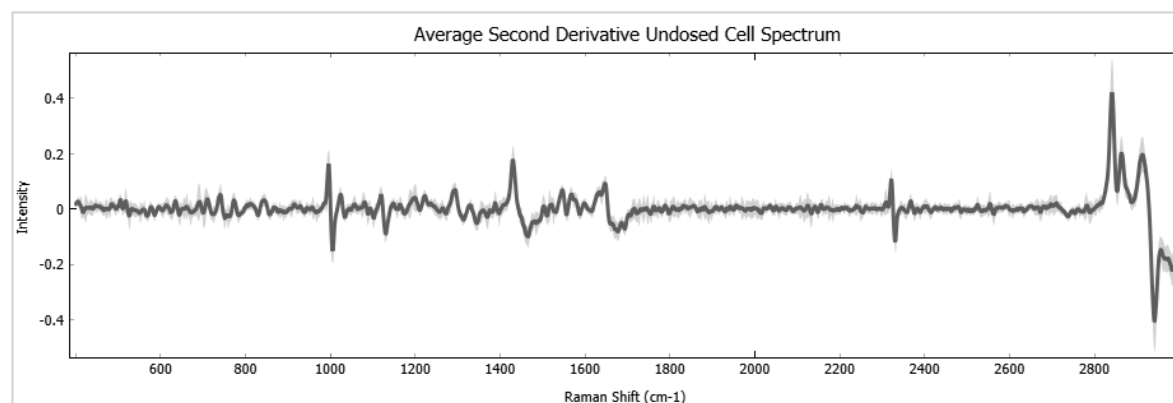


**Figure 14: Average second derivative Raman spectrum of cell samples.**

**Generated by increasing derivative order at the smoothing stage of spectral preprocessing.**

### 2.2.3. Raman Data Analysis

Following pre-processing, data were analysed using Orange (Quasar) software. First, manual peak identification was performed on average spectra. That is, average spectra were visually inspected and peaks identified, noting shift and changes in band intensity and consulting second derivative spectra for clarity where applicable. Bands were assigned to bond vibrations and potential molecules through literature consultation (see table 3).

**Table 3: Raman band assignments.**

Raman Band Region (cm <sup>-1</sup> )	Associated Bond Vibration	Molecular Family
<b>400-600</b>	CH <sub>2</sub> bending, C-C-C deformations	Polysaccharides/nucleic acids
<b>600-700</b>	CH <sub>2</sub> bending, amide IV, C-S stretching, nucleotide ring breathing	Polysaccharides/nucleic acids/proteins
<b>725</b>	Bond vibrations in adenine	Nucleic acids
<b>750</b>	Bond vibrations in thymine	Nucleic acids

<b>785</b>	Bond vibrations in cytosine	Nucleic acids
<b>825</b>	O-P-O stretching of nucleic acids	Nucleic acids
<b>852</b>	C-H ring breathing	Amino acids
<b>870-980</b>	C-O stretching, C-C-N asymmetric stretching, C-O-C ring deformation	Lipids/proteins/nucleic acids
<b>1005</b>	Symmetric ring breathing	Proteins
<b>1032</b>	CH <sub>3</sub> wagging	Proteins
<b>1050-1115</b>	C-O stretching, C-C stretch, C=O vibration	Lipids/proteins
<b>1128</b>	C-C stretch, CH <sub>2</sub> vibration	Lipids/glucose
<b>1145-1195</b>	C-C stretching, C-H bending, C-N vibration	Proteins/amino acids
<b>1195-1405</b>	Amide III, C-O stretching, C=C vibrations, CH <sub>2</sub> wagging	Lipids/proteins/polysaccharides
<b>1441</b>	CH <sub>2</sub> /CH <sub>3</sub> deformation	Lipids/proteins
<b>1540-1625</b>	C=C stretch, N-H bending, tryptophan ring stretching, C-C-H ring vibration	Proteins
<b>1659</b>	Amide I, C=O stretching	Lipids/proteins
<b>1720-1900</b>	C=O stretching	Lipids
<b>2830-2900</b>	CH <sub>2</sub> stretching	Lipids/proteins
<b>2900-3100</b>	CH <sub>3</sub> stretching	Lipids/proteins

Principal component analyses (PCAs) were conducted, also in Quasar software, with associated loadings plots generated from components. PCA was employed to enable visualisation of sample clustering and identification of variation sources through accompanying loadings plots. PCA was also used to reduce data dimensionality ahead of modelling in inflammation investigations. As Raman spectral data is highly dimensional (each wavenumber representing a different variable), PCA is an ideal method to transform data into a less varied format while still retaining valuable information.

PCA works by assigning variance in data to principal components (PCs). Principal components, calculated from data set covariance, indicate sites of variation in data, with principal component 1 (PC1) corresponding to the highest variance and the PCs that follow it (PC2, PC3 etc.) corresponding to reduced variances as they continue.

PC scores were employed to generate scatter plots enabling visualisation of data point clustering. Corresponding loadings plots enabled visualisation of variable participation in each principal component. By observing both scatter plots and loadings plots, sample clustering and its sources may be identified. In terms of spectral data, scatter plots of PCs may, for example, demonstrate significant

separate clustering of a dosed and undosed cell condition, which can be attributed to spectral variations identifiable by consulting the associated loadings plot.

In all sections of the present research, Principal Component Analysis was performed using Orange Quasar software. PCA was conducted before any non-linear predictive models to reduce data dimensionality. In inflammation investigations, predictive models were generated using Orange Quasar. Neural network was selected as the optimal model for use in this research due to its capacity to recognise patterns in data without the need to specify the nature of interaction.

To explain a neural network's functioning – each model is made up of components known as neurons, arranged into layers corresponding to inputs, computations, and outputs. Neurons in each layer are connected to neurons in the next layer, with each connection given a weight representing its importance. Initially weights are assigned random values, but as the model trains and learns these are adjusted to improve model performance.

Data is introduced through the input layer, with each neuron calculating a weighted sum of inputs before applying an activation function (which transforms neuron outputs into values for the next neuron in the network). Activation functions enable non-linear relationships between input and output data. Data then undergoes feedforward propagation, where neurons receive previous layers' outputs, apply computations, and apply the activation function. Finally, an output is generated in the output layer.

After generating an output, the model calculates the loss (error) by comparing the predicted output to the actual output using a loss function. The model is then able to learn through backpropagation, wherein the model works from the output layer back to the input layer, calculating error for each layer as it goes and updating weights accordingly.

Neural network models can predict data classifications through a repeat training and testing process where the model is trained on a dataset (repeatedly performing forward propagation and backpropagation to update weights). During testing, the model is then able to make predictions on new, unseen data based on generalisation of its findings from the training data including the weights of connections. This enables a neural network model to classify data based on what it has learned.

## 2.3. ATR-FTIR Spectroscopy of Cochlear Fibrocyte

### Supernatant

#### 2.3.1. The Dxcover Sampling System

During this research, all FTIR spectroscopy conducted at the Keele University Guy Hilton Research Centre site made use of a novel sampling setup generously provided by Dxcover Ltd., Glasgow. This setup combined a Specac Quest ATR accessory with a Dxcover® Sampling Unit and Dxcover® Sample Slides to enable rapid benchtop sampling (Fig. 15). Dxcover® technology focuses on the development of liquid biopsies for early detection of cancer and other diseases, thus the provided kit was ideally applied in the present research, wherein it is employed for the analysis of cell supernatant samples.



**Figure 15: Accessories employed in the ATR-FTIR setup.**

**A) The Specac Quest ATR accessory. B) The Dxcover® Sampling Unit and sample slides.**

The Dxcover® Sample Slides employed in this research consisted of four individual silicon wafers labelled 0 to 3 per slide (Fig. 16). This setup and the way it was used enabled a ‘triplicate per slide’ arrangement. That is, three technical replicates of the same sample could be present on a single slide alongside a single blank wafer used for background. This significantly streamlined the sampling process when compared with typically employed methods.

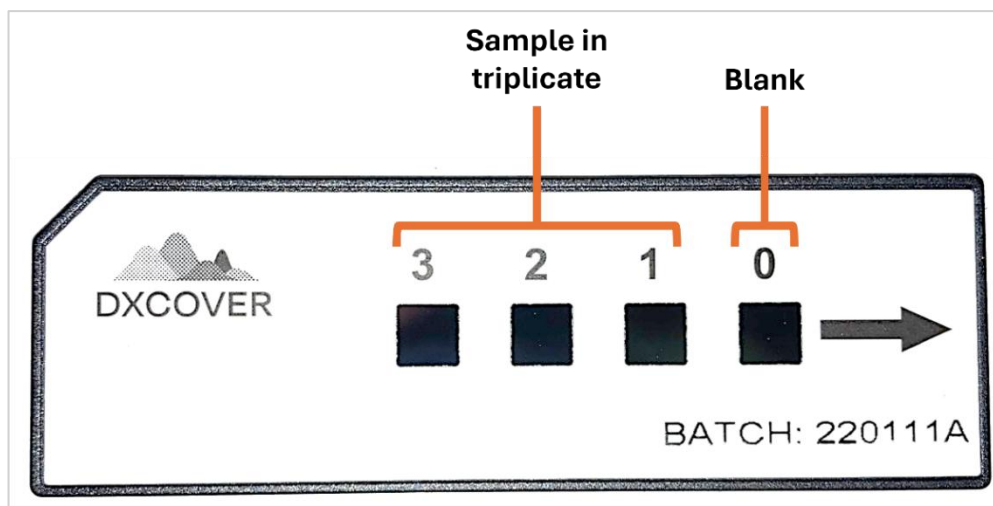


**Figure 16: A Dxcover® sample slide.**

**Photograph of a Dxcover® labelled according to the placement of samples and blank control.**

### **2.3.2. ATR-FTIR Sample Preparation and Sampling**

For ATR-FTIR spectroscopy, samples were prepared subject to specific experimental requirements in T25 flasks. Media samples from flask cell cultures were taken from populations of approximately 200,000 cells. Media-only samples were set up in flasks parallel to cell samples to ensure minimal variation from culture condition factors. Media samples were taken from cell culture flasks and relevant controls, centrifuged to separate any non-supernatant components, and 6µl of each pipetted onto the silicon wafers of Dxcover® Sample Slides (Dxcover). Each flask was sampled 3 times, with a single slide per sample employed and 3 available wafers on a slide forming a triplicate technical replicate as outlined in section 2.6.1. Samples were allowed to air dry in ambient conditions prior to measurement.

ATR-FTIR measurements were taken using a Thermo Scientific iS50 spectrometer coupled with the aforementioned Specac Quest ATR accessory onto which the Dxcover® autosampler was positioned. Dxcover® Sample Slides were loaded into the Dxcover® auto sampler for measurement.

Measurements were taken using Omnic software. Spectral parameters were set as follows: 128 co-added scans per spectrum with a resolution of 4cm<sup>-1</sup> across a 4000-400cm<sup>-1</sup> range. A background measurement was taken before each sample measurement using the same general parameters as

sample spectrum collection. All measurements were taken in absorbance mode with no corrections applied during sampling. Automatic atmospheric suppression was employed.

### 2.3.3. ATR-FTIR Data Processing and Analysis

As in Raman spectroscopy, ATR-FTIR data were pre-processed to reduce uncontrollable variation across samples. Following collection, spectra were opened in Omnic software and exported as .SPA files. All data processing and analysis was conducted in Orange Quasar software. Spectra were cut to remove noise where necessary, followed by a rubber band baseline correction. Data were then smoothed using Savitsky Golay (window 11, polynomial 2) and vector normalised. Finally, data were trimmed to regions of interest ( $400\text{-}3800\text{ cm}^{-1}$  for full spectra,  $400\text{-}1800\text{ cm}^{-1}$  for fingerprint,  $2800\text{-}3600\text{ cm}^{-1}$  for high wavenumber). Pre-processing steps are illustrated in figure 17 on overleaf.

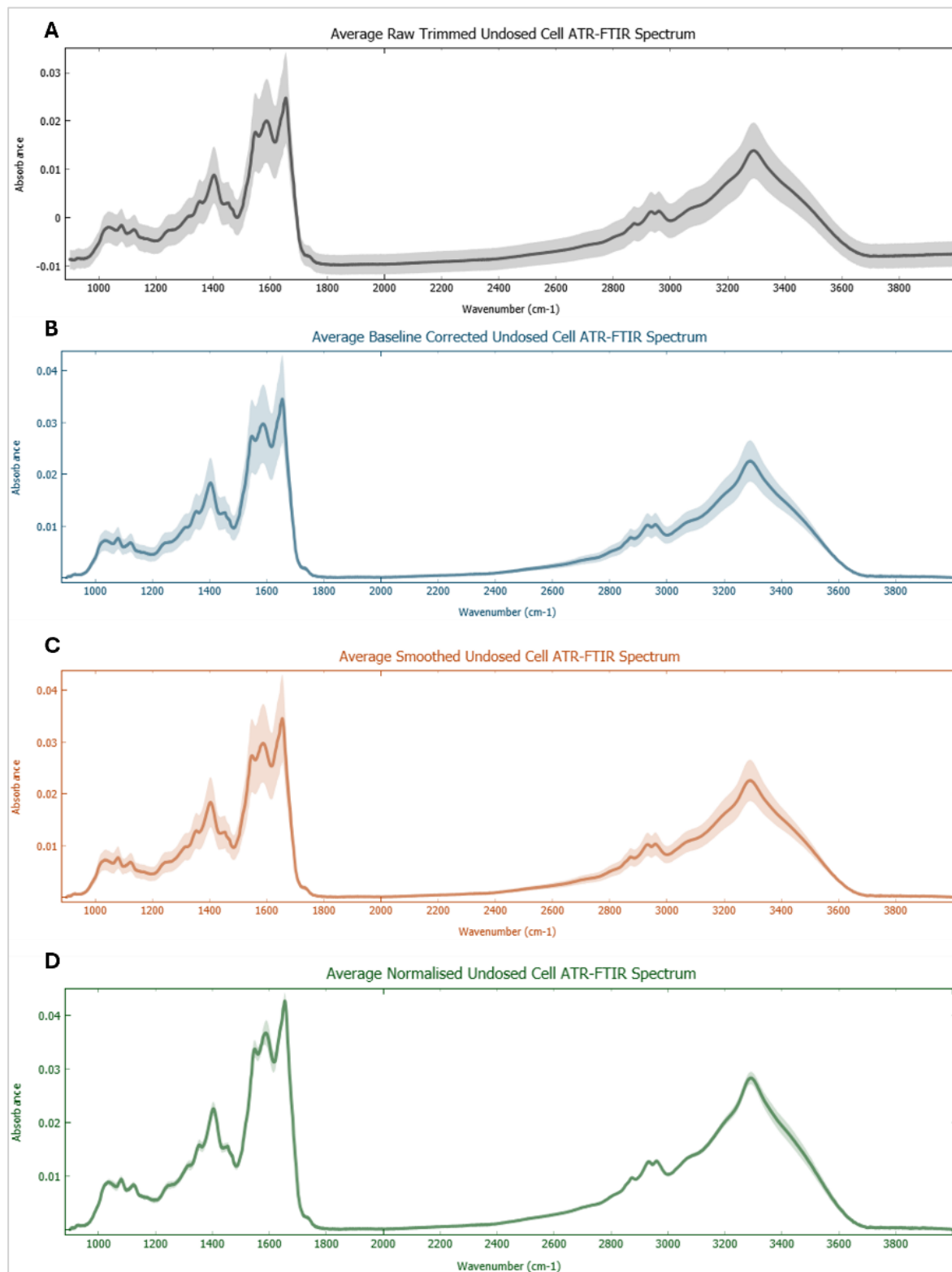


**Figure 17: Average ATR-FTIR spectra of cell samples at each pre-processing stage.**

**A) Trimmed raw spectrum. B) Rubber band baseline correction applied. C) Savitsky Golay smoothing applied. D) Vector normalisation applied.**

Second derivative spectra were generated by increasing derivative order at the Savitsky Golay smoothing stage. To counteract noise introduced by this, window was increased to 27. An example second derivative ATR-FTIR spectrum is shown in figure 18 below.

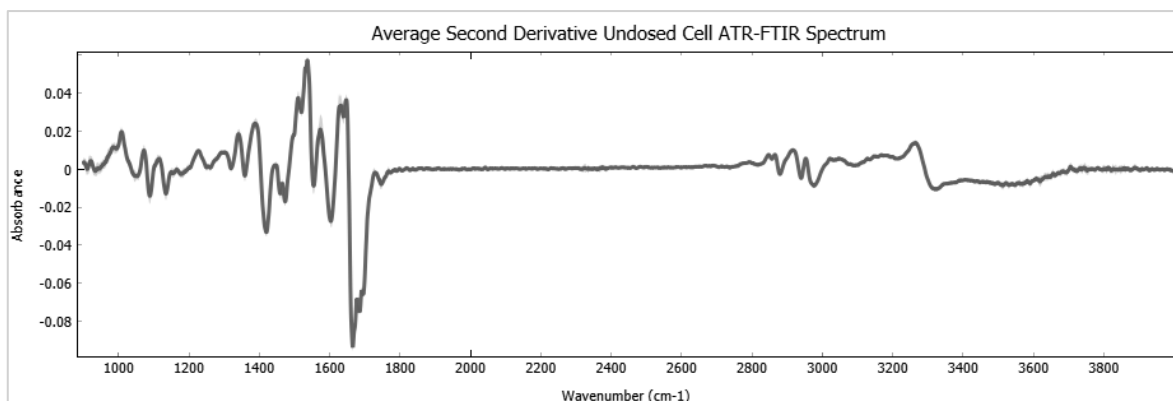


**Figure 18: Average second derivative ATR-FTIR spectrum of cell samples.**

Following pre-processing, data were analysed using Orange (Quasar) software. As for Raman data, manual peak identification was performed on average spectra, consulting second derivative spectra for clarity where applicable. Bands were assigned to bond vibrations and potential molecules through literature consultation (see table 4). PCA were conducted using the same methods as noted for Raman spectra in section 2.2.2., with associated loadings plots generated from components used to identify sources of variation.

**Table 4: ATR-FTIR band assignments.**

Wavenumber (cm <sup>-1</sup> )	Associated Bond Vibration	Molecular Family
<b>920-940</b>	DNA-linked deformations	Nucleic acids
<b>1030</b>	C-O stretching and C-O bending	Carbohydrates
<b>1070- 1105</b>	Phosphate group deformations	Nucleic acids/phospholipids
<b>1120-1240</b>	C-O stretching, C-OH antisymmetric stretching	Nucleic acids
<b>1305</b>	Amide III	Proteins
<b>1340</b>	CH <sub>2</sub> wagging	Lipids
<b>1400</b>	COO <sup>-</sup> symmetric stretching	Amino acids/fatty acids
<b>1450</b>	CH <sub>3</sub> antisymmetric stretching	Proteins
<b>1470</b>	CH <sub>2</sub> wagging	Lipids
<b>1520-1550</b>	N-H bending	Proteins
<b>1550</b>	Amide II	Proteins
<b>1615-1695</b>	C=O stretching	Proteins

<b>1650</b>	Amide I	Proteins
<b>1735</b>	C=O stretching of esters	Lipids
<b>2800-3100</b>	CH <sub>2</sub> stretching, CH <sub>3</sub> stretching, =CH stretching, amide B	Proteins/lipids
<b>3100-3600</b>	-OH stretching, -NH stretching, amide A.	Proteins

## 2.4. Synchrotron FTIR Spectroscopy (S-FTIR) and

## Hyperspectral Raman

### 2.4.1. Synchrotron Instrumentation and Sample Preparation

S-FTIR data were obtained from the Diamond Light Source (Oxford) using beamline station B22 (MIRIAM). This station is equipped with a Hyperion 3000 microscope (Bruker) and a Bruker 80V FTIR spectrometer, coupled with a liquid nitrogen managed 100 x 100µm<sup>2</sup> MCT/A detector. Spectra and images were obtained via a 36x Schwarzschild objective, managed by Opus software (Bruker). Hyperspectral benchtop Raman measurements were also conducted at the Diamond facility. Further details of the methods employed may be found in chapter 4, which focuses on the work conducted at Diamond Light Source.

### 2.4.2. Synchrotron Data Processing and Analysis

To enable comparison across samples taken using both standard benchtop and micro-Raman/synchrotron-FTIR instruments, data were subjected to the same pre-processing as applied to benchtop instrument results. This included a normalisation step to enable comparison. PCA were conducted in Orange Quasar software, with associated loadings plots generated from components. From S-FTIR data, predictive models were generated using Quasar software. Visualisations of Raman hyperspectral data were generated using Quasar software, including k-means analyses. Further particulars are discussed in chapter 4.

## 2.5. SIFT-MS of Cochlear Fibrocytes

### 2.5.1. SIFT-MS Instrumentation

Measures of VOCs in sample headspace were taken in house at Keele University using a Transpectra Profile 3 SIFT-MS instrument, from Instrument Science, UK. As described in chapter 1, selected reagent ions,  $\text{H}_3\text{O}^+$  and  $\text{NO}^+$ , were produced via microwave discharge through air and isolated by sorting via mass quadrupole filter. Within the SIFT-MS instrument, selected ions were reacted with sample headspace (taken up via heated sampling line) in helium (acting as an inert carrier gas) at a controlled flow rate in order to yield identifiable and quantifiable products for which absolute concentration may be calculated. SIFT-MS identification of product ions is conducted by mass spectrometer and counts of ions are conducted by electron multiplier, with concentration calculations conducted in real time by the attached computer system.

SIFT-MS was used in two sampling modes for this research: multi-ion monitor (MUI) mode and full scan (FS) mode. MUI mode allowed analysis of chosen analytes based upon an uploaded kinetic library, compiled based upon numerous ion-molecule reactions indicated in literature. FS mode allowed general analysis of analytes in the  $m/z$  range 1-180.

### 2.5.2. SIFT-MS Vessel Selection for Cell Sampling

Before beginning any SIFT-MS observation, viability counts were conducted on cells seeded into various containers to ascertain the most suitable vessel for SIFT-MS. Qualities assessed were cell viability, liquid capacity, and available headspace for sampling. The ideal container was that which yielded the best viability, the largest surface area for cell adherence and the largest headspace for VOC accumulation and sampling. Though larger headspaces may result in dilution of samples, they are preferable to smaller alternatives to allowing greater numbers of measurements to be taken.

This was conducted using MG63 rather than cochlear fibrocytes due to their rapid growth and lack of need for animal sacrifice. Samples of 15,000 and 150,000 cells were seeded into either- a 12mL vial, a 25mL bottle, a 30mL bottle, a 70mL bottle, or a 150mL bottle (all of which had rubber septum lids which could be pierced by the SIFT-MS instrument's sampling head) with 20mL media added to each. After incubation at 37°C (5% CO<sub>2</sub>) overnight, cells were retrieved and counted, using the trypan blue live/dead exclusion method.

To retrieve cells from bottles, supernatant media was first removed and kept separately in labelled 50mL conical test tubes. 3mL 8:6 trypsin: PBS was then added, and samples incubated for 10 minutes at 37°C (5% CO<sub>2</sub>) with manual aggravation. Samples were quenched with their corresponding supernatants and added to tubes as before. Samples were then centrifuged at 1200rpm for 5 minutes. Each pellet was resuspended in the 300µL of supernatant media retained. Each cell suspension was transferred to an Eppendorf tube and centrifuged at 1200rpm for 3 minutes. Following centrifugation, 200µL of supernatant was removed and each pellet was resuspended in the remaining 100µL. Live/dead cell counts were performed using a haemocytometer and trypan blue at a 1:1 ratio. Cells that appeared bright under trypan blue were counted as healthy, while those that stained dark blue were counted as dead/non-viable. Percentage viability was obtained by dividing live cell number by total cell number, with viability results averaged across conditions (Table 5).

**Table 5: Table of percentage viability for each potential SIFT-MS vessel.**

<b>Bottle Type</b>	<b>Average % Cell Viability</b>	<b>Likely Capacity</b>	<b>Media Available Headspace</b>
<i>150mL Glass Bottle</i>	78%	20mL	130mL
<i>70mL Glass Bottle</i>	43%	20mL	50mL
<i>30mL Glass Bottle</i>	40%	10mL	20mL
<i>25mL Glass Bottle</i>	75%	10mL	15mL
<i>12mL Glass Vial</i>	67%	5mL	5mL media

From this viability assessment, 150mL glass bottles were chosen as the best vessel for SIFT-MS investigations of cells. This vessel was employed in all SIFT-MS investigations throughout the research.

### 2.5.3. SIFT-MS Low Cell Number Testing

Following vessel selection, samples of MG63 cells were created in triplicate in 150mL bottles with black rubber septum lids, with either 15,000 cells, 150,000 cells or control media only (i.e. 9 bottles per experiment), in order to verify the ability of SIFT-MS to detect cell presence at low, physiologically relevant cell numbers (around 15,000 cochlear fibrocytes *in vivo*). Samples were seeded, air purged using dry compressed air, and incubated at 37°C for approximately 16 hours before measurement to allow sufficient accumulation of headspace<sup>[130]</sup>. During measurement, samples were heated in a 37°C water bath. Samples were normalised to a water vapour level of 4% (appropriate for wet samples) using in-software flow rate adjustment.

Measures of VOCs in the headspace of MG63s were conducted (using Transpectra Software, Transpectra UK), with observations across  $\text{H}_3\text{O}^+$  and  $\text{NO}^+$  precursors for compounds of  $m/z$  1-180. Multi-ion monitor mode samples were taken using an uploaded kinetic library (Appendix B) for 40 seconds in each bottle for both reagent ions. Average scans (each scan= average of 3 20 second scans) of each sample were also taken for both reagent ions. Headspace in bottles was topped up using a purge bag containing dry compressed air between each measurement in order to prevent depletion of gas headspace and maintain relative compound concentrations where possible.

Preliminary results confirmed the suitability of SIFT-MS in the detection of low, physiologically relevant cell numbers, with similar signal distinction proven possible at 15,000 and 100,000 cells per sample. These results are not included in the present thesis.

### 2.5.4. Fibrocyte Sample Preparation and SIFT- MS Sampling

As in MG63 tests, cochlear fibrocyte and associated control media samples were created in triplicate in 150mL bottles with black rubber septum lids, with conditions and number of samples employed dependent upon experiment (outlined in relevant experimental chapter methods). In general, samples were seeded, air purged using dry compressed air, and incubated at 37°C for approximately 16 hours before measurement. Where additional processing (e.g. incubation of

inflammatory agents) was required, 16 hour incubation time was factored into this (see relevant experimental chapters). As before, during measurement, samples were heated in a 37°C water bath and normalised to a water vapour level of 4% for wet samples using in-software flow rate adjustment.

Measures of VOCs in sample headspace were conducted (using Transpectra Software, Transpectra UK), with observations across  $\text{H}_3\text{O}^+$  and  $\text{NO}^+$  precursors for compounds of  $m/z$  1-180. Multi-ion monitor mode samples were taken using the uploaded kinetic library for 40 seconds in each bottle for both reagent ions. Average scans (each scan= average of 3 20 second scans) of each sample were also taken for both reagent ions. Headspace in bottles was topped up using a purge bag containing dry compressed air between each measurement.

### 2.5.5. SIFT-MS Data Processing and Analysis

As noted above, SIFT-MS sampling was conducted either in the form of a 40 second duration continuous abundance/time profile (MUI) or an average scan (3 scans of 20 seconds) of abundance per sample in counts/second (FS). SIFT-MS acquired profiles were handled in either SIFT time profile viewer or SIFT mass spectra software (for MUI and FS data respectively).

In time profile software, MUI data was opened and central 30 second samples of each 40 second time profile snippet logged individually into a Microsoft Excel 2016 sheet, ensuring data presentation in parts per billion (ppb). To ensure accurate relative quantification of compounds, samples were normalized via flow rate alteration/water value correction to 4% (wet samples) or 2% (dry samples) to account for variations in sample humidity and environment. Water correction percentages were set based on the average correction applied to the liquid to headspace ratio employed. Numerical data from time profile snippets was exported in .CSV format to Microsoft Excel 2016 for compilation and appropriate formatting. Statistical testing of MUI data was conducted via Mann Whitney U test or Kruskal Wallace H test (depending upon condition numbers), performed in SPSS data analysis software to a  $p \leq 0.05$  significance level. Bar charts presenting MUI data were generated in Microsoft Excel 2016.

In FS software, scans were normalized and averaged, before exporting into Microsoft Excel 2016 for compilation and formatting. For  $\text{H}_3\text{O}^+$  FS data,  $m/z$  17-180 were presented, with precursor isotopologues removed:  $m/z$ s 19, 20, 21, 30, 32, 34, 37, 38, 39, 48, 55, 56, 57, 66, 73, 74, 75, 91.  $\text{NO}^+$  data were treated similarly, with removal of  $m/z$  30.

FS data were generally presented as heat maps generated using Quasar software. Compounds of interest were manually identified based on literature.

### 2.5.6. Mann Whitney U Test and Kruskal Wallis H Test

Significance testing in the present research was conducted via Mann Whitney U or Kruskal Wallis H test. The Mann Whitney U test was employed when comparing two conditions, and the Kruskal Wallis H test was employed when comparing more than two conditions. These tests were chosen as they act as non-parametric alternatives to the Student's T-test and ANOVA respectively and data are not assumed to be normally distributed. These statistical tests allow comparison of means across sampling conditions, enabling significant differences (e.g. in compound levels) to be identified.

## 2.6. Cerumen Investigations

### 2.6.1. Human Cerumen Samples

All human cerumen samples employed in this research were commercially sourced via Caltag Medsystems (Buckingham). As samples were purchased through a commercial supplier and no patients were directly involved in the research, no patient-focused ethical clearance was necessitated. Nonetheless, ethical clearance for use of the biofluid was obtained via Keele University's Faculty of Medicine and Health Sciences Research Ethics Committee (Appendix C).

Due to the potential for tissue presence in cerumen samples and the resulting classification as a 'relevant material' (point 54, Human Tissue Act, 2004), all samples were handled, stored, transported and disposed of according to the Human Tissue Act (2004). Samples arrived on cotton swabs and were maintained as such, in the containers in which they arrived, until use. Samples were stored at room temperature, in their sealed containers to prevent effects of humidity variations.

## 2.6.2. Vibrational Spectroscopy of Cerumen

For the purposes of Raman spectroscopy, a single cerumen sample was transferred from the cotton swab upon which it arrived to a  $\text{CaF}_2$  substrate. No fixation or further treatment was applied. Sampling was conducted under the same methods as cellular samples (outlined in chapter 2.2.1), with 100 points sampled across the wax area. Data work was conducted as outlined in chapter 2.2.2 using Quasar software.

In preparation for ATR-FTIR, cerumen swabs trialled in both wet and 'processed' states. Dry wax was not subjected to any preparation. 'Processed' wax was submerged in 200  $\mu\text{L}$   $\text{dH}_2\text{O}$  and heated to 37°C for 10 minutes. Vials of  $\text{dH}_2\text{O}$  containing cerumen were then centrifuged at 1200RPM for 3 minutes. Supernatants were discarded and samples vortexed for 10 seconds followed by thorough mixing. Mixed samples were pipetted onto Dxcover® sample slides (6  $\mu\text{L}$  per silicon wafer) and air dried. Sampling was conducted under the same methods as cellular samples (outlined in chapter 2.3.2), with 100 points sampled across the wax area.

## 2.6.3. Headspace Analysis of Cerumen

To investigate the headspace of cerumen samples, SIFT-MS was employed. Cerumen samples on swabs were placed into 150mL glass bottles as used in cellular investigations, with swab stems trimmed consistently to allow sealing of bottles. Samples were air purged with dry compressed air prior to sampling to remove laboratory air and sealed with a black rubber septum lid to allow VOC accumulation. Samples were then incubated for 16 hours at 37°C.

Following incubation, measures of VOCs in sample headspace were taken as outlined in chapter 2.3.4. Data were processed as detailed in chapter 2.2.5, with Mann Whitney U test employed to test for differences between wax and non-wax conditions. Water correction was conducted at 2% rather than 4% to account for the use of dry samples.

Swab only 'blanks' were conducted alongside swabs with cerumen to act as a control. Blank swabs were prepared in the same manner as those containing sample.

### 3. Characterisation of Healthy and Inflamed Cochlear Fibrocyte Cultures by Raman Spectroscopy and ATR-FTIR

---

#### 3.1. Introduction

##### 3.1.1. The Healthy Cochlear Fibrocyte State

As discussed in section 1.4.1, the ability of sensory cells within the inner ear to depolarise and transduce signals is reliant upon the maintenance of ionic differences within the fluids of the *scala vestibuli*, *scala media*, and *scala tympani*. In their healthy state, the balance of such ionic differences is maintained by cochlear fibrocytes. To reiterate the information overviewed in chapter 1, high sodium, low potassium perilymph is contained within the upper and lower chambers, whereas low sodium, high potassium endolymph is contained within the central chamber <sup>[1, 37]</sup>, with the difference between ionic concentrations present across these chambers generating an 8090mV homeostatic trans-epithelial potential in the *scala media* <sup>[38]</sup>. This potential, the endolymphatic/endocochlear potential (EP), ensures that the endolymph within the central cochlear chamber has the appropriate potassium and sodium concentrations to facilitate depolarisation of hair cells and transmission of signals to auditory nerves.

##### 3.1.2. Cochlear Fibrocyte Classification

Cochlear fibrocytes, though primarily located in the spiral ligament (some occur in the spiral limbus) may be sub divided into five types (type I, type II, type III, type IV, type V) dependent upon their location (Fig. 19). Classification is also dependent upon expression of features including transporters, enzymes and channels <sup>[44,46]</sup>. The variation between these sub-types could potentially produce detectable differences when aiming to non-invasively identify fibrocyte damage, thus all sub-types must be considered.

Type I fibrocytes are found directly adjacent to the *stria vascularis* <sup>[40]</sup>. Like the majority of subtypes, these fibrocytes are also known to express the glutamate-aspartate transporter (GLAST), indicating a role in glutamate homeostasis <sup>[133]</sup>. This is consistent with the context of auditory function, as glutamate is the primary afferent neurotransmitter of the inner ear <sup>[134]</sup>. Additionally, type I enact

their role in potassium recycling via the expression of carbonic anhydrase (CA) and creatine kinase (CK), which convert  $\text{H}_2\text{O}$  and  $\text{CO}_2$  to  $\text{H}^+$  and  $\text{HCO}_3^-$ , and phosphate to ADP respectively.  $\text{H}^+$  and  $\text{HCO}_3^-$  exchange for sodium and potassium, contributing to fluid ion content regulation. Conversion of phosphate to ADP allows ATP production, enabling potassium recycling function [42, 43, 48].

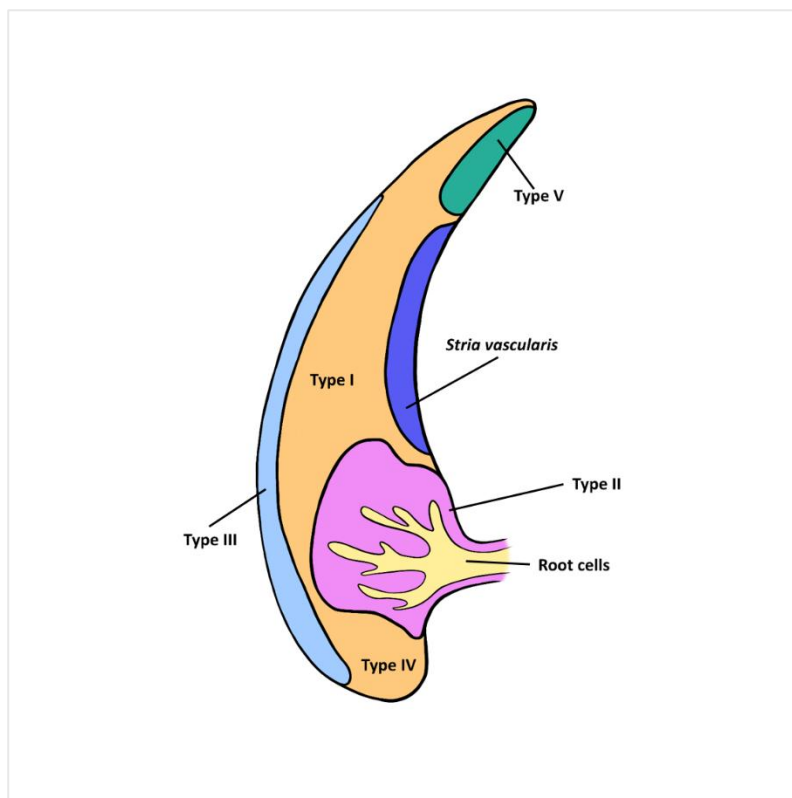


**Figure 19: Fibrocyte regions within the spiral ligament.**

**Diagram showing locations of fibrocyte sub-categories within the cochlea. Type I- lateral to stria vascularis; type II- lateral to spiral prominence epithelium; type III- marginal region; type IV- basilar crest region; type V- supra-strial (adapted from Kelly *et al.*, 2012).**

Type II fibrocytes are found at the point where the basilar membrane and LW intersect. This type of fibrocyte is known to express potassium uptake transporters ( $\text{Na}^+$ ,  $\text{K}^+$ -ATPases) enabling manipulation of local ion concentrations, as well as structural specialisation for ion pumping [40, 44, 45, 135]. This is evident of a significant role in potassium recycling. GLAST transporter expression across all SLFs is the highest in this sub type, suggesting a high level of glutamate homeostasis [133].

Type III fibrocytes, or tension fibrocytes (a name earned due to their role in basilar membrane contractility manipulation) are found in the marginal region of the spiral ligament [39, 136]. With a role in control of the basilar membrane, confirmed across multiple mammalian species, type III fibrocytes

demonstrate an effect on the tuning of hair cells, thus is it not beyond possibility that damage to this type in particular may exacerbate hearing losses without additional damage to other subtypes. Type III, like type I fibrocytes express CA and CK, as well as low levels of GLAST transporters<sup>[44]</sup>. In research it would appear that type III are the most prevalent and best identified sub type, with anti-aquaporin staining often used to classify the type *in vitro*<sup>[39, 40, 136]</sup>.

As there is limited research in the area, it is unclear whether the apparent prevalence of type III fibrocytes *in vitro* is due to their hardness in comparison to other sub-types, whether they serve as a base type from which other fibrocyte classifications stem, or due to another reason entirely. Thus, where modelling of fibrocyte death *in vitro* is concerned and where experimental time allows it would be prudent to trial different conditions, LW sectioning methods, and employ samples from a range of animal ages in aims to cover as broad a range of fibrocyte sub-types as possible.

Type IV fibrocytes are found in the basilar crest region at the lower point of the LW. They are known to express potassium uptake transporters Na<sup>+</sup>, K<sup>+</sup>-ATPase and Na<sup>+</sup>,K<sup>+</sup>,2Cl<sup>-</sup>-cotransporter (NKCC) on their membranes, as well as CA and CK internally, similarly to type II<sup>[40, 44, 135]</sup>. However, where potassium recycling function is concerned, type IV fibrocytes are suggested to serve little purpose due to their relative lack of connexins<sup>[137]</sup>. Like most other types, type IV fibrocytes express GLAST<sup>[133]</sup>.

Finally, type V fibrocytes primarily occur at the highest, innermost point of the LW, directly above the *stria vascularis*. Initially, it was suggested by suggestion by Qu *et al.*<sup>[138]</sup> that these fibrocytes showed low numbers of Na<sup>+</sup>, K<sup>+</sup>-ATPase transporters than other types. However, it has since been demonstrated that expression of these transporters in type V fibrocytes is of a similar level to that in type II<sup>[40]</sup>. Like other sub-types, type V demonstrate CA and CK expression, as well as the second highest GLAST expression across sub-types<sup>[44,133]</sup>.

In general, it is clear that fibrocytes play fundamental roles in auditory function, particularly where EP generation, tension regulation, and glutamate homeostasis are concerned. From this, it is possible to confirm that fibrocyte degeneration is a causative factor in many hearing loss types, metabolic ARHL in particular<sup>[9, 58]</sup>.

### 3.1.3. Traditional Methods of Cochlear Fibrocyte Observation

As outlined above, cochlear fibrocytes are typically distinguished into 5 sub-types based upon their location and on the expression of markers such as ion transport channels. As such, cells are typically characterised and monitored via the use of immunocytochemistry of cultured cells and tissue slices to identify sub type and track changes. Common proteins targeted for immunocytochemistry are outlined in table 6 below.

**Table 6: Fluorescence markers of cochlear fibrocytes (Adapted from Furness, 2019)**

Protein	Type I	Type II	Type III	Type IV	Type V
<b>Caldesmon</b>	-	-	X	-	-
<b>S-100</b>	X	X	-	-	X
<b>Na, K-ATPase</b>	-	X	-	-	X
<b>Ca, ATPase</b>	X	-	-	-	-
<b>Na, K, Cl-cotransporter</b>	-	X	-	X	X
<b>Kir5.1</b>	-	X	-	X	X
<b>AQP1</b>	-	-	X	-	-
<b>Carbonic anhydrase</b>	X	-	X	X	X
<b>Creatine kinase</b>	X	-	X	X	X
<b>CTGF</b>	-	-	-	X	-

### 3.1.4. Modelling Cochlear Fibrocyte Inflammation *In vitro*

As discussed in chapter 1, a particular pathology of interest in ARHL investigation is inflammation, with inflammatory markers such as IL-6 associated with inflammaging and ARHL<sup>[154]</sup>. It is understood that such inflammation contributes to further pathological development including mitochondrial damage, affecting the long term functioning of cells and diminishing potential for recovery<sup>[49]</sup>. In turn, mitochondrial damage in fibrocytes is known to lead to the onset of further inner ear damage and symptomatic ARHL<sup>[50]</sup>.

Where simulation and detection of the inflammatory state *in vitro* are concerned, it is of note that the majority of inflammaging appears to arise from similar mechanisms and proteins of interest (Table 7)<sup>[155]</sup>. A selection of these markers are used presently to produce an *in vitro* inflammatory state for detection- it should be noted that IL-6 particularly has been highly implicated in age-related conditions and, in previous studies of ARHL inflammation, has been shown as expressing within the spiral ligament<sup>[156]</sup>. This is taken into account when seeking to verify inflammation in cochlear fibrocytes.

**Table 7: Cytokines of interest in inflammation investigations (Adapted from Michaud *et al.*, 2013)**

<i>Item</i>	<i>Role in vivo</i>
<i>IL-1(IL-1<math>\beta</math> particularly)</i>	Essential to pro-inflammation cellular function. Associated with acute and chronic inflammation, among the first activated in the inflammatory response. Start of inflammatory cascade. Regulates cell proliferation and differentiation.
<i>IL-6</i>	Pro-inflammatory cytokine linked to aging tissue and hearing associated conditions (diabetes particularly). Commonly used to assess level of inflammation in inflammaging studies.
<i>TNF-<math>\alpha</math></i>	Central circulating factor that proliferates under pro-inflammatory conditions. Leads to leukocyte binding and promotes inflammatory response.
<i>TGF-<math>\beta</math></i>	Participates in chronic inflammation in ageing tissue. Assists in regulating cell regeneration, angiogenesis, and recruitment of other pro-inflammatory proteins.
<i>CRP</i>	Acute inflammatory protein that increases up to 1,000-fold at sites of infection or inflammation. Involved in the production of particularly interleukin-6 and tumour necrosis factor- $\alpha$ .
<i>IL-8</i>	Pro inflammatory chemoattractant cytokine produced by a variety of cells. Attracts and activated neutrophils in inflammatory regions.

### 3.1.5. The Role of TNF- $\alpha$ in Cochlear Fibrocyte Inflammation

In research to date, TNF- $\alpha$  has been highlighted as a crucial component of hearing loss pathogenesis. However, TNF- $\alpha$  does not appear to lead to cell death in cochlear sensory cells directly unless present in extremely high concentrations <sup>[157-159]</sup>. This has led some groups to suggest the presence of other molecules which may sensitise cells to TNF- $\alpha$ .

However, it may also be suggested that the death of cochlear sensory cells in such inflammatory conditions is due to dysfunction and death of support cells such as cochlear fibrocytes. This circumstance seems highly likely as research shows evidence of spiral ligament fibrocytes upregulating TNF- $\alpha$  in response to the inflammatory state <sup>[159]</sup>.

Such involvement of TNF- $\alpha$  has been highlighted in studies using knockout animals but efforts to induce cellular mitochondrial alteration via cytokine dosing do not appear to have been made to date <sup>[59]</sup>. Thus, the present section of research investigates the inflammation of cochlear fibrocytes by TNF- $\alpha$  dosage and the detection of downstream effects using methods previously unexplored in the field.

### 3.1.6. IL-1 $\beta$ and the NLRP3 Inflammasome

Additional to TNF- $\alpha$ , the cytokine interleukin-1 $\beta$  (IL-1 $\beta$ ) is significantly implicated in inflammation-associated inner ear damage <sup>[162]</sup>. As previously highlighted, IL-1 $\beta$  plays a fundamental role in the onset and perpetuation of the inflammatory state *in vivo*, contributing to the earliest stages of the inflammatory response in both acute and chronic inflammation.

In identifying the source of IL-1 $\beta$  upregulation in inflammation, complexes known as inflammasomes have become a target for investigation <sup>[163]</sup>. These complexes trigger the activation of caspase-1, a proteolytic enzyme responsible for the maturation of pro-inflammatory cytokines IL-1 $\beta$  and IL-18 from their precursors <sup>[164, 165]</sup> as well as the onset of an inflammation-associated form of cell death known as pyroptosis <sup>[166]</sup>. The activation of inflammasome complexes is triggered in response to either pathogen-associated or danger-associated molecular patterns (PAMPs or DAMPs), and is critical in inflammatory responses to pathogen invasion and other tissue damage. Of these patterns, DAMPs are of particular interest in the present research. DAMPs may be defined as endogenous signals of danger released by damaged cells during non-infectious cases of inflammation (with infectious inflammation leading to PAMPs) <sup>[167]</sup>.

Of those identified, the NLRP3 inflammasome is arguably the most well-understood, with variations to the gene encoding the complex highly implicated in genetic sensorineural hearing loss and other diseases that may lead to hearing deterioration such as cryopyrin-associated periodic syndrome (CAPS) <sup>[168, 169]</sup>.

The association of NLRP3 and IL-1 $\beta$  secretion in hearing loss is of particular interest to the present research due to the potential for the application of anti-interleukin-1 therapies, particularly in hearing losses that are not genetically predisposed such as ARHL <sup>[169]</sup>. It may be comfortably stated in

this case, therefore, that the detection of inflammation mediated by NLRP3 activation and resultant IL-1 $\beta$  secretion may allow more timely and targeted application of anti-interleukin-1 therapies.

Though other cochlear tissues such as the Organ of Corti lack macrophages <sup>[170, 171]</sup>, research has demonstrated that macrophages are present in all areas of the spiral ligament though their distribution varies through this tissue. Research suggests that macrophages of the spiral ligament are found most abundantly in those regions corresponding to type II and IV fibrocytes <sup>[172-175]</sup>, with a relatively lower concentration of macrophages in the areas immediately adjacent to the *stria vascularis* <sup>[176]</sup>, though no specific link between fibrocyte region and macrophage distribution is suggested.

For the purposes of the present research, wherein cultured fibrocytes are suggested to be of type II, IV, V, the presence of macrophages in local native tissue is highly likely. As such, activation of the NLRP3 complex may be relevant when considering lateral wall inflammation associated with these cochlear fibrocyte sub-types and is highly relevant where inflammaging is concerned <sup>[177]</sup>.

### 3.1.7. Anti-IL-1 Therapies Revisited

As mentioned in chapter 1, anti-interleukin-1 therapies are a potential target for the treatment of inflammation in ARHL. Such therapies, as discussed, prevent signal transduction of IL-1 $\beta$  and alleviate inflammatory symptoms. With this in mind, further necessity for the present section of research is evident, with the detection of IL-based inflammatory changes necessary to facilitate timely, targeted anti-interleukin-1 therapies.

Should the present section of research demonstrate capacity for minimally-invasive IL-1 $\beta$  detection, it is additionally feasible that the present methods be employed in the monitoring of therapeutic effects. That is, the present techniques, combined with appropriate patient sampling methods, may be used to follow-up anti-interleukin-1 therapies and ensure their success without reliance on symptom-based assessment as is currently typical of hearing testing.

### 3.1.8. Detection of Cochlear Fibrocyte Health via Raman and ATR-FTIR Spectroscopy

As a relatively small research niche when compared with studies into sensory cells of the inner ear, it is not surprising there have been very few investigations of cochlear fibrocyte health through the methods explored in the present research. To date, it would appear that there have been no studies involving the examination of cochlear fibrocytes via Raman spectroscopy or FTIR spectroscopy, with the most relevant studies to ARHL being those by Höhl *et al.* (2019) previously discussed.

Despite this, cellular health studies having been conducted for countless other cell types via the methods targeted, justifying their use in fibrocyte analyses. Nonetheless, it is safe to say that a distinct 'expected profile' is neither in place for vibrational spectra of cochlear fibrocyte cells or supernatant, with this research marking the first steps towards establishment of such profiles. From this, it is hoped that a deeper understanding of cochlear fibrocyte inflammatory pathology may be gleaned, and that this may aid in the development of diagnostic and therapeutic efforts moving forward.

With this in mind, the first stage of the research focused upon the characterisation of cochlear fibrocytes in their healthy and inflamed cultured states by way of Raman spectroscopy and ATR-FTIR spectroscopy.

## 3.2. Chapter Aims

The aims of this section of research are as follows:

1. Successfully explant, culture and, by way of immunocytochemistry, characterise murine cochlear fibrocytes.
2. Establish a spectral profile of murine cochlear fibrocytes in an untreated state using Raman Spectroscopy.
3. Establish a spectral profile of untreated murine cochlear fibrocyte culture supernatant using ATR-FTIR.
4. Induce inflammation-like responses in cochlear fibrocyte cultures using TNF- $\alpha$  and IL-1 $\beta$ .

5. Establish spectral profile of cytokine-dosed cochlear fibrocytes and distinguish between healthy and inflamed cells via Raman Spectroscopy.
6. Establish spectral profiles of cytokine -dosed murine cochlear fibrocyte culture supernatant and distinguish between healthy and inflamed cells via ATR-FTIR.

### 3.3. Materials and Methods

#### 3.3.1. Cochlear Fibrocyte Explantation, Growth and Maintenance

As outlined in section 2.1, murine cochlear fibrocytes were retrieved from CD/1 mice using methods adapted from the gerbil dissection protocol of Gratton *et al.* [89]. Mice were euthanized via injection of 0.05mL sodium pentobarbital, heads were detached and bisected sagittally, brains removed and otic capsules detached from the skull. Cochlear shells were peeled away to access spiral ligaments, which were removed to 6 well plates, topped with a coverslip and covered with culture media. Coverslips were removed once ligaments had adhered to plates. Ligaments were removed after around 1-2 weeks. Cells were cultured until confluent patches formed in wells, then split for use in experiments or frozen for future use according to the protocols outlined in section 2.1.3.

All cochlear fibrocyte cell culture was conducted under sterile conditions in a class 2 BSC. Cells were grown in a 37°C (5% CO<sub>2</sub>) incubator with media changes every other day. Cells were passaged and stored as outlined in section 2.1.3.

#### 3.3.2. Observation of Cell Outgrowth from the Spiral Ligament

Throughout the cell growth process, regular observations of cultures were made using via light microscopy conducted using an Olympus CKX41 microscope with a Q-Imaging Micropublisher 5.0 RTV camera attachment. Observations focused on examining cell population number, cell morphology, and general culture health.

To further visualise the outgrowth of cochlear fibrocytes from murine spiral ligaments *in vitro*, Vybrant™ Cell-Labeling Solution was employed. Following explantation, plating and topping with coverslips as detailed above, ligaments were allowed to sit for 2-3 hours before the removal of growth

media from wells and brief air drying in a BSC. Staining medium was prepared by adding 5  $\mu$ L of dye labelling solution to each 1 mL of pre-prepared growth medium. Staining medium was pipetted in increments of 100  $\mu$ L into the well until the coverslip and ligament pieces were fully immersed. Plates were then incubated at 37°C for 20 minutes to allow dye uptake. Following incubation, staining medium was removed and wells were washed 3 times by adding growth media to cover contents, incubating for 10 minutes, then repeating. The final addition of growth media was left on cells for incubation under observation using an Echo Cellcyte live cell analyser.

### 3.3.3. Characterisation of Cultured Cells by Immunocytochemistry

For characterisation via ICC, fibrocyte secondary cultures were established in 24-well plates alongside parallel MG63 cell line cultures (cultured as outlined in chapter 2) for use as negative controls. Cells were fixed in 4% PFA for 15 minutes followed by 3 washes with PBS. Fixed cultures were then incubated with 0.25% triton-X 100 in PBS with 1% Donkey Serum (DS) for 30 minutes. Cells were then washed once again 3 times with PBS. Washed samples were pre-blocked in 10% DS-PBS for 30 minutes followed by the addition of primary antibody diluted in 1% DS-PBS at room temperature for 2 hours. The primary antibodies selected were against AQP1 (rabbit anti-mouse, Sigma Aldrich, 1:100 dilution), S-100 (sheep anti-mouse, R&D Systems, 1:100 dilution) and NaK-ATPase (goat anti-mouse, Furness Lab, 1:50 dilution) to enable detection of all 5 fibrocyte sub types.

To enable further control in analysis and ensure awareness of any stain interactions and natural fluorescence, well-plates were stained as follows: 3 wells with no primary antibody applied (secondary only), 3 wells with no secondary antibody applied (primary only), 3 wells with AQP1 staining only, 3 wells with S100B staining only, 3 wells with NaK-ATPase staining only, 6 wells with both primary and secondary antibody for each target applied (triple staining).

Following primary incubation, cells were washed 3 times in 1% DS-PBS. Appropriate secondary antibody diluted in 1% DS-PBS was added to cells at room temperature for 2 hours (donkey anti-rabbit rhodamine (Sigma Aldrich), donkey anti-sheep far red (Sigma Aldrich), donkey anti-goat FITC (Sigma

Aldrich) – 1:100 dilution for all). Cells were then washed 3 times in PBS. DAPI staining solution (Sigma Aldrich) was added at room temperature for 5 minutes followed by 3 washes with PBS.

### 3.3.4. Induction of Inflammation and Confirmation of the Inflammatory State

Based upon the markers indicated (Table 6) and the influence of TNF- $\alpha$  and IL-1 $\beta$  in ARHL, it was decided that the *in vitro* inflammatory state for the present research be induced by addition of TNF- $\alpha$  or IL-1 $\beta$  to culture media. To do this, standard cochlear fibrocyte culture media was dosed with 1ng/mL, 5ng/mL, 10ng/mL, 25ng/mL and 50ng/mL of cytokine (TNF- $\alpha$  or IL-1 $\beta$ ) solution to produce conditions referred to as lowest, low, medium high and highest dosage respectively. Cells were then labelled and incubated under standard culture conditions in this media. Following a period of 24 hours incubation (37°C, 5% CO<sub>2</sub>) with dosed media, samples were subjected to relevant preparation and spectral analysis steps.

To confirm successful inflammation induction, inflamed cultures were subjected to immunocytochemistry for downstream inflammation indicators IL-6 and IL-8. Following primary antibody incubation, cells were washed 3 times in 1% DS-PBS. Appropriate secondary antibody diluted in 1% DS-PBS was added to cells at room temperature for 2 hours. Cells were then washed 3 times in PBS. DAPI staining solution was added at room temperature for 5 minutes followed by 3 washes with PBS.

### 3.3.5. Raman Spectroscopy of Healthy and Inflamed Cochlear Fibrocytes

Healthy and inflamed cochlear fibrocytes were detached via trypsin and cytospun onto CaF<sub>2</sub> slides as outlined in chapter 2.2.1. Sampling was conducted on all outlined conditions- 0ng/mL, 1ng/mL, 5ng/mL, 10ng/mL, 25ng/mL, 50ng/mL. Samples were analysed by Thermofisher DXR 3 Raman spectrometer (532nm laser, full range grating) as outlined in section 2.2.1. Typically, 100 spectra were collected per condition (1 point per cell with sampling conducted around the approximate nuclear region). A 120 second acquisition time was used for each sample point, with 3 scans per sample and 4 scans of background. Following every 25 cells sampled, a series of 'blank' spectra were taken from

cell free substrate regions. Sample spectra were collected at 20x magnification. Prior to sample spectrum collection, samples were photobleached for 30 seconds to mitigate sample fluorescence and improve the contrast of Raman bands in spectra. A high cosmic ray threshold was employed in order to minimise background noise and improve signal clarity in spectra despite lack of mechanical isolation in the benchtop setup. This, along with the relatively high spectral resolution employed ( $\sim 10\text{cm}^{-1}$  on average), is also supportive of comparative analyses across instruments with similar parameters e.g. hyperspectral Raman at Synchrotron facility.

### 3.3.6. ATR-FTIR Spectroscopy of Healthy and Inflamed Cochlear Fibrocyte Supernatant

Media samples from healthy and inflamed cochlear fibrocytes, as well as acellular controls were collected from flasks and transferred to Eppendorf tubes. Three samples were taken per flask, with three flasks created per sample condition. Ahead of slide preparation, samples were centrifuged to separate any non-supernatant components. Samples were allowed to air dry in ambient conditions prior to measurement.

ATR-FTIR measurements were taken using a Thermo Scientific iS50 spectrometer coupled with the Specac Quest ATR accessory onto which a Dxcover® autosampler was positioned. Dxcover® Sample Slides were loaded into the Dxcover® auto sampler for measurement as outlined in section 2.3.2.

Sampling was conducted on all outlined conditions- 0ng/mL, 1ng/mL, 5ng/mL, 10ng/mL, 25ng/mL, 50ng/mL. Measurements were taken using Omnic software. Spectral parameters were set as follows: 128 co-added scans per spectrum with a resolution of  $4\text{cm}^{-1}$  across a  $4000\text{-}400\text{cm}^{-1}$  range. A background measurement was taken before each sample measurement. All measurements were taken in absorbance mode with no corrections applied during sampling. Automatic atmospheric suppression was employed.

### 3.3.7. Data Processing and Analysis

Data were pre-processed and analysed as outlined in sections 2.2.2, 2.2.3 and 2.3.3. Raman spectroscopy data was pre-processed in Orange (Quasar) software. Spectra were first cut to remove

noise and the large  $\text{CaF}_2$  peak, followed by the application of a rubber band baseline correction. Following this, data were smoothed using Savitsky Golay (window 11, polynomial 2) and vector normalised. Finally, data were cut to regions of interest ( $400\text{-}3600\text{cm}^{-1}$  general,  $400\text{-}1800\text{cm}^{-1}$  fingerprint,  $2800\text{-}3600\text{cm}^{-1}$  high wavenumber). Anomalous spectra were excluded from data prior to analysis. Second derivative spectra were generated by increasing derivative order at the Savitsky-Golay smoothing stage. To reduce noise in second derivative spectra, Savitsky Golay filter window was increased to 27.

ATR-FTIR data spectroscopy data was pre-processed in Orange (Quasar) software. Spectra were first cut to remove noise, followed by the application of a rubber band baseline correction. Data was then smoothed using Savitsky Golay (window 11, polynomial 2) and vector normalised. Finally, data were cut to regions of interest ( $400\text{-}3800\text{cm}^{-1}$  general,  $400\text{-}1800\text{cm}^{-1}$  fingerprint,  $2800\text{-}3600\text{cm}^{-1}$  high wavenumber). Anomalous spectra were excluded from data prior to analysis. Second derivative spectra were generated by increasing derivative order at the Savitsky-Golay smoothing stage. To reduce noise in second derivative spectra, Savitsky Golay filter window was increased to 27.

For both Raman and ATR-FTIR data, samples were analysed using Orange (Quasar) software. Manual peak identification was performed on average spectra, consulting second derivative spectra for clarity where applicable. Bands were assigned to bond vibrations and potential molecules through literature consultation. Principal component analyses (PCAs) were conducted in Quasar software, with associated loadings plots generated from components.

Thanks to the relatively high sample number observed, Raman spectra of healthy and inflamed cells were utilised to produce a non-linear predictive model. This was conducted on pre-processed data following PCA to reduce dimensionality. Data was split randomly (50:50 train to test), and neural network modelling performed.

A 50:50 test to train split refers to presentation of condition labels for half of the data at random to the model, allowing it to predict the unseen half. This was performed using a 5-fold method, wherein data was re-randomised and independently tested 5-times with presented accuracy formed from an average across all folds.

## 3.4. Results and Interpretation

### 3.4.1. Explantation, Growth and Characterisation of Explanted Cochlear Fibrocytes

Following explantation of cochlear tissue from CD/1 mice to culture, adherent cells could be seen emerging from all edges of the tissue sections within 1-2 days of placement in culture (Fig. 20). This is consistent with expectations of the culture method used.

Light microscopy images (Fig. 21), though showing a large amount of debris (typical of explanted tissue cultures) demonstrate living cells continuing to proliferate over time suggesting a healthy culture. Rate of proliferation based on general observation appeared similar to that expected for the culture method used (growth measurements from Gratton paper). Where cells are seen emerging from the explanted tissue following several days of sterile culture, it is logical to assume that they have origins in murine cochlear tissue, though in their early stages cultures are likely to consist of both spiral ligament and *stria vascularis* cells. This is demonstrated presently by the presence of an

epithelial/fibroblastic mixed culture. This, however, is refined as culture progresses through the conditions chosen for cells.

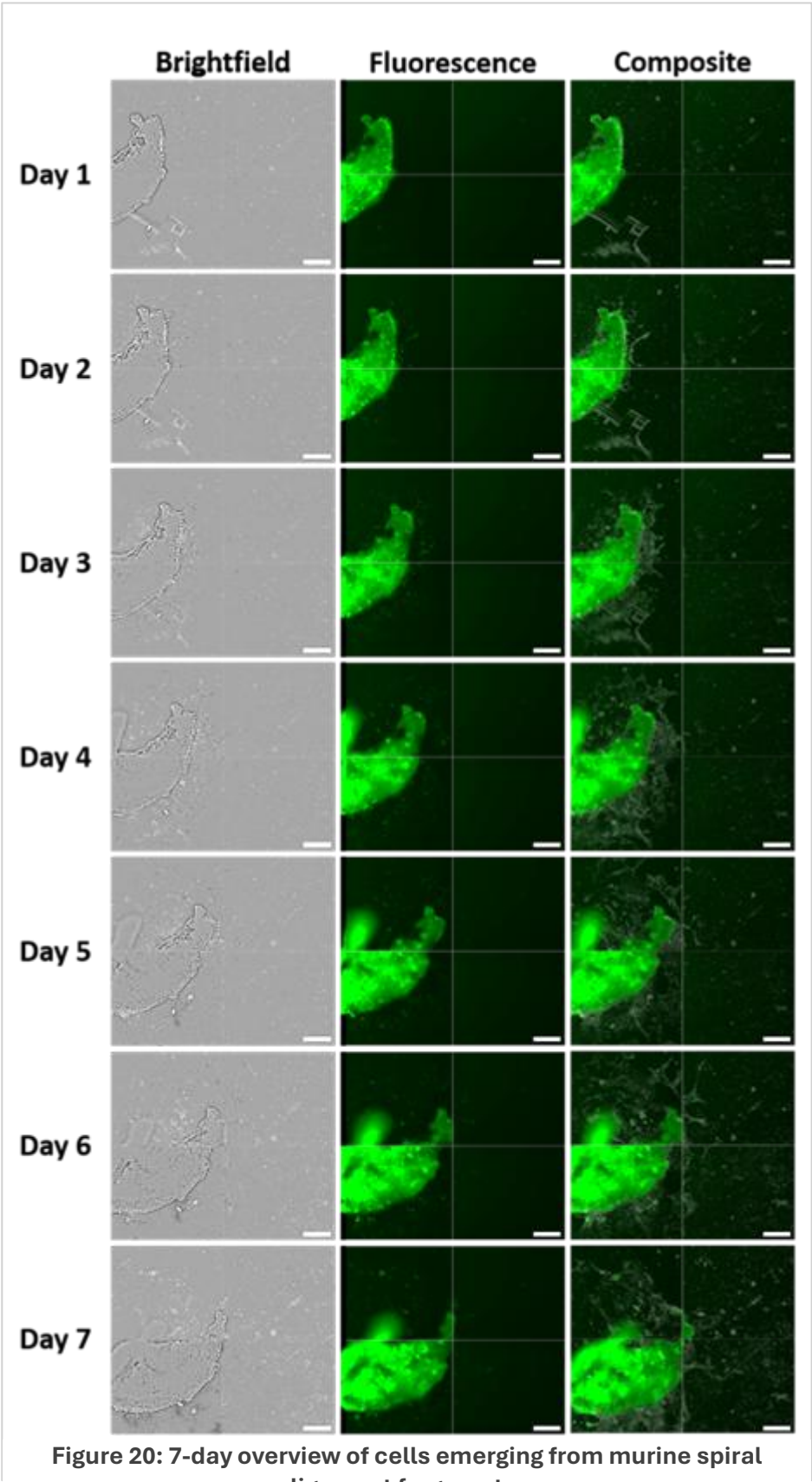
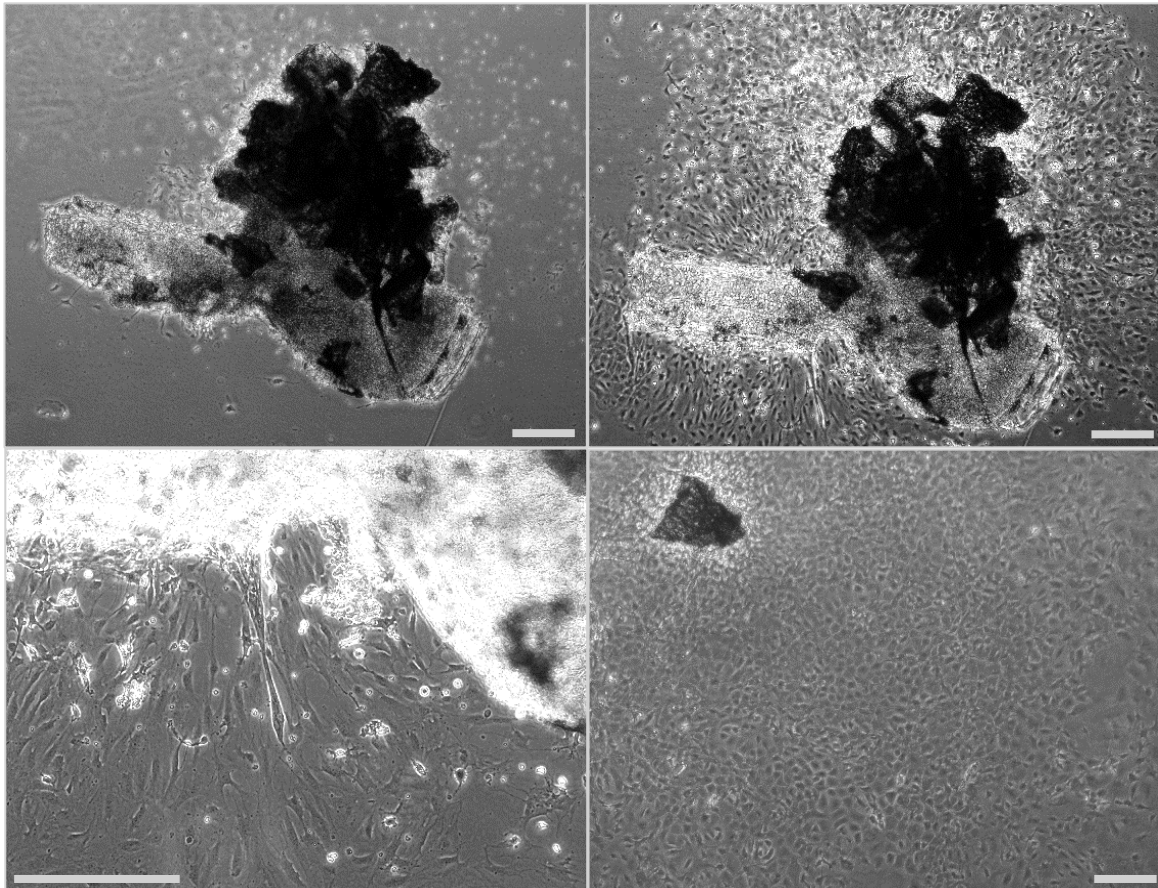


Figure 20: 7-day overview of cells emerging from murine spiral ligament fragments.

Stitched images from 4 adjacent photo sites. Staining conducted using Vybrant dye. Scale bars= 100µm.

Following passage, early secondary cultures consisted of adherent cells demonstrating typical fibrocyte morphology- that is fusiform-like cells with large nuclei and slender processes, as well as some multipolar and bipolar fibroblastic cells. Increase in cell number as cultures progressed yielded parallel-oriented cells with characteristic ‘whorls’ as seen in literature (Fig. 22). Such morphological characteristics suggest with confidence that cell seen are cochlear fibrocytes.



**Figure 21: Light microscopy images of cells emerging from tissue explants.**

**A) 1 day after removal from the animal. B) 1 week after removal from the animal, following coverslip removal. C) 1 week after removal from the animal, following coverslip removal. Cells may be seen actively proliferating from the explanted tissue. D) 2 weeks after removal from the animal, following main ligament removal. Cells take on a less characteristically fibrocyte-like morphology nearer the centre of the confluent patch where crowding occurs. Scale bars= 250µm.**

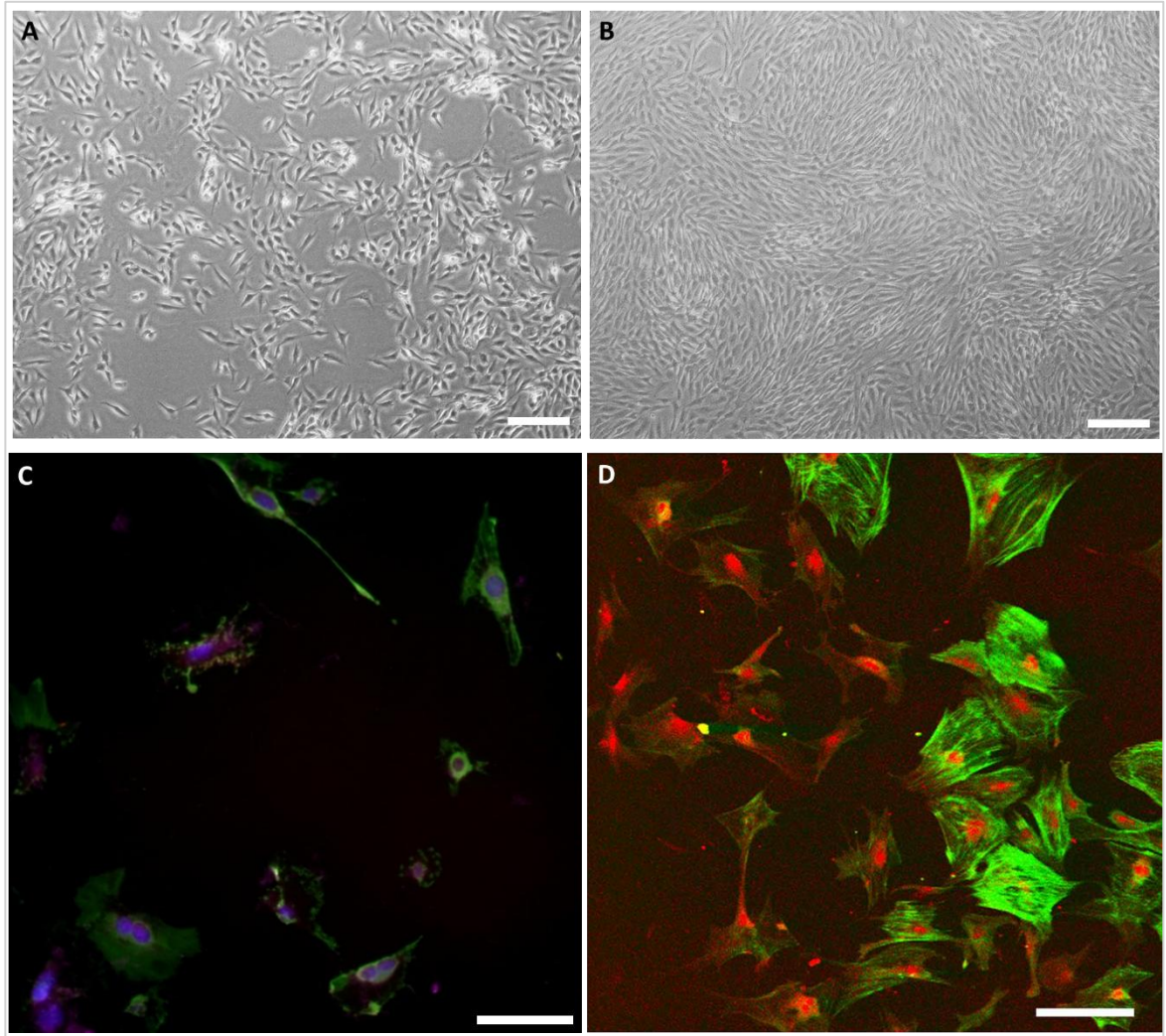


**Figure 22: Light microscopy and fluorescence microscopy images of monolayer secondary cultures.**

**A) Low confluence culture demonstrating fusiform and fibroblastic morphologies. B) Higher confluence culture demonstrating oriented cells and 'whorl' structures. C) Cells following immunofluorescence labelling for Na<sup>+</sup>, K<sup>+</sup>-ATPase (green), AQP-1 (red), DAPI (blue) and S-100β (magenta). D) Image from Furness (forgotten fibrocytes paper): cells following immunofluorescence labelling for caldesmon (green) and Na<sup>+</sup>, K<sup>+</sup>-ATPase (red). Scale bars= 100μm for fluorescence 250μm for brightfield.**

This does not, however, confirm these cells as cochlear fibrocytes as other cell types are present in the cochlea (though the use of serum containing media without the presence of growth factors does encourage the persistence of fibrocyte as opposed to epithelial outgrowth). In order to firmly identify the emerging cells as cochlear fibrocytes, immunocytochemical analysis was performed on secondary cultures (following one or more passages after the initial explant culture) in

comparison to known profiles from literature (though relatively little characterisation of *in vitro* fibrocytes is conducted as opposed to *in vivo* (assessed via sectioned cochleae)) (Fig. 23).

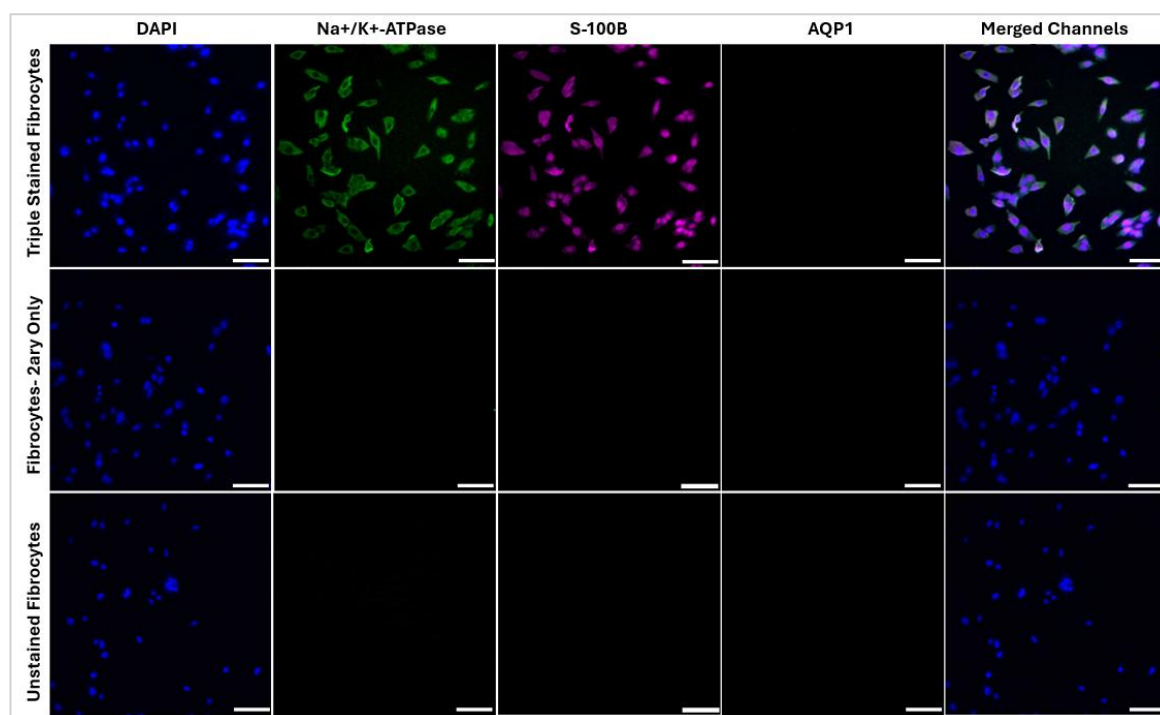


**Figure 23: Fluorescence images of cultured cells stained for common fibrocyte markers. Scale bars= 100µm.**

DAPI is present in all imaged cells indicating nuclei. Na<sup>+</sup>, K<sup>+</sup>-ATPase and S100-β are present in only triple stained cells indicating positive staining with no general dye adhesion to cells or autofluorescence. Cells did not stain positively for Aqp-1.

Positive staining of cells for Na<sup>+</sup>, K<sup>+</sup>-ATPase and S100-β, but not Aqp-1 indicates fibrocytes of type II, IV or V. MG63 osteosarcoma cells showed no fluorescence for these markers and were an appropriate negative control (Fig. 24). Lack of staining for Aqp-1 also serves to verify that the cultured cells no-longer contain those from the *stria vascularis* which are expected to stain positively <sup>[141]</sup>. Considering their distribution, cells seen are likely of type II or V (likely II as these have the largest and innermost area from which to harvest) this but cannot be made certain without further examination via distinguishing antibodies. Nonetheless, for the purposes of the present investigation there is no requirement for further assessment.

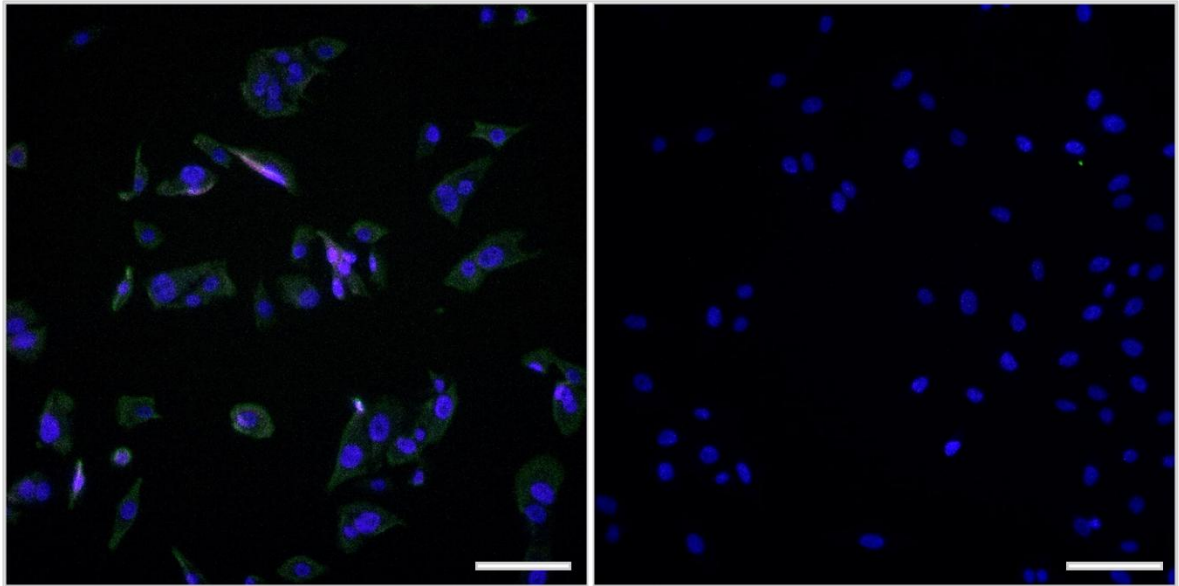


**Figure 24: Fluorescence microscopy images of monolayer secondary cultures- SLF vs. MG63.**

**Murine spiral ligament fibrocytes (left) and human MG63 osteosarcoma cell line (right). Immunofluorescence labelling is for Na<sup>+</sup>, K<sup>+</sup>-ATPase (green), AQP-1 (red), DAPI (blue) and S-100β (magenta). SLFs label for Na<sup>+</sup>, K<sup>+</sup>-ATPase and S-100β but do not appear to express AQP-1 indicating a sub-type of II, IV or V. MG63 cells do not label for any of the selected markers. Scale bars= 100μm.**

### 3.4.2. Raman Spectroscopy of Healthy Cochlear Fibrocytes

Raman spectroscopy of healthy cochlear fibrocytes may be used to observe the presence of key metabolic compounds and assess a general profile for these cells in their untreated state. The average Raman spectrum of healthy cochlear fibrocytes (Fig. 25) demonstrates a rich fingerprint region, consistent with expectations for a cellular sample. Visible are peaks in regions indicative of protein ( $\sim 1125\text{-}1450\text{cm}^{-1}$ ,  $\sim 1600\text{-}1660\text{cm}^{-1}$ ) [142-144] and DNA/RNA ( $\sim 780\text{-}790\text{cm}^{-1}$ ,  $\sim 897\text{cm}^{-1}$ ,  $\sim 1095\text{cm}^{-1}$ ,  $\sim 1320\text{-}1350\text{cm}^{-1}$ ,  $\sim 1575\text{cm}^{-1}$ ) [142, 144, 145], consistent with nuclear region sampling conducted. The presence of DNA-associated peaks ( $\sim 770\text{-}900\text{cm}^{-1}$ ) such as the ring stretching of cytosine, confirms cell viability immediately prior to fixation, and the presence of the O-P-O stretch band ( $\sim 790\text{cm}^{-1}$ ) indicates intact DNA strands in samples [146].

Additionally, peaks typically indicative of lipids are present between  $\sim 1065\text{cm}^{-1}$  and  $\sim 1125\text{cm}^{-1}$ , as well as  $\sim 1250\text{-}1300\text{cm}^{-1}$ ,  $\sim 1367\text{cm}^{-1}$  and  $\sim 1660\text{cm}^{-1}$  [142-144]. Peaks typically indicative of lipids at  $\sim 1149\text{cm}^{-1}$  and  $\sim 1460\text{cm}^{-1}$  were not clearly observed, though this is assumed to be due to overlap with more prominent protein regions present in spectra, and the relative higher protein load associated

with the nuclear region. Carbohydrate-associated peaks are also visible ( $\sim 1080\text{-}1095\text{cm}^{-1}$ ), as are a relatively prominent CH group rocking peak ( $\sim 1160\text{cm}^{-1}$ ) and C-H stretching bands attributable to lipids and proteins in the high wavenumber region ( $\sim 2900\text{-}3050\text{cm}^{-1}$ ) [143].

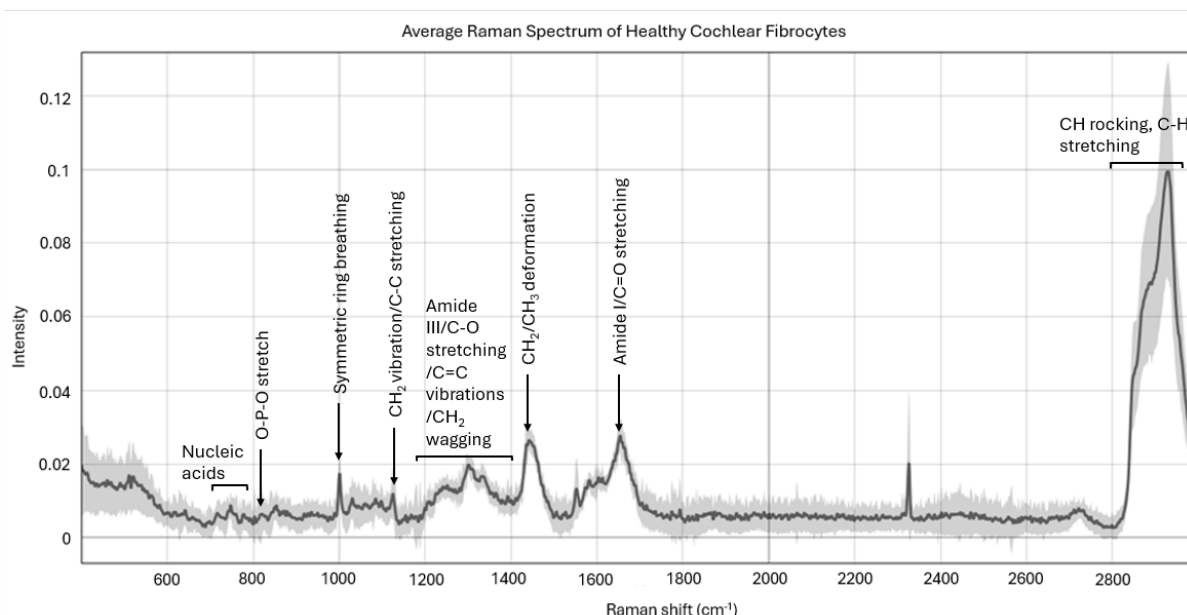


**Figure 25: Average Raman spectrum of healthy cochlear fibrocytes.**

**Average Raman spectrum of healthy cochlear fibrocytes (~250 individual cell spectra from a ~250k cell cytopspin monolayer of PFA fixed cells on CaF<sub>2</sub> - cells fixed at maximum P8), highlighting characteristic vibrational peaks corresponding to key molecular components.**

**Prominent bands are associated with proteins, lipids, nucleic acids, and other cellular biomolecules.**

It is important to note that the spectral features highlighted in regions 800–850, 1200–1300 and 1500–1600 cm<sup>-1</sup> are subject to some variation from expected peak wavenumbers, due predominantly to variation in cell cycle phase [142, 144, 145]. This should be kept in mind when moving towards observation of pathological conditions. Nonetheless, Raman spectra of cochlear fibrocytes clearly demonstrate that cell signals are discernible by presently employed methods.

### 3.4.3. ATR-FTIR Spectroscopy of Healthy Cochlear Fibrocyte Supernatant

ATR-FTIR Spectroscopy of culture media and cell supernatants allow comparison of cellular and acellular cultures and confirm the origins of visible compounds. Analysis of supernatant, when considered alongside Raman findings, enriches understanding of healthy cochlear fibrocyte function by providing insight into the external metabolic environment of cells.

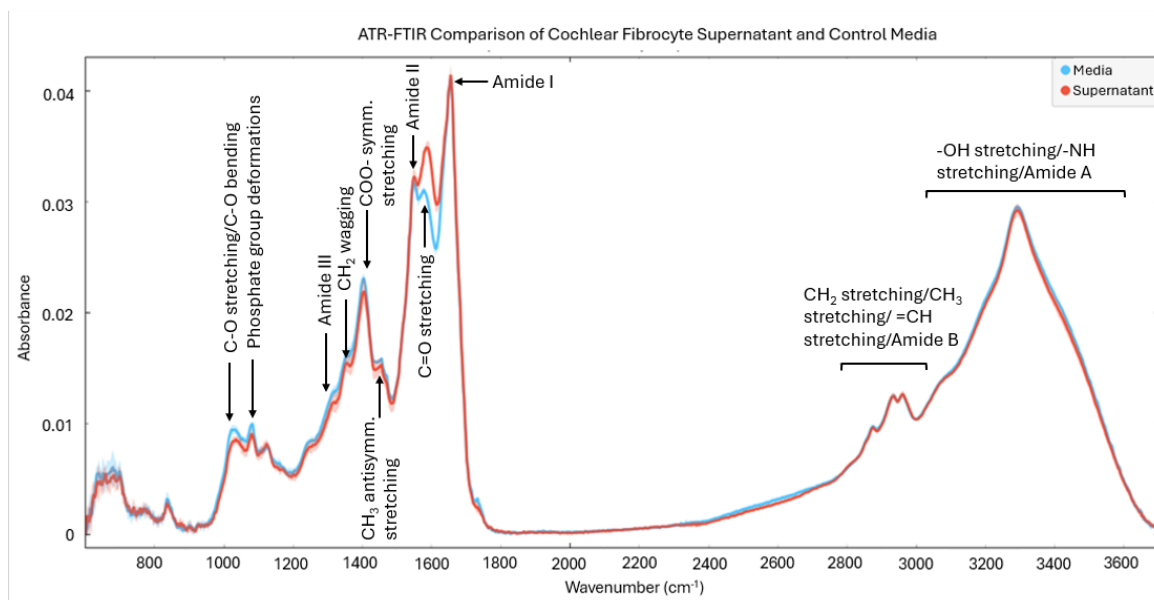


**Figure 26: ATR-FTIR spectra of cochlear fibrocyte supernatant and control media.**

**Average ATR-FTIR spectra of healthy cochlear fibrocyte supernatant vs control media.**

**Supernatant averages formed of 9 supernatant spectra (3 per slide, 3 slides) from a ~200k cell population of cells at maximum P8. Media averages formed of 9 control media spectra (3 per slide, 3 slides) from media exposed to the same conditions as cell cultures (flasks, incubation etc.).**

Visually comparing the spectra of cell supernatant and control media clearly indicates variation between cellular (supernatant) and acellular (media only) samples, though cellular and acellular media spectra are similar in general due to the presence of the same base media (Fig. 26). Areas of note in both media and supernatant spectra include bands attributed to C-OH vibration of carbohydrates ( $\sim 1030\text{-}1050\text{cm}^{-1}$ ), peptide bond changes (C=O stretching, C-N stretching, N-H bending) of amides (II-  $\sim 1540\text{cm}^{-1}$ , III-  $\sim 1305\text{cm}^{-1}$ ) and C=O stretching in lipids ( $\sim 1745\text{cm}^{-1}$ ). Particularly clear variation is seen in the wavenumber region  $1560\text{-}1630\text{cm}^{-1}$ , likely indicative of C=O stretching in proteins.

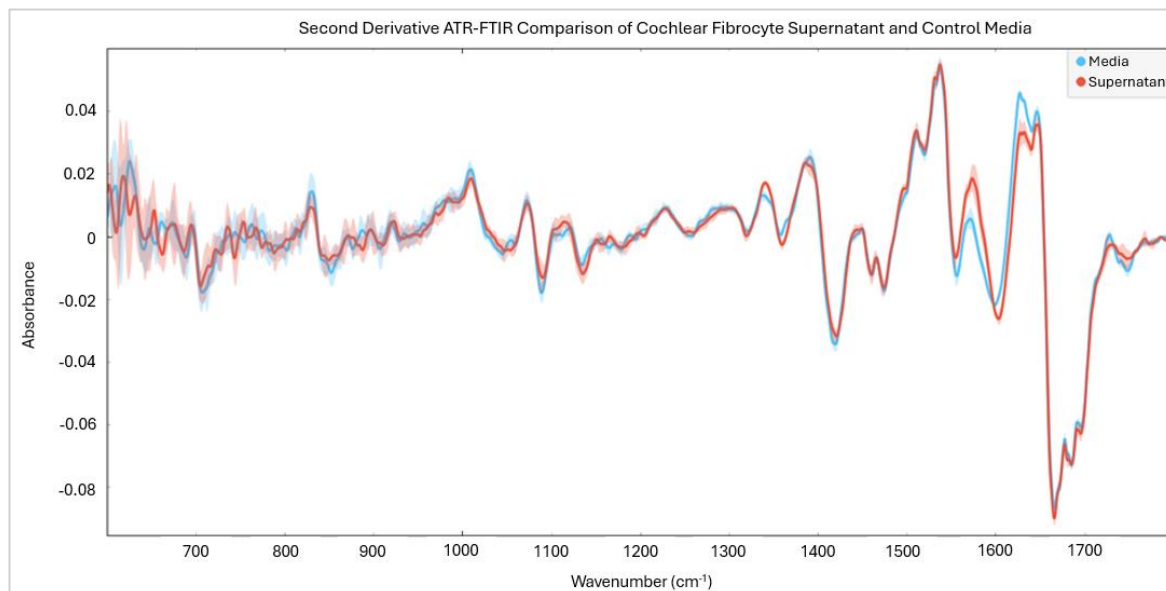


**Figure 27: Second derivative ATR-FTIR fingerprint region spectra of cochlear fibrocyte supernatant and control media.**

**Second derivative average ATR-FTIR spectra of healthy cochlear fibrocyte supernatant vs control media. Supernatant averages formed of 9 supernatant spectra (3 per slide, 3 slides) from a ~200k cell population of cells at maximum P8. Media averages formed of 9 control media spectra (3 per slide, 3 slides) from media exposed to the same conditions as cell cultures (flasks, incubation etc.).**

Examining second derivative spectra of the fingerprint region allows further clarity in distinguishing variations (Fig. 27). Distinction between cellular and acellular conditions is noted at  $1340\text{cm}^{-1}$  ( $\text{CH}_2$  wagging of lipids)  $1360\text{cm}^{-1}$  (glycine  $\text{CH}_2$  wagging <sup>[258]</sup>)  $1570\text{cm}^{-1}$  (amide II),  $1630\text{cm}^{-1}$  ( $\text{C}=\text{O}$  stretching of proteins),  $1650\text{cm}^{-1}$  (amide I). From this, it is concluded that the majority of variation between cellular and acellular conditions arises in the form of protein changes, with some alterations to lipids and amino acids also noted. It should be acknowledged that, though there are variations in nucleic acid associated regions (e.g.  $920\text{-}940\text{cm}^{-1}$ ) as would be expected for cellular vs acellular comparisons, these regions show substantial sample range overlap thus peaks cannot be reliably distinguished at this stage.

Interestingly, the peak noted at  $\sim 1595\text{cm}^{-1}$  demonstrates greatly increased absorbance in the supernatant condition, and may be indicative of histidine presence in cells. This is consistent with some mutations seen in cochlear fibrocytes and may be a feature of the mouse type (CD/1) used which, though typically of normal hearing status at birth, demonstrate ARHL like symptoms with age [149-152]. This may also be reflective of the possible amino acid peak noted in Raman results.

Comparing cellular and acellular conditions using PCA further highlights variation. PCA of the fingerprint region shows clear distinction between cellular and acellular conditions, with over 80% of variance explained by 6 principal components (Fig. 28). Associated loadings plots, though showing substantial spectral noise, validate the sources of variation previously identified.

PCA of the high wavenumber region, as anticipated, demonstrates fewer identified sources of variation than the fingerprint region, with 94% of variance explained by 6 principal components. Nonetheless, though variations in this region are difficult to visualise from spectra alone, PCA scatter plots confirm distinction between conditions (Fig. 29). Associated loadings plots demonstrate sources of noted variation, with the majority arising in  $\text{CH}_2$  stretching,  $\text{CH}_3$  stretching,  $=\text{CH}$  stretching, and amide B associated regions below  $3100\text{cm}^{-1}$ .

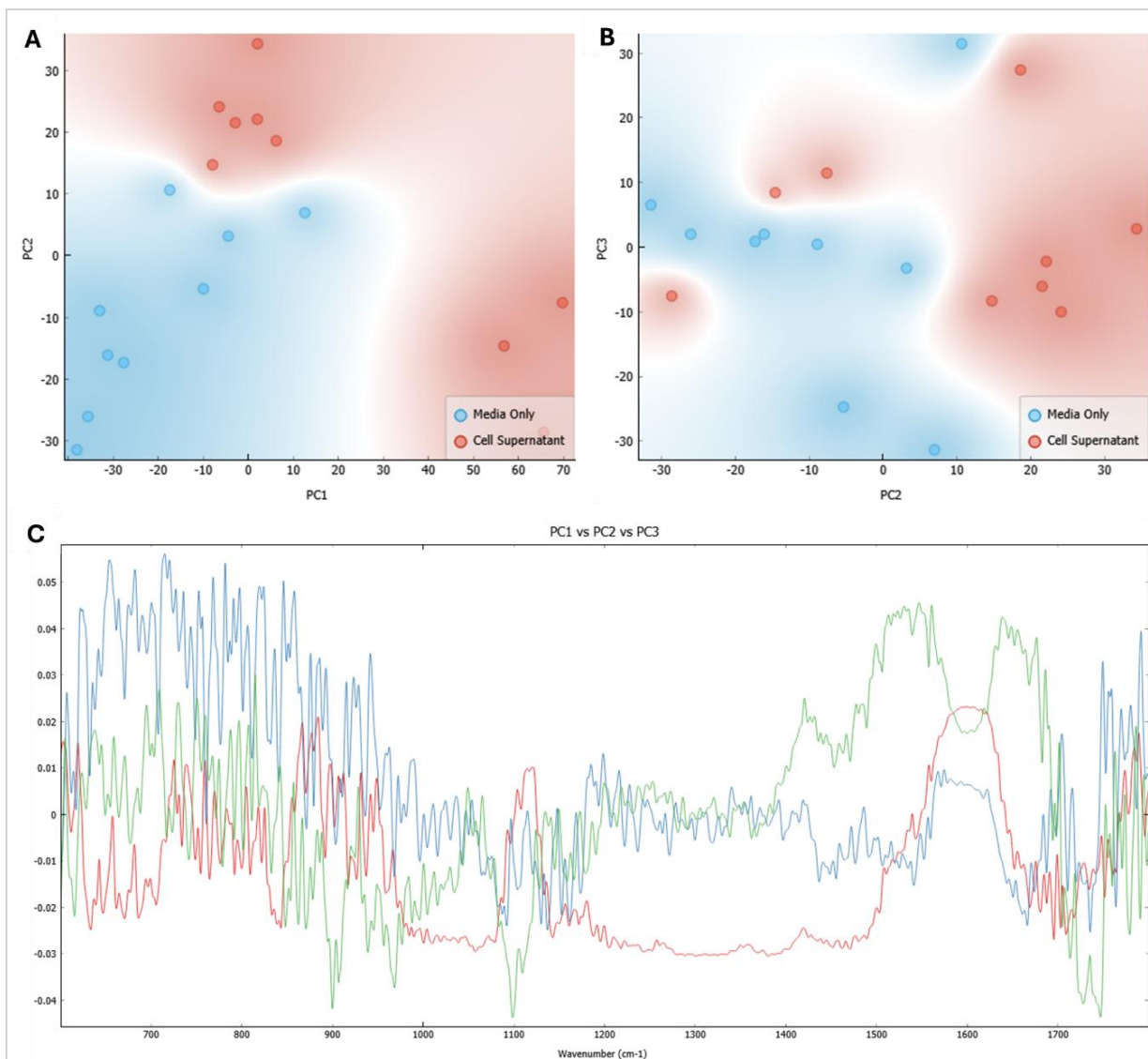


**Figure 28: PCA of the fingerprint region of cochlear fibrocyte supernatant vs control media.**  
**From average ATR-FTIR spectra of healthy cochlear fibrocyte supernatant vs control media.**  
**Supernatant averages formed of 9 supernatant spectra (3 per slide, 3 slides) from a ~200k cell population of cells at maximum P8. Media averages formed of 9 control media spectra (3 per slide, 3 slides) from media exposed to the same conditions as cell cultures (flasks, incubation etc.).**  
**A) Scatter plot of PC1 (41%) vs PC2 (15.4%). B) Scatter plot of PC2 (15.4%) vs PC3 (8.6%). C) Loadings plot of PC1 (red) vs PC2 (green) vs PC3 (blue).**

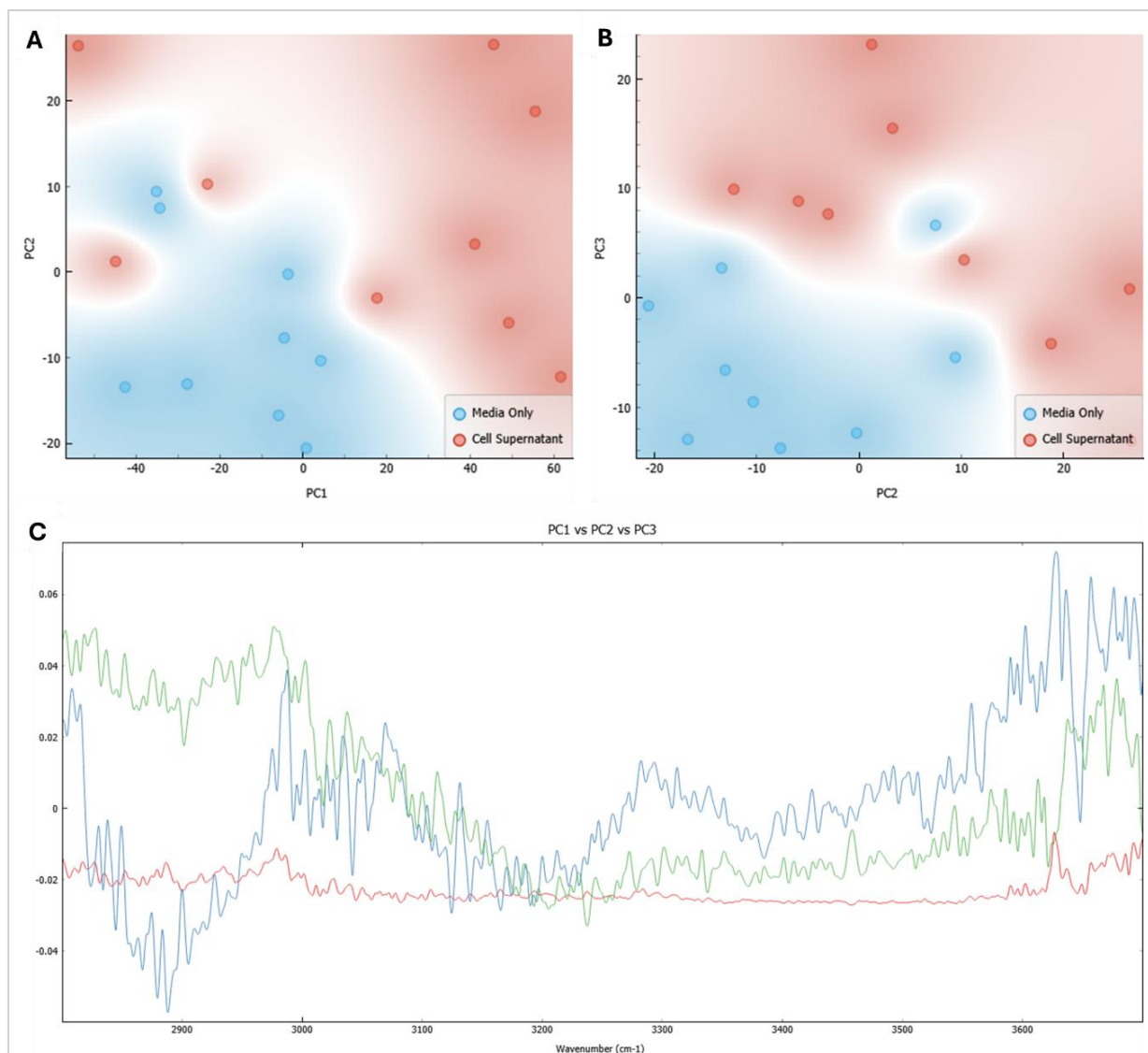


**Figure 29: PCA of the high wavenumber region of cochlear fibrocyte supernatant vs control media.**

From average ATR-FTIR spectra of healthy cochlear fibrocyte supernatant vs control media. Supernatant averages formed of 9 supernatant spectra (3 per slide, 3 slides) from a ~200k cell population of cells at maximum P8. Media averages formed of 9 control media spectra (3 per slide, 3 slides) from media exposed to the same conditions as cell cultures (flasks, incubation etc.). A) Scatter plot of PC1 (71%) vs PC2 (10.2%). B) Scatter plot of PC2 (10.2%) vs PC3 (5.8%). C) Loadings plot of PC1 (red) vs PC2 (green) vs PC3 (blue).

Based on the data presented, it is concluded that cell supernatant is distinct from control media, with variations detectable through ATR-FTIR. Spectra suggest that the majority of these variations arise in protein associated regions, with some variation in amino acid and lipid regions also noted.

### 3.4.4. The Induction of Inflammation in Cochlear Fibrocyte Cultures by TNF- $\alpha$ Dosage

Cochlear fibrocyte cultures appear, by immunocytochemistry examination, to have responded to the addition of TNF- $\alpha$  to culture media in a manner consistent with downstream inflammation effects.

Observing fluorescence imaging for IL-6 (Fig. 30), it is clear that undosed control cells do not express the targeted marker. However, at even 1ng/mL evidence of IL-6 presence may be seen in images. Such presence appears to be most prominent in 5ng/mL dosed cells, though the apparent depletion of cell numbers in later conditions may indicate otherwise. In any case, it is clear that a distinct expression difference is present between dosed and undosed conditions.

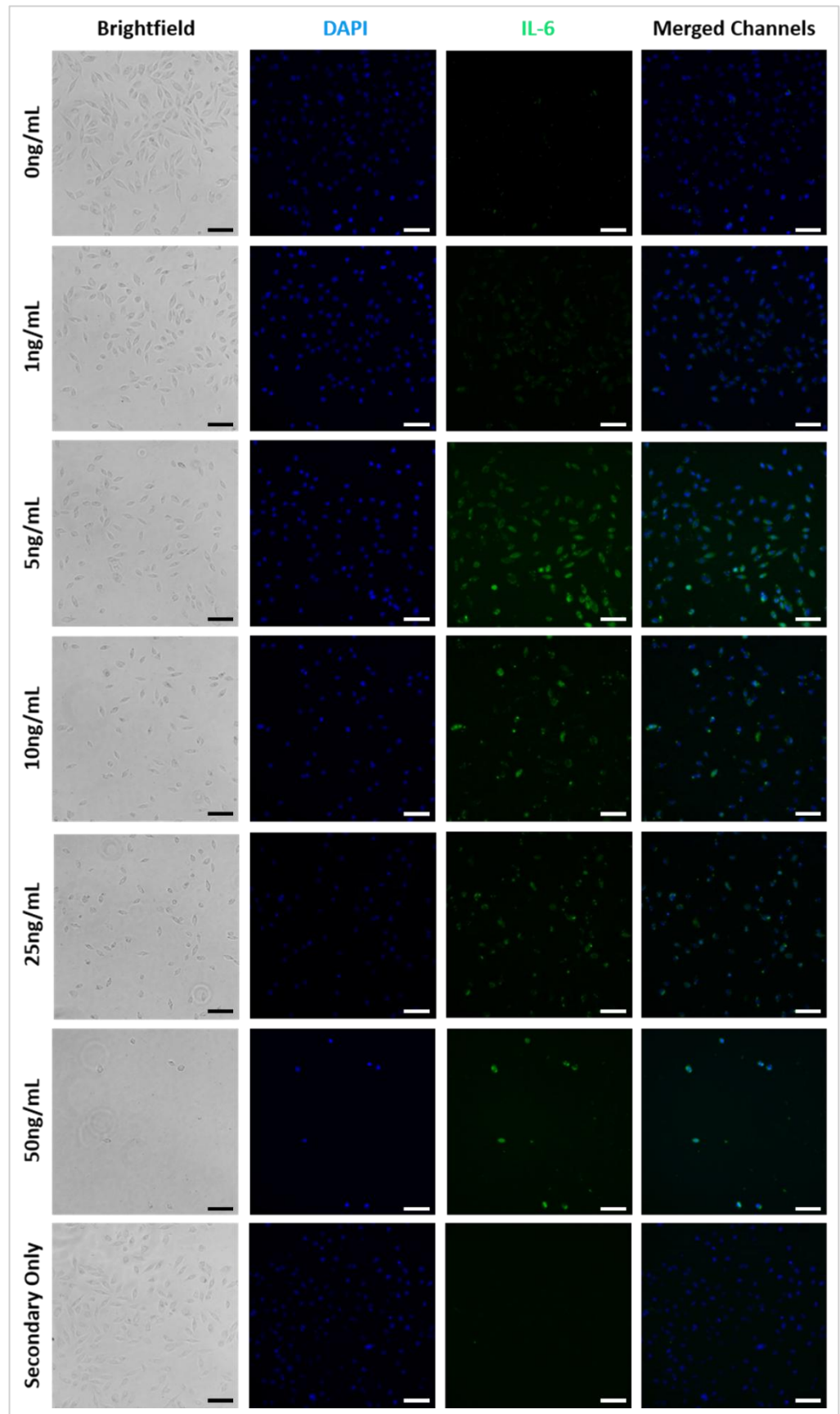


**Figure 30: Fluorescence imaging of TNF- $\alpha$ -dosed cochlear fibrocytes labelled for IL-6. Scale bars= 100 $\mu$ m.**

Similarly to IL-6, IL-8 is evidenced even in the lowest TNF dosage condition while undosed cells remain clear of the marker (Fig. 31). This further verifies the successful onset of inflammation in culture.

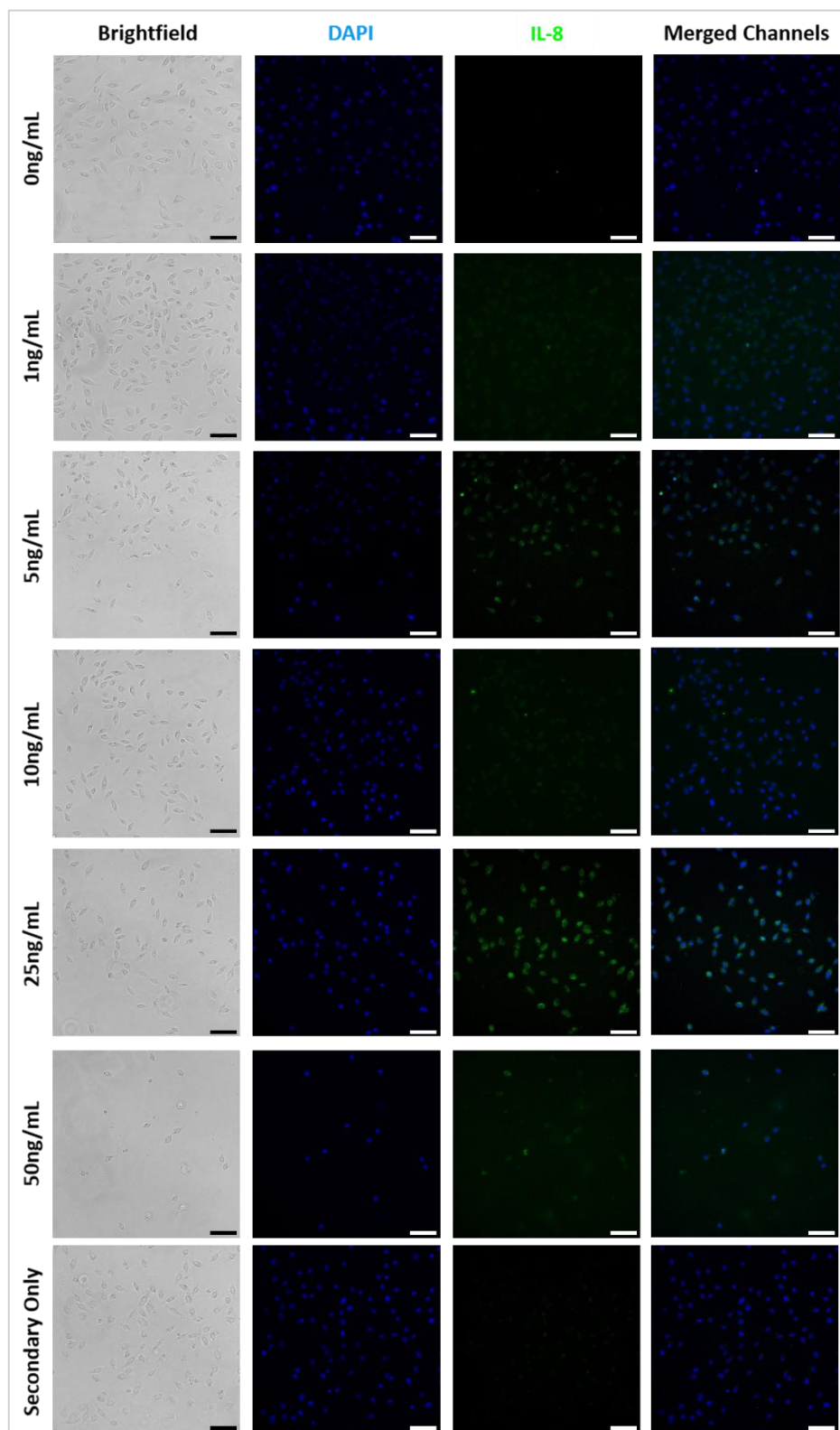


**Figure 31: Fluorescence imaging of TNF- $\alpha$ -dosed cochlear fibrocytes labelled for IL-6. Scale bars= 100 $\mu$ m.**

### 3.4.5. Raman Spectroscopy of TNF- $\alpha$ -dosed Cochlear Fibrocytes

Prior to analysis of Raman spectroscopy results it should be noted that the 25ng/mL dosage sample was not generated successfully despite multiple attempts using the same methods as all other Raman samples. The precise reason for this is unknown, though it is likely a failing stemming from human error in the cytospinning, fixation and wash stages of the preparation process. Some issues in culture were noted at this stage of research, but other samples in this set do not appear to have been affected. With this in mind, to preserve time and resources, a 25ng/mL TNF-dosed sample was not included in Raman analyses.

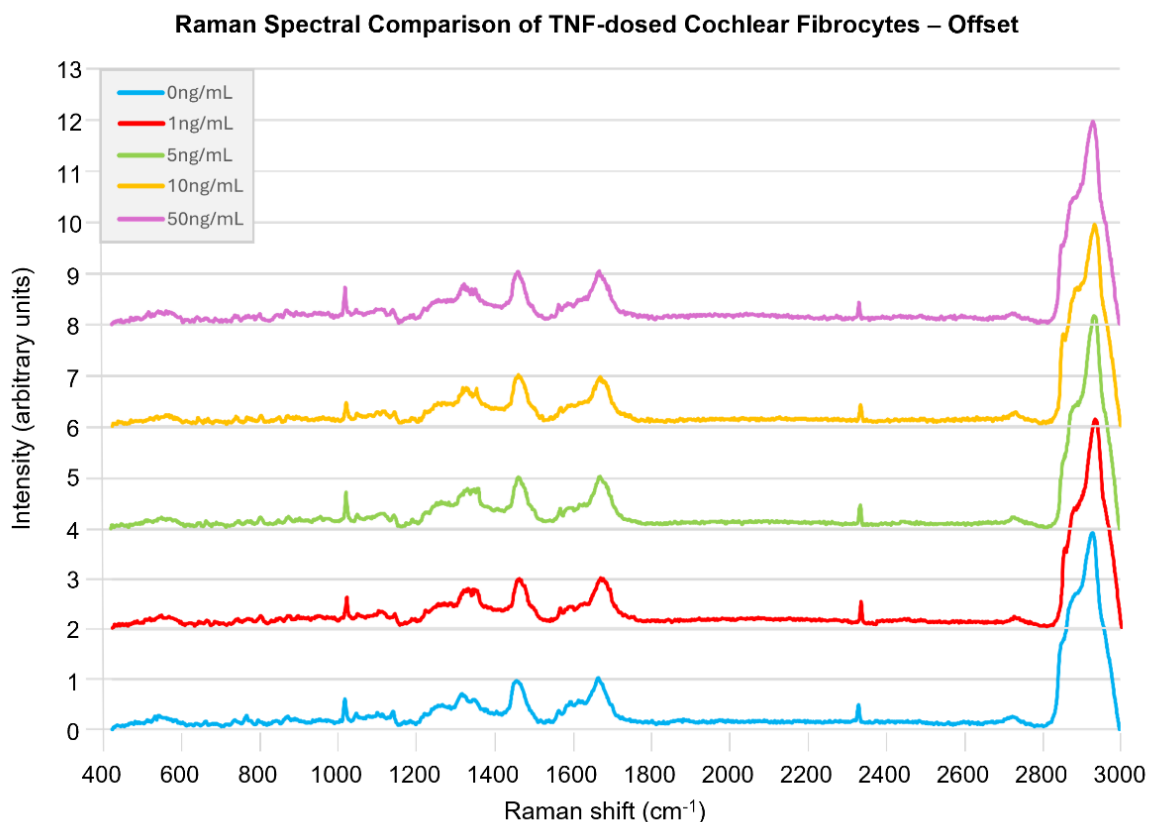


**Figure 32: Average Raman spectra of murine cochlear fibrocytes following 24hrs incubation with TNF- $\alpha$ .**

**Average Raman spectra of TNF-dosed cochlear fibrocytes - ~250 individual cell spectra per condition from individual samples each a ~250k cell cytospun monolayer of PFA fixed cells on CaF2 - cells fixed at maximum P8 following cytokine incubation.**

In examining the Raman spectra of TNF-dosed cochlear fibrocytes, it is clear that the general spectral profile of cells remains similar regardless of dose (Fig. 32). This is as expected as, despite potential changes in metabolic action, cells are anticipated to remain predominantly structurally

stable, particularly in the nuclear region where sampling was targeted. However, some variations are still visible in intensity of peaks.

From figure 32 it is clear that dosed and healthy cell signals are difficult to distinguish by eye from full spectra. This can be attributed to the complexity of signal seen as well as the overlaying of several dosage conditions and necessitates the closer examination of regions and conditions.

Examining spectral variations between dosed and undosed cells more closely, comparisons of each dose against undosed controls are made. In the fingerprint region of undosed and 1ng/mL dosed cells (Fig. 33), manual peak identification allows the distinction of visible variations across average spectra. It should be noted, however, that substantial variation around the average spectrum in dosed cells makes distinction of differences more uncertain.

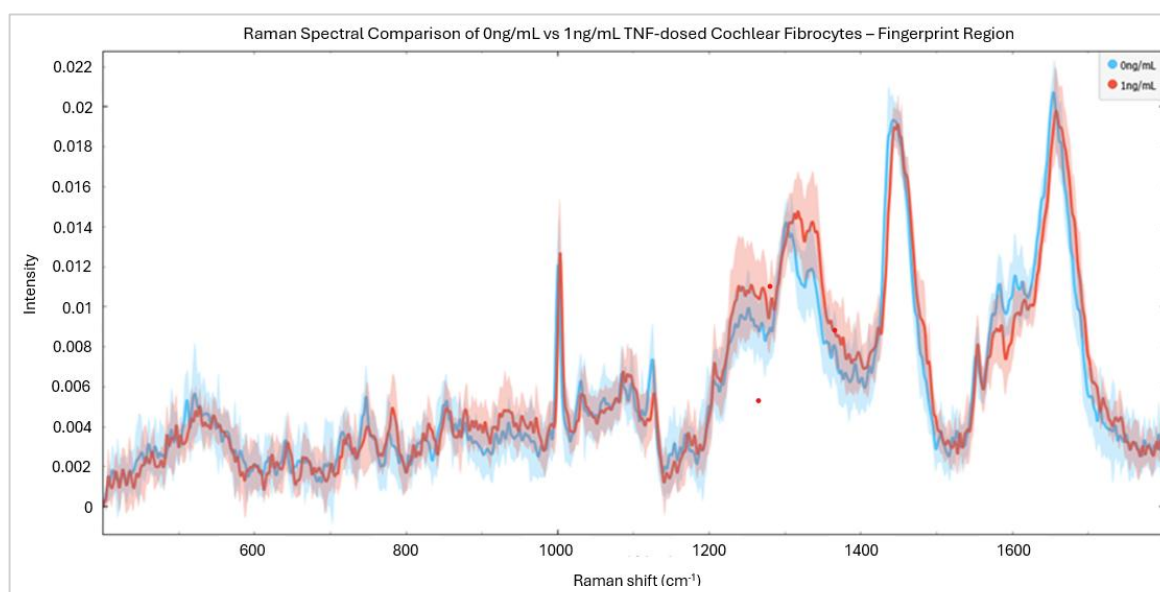


**Figure 33: Average Raman spectra of healthy and 1ng/mL-dosed cochlear fibrocytes following 24hrs incubation with TNF- $\alpha$  (fingerprint region).**

**Average Raman spectra (fingerprint region) of TNF-dosed vs healthy cochlear fibrocytes - ~250 individual cell spectra per condition, each from a separate (by condition) ~250k cell cytopun monolayer of PFA fixed cells on CaF<sub>2</sub> - cells fixed at maximum P8.**

Working from lower to higher Raman shift, there is little visible variation between samples below 600cm<sup>-1</sup>. A small reduction in intensity may be seen in the 1ng/mL dosed cell condition at

$\sim 650\text{cm}^{-1}$ , likely indicating changes in polysaccharides or nucleic acids ( $\text{CH}_2$  bending, C-C-C deformations). Any of these causes may be possible as a result of TNF dosage.

In the nucleic acid triple peak region ( $725\text{-}785\text{cm}^{-1}$ ) three contrasting interactions can be seen. In the adenine associated peak at  $725\text{cm}^{-1}$ , undosed and  $1\text{ng/mL}$  dosed cells demonstrate similar spectral intensity, with a slight shift towards the high wavenumber region visible in the dosed spectrum. In the thymine associated peak, dosed cell signal is less intense than that of undosed cells. Contrastingly, in the cytosine peak, dosed cell signal is more intense than that of undosed cells. These spectral variations suggest potential changes to nucleic acids as a result of inflammation. However, examination of further TNF dosages is required before this can be concluded.

Between  $\sim 870\text{cm}^{-1}$  and  $1000\text{cm}^{-1}$ , a region predominantly attributed to proteins, lipids and nucleic acids (C-O stretching, C-C-N asymmetric stretching, C-O-C ring deformation), there appears to be an increase in signal intensity in  $1\text{ng/mL}$ -dosed cells. This may be indicative of protein/lipid structural changes resulting from TNF dosage, though no firm conclusions may be drawn from undosed and  $1\text{ng/mL}$  comparisons alone.

At  $1000\text{cm}^{-1}$  both undosed and dosed cells demonstrate similar signal intensity, with the dosed condition demonstrating a negligible increase in intensity and shift towards the high wavenumber region. This band is typically associated with symmetric ring breathing of proteins, so alterations induced by inflammation are not unexpected. However, insufficient evidence is seen in undosed and  $1\text{ng/mL}$  comparison to draw any conclusions regarding TNF effects on this band.

In contrast, the  $\text{CH}_3$  wagging-associated peak at  $1032\text{cm}^{-1}$  appears to be of greater intensity in the undosed condition. Though this intensity difference is opposed to the previous peak, it may still indicate protein structural variability between conditions. Such variability is further evidenced by the spectral differences seen in region  $1145\text{-}1195\text{cm}^{-1}$ , attributable to C-C stretching, C-H bending and C-N vibrations in proteins.

At  $1128\text{cm}^{-1}$  signal intensity in the undosed condition is notably higher than that of the  $1\text{ng/mL}$  dosed condition. Differences in this band, typically attributed C-C stretching and  $\text{CH}_2$  vibration of lipids and glucose, may indicate changes in cellular processing of glucose during respiration. This is a

logical hypothesis given that inflammation typically results in mitochondrial dysfunction in cochlear fibrocytes.

In the spectral region  $1200\text{-}1400\text{cm}^{-1}$  (attributed to amide III, C-O stretching, C=C vibrations and  $\text{CH}_2$  wagging), the TNF dosed spectrum demonstrates a higher signal intensity than that of undosed cells. This is indicative of variations in lipids, proteins and polysaccharides between dosed and undosed cells. This relationship is of interest when examining further dosed cell conditions against undosed cells as it may be indicative of lipid accumulation as a result of inflammation, alterations to protein structure and function, and variations in cellular processing of polysaccharides.

The  $\text{CH}_2/\text{CH}_3$  deformation associated band at  $\sim 1450\text{cm}^{-1}$  does not show substantial difference between undosed and  $1\text{ng/mL}$  TNF dosed cells. Nonetheless, this band is of interest when examining the effect of TNF at higher doses.

In the protein region  $1540\text{-}1625\text{cm}^{-1}$  (associated with C=C stretching, N-H bending, tryptophan ring stretching and C-C-H ring vibration) signal intensity appears generally greater in the undosed cell condition than in  $1\text{ng/mL}$  dosed cells. This is further indicative of protein alterations arising in the inflamed condition and is a focus of further examination across dosages.

The amide I/C=O stretching band at  $\sim 1650\text{cm}^{-1}$ , similarly to the preceding protein region, demonstrates a higher signal intensity in the undosed cell condition than in the dosed cell condition. There also appears to be a slight shift towards the high wavenumber region in the dosed cell condition. This appears to support the previous suggested protein alterations but requires further verification through analysis of higher dosages.

Second derivative spectra of  $0\text{ng/mL}$  and  $1\text{ng/mL}$  TNF-dosed cells further illustrate differences in the fingerprint region (Fig. 34). Differences are particularly visible at  $1032\text{cm}^{-1}$  ( $\text{CH}_3$  wagging of proteins),  $1128\text{cm}^{-1}$  (C-C stretch/ $\text{CH}_2$  vibration of lipids/glucose) and  $1450\text{cm}^{-1}$  ( $\text{CH}_2/\text{CH}_3$  deformation of lipids/proteins). This implies that the primary differences between undosed and dosed

spectra arise in CH<sub>2</sub> and CH<sub>3</sub> associated regions, though this requires verification through the examination of further dosages.

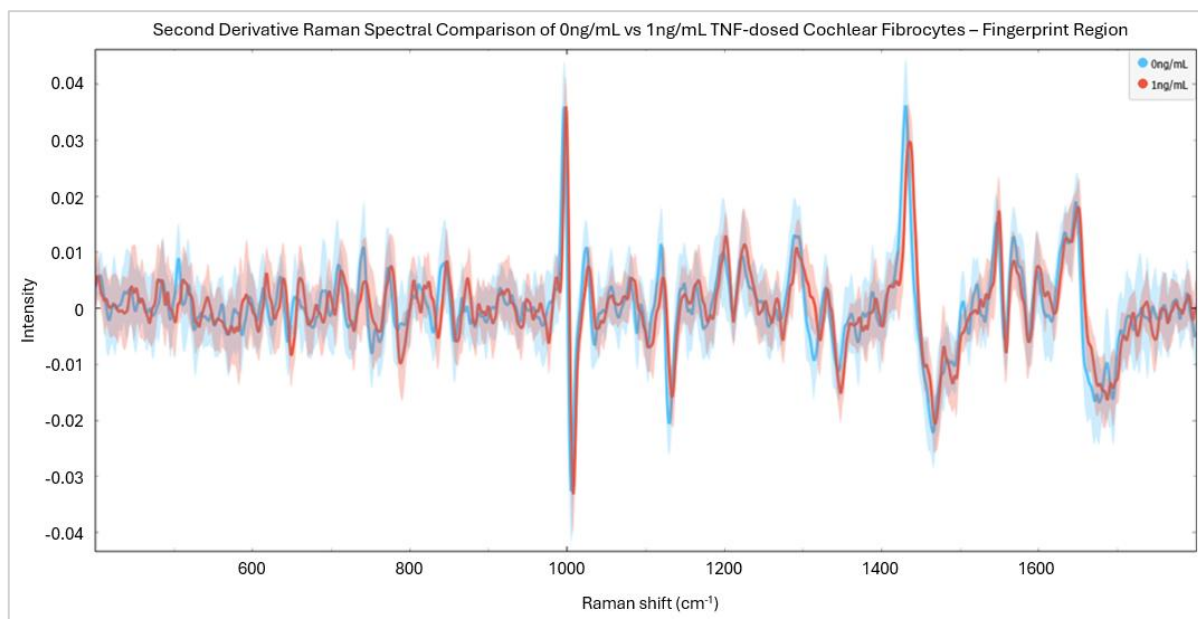


**Figure 34: Second derivative Raman fingerprint region spectra of 0ng/mL and 1ng/mL TNF-dosed cochlear fibrocytes.**

Second derivative average Raman spectra (fingerprint region) of TNF-dosed vs healthy cochlear fibrocytes - ~250 individual cell spectra per condition, each from a separate (by condition) ~250k cell cytopspin monolayer of PFA fixed cells on CaF<sub>2</sub> - cells fixed at maximum

P8.

In the high wavenumber region of 0ng/mL and 1ng/mL TNF-dosed cells, further differences are apparent (Fig. 35). The dosed spectrum in this region appears to demonstrate a shift towards the high wavenumber end of the spectrum. Additionally, intensity variations are noted throughout the dosed condition compared with undosed cells. In the CH<sub>2</sub> stretching region below ~2920cm<sup>-1</sup>, dosed cells are of lower signal intensity than undosed cells. Contrastingly, above 2920cm<sup>-1</sup>, in the CH<sub>3</sub> stretching region, dosed cells demonstrate higher signal intensity than undosed cells. Both differences illustrate variations in lipids and proteins arising from TNF dosage.

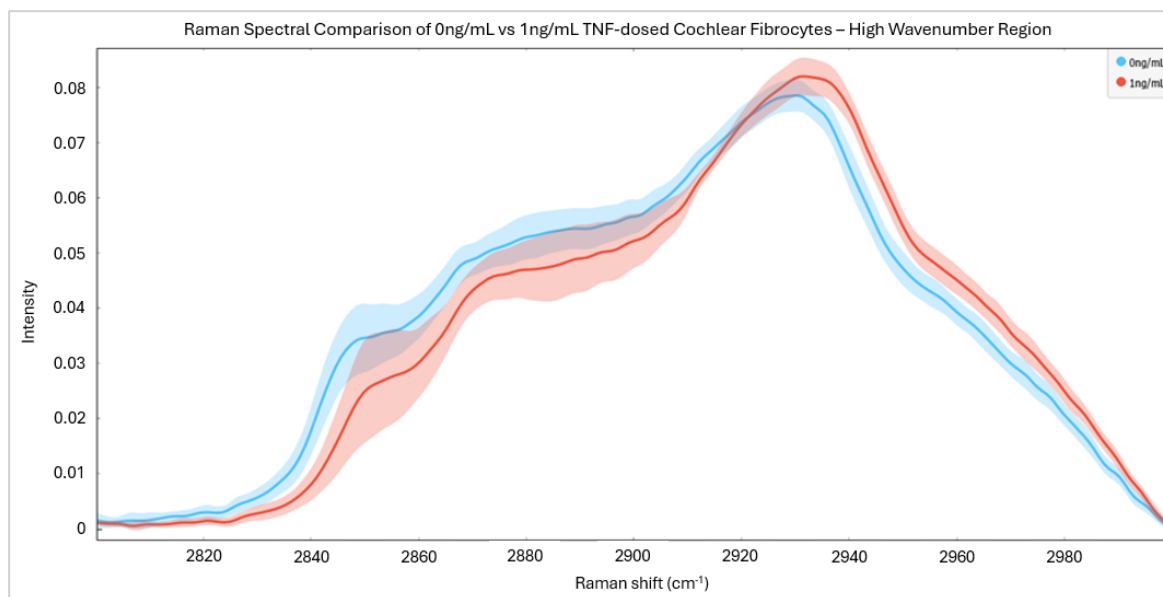


**Figure 35: Average Raman spectra of healthy and 1ng/mL-dosed cochlear fibrocytes following 24hrs incubation with TNF- $\alpha$  (high wavenumber region).**

**Average Raman spectra (high wavenumber region) of TNF-dosed vs healthy cochlear fibrocytes - ~250 individual cell spectra per condition, each from a separate (by condition) ~250k cell cytopspin monolayer of PFA fixed cells on CaF<sub>2</sub> - cells fixed at maximum P8.**

Second derivative spectra of 0ng/mL and 1ng/mL TNF-dosed cells in the high wavenumber region lend further clarity to the differences seen (Fig. 36). In particular, differences between dosed and undosed cells can be seen at ~2850cm<sup>-1</sup>.

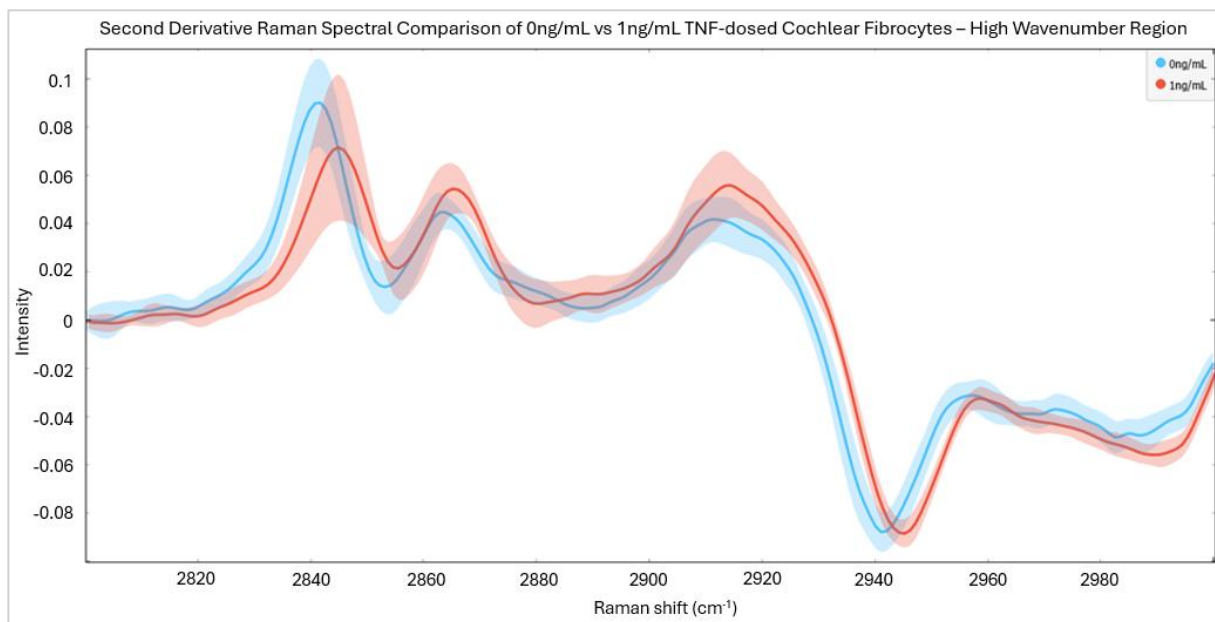


**Figure 36: Second derivative Raman high wavenumber region spectra of 0ng/mL and 1ng/mL TNF-dosed cochlear fibrocytes.**

**Second derivative average Raman spectra (high wavenumber region) of TNF-dosed vs healthy cochlear fibrocytes - ~250 individual cell spectra per condition, each from a separate (by condition) ~250k cell cytopspin monolayer of PFA fixed cells on CaF<sub>2</sub> - cells fixed at maximum P8.**

Viewing the fingerprint region of undosed and 5ng/mL dosed cells (Fig. 37), greater variation between conditions than that seen between undosed and 1ng/mL dosed cells is seen. Once again, variation around average spectra cells makes distinction of differences difficult.

Beginning once again in the lower end of the spectrum, variation between samples below 600cm<sup>-1</sup> appears to be greater than that seen in the previous comparison, with 5ng/mL dosed cell signal intensity generally lower than that of undosed cells. This, as before is likely indicative of changes in polysaccharides or nucleic acids (CH<sub>2</sub> bending, C-C-C deformations).

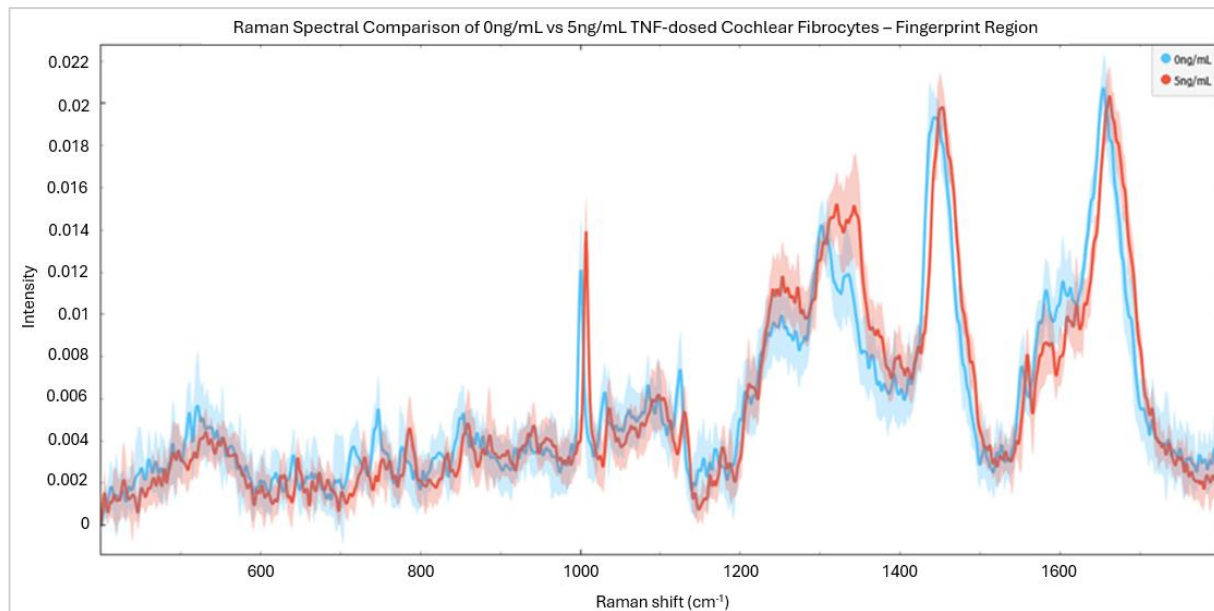


**Figure 37: Average Raman spectra of healthy and 5ng/mL-dosed cochlear fibrocytes following 24hrs incubation with TNF- $\alpha$  (fingerprint region).**

**Average Raman spectra (fingerprint region) of TNF-dosed vs healthy cochlear fibrocytes - ~250 individual cell spectra per condition, each from a separate (by condition) ~250k cell cytospun monolayer of PFA fixed cells on CaF<sub>2</sub> - cells fixed at maximum P8.**

In the nucleic acid triple peak region (725-785 $\text{cm}^{-1}$ ) a general intensity decrease is seen in 5ng/mL dosed cells compared to previously observed 1ng/mL dosed cells. This is coupled with a shift towards the high wavenumber region. In contrast to the previous comparison, the adenine associated peak shows a reduced signal intensity in dosed cells. Once again, the thymine peak shows a dosed cell signal less intense than that of undosed cells. The cytosine peak retains dosed cell signal more intense than that of undosed cells. Noted spectral variations, when compared with those of 1ng/mL dosed cells, further suggest alterations to nucleic acids as a result of inflammation.

Between ~870 $\text{cm}^{-1}$  and 1000 $\text{cm}^{-1}$ , there once again appears to be an increase in signal intensity in dosed cells, though this is less apparent than that seen in the 1ng/mL spectrum. Nonetheless, this supports the suggestion of protein/lipid changes arising from TNF application.

At 1000 $\text{cm}^{-1}$  5ng/mL dosed cells demonstrate both an increased signal intensity and a peak shift towards the high wavenumber region. This is further suggestive of protein alterations induced by inflammation. Though, it should be noted that alterations in protein-related bands may not only imply

structural and functional changes in cells, they may also indicate presence of the pro-inflammatory cytokine TNF.

As seen in 1ng/mL dosed cells, the CH<sub>3</sub> wagging-associated peak at 1032cm<sup>-1</sup>, and 1128cm<sup>-1</sup> C-C stretching/CH<sub>2</sub> vibration bands are of greater intensity in the undosed condition. This further suggests differences in protein structures and metabolic features between dosed and undosed cells.

Between 1200-1400cm<sup>-1</sup> (amide III, C-O stretching, C=C vibrations and CH<sub>2</sub> wagging), the TNF dosed spectrum again demonstrates a higher signal intensity than that of undosed cells. In fact, the 5ng/mL dosage condition appears to yield a slightly greater signal intensity in this region than 1ng/mL dosed cells. This may indicate a correlation between dosage and signal intensity in this region, though further verification is needed.

In contrast to the previous spectrum of this region, the 5ng/mL dosed condition demonstrates greater signal intensity at ~1450cm<sup>-1</sup> than the undosed condition. This is accompanied by a slight shift towards the high wavenumber end of the spectrum. Variations in this band, attributed to CH<sub>2</sub>/CH<sub>3</sub> deformation, suggest inflammation induced changes in lipid and protein structures and abundance.

Once again, the protein region 1540-1625cm<sup>-1</sup> (associated with C=C stretching, N-H bending, tryptophan ring stretching and C-C-H ring vibration) demonstrates higher signal intensity in the undosed cell condition, with little visible difference from the previous spectrum. A slight shift towards the high wavenumber end of the spectrum is present in the dosed condition and, alongside difference in signal intensity, indicates protein variation between dosed and undosed conditions.

As noted previously for this spectrum, a slight shift towards the high wavenumber region may be seen in the amide I/C=O stretching band at  $\sim 1650\text{cm}^{-1}$ . Once again this band demonstrates a higher signal intensity in the undosed cell condition than in the dosed cell condition, though 5ng/mL dosed cell signal intensity appears higher than that of 1ng/mL dosed cells. This supports the previous suggestion of protein variations in dosed cells.

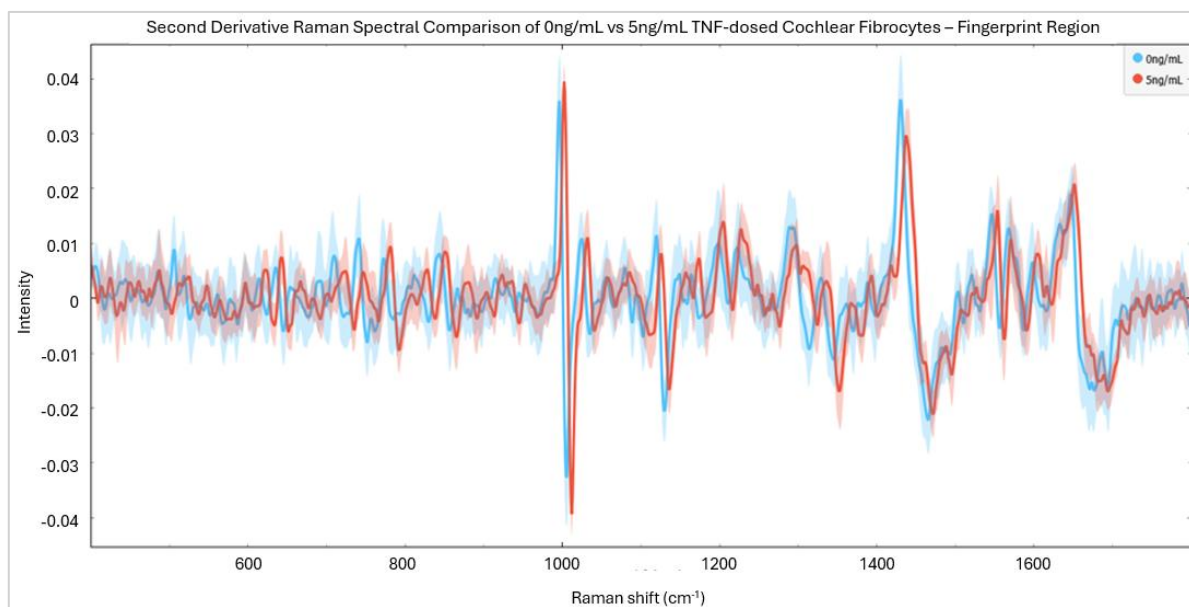


**Figure 38: Second derivative Raman fingerprint region spectra of 0ng/mL and 5ng/mL TNF-dosed cochlear fibrocytes.**

**Second derivative average Raman spectra (fingerprint region) of TNF-dosed vs healthy cochlear fibrocytes - ~250 individual cell spectra per condition, each from a separate (by condition) ~250k cell cytospun monolayer of PFA fixed cells on CaF<sub>2</sub> - cells fixed at maximum**

**P8.**

Second derivative spectra of 0ng/mL and 5ng/mL TNF-dosed cells further illustrate differences in the fingerprint region (Fig. 38), particularly the spectral shift towards the high wavenumber region previously noted. Unlike 1ng/mL dosed cells, differences between dosed and undosed spectra are not particularly visible at  $1032\text{cm}^{-1}$  ( $\text{CH}_3$  wagging of proteins), though variations at  $1128\text{cm}^{-1}$  (C-C stretch/ $\text{CH}_2$  vibration of lipids/glucose) may still be seen. A clear difference at

1450cm<sup>-1</sup> (CH<sub>2</sub>/CH<sub>3</sub> deformation of lipids/proteins) is still seen. Additionally, a difference at 1000cm<sup>-1</sup> (symmetric ring breathing of proteins) is visible.

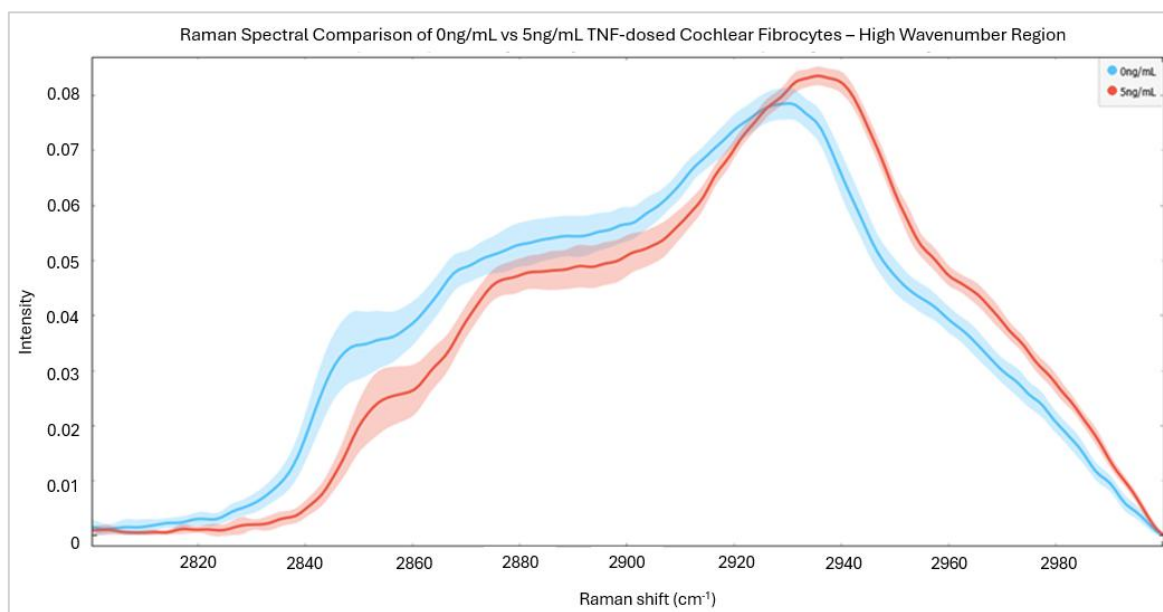


**Figure 39: Average Raman spectra of healthy and 5ng/mL-dosed cochlear fibrocytes following 24hrs incubation with TNF- $\alpha$  (high wavenumber region).**

**Average Raman spectra (high wavenumber region) of TNF-dosed vs healthy cochlear fibrocytes - ~250 individual cell spectra per condition, each from a separate (by condition) ~250k cell cytopspin monolayer of PFA fixed cells on CaF<sub>2</sub> - cells fixed at maximum P8.**

The high wavenumber region of 0ng/mL and 5ng/mL TNF-dosed cells demonstrates further differences between dosed and undosed cell spectra (Fig. 39). As in 1ng/mL TNF-dosed cells, the dosed spectrum in this region appears to demonstrate a shift towards the high wavenumber end of the spectrum, with this shift appearing more substantial than in the lower dose seen. Once again, intensity variations are noted throughout the dosed condition compared with undosed cells with the CH<sub>2</sub> stretching region below ~2920cm<sup>-1</sup> showing a lower signal intensity in dosed cells and the CH<sub>3</sub> stretching region above ~2920cm<sup>-1</sup> showing a higher signal intensity in dosed cells.

Second derivative spectra of 0ng/mL and 5ng/mL TNF-dosed cells in the high wavenumber region lend further clarity differences between dosed and undosed conditions (Fig. 40), with spectral shift once again noted in the dosed condition. Additionally, signal intensity differences between dosed and undosed are again seen around 2850cm<sup>-1</sup>.

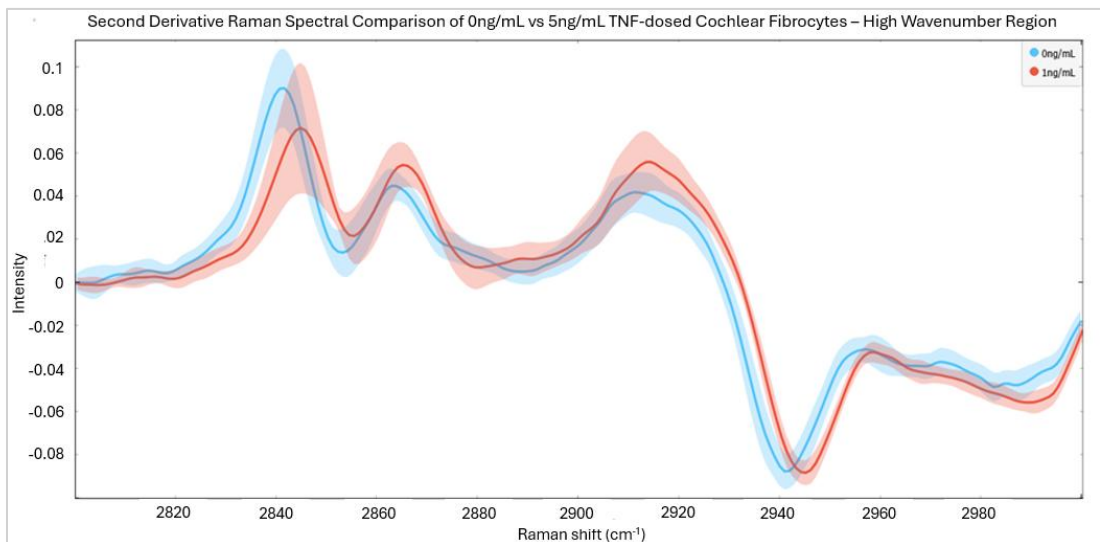


**Figure 41: Second derivative Raman high wavenumber region spectra of 0ng/mL and 5ng/mL TNF-dosed cochlear fibrocytes.**

**Second derivative average Raman spectra (high wavenumber region) of TNF-dosed vs healthy cochlear fibrocytes - ~250 individual cell spectra per condition, each from a separate (by condition) ~250k cell cytopspin monolayer of PFA fixed cells on CaF<sub>2</sub> - cells fixed at maximum P8.**

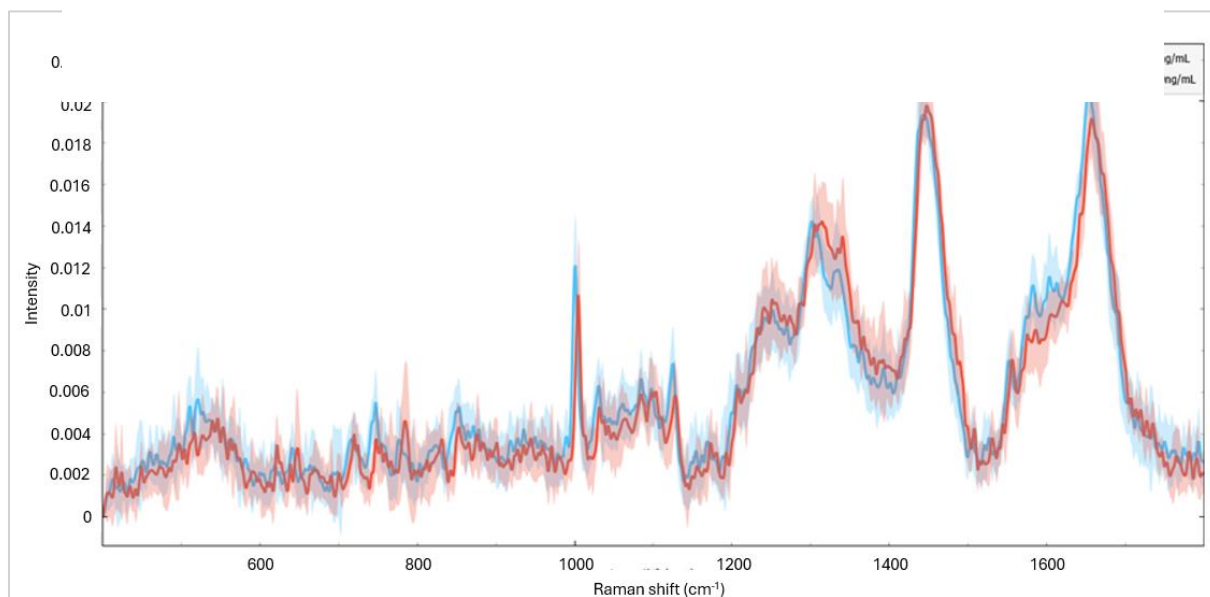


**Figure 40: Average Raman spectra of healthy and 10ng/mL-dosed cochlear fibrocytes following 24hrs incubation with TNF- $\alpha$  (fingerprint region).**

**Average Raman spectra (fingerprint region) of TNF-dosed vs healthy cochlear fibrocytes - ~250 individual cell spectra per condition, each from a separate (by condition) ~250k cell cytopspin monolayer of PFA fixed cells on CaF<sub>2</sub> - cells fixed at maximum P8.**

In the fingerprint region of undosed and 10ng/mL dosed cells (Fig. 41), further variati98

between conditions can be seen, with some changes notable between 5ng/mL and 10ng/mL dosage conditions. Once again, variation around average spectra may indicate less variation between conditions than apparent.

Variation between samples below  $600\text{cm}^{-1}$  does not vary substantially from that seen in undosed and 5ng/mL comparisons. Nonetheless, the presence of intensity differences in this region indicates polysaccharide/nucleic acid ( $\text{CH}_2$  bending, C-C-C deformations) changes arising from TNF dosage.

In the nucleic acid triple peak region ( $725\text{-}785\text{cm}^{-1}$ ) signal intensity is generally similar in the 10ng/mL spectrum to that seen in 5ng/mL dosed cells. In contrast to the previous comparison, the adenine associated peak shows an increased signal intensity in dosed cells.

Between  $\sim 870\text{cm}^{-1}$  and  $1000\text{cm}^{-1}$ , signal intensity in 10ng/mL dosed cells is reduced compared with previous dosages. Nonetheless, this supports the suggestion of protein/lipid changes arising from TNF application as signal in the dosed condition still differs from that of the undosed condition.

In contrast to previous spectra, 10ng/mL dosed cells show a decrease in signal intensity at  $1000\text{cm}^{-1}$ , with dosed signal now less intense than undosed. Though this does not correlate with trends suggested in previous spectra, protein alterations are still suggested.

As seen in previous spectra cells,  $1032\text{cm}^{-1}$  and  $1128\text{cm}^{-1}$  bands are of greater intensity in the undosed condition than in dosed cells. This relationship appears to suggest consistent differences in protein structure/abundance and metabolic features between dosed and undosed cells and may be indicative of TNF presence.

As in previous spectra, between  $1200\text{-}1400\text{cm}^{-1}$  (amide III, C-O stretching, C=C vibrations and  $\text{CH}_2$  wagging), the TNF dosed spectrum demonstrates a higher signal intensity than that of undosed cells. However, signal intensity in this region is not as high in 10ng/mL cells than 5ng/mL and 1ng/mL dosed cells. This goes against the previous suggestion of correlation between dosage and signal intensity in this region.

Similarly to 5ng/mL dosed cells, 10ng/mL dosed cells demonstrate greater signal intensity than undosed cells at  $\sim 1450\text{cm}^{-1}$ . However, this variation is small and may be accounted for by variation around the dosage average. Once again, a slight shift towards the high wavenumber end of the spectrum is seen.

As before, the protein region  $1540\text{--}1625\text{cm}^{-1}$  demonstrates higher signal intensity in the undosed cell condition than in dosed cells. This region is associated with C=C stretching, N-H bending, tryptophan ring stretching and C-C-H ring vibration. The difference noted between dosed and undosed cells appears consistent across dosage conditions and suggests differences in protein structure/abundance between dosed and undosed cells. This may be indicative of TNF presence.

At  $\sim 1650\text{cm}^{-1}$ , a slight shift towards the high wavenumber region may be seen in 10ng/mL dosed cells, though this is less substantial than that noted in 5ng/mL dosed cells. Nonetheless, this band demonstrates a higher signal intensity in the undosed cell condition than in the dosed cell condition, supporting the previous suggestion of protein variations in dosed cells.

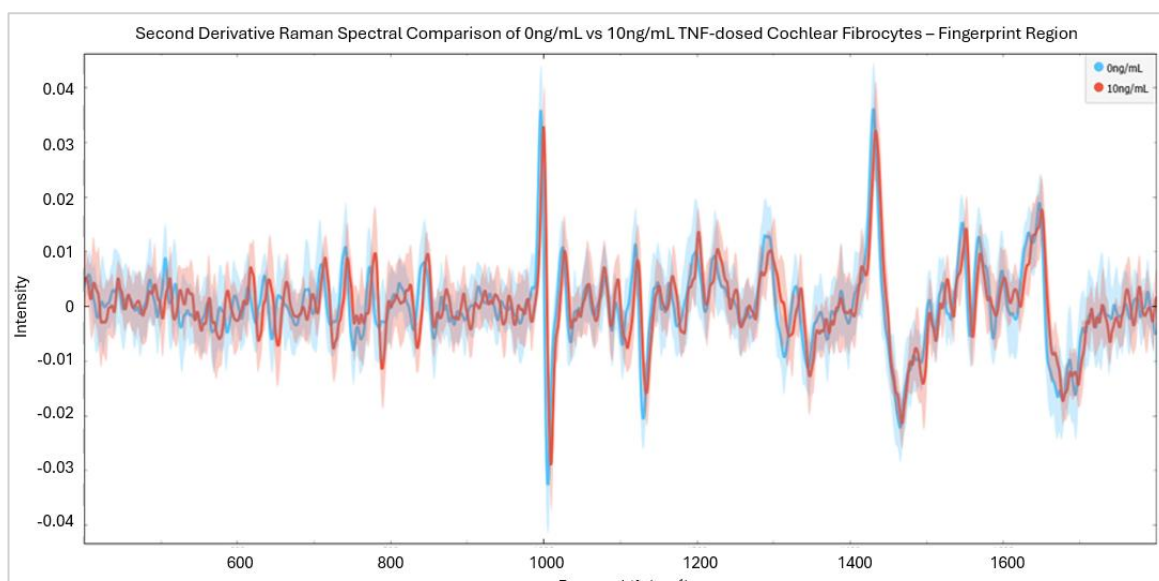


**Figure 42: Second derivative Raman fingerprint region spectra of 0ng/mL and 10ng/mL TNF-dosed cochlear fibrocytes.**

**Second derivative average Raman spectra (fingerprint region) of TNF-dosed vs healthy cochlear fibrocytes - ~250 individual cell spectra per condition, each from a separate (by condition) ~250k cell cytopun monolayer of PFA fixed cells on CaF<sub>2</sub> - cells fixed at maximum P8.**

Second derivative spectra of 0ng/mL and 10ng/mL TNF-dosed cells further illustrate differences in the fingerprint region (Fig. 42), though the spectral shift previously noted is not as clear. Though differences between dosed and undosed spectra are not as visible as in previous dosage at  $1032\text{cm}^{-1}$  ( $\text{CH}_3$  wagging of proteins) and  $1128\text{cm}^{-1}$  (C-C stretch/ $\text{CH}_2$  vibration of lipids/glucose), differences at  $1000\text{cm}^{-1}$  (symmetric ring breathing of proteins) and  $1450\text{cm}^{-1}$  ( $\text{CH}_2/\text{CH}_3$  deformation of lipids/proteins) are still seen.

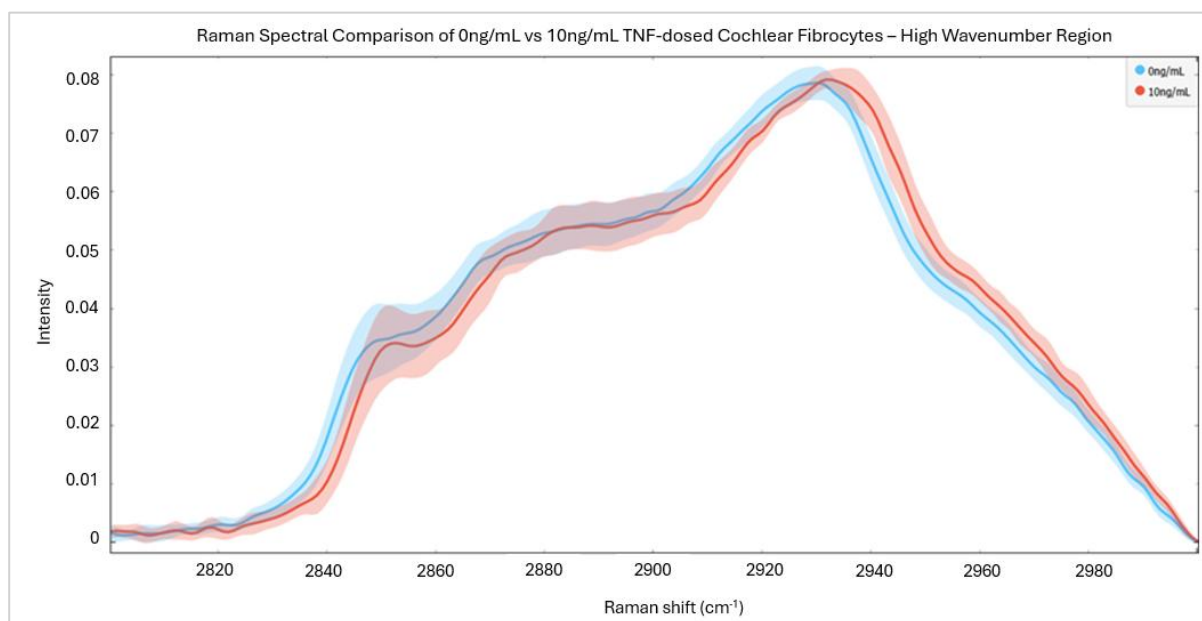


**Figure 43: Average Raman spectra of healthy and 10ng/mL-dosed cochlear fibrocytes following 24hrs incubation with TNF- $\alpha$  (high wavenumber region).**

**Average Raman spectra (high wavenumber region) of TNF-dosed vs healthy cochlear fibrocytes**

**- ~250 individual cell spectra per condition, each from a separate (by condition) ~250k cell cytopun monolayer of PFA fixed cells on CaF2 - cells fixed at maximum P8.**

In contrast to 1ng/mL and 5ng/mL TNF-dosed cells, the spectrum of 10ng/mL TNF-dosed cells shows only a slight shift in the high wavenumber region towards the  $3600\text{cm}^{-1}$  end of the spectrum (Fig 43). Nonetheless, intensity variations are still visible, though these too are of reduced magnitude compared with lower dosages observed. As seen previously, the dosed condition appears of lower intensity than undosed in the  $\text{CH}_2$  stretching region and higher signal intensity than undosed cells in the  $\text{CH}_3$  stretching region, though there is considerable overlap across averages.

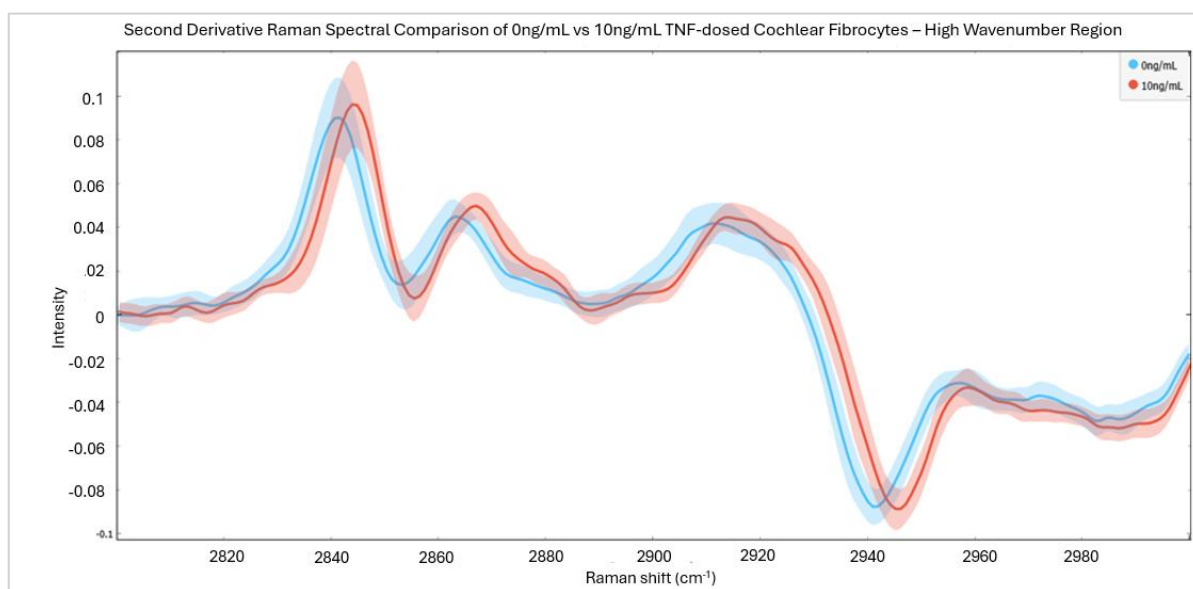


**Figure 44: Second derivative Raman high wavenumber region spectra of 0ng/mL and 10ng/mL TNF-dosed cochlear fibrocytes.**

**Second derivative average Raman spectra (high wavenumber region) of TNF-dosed vs healthy cochlear fibrocytes - ~250 individual cell spectra per condition, each from a separate (by condition) ~250k cell cytopspin monolayer of PFA fixed cells on CaF2 - cells fixed at maximum P8.**

Second derivative spectra of 0ng/mL and 10ng/mL TNF-dosed cells in the high wavenumber region again aid in clarifying differences between dosed and undosed conditions (Fig. 44). Signal intensity differences between dosed and undosed are again seen around  $2850\text{cm}^{-1}$ , though the nature of this difference appears to vary from lower dose spectra.

Finally, in the fingerprint region of undosed and 50ng/mL dosed cells (Fig. 45), points of variation between conditions can be seen once again. At this dosage level, variation around the average spectrum is substantial, with true variation between conditions difficult to visualise as a

result. This variation around the average likely arises because of varying cell health due to inflammation, with many cells having died off at this level.

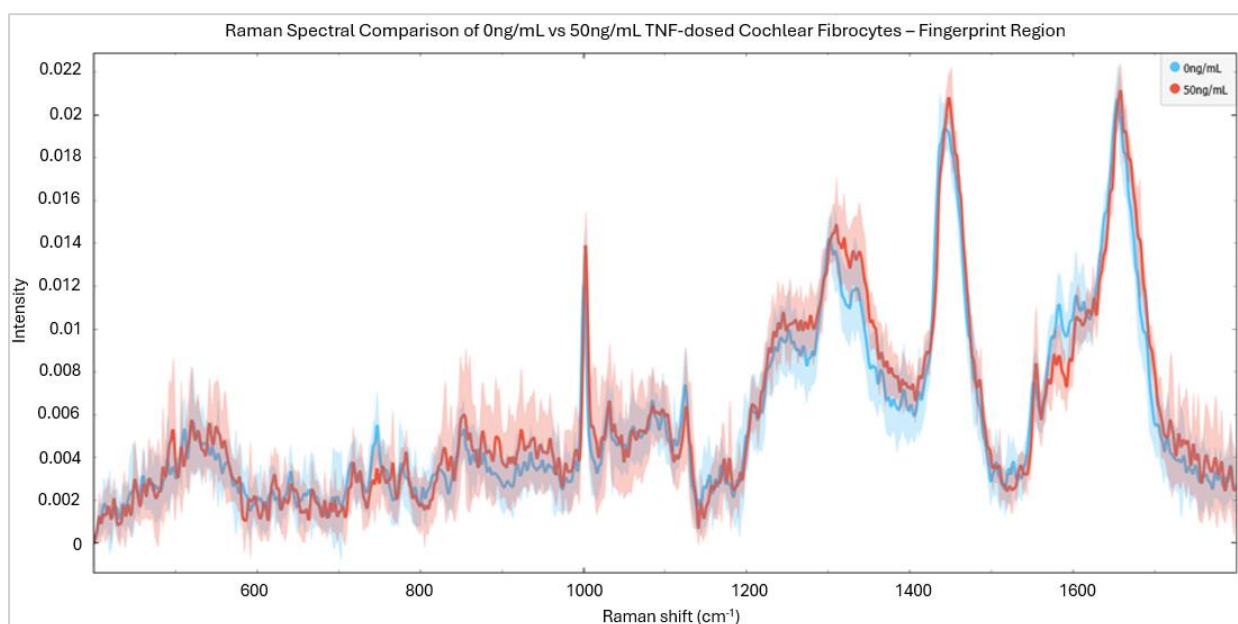


**Figure 45: Average Raman spectra of healthy and 50ng/mL-dosed cochlear fibrocytes following 24hrs incubation with TNF- $\alpha$  (fingerprint region).**

**Average Raman spectra (fingerprint region) of TNF-dosed vs healthy cochlear fibrocytes - ~250 individual cell spectra per condition, each from a separate (by condition) ~250k cell cytospun monolayer of PFA fixed cells on CaF<sub>2</sub> - cells fixed at maximum P8.**

In contrast to previous dosed spectra, below 600cm<sup>-1</sup> the 50ng/mL dosage condition demonstrates a higher signal intensity than undosed cells. Though this relationship differs from that previously seen, intensity differences in this region suggest polysaccharide/nucleic acid (CH<sub>2</sub> bending, C-C-C deformations) changes arising from TNF dosage.

In the nucleic acid triple peak region (725-785cm<sup>-1</sup>) signal intensity in 50ng/mL cells is slightly lower than in previous dosage conditions. This is particularly apparent from the cytosine peak. This, alongside variations below 600cm<sup>-1</sup>, is suggestive of nucleic acid alterations as a result of TNF dosage, particularly at higher dosages such as 50ng/mL.

Between ~870cm<sup>-1</sup> and 1000cm<sup>-1</sup>, signal intensity in 50ng/mL dosed cells is increased compared with previous dosages, with much of this region now demonstrating greater signal intensity than undosed cells. Though this contrasts with previous spectra, variations in this region support the

suggestion of protein/lipid changes arising from TNF application. Increased signal intensity in this region at this dosage may be associated with the lipid accumulation expected from apoptotic cells.

Similarly to 1ng/mL and 5ng/mL spectra, 50ng/mL dosed cells show increased signal intensity at  $1000\text{cm}^{-1}$  compared to undosed cells. This suggests that the decreased intensity seen at 10ng/mL is somewhat abnormal, with other dosed spectra demonstrating a trend of increasing signal intensity with higher dosage. Regardless of this trend, variations from undosed cells at this band location are further indicative of protein variations in TNF-dosed samples.

In contrast to previous spectra, the protein-associated  $\text{CH}_3$  wagging band at  $1032\text{cm}^{-1}$  demonstrates signal intensity similar to that of undosed cells. Though different from previous dosed spectra, this does not rule out protein variation from inflammation, though increase in intensity of this band is likely linked to the presence of TNF at high dosage (50ng/mL) rather than due to structural/functional changes.

At  $1128\text{cm}^{-1}$ , signal remains of greater intensity in the undosed condition. However, signal intensity appears to be increased in 50ng/mL dosed cells compared with lower dosages. This may suggest inflammation associated lipid accumulation at high TNF levels.

As in previous spectra, between  $1200\text{-}1400\text{cm}^{-1}$  (amide III, C-O stretching, C=C vibrations and  $\text{CH}_2$  wagging), the TNF dosed spectrum demonstrates a higher signal intensity than that of undosed cells. This further validates noted differences between dosed and undosed cell spectra.

Similarly to 5ng/mL and 10ng/mL dosed cells, 50ng/mL dosed cells demonstrate greater signal intensity than undosed cells at  $\sim 1450\text{cm}^{-1}$ . This variation appears to be greater than that seen in previous comparisons and is indicative of greater degrees of  $\text{CH}_2$  and  $\text{CH}_3$  deformation arising at higher dosages. Unlike previous spectra, no shift in this band is seen in the dosed condition.

As before, the protein region  $1540\text{-}1625\text{cm}^{-1}$  demonstrates higher signal intensity in the undosed cell condition than in dosed cells. This validates that the difference noted between dosed and undosed cells is consistent across dosage conditions and suggests differences in protein structure/abundance between dosed and undosed cells. The consistency seen across dosages

additionally suggests that variation seen between dosed and undosed cells arises due to genuine structural and functional changes rather than from TNF presence.

Unlike the previous dosed spectra, 50ng/mL dosed cells demonstrate slightly greater signal intensity at  $\sim 1650\text{cm}^{-1}$  than undosed cells. Additionally, though a slight shift towards the high wavenumber region is still present, this is less substantial than in other dosage conditions. With the previous analyses in mind, this may be indicative of either TNF dosage or protein variation arising from it.

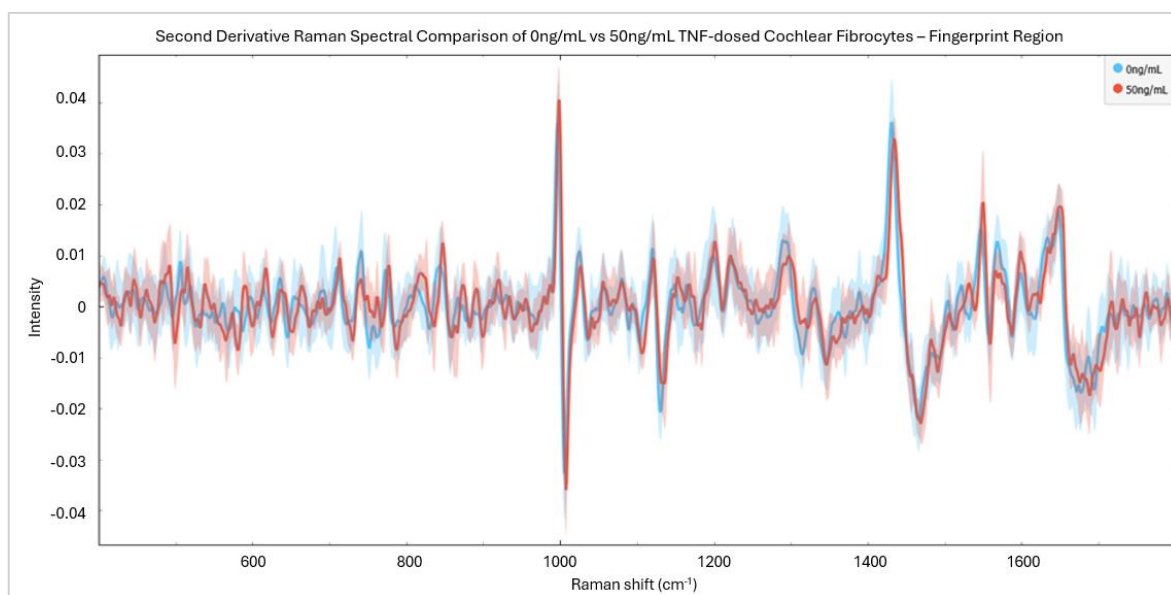


**Figure 46: Second derivative Raman fingerprint region spectra of 0ng/mL and 50ng/mL TNF-dosed cochlear fibrocytes.**

**Second derivative average Raman spectra (fingerprint region) of TNF-dosed vs healthy cochlear fibrocytes - ~250 individual cell spectra per condition, each from a separate (by condition) ~250k cell cytospun monolayer of PFA fixed cells on CaF<sub>2</sub> - cells fixed at maximum P8.**

Second derivative spectra of 0ng/mL and 50ng/mL TNF-dosed cells further clarify differences in the fingerprint region (Fig. 46). Though clear differences between dosed and undosed spectra are no longer visible at  $1000\text{cm}^{-1}$  (symmetric ring breathing of proteins), variations can once again be seen at  $1032\text{cm}^{-1}$  ( $\text{CH}_3$  wagging of proteins) and  $1128\text{cm}^{-1}$  (C-C stretch/ $\text{CH}_2$  vibration of lipids/glucose). As before, differences at and  $1450\text{cm}^{-1}$  ( $\text{CH}_2/\text{CH}_3$  deformation of lipids/proteins) are seen. From this visual analysis, protein and lipid alterations (particularly in  $\text{CH}_2/\text{CH}_3$  associated regions) appear to be the main source of variation between dosed and undosed cells. However, it should be noted that level of difference varies across dosage conditions.

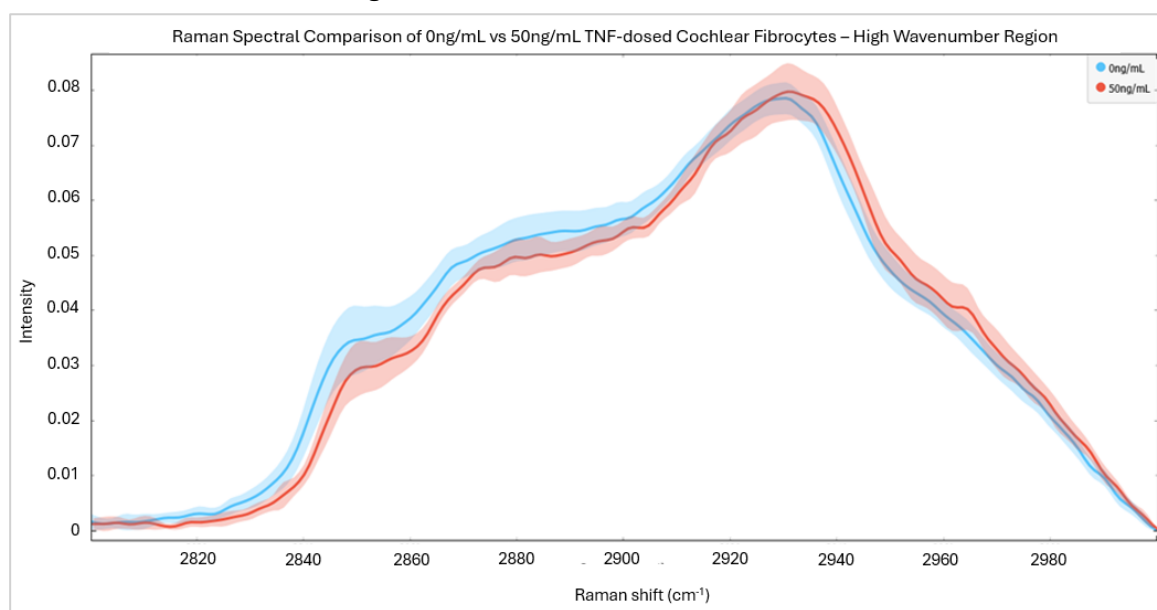


**Figure 47: Average Raman spectra of healthy and 50ng/mL-dosed cochlear fibrocytes following 24hrs incubation with TNF- $\alpha$  (high wavenumber region).**

**Average Raman spectra (high wavenumber region) of TNF-dosed vs healthy cochlear fibrocytes - ~250 individual cell spectra per condition, each from a separate (by condition) ~250k cell cytopspin monolayer of PFA fixed cells on CaF<sub>2</sub> - cells fixed at maximum P8.**

As seen in 10ng/mL TNF-dosed cells, the spectrum of 50ng/mL TNF-dosed cells shows only a slight shift in the high wavenumber region (Fig.47). Once again, intensity variations are visible between dosed and undosed cell spectra, with the dosed condition of lower intensity in the  $\text{CH}_2$  stretching region and higher signal intensity in the  $\text{CH}_3$  stretching region.

Second derivative spectra once again aid in clarifying differences between dosed and undosed conditions (Fig. 48). Signal intensity differences between dosed and undosed can be seen around  $2850\text{cm}^{-1}$ , with additional differences arising at around  $2910\text{cm}^{-1}$ .

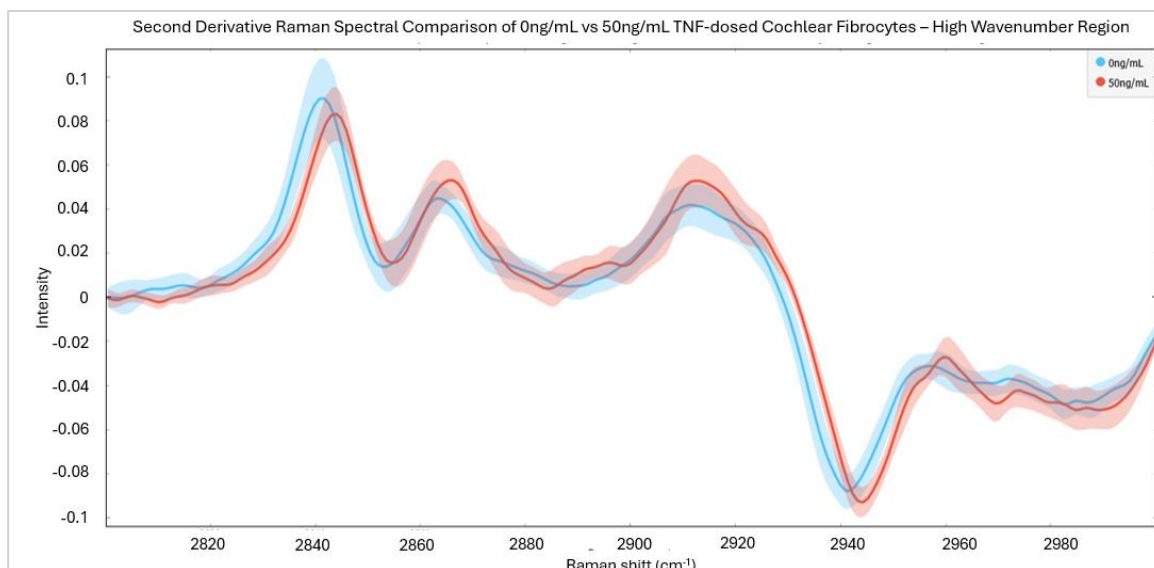


**Figure 48: Second derivative Raman high wavenumber region spectra of 0ng/mL and 50ng/mL TNF-dosed cochlear fibrocytes.**

**Second derivative average Raman spectra (high wavenumber region) of TNF-dosed vs healthy cochlear fibrocytes - ~250 individual cell spectra per condition, each from a separate (by condition) ~250k cell cytopun monolayer of PFA fixed cells on CaF<sub>2</sub> - cells fixed at maximum P8.**

Examining spectral changes across conditions statistically, PCA of the fingerprint (Fig. 49) and high wavenumber (Fig. 50) regions demonstrates clear clustering of samples based upon dosage condition. Scatter plots of fingerprint region PCA reveal distinct groupings among samples, with smaller sub-groups visible in some dosage conditions. This sub-grouping is not present among undosed cells and suggests inter-condition variation among dosed samples only. In this case, such variation has likely arisen due to variable uptake of TNF by cells based on factors such as cell cycle stage, as well as variable inflammatory response. Nonetheless, condition-based clustering is clear, with the corresponding loadings plot indicating sources of variation at previously identified spectral regions.

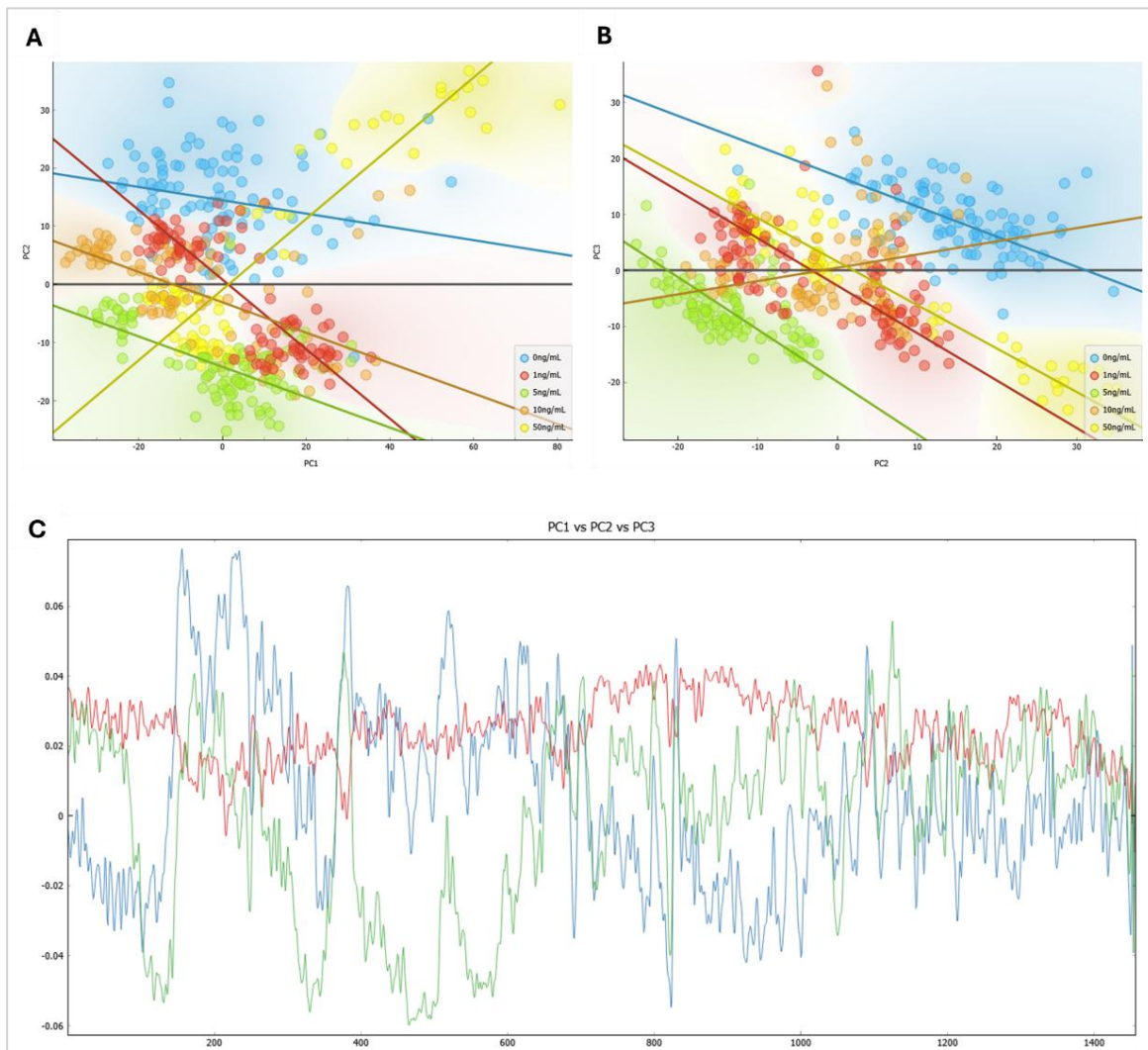


**Figure 49: PCA of the fingerprint region of undosed vs TNF-dosed cochlear fibrocytes.**

**From average Raman spectra (fingerprint region) of TNF-dosed vs healthy cochlear fibrocytes - ~250 individual cell spectra per condition, each from a separate (by condition) ~250k cell cytopspin monolayer of PFA fixed cells on CaF<sub>2</sub> - cells fixed at maximum P8. A) Scatter plot of PC1 (23%) vs PC2 (14%). B) Scatter plot of PC2 (14%) vs PC3 (6%). C) Loadings plot of PC1 (red) vs PC2 (green) vs PC3 (blue).**

Similarly, scatter plots of high wavenumber region PCA demonstrate condition-based groupings, with smaller sub-groups once again visible in dosed conditions (Fig. 50). This is most apparent in the 1ng/mL dosage condition, with some samples appearing to sit among undosed samples, while others sit closer to other dosed samples.

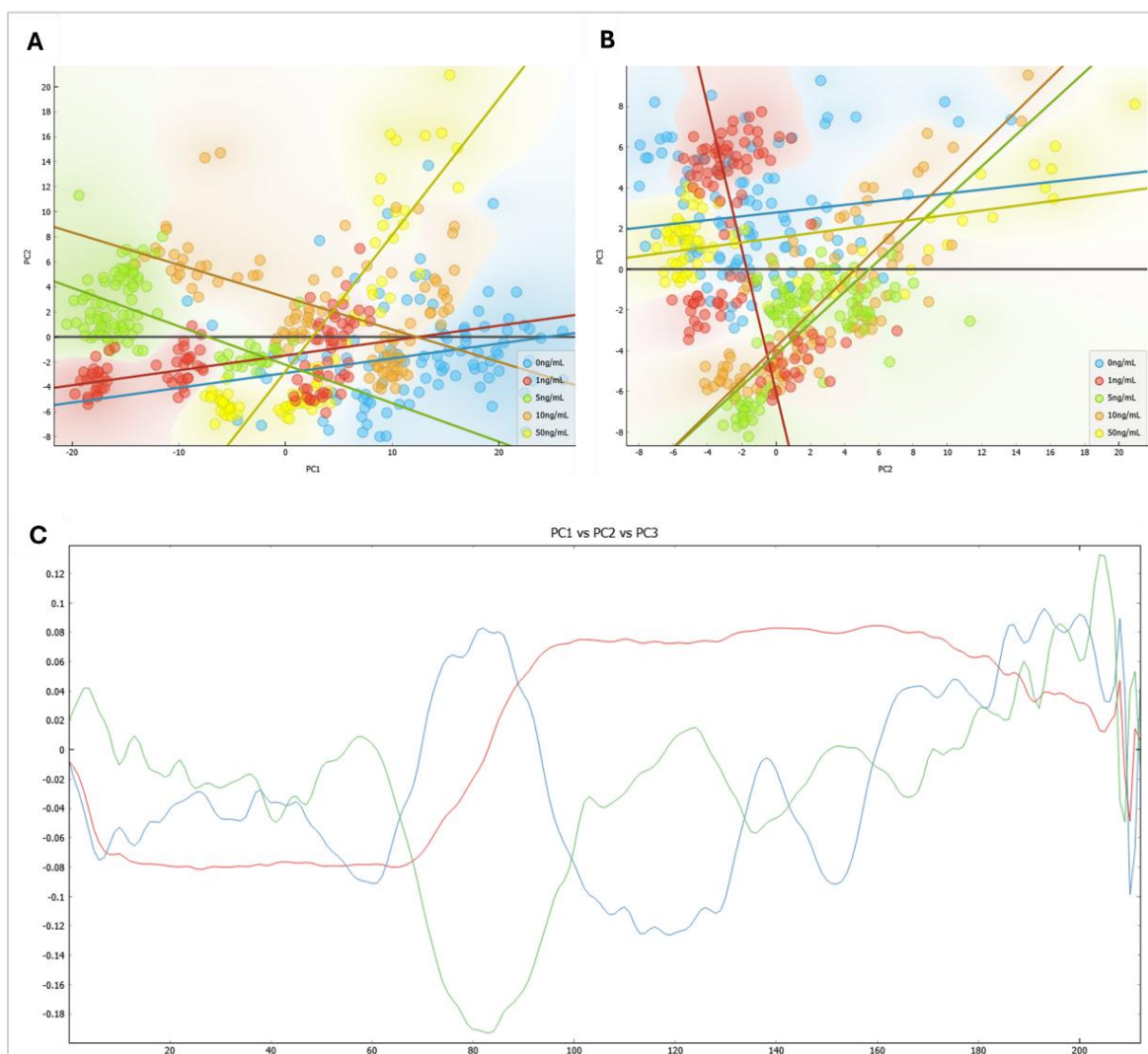


**Figure 50: PCA of the fingerprint region of undosed vs TNF-dosed cochlear fibrocytes. From average Raman spectra (fingerprint region) of TNF-dosed vs healthy cochlear fibrocytes - ~250 individual cell spectra per condition, each from a separate (by condition) ~250k cell cytopspun monolayer of PFA fixed cells on CaF<sub>2</sub> - cells fixed at maximum P8. A) Scatter plot of PC1 (62%) vs PC2 (10%). B) Scatter plot of PC2 (10%) vs PC3 (8%). C) Loadings plot of PC1 (red) vs PC2 (green) vs PC3 (blue).**

The distinction between undosed cells as well as TNF dosage conditions is further validated through predictive modelling. A neural network model yields high prediction accuracy for both the fingerprint and high wavenumber regions, evidencing detectable differences between conditions, even where manual distinction proves troublesome. This is shown via confidence tables in figure 51 below.

		Predicted					$\Sigma$
		0ng/mL	1ng/mL	5ng/mL	10ng/mL	50ng/mL	
Actual	0ng/mL	98.8 %	1.2 %	0.0 %	0.0 %	0.0 %	249
	1ng/mL	0.0 %	98.8 %	0.4 %	0.4 %	0.4 %	250
	5ng/mL	0.0 %	0.4 %	99.6 %	0.0 %	0.0 %	250
	10ng/mL	0.4 %	0.0 %	0.0 %	98.4 %	1.2 %	250
	50ng/mL	0.0 %	0.0 %	0.0 %	0.0 %	100.0 %	186
	$\Sigma$	247	251	250	247	190	1185

		Predicted					$\Sigma$
		0ng/mL	1ng/mL	5ng/mL	10ng/mL	50ng/mL	
Actual	0ng/mL	95.6 %	1.6 %	0.0 %	1.2 %	1.6 %	249
	1ng/mL	2.4 %	96.8 %	0.0 %	0.8 %	0.0 %	250
	5ng/mL	0.0 %	0.0 %	99.6 %	0.4 %	0.0 %	250
	10ng/mL	0.4 %	0.0 %	0.0 %	98.8 %	0.8 %	250
	50ng/mL	0.0 %	0.0 %	0.0 %	0.0 %	100.0 %	186
	$\Sigma$	245	246	249	253	192	1185

**Figure 51: Confidence tables for neural network modelling of Raman spectra of murine cochlear fibrocytes following 24hrs incubation with TNF- $\alpha$ .**

**From Raman spectra of TNF-dosed vs healthy cochlear fibrocytes each from a separate (by condition) ~250k cell cytopun monolayer of PFA fixed cells on CaF2 - cells fixed at maximum P8. A) Fingerprint region B) High wavenumber region.**

To summarise the findings of TNF-dosed cell Raman examinations, visible differences could be seen between dosed and undosed spectra at all dosage levels. Manual comparison of spectra indicates these differences arise in multiple regions, including those attributed to nucleic acids, proteins, lipids, polysaccharides, and amino acids. In particular, protein and lipid alterations originating in CH<sub>2</sub> and CH<sub>3</sub> vibrational modes (e.g. 1450cm<sup>-1</sup>, high wavenumber region) are implicated both in fingerprint and high wavenumber region analyses. Some evidence of lipid accumulation is seen at high TNF dosages (870-1000cm<sup>-1</sup>, 1128cm<sup>-1</sup>)- a finding consistent with expectations for inflamed and apoptotic cells. Regions of varied association (1200-1400cm<sup>-1</sup>, 1540-1625cm<sup>-1</sup>) consistent differences in intensity are noted between dosed and undosed cell conditions, though no dosage-

based correlation is found. Distinction of dosage conditions as well as healthy cells is verified by both multivariate analysis (PCA) and neural network.

#### 3.4.6. ATR-FTIR of TNF- $\alpha$ -dosed Cochlear Fibrocyte Supernatant

In analysing the FTIR spectra of TNF-dosed cochlear fibrocyte supernatants (Fig. 52), it must first be noted that the spectra show a slightly lower overall absorbance than those seen in the first set of undosed cells examined. This is attributed to variations in sample preparation conditions such as laboratory temperature and humidity, as well as general variation in individual cell populations due to factors including cell cycle stage. As undosed supernatant was included in this stage of research, comparison across dosage conditions and undosed cells is still possible. Cell supernatants were distinct in all cases from matched media controls.

All supernatant spectra demonstrate bands indicating cellular presence via DNA (950-1200 $\text{cm}^{-1}$ ), glycogen and carbohydrates (~1030-1080 $\text{cm}^{-1}$ ), amides (I- ~1650 $\text{cm}^{-1}$ , II- ~1540 $\text{cm}^{-1}$ , III- 1300-1500 $\text{cm}^{-1}$ ), and lipids (~1745 $\text{cm}^{-1}$ , 2800-3050 $\text{cm}^{-1}$ ). Comparing spectra by eye, general peaks appear to be similar in the majority of conditions, with the largest variations from trends appearing in the 1ng/mL spectra. This spectrum demonstrates increased intensity and peak variations in the DNA/carbohydrate associated region (950-1200 $\text{cm}^{-1}$ ) and a relatively smaller decrease in intensity in the high wavenumber region.

It should also be noted that the peak previously attributed to histidine ( $1590\text{cm}^{-1}$ ) seemingly demonstrates the most distinct variation across all conditions, with intensity appearing to increase as dosage level rises.

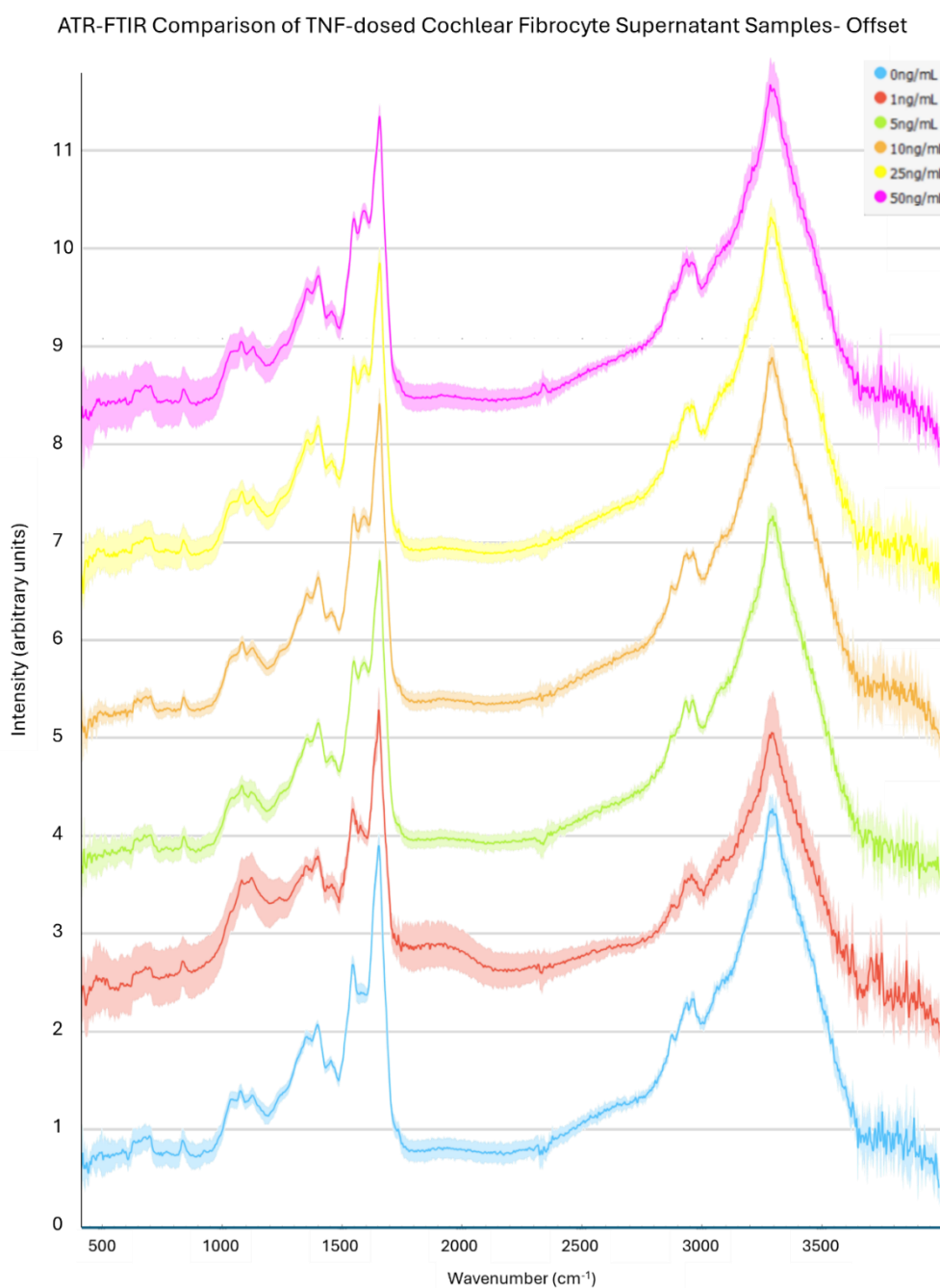


**Figure 52: ATR-FTIR spectra of TNF-dosed cochlear fibrocyte supernatant samples.**  
Average ATR-FTIR spectra of supernatant from healthy vs TNF-dosed cochlear fibrocyte cultures. Supernatant averages formed of 9 spectra (3 per slide, 3 slides) from a ~200k cell population of cells at maximum P8.

Second derivative spectra demonstrate variations further, with particular clarity arising in the distinction of the 1ng/mL dosage condition from others trialled (Fig. 53). As noted above, variations between conditions are seen in regions denoting glycogen and carbohydrates ( $\sim 1030\text{-}1080\text{cm}^{-1}$ ) and amide 1 ( $1650\text{cm}^{-1}$ ). Once again, the peak previously attributed to histidine demonstrates clear variation, with the undosed and lowest dosage conditions appearing distinct from others trialled.

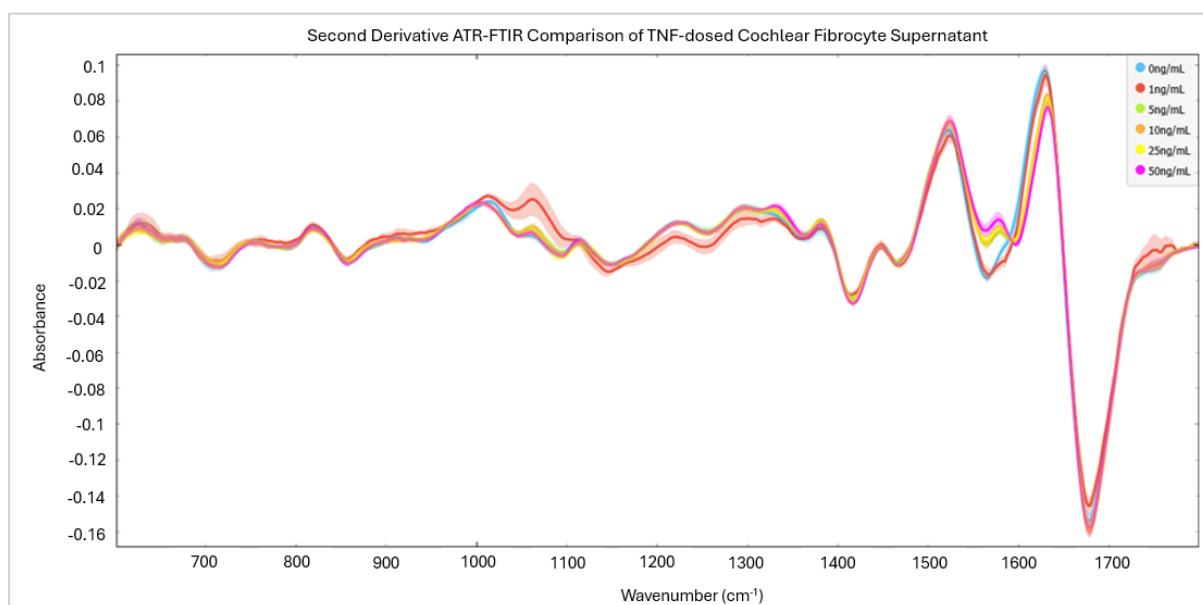


**Figure 53: Second derivative ATR-FTIR fingerprint region spectra of TNF-dosed cochlear fibrocyte supernatants.**

**Second derivative average ATR-FTIR spectra of supernatant from healthy vs TNF-dosed cochlear fibrocyte cultures. Supernatant averages formed of 9 spectra (3 per slide, 3 slides) from a  $\sim 200\text{k}$  cell population of cells at maximum P8.**

Principal component analysis of spectra indicate differences between spectra, though visualisation of other conditions is limited by the more substantially different 1ng/mL dosage sample. PCA of all dosage samples in the fingerprint region revealed 97% of variance accounted for by 6 principal components. The corresponding scatter plot (Fig. 54) shows some evidence of clustering in conditions, with 1ng/mL forming a distinct group. Clustering of 0ng/mL samples can also be seen. The loadings plot for this analysis indicates variation arising from amide and other protein vibrations ( $1450\text{cm}^{-1}$ ,  $1550\text{cm}^{-1}$ ,  $1650\text{cm}^{-1}$ ). This supports the findings of other experiments, with protein variation noted to arise from inflammation.

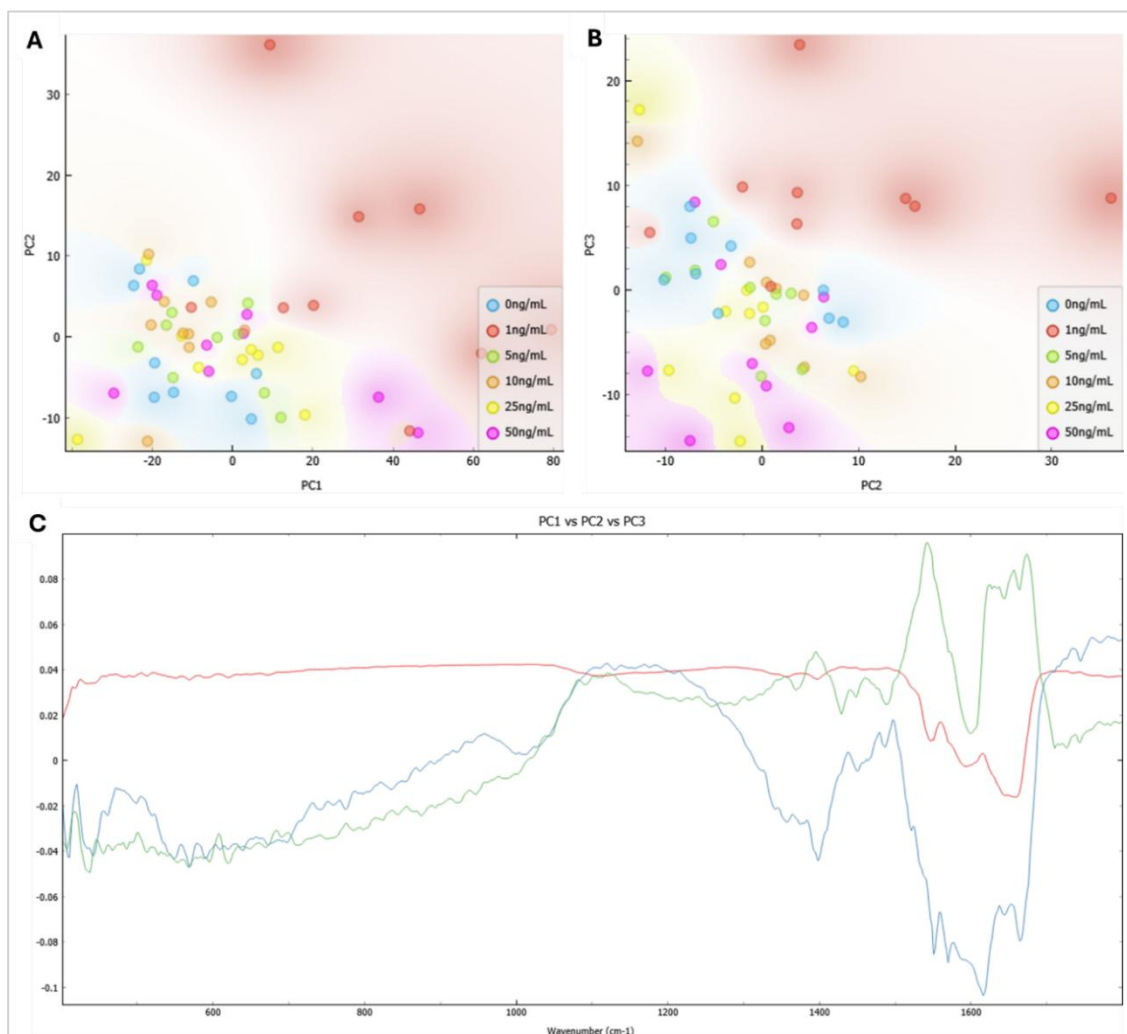


**Figure 54: PCA of the fingerprint region of TNF-dosed cochlear fibrocyte supernatant.**

**Average ATR-FTIR spectra of supernatant from healthy vs TNF-dosed cochlear fibrocyte cultures. Supernatant averages formed of 9 spectra (3 per slide, 3 slides) from a ~200k cell population of cells at maximum P8. A) Scatter plot of PC1 (76%) vs PC2 (10%). B) Scatter plot of PC2 (10%) vs PC3 (7.1%). C) Loadings plot of PC1 (red) vs PC2 (green) vs PC3 (blue).**

PCA of the high wavenumber region supports this hypothesis, with further protein-related variation identified. Scatter plots of samples once again show grouping in the 1ng/mL dosage, as well as in 0ng/mL, 50ng/mL and 25ng/mL conditions (Fig. 55). The 5ng/mL and 10ng/mL conditions do not demonstrate distinct sample clusters. Corresponding loadings plots suggest, once again, that the majority of variation across conditions arises in protein-related regions.

Based upon ATR-FTIR analysis, the 1ng/mL dosage condition appears to be distinct from both other dosage and undosed control conditions. Whether this arises as a result of dosage-induced cell

changes or as a variation arising during sampling through human error or lack of sample homogeneity is unknown. The latter is assumed presently due to the increased baseline intensity seen.

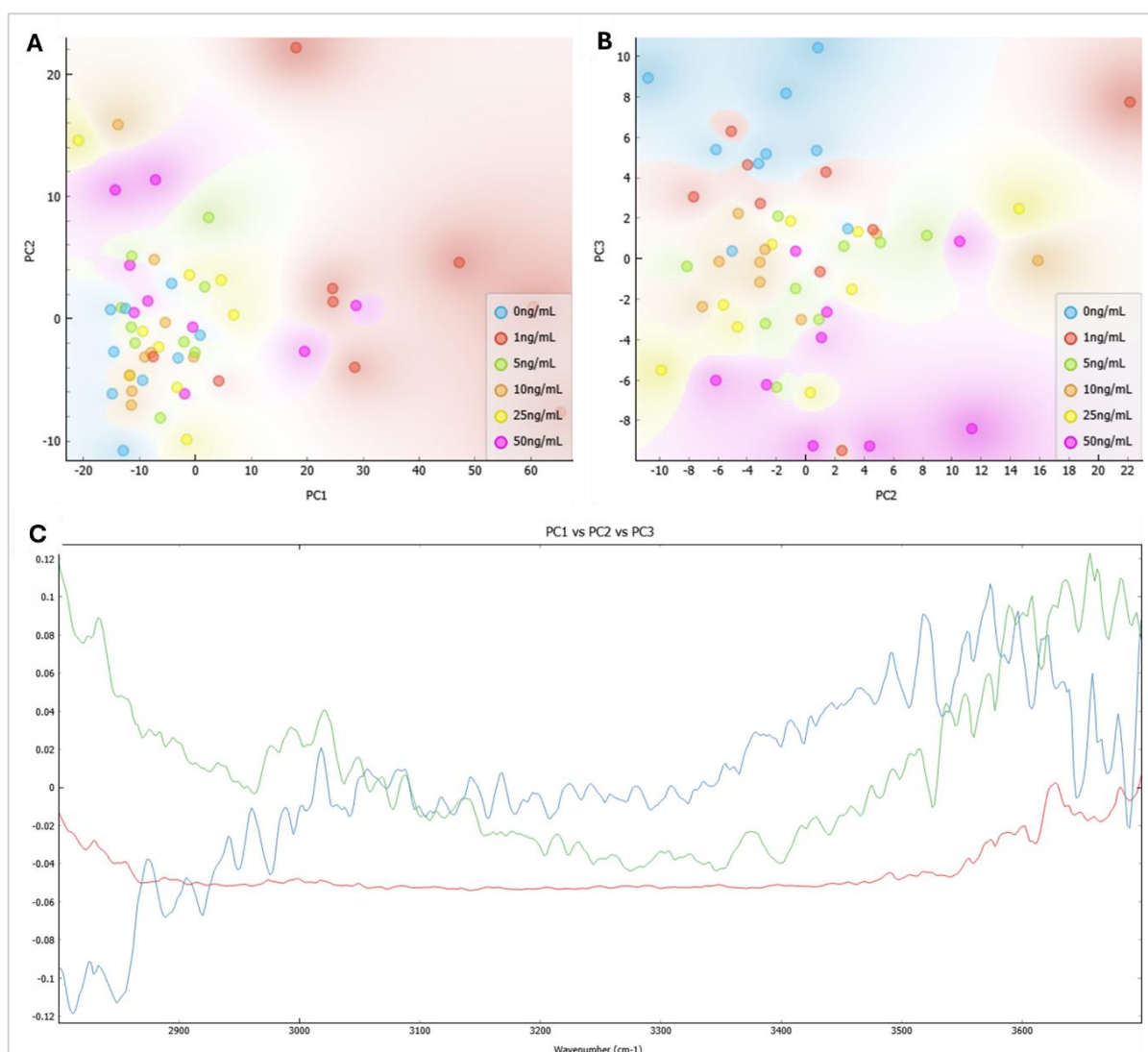


**Figure 55: PCA of the high wavenumber region of TNF-dosed cochlear fibrocyte supernatant.**

From average ATR-FTIR spectra of supernatant from healthy vs TNF-dosed cochlear fibrocyte cultures. Supernatant averages formed of 9 spectra (3 per slide, 3 slides) from a ~200k cell population of cells at maximum P8. A) Scatter plot of PC1 (65%) vs PC2 (7.1%). B) Scatter plot of PC2 (7.1%) vs PC3 (4.2%). C) Loadings plot of PC1 (red) vs PC2 (green) vs PC3 (blue).

In general, this data serves to demonstrate detectable differences between dosage conditions from TNF-dosed cochlear fibrocyte supernatant. Protein-related variations are believed to be the source of these differences, consistent with presence of pro-inflammatory cytokines as well as structural/functional changes to proteins that may indicate inflammation. Of particular interest is the

variation seen at  $1590\text{cm}^{-1}$  which is presently attributed to histidine. This appears to be a source of great variation across PC2 and PC3 particularly.

### 3.4.7. The Induction of Inflammation in Cochlear Fibrocyte Cultures by IL-1 $\beta$ Dosage

Immunocytochemistry demonstrates that, even at the lowest administered dose (1ng/mL), the beginnings of IL-6 accumulation in cells may be seen (Fig. 56). Results seem to become more inconsistent above 10ng/mL dosage, implying a variable cellular response to cytokine administration above this level. This may be due to reduced culture viability and downstream effects of inflammation such as shifts in cytokine expression.

In IL-8 immunocytochemistry, similar fluorescence may be seen in dosed conditions with none in undosed (Fig. 57). Though intensity does not seem as great as in IL-6 examination, both downstream markers evidence inflammation in cultures as a result of IL-1 dosage.

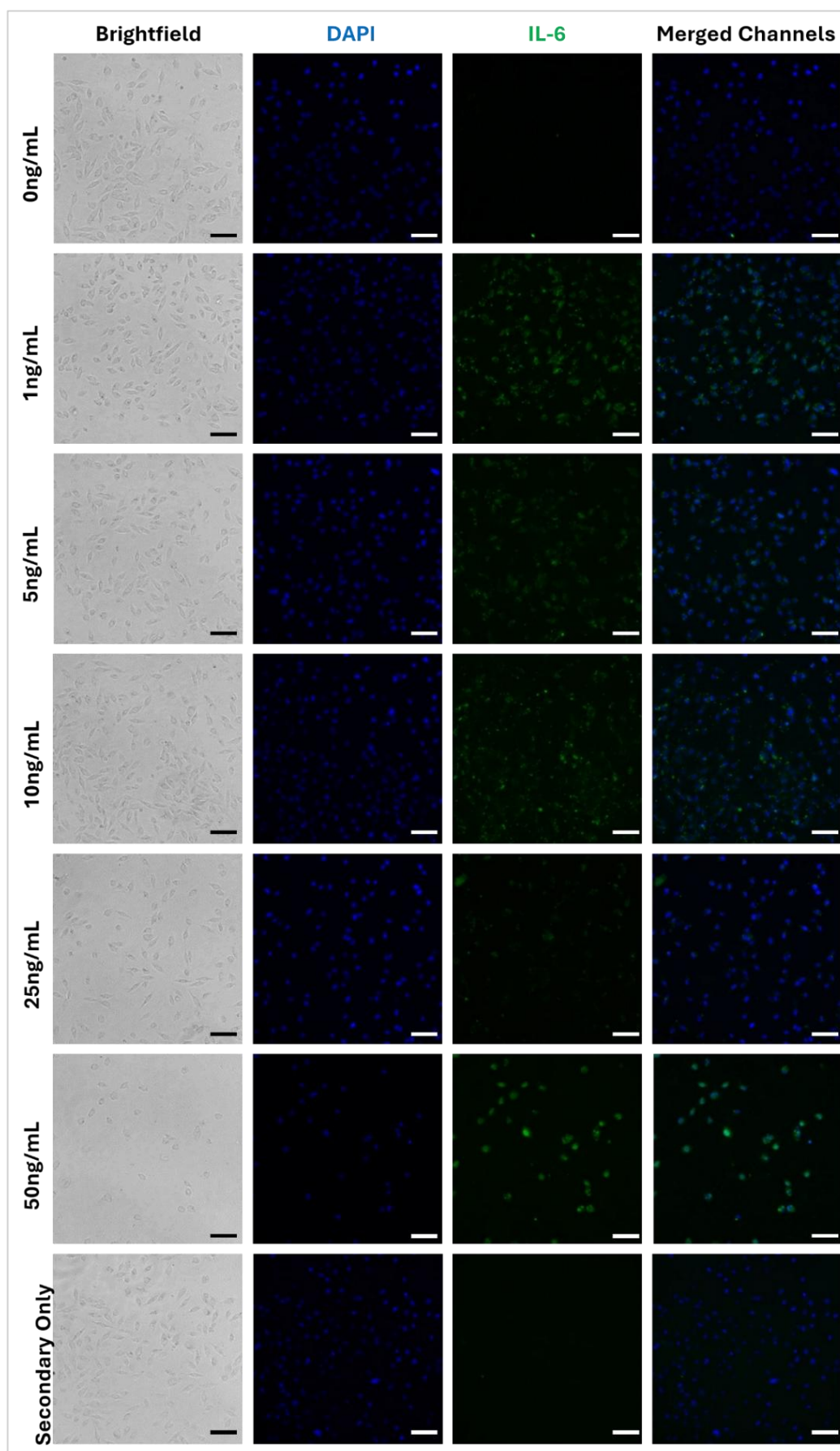
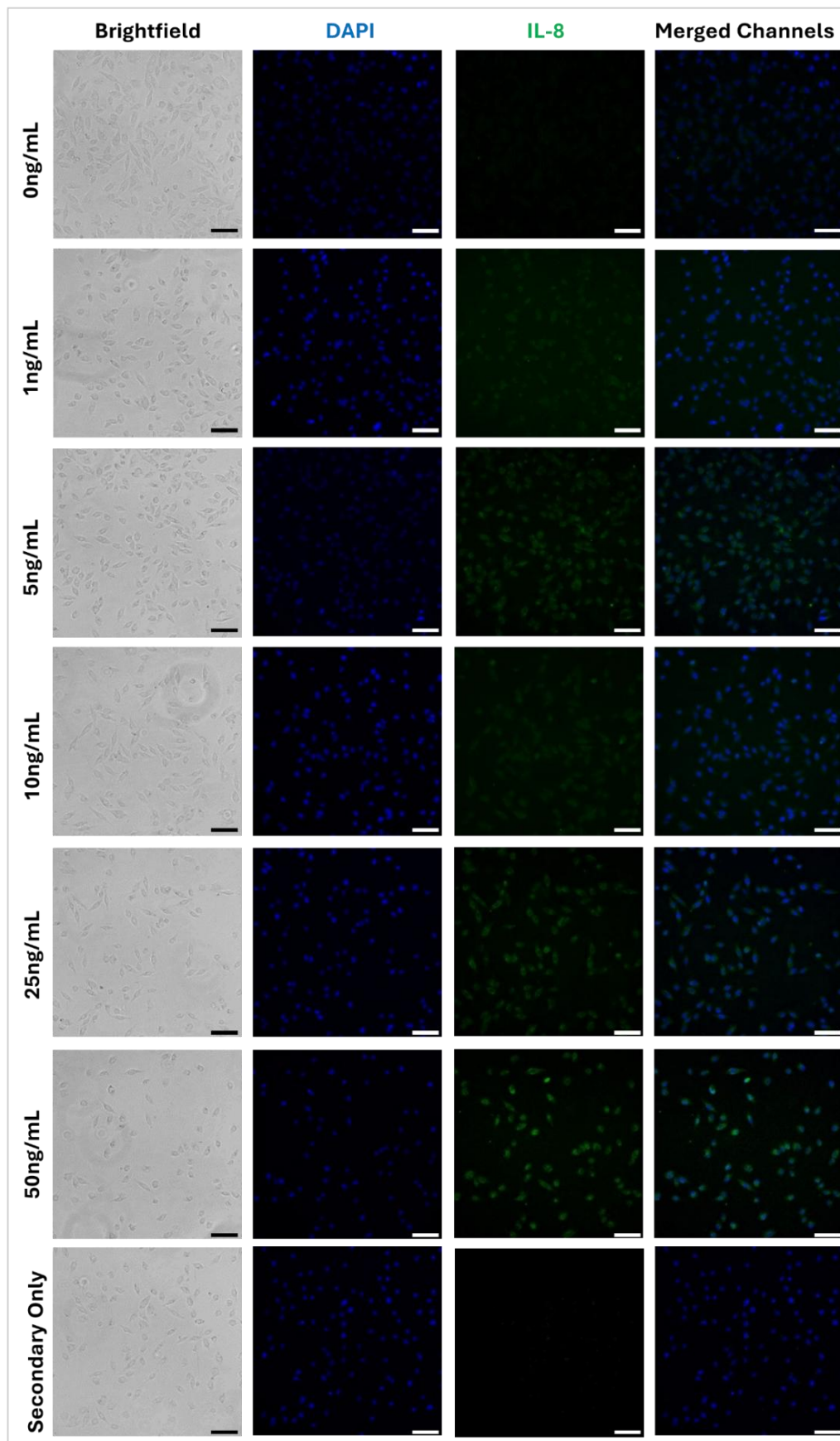


Figure 56: Fluorescence imaging of IL-1 $\beta$ -dosed cochlear fibrocytes labelled for IL-6. Scale bars= 100 $\mu$ m



**Figure 57: Fluorescence imaging of IL-1 $\beta$ -dosed cochlear fibrocytes labelled for IL-8. Scale bars= 100 $\mu$ m.**

### 3.4.8. Raman Spectroscopy of IL-1 $\beta$ -dosed Cochlear Fibrocytes

In examining the Raman spectra of IL-dosed cochlear fibrocytes, similarly to TNF-dosed cells, general spectral profile of cells remains similar regardless of dose (Fig. 58). At face value, it would appear that spectral changes (including differences in intensity) across conditions are larger between IL-dosed cell conditions than those of TNF, though this requires more detailed examination.

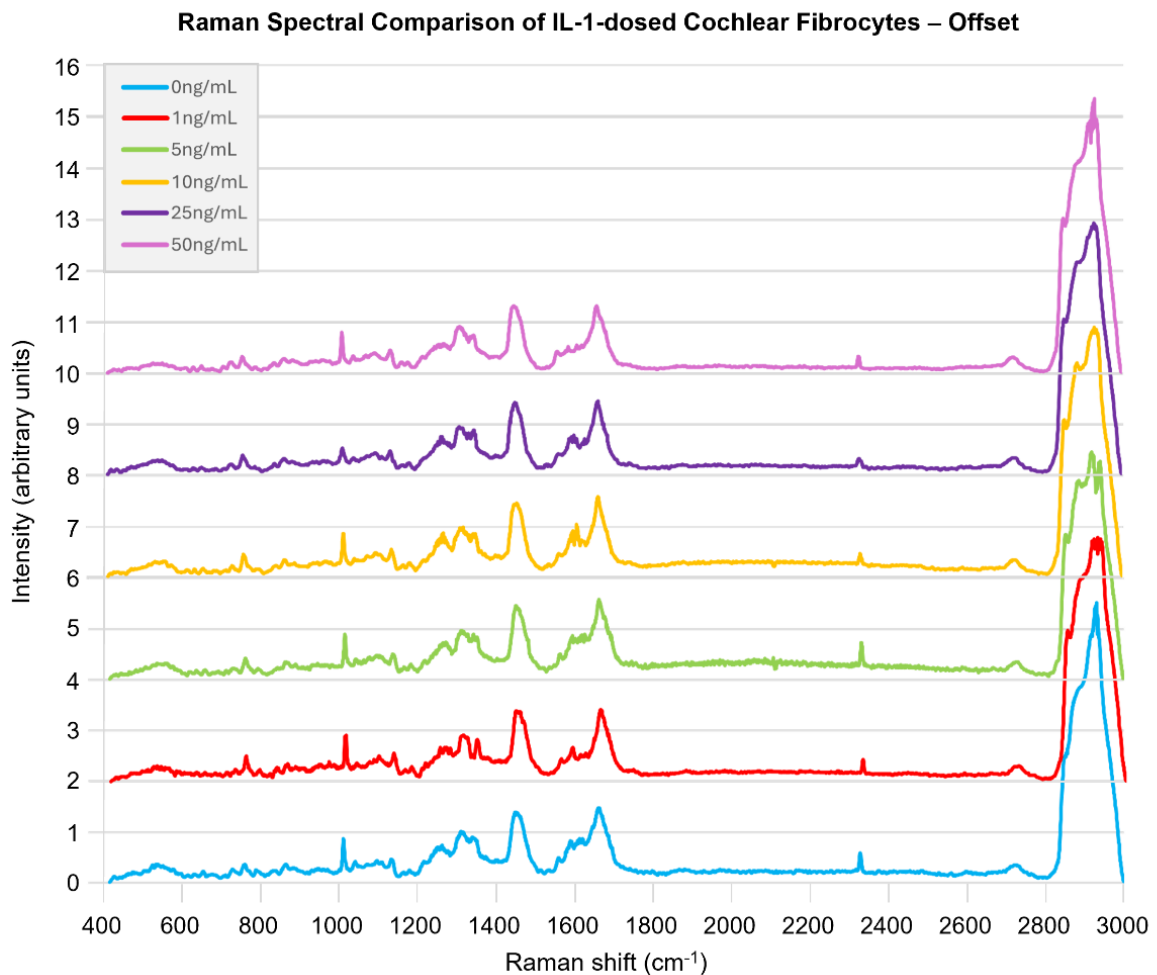


**Figure 58: Average Raman spectra of murine cochlear fibrocytes following 24hrs incubation with IL-1 $\beta$ .**

**Average Raman spectra of IL-dosed vs healthy cochlear fibrocytes - ~250 individual cell spectra per condition, each from a separate (by condition) ~250k cell cytopspin monolayer of PFA fixed cells on CaF<sub>2</sub> - cells fixed at maximum P8.**

Interestingly, it is of note that where signal intensity appears stronger in the fingerprint region, a lower signal intensity is seen in the high wavenumber region. This is presumably down to topographic variations in samples. There is also a clear difference in the overall signal intensity of these regions,

with fingerprint region intensity appearing lower than that of the high wavenumber region. Such alteration suggests variation in relative lipid levels, potentially indicative of lipid accumulation as a result of inflammation similar to that hypothesised in TNF investigations.

Similarly to TNF-dosed cells, dosed and healthy cell signals are difficult to distinguish by eye from full spectra, with condition samples appearing to show a large variation around averages. This is consistent with the expectations due to the large number of cells sampled and the individual variations arising between them including cell cycle stage etc. Variations in cell cycle stage across populations are anticipated to yield differences in uptake of cytokine and thus differing responses.

To examine spectral variations between IL-dosed and undosed cells in further detail, pairwise comparisons of each dosage against undosed cells is made. Beginning with undosed cells and 1ng/mL IL-dosed cells (Fig. 59), manual peak identification allows the distinction of variations in spectra.

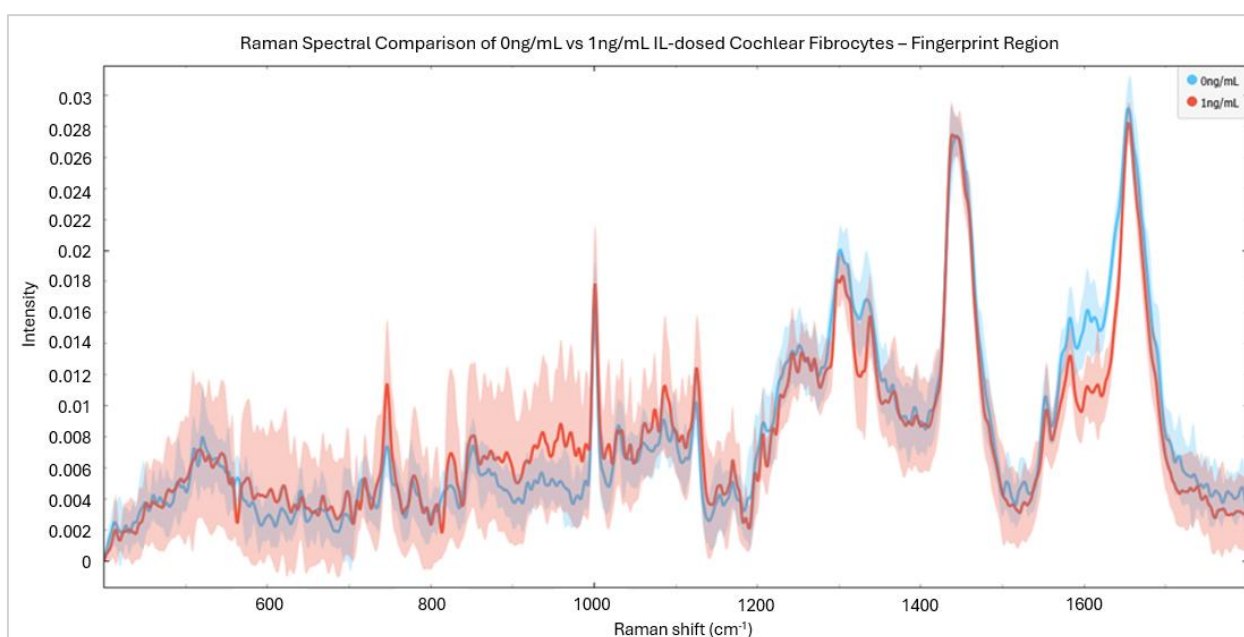


**Figure 59: Average Raman spectra of healthy and 1ng/mL-dosed cochlear fibrocytes following 24hrs incubation with IL-1 $\beta$  (fingerprint region).**

**Average Raman spectra (fingerprint region) of IL-dosed vs healthy cochlear fibrocytes - ~250**

**individual cell spectra per condition, each from a separate (by condition) ~250k cell cytopun**

**monolayer of PFA fixed cells on CaF<sub>2</sub> - cells fixed at maximum P8.**

Working from lower to higher Raman shift as with TNF analyses, there is little visible variation between samples below  $600\text{cm}^{-1}$ . Dosed cells in particular show substantial variation around their average spectrum in this region making any true differences difficult to isolate. This variation is believed to arise due to differences in cytokine response across cells at this dosage as such variation is not seen to the same extent in other dosages. That is, at  $1\text{ng/mL}$  some cells behave as if they are inflamed where others remain relatively healthy.

In the nucleic acid triple peak region ( $725\text{--}785\text{cm}^{-1}$ ),  $1\text{ng/mL}$  IL-dosed cells show contrasting spectral features to TNF dosed cells of the same dosage. In  $1\text{ng/mL}$  IL-dosed cells similar signal intensity to undosed cells is seen for adenine and cytosine bands, while a far greater signal intensity is noted at the central thymine band. While such spectral features still suggest differences in nucleic acid structure between dosed and undosed cells, these differences appear to vary from those seen in TNF-dosed cells. This implies that these cytokines, if to blame for the changes seen, yield differing alterations to nucleic acids.

Between  $\sim 870\text{cm}^{-1}$  and  $1000\text{cm}^{-1}$  (C-O stretching, C-C-N asymmetric stretching, C-O-C ring deformation), dosed cells demonstrate increased signal intensity compared with undosed cells. This was also seen in TNF-dosed cells at the same dosage and is likely indicative of protein/lipid structural changes resulting from inflammation.

As seen in TNF-dosed cells at the same dosage, at  $1000\text{cm}^{-1}$  both undosed and dosed cells demonstrate similar signal intensity. This band is typically associated with symmetric ring breathing of proteins, so alterations induced by inflammation are not unexpected. However, it does not appear that any arise at this dosage based upon manual analysis.

The  $\text{CH}_3$  wagging protein-associated peak at  $1032\text{cm}^{-1}$  appears to be of slightly reduced intensity in the IL-dosed condition, again similar to TNF-dosed cells at this dosage. This intensity difference may indicate some protein structural variability between conditions.

At  $1128\text{cm}^{-1}$ , in contrast to TNF-dosed cells at this dosage, signal intensity in the IL-dosed condition is notably higher than that of undosed cells. Differences in this band, attributed C-C

stretching and CH<sub>2</sub> vibration of lipids and glucose, may indicate changes in cellular processing of glucose during respiration. An increase in intensity at this band for dosed cells may suggest accumulation of glucose in cells, potentially due to inability to correctly process it. Further analysis of other dosages is required to confirm this.

In the spectral region 1200-1400cm<sup>-1</sup> (attributed to amide III, C-O stretching, C=C vibrations and CH<sub>2</sub> wagging), the IL dosed spectrum demonstrates a lower signal intensity than that of undosed cells. This contrasts with TNF-dosed cells at the same dosage. Though spectral features vary across cytokines, differences between dosed and undosed cells in both cases indicate variations in lipids, proteins, and polysaccharides between dosed and undosed cells.

Similarly to TNF-dosed cells at this dosage, the CH<sub>2</sub>/CH<sub>3</sub> deformation associated band at ~1450cm<sup>-1</sup> does not show substantial difference between undosed and 1ng/mL IL-dosed cells. This may be due to the relatively low dosage employed; thus this band remains of interest when examining differences at higher dosages.

In the protein region 1540-1625cm<sup>-1</sup> (associated with C=C stretching, N-H bending, tryptophan ring stretching and C-C-H ring vibration) signal intensity appears generally greater in the undosed cell condition than in 1ng/mL dosed cells. This relationship is also seen in TNF-dosed cells of the same dosage. Differences between dosed and undosed cells in this further suggest protein alterations arising in the inflamed condition.

The amide I/C=O stretching band at ~1650cm<sup>-1</sup>, similarly to TNF-dosed cells of the same dosage, demonstrates a lower signal intensity in the 1ng/mL IL-dosed cell condition than in the undosed cell condition. Unlike TNF-dosed cells, no shift is seen. Nonetheless, this supports the previous suggestion of protein alterations between dosed and undosed cells. Whether this is a product of inflammatory changes, or merely a sign of cytokine presence in cells is unclear.

Second derivative spectra enable further analysis of the fingerprint region for undosed and 1n/mL IL-dosed cells (Fig. 60). From this comparison, differences between dosed and undosed

spectra are particularly visible at 700-800 $\text{cm}^{-1}$ , 950-1000 $\text{cm}^{-1}$ , 1032 $\text{cm}^{-1}$ , and 1600-1650 $\text{cm}^{-1}$ . These regions may be associated with bond vibrations in nucleic acids, proteins, and lipids.

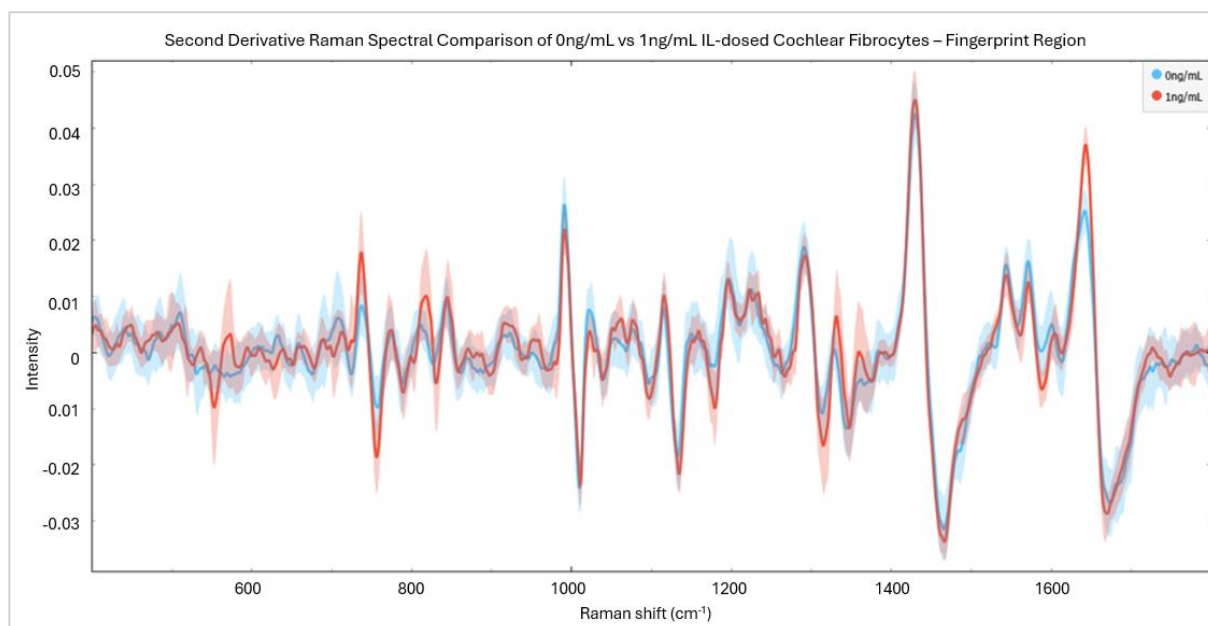


**Figure 60: Second derivative Raman spectra of healthy and 1ng/mL-dosed cochlear fibrocytes following 24hrs incubation with IL-1 $\beta$  (fingerprint region).**

**Second derivative average Raman spectra (fingerprint region) of IL-dosed vs healthy cochlear fibrocytes - ~250 individual cell spectra per condition, each from a separate (by condition) ~250k cell cytopspin monolayer of PFA fixed cells on CaF<sub>2</sub> - cells fixed at maximum P8.**

In the high wavenumber region, 0ng/mL and 1ng/mL IL-dosed cells differ slightly (Fig. 61), though this difference is not as substantial as that noted for TNF-dosed cells of the same level. In contrast to TNF-dosed cells, dosed signal intensity below ~2910 $\text{cm}^{-1}$  is greater than undosed and above 2910 $\text{cm}^{-1}$  is lower than undosed. This further evidences differing modes of action across cytokines. In particular, difference is noted between undosed and 1ng/mL IL-dosed cells at ~2850 $\text{cm}^{-1}$ , in the region typically associated with CH<sub>2</sub> stretching.

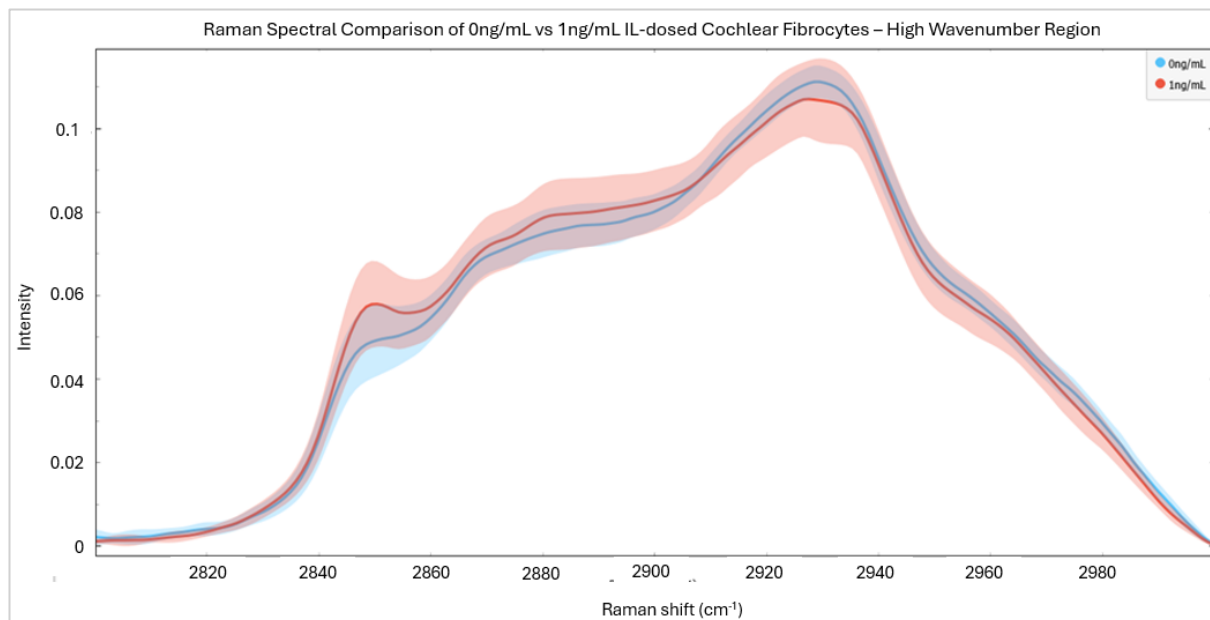


**Figure 61: Average Raman spectra of healthy and 1ng/mL-dosed cochlear fibrocytes following 24hrs incubation with IL-1 $\beta$  (high wavenumber region).**

**Average Raman spectra (high wavenumber region) of IL-dosed vs healthy cochlear fibrocytes - ~250 individual cell spectra per condition, each from a separate (by condition) ~250k cell cytopun monolayer of PFA fixed cells on CaF2 - cells fixed at maximum P8.**

Second derivative spectra of the high wavenumber region further clarify differences, though overlap of spectra is still substantial (Fig. 62). Signal intensity variations are most clear in the region surrounding 2850cm<sup>-1</sup> as previously noted. This is kept in mind when moving to higher IL doses.

Viewing the fingerprint region of undosed and 5ng/mL IL-dosed cells (Fig. 63), greater variation between conditions is still apparent, though arguably less so than in the previous dosage condition. However, variation around the average spectrum is reduced at this dosage level, suggesting a more consistent cellular response to cytokine application.

Beginning once again in the lower end of the spectrum, variation between samples below 600cm<sup>-1</sup> is once again negligible based on manual analysis. This is due to both noise in the region and variation around sample averages. As such, no differences in polysaccharides or nucleic acids can be firmly identified from this spectral region.

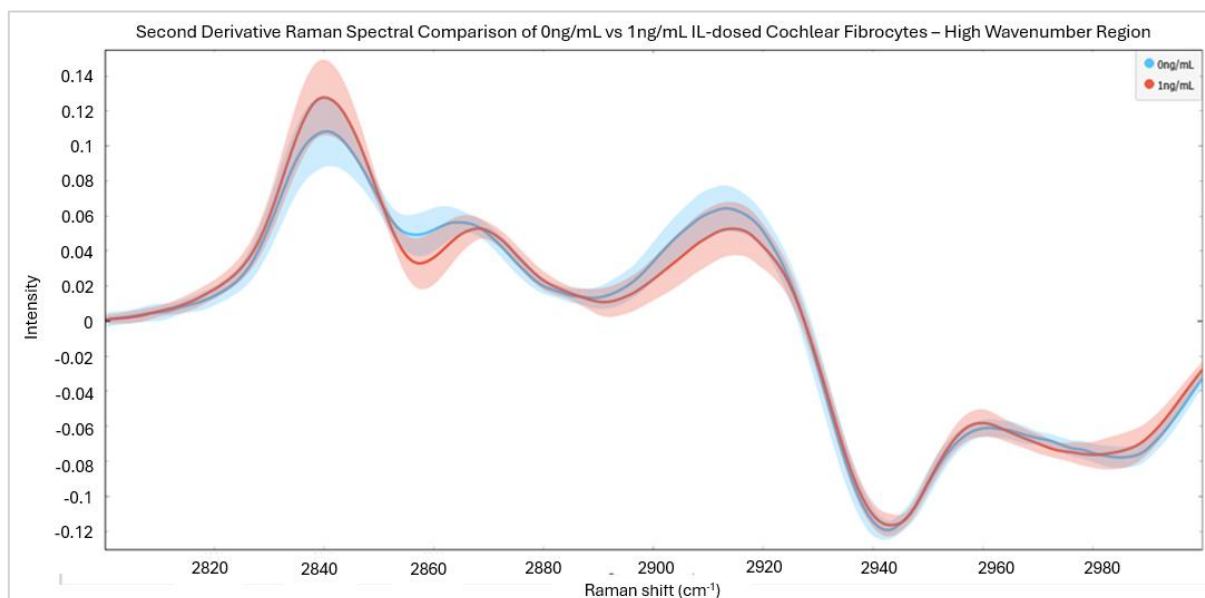


**Figure 62: Second derivative Raman spectra of healthy and 1ng/mL-dosed cochlear fibrocytes following 24hrs incubation with IL-1 $\beta$  (high wavenumber region).**

**Second derivative average Raman spectra (high wavenumber region) of IL-dosed vs healthy cochlear fibrocytes - ~250 individual cell spectra per condition, each from a separate (by condition) ~250k cell cytopspin monolayer of PFA fixed cells on CaF<sub>2</sub> – fixed at maximum P8.**

In the nucleic acid triple peak region (725-785cm<sup>-1</sup>), similarly to the previous dosage, 5ng/mL IL-dosed cells show contrasting spectral features to TNF dosed cells. Once again, IL-dosed cells show similar (slightly lower) signal intensity to undosed cells for adenine and cytosine bands, with greater signal intensity in the thymine band. This is consistent with 1ng/mL IL-dosed cells and further implies that the administered cytokines yield different alterations to nucleic acids.

Between ~870cm<sup>-1</sup> and 1000cm<sup>-1</sup>, as in TNF-dosed cells, appears to be an increase in signal intensity in dosed cells compared with undosed. Though, this is less substantial than that seen in the 1ng/mL spectrum. Nonetheless, variations in this region support the suggestion of protein/lipid changes arising IL application, with a potential inverse correlation between dosage and effect suggested.

Once again, at 1000cm<sup>-1</sup> 5ng/mL IL-dosed cells demonstrate similar signal intensity to undosed cells. Additionally, a slight shift towards the high wavenumber end of the spectrum is seen in the dosed condition. This contrasts with TNF-dosed cells at 5ng/mL where both an increased signal

intensity and a peak shift are seen. This further suggests variations in protein alterations depending on the cytokine responsible.

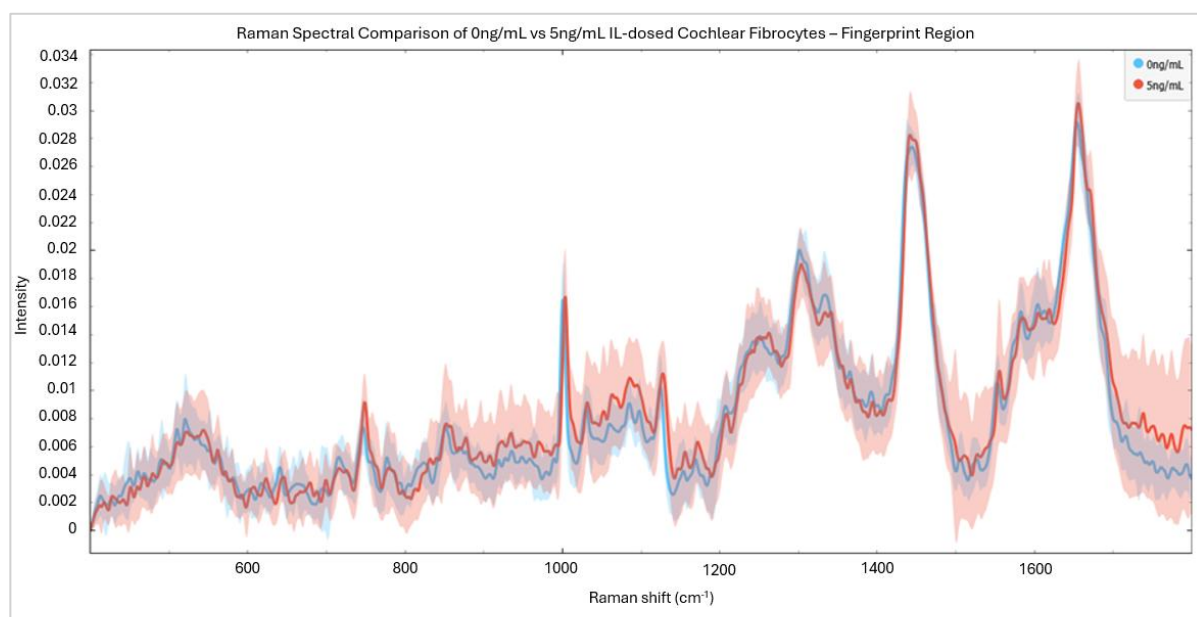


**Figure 63: Average Raman spectra of healthy and 5ng/mL-dosed cochlear fibrocytes following 24hrs incubation with IL-1 $\beta$  (fingerprint region).**

**Average Raman spectra (fingerprint region) of IL-dosed vs healthy cochlear fibrocytes - ~250 individual cell spectra per condition, each from a separate (by condition) ~250k cell cytopspin monolayer of PFA fixed cells on CaF<sub>2</sub> - cells fixed at maximum P8.**

In contrast to the previous IL dosage as well as to TNF-dosed cells at the same level, the CH<sub>3</sub> wagging-associated band at 1032cm<sup>-1</sup> and the C-C stretching/CH<sub>2</sub> vibration bands at 1128cm<sup>-1</sup> are both of greater intensity in the IL-dosed condition. This further suggests differences in protein structures and metabolic features between dosed and undosed cells. Though not as clear as in 1ng/mL dosed cells, increased signal intensity at 1128cm<sup>-1</sup> may suggest accumulation of glucose in cells [216].

Between 1200-1400cm<sup>-1</sup>, the undosed cell spectrum is once again generally of greater intensity than that of dosed cells. Similarly to TNF-dosed cells, the 5ng/mL IL dosage condition appears to yield a slightly greater signal intensity in this region than 1ng/mL dosed cells. This may indicate a correlation between dosage and signal intensity in this region. As this region may be associated with lipids, proteins, polysaccharides and amino acids, variations may arise from a range of sources.

At  $\sim 1450\text{cm}^{-1}$ , in contrast to 1ng/mL IL-dosed cells, 5ng/mL dosed cells demonstrate slightly greater signal intensity than undosed cells. This trend is also seen in TNF-dosed cells of the same dosage, though no accompanying peak shift is noted. Variations in this band, attributed to  $\text{CH}_2/\text{CH}_3$  deformation, suggest differences in lipid and protein structure/abundance between dosed and undosed cells.

Unlike 1ng/mL IL-dosed cells, the protein region  $1540\text{-}1625\text{cm}^{-1}$  demonstrates similar signal intensity in both dosed and undosed conditions. This is due to a substantial increase in signal intensity of 5ng/mL dosed cells compared with 1ng/mL dosed cells. This increase may be indicative of inflammation induced variations or the presence of IL-1 in cells.

Further contrasting from 1ng/mL IL-dosed cells, the band at  $\sim 1650\text{cm}^{-1}$  demonstrates greater signal intensity in 5ng/mL dosed cells than undosed cells. This additionally contrast with TNF-dosed cells at the same level. Once again, this is suggestive of protein variations between dosed and undosed cells, with the nature of variation differing depending on the cytokine responsible.

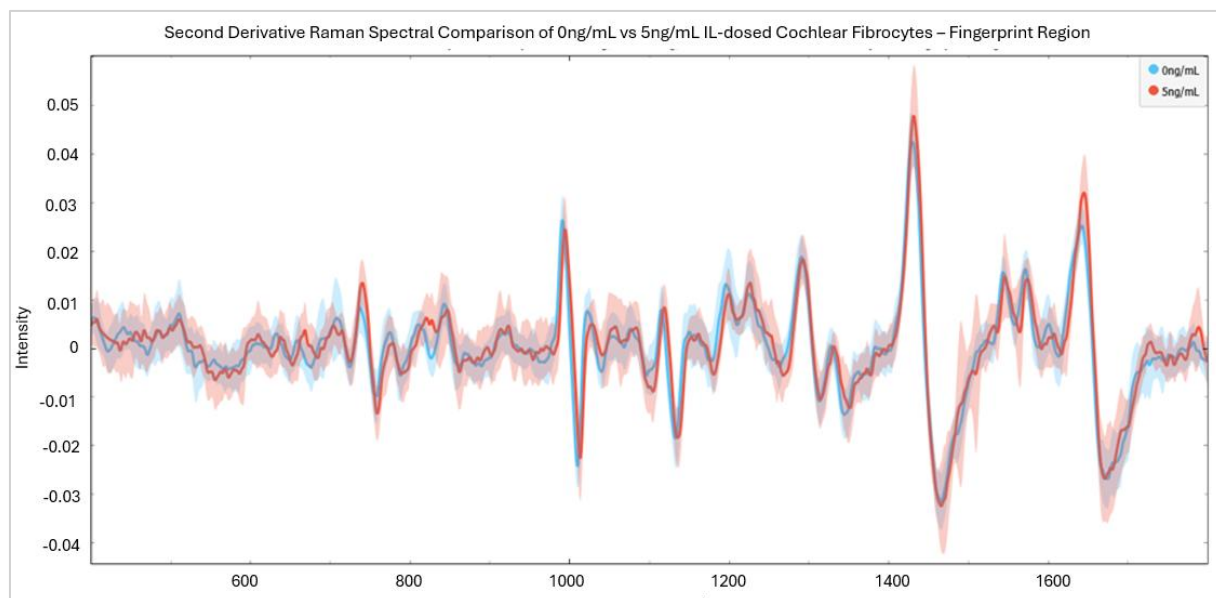


**Figure 64: Second derivative Raman spectra of healthy and 5ng/mL-dosed cochlear fibrocytes following 24hrs incubation with IL-1 $\beta$  (fingerprint region).**

**Second derivative average Raman spectra (fingerprint region) of IL-dosed vs healthy cochlear fibrocytes - ~250 individual cell spectra per condition, each from a separate (by condition) ~250k cell cytopun monolayer of PFA fixed cells on CaF<sub>2</sub> - cells fixed at maximum P8.**

Second derivative spectra demonstrate subtler differences between spectra (Fig. 64), with variation below  $600\text{cm}^{-1}$  now visible. This, however, does not appear to be substantial outside of deviation around spectral averages. Potentially significant differences are noted at  $700\text{-}800\text{cm}^{-1}$  and  $1600\text{-}1650\text{cm}^{-1}$ , with evidence of difference around  $1032\text{cm}^{-1}$  and  $1200\text{cm}^{-1}$ . These regions are associated with bond vibrations in nucleic acids, proteins, lipids, and polysaccharides.

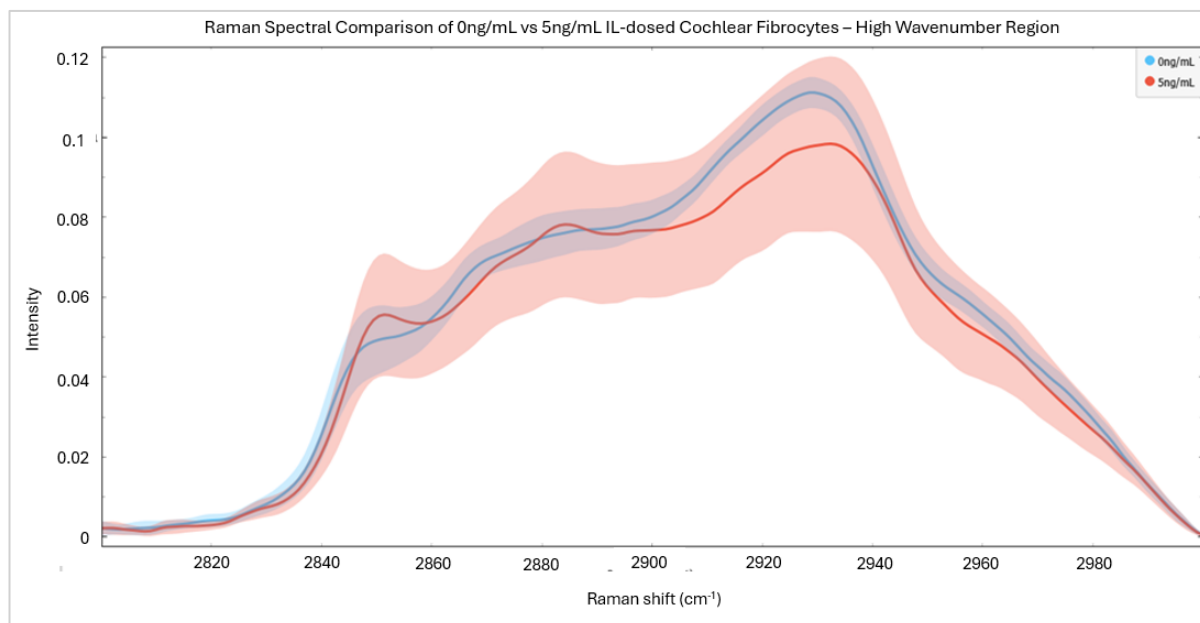


**Figure 65: Average Raman spectra of healthy and 5ng/mL-dosed cochlear fibrocytes following 24hrs incubation with IL-1 $\beta$  (high wavenumber region).**

**Average Raman spectra (high wavenumber region) of IL-dosed vs healthy cochlear fibrocytes -  
~250 individual cell spectra per condition, each from a separate (by condition) ~250k cell  
cytopun monolayer of PFA fixed cells on CaF<sub>2</sub> - cells fixed at maximum P8.**

In the high wavenumber region, 5ng/mL dosed spectra demonstrate substantial variability around the spectral average (Fig. 65). Nonetheless, similar spectral features to those seen in 1ng/mL dosed cells are present. Below  $2900\text{cm}^{-1}$ , dosed cell signal intensity is not consistently above that of undosed cells as seen in 1ng/mL, instead fluctuating. Above  $2900\text{cm}^{-1}$ , dosed cell signal intensity is still lower than that of undosed cells, to a greater degree than that seen in 1ng/mL analysis. The nature of differences between dosed and undosed cells once again directly contrasts with TNF-dosed cells at the same level.

Second derivative spectral comparison of 0ng/mL and 5ng/mL high wavenumber regions lends clarity to spectra (Fig. 66). Though variation around the average spectrum is still clear, differences between dosed and undosed cells are distinguishable in regions identified in 1ng/mL dosed spectra such as 2850-2870cm<sup>-1</sup> and 2900-2920cm<sup>-1</sup>. Though there is overlap between conditions, intensity variation is visible in the region surrounding 2850cm<sup>-1</sup> as previously noted.

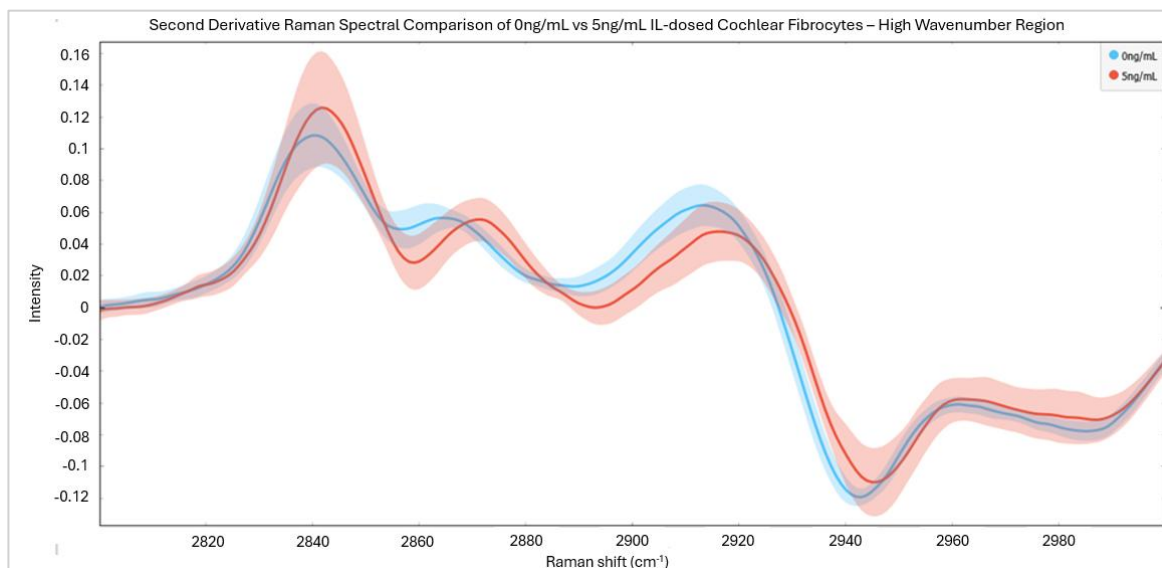


**Figure 66: Second derivative Raman spectra of healthy and 5ng/mL-dosed cochlear fibrocytes following 24hrs incubation with IL-1 $\beta$  (high wavenumber region).**

**Second derivative average Raman spectra (high wavenumber region) of IL-dosed vs healthy cochlear fibrocytes - ~250 individual cell spectra per condition, each from a separate (by condition) ~250k cell cytopspin monolayer of PFA fixed cells on CaF<sub>2</sub> - cells fixed at maximum P8.**

In the fingerprint region of undosed and 10ng/mL IL-dosed cells (Fig. 67), visible variation between conditions is once again demonstrated. As before, variation around average spectra makes differences more uncertain, though variation around the dosed average spectrum is again reduced compared with the previous dosage.

Below 600cm<sup>-1</sup>, variation between dosed and undosed conditions arises at 10ng/mL. At this dosage, signal intensity is reduced compared with undosed cells with presence of intensity differences in this region indicative of polysaccharide/nucleic acid (CH<sub>2</sub> bending, C-C-C

deformations) changes arising from inflammation. Similar variations were not observed in TNF-dosed cells of the same level, further illustrating differences in cytokine modes of action.

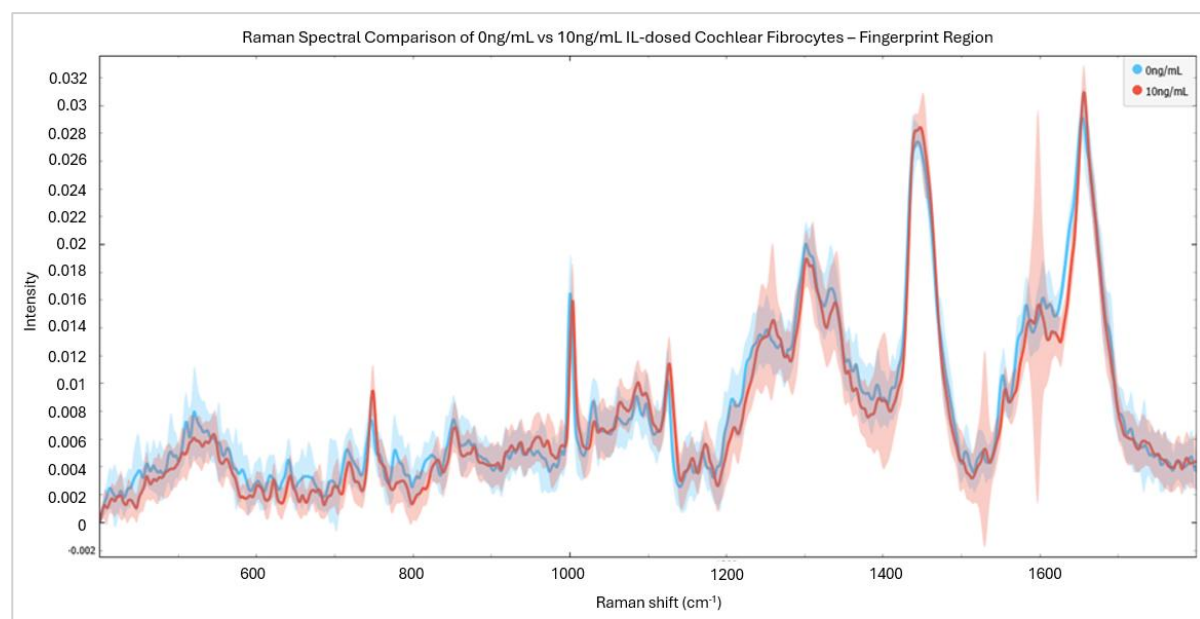


**Figure 67: Average Raman spectra of healthy and 10ng/mL-dosed cochlear fibrocytes following 24hrs incubation with IL-1 $\beta$  (fingerprint region).**

**Average Raman spectra (fingerprint region) of IL-dosed vs healthy cochlear fibrocytes - ~250 individual cell spectra per condition, each from a separate (by condition) ~250k cell cytospun monolayer of PFA fixed cells on CaF2 - cells fixed at maximum P8.**

In the nucleic acid region (725-785 $\text{cm}^{-1}$ ), the trend noted in 1ng/mL and 5ng/mL dosed cells persists, with dosed cells showing slightly lower signal intensity than undosed cells for adenine and cytosine bands, and greater signal intensity in the thymine band. This once again varies from the spectra of TNF-dosed cells at the same level. This is not only consistent with varying responses across cytokines but also indicates potential correlations between signal intensity and IL dosage at each nucleic acid band.

Between ~870 $\text{cm}^{-1}$  and 1000 $\text{cm}^{-1}$ , as previously, there is a slight increase in signal intensity in dosed cells compared with undosed. Though, again, this is less substantial than that seen in lower dosages and further implies an inverse correlation between dosage and effect. This region contains C-O stretching, C-C-N asymmetric stretching and C-O-C ring deformation attributable to lipids, proteins, and nucleic acids. As such, dosage-based variation across all of these parameters to some extent is suggested,

Again, at  $1000\text{cm}^{-1}$  10ng/mL IL-dosed cells demonstrate similar signal intensity to undosed cells, with a slightly lower intensity and slight shift towards the high wavenumber end of the spectrum seen in the dosed condition. This further suggests variations in protein structure and abundance resulting from cytokine administration.

Similarly to 1ng/mL IL-dosed cells, the 10ng/mL IL-dosed cell condition demonstrates reduced signal intensity at  $1032\text{cm}^{-1}$  compared with undosed cells. This reduction is far clearer than that seen at lower dosages and strongly implies alterations to structure/function of proteins at  $\text{CH}_3$  sites arising at 10ng/mL IL dosage.

In contrast, similarly to previous dosages, the C-C stretching/ $\text{CH}_2$  vibration band at  $1128\text{cm}^{-1}$  demonstrates greater signal intensity in the IL-dosed condition. This is further suggestive of lipid/glucose accumulation in IL-inflamed cells and contrasts with the findings from TNF-dosed cells at this level.

Between  $1200\text{-}1400\text{cm}^{-1}$ , the undosed cell spectrum is again generally of greater intensity than that of dosed cells, with little apparent change between 5ng/mL and 10ng/mL dosed cell spectra in this region besides a slight reduction in dosed cell signal intensity. This further indicates variations to lipids, proteins, polysaccharides, and amino acids in response to inflammation, though a clear dose-response correlation cannot be seen.

At  $\sim 1450\text{cm}^{-1}$ , the trend of increased signal intensity in IL dosed cells continues. This trend is also seen in TNF-dosed cells of the same dosage. It is hence suggested at this stage that signal intensity in this band may correlate with dosage level and indicate differences in lipid and protein structure/abundance between dosed and undosed cells. Increased signal intensity in dosed conditions at this band may be demonstrative of cytokine presence in cells.

Once again, the protein region  $1540\text{-}1625\text{cm}^{-1}$  demonstrates similar signal intensity in both dosed and undosed conditions. Though, it should be noted that there are some sites of substantial variation around the average dosed spectrum in this region. This increase, similar to that seen in

5ng/mL dosed cells, may be indicative of inflammation induced variations or the presence of IL-1 in cells.

Further similarities to 5ng/mL dosed cells arise at  $\sim 1650\text{cm}^{-1}$ , with greater signal intensity noted in dosed cells than undosed cells. This contrasts with TNF-dosed cells at the same level as well as with 1ng/mL IL-dosed cells. Once again, this is suggestive of protein variations between dosed and undosed cells, with the nature of variation differing depending on the cytokine responsible.

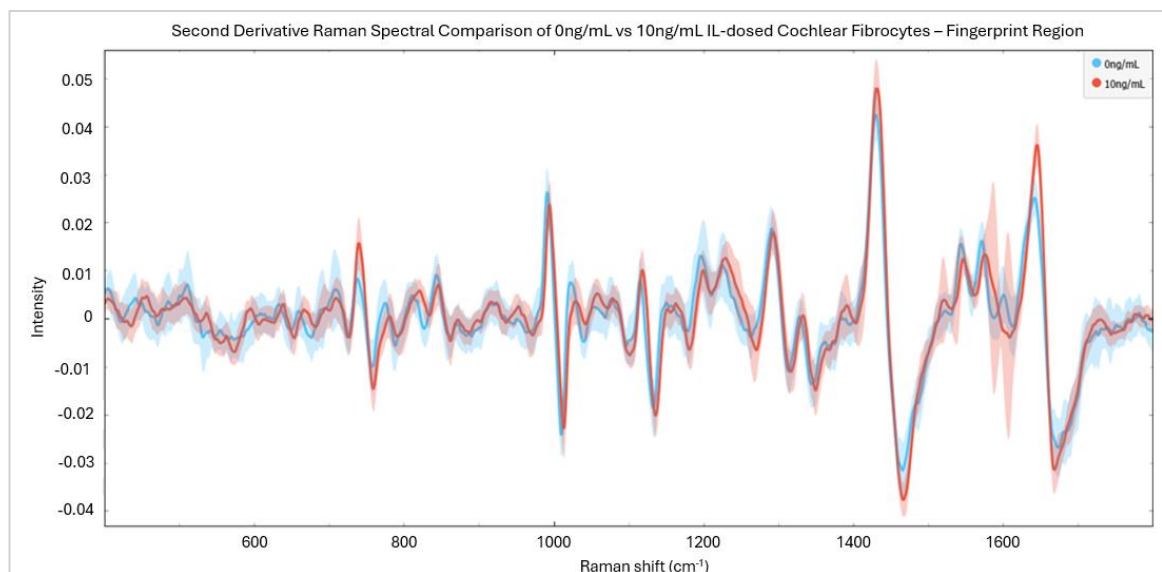


**Figure 68: Second derivative Raman spectra of healthy and 10ng/mL-dosed cochlear fibrocytes following 24hrs incubation with IL-1 $\beta$  (fingerprint region).**

**Second derivative average Raman spectra (fingerprint region) of IL-dosed vs healthy cochlear fibrocytes - ~250 individual cell spectra per condition, each from a separate (by condition) ~250k cell cytopspin monolayer of PFA fixed cells on CaF<sub>2</sub> - cells fixed at maximum P8.**

Second derivative spectra lend further clarity in the distinction of differences between spectra (Fig. 68). Potentially significant differences are once again noted at  $700\text{-}800\text{cm}^{-1}$ ,  $950\text{-}1000\text{cm}^{-1}$ ,  $1032\text{cm}^{-1}$ ,  $1400\text{-}1500\text{cm}^{-1}$  and  $1600\text{-}1650\text{cm}^{-1}$ . These regions are predominantly associated with bond vibrations in nucleic acids, proteins and lipids.

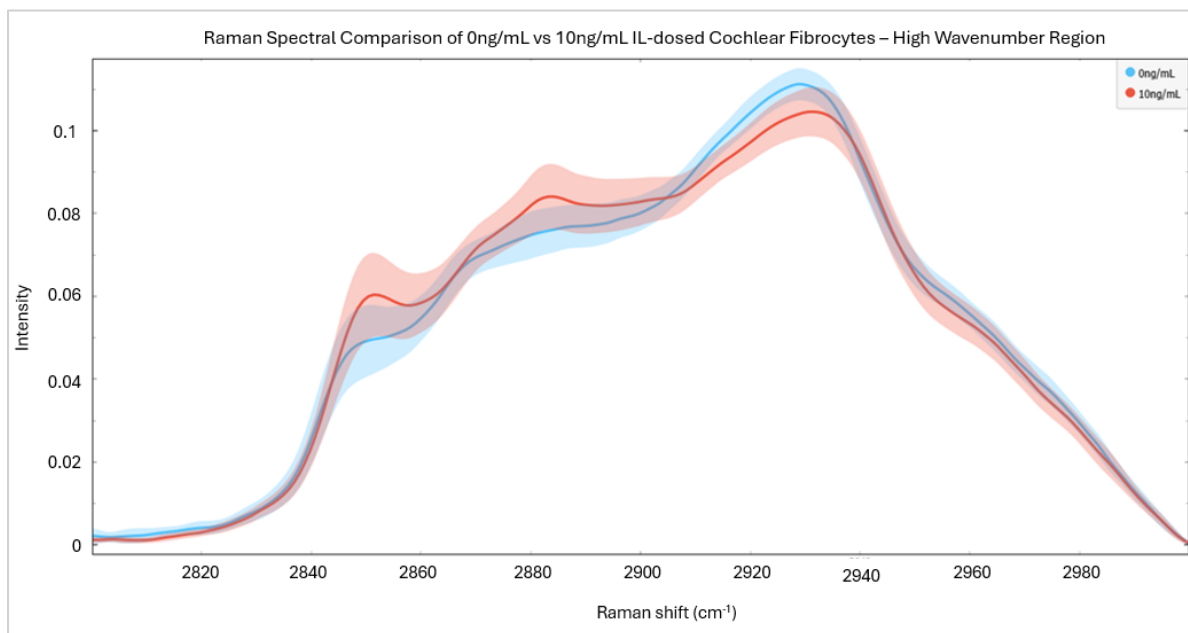


**Figure 69: Average Raman spectra of healthy and 10ng/mL-dosed cochlear fibrocytes following 24hrs incubation with IL-1 $\beta$  (high wavenumber region).**

**Average Raman spectra (high wavenumber region) of IL-dosed vs healthy cochlear fibrocytes - ~250 individual cell spectra per condition, each from a separate (by condition) ~250k cell cytopun monolayer of PFA fixed cells on CaF2 - cells fixed at maximum P8.**

In the high wavenumber region, the 10ng/mL IL-dosed cell spectrum resembles that of 1ng/mL dosed cells (Fig. 69). This, along with the variation around average spectrum noted implies that 5ng/mL results do not follow the trend in dose-response seen. As in 1ng/mL IL-dosed cells, 10ng/mL dosed cells demonstrate greater signal intensity than undosed cells below  $\sim 2900\text{cm}^{-1}$  and lower signal intensity than undosed cells above  $2900\text{cm}^{-1}$ , with differences between dosed and undosed spectra made clearer by increased magnitude of difference and reduction in variation around the spectral average. Once again, an interesting site of intensity variation is visible around  $2850\text{cm}^{-1}$ . The demonstrated differences are evidence of dosage induced changes in  $\text{CH}_2$  and  $\text{CH}_3$  stretching of proteins and lipids and are potentially indicative of dose-response correlative effects.

Second derivative high wavenumber region spectra further demonstrate the noted differences (Fig. 70). Clear differences in signal intensity and band location are notable at  $2830\text{-}2850\text{cm}^{-1}$ ,  $2850\text{-}2880\text{cm}^{-1}$ ,  $2900\text{-}2920\text{cm}^{-1}$  and  $2940\text{cm}^{-1}$ .

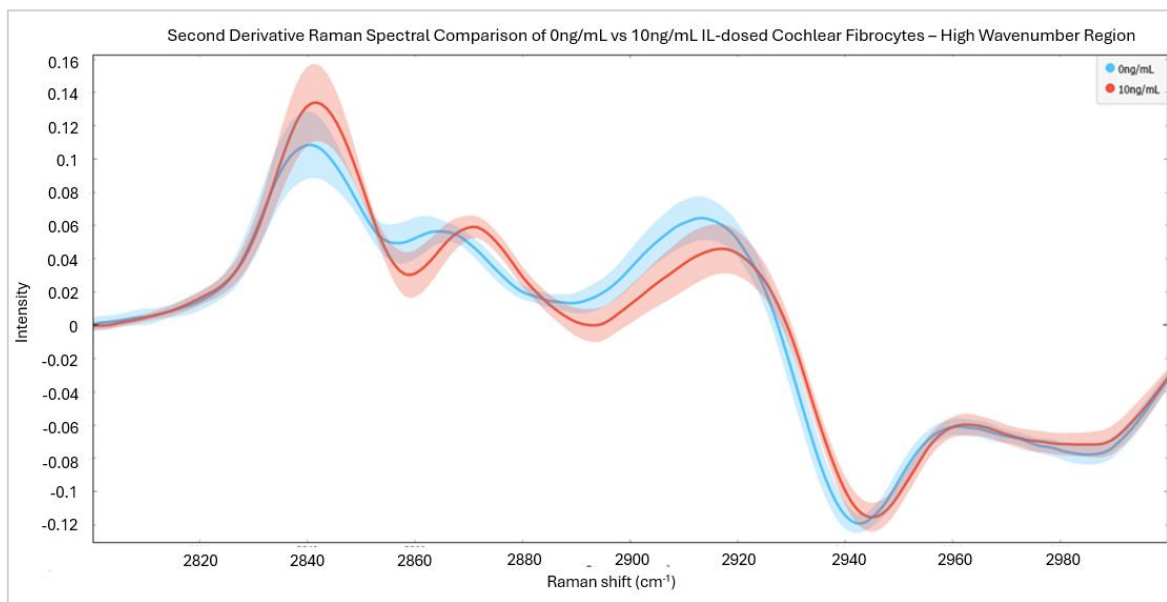


**Figure 70: Second derivative Raman spectra of healthy and 1ng/mL-dosed cochlear fibrocytes following 24hrs incubation with IL-1 $\beta$  (high wavenumber region).**

**Second derivative average Raman spectra (high wavenumber region) of IL-dosed vs healthy cochlear fibrocytes - ~250 individual cell spectra per condition, each from a separate (by condition) ~250k cell cytopun monolayer of PFA fixed cells on CaF2 - cells fixed at maximum P8.**

The fingerprint region of undosed and 25ng/mL IL-dosed cells (Fig. 71), once again demonstrates variation between conditions, with dosed and undosed spectra generally demonstrating a similar relationship to that seen in 10ng/mL comparisons. As before, variation around the dosed average spectrum is reduced compared with previous dosages. No comparisons with TNF dosed cells are made at this level as a comparable TNF spectrum is not available.

In the spectral region indicative of polysaccharide/nucleic acids (below 600cm<sup>-1</sup>), variation between dosed and undosed cells similar to that of 10ng/mL dosed cells is seen. Once again, differences between dosed and undosed cells in this region imply variations in nucleic acid structure and cell metabolism arising from inflammation.

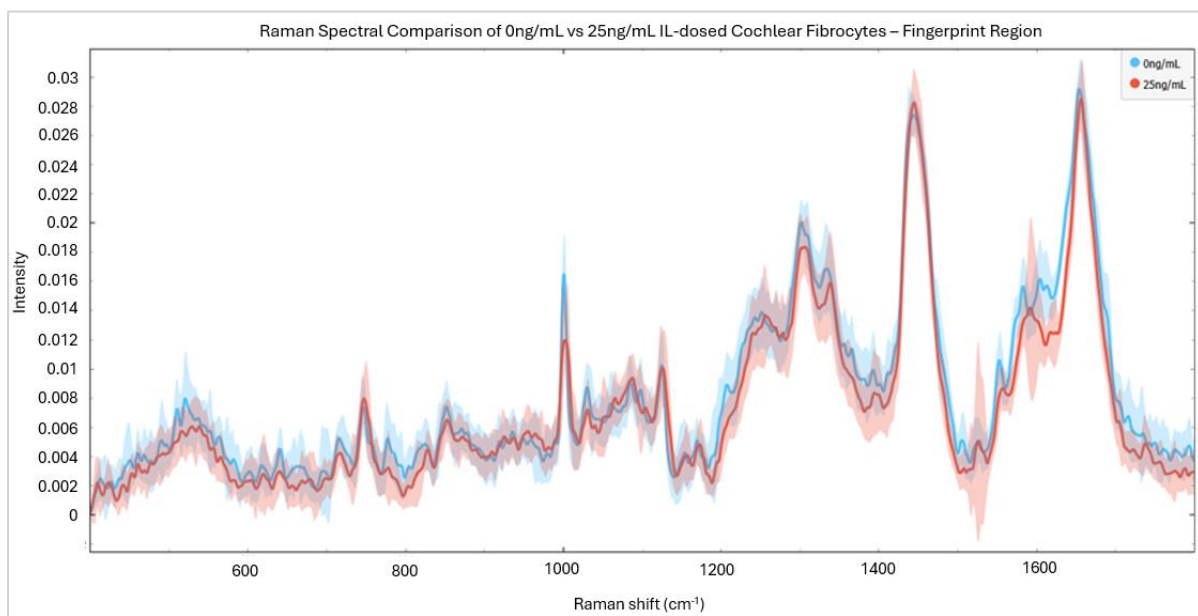


**Figure 71: Average Raman spectra of healthy and 25ng/mL-dosed cochlear fibrocytes following 24hrs incubation with IL-1 $\beta$  (fingerprint region).**

**Average Raman spectra (fingerprint region) of IL-dosed vs healthy cochlear fibrocytes - ~250 individual cell spectra per condition, each from a separate (by condition) ~250k cell cytopspin monolayer of PFA fixed cells on CaF<sub>2</sub> - cells fixed at maximum P8.**

As in previous dosages, nucleic acid region (725-785cm<sup>-1</sup>) signal intensity is further reduced in 25ng/mL dosed cells, with dosed cells now showing similar or lower signal intensity than undosed cells for all bands. This further validates the potential inverse correlation between signal intensity and IL dosage in this spectral region.

Between ~870cm<sup>-1</sup> and 1000cm<sup>-1</sup>, signal intensity in 25ng/mL dosed cells is marginally reduced compared to 10ng/mL dosed cells. Signal intensity in this region is similar in both undosed and dosed cell conditions, further implying an inverse correlation between dosage and signal intensity similar to that hypothesised for 725-785cm<sup>-1</sup>. Based upon this, it is hypothesised that variations across dosages in this spectral region are predominantly attributable to nucleic acid changes.

In contrast to lower dosages, at 1000cm<sup>-1</sup>, 25ng/mL IL-dosed cells demonstrate a clear lower signal intensity than undosed cells. Building on the findings of previous dosages, an inverse correlation between dosage and signal intensity is implied at this band. This is suggestive of variations in protein structure and abundance resulting from cytokine administration.

As seen in 1ng/mL and 10ng/mL IL-dosed cells, 25ng/mL dosed cells demonstrate a reduced signal intensity compared to undosed cells at  $1032\text{cm}^{-1}$ . Though this reduction is clear, there does not appear to be a particular change in intensity between 10ng/mL and 25ng/mL dosages, thus no distinct correlation is implied. Nonetheless, intensity variation in this band strongly implies alterations to structure/function of proteins consistent with inflammation.

Contrary to previous dosages, the C-C stretching/ $\text{CH}_2$  vibration band at  $1128\text{cm}^{-1}$  demonstrates similar signal intensity both dosed and undosed conditions. This goes against the suggestion of lipid/glucose accumulation in IL-inflamed cells, instead implying a reduction in abundance at higher dosages.

Between  $1200\text{-}1400\text{cm}^{-1}$ , the undosed cell spectrum remains of greater intensity generally than that of dosed cells. This further indicates consistent differences in lipids, proteins, polysaccharides, and amino acids between dosed and undosed cells.

At  $\sim 1450\text{cm}^{-1}$ , increased signal intensity in IL dosed cells is once again visible, though there is little change in intensity between 10ng/mL and 25ng/mL dosed cells. This goes against the previous suggestion of correlation. Nonetheless, visible differences in this band imply changes to lipid and protein structure/abundance as a result of cytokine administration.

As before, the protein region  $1540\text{-}1625\text{cm}^{-1}$  demonstrates similar signal intensity in both dosed and undosed conditions, with the dosed spectrum now appearing to be somewhat reduced in intensity compared with previous dosages. This implies that variations in this region are not merely indicative of IL presence. Instead, the return to a lower dose-like spectral profile implies a change, plateau, or resolution to inflammation effects.

As in the protein region  $1540\text{-}1625\text{cm}^{-1}$ ,  $25\text{ng/mL}$  dosed cells demonstrate reduced signal intensity at  $\sim 1650\text{cm}^{-1}$ . This contrasts with  $5\text{ng/mL}$  and  $10\text{ng/mL}$  findings and is suggestive of a change, plateau, or resolution to protein variations at this dosage.

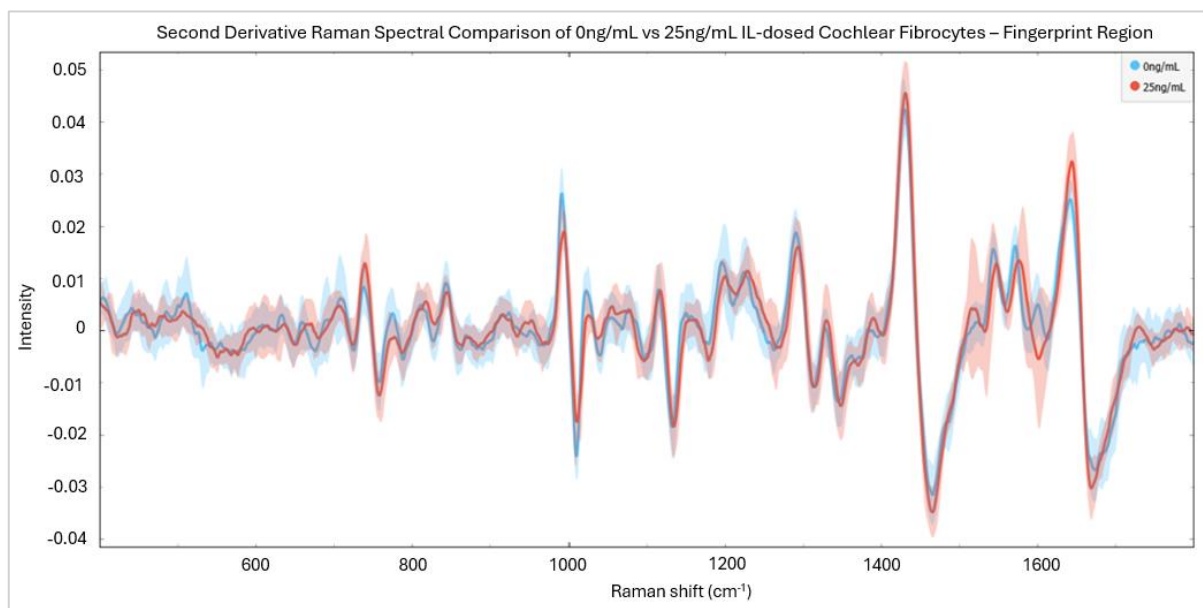


**Figure 72: Second derivative Raman spectra of healthy and  $25\text{ng/mL}$ -dosed cochlear fibrocytes following 24hrs incubation with  $\text{IL-1}\beta$  (fingerprint region).**

**Second derivative average Raman spectra (fingerprint region) of IL-dosed vs healthy cochlear fibrocytes -  $\sim 250$  individual cell spectra per condition, each from a separate (by condition)  $\sim 250\text{k}$  cell cytopun monolayer of PFA fixed cells on  $\text{CaF}_2$  - cells fixed at maximum P8.**

Second derivative spectra at this dosage further demonstrate differences between dosed and undosed conditions (Fig. 72). As in lower dose analyses, potential significant differences are noted at  $700\text{-}800\text{cm}^{-1}$ ,  $950\text{-}1000\text{cm}^{-1}$ ,  $1032\text{cm}^{-1}$ ,  $1400\text{-}1500\text{cm}^{-1}$  and  $1600\text{-}1650\text{cm}^{-1}$ .

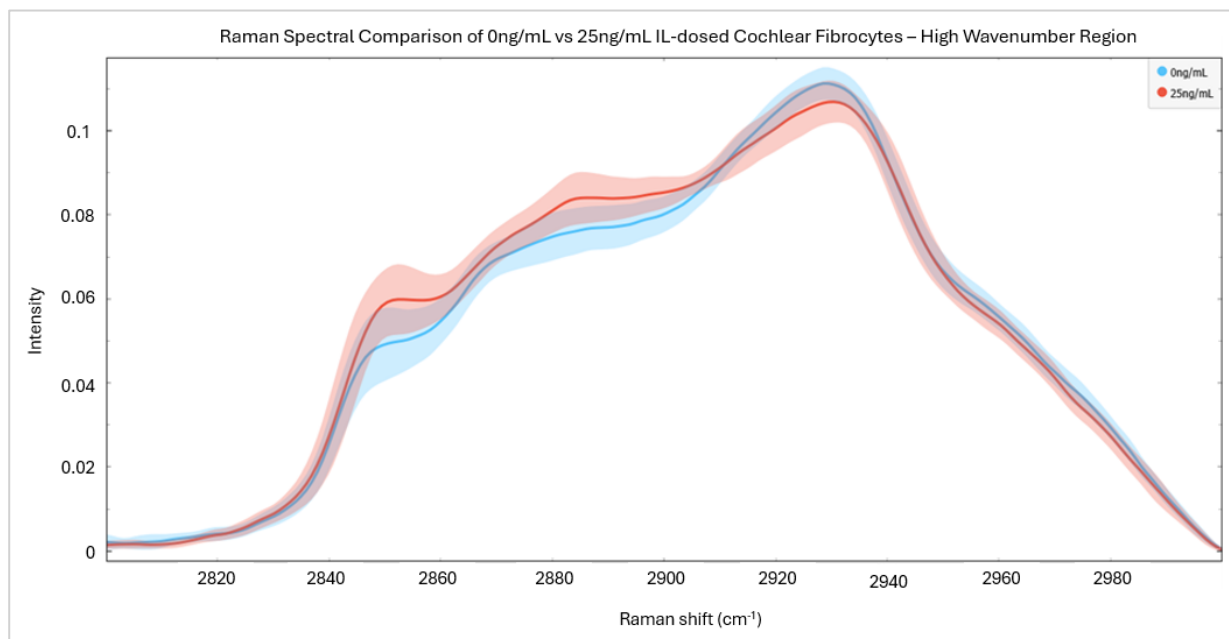


**Figure 73: Average Raman spectra of healthy and 25ng/mL-dosed cochlear fibrocytes following 24hrs incubation with IL-1 $\beta$  (high wavenumber region).**

**Average Raman spectra (high wavenumber region) of IL-dosed vs healthy cochlear fibrocytes -  
~250 individual cell spectra per condition, each from a separate (by condition) ~250k cell  
cytospun monolayer of PFA fixed cells on CaF<sub>2</sub> - cells fixed at maximum P8.**

In the high wavenumber region, the 25ng/mL dosed spectrum resembles that seen in 1ng/mL and 10ng/mL analyses (Fig. 73). As before, dosed cells demonstrate greater signal intensity than undosed cells below  $\sim 2900\text{cm}^{-1}$  and lower signal intensity than undosed cells above  $2900\text{cm}^{-1}$ . Again, intensity variation is seen around  $2850\text{cm}^{-1}$ . These differences imply dosage induced changes in proteins and lipids, though no correlation is implied as previously suggested.

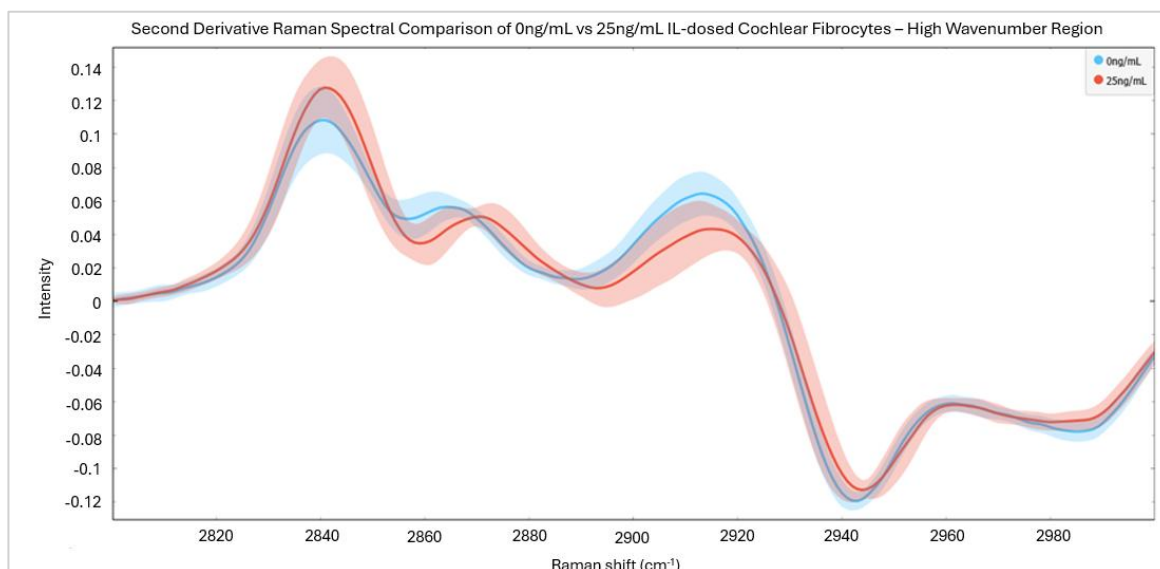


**Figure 74: Second derivative Raman spectra of healthy and 25ng/mL-dosed cochlear fibrocytes following 24hrs incubation with IL-1 $\beta$  (high wavenumber region).**

**Second derivative average Raman spectra (high wavenumber region) of IL-dosed vs healthy cochlear fibrocytes - ~250 individual cell spectra per condition, each from a separate (by condition) ~250k cell cytospun monolayer of PFA fixed cells on CaF<sub>2</sub> - cells fixed at maximum P8.**

Second derivative spectra once again demonstrate noted differences (Fig. 74). As in 10ng/mL IL-dosed cells, differences in signal intensity and band location are notable at 2830-2850cm<sup>-1</sup>, 2850-2880cm<sup>-1</sup>, and 2900-2920cm<sup>-1</sup>. This is suggestive of dosage-induced changes to both CH<sub>2</sub> and CH<sub>3</sub> stretching vibrational modes.

Finally, in the fingerprint region of undosed and 50ng/mL dosed cells (Fig. 75), dosed cell signal intensity appears overall lower than that of undosed cells. This strongly implies detectable effects of inflammation at this dosage level. Once again, compared with lower dosages, variation around the dosed average spectrum is reduced. This implies more consistency in cell response to IL at this dosage level, likely due to cell population being reduced. That is, with many poorly responding cells having already died at lower dosage levels, only those that consistently respond better to such high IL doses remain. This contrasts with TNF results, implying that TNF- $\alpha$  may be better tolerated by cells than IL-1 $\beta$ .

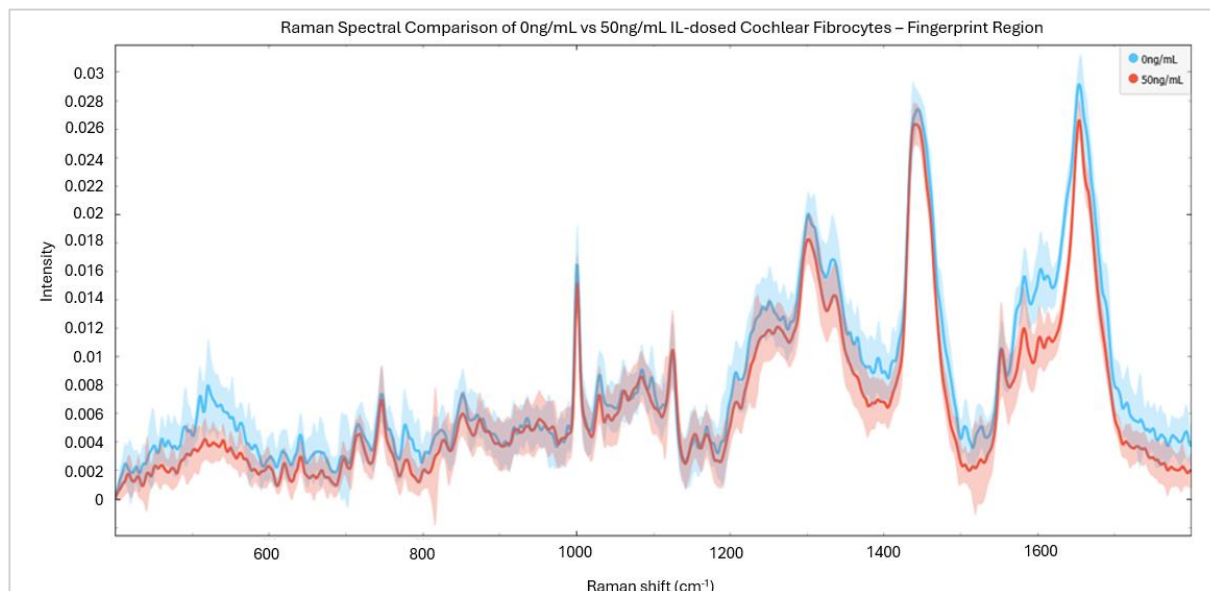


**Figure 75: Average Raman spectra of healthy and 50ng/mL-dosed cochlear fibrocytes following 24hrs incubation with IL-1 $\beta$  (fingerprint region).**

**Average Raman spectra (fingerprint region) of IL-dosed vs healthy cochlear fibrocytes - ~250 individual cell spectra per condition, each from a separate (by condition) ~250k cell cytopun monolayer of PFA fixed cells on CaF<sub>2</sub> - cells fixed at maximum P8.**

In contrast to previous dosed spectra, signal intensity below 600cm<sup>-1</sup> is drastically reduced in the 50ng/mL dosage condition. This opposes TNF-dosed cells at the same level which demonstrate higher signal intensity than undosed cells. Though at lower dosages dosed cell spectra appeared similar to undosed cells, a gradual reduction in signal intensity is implied in this region with dosage increase. Though a definite correlation is not observed, this difference further suggests polysaccharide/nucleic acid (CH<sub>2</sub> bending, C-C-C deformations) changes arising from IL dosage. This may indicate variations in metabolic properties of cells at this dosage level.

As in lower dosages, signal intensity in the nucleic acid triple peak region (725-785cm<sup>-1</sup>) is further reduced in 50ng/mL dosed cells, with the thymine band now demonstrating lower signal intensity in dosed cells compared with undosed. This further validates the proposed inverse correlation between signal intensity and IL dosage in this spectral region. Similar reduced intensity is seen at this dosage of TNF, though spectra for each cytokine are still distinct in this region.

Between ~870cm<sup>-1</sup> and 1000cm<sup>-1</sup>, signal intensity in 50ng/mL dosed cells is once again reduced compared to previous dosages, now appearing similar to that of undosed cells. This validates

the proposed inverse correlation between dosage and signal intensity in this spectral region, likely arising because of nucleic acid changes. This correlation contrasts with the results of TNF analysis, wherein much of this region demonstrated greater signal intensity than undosed cells at this dosage. Increased signal intensity in this case was associated lipid accumulation, further demonstrating the different actions of administered cytokines.

Though not as reduced as in 25ng/mL dosed cells, signal intensity of 50ng/mL IL-dosed cells is lower than that of undosed cells at  $1000\text{cm}^{-1}$ . This goes against the previous suggestion of an inverse correlation between dosage and signal intensity, though this may imply that 25ng/mL dosed cells are the outlier. Nonetheless, differences in signal intensity at this band are suggestive of variations in protein structure and abundance between dosed and undosed cells. Reduced signal intensity in this region directly contrasts with TNF-dosed cells at this dosage and further demonstrates differences between the two cytokines trialled.

Once again, as seen in all but 5ng/mL IL-dosed cells, a reduced signal intensity is seen in dosed cells compared to undosed cells at  $1032\text{cm}^{-1}$ . Again, there does not appear to be a particular change in intensity between 10ng/mL, 25ng/mL and 50ng/mL dosages. As before, intensity variation in this band implies alterations to structure/function of proteins consistent with expectations of inflammation. Such variation is not seen in TNF-dosed cells at the same level.

As noted in 25ng/mL dosed cells, the C-C stretching/ $\text{CH}_2$  vibration band at  $1128\text{cm}^{-1}$  demonstrates similar signal intensity both dosed and undosed conditions. This once again opposes the suggestion of lipid/glucose accumulation in IL-inflamed cells, instead indicating limited differences above a certain dosage level. This contrasts with the findings of TNF-dosed cells at the same level, wherein a clear increase in signal intensity was observed in the dosed cell condition.

As for lower dosages, in the  $1200\text{-}1400\text{cm}^{-1}$  spectral region, the undosed cell spectrum remains of greater intensity generally than that of dosed cells. This signal intensity difference is more apparent than at lower dosages, with the 50ng/mL dosed cell spectrum demonstrating the lowest signal intensity seen across dosed cells. This further indicates consistent differences in lipids, proteins, polysaccharides, and amino acids between dosed and undosed cells, and implies a level of

inverse correlation between signal intensity and IL dosage in this region. This, again, contrasts with the findings of TNF investigations.

At  $\sim 1450\text{cm}^{-1}$ , in contrast to lower dosages, a reduced signal intensity in IL dosed cells is seen compared with undosed cells. This contradicts the previous suggestion of correlation, with reduction in signal intensity at this dosage further implying an alteration in lipid effects at high dosages. This, once again, contrasts with the findings of TNF investigations.

As seen in 25ng/mL dosed cells, the protein region  $1540\text{-}1625\text{cm}^{-1}$  demonstrates a lower signal intensity in the dosed condition than undosed. This return to a lower dose-like spectral profile further implies a change, plateau, or resolution to inflammation effects occurring at higher dosages. Differences seen at this dosage level are similar to those noted for TNF-dosed cells.

Once again, 50ng/mL dosed cells demonstrate reduced signal intensity at  $\sim 1650\text{cm}^{-1}$  compared to undosed cells. This is similar to 25ng/mL dosage results and again contrasts with 5ng/mL and 10ng/mL spectra, again implying a change, plateau, or resolution to protein/lipid variations of this type (Amide I, C=O stretching) at higher dosages. Reduced signal intensity in dosed cells for this band contrasts with the findings of TNF-dosed cells at this dosage and is further demonstrative of differing modes of action across the administered cytokines.

Second derivative spectra of undosed and 50ng/ml IL-dosed cells further demonstrate differences between spectra (Fig. 76), with numerous points of variation visible throughout. Potentially significant differences are again noted at  $700\text{-}800\text{cm}^{-1}$ ,  $950\text{-}1000\text{cm}^{-1}$ ,  $1032\text{cm}^{-1}$ ,  $1400\text{-}1500\text{cm}^{-1}$  and  $1600\text{-}1650\text{cm}^{-1}$ . These regions are predominantly associated with bond vibrations in nucleic acids, proteins and lipids. Additional variations of interest are noted below  $600\text{cm}^{-1}$  and in the region  $1550\text{-}1600\text{cm}^{-1}$ , and are attributed to bond vibrations in nucleic acids, polysaccharides and proteins.

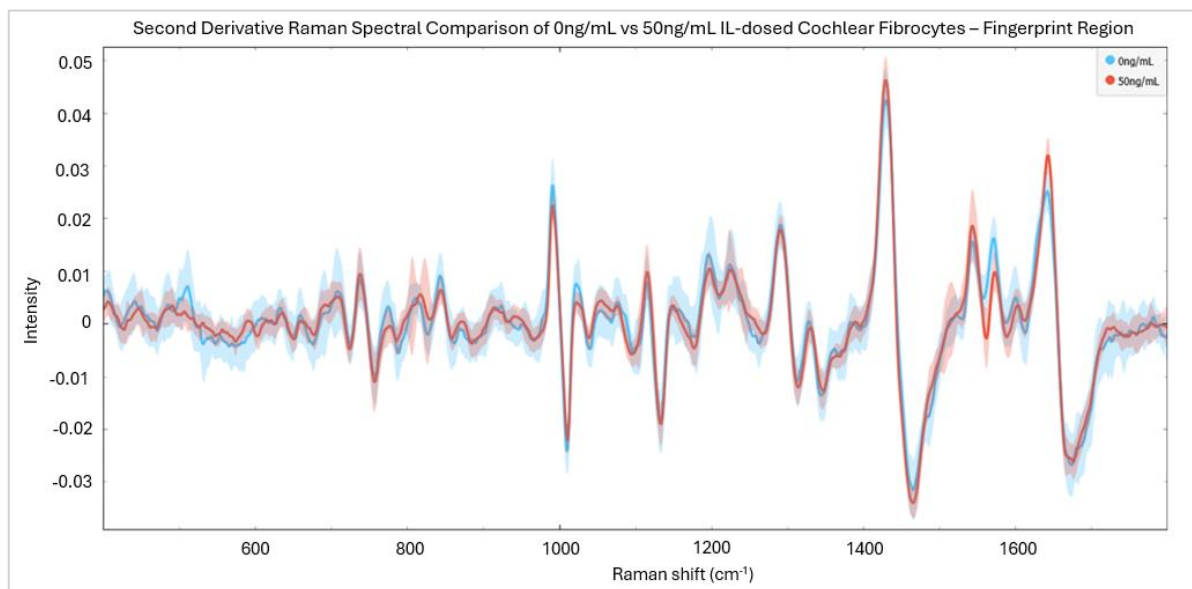


**Figure 76: Second derivative Raman spectra of healthy and 50ng/mL-dosed cochlear fibrocytes following 24hrs incubation with IL-1 $\beta$  (fingerprint region).**

**Second derivative average Raman spectra (fingerprint region) of IL-dosed vs healthy cochlear fibrocytes - ~250 individual cell spectra per condition, each from a separate (by condition) ~250k cell cytopun monolayer of PFA fixed cells on CaF2 - cells fixed at maximum P8.**

In the high wavenumber region, the 50ng/mL dosed spectrum resembles those seen at lower doses, though changes in signal intensity are visible (Fig. 77). As in previous doses, dosed cells demonstrate greater signal intensity than undosed cells below  $\sim 2900\text{cm}^{-1}$  and lower signal intensity than undosed cells above  $2900\text{cm}^{-1}$ . However, it should be noted that there is little difference between dosed and undosed spectra above  $2920\text{cm}^{-1}$  at this dosage level. In contrast, the difference noted around  $2850\text{cm}^{-1}$  seems of greater magnitude than in previous dosages.

Second derivative spectra once again demonstrate noted differences between dosed and undosed spectra (Fig. 78). Differences in signal intensity and band location are clearly visible at  $2830\text{--}2850\text{cm}^{-1}$ ,  $2850\text{--}2880\text{cm}^{-1}$ , and  $2900\text{--}2920\text{cm}^{-1}$ . This verified the suggestion of dosage-induced changes to both  $\text{CH}_2$  and  $\text{CH}_3$  stretching vibrational modes. Whether these changes are a result of IL-1 presence in cells or inflammatory effects are unclear.

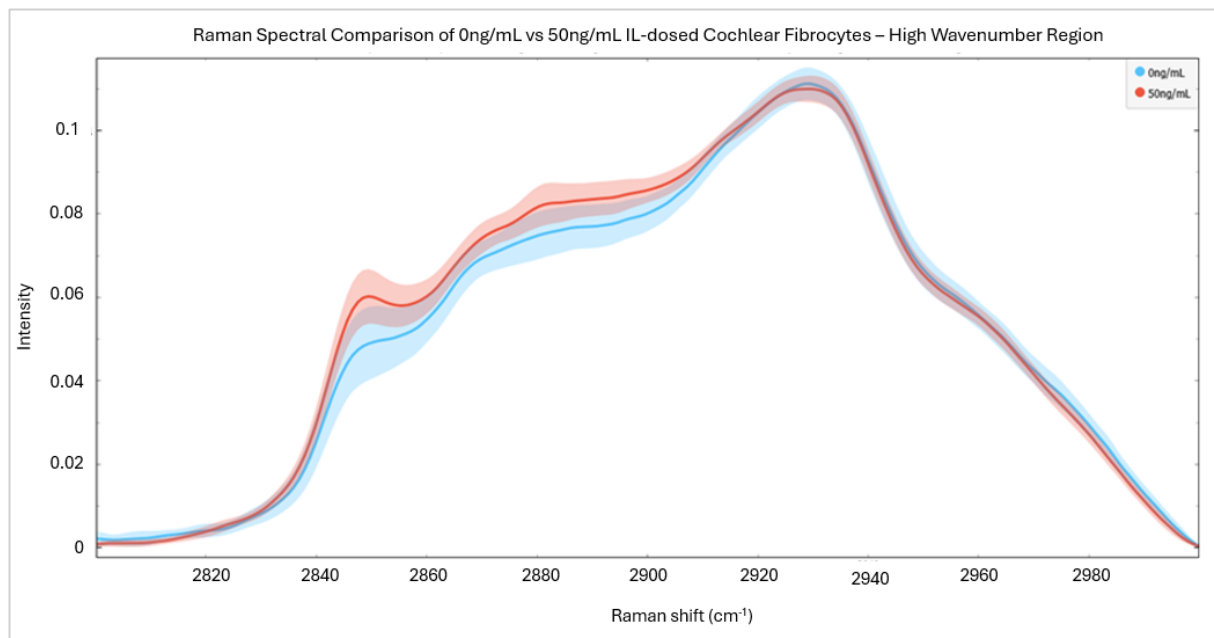


**Figure 78: Average Raman spectra of healthy and 50ng/mL-dosed cochlear fibrocytes following 24hrs incubation with IL-1 $\beta$  (high wavenumber region).**

**Average Raman spectra (high wavenumber region) of IL-dosed vs healthy cochlear fibrocytes -**  
**~250 individual cell spectra per condition, each from a separate (by condition) ~250k cell**  
**cytospun monolayer of PFA fixed cells on CaF2 - cells fixed at maximum P8.**

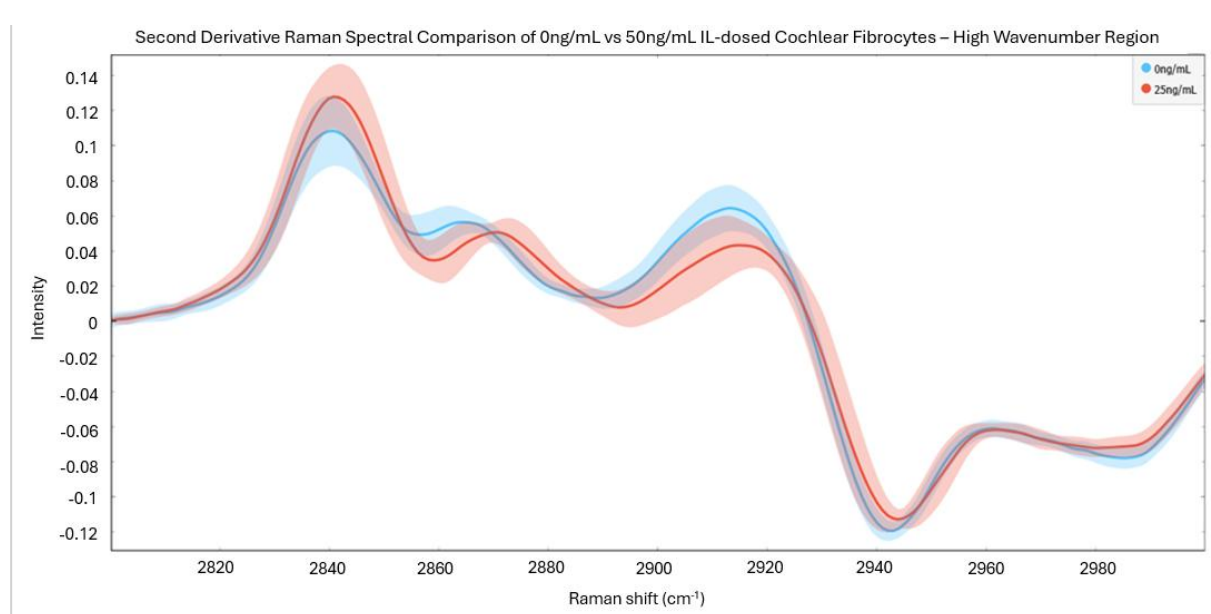


**Figure 77: Second derivative Raman spectra of healthy and 50ng/mL-dosed cochlear fibrocytes following 24hrs incubation with IL-1 $\beta$  (high wavenumber region).**

**Second derivative average Raman spectra (high wavenumber region) of IL-dosed vs healthy**  
**cochlear fibrocytes - ~250 individual cell spectra per condition, each from a separate (by**  
**condition) ~250k cell cytospun monolayer of PFA fixed cells on CaF2 - fixed at maximum P8.**

Examining spectral changes across conditions statistically, PCA demonstrates clustering of sample conditions, though this is far more difficult to visualise in scatter plots (Fig. 79) than those of TNF-dosed cells. Nonetheless, grouping of samples by dosage condition can be seen. This appears to be clearer in high wavenumber region analysis (Fig. 80) than in fingerprint region analysis.

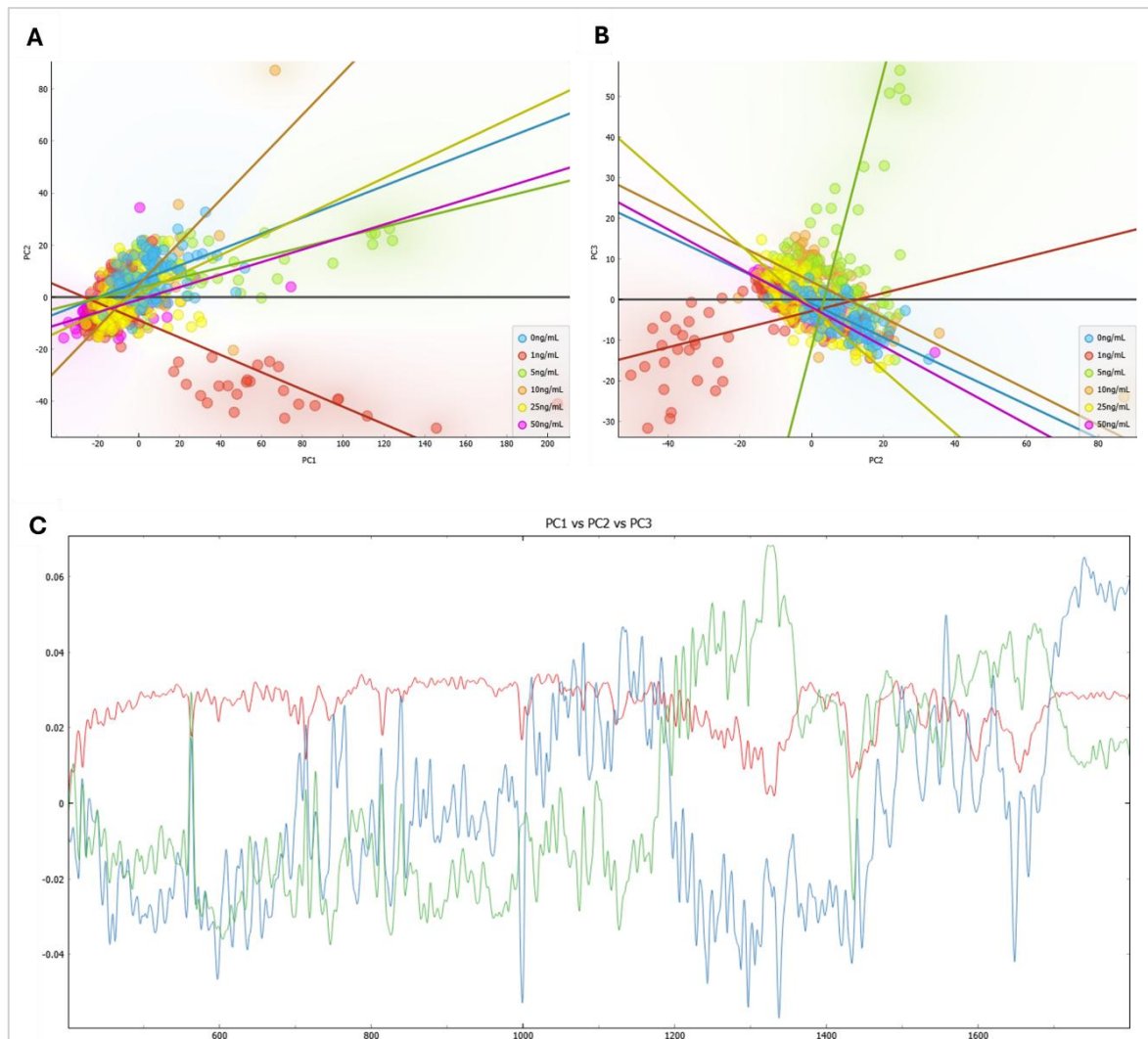


**Figure 79: PCA of the fingerprint region of undosed vs IL-dosed cochlear fibrocytes.**

**From average Raman spectra (fingerprint region) of IL-dosed vs healthy cochlear fibrocytes**  
**- ~250 individual cell spectra per condition, each from a separate (by condition) ~250k cell**  
**cytopun monolayer of PFA fixed cells on CaF2 - cells fixed at maximum P8. A) Scatter plot**  
**of PC1 (45.5%) vs PC2 (11%). B) Scatter plot of PC2 (11%) vs PC3 (5.1%). C) Loadings plot of**  
**PC1 (red) vs PC2 (green) vs PC3 (blue).**

Accompanying loadings plots validate sources of variation at sites identified in manual analysis. In the fingerprint region (Fig. 79) these include below  $600\text{cm}^{-1}$ ,  $1000\text{cm}^{-1}$ ,  $1032\text{cm}^{-1}$  and  $1600\text{--}1650\text{cm}^{-1}$ . Associated bond vibrations in these regions are  $\text{CH}_2$  bending/C-C-C deformations of polysaccharides and nucleic acids, symmetric ring breathing of proteins,  $\text{CH}_3$  wagging of proteins, and amide I/C=O stretching of lipids and proteins respectively. In the high wavenumber region (Fig. 80), these  $2830\text{--}2850\text{cm}^{-1}$ ,  $2850\text{--}2880\text{cm}^{-1}$ , and  $2900\text{--}2940\text{cm}^{-1}$ . Associated bond vibrations are  $\text{CH}_2$  and  $\text{CH}_3$  stretching of proteins and lipids.

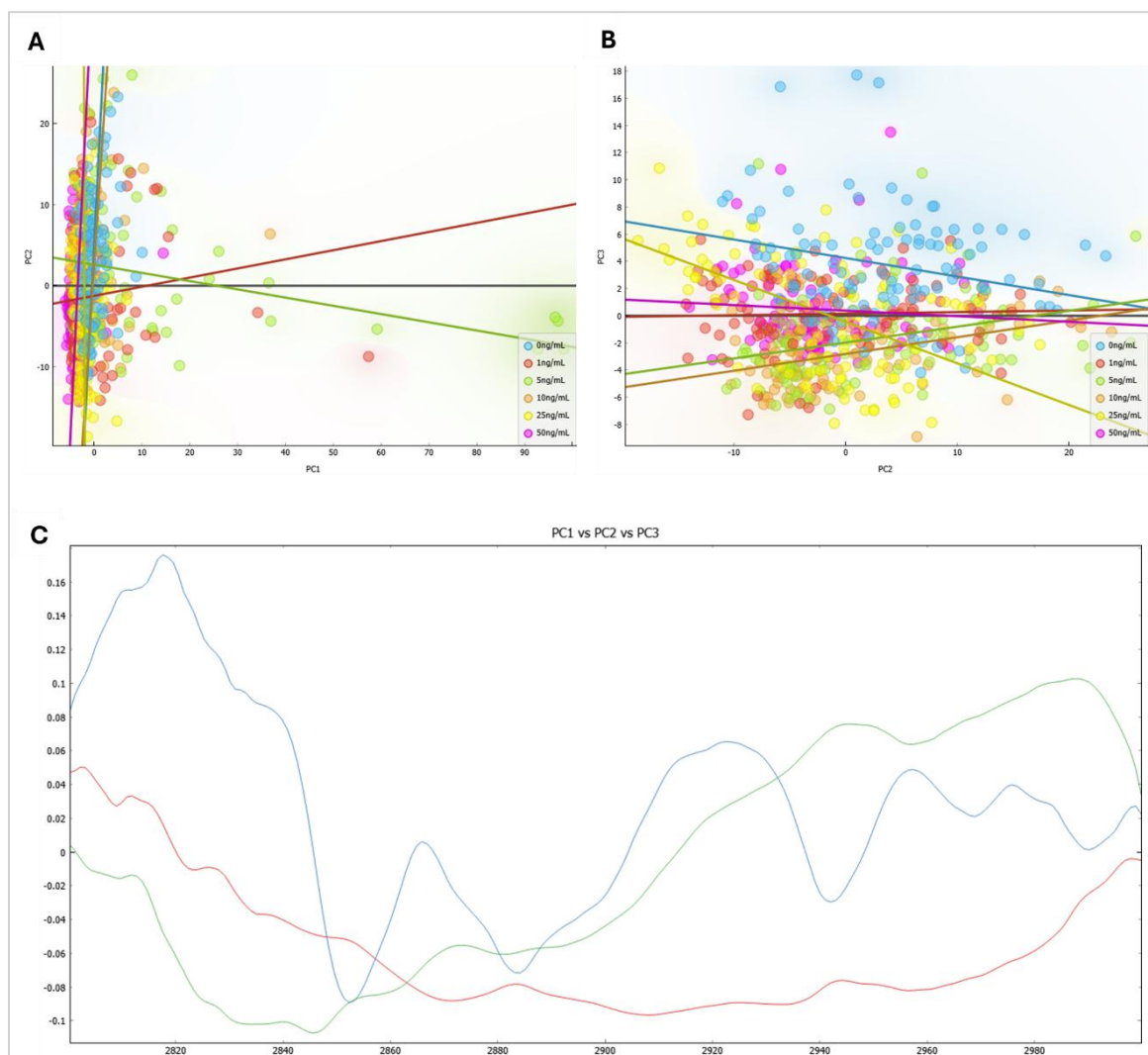


**Figure 80: PCA of the high-wavenumber region of undosed vs IL-dosed cells.**

From average Raman spectra (high wavenumber region) of IL-dosed vs healthy cochlear fibrocytes - ~250 individual cell spectra per condition, each from a separate (by condition) ~250k cell cytopspin monolayer of PFA fixed cells on CaF<sub>2</sub> - cells fixed at maximum P8. A) Scatter plot of PC1 (47%) vs PC2 (30%). B) Scatter plot of PC2 (30%) vs PC3 (7.3). C) Loadings plot of PC1 (red) vs PC2 (green) vs PC3 (blue).

Once again, the large number of samples employed in Raman spectroscopy investigation facilitated the application of predictive modelling using a neural network. As evidenced by the confidence tables in figure 81, though this model had slightly less accuracy than of TNF-dosed cells (likely due to the additional variable incorporated), it is clear that detectable differences between undosed cells and dosage conditions are present. This is particularly evident in the fingerprint region.

		Predicted						$\Sigma$
		0ng/mL	1ng/mL	5ng/mL	10ng/mL	25ng/mL	50ng/mL	
Actual	0ng/mL	96.4 %	0.0 %	0.0 %	0.4 %	0.8 %	2.4 %	249
	1ng/mL	0.0 %	98.4 %	0.0 %	0.0 %	0.4 %	1.2 %	250
	5ng/mL	0.4 %	0.0 %	93.5 %	5.3 %	0.8 %	0.0 %	246
	10ng/mL	0.4 %	1.2 %	6.5 %	79.0 %	12.9 %	0.0 %	248
	25ng/mL	0.8 %	0.0 %	1.2 %	11.3 %	85.0 %	1.6 %	247
	50ng/mL	1.2 %	0.0 %	0.0 %	0.0 %	0.4 %	98.4 %	250
	$\Sigma$	247	249	249	238	248	259	1490

		Predicted						$\Sigma$
		0ng/mL	1ng/mL	5ng/mL	10ng/mL	25ng/mL	50ng/mL	
Actual	0ng/mL	81.5 %	2.8 %	4.0 %	2.0 %	4.4 %	5.2 %	249
	1ng/mL	4.0 %	73.6 %	3.2 %	4.4 %	0.0 %	14.8 %	250
	5ng/mL	1.2 %	2.0 %	75.6 %	13.8 %	7.3 %	0.0 %	246
	10ng/mL	1.6 %	2.0 %	15.7 %	76.2 %	4.4 %	0.0 %	248
	25ng/mL	6.1 %	0.8 %	4.5 %	8.1 %	76.5 %	4.0 %	247
	50ng/mL	9.2 %	7.6 %	0.4 %	0.0 %	3.6 %	79.2 %	250
	$\Sigma$	258	222	255	259	238	258	1490

Figure 81: Confidence tables for neural network modelling of Raman spectra of murine cochlear fibrocytes following 24hrs incubation with IL-1 $\beta$ .

From Raman spectra of IL-dosed vs healthy cochlear fibrocytes each from a separate (by condition) ~250k cell cytopspin monolayer of PFA fixed cells on CaF<sub>2</sub> - cells fixed at maximum P8. A) Fingerprint region B) High wavenumber region.

To summarise the findings of IL-dosed cell Raman examinations, visible differences could be seen between dosed and undosed spectra at all dosage levels. These differences directly contrasted with observed TNF-based variations, strongly implying different modes of action in each cytokine's interaction with cochlear fibrocytes. This contrast is particularly notable at CH<sub>2</sub> and CH<sub>3</sub> bond vibration-associated sites.

Manual comparison of IL-dosed and undosed spectra indicates differences arising in multiple regions, including those attributed to nucleic acids, proteins, lipids, polysaccharides. Below 600cm<sup>-1</sup>, alterations to polysaccharide/nucleic acid signal intensity are seen at higher dosage levels. Likewise, nucleic acid variations in the region 700-1000cm<sup>-1</sup> demonstrate signal intensity variations between dosed and undosed conditions. In this region, signal intensity reductions correlate with dosage increase across all dose parameters. An inverse correlation between dosage and signal intensity is also noted in the symmetric ring breathing protein band at 1000cm<sup>-1</sup>. Such intensity decrease with dosage increase is unlikely to arise from IL presence in cells alone and indicated structural and functional changes to proteins in response to IL dosage. Differences noted at 1128cm<sup>-1</sup>, similar to those below 600cm<sup>-1</sup> arising at higher dosages, imply changes to glucose processing in cells in response to IL dosage. At higher dosages (25ng/mL, 50ng/mL) variations in lipid signal intensity may also be seen, with a reduction in signal intensity at these doses compared to the lower doses explored. As in TNF results, consistent differences in signal intensity are noted between dosed and undosed cell conditions in the region 1200-1400cm<sup>-1</sup>. In the high wavenumber region, signal intensity variations between dosed and undosed conditions contrast with those seen in TNF analyses, with variation at 2850cm<sup>-1</sup> seemingly unique to IL-dosed cells. Once again, successful distinction of dosage conditions and healthy cells is verified by both multivariate analysis (PCA) and neural network model.

#### 3.4.9. ATR-FTIR of IL-1 $\beta$ -dosed Cochlear Fibrocyte Supernatant

As seen with TNF-dosed samples, spectra of IL-dosed cochlear fibrocyte supernatants (Fig. 82) spectra show a lower overall absorbance than those seen in the first set of undosed cells examined. This is once again attributed to variations in sample preparation conditions and variation

in individual cell populations, though data appear to be of far greater consistency than those of TNF-dosed cells, likely due to the culture issues mentioned. As before, undosed supernatant was included in this stage of research enabling comparison across dosage conditions and undosed cells. Cell supernatants were distinct in all cases from matched media controls.

As anticipated based on previous supernatant analyses, all supernatant spectra, both undosed and dosed appear to demonstrate bands indicating DNA ( $950\text{-}1200\text{cm}^{-1}$ ), glycogen and carbohydrates ( $\sim 1030\text{-}1080\text{cm}^{-1}$ ), amides (I-  $\sim 1650\text{cm}^{-1}$ , II-  $\sim 1540\text{cm}^{-1}$ , III-  $1300\text{-}1500\text{cm}^{-1}$ ), and lipids ( $\sim 1745\text{cm}^{-1}$ ,  $2800\text{-}3050\text{cm}^{-1}$ ). Visually comparing spectra, there do not appear to be any large differences in absorbance or peak shifts across dosage conditions, with intra-condition sample variations around means making differences between conditions challenging to identify by eye.

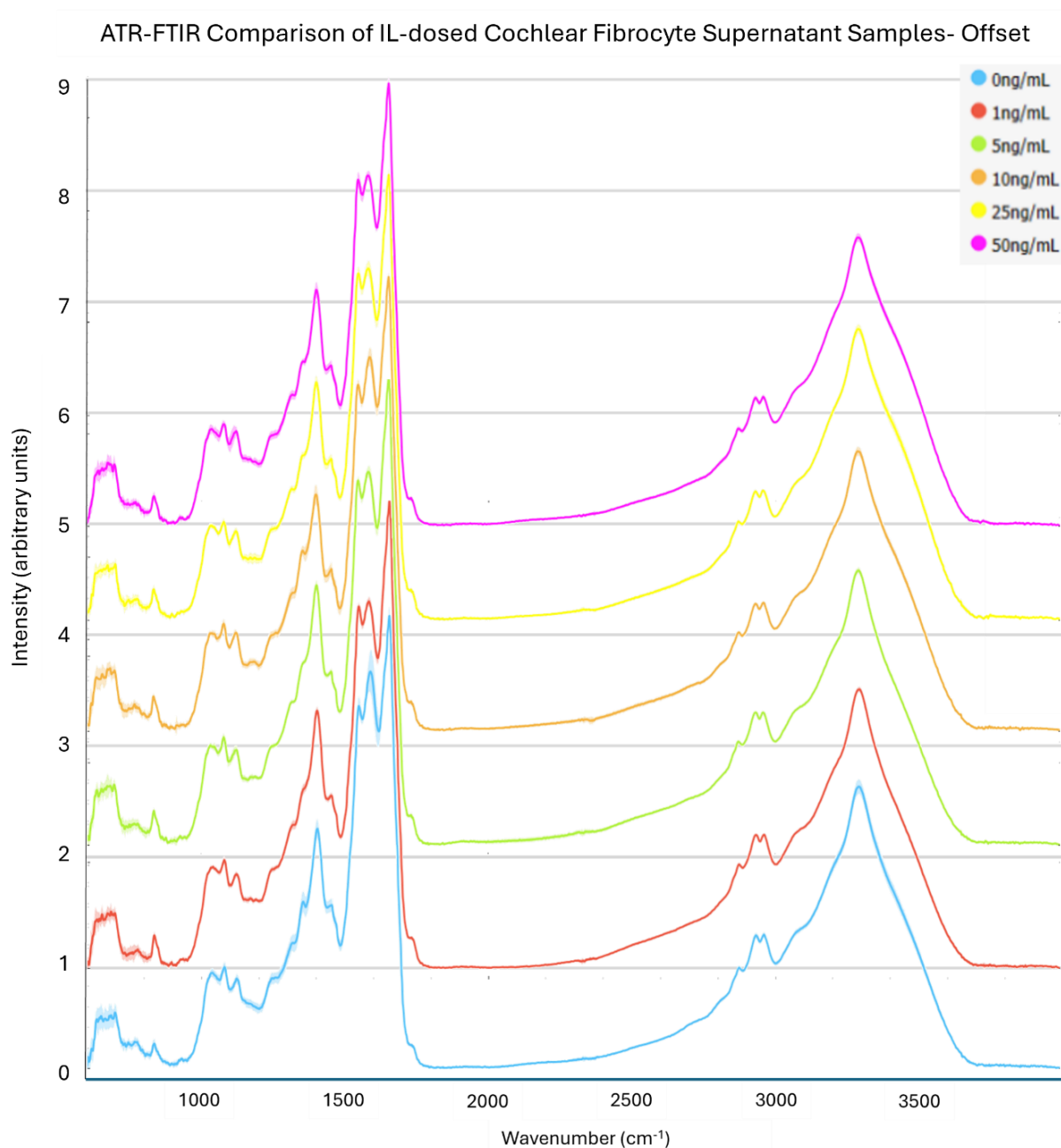


**Figure 82: ATR-FTIR spectra of IL-dosed cochlear fibrocyte supernatant samples.**

**Average ATR-FTIR spectra of supernatant from healthy vs IL-dosed cochlear fibrocyte cultures.**

**Supernatant averages formed of 9 spectra (3 per slide, 3 slides) from a ~200k cell population of cells at maximum P8.**

Nonetheless, some variations across conditions can be noted in the fingerprint region. Similar to TNF data, variation appears between conditions at  $\sim 1590\text{cm}^{-1}$ , previously attributed to histidine. As before, this is believed to indicate potential changes cell respiration, though VOC data must be examined to verify this. The greatest source of variation noted by eye arises in the region  $1095\text{--}1140\text{cm}^{-1}$ .

<sup>1</sup>, and is linked to phosphate group deformations, C-O stretching and C-OH antisymmetric stretching of nucleic acids.

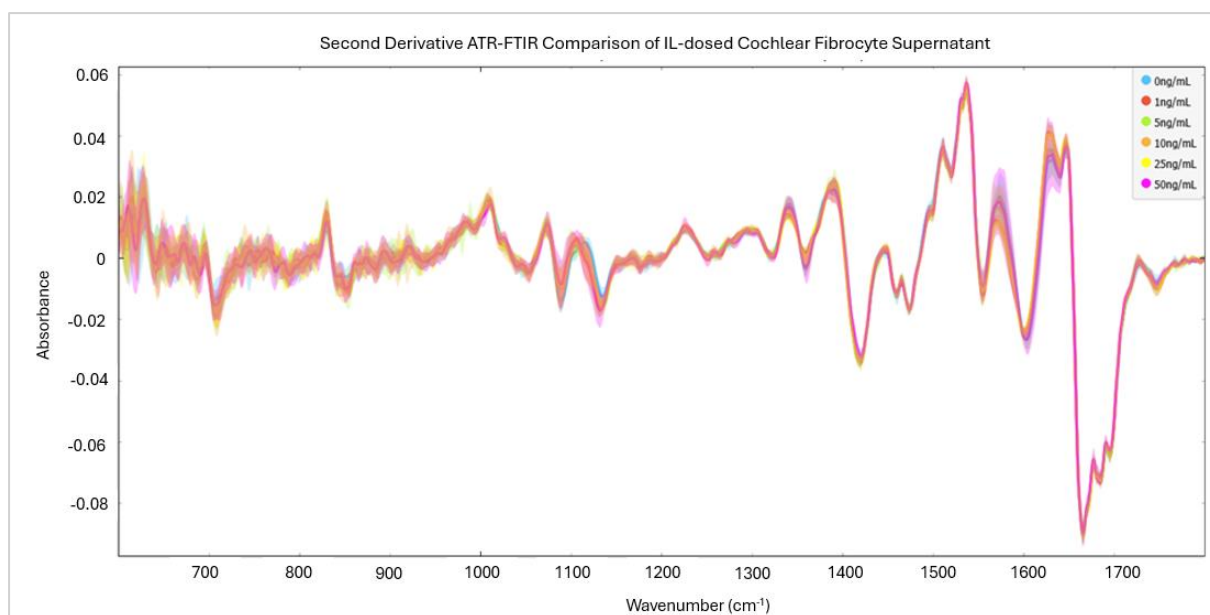


**Figure 83: Second derivative ATR-FTIR fingerprint region spectra of IL-dosed cochlear fibrocyte supernatants.**

**Second derivative average ATR-FTIR spectra of supernatant from healthy vs IL-dosed cochlear fibrocyte cultures. Supernatant averages formed of 9 spectra (3 per slide, 3 slides) from a ~200k cell population of cells at maximum P8.**

Second derivative spectra further demonstrate the noted variations, though intra-condition sample variation once again present a challenge to distinction (Fig. 83). As noted previously, the region 1095-1140cm<sup>-1</sup> appears to represent the greatest variation between conditions.

Examining fingerprint region PCA of IL-dosed cell FTIR, more sources of variation between conditions are noted than in TNF-dosed investigations, with only 76% of variation accounted for by 6 principal components. Scatter plots (Fig. 84) show some clustering of data points based upon dosage, though samples appear to cluster into several smaller groups within conditions in some areas. This is likely due to variations arising from sample prep and is considered human error. Nonetheless, variation between conditions is clear, with the corresponding loadings plot highlighting sources in regions below 800cm<sup>-1</sup>, 1030cm<sup>-1</sup> (C-O stretching and bending), 1095-1140cm<sup>-1</sup> (phosphate group deformations, C-O stretching and C-OH antisymmetric stretching) and 1500-1700cm<sup>-1</sup> (N-H bending, amide II, C=O stretching and amide I).

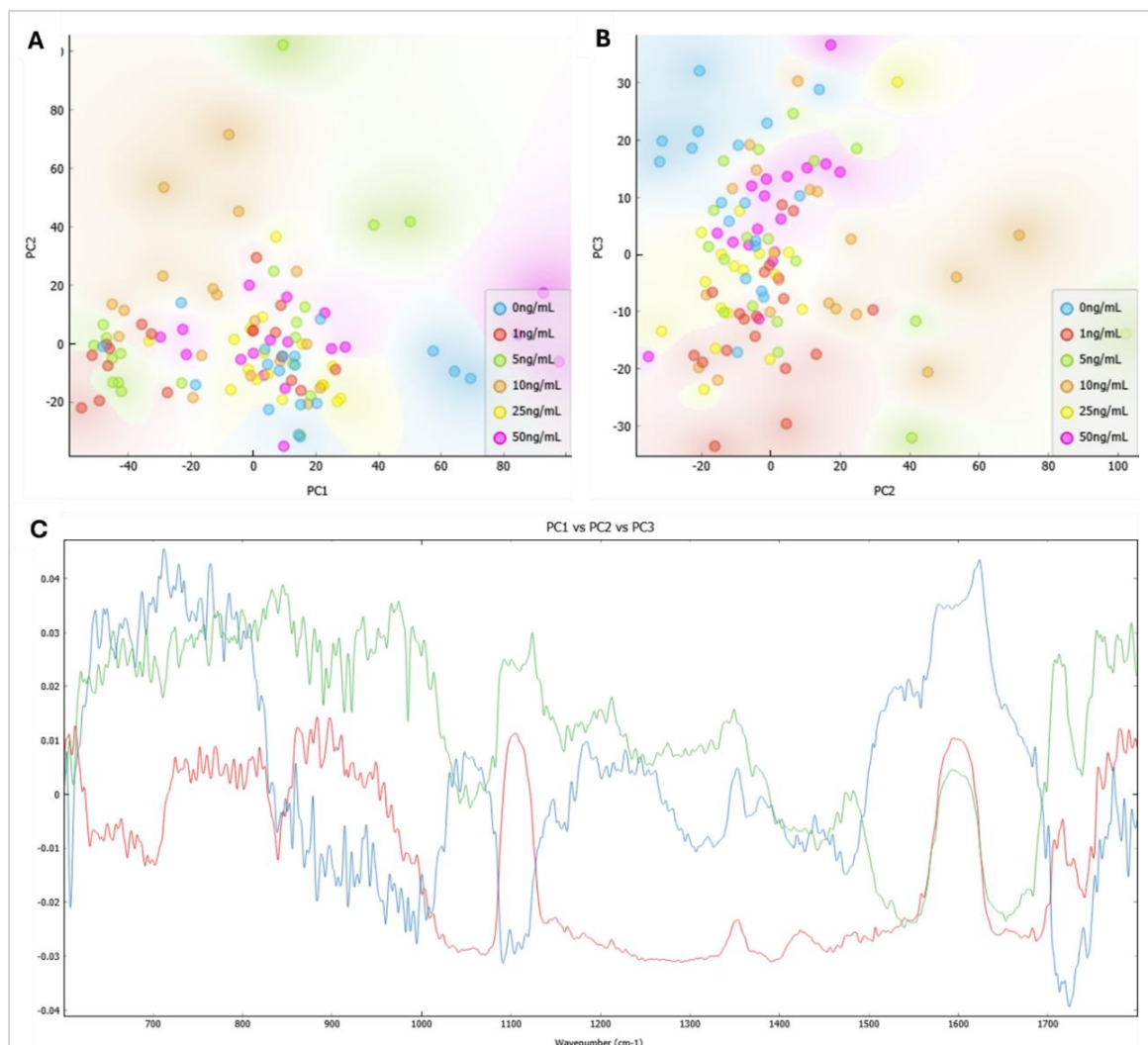


**Figure 84: PCA of the fingerprint region of IL-dosed cochlear fibrocyte supernatant.**

**From average ATR-FTIR spectra of supernatant from healthy vs IL-dosed cochlear fibrocyte cultures. Supernatant averages formed of 9 spectra (3 per slide, 3 slides) from a ~200k cell population of cells at maximum P8. A) Scatter plot of PC1 (40%) vs PC2 (24%). B) Scatter plot of PC2 (24%) vs PC3 (6%). C) Loadings plot of PC1 (red) vs PC2 (green) vs PC3 (blue).**

Turning to the high wavenumber region, as anticipated from spectra, fewer sources of variation are noted, with 80% of variance accounted for in 6 principal components. Scatter plots (Fig. 85) once again demonstrate clustering of samples, though small groupings within conditions are noted similarly to the fingerprint region. The corresponding loadings plot highlights sources of noted variations, with the majority appearing to arise below  $3000\text{cm}^{-1}$ , consistent with  $\text{CH}_2$  stretching,  $\text{CH}_3$  stretching,  $=\text{CH}$  stretching and amide B bond vibrations in proteins and lipids.

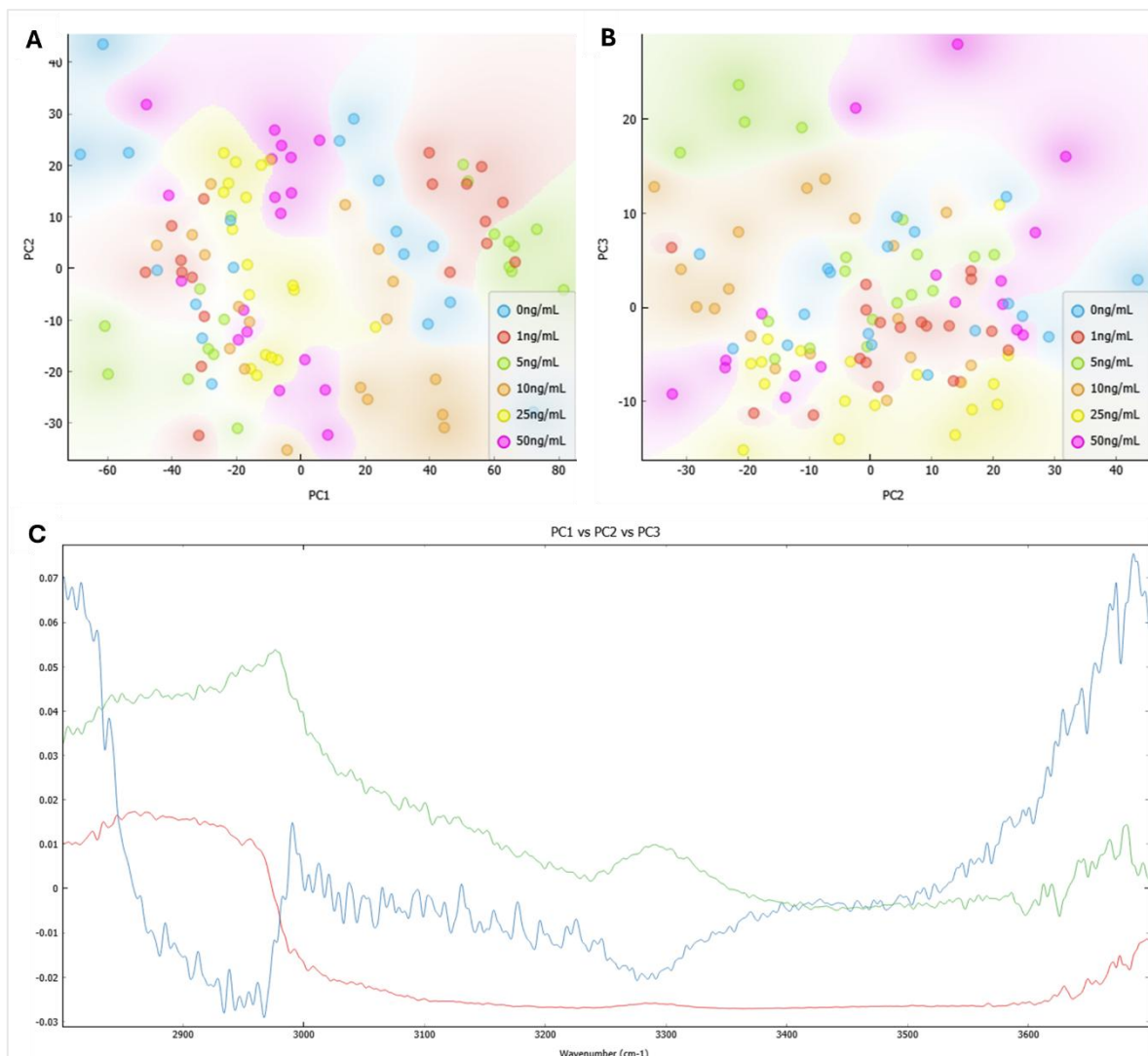


**Figure 85: PCA of the high wavenumber region of TNF-dosed cochlear fibrocyte supernatant. From average ATR-FTIR spectra of supernatant from healthy vs IL-dosed cochlear fibrocyte cultures. Supernatant averages formed of 9 spectra (3 per slide, 3 slides) from a ~200k cell population of cells at maximum P8. A) Scatter plot of PC1 (45%) vs PC2 (15%). B) Scatter plot of PC2 (15%) vs PC3 (8.5%). C) Loadings plot of PC1 (red) vs PC2 (green) vs PC3 (blue).**

Overall, ATR-FTIR analysis of IL-1-dosed cochlear fibrocyte supernatant samples reveals distinguishable differences between dosage conditions. These differences arise predominantly in regions associated with nucleic acids, amino acids and proteins, similar to outcomes of TNF-dosed cell examinations. Once again, variation is noted at  $1590\text{cm}^{-1}$ , likely indicative of bond vibrations in amino acids – potentially histidine as previously discussed.

### 3.5. Discussion

In general, this section of research was successful, with spectral profiles of healthy and inflamed cochlear fibrocytes successfully established using the experimental methods. Findings of this chapter further elucidate the pathology of inflammation in cochlear fibrocytes and form the first step in development of a pre-symptom detection method for cochlear fibrocyte damage. Both Raman spectroscopy data and ATR-FTIR spectroscopy data provide insight into the process of cochlear fibrocyte inflammation *in vitro* via cytokine administration and thus add value to the field.

Cochlear fibrocytes were successfully cultured from explanted spiral ligaments, with verification of sub-type by immunocytochemistry. Cells were confidently identified as cochlear fibrocytes, likely of sub-type II, IV or V.

Raman spectroscopy analysis of healthy cochlear fibrocytes demonstrated signals consistent with those expected of fixed cells, with peaks indicative of typical cellular constituents such as proteins, lipids, amino acids and DNA components. It should be noted, however, that some spectral noise and variation around sample averages is seen likely due to factors including lack of sensitivity in the optical platform employed and differences in cell cycle stage.

ATR-FTIR analysis, similarly to Raman spectroscopy, demonstrated signals consistent with expectations and confirmed the ability to distinguish cell supernatant from control media. Of particular interest in inflammation analysis was the peak attributed to histidine as this appeared to only be present in the cellular condition. The fingerprint region of both cochlear fibrocyte supernatant and control media showed clear peaks of amide I at  $\sim 1645\text{ cm}^{-1}$  and amide II at  $\sim 1550\text{ cm}^{-1}$ , though absorbance was shown to be stronger in cell supernatant samples - indicative of a higher protein content in media which has contained cells.

Induction of inflammation in cochlear fibrocytes via TNF- $\alpha$  administration was confirmed via the downstream expression of IL-6 and IL-8. Both of these inflammatory markers are associated with inflammaging and ARHL<sup>[154]</sup> and appropriately confirm the desired effect of TNF application to cultures.

Raman spectroscopy analysis of TNF-dosed cochlear fibrocytes demonstrated detectable differences between dosed and undosed cells at all dosage levels. In contrast to sensory cells, which do not experience damage from TNF- $\alpha$  unless present in extremely high concentrations <sup>[157-159]</sup>, cochlear fibrocytes appear to show TNF-induced alterations at even 1ng/mL. This supports the hypothesis that damage to sensory cells in the presence of TNF arises in part from changes to cochlear homeostasis due to support cell damage.

The nature of this damage in cochlear fibrocytes is implied to arise due to multiple factors, with spectral differences between healthy and inflamed cells noted in regions associated with nucleic acids, proteins, lipids, polysaccharides, and amino acids. In particular, protein and lipid alterations originating in CH<sub>2</sub> and CH<sub>3</sub> vibrational modes are implicated. Such variations are believed to indicate inflammation-consistent factors such as changes to mitochondrial protein and lipid ratios as well as apoptosis-associated lipid accumulation <sup>[257,125]</sup>.

Distinction of dosage conditions as well as healthy cells in TNF-dosed cochlear fibrocytes was verified by both multivariate analysis (PCA) and neural network model. Both analyses demonstrated capacity for the distinction of healthy and inflamed cells, even at low cytokine dosage.

ATR-FTIR analysis of TNF-dosed cochlear fibrocyte supernatant further demonstrated detectable differences between dosage conditions. This is particularly encouraging when considering potential clinical translation and the use of cochlear fluid sampling <sup>[110,111]</sup>. The most notable variations seen in ATR-FTIR analyses were protein related and appeared consistent with the presence of pro-inflammatory cytokines in supernatant. This likely indicates TNF, IL-6 and IL-8 presence and supports evidence from literature of spiral ligament fibrocytes upregulating TNF- $\alpha$  in response to the inflammatory state <sup>[159]</sup>. A distinct variation was seen between samples at 1590cm<sup>-1</sup> which is presently attributed to histidine. This appears to be a source of great variation across PC2 and PC3 particularly. Variation in this band indirectly implies mitochondrial changes arising from TNF dosage, as histidine present in the mitochondria of all mammals <sup>[153]</sup>. In other cell types such as endothelial cells histidine is shown to demonstrate anti-inflammatory effects <sup>[124]</sup>, so its presence may alternatively indicate an anti-inflammatory effect in cochlear fibrocytes. Should this band represent another amino acid

susceptible to similar bond deformation to histidine such as tryptophan data are still of value, with such amino acids highly implicated in inflammation research <sup>[160, 161]</sup>.

In the context of ARHL, Johnson *et al.* <sup>[153]</sup> elucidated genetic mechanisms behind ARHL development in A/J mice, a popular mouse model of ARHL by mitochondrial dysfunction and rapid hair cell loss. This study highlighted an amino acid change in the citrate synthase protein of such mice, from histidine to asparagine, contributing to a mutation in said gene and subsequent mitochondrial dysfunction. It is, thus, not unsupported to suggest that variation in histidine level with inflammation may indicate alterations to citrate synthase action and mitochondria in general. However, given the presence of this signal in supernatant samples, it is more likely that mitochondrial degradation is to blame or that cochlear fibrocytes produce histidine in response to inflammation similarly to endothelial cells.

As in TNF- $\alpha$ -dosed cells, induction of inflammation in cochlear fibrocytes via IL-1 $\beta$  administration was confirmed via the downstream expression of IL-6 and IL-8. Such markers appropriately confirm the desired effect of IL-1 application to cultures.

Raman spectroscopy analysis of IL-dosed cochlear fibrocytes, as in TNF-dosed cells, demonstrated detectable differences between dosed and undosed cells at all dosage levels. Once again, successful distinction of dosage conditions and healthy cells was verified by both multivariate analysis (PCA) and neural network model. However, it is notable that effects of inflammation appear varied, with cells at higher dosages (25ng/mL, 50ng/mL) responding differently in some spectral regions than lower dosed cells.

Comparison of IL-dosed and undosed spectra indicated notable differences arising in regions attributed to nucleic acids and polysaccharides. In the characteristic triple peak region, nucleic acid signal intensity reductions were shown to correlate with dosage increase across all dose parameters, strongly implying alterations to DNA arising from inflammation. Differences noted at 1128cm<sup>-1</sup> imply changes to glucose processing (and consequently mitochondrial function) in response to IL dosage. These findings are consistent with expectations of damage to cells undergoing inflammation <sup>[215]</sup>.

Differences seen between IL-dosed and healthy cells often directly contrasted with observed differences in TNF-dosed and undosed cells, illustrating the different signalling pathways of inflammatory action in the two cytokines examined. Such contrasting observations include an inverse correlation between dosage and signal intensity in the symmetric ring breathing protein band at  $1000\text{cm}^{-1}$ , suggestive of structural and functional changes to proteins in response to IL dosage. This may include the maturation of pro-inflammatory cytokines IL- $1\beta$  and IL-18 from their precursors <sup>[164, 165]</sup>.

Though no firm conclusion may be made at present, capacity to distinguish the nature of inflammatory action may enable differentiation between apoptosis and the inflammasome-associated form of cell death pyroptosis <sup>[166]</sup>. In seeking to verify the induction of potential pyroptosis-like responses *in vitro*, hyperspectral Raman analysis is recommended in order to assess plasma membrane integrity.

Further distinctions from TNF-dosed cells is particularly notable at  $\text{CH}_2$  and  $\text{CH}_3$  bond vibration-associated sites attributed to both lipids and proteins. This is noted both in the fingerprint and high wavenumber regions of IL-dosed cell spectra. At higher IL dosages (25ng/mL, 50ng/mL) a reduction in lipid associated  $\text{CH}_2/\text{CH}_3$  signal intensity was noted compared to the lower doses explored. This both contrasts with findings from TNF-dosed cells at the same level, and suggests accumulation of lipids consistent with apoptosis progression at lower doses followed by cell degradation above 25ng/mL. With these findings in mind, where time and resources were limited, it was decided that further investigation of IL- $1\beta$  inflammatory responses would be conducted in preference to TNF- $\alpha$  analyses at the Diamond Light Source (Oxford, UK), with only 1ng/mL, 5ng/mL and 10ng/mL conditions carried forward in investigations.

ATR-FTIR analysis of IL-1-dosed cochlear fibrocyte supernatant samples, similarly to TNF analysis, revealed distinguishable differences between dosage conditions. This, again, is good news when seeking to translate the trialled techniques to cochlear fluid sampling <sup>[110,111]</sup>. Differences between dosed and undosed supernatant conditions were shown to arise predominantly in regions associated with nucleic acids, amino acids and proteins, similar to outcomes of TNF-dosed cell examinations. Once again, variation was noted at  $1590\text{cm}^{-1}$ , likely indicative of bond vibrations in

amino acids – potentially indicative of histidine alterations as previously discussed <sup>[153]</sup>. Though not previously studied in the present context, variations in proteins detectable through cochlear fluids are of interest in future investigations when considering the work of Höhl *et al.* (2019) and the potential effects of the inner ear stress proteome discussed in section 1.7.4.

The noted distinct differences in response to TNF- $\alpha$  and IL-1 $\beta$  dosage are not unexpected and may arise through several routes. One causative factor may be variation in receptor expression. Though cultured spiral ligament fibrocytes have been shown to secrete chemokines and other mediators after stimulation of proinflammatory cytokine TNF- $\alpha$  or IL-1 $\beta$ , indicating appropriate receptor presence, quantification has not been performed and their relative abundance on the varied sub-types of cochlear fibrocytes is yet unconfirmed. Thus, it is plausible that some of the response variation seen is a result of this.

It is also notable that, while both IL-1 $\beta$  and TNF- $\alpha$  are pro-inflammatory cytokines, they have distinct mechanisms of action, signalling pathways, and physiological effects as alluded to in Table 7. For example, while both pro-inflammatory cytokines studied yield an increase in IL-6 and IL-8 secretion<sup>[273]</sup>, TNF- $\alpha$  may cause a more prolonged inflammatory state due to its role in chronic inflammation – a factor which may not be fully represented in this study due to the 24 hour dosage period. IL-1 $\beta$ , however, being more focused on acute inflammation and initiation of inflammatory pathways, may induce a quicker but more transient response. For greater representation of cytokine effects, future experiments may consider incorporating time-course analyses to capture early and late phase effects, measurement of fibrosis markers to assess prolonged inflammation and similarity of cochlear fibrocytes to circulating fibrocytes <sup>[274]</sup> and the addition of other cytokines or cell types to the model.

While reviewing future study improvements, it is of value, in examining the data presented within this chapter, to note that the noise seen in ATR-FTIR loadings plots is likely due to the small number of samples compared to the number of features analysed. That is, for each dosage condition, 9 sample points are considered, while the PCA notes 1868 features. This is supported by the lack of noise in S-FTIR data (chapter 4), wherein sample number is far greater. Similar may be said for benchtop Raman analyses, wherein number of features greatly outnumber sample size, yielding noise in loadings plots.

Where benchtop Raman data is concerned, the previously noted factors such as laser age and lack of vibrational dampening must also be considered as these may yield noise that, while not immediately apparent in raw data, may become visible in PCA loadings.

In cases such as this, trialling alternate clustering methods is of value in ensuring that data are represented appropriately. Such steps were taken in the present research, though methods are not explored in this report as they were not utilised for all data, rather to verify existing PCAs. Trialling t-SNE (which deals better with nonlinear data than traditional PCA), yields visible clustering across samples lending confidence to the PCA results presented. However, no loadings plots are generated from this method, meaning that variation sources still require additional data processing to be identified and making tSNE an inadequate alternative to PCA in the present case. Sparse PCA (which deals better with small sample numbers), yields clustering near-identical to that of the presented data, again lending confidence to results presented. Using this method, noise in loadings plots is reduced for data where features outweigh sample number but lend no additional insight to standard PCA in terms of variation origins etc. As sparse PCA is not ideal for other data in this manuscript such as HW region plots and synchrotron data, analysis was conducted with standard PCA only to ensure consistency across experiments of varying scale. However, though noise is seen, it can be comfortably stated that PCA results shown are verified.

In the presented Raman data, where PCA did not produce overly strong group separation, it is important to note both the limitations of PCA use and the value that the technique still holds in dimensionality reduction for neural network modelling. For Raman data, factors such as laser aging may introduce noise that PCA amplifies during decomposition, even if imperceptible in raw spectra. This is consistent with PCA's tendency to magnify subtle artifacts in high-dimensional data. Even under ideal experimental conditions, PCA's reliance on linear variance maximisation inherently limits its ability to capture complex, nonlinear relationships such as those seen in Raman data <sup>[276]</sup>. In contrast, neural networks can model such nonlinearities, allowing them to distinguish patterns that may not be immediately visible in a PCA scatter plot. Thus, the differing outcomes of PCA analysis and neural network modelling of Raman spectra in this chapter can be attributed to the distinct ways in which these methods process and interpret data.

Considering this, it should be noted that lack of group separation in PCA scores plots does not preclude its use in downstream classification. As a preprocessing step, PCA reduces data dimensionality while retaining critical spectral variance, enabling neural network models to extract previously unseen trends. As such, PCA is often accompanied by downstream modelling in spectral data processing <sup>[276]</sup>. By compressing Raman spectra into a lower-dimensional space while preserving maximal variance, PCA likely mitigated some high-frequency noise and redundant features, improving neural network training efficiency. As such, even if PCA did not visibly separate groups, it likely retained spectral features that were relevant for classification when processed through the neural network's weighted layers and activation functions. This highlights the advantage of combining PCA with machine learning approaches in a setup where PCA organises data into a lower-dimensional space, and the neural network builds upon this foundation to identify meaningful nonlinear patterns that PCA alone cannot resolve.

Overall, the findings of chapter 3 illustrate great progress in furthering the understanding of cochlear fibrocyte inflammation. The chapter also illustrates further the potential for application of vibrational spectroscopy techniques in the *in vitro* examination of cochlear fibrocyte health and the acquisition of inner ear health information from fluids surrounding cells. From the differences detected through the techniques applied, it is clear that with a sufficient sample size, similar predictive modelling methods to those employed in Raman analysis may be viable in ATR-FTIR liquid investigations. Where potential clinical translation is concerned this is highly desirable when seeking to undertake analysis of patient perilymph samples.

### 3.6. Conclusions

To conclude, this section of research meets the aims outlined within section 3.2.

Aim 1 was met through the successful explantation, culture and immunocytochemical characterisation of murine cochlear fibrocytes. Fibrocytes were noted as of sub-type II, IV or V.

Aim 2 was met through the successful establishment of a healthy murine cochlear fibrocyte spectral profile using Raman spectroscopy. Cell spectra were as expected for mammalian cells in culture.

Aim 3 was met through the successful establishment of a healthy murine cochlear fibrocyte supernatant spectral profile using ATR-FTIR spectroscopy. Cell supernatant spectra were distinct from culture media alone, demonstrating bands unique to cells.

Aim 4 was met through the successful induction of inflammation-like responses in cochlear fibrocyte cultures using TNF- $\alpha$  and IL-1 $\beta$  administration via culture media. Downstream inflammatory effects were confirmed by positive staining for IL-6 and IL-8 in dosed conditions.

Aim 5 was met through the successful establishment of differing spectral profiles for TNF- $\alpha$  and IL-1 $\beta$ -dosed cochlear fibrocytes and the distinction between healthy and inflamed cells via Raman spectroscopy. In both TNF- $\alpha$  and IL-1 $\beta$ -dosed investigations, detectable differences between healthy and inflamed cells were verified using multivariate analysis and neural network modelling.

Finally, aim 6 was met through the successful establishment of differing spectral profiles for TNF- $\alpha$  and IL-1 $\beta$ -dosed cochlear fibrocyte supernatant samples, and the distinction between healthy and inflamed cell supernatants via ATR-FTIR spectroscopy. In both TNF- $\alpha$  and IL-1 $\beta$ -dosed investigations, detectable differences between healthy and inflamed cell supernatants were verified using multivariate analysis.

With these findings in mind, it is clear that the techniques demonstrated show great promise in the advancement of ARHL understanding and treatment. To further improve understanding of the inflammatory states observed, further study is recommended in order to build a sample database from which further modelling and analysis may be conducted. Should such modelling prove successful and accurate in ATR-FTIR based liquid analysis, opportunities to employ patient perilymph sampling in inner ear health examination may be improved.

## 4. Hyperspectral Raman Spectroscopy and Synchrotron micro-FTIR of Interleukin-1 $\beta$ Induced Inflammatory Changes in Cochlear Fibrocyte Cultures

---

### 4.1. Introduction

Building on the findings of previous chapters, it is of undeniable value to explore higher spectral and spatial resolution data, to gain greater insight into inter- and intra-cellular changes induced by inflammation in cochlear fibrocytes. In pursuit of such high-resolution investigations, the research group employed time at the Diamond Light Source synchrotron facility at the Harwell Campus, Oxford, UK. Experimental time at the facility was granted to conduct measurements of healthy and IL-1 $\beta$ -inflamed cochlear fibrocytes using synchrotron micro-FTIR and hyperspectral Raman spectroscopy. These techniques are ideal for investigations of this nature as, unlike other techniques that may be employed, they can be kept relatively non-destructive to samples and allow the definitive description of cell phenotype in the form of a cell ‘fingerprint’. In addition to this, these techniques feasibly allow the detection of previously unseen biochemical variations between inflamed and control cells due to their high-resolution capacity. This is of great value in building the knowledge base surrounding cochlear fibrocytes and their related pathologies which, as mentioned previously, are considerably under-researched compared to other cell types of the inner ear.

As previous chapters have discussed the lack of cochlear fibrocyte analysis using benchtop FTIR and Raman, it comes as little surprise that such cells have not been subject to observation at synchrotron level. Arguably, the nearest these cells have come to vibrational spectroscopic analysis is in the form of bone-marrow derived fibrocytes associated with wound healing and inflammation <sup>[209,210]</sup>. That is, in the study by Becker *et al.* (2023) <sup>[211]</sup>, fibrotic tissue was examined via Raman microspectroscopy. Though successful in the discrimination of fibrotic and non-fibrotic tissue, this study is of limited relevance to the cellular analysis focus of the present research as it instead centres on extracellular matrix structure in sample tissues. Instead, where

seeking to apply literature findings to the present context, it is prudent to explore a wider field of reference material. That is, though not employed to date in the present context, S-FTIR hyperspectral Raman spectroscopy have a considerable history of successful employment in biological investigations. Examples include the use of S-FTIR in tracking anticancer drugs <sup>[212]</sup>, assessing biochemical variations across the cell cycle <sup>[213]</sup> and studying the effect of ionising radiation on cells <sup>[214]</sup>.

Of particular interest to the present context is the study by Dunkhunthod *et al.* (2020) <sup>[215]</sup>, who demonstrated use of S-FTIR in the examination of anti-inflammatory activity in murine macrophages. Though not directly relatable to the present research, the group's findings surrounding protein and lipid alterations are of great relevance when considering previous chapter findings (see chapter 5) as they imply that cochlear fibrocytes do not undergo activation in response to inflammatory signals in the manner that macrophages do. This is suggested by Dunkhunthod *et al.*'s finding that healthy (unactivated) macrophages demonstrate greater protein abundance than those that are activated, in contrast to the findings in chapter 5 which demonstrate an increase in protein peak intensity for higher inflammation dosages. This certainly warrants further investigation using S-FTIR to elucidate the biochemical mechanisms behind this response, with accompanying Raman spectroscopic analysis enabling observations of molecular localisation within cells.

#### 4.1.1. Infrared Spectroscopy- Synchrotron vs. Benchtop

As opposed to benchtop FTIR which uses IR (infrared) radiation produced via Global source, synchrotron based FTIR employs radiation produced by the rapid circular orbit of electrons around a synchrotron ring. Magnetic fields around the ring enable the paths of electrons to be bent, maintaining their circular movement in a controlled path at relativistic velocity. This source produces IR light with extremely high brightness, far greater than that possible with Global light sources <sup>[178, 179]</sup>. Specifically, the IR radiation produced at the Diamond Light Source available to the MIRIAM (B22) beamline spans the largest possible infrared spectral range (from near-IR to far-IR) and is capable of up to 1000 times the brightness of conventional IR sources. As a result of this

increased capacity for brightness, synchrotron-based sampling yields a far greater spatial resolution than benchtop sampling, with a signal to noise ratio unachievable by conventional FTIR methods. It is thus ideal for the examination of cellular samples and can facilitate the examination of molecular components at subcellular level in larger cells such as cochlear fibrocytes (typically ~50µm diameter). Such subcellular components may include mitochondria which, though they cannot be analysed in detail due to their extremely small size (mitochondria are typically <3µm while the MIRIAM FTIR instrument offers a spot size of approximately 15µm) may still be influential in cell spectra (for dedicated investigation of subcellular structures, employment of B22's scattering SNOM or photothermal contact resonance modes are recommended). This is of particular interest in the context of the present research, wherein interactions in both inter and intra-cellular contexts are of great value in interpreting the metabolic behaviour of cell populations under inflammatory stress.

With this in mind, IL-1β dosed cellular samples were subjected to analysis at the Diamond Light Source synchrotron facility (Oxford, UK). Analysis was conducted both via hyperspectral Raman spectroscopy and infrared micro-spectroscopy using synchrotron-produced radiation.

#### 4.1.2. The Present Investigation – The Study of Biochemical Changes in Murine Cochlear Fibrocytes due to Inflammation using Synchrotron-based MicroFTIR (S-FTIR)

Research time was granted on B22 (MIRIAM) of the Diamond Light Source synchrotron facility (Oxford, UK) for late 2022 (experiment number: SM-32158). The approved research proposal outlined plans to obtain S-FTIR spectra murine cochlea fibrocytes fixed on CaF<sub>2</sub> slides, and to conduct complementary measurements on the same samples using the confocal Raman microscope also located at B22. B22 facilities provided the high spectral and spatial resolution required to observe the inter- and intra-cellular changes induced in cochlear fibrocytes by cytokine administration.

In contrast to previous chapters, cellular samples examined in this section of research were not cytopun but grown directly onto substrates and fixed *in situ*. This is arguably of greater physiological relevance than cytopun cells when considering the general culture environment and the replication of *in vivo* conditions. This is particularly relevant where examining cell interactions via hyperspectral Raman spectroscopy. It is, however, important to note that the use of grown cells rather than cytopun cells increases the risk of uneven cell topography and may impact reproducibility of results. That is, surface irregularities in samples may alter the way in which incident light interacts with the sample affecting Raman laser focus, scattering and signal intensity, and yielding potentially inconsistent results.

## 4.2. Chapter Aims

The aims of this section of research are as follows:

1. Examine, by hyperspectral Raman spectroscopy, the effect of IL-1 $\beta$  dosage on murine cochlear fibrocytes, examining cell nuclei, cytoplasm, membranes and intersections with neighbouring cells.
2. Explore, by S-FTIR, the effect of the effect of IL-1 $\beta$  dosage on murine cochlear fibrocytes.
3. Accurately distinguish, through the use of a non-linear predictive model, the cytokine dosage applied to cultured cells.

## 4.3. Materials and Methods

### 4.3.1. Sample Preparation

In preparation for measurement, cells were seeded onto 0.5mm thick IR/Raman grade CaF<sub>2</sub> slides and topped with a ~1mL droplet of cochlear fibrocyte culture media. Slides were placed in individual petri dishes and supported with a plastic ring above a reservoir of dH<sub>2</sub>O in order to maintain humidity. Samples were incubated (37°C, 5% CO<sub>2</sub>) to allow for cell adherence. Once cells were adhered, the media droplet was aspirated and appropriate control or IL-1 $\beta$  dose media added

(1ng/mL, 5ng/mL, 10ng/mL). Only conditions IL-1 $\beta$ -dosed 0ng/mL, 1ng/mL, 5ng/mL and 10ng/mL were established for synchrotron analysis in order to efficiently use the time available at the facility (see Fig. 42, chapter 5). Samples were incubated (37°C, 5% CO<sub>2</sub>) for 24 hours to allow cytokine effect. After 24 hours <sup>[247]</sup>, dose media was aspirated and cells fixed for 10-15 minutes at room temperature using 4% PFA in 0.9% NaCl, followed by 3 washes with 0.9% NaCl solution and 1 wash with dH<sub>2</sub>O. Fixed samples were left to air dry in ambient conditions before storage.

#### 4.3.2. Synchrotron Facility at Diamond Light Source, UK

Synchrotron-source infrared micro-spectroscopy data were gathered at the Diamond Light Source, Oxford, UK using beamline station B22 (MIRIAM). This station is equipped with a Bruker Vertex 80 V Fourier Transform IR Interferometer with a Hyperion 3000 microscope (Fig. 86). Raman data were gathered in the B22 sample preparation area laboratory, using a Raman microspectrometer. We thank Diamond Light Source for access to the MIRIAM beamline, B22, (experiment number: SM-32158) that contributed to the results presented here.



Figure 86: The end station of B22 (MIRIAM), Diamond Light Source, Oxford, UK.

### 4.3.3. S-FTIR Sampling

Samples, prepared as detailed above, were subjected to single cell measurements using standard user mode of the B22 IR microscope. An MCT broadband detector was employed. As standard, cell measurements were taken at 36x magnification, with the beam approximately focused on the centre of each cell in efforts to sample the nuclear region or adjacent cytoplasm. Spectral parameters were ascertained following initial test measurements. Following these, 128 scans per sample were taken with a 20x20 $\mu\text{m}$  aperture. Background measurements were taken from clear substrate regions with no cells or debris using the same general parameters as sample measurements and acquiring 256 scans/background. A new background was acquired for each sample analysed, with background collected after approximately every 100 cell measurements acquired to ensure stability.

### 4.3.4. Raman Sampling

In addition to S-FTIR, hyperspectral Raman microspectroscopy was conducted on the prepared samples. Raman sampling was conducted using the SENTERRA confocal system at B22 using a 532nm laser operating at 50mW power with grating 400lines/mm. A 50x objective over a spectral range of 400 $\text{cm}^{-1}$  – 3500 $\text{cm}^{-1}$  was employed. A 50 $\mu\text{m}$  aperture was employed. Resolution was determined to be  $\sim 9\text{cm}^{-1}$  on average. No automatic background correction was conducted, scattering correction was applied during acquisition. Comparison was made between undosed cells and cells dosed with 10ng/mL IL-1 $\beta$ , with limited sampling conducted due to time constraints.

### 4.3.5. Data Processing

All data processing and analysis was conducted in Orange (Quasar) software as detailed in chapter 2.4.2. That is, spectra were cut for noise, baseline corrected (rubber band), smoothed (Savitsky-Golay), normalised (vector normalisation) and cut to areas of interest. As synchrotron data typically requires less smoothing than benchtop data, Savitsky-Golay filter was applied at window 5 to avoid over-processing. Second derivative spectra, similarly to benchtop data, received

greater smoothing to account for noise, with window of Savitsky-Golay set to 11 for second derivative spectra.

Similarly to Raman data presented in chapter 3, results of synchrotron FTIR analysis were utilised to produce a machine learning algorithm with the aim of reliably distinguishing dosage classes of examined samples. A neural network model was applied to the data. Data was split randomly into training and testing groups (50:50 train to test and 70:30 train to test), enabling separate data to be used to train and evaluate the accuracy of the model. This is discussed further in section 4.4.3.

Hyperspectral Raman data were presented both as spectra and accompanying images, as well as through k-means clustering. K-means cluster analysis is a popular clustering method found in Raman spectroscopy<sup>[263]</sup>. This unsupervised machine learning algorithm is used to group data into clusters based on similarity. The algorithm begins by randomly choosing a defined number (k) of cluster centres. Each pixel in the analysed image is then assigned to its nearest cluster centre. Cluster centres (centroids) are then iteratively adjusted to minimise the sum of distances. Spectra that no longer match their assigned cluster are reassigned to the nearest cluster. This process repeats until no further reassignment of spectra can occur or until a desired stopping point is reached (e.g. max iterations). Once this process is completed, clusters are colour coded yielding both a cluster group on the image and an associated spectrum. In summary, K-means clustering groups pixels with similar spectral characteristics into clusters. In the present data, 3 clusters were shown to be optimum for the data presented, with a maximum of 300 iterations specified for analysis.

## 4.4. Results and Interpretation

### 4.4.1. Raman Spectroscopy

In examination of cochlear fibrocytes by hyperspectral Raman spectroscopy, it is first important to note that, due to experimental time constraints and the acquisition time for each area map (up to 10 hours in some cases), few samples were collected. With this in mind, comparison of

undosed cells against 10ng/mL dosed cells (the highest dosage class taken to the facility) was prioritised to facilitate observation of the maximum possible sample variation within the granted time at the synchrotron facility. Further to this, where possible the group aimed to compare single cells and cells with neighbours, though such examples were not always available. As such, four samples are presented in depth below- an undosed single cell, two undosed cells in contact, two 10ng/mL dosed cells in contact, and a 10ng/mL in contact with other cells showing unusual granulations.

Beginning with examination of undosed cells alone vs in contact, it is clear that there are variations in overall spectra, with general signal intensity in the fingerprint region higher in interacting cells than a cell alone (Fig. 87). This contrasts with the high wavenumber region which demonstrates the opposite result, albeit more subtle. Of particular interest are the intensity increases demonstrated in the intersecting cells at wavenumbers  $<600\text{cm}^{-1}$ . However, this variation may be due to diffraction variations in samples.

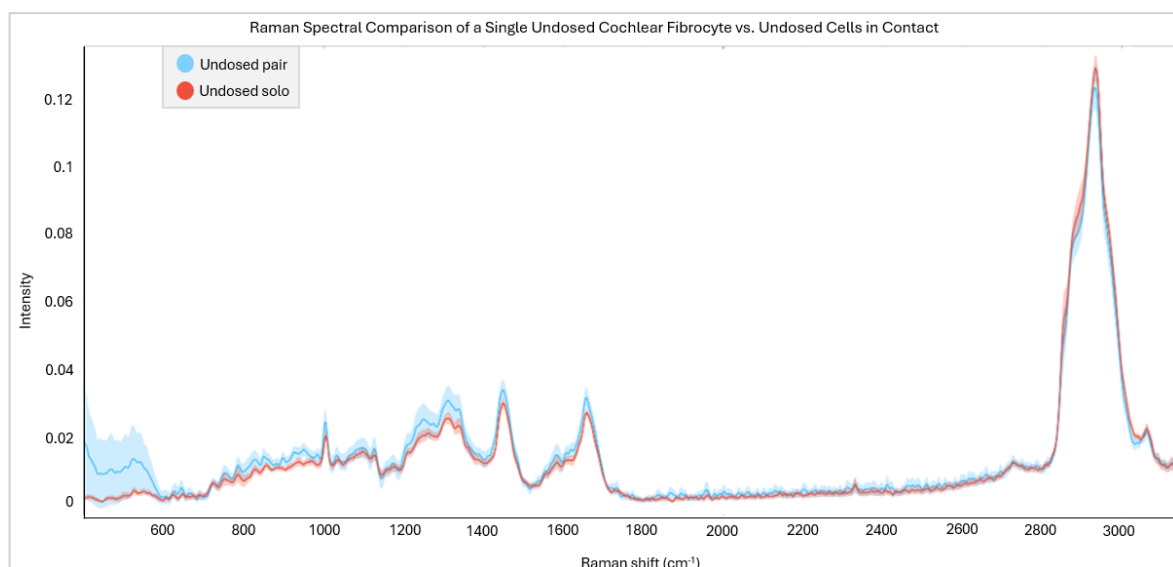


**Figure 87: Comparison of undosed cell spectra- a single undosed cell vs neighbouring undosed cells in contact.**

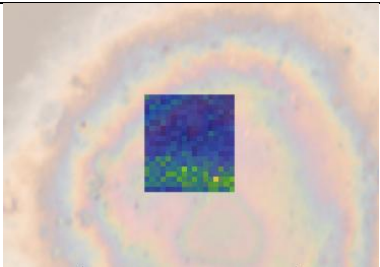
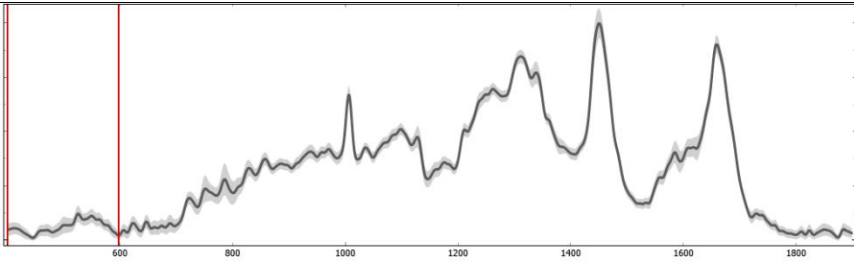
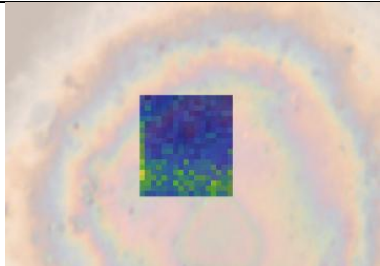
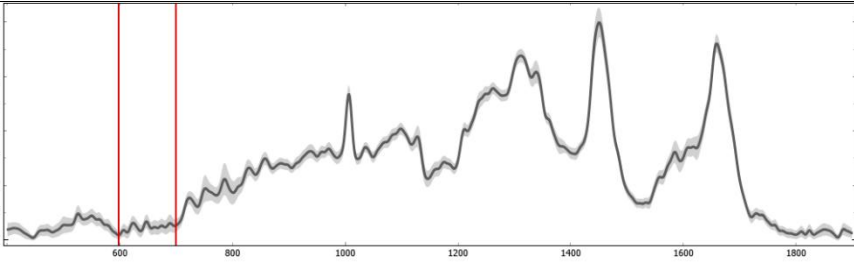
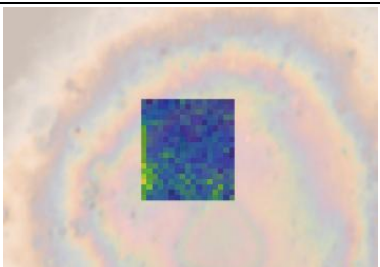
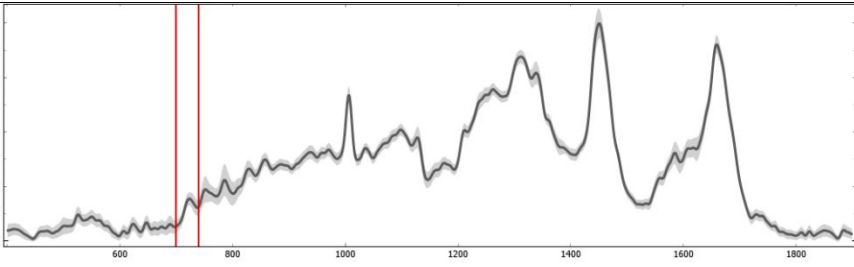
**Average spectra from hyperspectral Raman area maps of cochlear fibrocytes grown on  $\text{CaF}_2$ .**

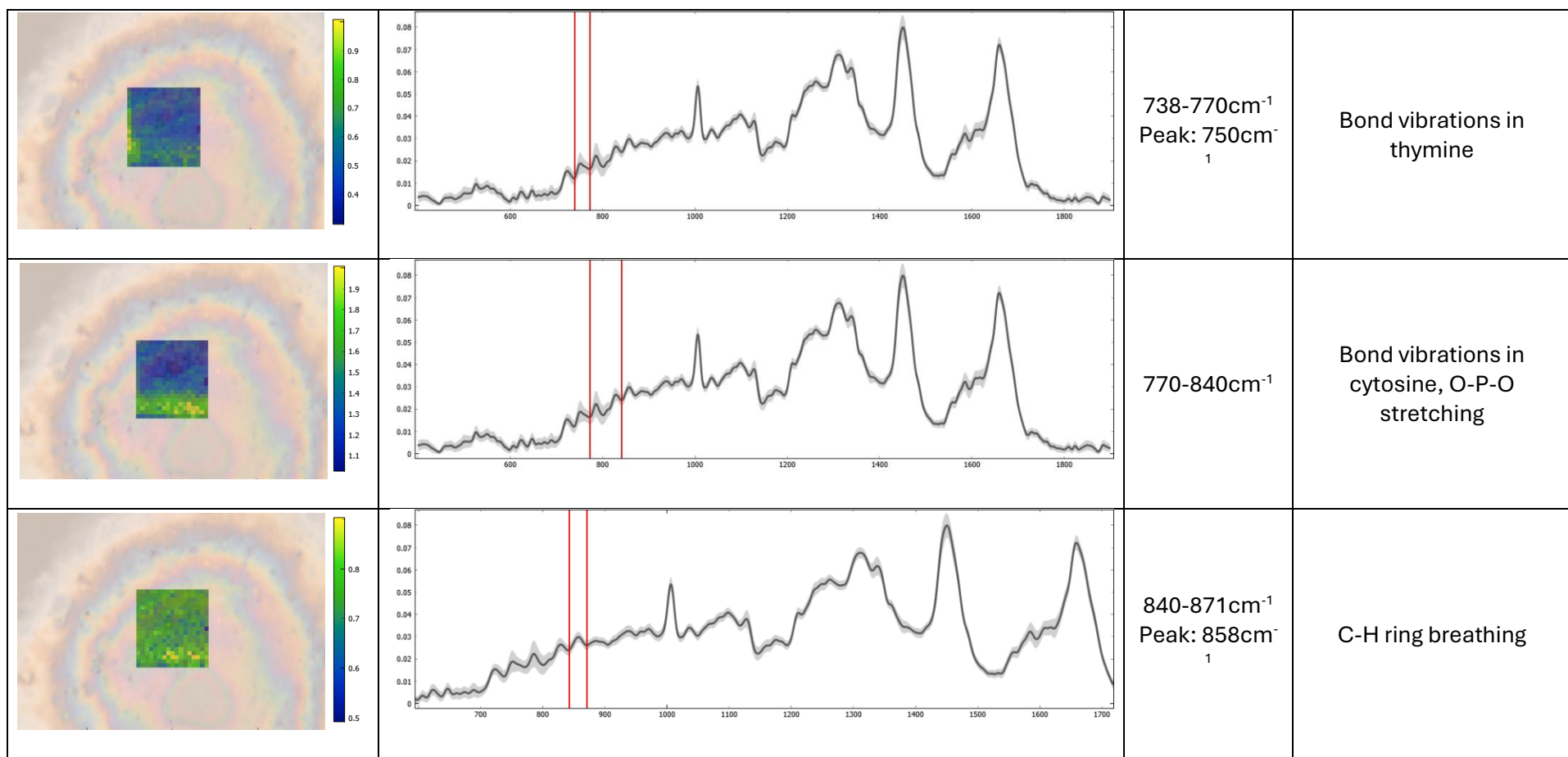
**Approx. 250k cell seeding density. Spectra collected at Diamond Light Source, Oxford, UK.**

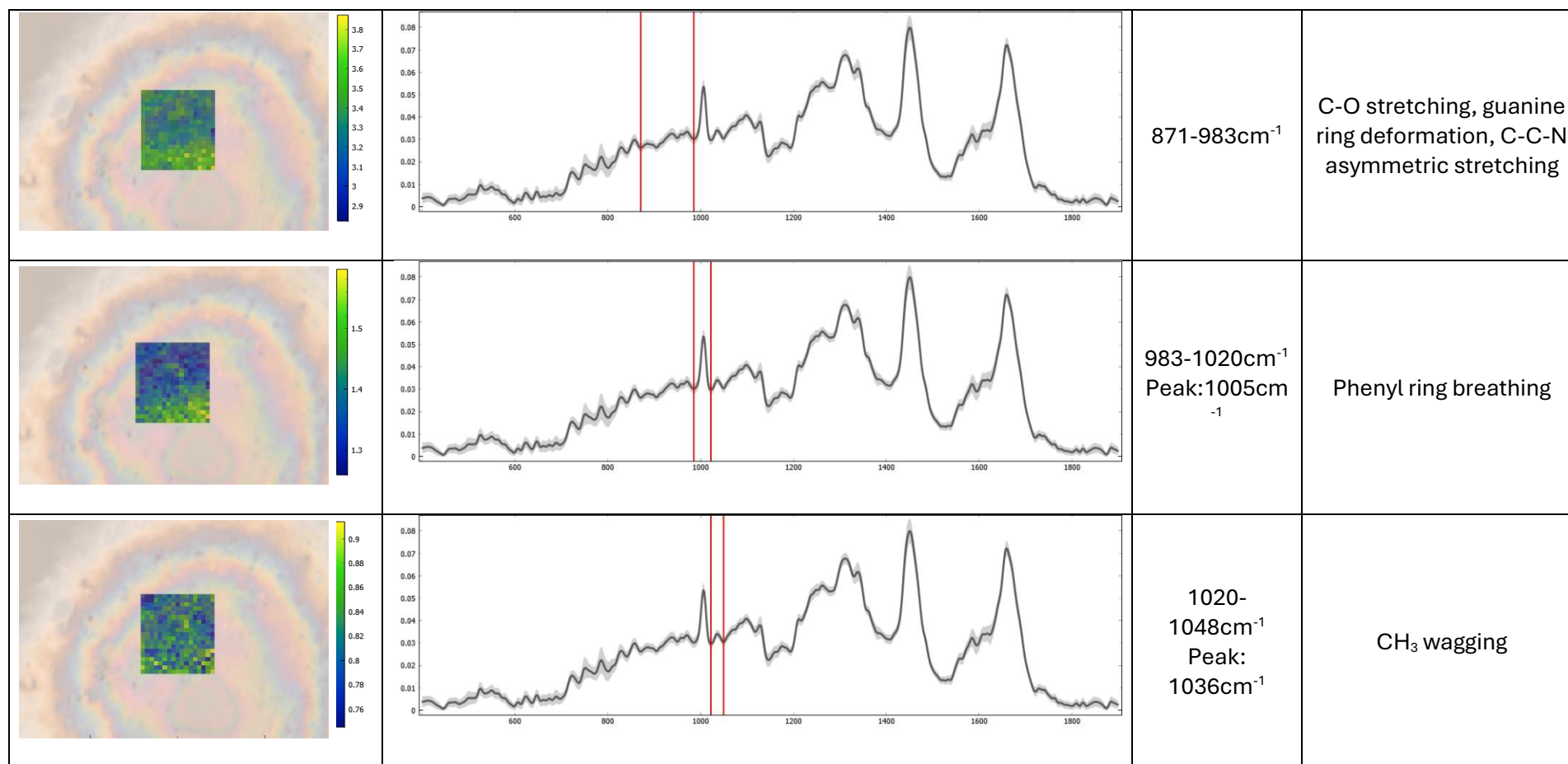
To examine these findings more thoroughly, hyperspectral data is of great value in assigning location to molecular features. Such capacity for localisation, even if spectral intensity appears similar at some wavenumbers, may indicate alterations in cells that have not been visible in previous chapters.

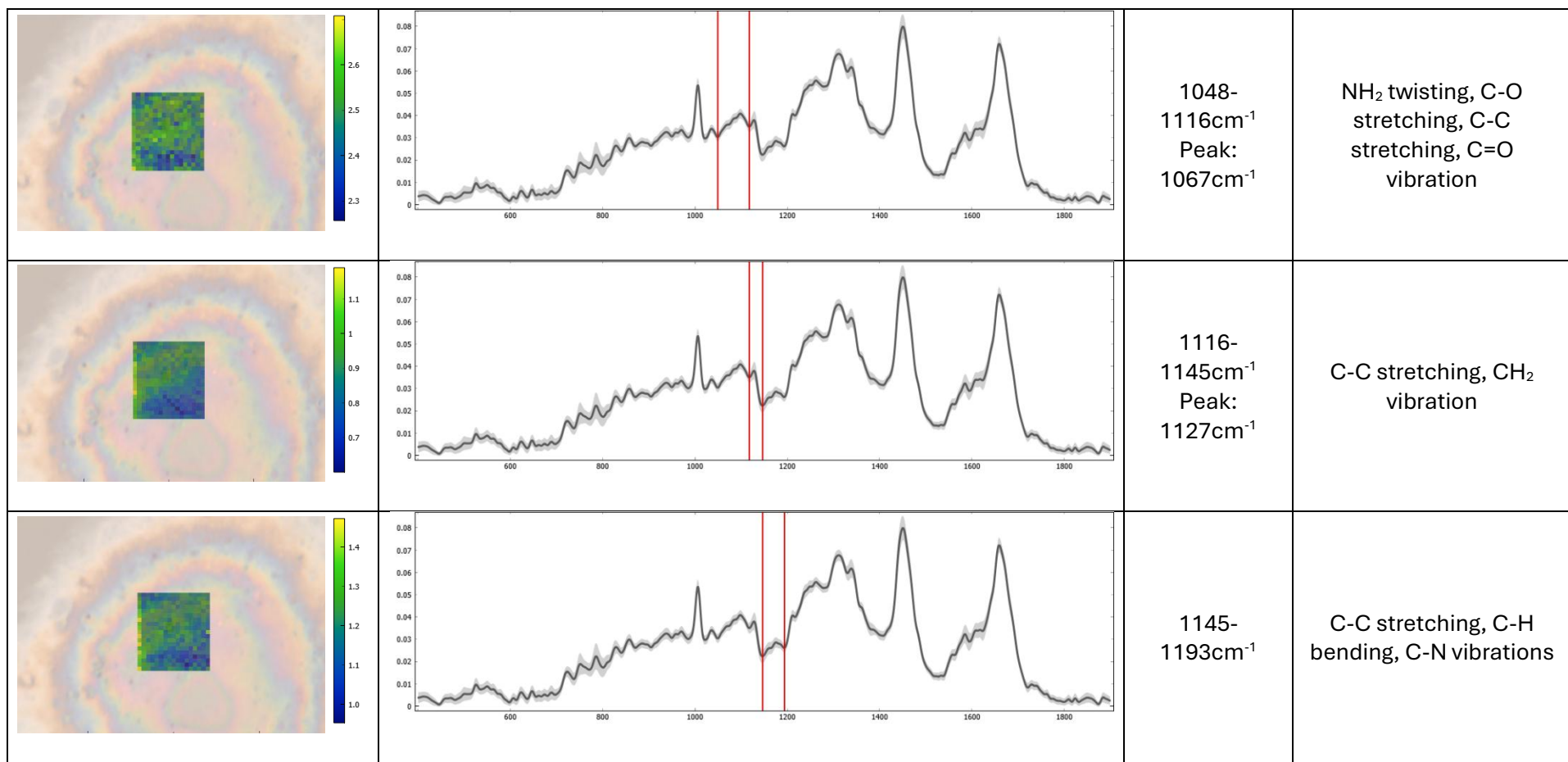
Beginning this analysis, the undosed single cell spectrum is presented in tables 7 and 8 below. Bands of interest are manually identified with accompanying chemical maps indicating molecular localisation. In addition, wavenumber and relevant bond vibrations are noted. The fingerprint region and high wavenumber region are presented separately, with the silent region disregarded.

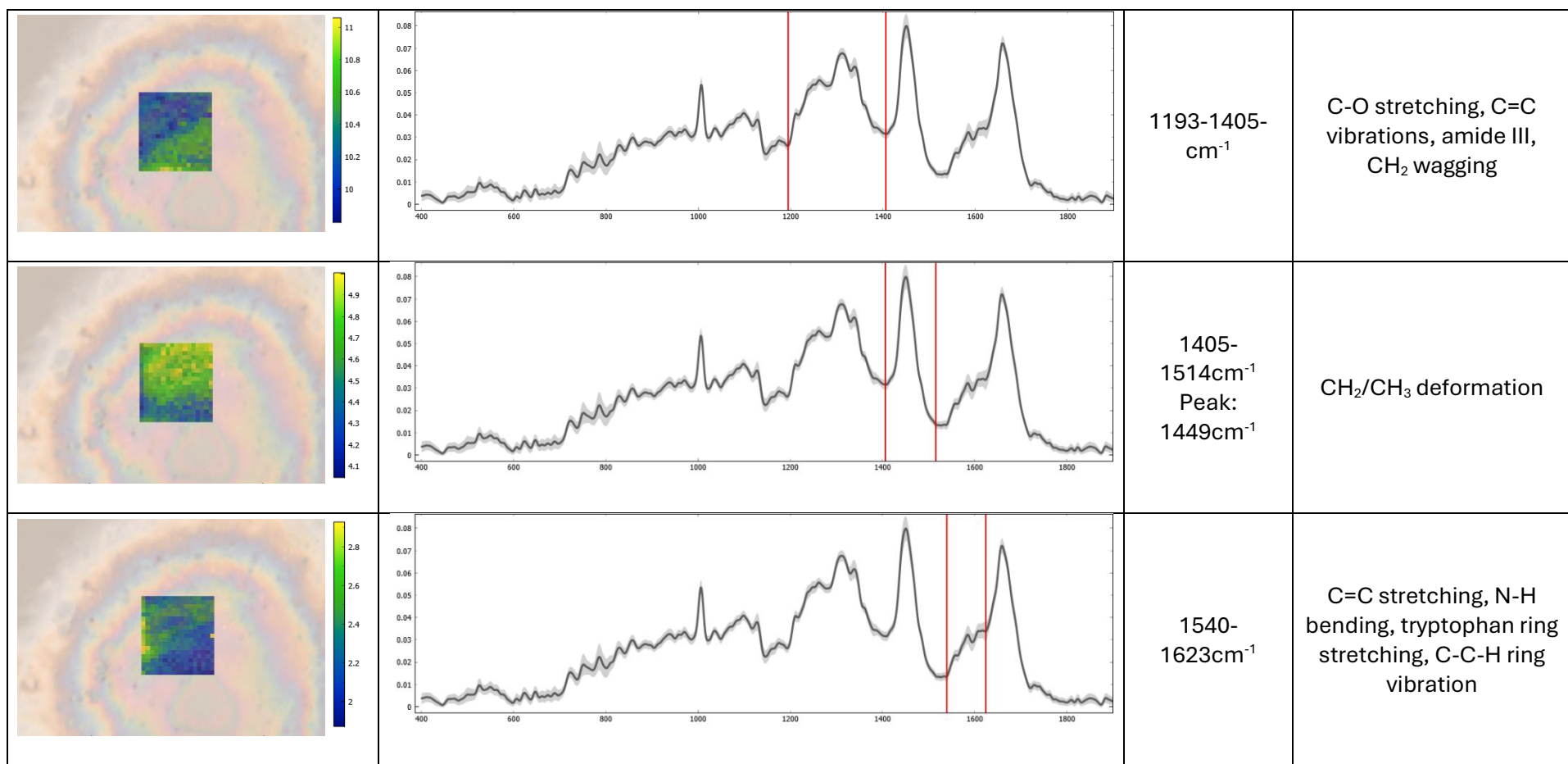
**Table 8: Chemical maps, wavenumbers and localisations of molecules in the fingerprint region of a single undosed cochlear fibrocyte spectrum analysed by hyperspectral Raman spectroscopy.**

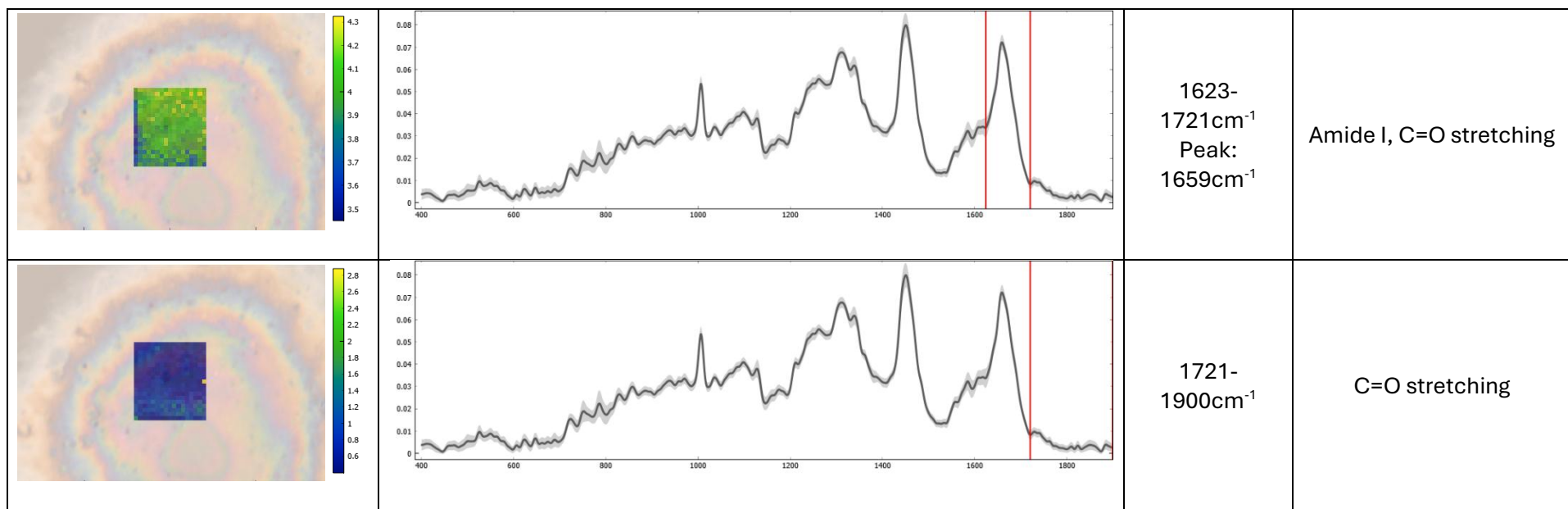
Image	Spectrum	Wavenumber	Relevant Bond Vibrations
		400-597cm <sup>-1</sup>	CH <sub>2</sub> bending, C-C-C deformations
		598-699cm <sup>-1</sup>	CH <sub>2</sub> bending, amide IV, C-S stretching, nucleotide ring breathing
		699-738cm <sup>-1</sup> Peak: 723cm <sup>-1</sup>	Bond vibrations in adenine



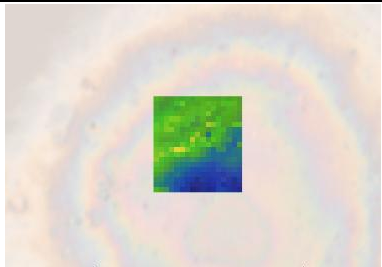
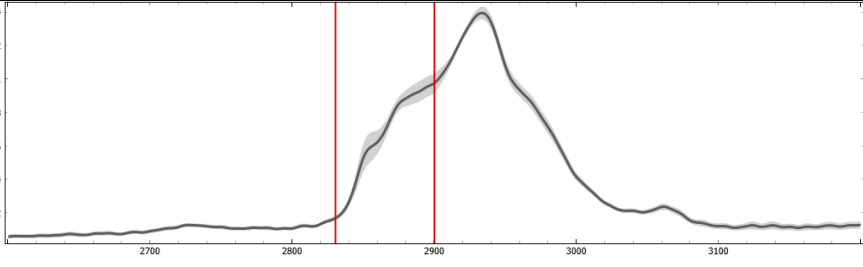
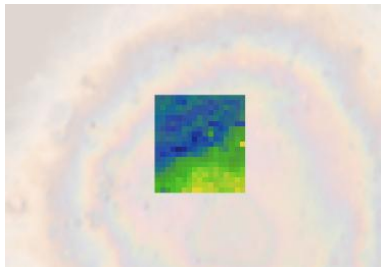
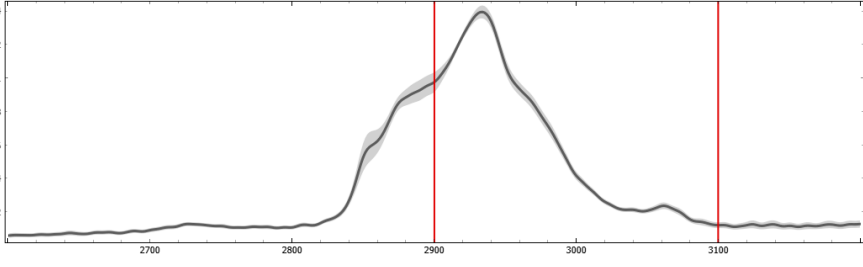








**Table 9: Chemical maps, wavenumbers and localisations of molecules in the high wavenumber region of a single undosed cochlear fibrocyte spectrum analysed by hyperspectral Raman spectroscopy.**

Image	Spectrum	Wavenumber	Strongest localisation
		2829-2900cm <sup>-1</sup>	CH <sub>2</sub> stretching
		2900-3100cm <sup>-1</sup>	CH <sub>3</sub> stretching

It is clear from the presented spectrum alone that the undosed single cell examined above demonstrates a profile comparable to that seen in benchtop Raman spectroscopy experiments. Though, is worthy of note that signal intensity for both the fingerprint and high wavenumber region is greater in the Raman spectrum obtained at Diamond Light Source than in spectra obtained on the benchtop instrument at Keele University. This is assumed to be due to the performance variability across instruments (with different optics and detectors) and the sample preparation methods employed presently (i.e. cell growth on slides). Consequently, due to the application of varied methods and instrumentation, comparison of Raman spectral data across chapters is considered only superficially.

Focusing on the spectral features of the examined undosed cell, localisation clearly varies substantially across the presented spectrum, even within the small cellular area examined. Beginning analysis in the lower end of the fingerprint region, it seems that below  $600\text{cm}^{-1}$  localisation is primarily in the region surrounding the nucleus. This is supported by the k-means analysis shown in Figure 89. Peaks noted in this region arise at  $412\text{cm}^{-1}$ ,  $498\text{cm}^{-1}$ ,  $524\text{cm}^{-1}$ ,  $550\text{cm}^{-1}$ ,  $565\text{cm}^{-1}$  and  $578\text{cm}^{-1}$ . Though peaks in this region are difficult to attribute with great confidence due to relative lack of reference material compared with other regions, literature suggests that this area in biological samples predominantly reflects peaks arising from phospholipids and DNA components <sup>[216]</sup>. This, in the present context, leads to the suggestion that peaks at  $498\text{cm}^{-1}$ ,  $550\text{cm}^{-1}$  represent ring  $\text{CH}_2$  bending of cholesterol, with the latter potentially indicating C-C-C deformations of glycerol. Similarly, the peak noted at  $524\text{cm}^{-1}$  is likely attributable to bond vibrations in saccharides <sup>[217]</sup>. Vibrational modes corresponding to the other peaks identified within this region cannot be identified confidently at this stage.

Moving to the area  $598\text{--}699\text{cm}^{-1}$ , several more peaks demonstrating nuclear localisation are seen. These peaks appear to arise at  $607\text{cm}^{-1}$ ,  $625\text{cm}^{-1}$ ,  $648\text{cm}^{-1}$ ,  $660\text{cm}^{-1}$ ,  $675\text{cm}^{-1}$  and  $689\text{cm}^{-1}$ . Based upon the observation of peaks at  $498\text{cm}^{-1}$  and  $550\text{cm}^{-1}$ , it is assumed that the peak at  $607\text{cm}^{-1}$  may likewise be attributed to cholesterol presence in the region of localisation <sup>[216]</sup>. Cholesterol in the nuclear region is consistent with evidence of cholesterol presence in the nuclear envelope <sup>[218, 219]</sup>. The peak seen at  $625\text{cm}^{-1}$  demonstrates the greatest signal intensity and strongest localisation to its

observed region, and likely corresponds to vibrations in amide IV – a common protein/DNA component. This is consistent with expectations of the nucleus though, it is notable that this band along with others in the surrounding spectral region may additionally be attributed to C-S stretching of methionine – an essential component in the synthesis of DNA, RNA, proteins and phospholipids [220, 221]. The band of similar intensity seen at  $648\text{cm}^{-1}$  may similarly be attributed to amide bond vibration and, in addition to general protein expression, may indicate nuclear presence of ATP [216]. In seeking to assign origins for the other noted peaks in this area, it is known the interval between  $600\text{cm}^{-1}$  and  $800\text{cm}^{-1}$  contains signals attributable to nucleotide ring breathing vibrations [222, 223]. Thus, bands at  $660\text{cm}^{-1}$ ,  $675\text{cm}^{-1}$  and  $689\text{cm}^{-1}$  are taken to indicate nucleotide presence, C-S stretching and amide bond vibrations indicative of the healthy nuclear environment.

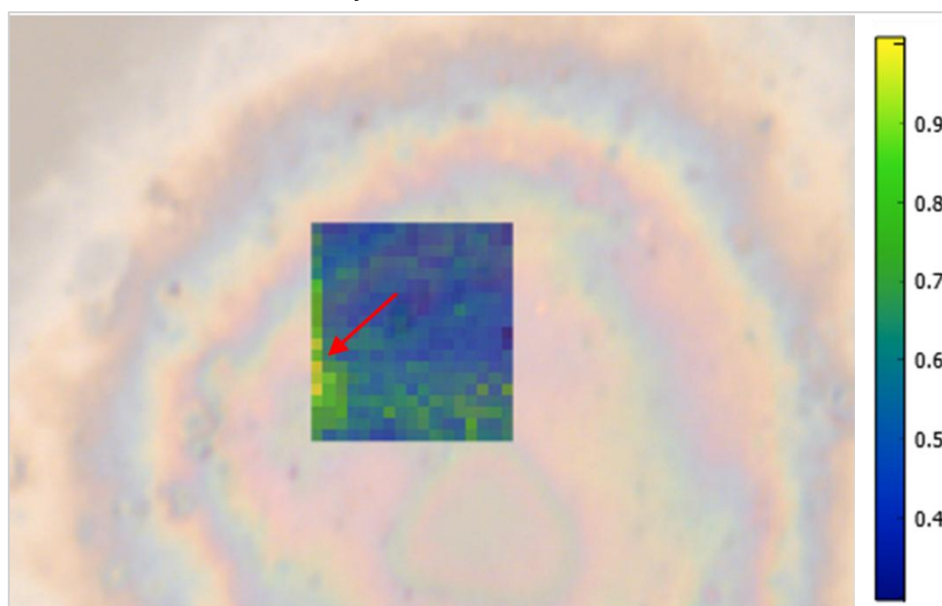


**Figure 88: Raman hyperspectral heat map of 0ng/mL dosed cell at  $750\text{cm}^{-1}$ .**

**Red arrow indicates region of intense signal believed to arise from mitochondrial presence.**

Continuing to the spectral region  $699\text{--}801\text{cm}^{-1}$  the expected nucleotide bands corresponding to ring vibrations in adenine, thymine and cytosine are present at  $723\text{cm}^{-1}$ ,  $750\text{cm}^{-1}$  and  $787\text{cm}^{-1}$  respectively [224–227]. Though, it is interesting to note that spectral signal does not appear to be as strongly localised in/around the cell nucleus as expected for bands  $723\text{cm}^{-1}$  and  $750\text{cm}^{-1}$ , instead appearing most intense in a small section to the left of the sampled area (Fig 88). This may indicate alternate vibrational origins for this band or signify mitochondrial presence. This is further supported by the k-means analysis shown in Figure 88.

Examining the region 801-983cm<sup>-1</sup> noted in previous chapters to predominantly contain bands indicative of amide and lipid bond vibrations, peaks at 830cm<sup>-1</sup>, 858cm<sup>-1</sup>, 938cm<sup>-1</sup>, 957cm<sup>-1</sup> and 971cm<sup>-1</sup> are seen. The band noted at 830cm<sup>-1</sup> is consistent with ring breathing of cytosine and is a logical assignment based upon the strong nuclear localisation noted <sup>[216]</sup>. In contrast, the band at 858cm<sup>-1</sup> which demonstrates similar presence throughout the examined cell area likely arises as a product of out-of-plane C-H ring bending, feasibly from phenylalanine <sup>[228]</sup>. The peak at 938cm<sup>-1</sup> attributable to C-O stretching of glycosidic bonds, in contrast, appears localised primarily in the region surrounding the nucleus though some cytoplasmic distribution is noted <sup>[224-227]</sup>. This peak also demonstrates a weak shoulder at ~911cm<sup>-1</sup>, likely arising from trace amounts of glucose from cell culture media <sup>[216]</sup>. The small peak at 957cm<sup>-1</sup>, though relatively tricky to identify with confidence due to overlap with its neighbour at 971cm<sup>-1</sup>, is deduced in the present context to correspond to ring deformation within guanine and is consistent with the nuclear localisation seen <sup>[216]</sup>. The overlapping band at 971cm<sup>-1</sup> is understood to arise from bending and rocking of hydrogen-containing structures, but a confident assignment is not made presently.

Examining the intense, narrow peak at 1005cm<sup>-1</sup> individually, a confident origin of phenyl ring breathing, likely from tyrosine and phenylalanine, is assigned <sup>[230, 231]</sup>. Such amino acids are vital components of cells and contribute to the formation of fundamental proteins throughout tissue structures. The localisation seen – predominantly nuclear with extension into the cytoplasm – is consistent with well-established cell biology knowledge regarding these molecules' presence in the nuclear envelope and nuclear pore complexes <sup>[232]</sup>.

Continuing to the spectral region 1020-1145cm<sup>-1</sup> molecular localisation shifts from primarily nuclear as seen in lower wavenumbers, to a more cytoplasmic distribution. Spectral peaks in this region arise at 1036cm<sup>-1</sup>, 1067cm<sup>-1</sup>, 1085cm<sup>-1</sup>, 1098cm<sup>-1</sup> and 1127cm<sup>-1</sup>, though whether the peaks at 1067cm<sup>-1</sup> and 1085cm<sup>-1</sup> are true peaks or shoulders of that at 1098cm<sup>-1</sup> is uncertain due to evident overlap. The first band in this section, at 1036cm<sup>-1</sup>, demonstrates a similar intensity across the cellular area sampled and is assigned to CH<sub>3</sub> wagging within cytosine based upon literature <sup>[216]</sup>. However, this is not as consistent with expectations of molecular localisation as hoped and leaves the origins of this band open to debate. Similarly, the band at 1067cm<sup>-1</sup> is assigned to twisting of the NH<sub>2</sub> amino group

present in phenylalanine <sup>[233]</sup>. A logical origin for the band at  $1085\text{cm}^{-1}$  could not be deduced based upon the data available. Once again, though the band at  $1098\text{cm}^{-1}$  is of relatively high signal intensity and demonstrates clear cytoplasmic localisation, a confident vibrational mode assignment cannot be made due to strong signal overlap in this spectral region. Nonetheless, provisional suggestions of lipid or amino acid-based bond vibrations are suggested based on literature wherein researchers experienced similar issues with peak overlap <sup>[216]</sup>. Fortunately, the band at  $1127\text{cm}^{-1}$  is not subject to such overlap and is assigned based on the cytoplasmic localisation seen to various bond vibrations in lipids and glucose (e.g. C-C stretching) <sup>[216]</sup>.

Focusing next on the small spectral region  $1145\text{-}1193\text{cm}^{-1}$ , a dominant peak at  $1176\text{cm}^{-1}$  is clearly visible with a weak shoulder at  $1185\text{cm}^{-1}$ , and an overlapping peak at  $1159\text{cm}^{-1}$ . It is unclear based on the data available whether the peak at  $1159\text{cm}^{-1}$  is an overlapping band or a stronger shoulder of the peak at  $1176\text{cm}^{-1}$ . This peak is assigned to C-C stretching activity in the present research and may indicate the presence of taurine in cochlear fibrocytes – a conceivable interpretation given the endogenous presence of taurine in numerous mammalian tissues <sup>[216, 234]</sup>. The identity of the band at  $1176\text{cm}^{-1}$  is suggested with equal uncertainty due to the overlap seen, with origin assumed to be C-H bending <sup>[216]</sup>.

Looking to the larger spectral region  $1193\text{-}1405\text{cm}^{-1}$  localisation of most signals once again returns to the nuclear region and its surroundings. The peak at  $1211\text{cm}^{-1}$ , though overlap with the neighbouring band is seen, is assigned presently to C-O stretching likely of tyrosine or phenylalanine origin <sup>[216]</sup>. Though a peak location is provisionally noted at  $1263\text{cm}^{-1}$ , the area  $1212\text{-}1280\text{cm}^{-1}$  appears to in fact contain three considerably overlapped peaks of similar intensity. These peaks, localised primarily in the nuclear region, may originate from C-O stretching, C=C vibrations or amide III alterations, with precise assignation unfeasible from the data available <sup>[235, 236]</sup>. The broad band at  $1312\text{cm}^{-1}$ , like its neighbours, is believed to originate from C-O stretching and is overlapped by a band at  $1339\text{cm}^{-1}$  similarly characteristic of C-O stretching potentially indicative of glutathione <sup>[216]</sup>. The remaining bands in this spectral region, identified at  $1362\text{cm}^{-1}$  and  $1387\text{cm}^{-1}$  are not confidently identified in the present research.

The high-intensity band at  $1449\text{cm}^{-1}$  is common to cellular samples and is confidently attributed to  $\text{CH}_2$  bending of lipids. Interestingly, examining the associated heat map it appears that there are small regions of high intensity signal distributed throughout the cytoplasm. These regions likely correspond to cell organelles, the lipid compositions of which reflect their distinct functions <sup>[237]</sup>.

Following this band, in the region  $1514\text{-}1623\text{cm}^{-1}$  signals are of substantially weaker intensity and a large amount of overlap between peaks is noted. The two low intensity, overlapping peaks between  $1514\text{cm}^{-1}$  and  $1540\text{cm}^{-1}$  are considered to fall in the 'amide II zone' and are believed to mainly be contributed by N-H bending <sup>[216]</sup>. Likewise, assignment of ring stretching in tryptophan is given to the band seen at  $1558\text{cm}^{-1}$  <sup>[216]</sup>. The peak at  $1585\text{cm}^{-1}$  demonstrates a weak shoulder and primarily cytoplasmic localisation consistent with its suggested origin of aromatic ring C-C-H vibration <sup>[238]</sup>. The precise aromatic ring in question is unknown based on the present data. Finally, the small overlapping peaks noted in the region  $1593\text{-}1623\text{cm}^{-1}$  are attributed to tyrosine and phenylalanine-related vibrational modes <sup>[216, 238]</sup>. Similarly to the nucleic acid bands identified previously, intense signal can be seen in this region on the left of the presented heat map, possibly indicating mitochondrial (or other organelle) presence.

Observing alone the clear high intensity band at  $1659\text{cm}^{-1}$  localisation is seen throughout the cell area samples, with small regions of high intensity similar to those seen for the lipid bending band at  $1149\text{cm}^{-1}$ . Though sources suggest contribution from lipids in this region, this band is largely attributable to the amide I mode of C=O stretching presently <sup>[216]</sup>, with both of these origins logically yielding the cellular distribution seen in chemical maps.

Finally, in examining the undosed cell fingerprint region bands are identified in the area  $1721\text{-}1900\text{cm}^{-1}$  demonstrating localisation throughout the cell region samples, albeit of relatively low intensity. Though little band distinction can be made in the spectral region  $1721\text{-}1757\text{cm}^{-1}$ , there appear to be two overlapping peaks within this area. These are believed to originate from C=O bond stretching in the phospholipids phosphatidylserine and phosphatidylinositol respectively, both of which are contributors to the regulation of subcellular processes in eukaryotes <sup>[216, 239, 240]</sup>. Likewise, the clearer band at  $1763\text{cm}^{-1}$  likely originates from similar C=O stretching in phosphatidylethanolamine, understood as the second most abundant phospholipid in eukaryotic

cells <sup>[216, 241]</sup>. Once again, the small overlapping peaks in the region 1770-1801cm<sup>-1</sup>, though origins cannot be stated confidently from data available, likely originate from phospholipids <sup>[216]</sup>. Further peaks in this region (i.e. 1800-1900cm<sup>-1</sup>) are not identified presently due relative lack of literature regarding these wavenumbers. Nonetheless, above ~1720cm<sup>-1</sup> bands in the fingerprint region of samples are presumed to correspond to lipids and their derivatives.

K-means analysis (Fig. 89), as noted above, demonstrates distinction between nucleic, cytoplasmic and potential mitochondrial cellular regions. The region associated with the nucleus demonstrates peaks in signal intensity at wavenumbers indicating nucleic acids and polysaccharides. The cytoplasmic region, meanwhile, demonstrates predominantly lipid and protein signal, Finally, the region believed to be mitochondrial shows signal intensity for lipids, amino acids, and nucleic acids.

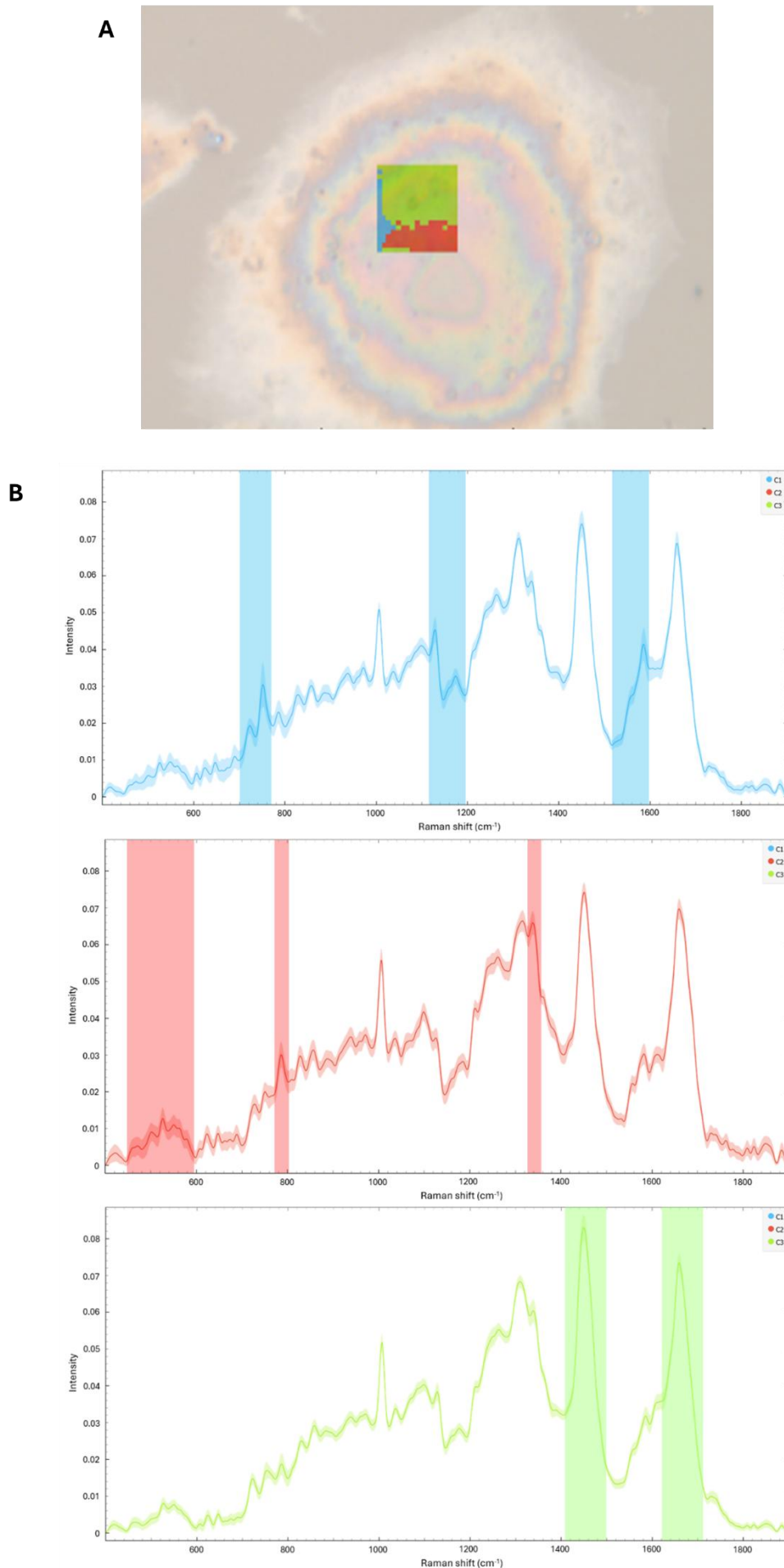


Figure 89: K-means clustering of hyperspectral Raman data – 0ng/mL dosed single cell.

A) Chemical map. B) Spectra.

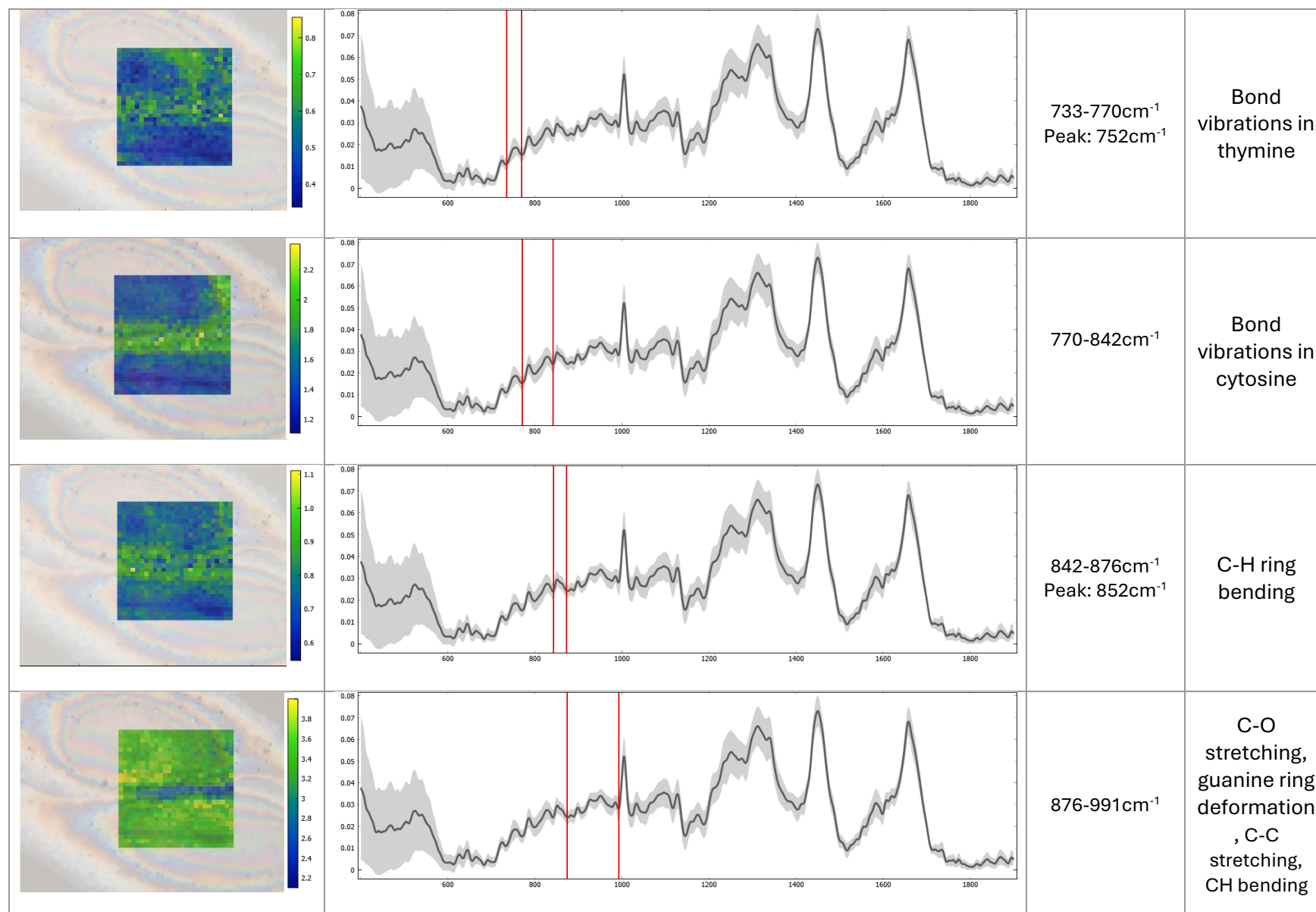
Briefly reviewing the high wavenumber region of the cell sampled, it is clear that the fingerprint region is far more data rich in comparison. This is as expected for biological samples. Nonetheless, bands may still be identified in this region, though several appear to overlap with the larger peak at  $2933\text{cm}^{-1}$ . Generally, the shoulder-like bands overlapping with the larger peak in the region  $2829\text{--}2900\text{cm}^{-1}$  are attributed to  $\text{CH}_2$  stretching in fatty acids, lipids or proteins, with the former arguably most likely based on the cytoplasmic distribution seen <sup>[242]</sup>. In contrast, the high intensity band peaking at  $2933\text{cm}^{-1}$  is assigned to  $\text{CH}_3$  stretching of proteins and is reflected in the nuclear localisation shown in the accompanying heat map <sup>[242]</sup>. The lower intensity band at  $3061\text{cm}^{-1}$  is not identified presently but shows similar nuclear localisation to the previous band identified. No K-means analysis was conducted on high wavenumber region data due to relative lack of localisation in this spectral region.

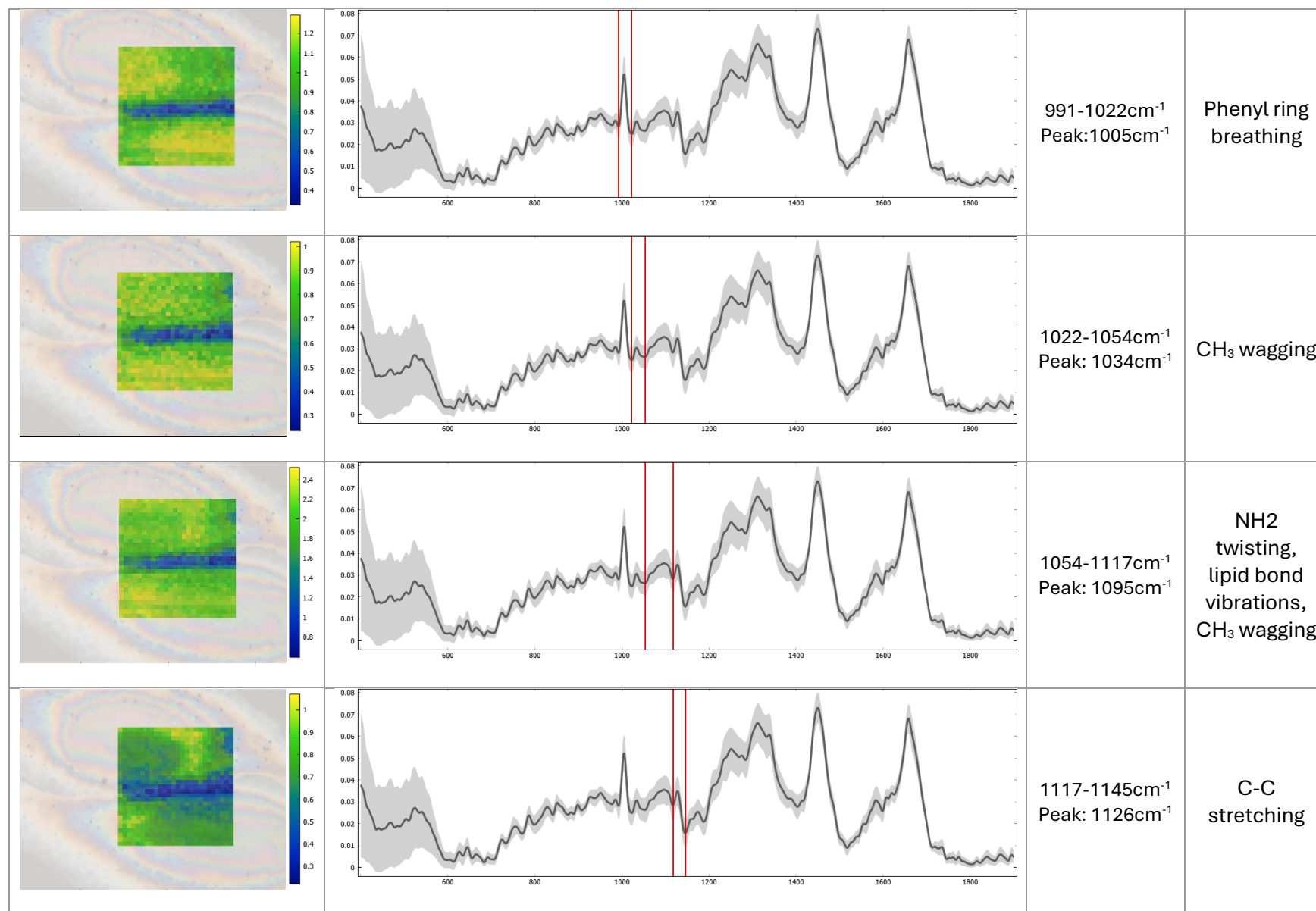
In general, Raman spectral results for the undosed cell presented are as expected. The overall spectrum resembles that of healthy cells in previous chapters, with variations attributable to the performance variation across each instrument employed in this stage of research. Molecular localisation visualised using chemical maps appears consistent with identified peak origins and lends insight into the subcellular environment of a ‘normal’ cochlear fibrocyte *in vitro*.

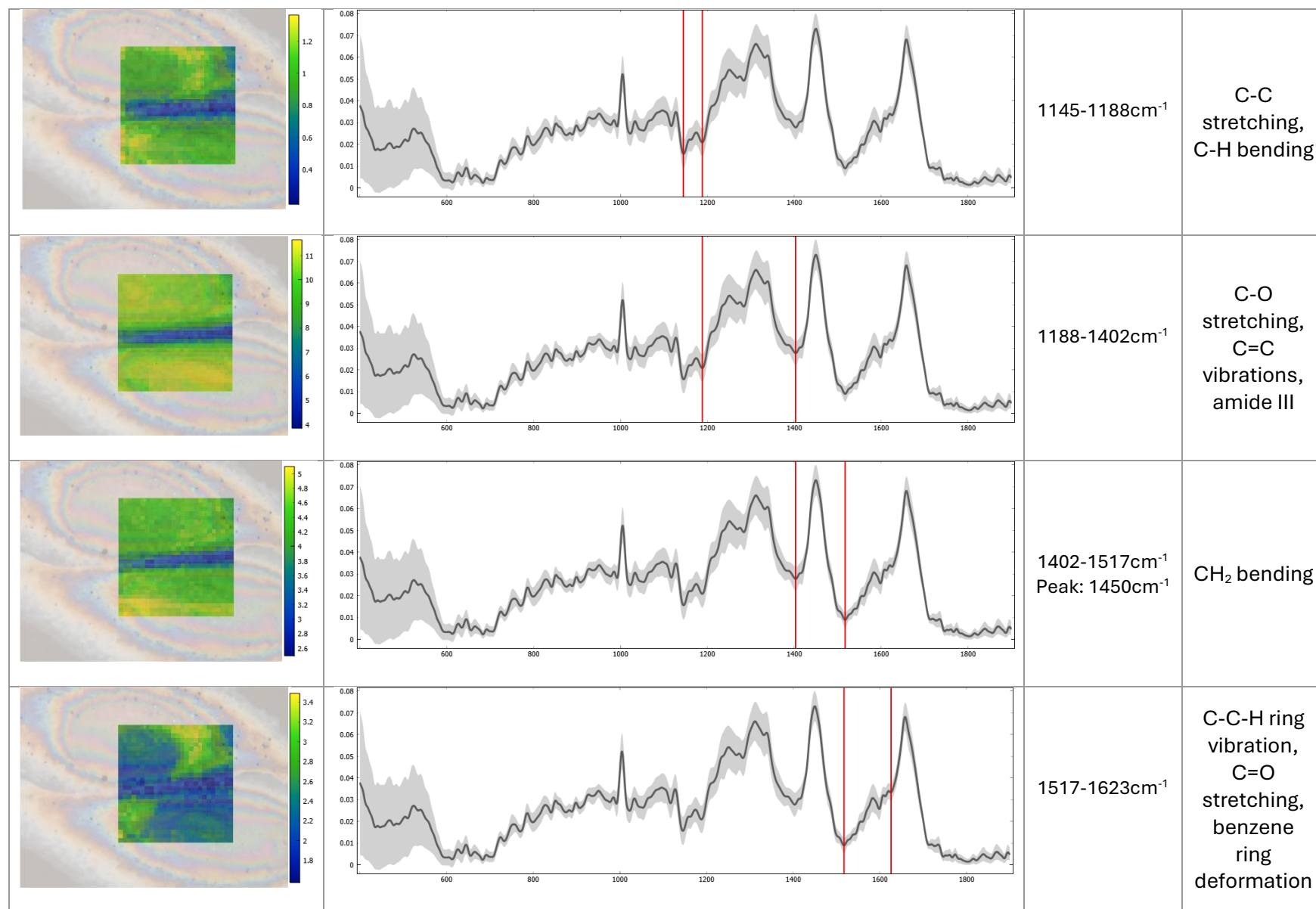
Moving to the analysis of intersecting undosed cells, tables 10 and 11 below display the spectrum and associated chemical maps for a pair of undosed cells in contact. Though, as mentioned previously, it is clear from spectral comparison alone that single cells and cells in contact with neighbours show variation, exploring feature localisation within these neighbouring cells in more depth is essential to understanding.

**Table 10: Chemical maps, wavenumbers and localisations of molecules in the fingerprint region of a pair of undosed cochlear fibrocytes' spectrum analysed by hyperspectral Raman spectroscopy.**

Image	Spectrum	Wavenumber	Strongest localisation
		400-594cm <sup>-1</sup>	CH <sub>2</sub> bending, C-C-C deformations
		594-705cm <sup>-1</sup>	CH <sub>2</sub> bending, amide IV, C-S stretching, nucleotide ring breathing
		706-733cm <sup>-1</sup> Peak: 723cm <sup>-1</sup>	Bond vibrations in adenine







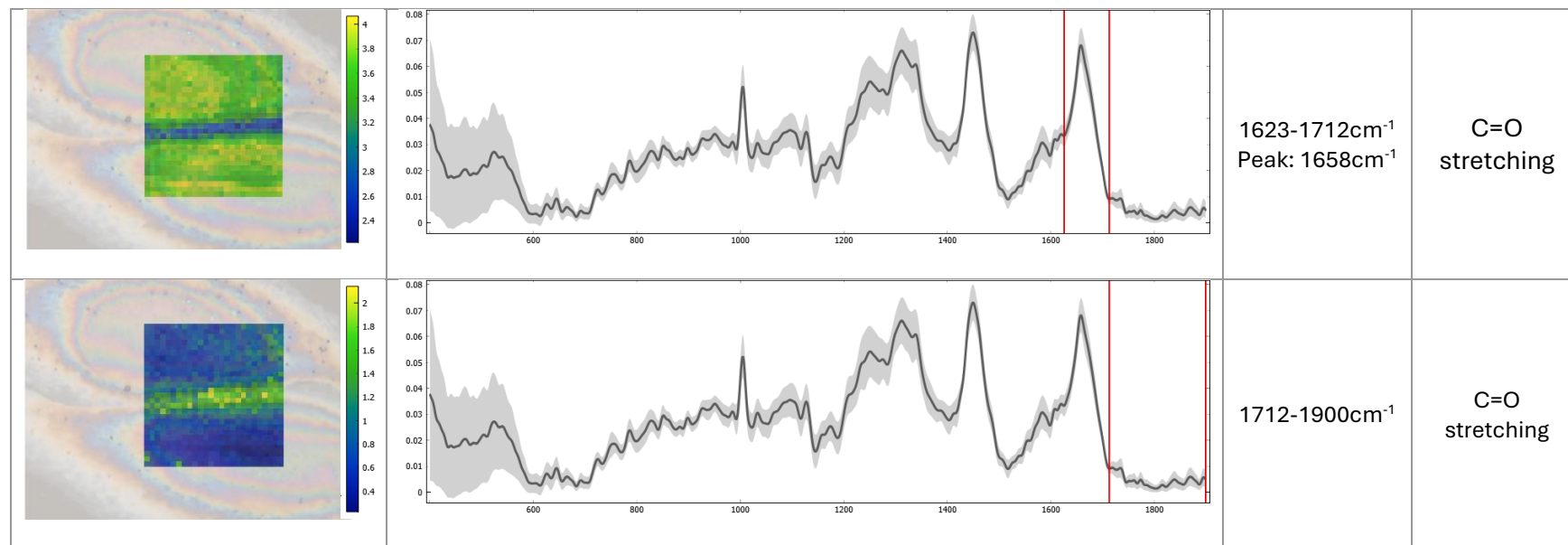
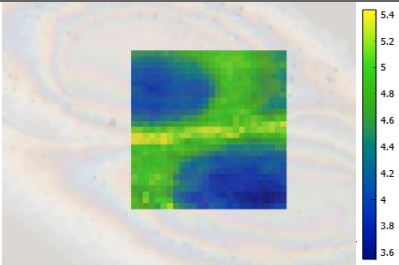
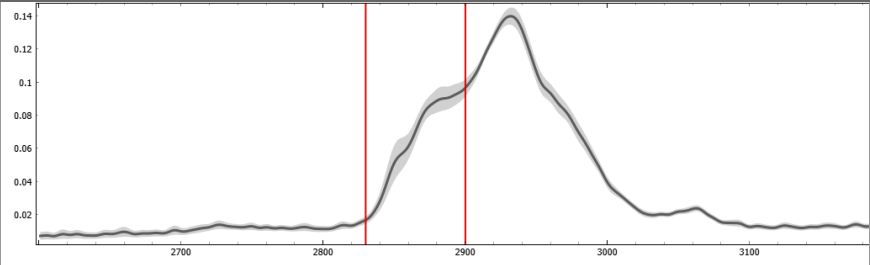
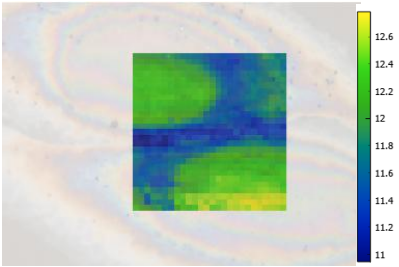
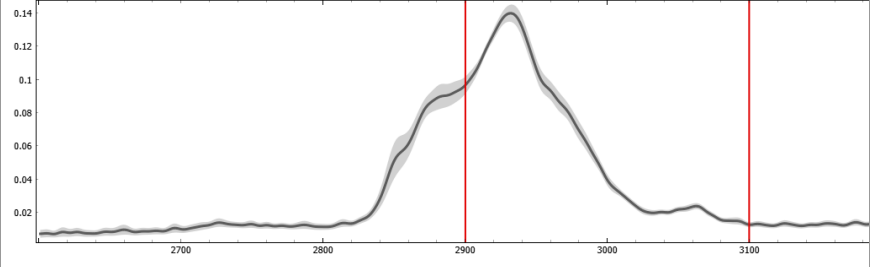


Table 11: Chemical maps, wavenumbers and localisations of molecules in the high wavenumber region of a pair of undosed cochlear fibrocytes' spectrum analysed by hyperspectral Raman spectroscopy.

Image	Spectrum	Wavenumber	Strongest localisation
		2829-2900cm <sup>-1</sup>	CH <sub>2</sub> stretching
		2900-3100cm <sup>-1</sup>	CH <sub>3</sub> stretching

Beginning in the lower end of the fingerprint region, it is evident from the chemical maps presented in table 10 that below  $\sim 700\text{cm}^{-1}$  localisation is primarily focused in the cell membrane region where the neighbouring cells intersect. This contrasts with the single undosed cell observed, where localisation appears focused in the area surrounding the nucleus, albeit at a lower intensity. Whether this feature is present in the membrane of single cells and throughout the membranes of the neighbouring cells is unclear from the data available. Nonetheless, variations are seen in this region in peak intensity, band location, and molecular localisation. This is supported by the k-means analysis shown in Figure 90.

Below  $600\text{cm}^{-1}$ , where the single control cell showed a broad, singular peak in the region  $440\text{-}444\text{cm}^{-1}$ , cells in contact demonstrate a sloping shoulder-like signal below  $435\text{cm}^{-1}$  and a small peak at  $440\text{cm}^{-1}$ , both of greater signal intensity than noted in this region for the single cell. The origins of these bands are unknown. Further variation is seen in the  $444\text{-}480\text{cm}^{-1}$  region, where the single control cell showed evidence of two overlapping low intensity peaks. Intersecting cells, in contrast, appear to demonstrate a single, higher intensity peak at  $469\text{cm}^{-1}$  in this spectral region. Again, the origins of this band cannot be confidently suggested from the data. Where more identifiable peaks arise in the single cell spectrum (at  $498\text{cm}^{-1}$ ,  $524\text{cm}^{-1}$ ,  $550\text{cm}^{-1}$ ) variations are further seen in intersecting cells, with peaks arising at  $485\text{cm}^{-1}$  and  $504\text{cm}^{-1}$  rather than  $498\text{cm}^{-1}$ , a shift of  $\sim 1\text{cm}^{-1}$  in the peak noted previously at  $524\text{cm}^{-1}$ , and indication of a shift of  $10\text{cm}^{-1}$  in the peak previously identified at  $550\text{cm}^{-1}$ . The newly noted peaks appearing at  $485\text{cm}^{-1}$  and glycerol and glycine respectively<sup>[217]</sup>. The unique appearance of these bands in intersecting cells, along with the membrane/intersection localisation seen, suggests involvement of these molecules in intercellular transport *in vitro*. As in the single cell, peaks noted at  $523\text{cm}^{-1}$  and  $540\text{cm}^{-1}$  are attributed to bond vibrations in saccharides and cholesterol respectively. Though this region varies substantially from that seen in the single cell sample, consideration should be given to the level of variation around the average spectrum in intersecting cells for this region. With this in mind, conclusions regarding differences between cells alone and cells in contact for this spectral region cannot be made presently.

Moving to spectral region  $595\text{-}690\text{cm}^{-1}$ , localisation is once again focused in the cell membrane/intersection region in neighbouring cells, in contrast to the single cell which demonstrated a nuclear focus. Unlike the previous region identified, bands in this spectral region show similar signal intensity in both samples suggesting distribution of identified molecules in both the nuclear and membrane regions. Generally, bands in this region resemble those seen in the single cell, with peaks identified at  $604\text{cm}^{-1}$ ,  $625\text{cm}^{-1}$ ,  $644\text{cm}^{-1}$ ,  $665\text{cm}^{-1}$  and  $690\text{cm}^{-1}$ . The band at  $604\text{cm}^{-1}$  is taken to represent a shift of  $\sim 3\text{cm}^{-1}$  in the band previously noted at  $607\text{cm}^{-1}$  and is assumed to be attributable to bond vibrations in cholesterol, commonly noted in cell membranes as well as the nucleus <sup>[216]</sup>. The band at  $625\text{cm}^{-1}$  appears as in the single cell and is once again attributed to amide IV bond vibrations, though methionine contribution should once again be considered due to its contribution to phospholipid formation. Similarly, the band seen at  $644\text{cm}^{-1}$  is taken to represent a  $\sim 4\text{cm}^{-1}$  shift in the amide band noted in the single cell at  $648\text{cm}^{-1}$ . Arguably the greatest variation in this region is seen in that peaks previously noted at  $660\text{cm}^{-1}$  and  $675\text{cm}^{-1}$  are not present in neighbouring cells, with the spectrum shown instead demonstrating a band peaking at  $665\text{cm}^{-1}$  across these wavenumbers. This alteration is likely a result of cell membranes lacking strong nucleotide expression, with signal attributable to amino acids dominating the spectrum in this cellular area <sup>[217]</sup>. Similarly, the band at  $690\text{cm}^{-1}$  is taken to indicate a shift in the band previously noted at  $689\text{cm}^{-1}$ , likely indicative of protein presence consistent with cell membranes. Again, this is supported by the k-means analysis shown in Figure 90 wherein many bands below  $1000\text{cm}^{-1}$  are prominent in the membrane/intersection region.

Continuing to the spectral region  $706\text{-}800\text{cm}^{-1}$ , the nucleotide bands identified in the single cell occur to a similar signal intensity, with the  $725\text{cm}^{-1}$  band appearing the same, and a shift of  $2\text{cm}^{-1}$  and  $3\text{cm}^{-1}$  in the thymine and cytosine bands respectively. The primary variation in this spectral region comes from the localisation seen within cells where, in contrast to the single cell, identified molecules appear to show their strongest localisation in the cell membrane and at points throughout the cytoplasm, likely indicative of small organelles.

Examining next the region  $800\text{-}991\text{cm}^{-1}$ , bands appear at similar wavenumbers and intensities as in the single cell, but once again localisation is varied. Based upon its shape and

intensity, the band at  $824\text{cm}^{-1}$  appears to represent a  $\sim 6\text{cm}^{-1}$  shift in the cytosine ring breathing band previously identified at  $830\text{cm}^{-1}$ . However, this is not consistent with the nuclear localisation expected for this molecule, suggesting that an alternate origin such as the essential amino acid histidine may be responsible <sup>[217]</sup>. In contrast, the band noted at  $852\text{cm}^{-1}$  is more confidently accepted as a  $\sim 6\text{cm}^{-1}$  shift of the C-H ring bending signal previously noted at  $858\text{cm}^{-1}$ . This confidence is a result of the similar cytoplasmic distribution of signal, with the addition of presence in cell membranes consistent with phenylalanine. Notably, in the spectral region  $871\text{-}905\text{cm}^{-1}$  two signal peaks can now be resolved where not previously feasible. These peaks are noted at  $883\text{cm}^{-1}$  and  $898\text{cm}^{-1}$  and are believed to arise from C-C stretching and CH bending respectively <sup>[216]</sup>.

In what, at first glance, appears to be the most substantial peak shift noted thus far, the band seen at  $938\text{cm}^{-1}$  in the observed single cell seems to shift by  $\sim 11\text{cm}^{-1}$  to  $927\text{cm}^{-1}$ . Viewing the intensity and overlap of neighbouring bands, it is arguably just as likely that the  $938\text{cm}^{-1}$  band is absent entirely, with the adjoining peaks seen at  $927\text{cm}^{-1}$  and  $950\text{cm}^{-1}$  representing an even more substantial shift of  $20\text{-}30\text{cm}^{-1}$  in those of similar formation seen previously at  $957\text{cm}^{-1}$  and  $971\text{cm}^{-1}$ . However, considering the similar peak intensities and contrasting localisations seen across these samples, neither of these options seems probable. Instead, alternate origins for the noted peaks are presented. Peaks are identified in the neighbouring cells at  $927\text{cm}^{-1}$ ,  $950\text{cm}^{-1}$  and  $984\text{cm}^{-1}$  and are taken to indicate moderate cytosolic presence of coenzyme A ( $927\text{cm}^{-1}$  and  $950\text{cm}^{-1}$ ) and taurine precursor hypotaurine ( $984\text{cm}^{-1}$ ) respectively <sup>[216, 217]</sup>. The former is consistent with expectations for eukaryotic cells conducting successful biosynthesis of essential molecules, while the latter supports the evidence of taurine presence noted in the single cell. Why such a substantial variation is possible between single and neighbouring cells is at present unclear.

As in the single cell, the band at  $1005\text{cm}^{-1}$  is confidently identified to arise due to phenyl ring breathing, likely from tyrosine and phenylalanine. Strong nuclear localisation with additional presence in cytoplasm is consistent with established knowledge of these molecules and their biological roles. This is further evidenced by k-means analysis shown in Figure 90.

Continuing to the spectral region  $1022\text{-}1145\text{cm}^{-1}$ , as in the single cell, molecular localisation appears predominantly cytoplasmic. Spectral peaks previously identified at  $1036\text{cm}^{-1}$ ,  $1067\text{cm}^{-1}$ ,  $1085\text{cm}^{-1}$ ,  $1098\text{cm}^{-1}$  and  $1127\text{cm}^{-1}$ , appear present but shifted, with the peaks at  $1067\text{cm}^{-1}$  and  $1085\text{cm}^{-1}$  noted as possible shoulders of  $1098\text{cm}^{-1}$  appearing even less distinct. As such, the identified peaks at  $1034\text{cm}^{-1}$ ,  $1095\text{cm}^{-1}$  and  $1126\text{cm}^{-1}$  are taken as shifts of  $\sim 2\text{cm}^{-1}$ ,  $\sim 3\text{cm}^{-1}$  and  $1\text{cm}^{-1}$  of  $\text{CH}_3$  wagging, bond vibrations in phenylalanine and lipid bond vibrations (e.g. C-C stretching) respectively.

Similarly, the small spectral region  $1145\text{-}1188\text{cm}^{-1}$  demonstrates a similar overlapping peak pair to that seen in the single cell spectrum, though at a marginally lower signal intensity. Peaks noted at  $1158\text{cm}^{-1}$  and  $1174\text{cm}^{-1}$  are taken to represent shifts of  $1\text{cm}^{-1}$  and  $2\text{cm}^{-1}$  in bands associated with C-C stretching and C-H bending.

Looking to the larger spectral region  $1188\text{-}1402\text{cm}^{-1}$ , localisation of most signals demonstrates strength in the nuclear regions of cells and their surroundings, similarly to the single cell observed. The C-O stretch band demonstrates a  $\sim 1\text{cm}^{-1}$  shift to  $1210\text{cm}^{-1}$  with nuclear localisation noted once again. The region previously believed to contain three peaks ( $1212\text{-}1280\text{cm}^{-1}$ ) instead appears to contain two distinct peaks and a shoulder for this sample. These peaks are identified at  $1250\text{cm}^{-1}$  and  $1276\text{cm}^{-1}$  and, though firm assignment cannot be made, likely correspond to bond vibrations in lipids and proteins. As in the single cell, the band at  $1313\text{cm}^{-1}$  and its overlapping neighbour at  $1338\text{cm}^{-1}$  (a  $\sim 1\text{cm}^{-1}$  shift from the single cell band in both cases) show strong distribution throughout the cell areas sampled and are believed to correspond to C-O stretching. In contrast to the single cell, of the peaks previously noted at  $1362\text{cm}^{-1}$  and  $1387\text{cm}^{-1}$  only one is present – a  $\sim 2\text{cm}^{-1}$  shift of the latter seen at  $1389\text{cm}^{-1}$  likely originating from bond vibrations in an amino acid (e.g. proline) [217].

As noted in the single cell, the high-intensity band at  $1450\text{cm}^{-1}$  is common to cellular samples and is confidently attributed to  $\text{CH}_2$  bending of lipids. In the neighbouring cells observed, small shoulders are also noted at  $1412\text{cm}^{-1}$  and  $1507\text{cm}^{-1}$  and are attributed to bond vibrations in dATP [216].

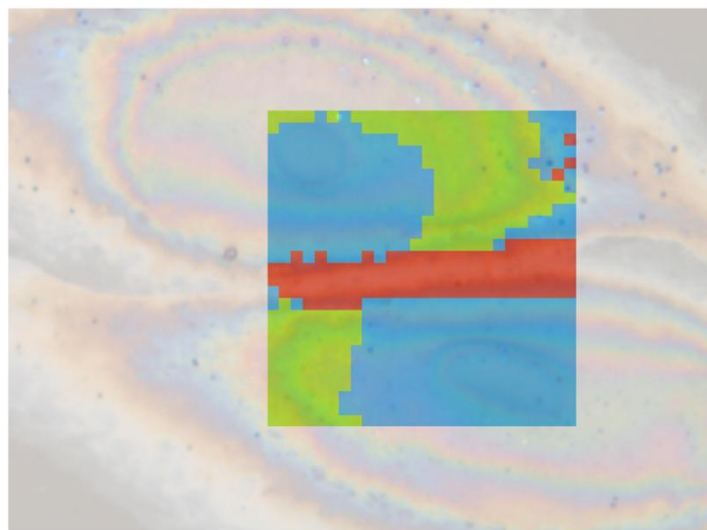
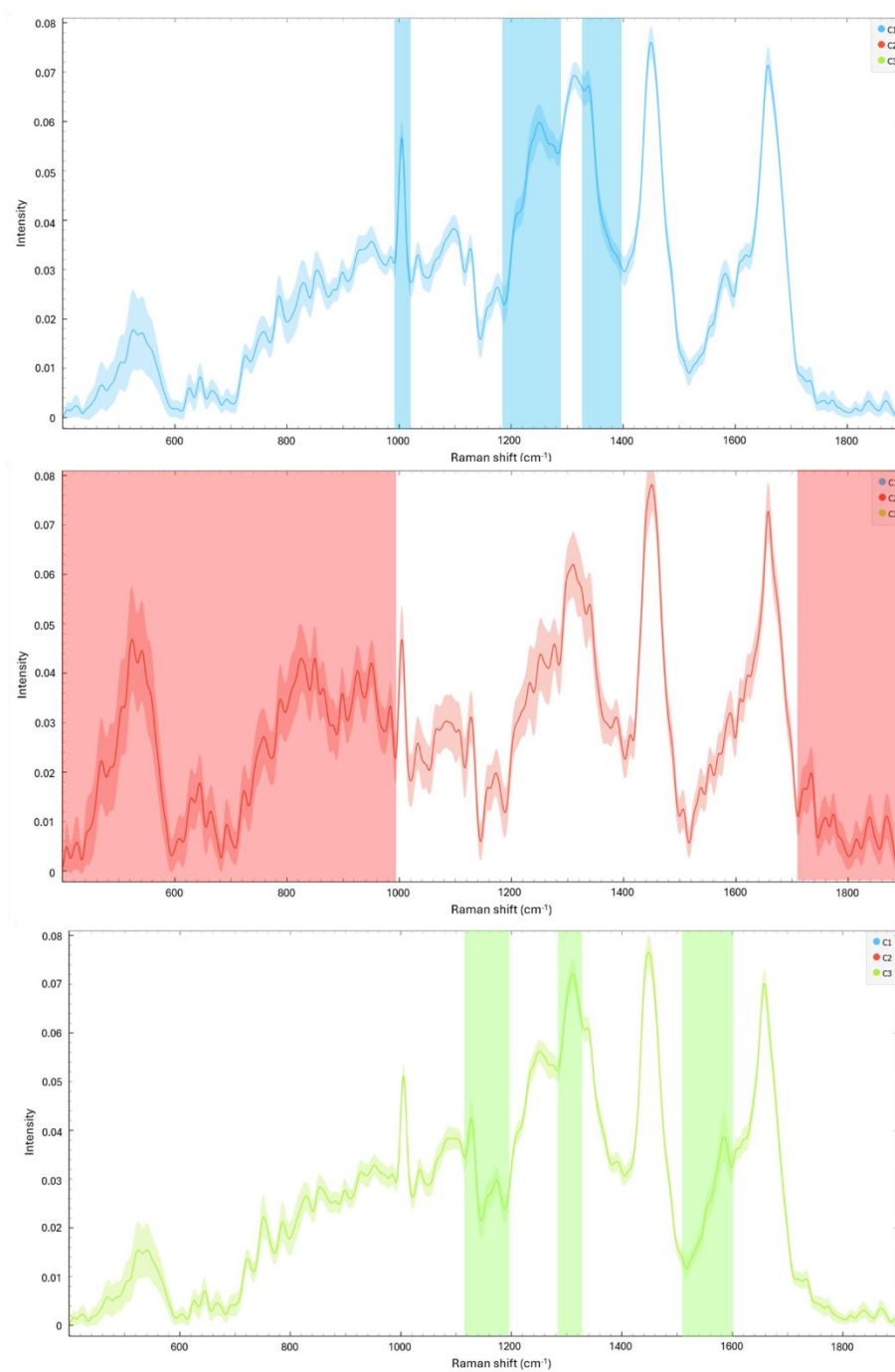
Following this band, in the region 1517-1623cm<sup>-1</sup> signals are of weaker intensity and a large amount of overlap between peaks is noted. The two low intensity, overlapping peaks identified in the region 1514-1540cm<sup>-1</sup> in the single cell spectrum are identified at 1524cm<sup>-1</sup> and 1537cm<sup>-1</sup> and are once again assigned to amide bond vibrations. The peak at 1553cm<sup>-1</sup> is assumed to be a ~5cm<sup>-1</sup> shift of the tryptophan stretching band noted in the single cell. Similarly, the band at 1582cm<sup>-1</sup> is assumed to be a ~3cm<sup>-1</sup> shift of the aromatic ring vibration band noted. Finally, the small overlapping peaks noted in the region 1593-1623cm<sup>-1</sup> in the single cell are resolved at 1606cm<sup>-1</sup> and 1618cm<sup>-1</sup> in the cell neighbours and support the assertion that this region represents tyrosine and phenylalanine-related vibrational modes (C=O stretching and benzene ring deformation respectively) [216].

The clear, high intensity band attributed previously to C=O stretching occurs at similar intensity in both the single cell and neighbouring cells observed. A slight shift of ~1cm<sup>-1</sup> is noted between the two spectra. Localisation of this molecule is also similar, though a slight increase in nuclear localisation is seen in the neighbouring cells compared with the single cell.

Finally, in the region 1712-1900cm<sup>-1</sup>, in contrast to the single cell observed, molecular localisation appears strongly focused on the intersection between the neighbouring cells. Thus, changes seen in this region are deduced to arise as a result of intercellular communication mechanisms. Though little band distinction was made in the spectral region 1721-1757cm<sup>-1</sup> in the single cell spectrum, the overlapping peaks are resolved in the present spectrum as 1719cm<sup>-1</sup> and 1735cm<sup>-1</sup> (some shift in this region is inferred). These bands are once again attributed to C=O bond stretching of phospholipids and are consistent with membrane localisation. In contrast, the band previously identified at 1763cm<sup>-1</sup> is not resolved in cell neighbours, with the surrounding region demonstrating evidence of two low intensity overlapping peaks here instead. These are likely still attributable to lipid bond vibrations, nevertheless. The small overlapping peaks previously noted in the region 1770-1801cm<sup>-1</sup>, are resolved presently to a single peak at 1772cm<sup>-1</sup>, still likely indicative of phospholipids and potentially showing greater clarity in the cell neighbours' spectrum due to the presence of cell membrane in the sampled area. As before, further peaks in this region (i.e. 1800-

1900cm<sup>-1</sup>) are not identified due relative lack of literature regarding these wavenumbers but are presumed to correspond to lipids in cell membranes.

K-means analysis (Fig. 90) demonstrates distinction between nucleic, cytoplasmic and membrane/intersection regions. The region associated with the nucleus predominantly demonstrates bands associated with protein presence, as well as key molecules such as tyrosine/phenylalanine (1005cm<sup>-1</sup>). This is consistent with expectations, though nucleic acid signals do not appear to be strongly associated with this region. The membrane/intersection region strongly demonstrates bands associated with polysaccharides, as well as lipids and proteins. Such signals may evidence the lipid cell membrane, transport proteins and transported molecules.

**A****B**

**Figure 90: K-means clustering of hyperspectral Raman data – 0ng/mL dosed cell pair.**

**A) Chemical map. B) Spectra.**

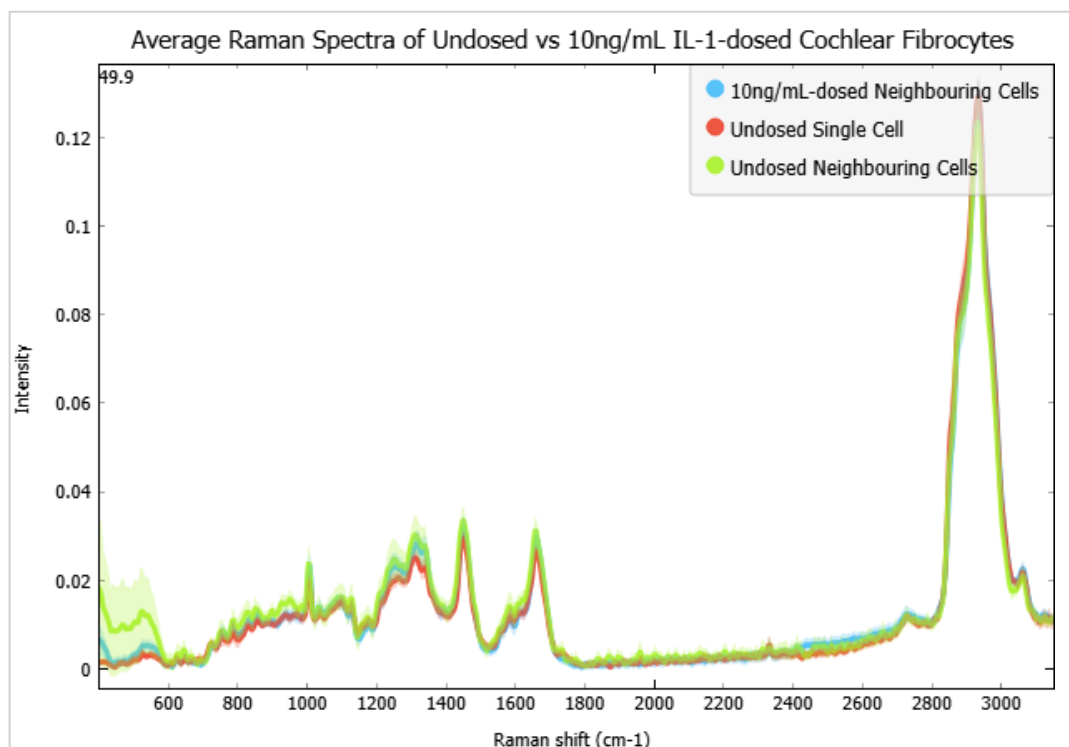
As observed in the single cell spectrum, the high wavenumber region of cell neighbours demonstrates a large central peak at  $2931\text{cm}^{-1}$  (shift of  $\sim 2\text{cm}^{-1}$  from the single cell), with overlapping shoulder like peaks in the region  $2819\text{--}2891\text{cm}^{-1}$  and a smaller neighbouring band at  $3063\text{cm}^{-1}$  (shift of  $\sim 2\text{cm}^{-1}$  from the single cell). These bands demonstrate similar signal intensity and molecular localisation and are once again assumed to arise due to bond vibrations in proteins. No K-means analysis was conducted on high wavenumber region data due to relative lack of localisation in this spectral region.

In general, spectral results for the undosed neighbouring cells observed are similar to the single cell, with the majority of variations occurring as small shifts in bands. Such small shifts ( $<9\text{cm}^{-1}$ ) are considered negligible in the present context due to the resolution of the instrument employed. Nonetheless, changes between single and neighbouring cells are still noted, with the regions  $<700\text{cm}^{-1}$  and  $>1712\text{cm}^{-1}$  believed to be of value in the distinction of cells alone from cells in contact due to evidence of strong membrane/intersection localisation of molecules. However, at this stage of research, where only a single sample is presented, firm conclusions cannot be drawn as to the significance of the variations seen.

Though it would undoubtedly be useful to compare dosed single and neighbouring cells with undosed controls of the same configuration, the present research is limited to comparison of cells with neighbours only, as a suitable single dosed cell could not be found in the examined sample within the allocated research time. However, though only dosed cells with neighbours are analysed presently, valuable insight may still be gleaned from comparison. In lieu of a dosed single cell, a pair of dosed cells showing unusual granulations (seen only in a small number of other cells within the  $10\text{ng/mL}$  dosed sample) is presented. Whether these granulations are a product of interleukin dosage is unclear from the samples obtained- however, it should be noted that such features are not present in undosed control cells.

Beginning with the non-granulated dosed cell neighbours, it is clear from spectral comparison alone that there are differences to be found between dosed and undosed cells in contact with neighbours (Fig. 91). It is particularly interesting to note that, in the regions previously

identified as relevant to the distinction of cells with neighbours ( $<700\text{cm}^{-1}$ ,  $>1712\text{cm}^{-1}$ ), the neighbouring 10ng/mL dosed cells examined show an average spectral profile and peak intensities more resemblant of a cell alone than in contact with others when compared to controls.

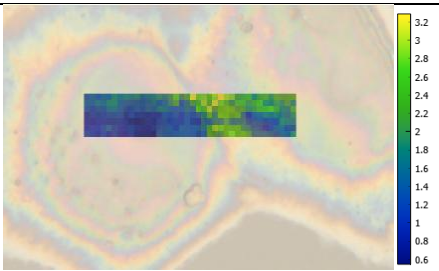
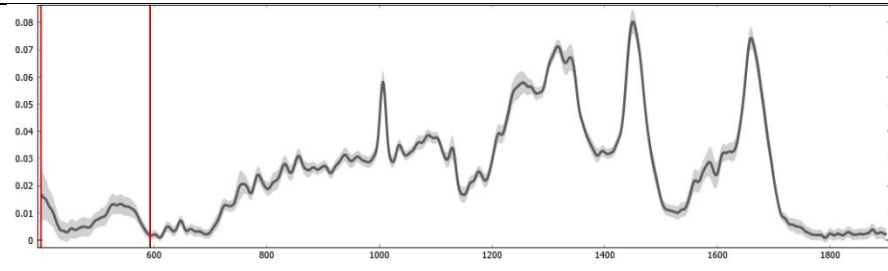
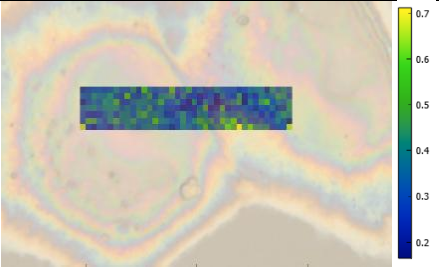
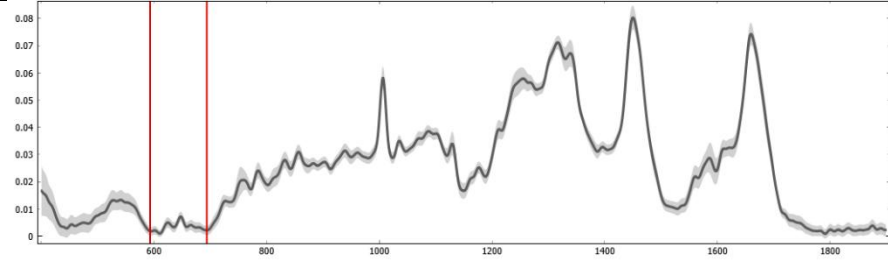
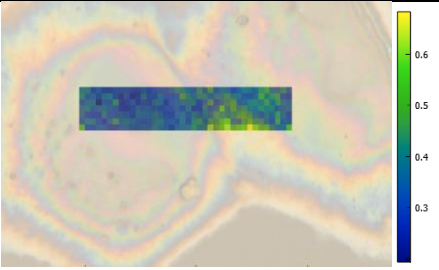
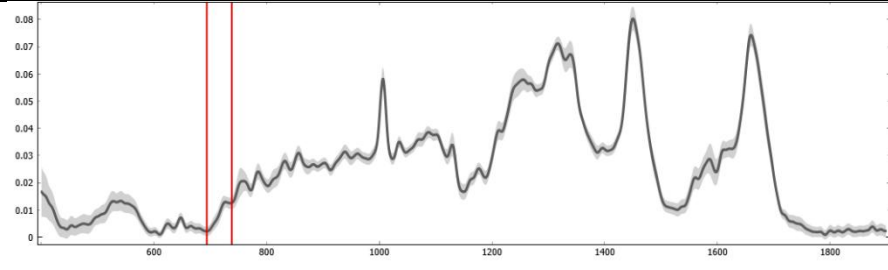


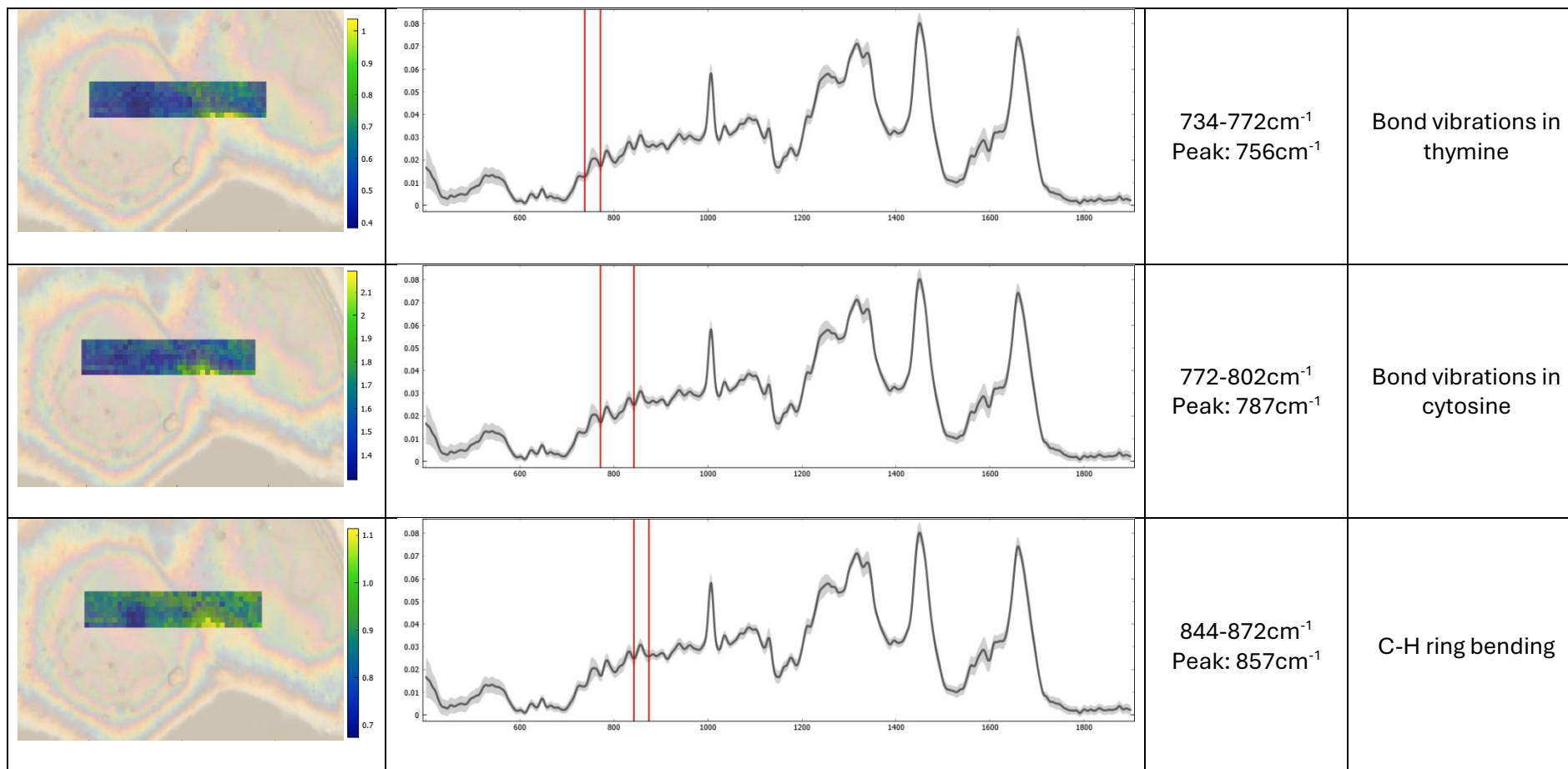
**Figure 91: Comparison of dosed and undosed cell spectra- a single undosed cell vs neighbouring undosed cells in contact vs 10ng/mL interleukin-1-dosed cells in contact.**

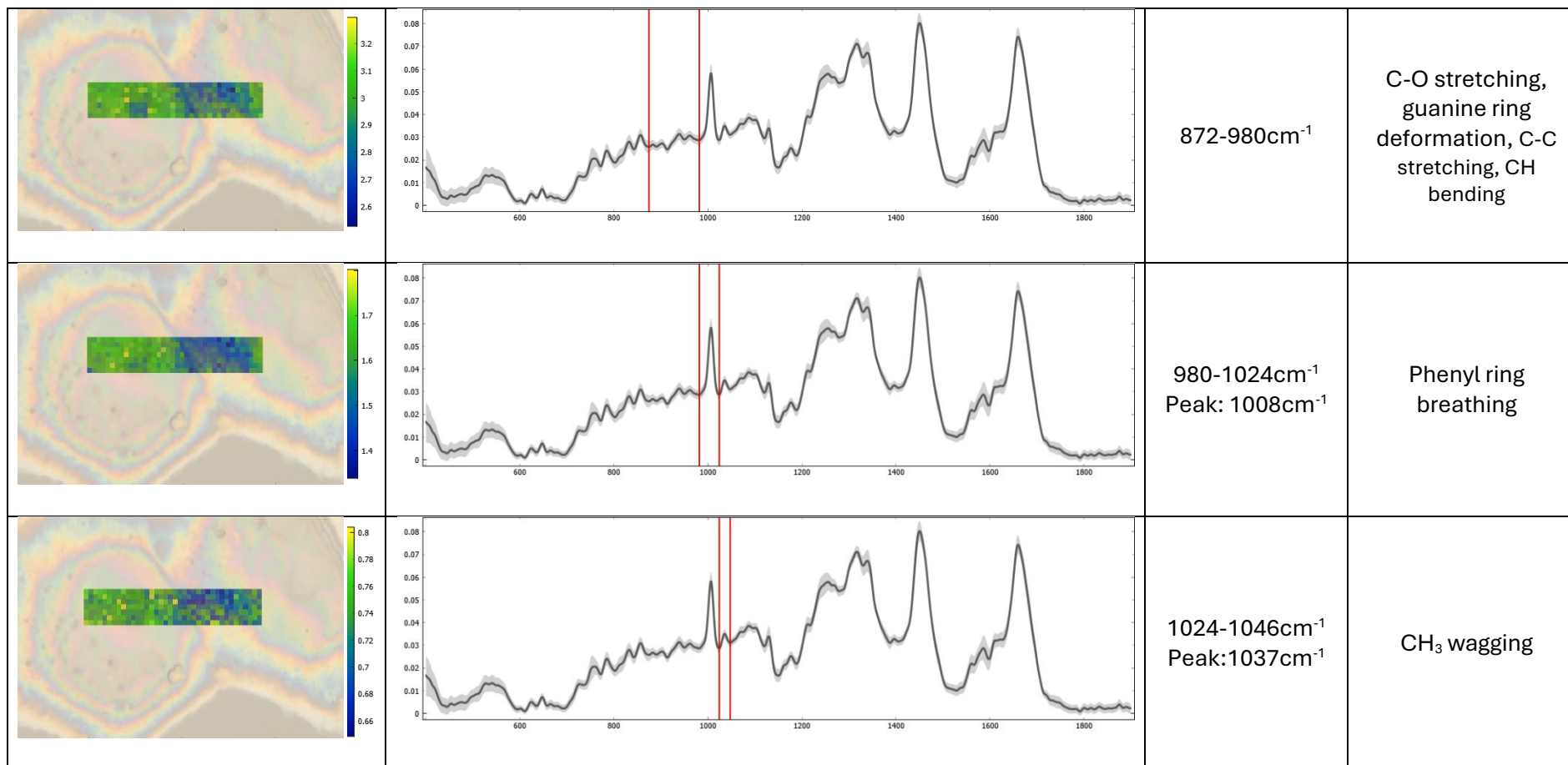
**Average spectra from hyperspectral Raman area maps of cochlear fibrocytes grown on  $\text{CaF}_2$ . Approx. 250k cell seeding density. Spectra collected at Diamond Light Source, Oxford, UK.**

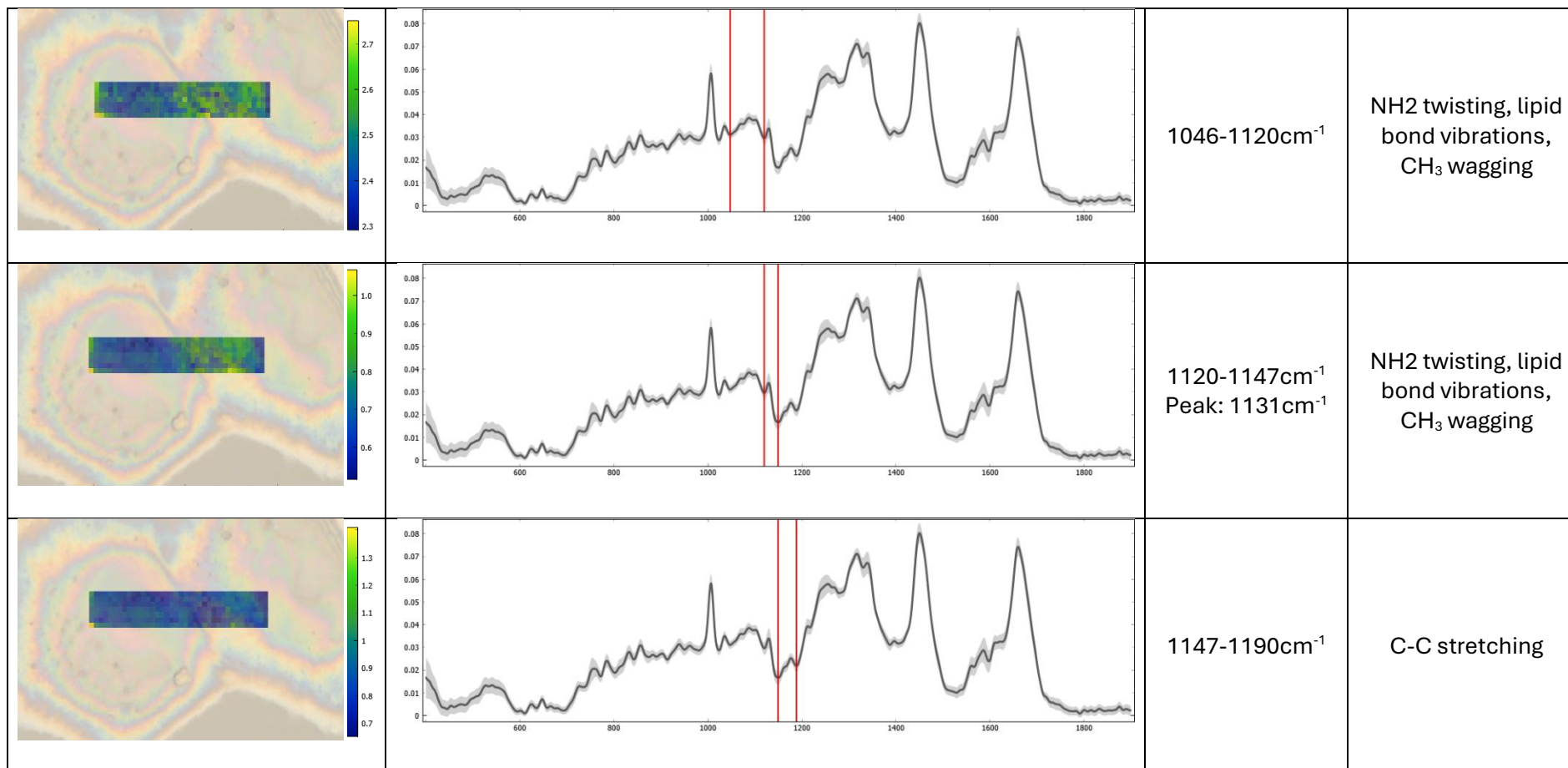
Analysing the spectrum of these cells peak-by-peak, and correlating this with accompanying chemical maps enables further insight into the observed variation and its potential source. To this end, the spectrum and associated chemical maps of 10ng/mL dosed neighbouring cells are presented in tables 12 and 13 below.

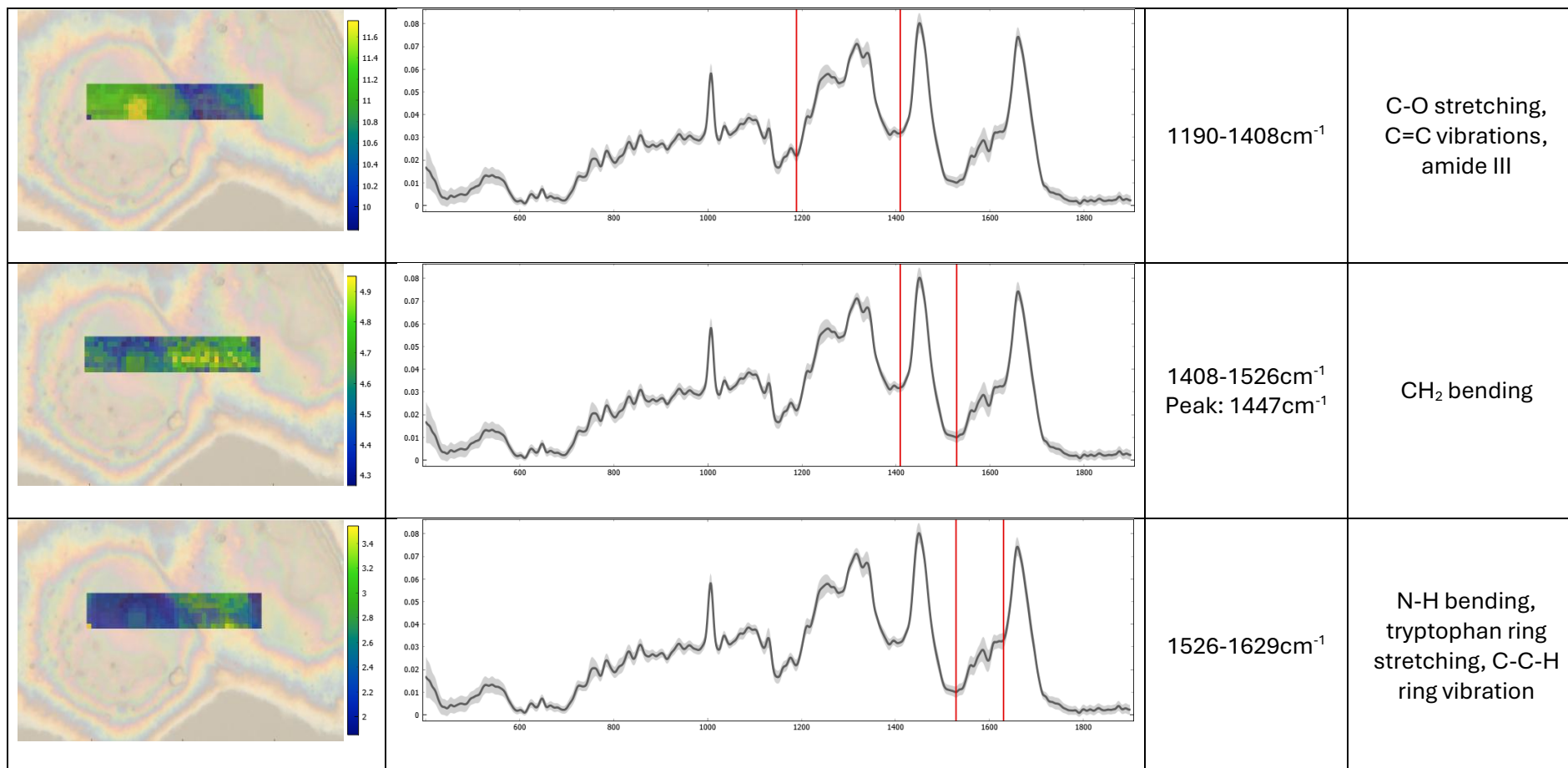
**Table 12: Chemical maps, wavenumbers and localisations of molecules in the fingerprint region of a pair of 10ng/mL dosed cochlear fibrocytes' spectrum analysed by hyperspectral Raman spectroscopy.**

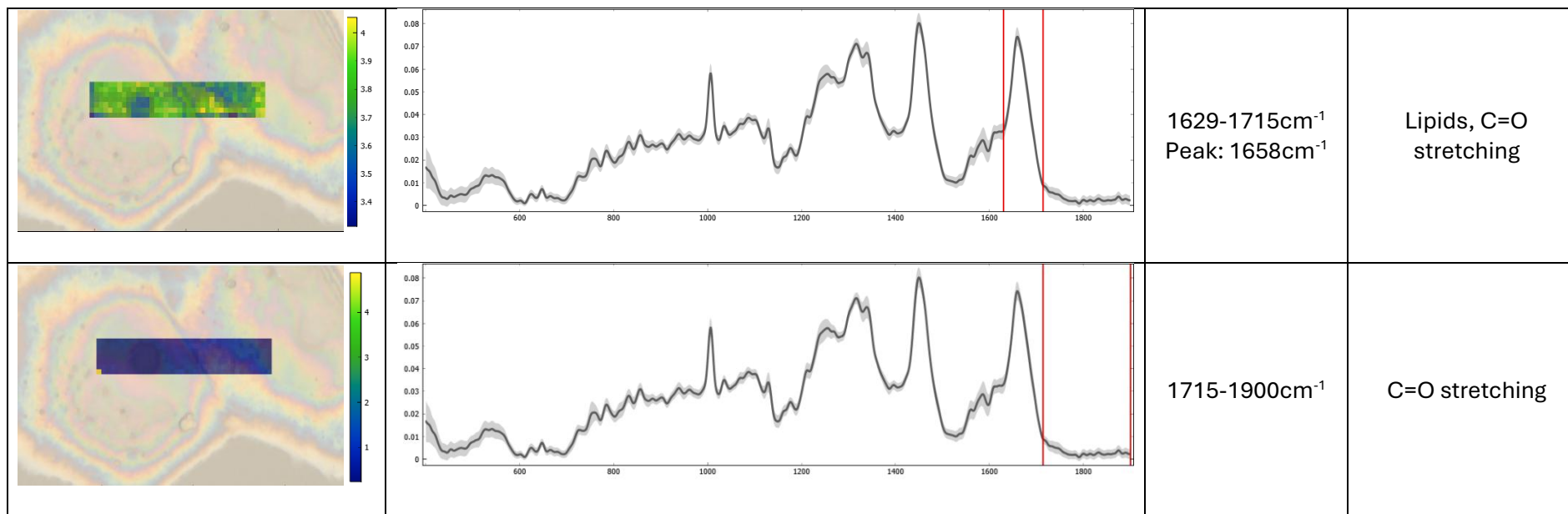
Image	Spectrum	Wavenumber	Strongest localisation
		400-593cm <sup>-1</sup>	CH <sub>2</sub> bending, C-C-C deformations
		593-693cm <sup>-1</sup>	CH <sub>2</sub> bending, amide IV, C-S stretching, nucleotide ring breathing
		693-734cm <sup>-1</sup> Peak: 725cm <sup>-1</sup>	Bond vibrations in adenine



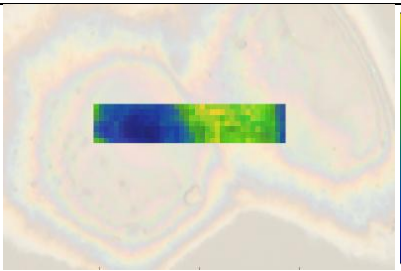
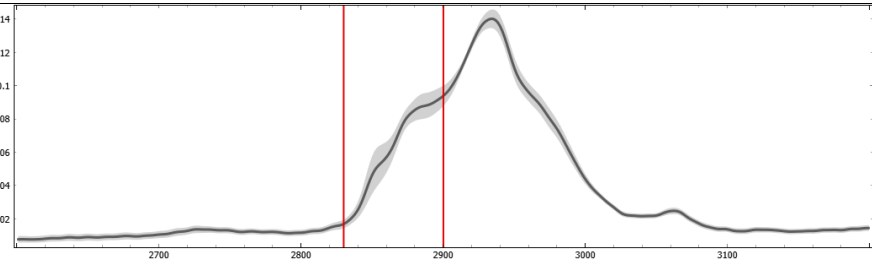
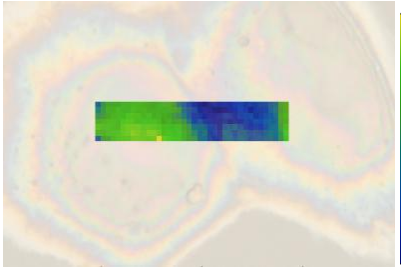
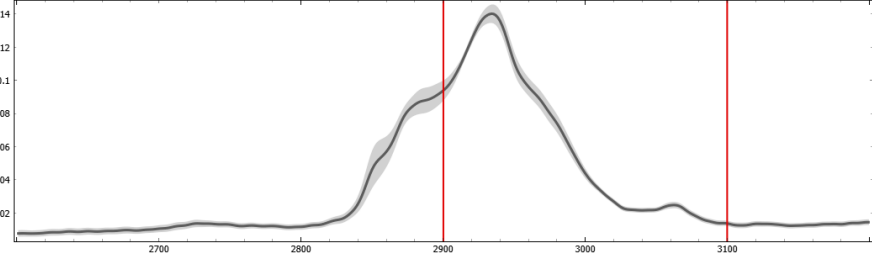








**Table 13: Chemical maps, wavenumbers and localisations of molecules in the high wavenumber region of a pair of 10ng/mL dosed cochlear fibrocytes' spectrum analysed by hyperspectral Raman spectroscopy.**

Image	Spectrum	Wavenumber	Strongest localisation
		2824-2900cm <sup>-1</sup>	CH <sub>2</sub> stretching
		2891-3100cm <sup>-1</sup> Peak: 2934cm <sup>-1</sup>	CH <sub>2</sub> stretching

Beginning in the lower end of the fingerprint region ( $<600\text{cm}^{-1}$ ), as stated above the spectrum of dosed cells demonstrates greatly reduced signal intensity. This is accompanied by a reduction in the clarity of peaks in this region, with fewer identifiable bands arising in this region for dosed cells. As seen in undosed neighbouring cells, the above spectrum shows a sloping shoulder-like signal below  $438\text{cm}^{-1}$  and a small peak at  $440\text{cm}^{-1}$ . This suggests that this feature is consistent across neighbouring cells and may distinguish them from isolated cells. Further bands identified in this region are difficult to resolve from their neighbours due to overlap and lack of signal intensity. This includes the absence of bands previously noted at  $485\text{cm}^{-1}$ ,  $504\text{cm}^{-1}$ ,  $523\text{cm}^{-1}$  and  $540\text{cm}^{-1}$ . Nonetheless, this region is considered of value and the alterations seen between undosed and dosed cells, given the localisation shown in associated chemical maps (Fig. 92), are taken to indicate reductions in intercellular transport of molecules such as saccharides. This is consistent with expectations of dosed cells from previous chapters.

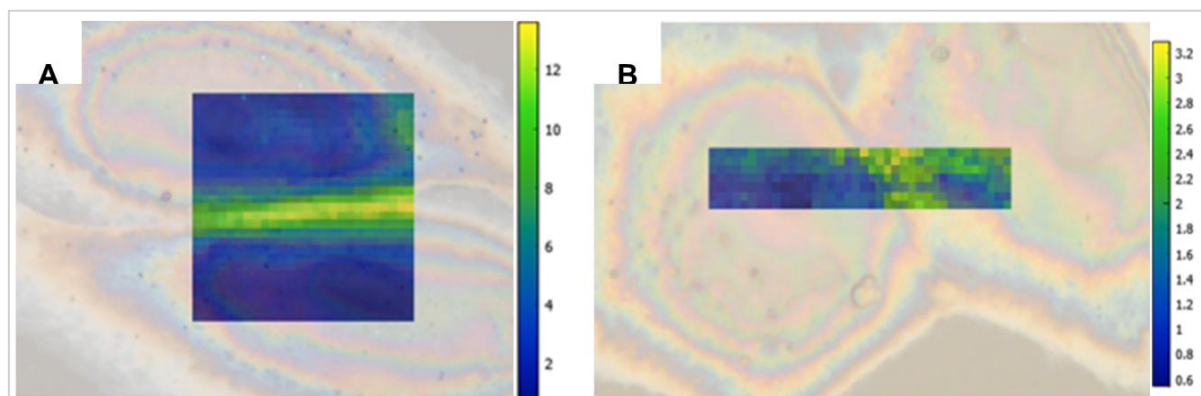


**Figure 92: Raman hyperspectral chemical maps of 0ng/mL dosed vs 10ng/mL dosed cell pairs below  $600\text{cm}^{-1}$ .**

**A) 0ng/mL cells. B) 10ng/mL cells. Note the heat map keys which indicate reduced signal intensity in dosed cells.**

Moving to spectral region  $592\text{--}693\text{cm}^{-1}$ , localisation is once again primarily focused in the cell membrane/intersection region in neighbouring cells, with signals of a similar intensity in both undosed and dosed cell pairs suggesting minimal alterations to structure and function represented by bands in this spectral region. Clear peaks at  $604\text{cm}^{-1}$  (no shift from undosed),  $625\text{cm}^{-1}$  (no shift from undosed) and  $644\text{cm}^{-1}$  ( $\sim 3\text{cm}^{-1}$  shift from undosed) are once again visible, with localisation to the cell intersection in both conditions. These peaks are attributed to bond vibrations of

cholesterol, amide IV/methionine and amide respectively. Though the bands noted in neighbouring control cells at  $665\text{cm}^{-1}$  and  $690\text{cm}^{-1}$  are noted in dosed cells at  $667\text{cm}^{-1}$  ( $\sim 2\text{cm}^{-1}$  shift) and  $682\text{cm}^{-1}$  ( $\sim 8\text{cm}^{-1}$  shift), localisation varies across conditions. This is assumed to be due to reduced amino acid content in dosed cell membranes, potentially indicative of alterations to transport proteins. Alternatively, these bands may represent nucleotide presence rather than a shift in amino acid peaks, based upon the nuclear localisation seen <sup>[216]</sup>.

Bands in the region  $693\text{--}802\text{cm}^{-1}$ , occur at similar intensities with similar distribution in cells in both dosed and undosed cell neighbours. Bands arise at  $725\text{cm}^{-1}$  ( $\sim 2\text{cm}^{-1}$  shift),  $756\text{cm}^{-1}$  ( $\sim 4\text{cm}^{-1}$  shift),  $787\text{cm}^{-1}$  ( $\sim 3\text{cm}^{-1}$  shift) and are attributed to nucleotides. No experimentally significant variation is noted in this spectral region.

At first glance, the spectral region  $802\text{--}980\text{cm}^{-1}$  demonstrates little variation in bands, peak intensity and molecular localisation across undosed and dosed cell samples. However, upon closer inspection it is evident that the spectrum of dosed cell neighbours in this region more closely resembles that of an isolated undosed cell than that of undosed cell neighbours, both in intensity and in bands. This is supported by bands arising at  $833\text{cm}^{-1}$  ( $\sim 3\text{cm}^{-1}$  shift from undosed single cell),  $857\text{cm}^{-1}$  ( $\sim 1\text{cm}^{-1}$  shift from undosed single cell) and  $938\text{cm}^{-1}$ , as well as by the lack of the coenzyme A-associated bands identified in undosed cell neighbours. Though uncertain, this may imply a reduction in cell production of coenzyme A and could indicate reduced capacity for biosynthesis of essential molecules in dosed cells. Further evidence of alterations in dosed cells is seen in the band at  $962\text{cm}^{-1}$ , noted as a fingerprint of peroxytaurine – a product of taurine/hypotaurine reactions with reactive oxygen species <sup>[216, 243, 244]</sup>.

As in the previous spectra, the band at  $1008\text{cm}^{-1}$  is identified as arising due to phenyl ring breathing, likely from tyrosine and phenylalanine. The localisation seen within the cells observed is consistent with established knowledge of these molecules and their biological roles. Interestingly, there appears to be a slight increase in signal intensity of this band in the dosed condition. This is likely indicative of an anti-inflammatory response in dosed cells <sup>[245]</sup>.

Continuing to the spectral region 1024-1147 $\text{cm}^{-1}$ , bands, intensity and molecular localisation appear generally similar to the undosed cell pair. The band seen at 1034 $\text{cm}^{-1}$  demonstrates a  $\sim 3\text{cm}^{-1}$  shift to 1037 $\text{cm}^{-1}$  and is attributed to  $\text{CH}_3$  wagging. The triple peak region noted previously at 1054-1117 $\text{cm}^{-1}$  is resolved to three clear bands at 1070 $\text{cm}^{-1}$ , 1085 $\text{cm}^{-1}$ , 1103 $\text{cm}^{-1}$ , attributed to bond vibrations in lipids. The band previously seen at 1126 $\text{cm}^{-1}$  demonstrates a  $\sim 5\text{cm}^{-1}$  shift to 1131 $\text{cm}^{-1}$  and is attributed to  $\text{CH}_3$  wagging. No experimentally significant variation is noted in this spectral region.

Similarly, the spectral region 1147-1190 $\text{cm}^{-1}$  demonstrates bands, intensity and molecular localisation generally similar to the undosed cell pair. The pair of bands in this region are attributed to C-C stretching and C-H bending. No experimentally significant variation is noted in this spectral region.

For the most part, the spectral region 1190-1408 $\text{cm}^{-1}$  demonstrates bands, intensity and molecular localisation similar to that seen in the undosed cell pair. Similar bands arise at 1210 $\text{cm}^{-1}$ , 1254 $\text{cm}^{-1}$  ( $\sim 4\text{cm}^{-1}$  shift), 1269 $\text{cm}^{-1}$  ( $\sim 7\text{cm}^{-1}$  shift), and 1337 $\text{cm}^{-1}$  ( $\sim 1\text{cm}^{-1}$  shift) and are attributed to C-O stretching and lipid/protein bond vibrations. Interestingly, the band at 1318 $\text{cm}^{-1}$  ( $\sim 5\text{cm}^{-1}$  shift) shows stronger nuclear localisation than that seen in the undosed cell pair, as well as a slightly increased signal intensity. This band is attributed to C-O stretching. Additionally, a unique band demonstrating strong nuclear localisation seen in neither undosed sample is identified at 1395 $\text{cm}^{-1}$ . The origins of this band are unknown.

Of further interest, the high-intensity band previously noted at 1450 $\text{cm}^{-1}$ , though showing similar molecular localisation, demonstrates a  $\sim 3\text{cm}^{-1}$  shift to 1447 $\text{cm}^{-1}$  in the dosed condition. Additionally, increased signal intensity is seen in this condition, implying lipid accumulation within cells similar to that hypothesised previously.

The spectral region 1526-1629 $\text{cm}^{-1}$  demonstrates bands, intensity and molecular localisation generally similar to the undosed cell pair, though clarity of overlapping bands is reduced in the dosed condition. Bands are attributed as before to amide bond vibrations,

tryptophan stretching, aromatic ring vibrations, C=O stretching and benzene ring deformations. No experimentally significant variation is noted in this spectral region.

The high-intensity band at  $1658\text{cm}^{-1}$  demonstrates differing molecular localisation to that seen in undosed neighbouring cells (Fig. 90), in that distribution of signal is seen throughout cytoplasm and the membrane region. It is notable that there are areas of strong localisation within the cell membrane region of dosed cells. Such regions may be indicative of protein/lipid accumulation and further suggest changes in cell membrane integrity. In this wavenumber region, an increase in signal intensity in the dosed condition is noted, further indicating protein accumulation and/or alterations in protein secondary structures as noted in chapters 4 and 5. It is, however, unclear from the data available whether this evidences changes induced by dosage (e.g. proinflammatory cytokine accumulation <sup>[57]</sup>) or merely the presence of up-taken IL- $1\beta$  in the cytoplasm of dosed cells.

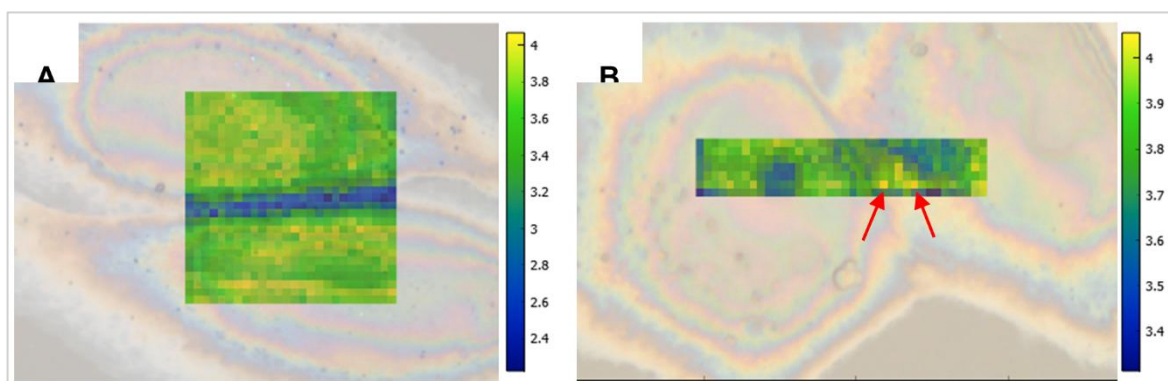


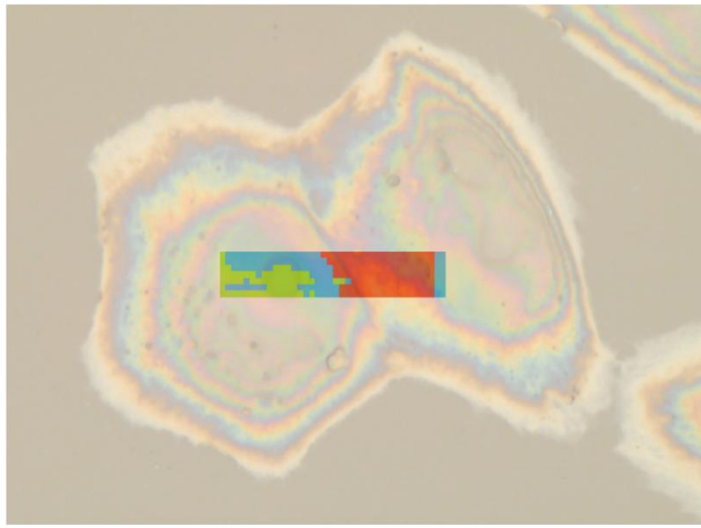
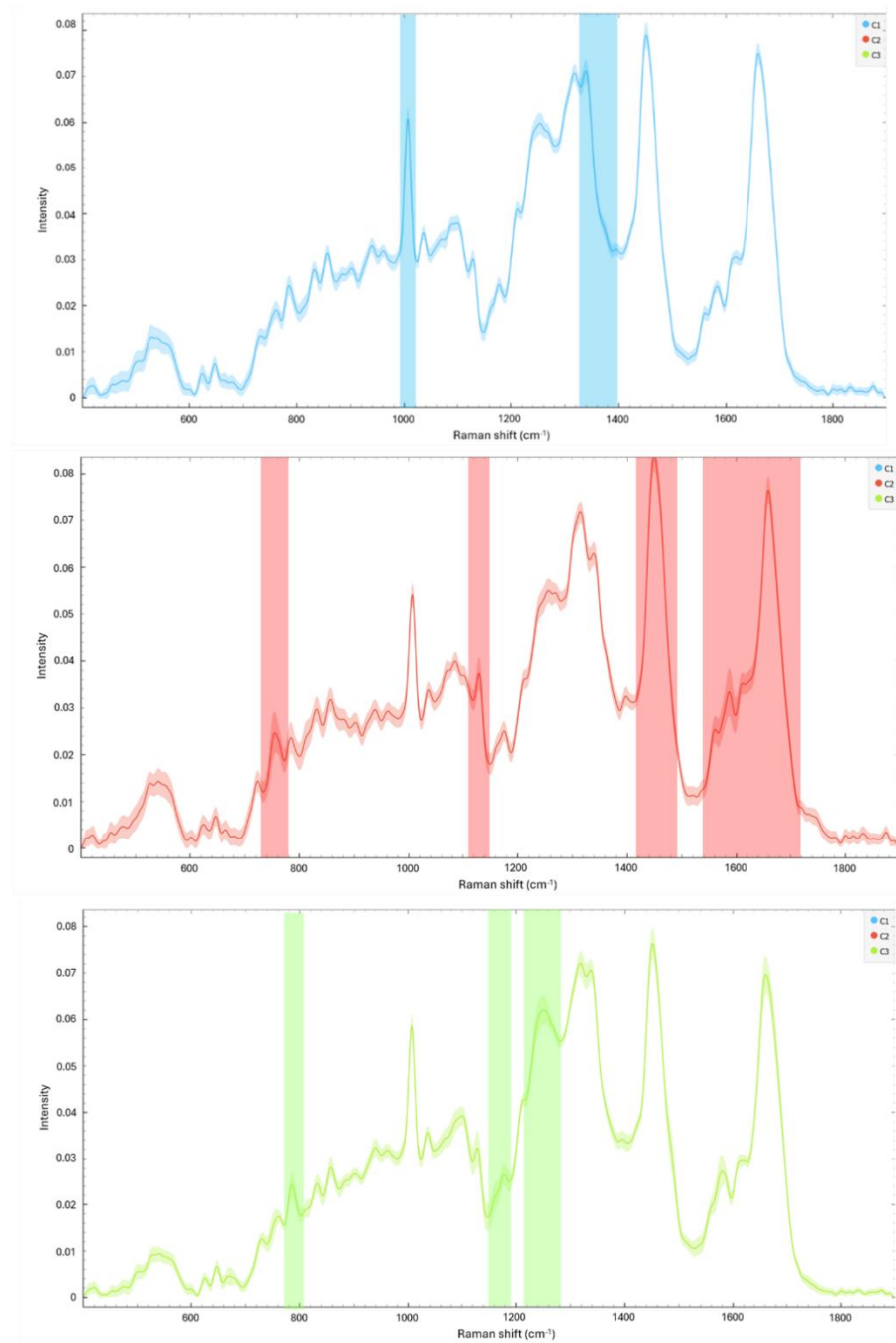
**Figure 93: Raman hyperspectral chemical maps of 0ng/mL dosed vs 10ng/mL dosed cell pairs at  $\sim 1650\text{cm}^{-1}$ .**

**A) 0ng/mL cells. B) 10ng/mL cells. Arrows indicate small areas of high intensity signal in the membrane region.**

Finally, in the region  $1715\text{--}1900\text{cm}^{-1}$  noticeable variation is observed between undosed and dosed cell pairs. This variation occurs in band location, band clarity, signal intensity and localisation. Where some bands noted in the undosed cell neighbours are seen shifted in the dosed condition (e.g.  $1813\text{cm}^{-1}$  band at  $1816\text{cm}^{-1}$ ,  $1839\text{cm}^{-1}$  band at  $1833\text{cm}^{-1}$ ,  $1894\text{cm}^{-1}$  band at  $1890\text{cm}^{-1}$ ), these occur at a reduced intensity and broader distribution throughout the sampled cell area rather than in the intersection/membrane region. Other previously noted bands are indistinguishable all together. As previously stated, this spectral region is typically associated with

lipid bond vibrations, particularly where phospholipids are concerned. Thus, the variation seen between undosed and dosed cell pairs is taken to indicate potential cell membrane degradation<sup>[223]</sup> and altered capacity for/mechanisms of intercellular communication<sup>[246]</sup>.

K-means analysis (Fig. 94) once again demonstrates distinction between nucleic, cytoplasmic and membrane/intersection regions, though the membrane-associated region is far less distinct than in undosed cells. Examining this region, it is notable that the strong polysaccharide-assigned signals noted in the undosed cell pair are not clearly localised in dosed cells in contact. This, as discussed above, is believed to indicate alterations to intercellular transport arising from inflammatory changes. The strong presence of thymine in this region is unexpected, though may be indicative of damage to mitochondria or nuclei. The nuclear region, though not demonstrating strong thymine signal, demonstrates bands for cytosine, proteins and amino acids, suggesting that the thymine presence in the membrane/cytoplasm is of mitochondrial origin.

**A****B**

**Figure 94: K-means clustering of hyperspectral Raman data – 10ng/mL dosed cell pair.**

**A) Chemical map. B) Spectra.**

As observed previously, the high wavenumber region of dosed cell neighbours demonstrates a large central peak at  $2934\text{cm}^{-1}$  (shift of  $\sim 3\text{cm}^{-1}$  from the undosed cell pair), with overlapping shoulder like peaks in the region  $2824\text{--}2891\text{cm}^{-1}$  and a smaller neighbouring band at  $3062\text{cm}^{-1}$  (shift of  $\sim 1\text{cm}^{-1}$  from the undosed cell pair). These bands demonstrate similar signal intensity and molecular localisation and are once again assumed to arise due to bond vibrations in proteins. As such, no experimentally significant variation is noted in this spectral region based on Raman results. No K-means analysis was conducted on high wavenumber region data due to relative lack of localisation in this spectral region.

Overall, spectral results for the dosed neighbouring cells demonstrate several sites of clear variation from their undosed counterparts, whether this be in the form of band presence, signal intensity, or molecular localisation. In particular, alterations are suggested in intercellular transport, membrane integrity/content, biosynthesis in cytoplasm, and molecular accumulation within cells. Such changes are consistent with previous chapter findings and with literature surrounding cellular inflammation.

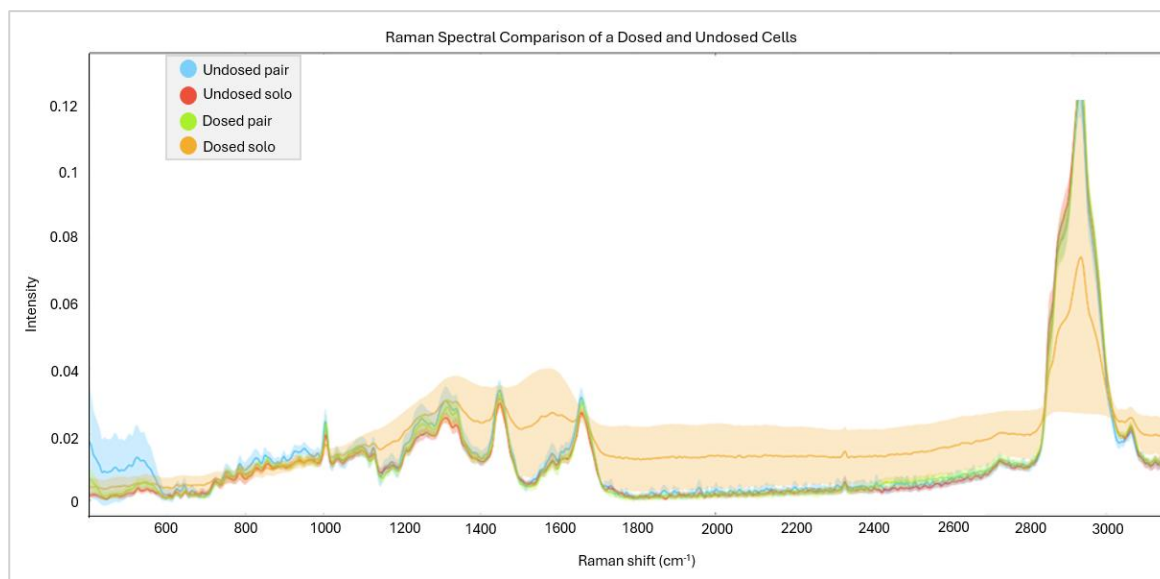


**Figure 95: Comparison of dosed and undosed cell spectra via hyperspectral Raman spectroscopy.**

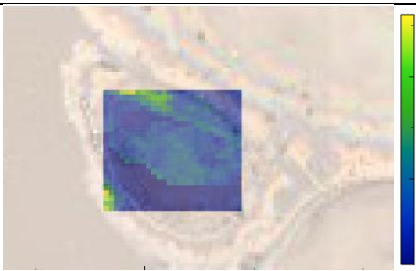
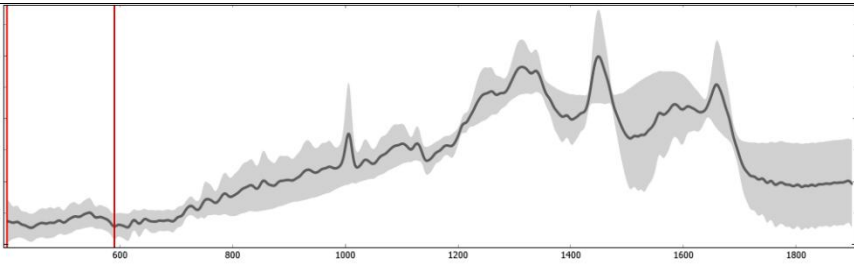
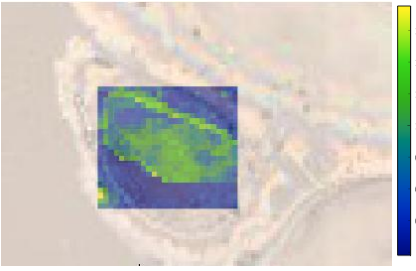
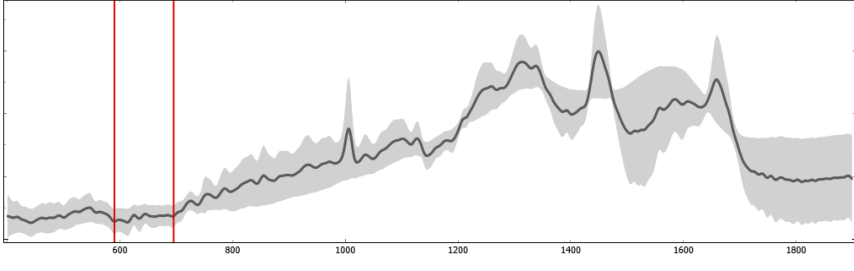
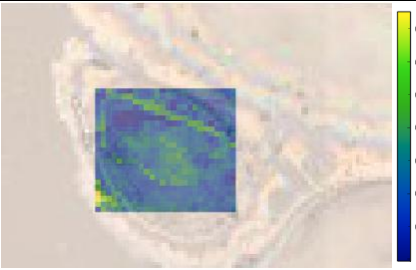
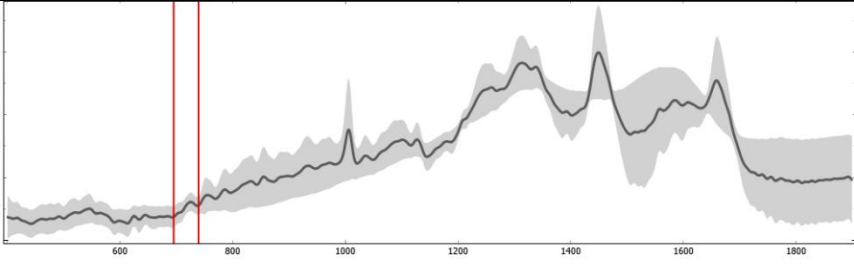
**Average spectra from hyperspectral Raman area maps of cochlear fibrocytes grown on  $\text{CaF}_2$ . Approx. 250k cell seeding density. Spectra collected at Diamond Light Source, Oxford, UK.**

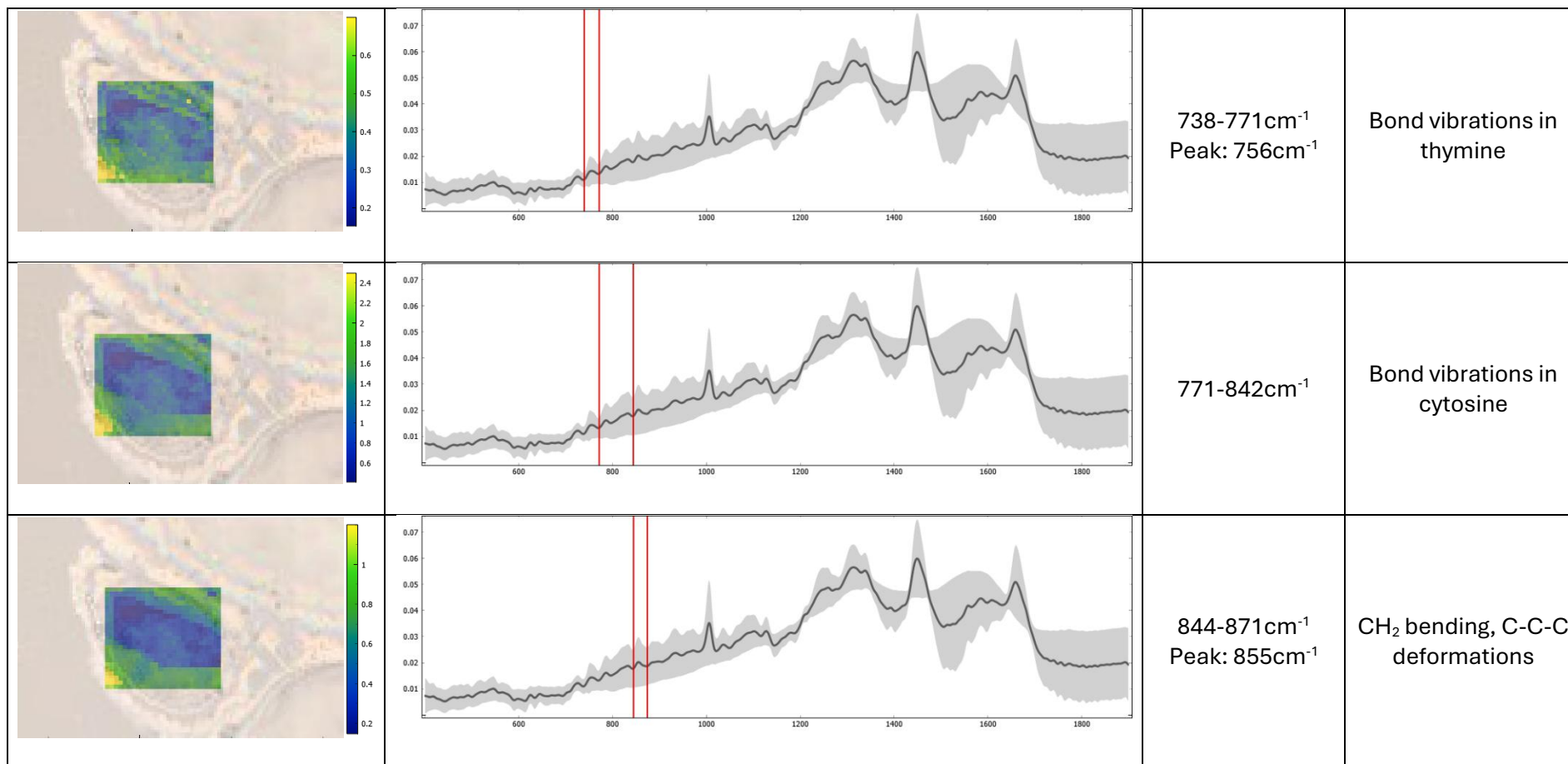
For further comparison, a second pair of neighbouring 10ng/mL dosed cells are presented. These cells, unlike those above, show unusual granulations in their cytoplasm and near their membranes. Such granulations were seen in several cells in this dosage sample but were not present in the undosed cells observed.

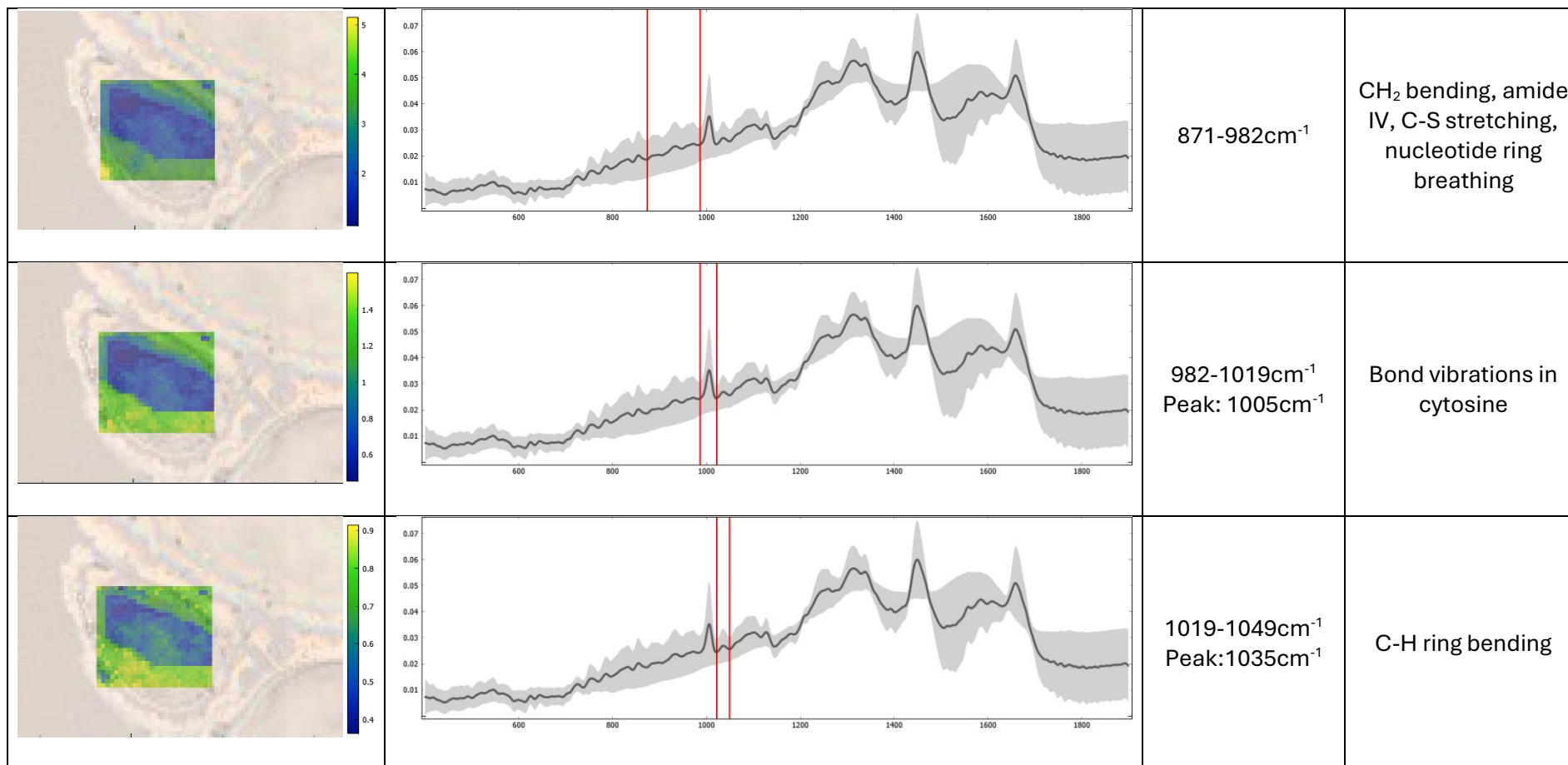
Comparing the spectrum of these cells with those previously observed, there are clear differences, with signals demonstrating variable intensity, poor peak resolution and wide margins of error (Fig. 95). Whether these variations arise as a result of molecular characteristics, or changes to scattering due to structural differences in the granular cells, they are valuable to note in seeking to observe the dosed cell condition in its entirety. This is particularly relevant where considering variation of cells within the 10ng/mL condition and other cytokine dosages that may yield error in differentiation of conditions.

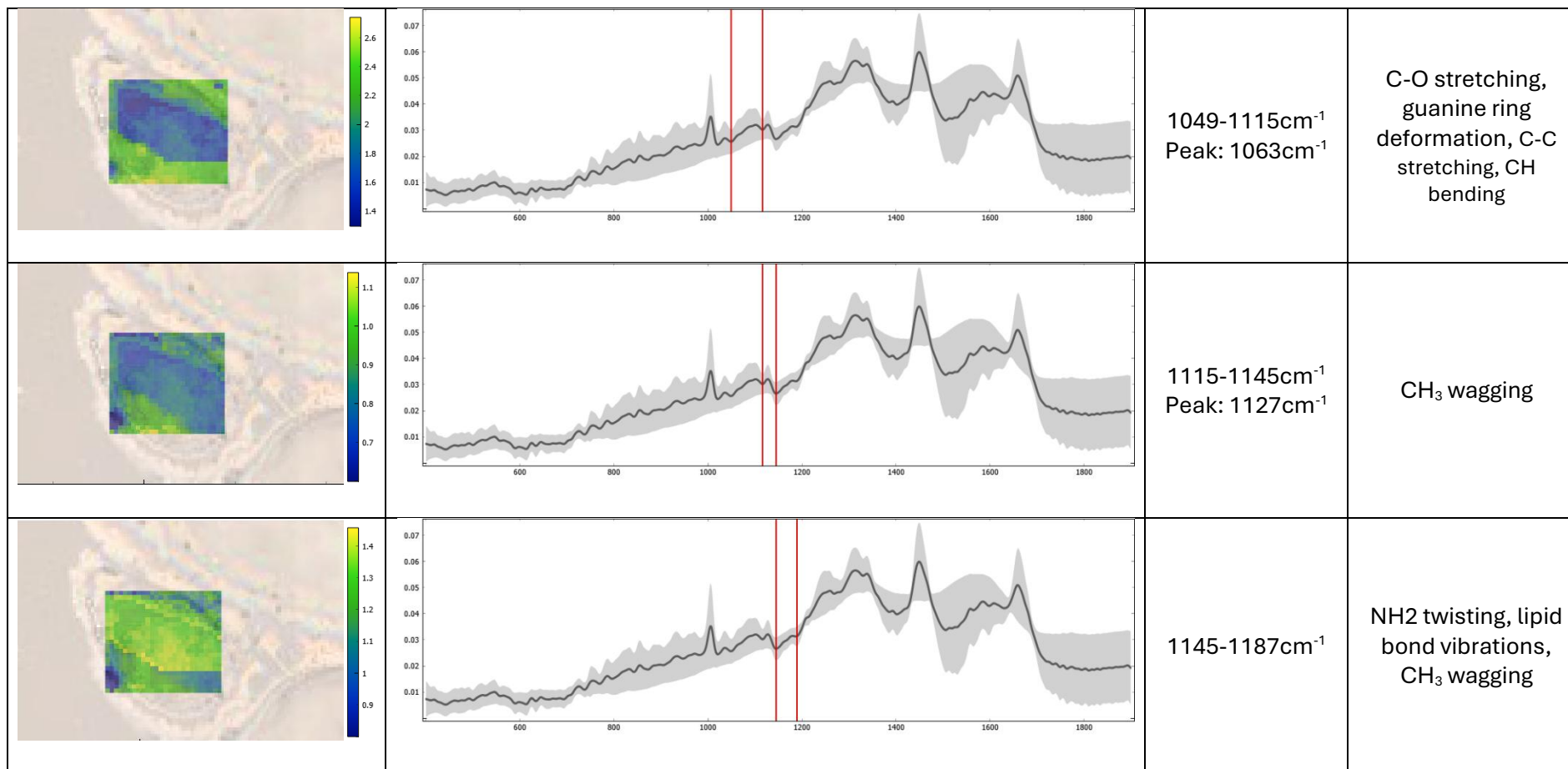
To examine the spectral changes noted, the spectrum and associated chemical maps of the granular 10ng/mL dosed cells are presented in tables 14 and 15 below.

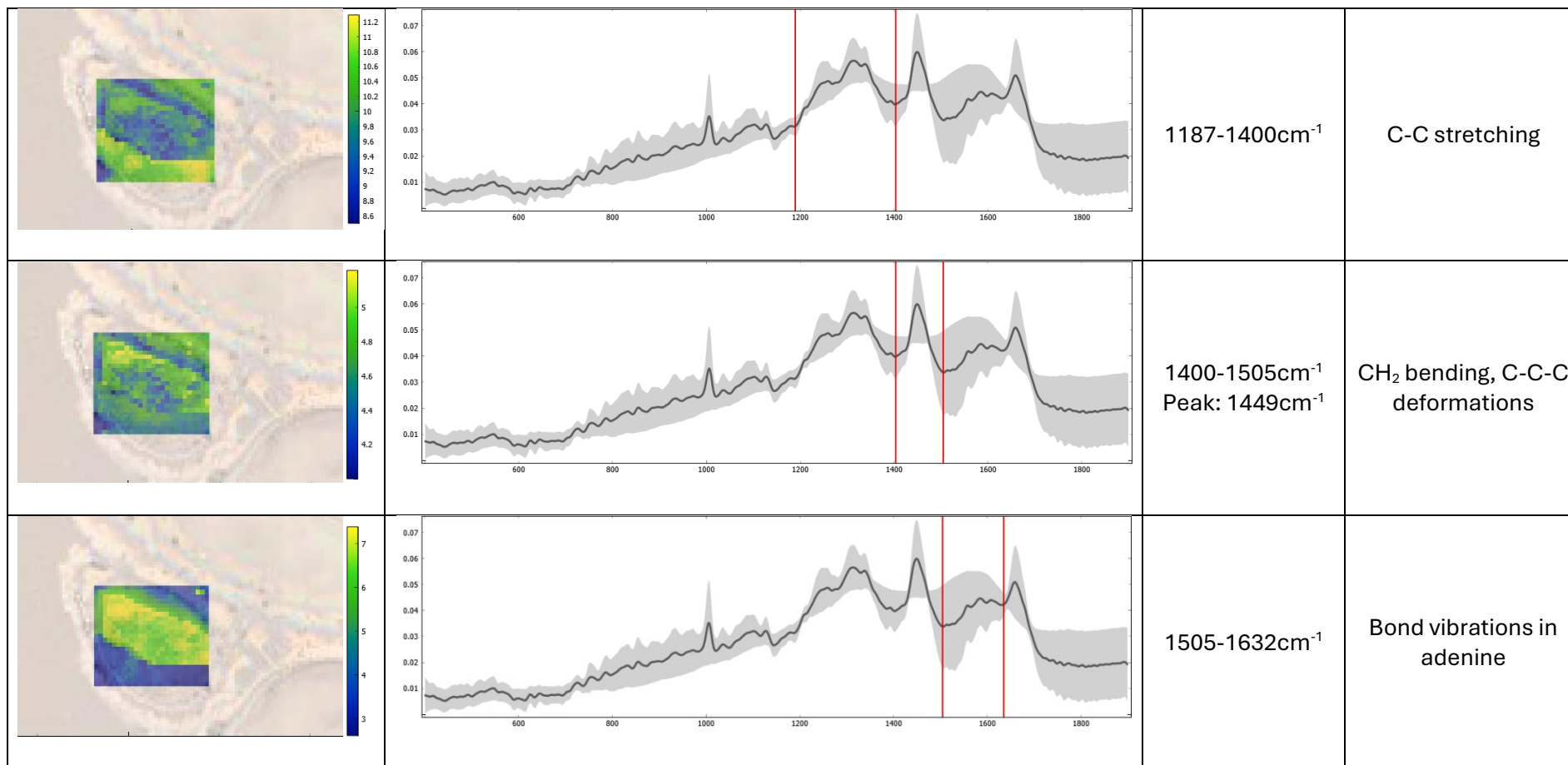
**Table 14: Chemical maps, wavenumbers and localisations of molecules in the fingerprint region of granulated 10ng/mL dosed cochlear fibrocytes' spectrum analysed by hyperspectral Raman spectroscopy.**

Image	Spectrum	Wavenumber	Strongest localisation
		400-589cm <sup>-1</sup>	CH <sub>2</sub> bending, C-C-C deformations
		589-693cm <sup>-1</sup>	CH <sub>2</sub> bending, amide IV, C-S stretching, nucleotide ring breathing
		693-738cm <sup>-1</sup> Peak: 725cm <sup>-1</sup>	Bond vibrations in adenine









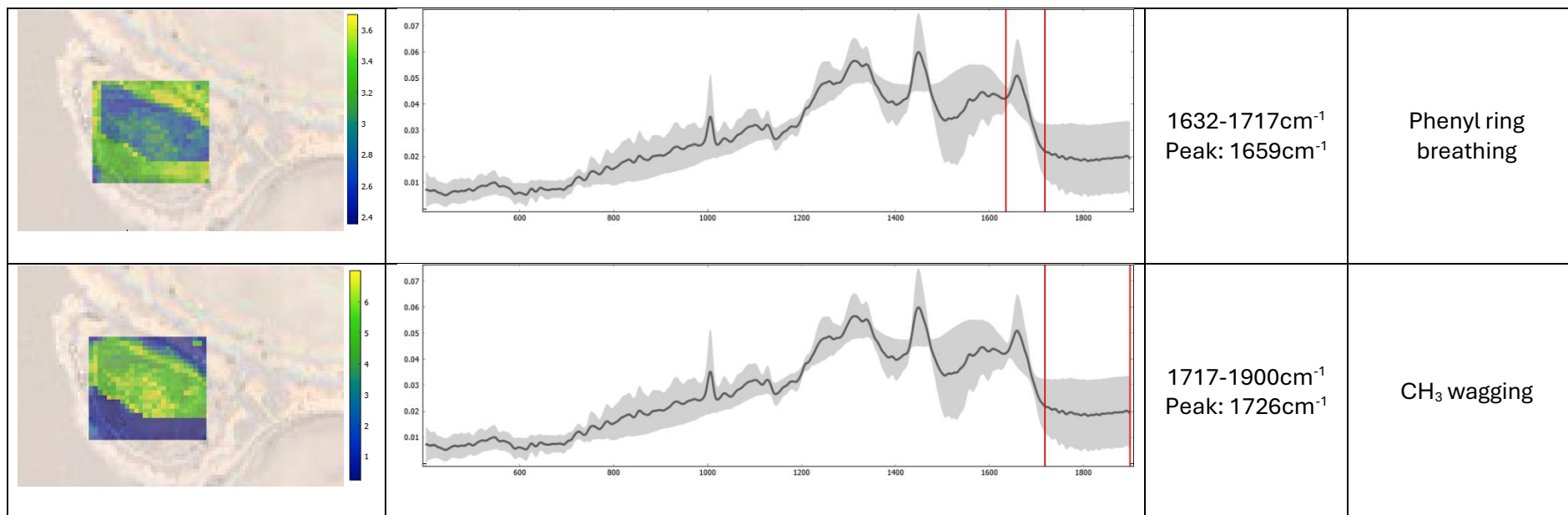
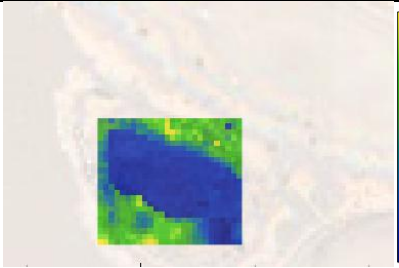
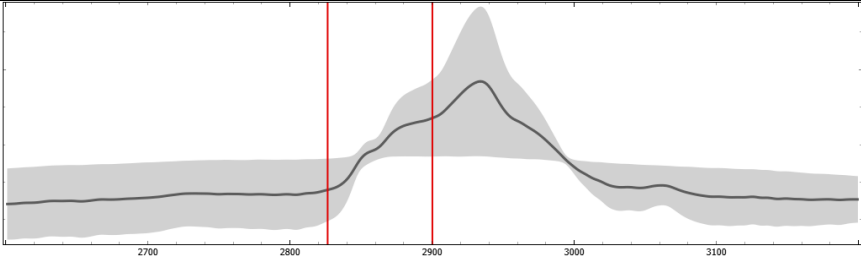
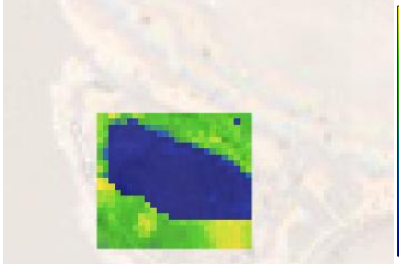
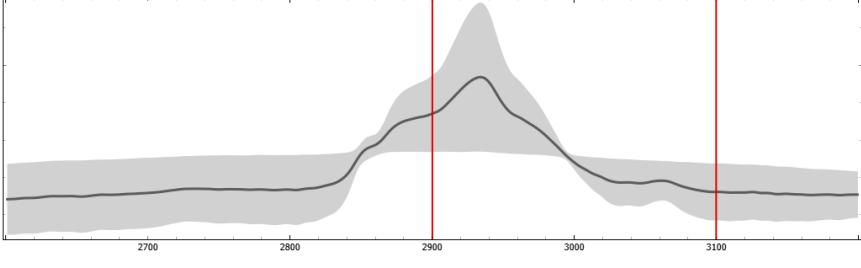


Table 15: Chemical maps, wavenumbers and localisations of molecules in the high wavenumber region of granulated 10ng/mL dosed cochlear fibrocytes’ spectrum analysed by hyperspectral Raman spectroscopy.

Image	Spectrum	Wavenumber	Strongest localisation
		2824-2896cm <sup>-1</sup>	Nucleus and surroundings
		2896-3100cm <sup>-1</sup>	Cytoplasm

Beginning, as before in the lower end of the fingerprint region ( $<600\text{cm}^{-1}$ ), visible differences may be identified in bands, signal intensity, and localisation. Though some bands are identified, true peaks in this region are scarce and of greatly reduced intensity in comparison to both the undosed pair and non-granulated pair of cells observed. This reduced intensity is accompanied by ambiguous chemical maps, with minimal evidence of membrane localisation seen. Considering the intensity reduction noted in non-granulated dosed cells, it may be speculated that the spectral results seen for granulated cells reflect a more severe form of the intercellular transport decline hypothesised.

Moving to spectral region  $589\text{-}692\text{cm}^{-1}$ , localisation is once again ambiguous. Nonetheless, bands identified in the previously observed dosed cells are noted in the granular cells at  $600\text{cm}^{-1}$  ( $\sim 4\text{cm}^{-1}$  shift from non-granular cells),  $626\text{cm}^{-1}$  ( $\sim 1\text{cm}^{-1}$  shift from non-granular cells),  $645\text{cm}^{-1}$  ( $\sim 2\text{cm}^{-1}$  shift from non-granular cells),  $670\text{cm}^{-1}$  ( $\sim 3\text{cm}^{-1}$  shift from non-granular cells) and  $686\text{cm}^{-1}$  ( $\sim 4\text{cm}^{-1}$  shift from non-granular cells). Interestingly, the bands seen at  $600\text{cm}^{-1}$ ,  $670\text{cm}^{-1}$  and  $686\text{cm}^{-1}$  demonstrate slightly increased signal intensity compared to non-granular cells. This is potentially indicative of further alterations to amino acids and similar molecules in dosed cells and may again evidence a more severely inflamed cell.

Nucleotide bands in the region  $692\text{-}795\text{cm}^{-1}$ , occur in granulated cells with minimal shift from non-granulated counterparts at  $725\text{cm}^{-1}$ ,  $756\text{cm}^{-1}$  and  $785\text{cm}^{-1}$  ( $\sim 2\text{cm}^{-1}$  shift). These bands, however, demonstrate reduced signal intensity and ambiguous localisation in the granulated cell sample. Such reduced signal intensity in DNA/RNA associated bands is consistent with apoptotic cells <sup>[223]</sup> and supports the hypothesis that the granular cells seen are, for some reason, more severely inflamed.

In the  $795\text{-}982\text{cm}^{-1}$  region, reduced signal intensity, ambiguous localisation and difficulty in resolving peaks is seen in the granular cell sample, though the spectrum seen clearly resembles the non-granulated dosed cell in peak locations. This is deduced as band shifts, where seen, are of  $<9\text{cm}^{-1}$  and are considered negligible. As such, the reduction in signal intensity across all noted peaks in this region implies a further worsened capacity for biosynthesis of coenzyme A in the observed granulated cells. This further supports the severe inflammation hypothesis for these cells.

Similarly, though the band previously identified at  $1008\text{cm}^{-1}$  is present in the granulated cell spectrum at  $1005\text{cm}^{-1}$  (shift of  $\sim 3\text{cm}^{-1}$ ), a drastically reduced signal intensity is seen compared to non-

granulated dosed cells and undosed neighbouring cells observed. This not only implies the termination of anti-inflammatory responses hypothesized in the previous dosed sample, it further suggests that granulated dosed cells such as those observed are subject to reduced capacity for biosynthesis.

Again, in the region  $1019\text{-}1145\text{cm}^{-1}$ , though peak resolution is tricky, bands resemble those seen in non-granulated dosed cells with signal intensity in most cases reduced. However, despite this reduced signal intensity, lipid-associated areas seem to arise more widely in granulated cells than their non-granulated counterparts. Whether this occurs as a result of lipid accumulation/depletion in certain cell areas, or as a by-product of reduced organelle membrane integrity within cells is unclear.

In contrast, the bands noted at  $1160\text{cm}^{-1}$  and  $1179\text{cm}^{-1}$  demonstrate a greater signal intensity in granulated dosed cells as well as a more widespread molecular distribution in the sampled area. Though precise origins of these bands are unknown in terms of molecule, such increases in signal intensity may imply fatty acid accumulation in the granulated cells observed.

Unlike previous spectral regions noted, where variation appears to arise predominantly from signal intensity changes across samples, the region  $1187\text{-}1423\text{cm}^{-1}$  demonstrates differences in both signal intensity and molecular localisation. The band at  $1208\text{cm}^{-1}$  ( $\sim 2\text{cm}^{-1}$  shift from non-granular cells) demonstrates a reduced peak clarity and strong molecular localisation at a point in the cytoplasm potentially indicative of a large organelle. The band at  $1257\text{cm}^{-1}$  ( $\sim 3\text{cm}^{-1}$  shift from non-granular cells) demonstrates reduced signal intensity and a lack of presence in the nucleus. The band at  $1277\text{cm}^{-1}$  ( $\sim 8\text{cm}^{-1}$  shift from non-granular cells) demonstrates a similar intensity reduction. The band at  $1313\text{cm}^{-1}$  ( $\sim 5\text{cm}^{-1}$  shift from non-granular cells), like that at  $1257\text{cm}^{-1}$ , demonstrates reduced signal intensity and a lack of presence in the nucleus. The band at  $1340\text{cm}^{-1}$  ( $\sim 3\text{cm}^{-1}$  shift from non-granular cells) demonstrates a similar intensity reduction. In contrast, the band at  $1393\text{cm}^{-1}$  ( $\sim 2\text{cm}^{-1}$  shift from non-granular cells) demonstrates a slight increase in signal intensity. Based upon these observations, and the prior identification of bands in this region as attributable to C-O stretching, this spectral region is assumed to predominantly correspond to proteins. This being assumed, the reductions in signal intensity, where seen, are consistent expectations of apoptotic cells <sup>[223]</sup>. This further implies that, where increased intensity is seen, lipid bond vibrations may be implicated.

This, however, is contrasted by the band at  $1449\text{cm}^{-1}$  ( $\sim 1\text{cm}^{-1}$  shift from non-granular cells), which demonstrates a substantially reduced signal intensity in comparison with non-granular dosed cells. This contrasts with the findings of previous chapters and lends uncertainty as to the reliability of the spectral variations seen across the granulated cell sample. Nonetheless, considering the wide error margin noted for this sample, the hypothesis outlined is still feasible within the bounds of observed error.

In contrast to non-granular dosed cells, the granular cells samples demonstrate peaks at  $1512\text{cm}^{-1}$  and  $1525\text{cm}^{-1}$  similar to those seen in the undosed cell pair. These peaks arise in both nuclear and cytoplasmic regions at greater signal intensity than in other spectra and are attributed to amide bond vibrations. This contrasts with the findings of previous chapters and suggests potential structural changes in proteins in the granulated cells observed, particularly in the nuclear region where molecular distribution was previously not noted.

Similarly, in the region  $1531\text{-}1632\text{cm}^{-1}$ , the bands seen resemble those noted in the non-granulated dosed cell, though they demonstrate increased signal intensity and presence in the nucleus of cells as well as the cytoplasm. These bands are attributed to tryptophan stretching, aromatic ring vibrations, C=O stretching and benzene ring deformations, with their increased intensity in granulated cell nuclei further suggesting protein alterations and changes to essential molecules such as phenylalanine.

The clear band at  $1659\text{cm}^{-1}$  ( $\sim 1\text{cm}^{-1}$  shift from non-granular cells) demonstrates similar localisation to that seen in non-granular dosed cells, though signal intensity is substantially reduced compared to both dosed and undosed cell pairs previously examined. This contrasts with other protein-associated spectral regions identified in granular cells as well as with expectations of further signal intensity increase based on non-granular dosed cells and previous chapter results. However, intensity reduction in this band is consistent with literature surrounding apoptosis and further emphasises likely changes to protein structure and abundance in inflamed cells.

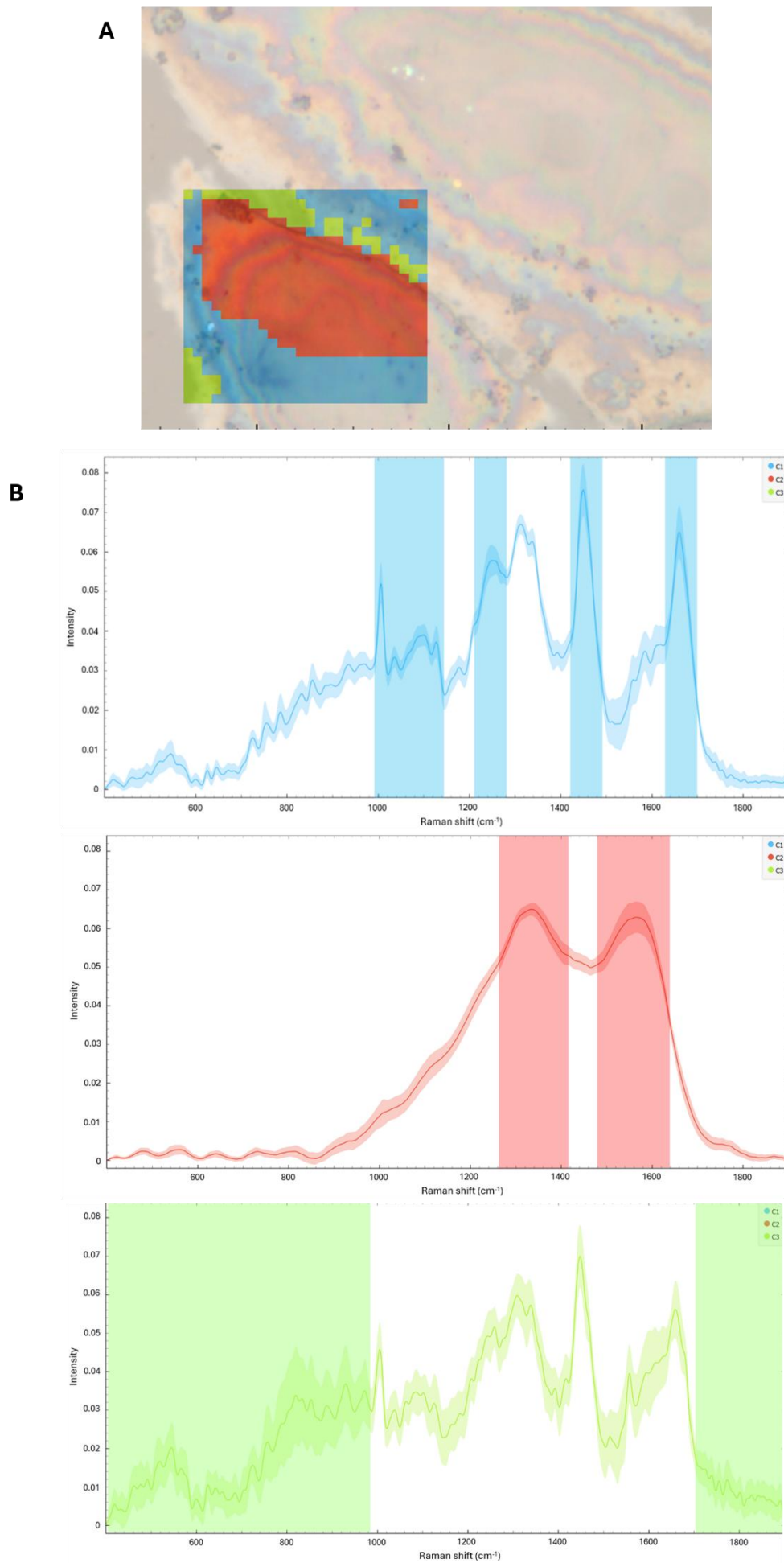


**Figure 96: K-means clustering of hyperspectral Raman data – 10ng/mL dosed granular cell.**

**A) Chemical map. B) Spectra.**

Finally, in the region  $1717\text{-}1900\text{cm}^{-1}$  clear peaks cannot be resolved with confidence. Nonetheless, this region appears to demonstrate increased signal intensity compared to other samples examined as well as molecular distribution throughout cytoplasmic and nuclear regions. This observation may indicate alterations to lipid abundance in cells, but firm conclusions cannot be made based on the data shown. Arguably, it is equally feasible that the variation seen in this spectral region is a result of spectral baseline deformation due to abnormal cell topography/density.

K-means analysis (Fig. 96) once again demonstrates distinction between nucleic, cytoplasmic and membrane/intersection regions, though distinction across these regions is less clear than in other samples. In particular, the nuclear and surrounding region demonstrates an unusual spectrum which, though dominated by protein-attributable signal, indicates poor localisation, limited nucleic acid signal and potential changes to nuclear envelope integrity. Contrary to expectations, membrane related signal in this cell pair appears to demonstrate polysaccharide and protein signal indicative of intercellular transport. However, localisation is indistinct and variation around the spectral average suggests large variability. As such, transport is believed to still be impaired in comparison to undosed cells in contact.

In the high wavenumber region, a substantial reduction in signal intensity is seen in the granulated cell pair compared with other samples. The large central peak at  $2934\text{cm}^{-1}$  is still present though, unlike other samples, does not show nuclear presence in cell chemical maps. In contrast, the smaller neighbouring band at  $3062\text{cm}^{-1}$  demonstrates nuclear presence where previously unseen. These results further imply protein alterations in the granulated cell observed. No K-means analysis was conducted on high wavenumber region data due to relative lack of localisation in this spectral region.

Overall, spectral results for the granulated cell demonstrate various alterations consistent with increased cell inflammation and potential apoptosis, as well as some alterations that challenge this suggestion. Due to the large error margin noted for this sample as well as potential baseline changes, the non-granular dosed cell is considered a more reliable example of inflammatory response in cochlear fibrocytes, with an overview of spectral changes between non-granular dosed and undosed cell pairs presented in Table 16 below. Nonetheless, the presence of such granular cells with

unusual spectral profiles should not be ignored, as such cells may represent a portion of the intra-condition variation seen in other results. Such factors are considered when examining FTIR data.

**Table 16: Summary of Raman Spectral Changes in Cochlear Fibrocytes in Response to IL-1 $\beta$  Stimulation**

Wavenumber Region (cm <sup>-1</sup> )	Peak Assignment	Change in Response to Cytokine Stimulation (10 ng/mL IL-1 $\beta$ )
400–593	CH <sub>2</sub> bending, C-C-C deformations	Reduced signal intensity and clarity of bands observed in undosed cells, indicating altered intercellular transport.
593–693	CH <sub>2</sub> bending, amide IV, C-S stretching, nucleotide ring breathing	Peak shift ( $\sim 3\text{cm}^{-1}$ ) noted in $644\text{cm}^{-1}$ band (amide). Peak shift ( $\sim 2\text{cm}^{-1}$ ) in $667\text{cm}^{-1}$ and ( $\sim 8\text{cm}^{-1}$ ) in $682\text{cm}^{-1}$ band, potentially indicative of alterations to amino acid or nucleotide presence. Localisation variation.
693–734	Adenine bond vibrations	Peak shift ( $\sim 2\text{cm}^{-1}$ ) in $725\text{cm}^{-1}$ band, potentially indicative of nucleotide modifications.
734–772	Thymine bond vibrations	Peak shift ( $\sim 3\text{cm}^{-1}$ ) in $725\text{cm}^{-1}$ band, potentially indicative of nucleotide modifications.
772–802	Cytosine bond vibrations	Peak shift ( $\sim 4\text{cm}^{-1}$ ) in $725\text{cm}^{-1}$ band, potentially indicative of nucleotide modifications.
802–890	C-H ring bending, C-O stretching, guanine ring deformation, C-C stretching, CH bending	Peak shift ( $\sim 3\text{cm}^{-1}$ ) in $833\text{cm}^{-1}$ band, ( $\sim 1\text{cm}^{-1}$ ) in $857\text{cm}^{-1}$ band. Lack of coenzyme A-associated bands identified in undosed cells may imply a reduction in coenzyme A production – potential reduced capacity for biosynthesis of essential molecules.
980–1024	Phenyl ring breathing (Tyrosine, Phenylalanine)	Increased intensity, potential evidence of anti-inflammatory response.
1024–1046	CH <sub>3</sub> wagging	Slight peak shift ( $\sim 3\text{cm}^{-1}$ ), similar intensity.
1046–1147	NH <sub>2</sub> twisting, lipid bond vibrations, CH <sub>3</sub> wagging	Triple peak region is resolved to three clear bands at $1070\text{cm}^{-1}$ , $1085\text{cm}^{-1}$ , $1103\text{cm}^{-1}$ . Peak shift ( $\sim 5\text{cm}^{-1}$ ) in $1131\text{cm}^{-1}$ band suggesting potential lipid alterations.
1147–1190	C-C stretching, lipid bond vibrations	No notable variations seen.
1190–1408	C-O stretching, C=C vibrations, amide III	Peak shift ( $\sim 4\text{cm}^{-1}$ ) in $1254\text{cm}^{-1}$ band, ( $\sim 7\text{cm}^{-1}$ shift) in $1269\text{cm}^{-1}$ band and ( $\sim 1\text{cm}^{-1}$ shift) in $1337\text{cm}^{-1}$ band, suggestive of potential lipid/protein variations. Peak shift ( $\sim 5\text{cm}^{-1}$ ) and increased signal intensity in $1318\text{cm}^{-1}$ suggestive of C-O stretching alterations. Some localisation variation.
1408–1526	CH <sub>2</sub> /CH <sub>3</sub> bending (Lipids)	Peak shift ( $\sim 3\text{cm}^{-1}$ ) and increased intensity, suggesting lipid accumulation.

1526-1629	Amide bond vibrations, tryptophan stretching, aromatic ring vibrations, C=O stretching, benzene ring deformations.	Clarity of bands reduced.
1629-1715	C=O stretching	Increased signal intensity and altered localisation - distribution of signal throughout cytoplasm and membrane. Potentially indicative of protein/lipid accumulation, alterations in protein secondary structures and changes in membrane integrity.
1715–1900	C=O stretching	Changes in band location, band clarity, signal intensity and localisation. Peak shifts ( $\sim 3\text{ cm}^{-1}$ ) in $1816\text{cm}^{-1}$ band, ( $\sim 6\text{cm}^{-1}$ ) in $1833\text{cm}^{-1}$ band, ( $\sim 4\text{cm}^{-1}$ ) in $1890\text{cm}^{-1}$ band. Reduced band intensity and broader localisation throughout sampled cell area. Some bands noted in undosed cells not distinguished. Potentially indicative of membrane degradation and transport alterations.
2824–3100	$\text{CH}_2/\text{CH}_3$ stretching (Proteins)	Peak shift ( $\sim 3\text{ cm}^{-1}$ ), similar localisation and intensity.

Focusing in particular on variations between undosed and dosed (non-granular) cell pairs, findings from Raman spectral analysis of cochlear fibrocytes stimulated with IL-1 $\beta$  reveal distinct molecular changes when compared to undosed controls. Though it should be noted that many peak shifts observed fall below the spectral resolution of the instrument (maximum  $5\text{cm}^{-1}$ ) and cannot be taken as reliable alone, overall spectral variations reflect alterations in protein, lipid, and nucleotide-associated regions, suggesting cellular responses to cytokine exposure.

Notable variations are summarised as follows (around Table 16)- peaks associated with nucleotide vibrations indicate potential modifications in DNA/RNA structures or interactions. The absence of coenzyme A-associated peaks in dosed cells may suggest a reduced biosynthetic capacity in stimulated fibrocytes. Increased intensity in the phenyl ring breathing region implies upregulated protein synthesis, possibly as part of an anti-inflammatory or stress response. Shifts, localisation and intensity changes in lipid-associated regions suggest alterations in membrane composition<sup>[223]</sup> and potential lipid accumulation (commonly associated with inflammation and inherently linked to cytokine secretion<sup>[275]</sup>). Increased intensity in protein-related bands suggests protein accumulation, potentially reflecting inflammation-associated structural changes or downstream cytokine production.

While such downstream cytokine production such as IL-6 and IL-8 accumulation cannot be directly identified from spectral results, observed spectral changes may be linked to their production. As mentioned, increased intensity in the phenyl ring breathing-associated region suggests upregulated protein synthesis which, in an inflammatory response, could indicate presence of downstream cytokines such as IL-6 and IL-8 <sup>[217]</sup>. Similarly, changes in other protein associated regions (e.g. amide I) may indicate protein accumulation possibly related to cytokine production. Similarly, the noted lipid accumulation, believed to be suggestive of membrane alterations <sup>[223]</sup>, may also be linked to cytokine secretion pathways. Alterations in these spectral regions (particularly in protein-related and lipid-associated peaks) align with known biological mechanisms of cytokine response. If desired in future research, to definitively confirm IL-6 and IL-8 presence, complementary biochemical assays are recommended.

Overall, though not associated with distinct downstream cytokine production, Raman findings indicate that IL-1 $\beta$  stimulation elicits notable biochemical alterations in fibrocytes consistent with expected inflammatory and cellular stress responses. Thus, findings demonstrate promise in seeking to distinguish between inflamed and healthy cells via spectroscopic methods.

#### 4.4.2. S-FTIR – Spectral Analysis and PCA

Ahead of analysing S-FTIR dosage data, similarity of low and high seeding density cell samples must be assessed. With this in mind, PCA of low vs high seeding density controls is presented in figure 97 below. In this analysis, 87% of variance was accounted for in 3 principal components.

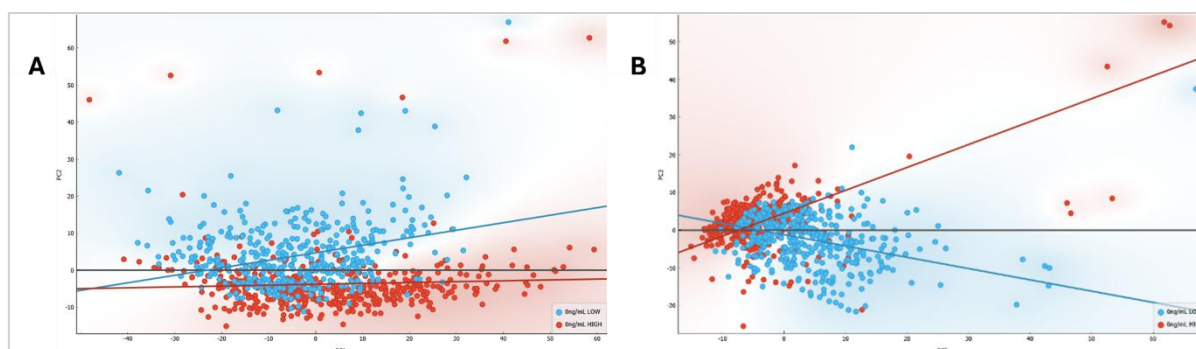


**Figure 97: PCA scatter plots of low vs high cell seeding density samples analysed by S-FTIR. From average S-FTIR spectra of ~1000 (per dosage condition and seeding density) cochlear fibrocytes cytospun on CaF<sub>2</sub>. Cells cytospun and fixed at maximum P8. Spectra collected at Diamond Light Source, Oxford, UK. A) PC1 (58%) vs PC2 (18.4%) B) PC2 (18.4%) vs PC3 (10.4%)**

It is clear from these plots that cell spectra are variable depending on seeding condition, with some overlap between groups where cell spectra are similar. Sources of variation may be seen from the loadings plot below (Fig. 98) This is as expected based Raman hyperspectral data, which indicated spectral changes arising from contact with neighbouring cells. Cells are more likely to be in contact with neighbours in the high seeding density condition. Both conditions may be considered physiologically relevant as *in vivo* cochlear fibrocytes are densely packed when healthy, with numbers and density depleting as cells become inflamed and die off.

From the loadings plot of the first three principal components, it is apparent that variation between seeding density groups arises mainly from protein-associated regions. This is consistent with expectations of inflammation.

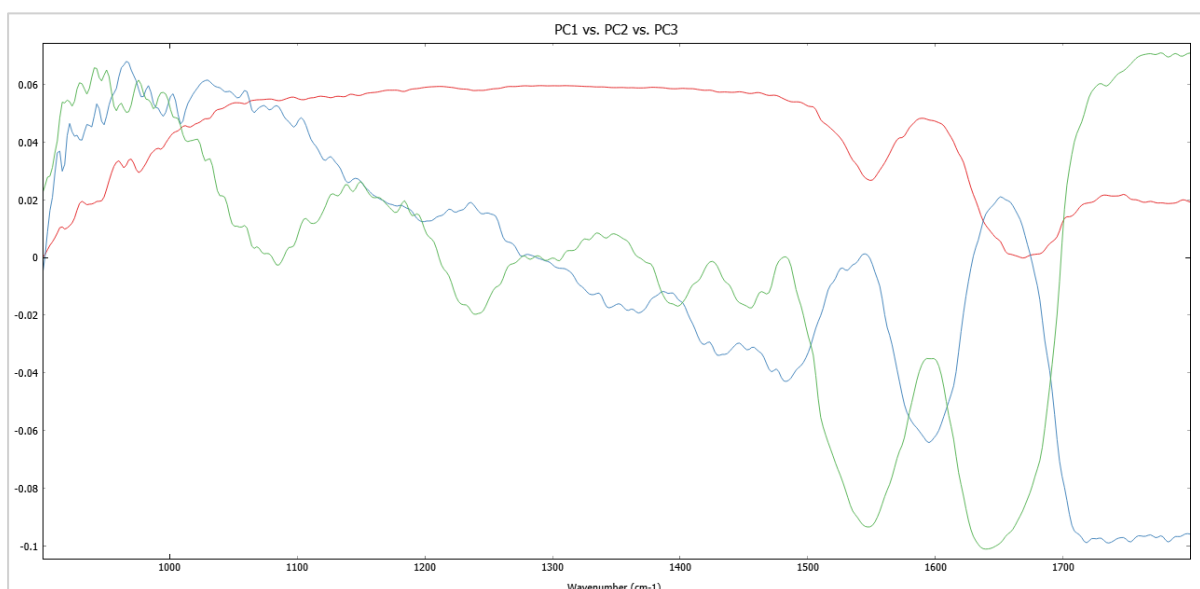


**Figure 98: Loadings plot of low vs high cell seeding density sample PCA.**

**From PCA of average S-FTIR spectra of ~1000 (per dosage condition and seeding density) cochlear fibrocytes cytopun on CaF<sub>2</sub>. Cells cytopun and fixed at maximum P8. Spectra collected at Diamond Light Source, Oxford, UK.**

In the interest of maintaining accuracy whilst enabling the broadest representation of cell variables, comparisons of neural network dosage classification performance were made between low, high and mixed groups. As shown in table 17 below, mixing seeding density conditions does not appear to greatly affect model confidence, with only a slight reduction in accuracy noted. This suggests that, while seeding is a source of variation, dosage condition can still be distinguished above this. By increasing training data access (from 50:50 to 70:30 train to test) the model is improved (table 18). Again, mixing cell seeding density has only a small effect on model confidence. With this in mind, further comparisons are made on low and high seeded cells together to allow for broader representation of cell variety in dosage distinction analyses.

**Table 17: Confidence tables for 50:50 neural network modelling of low, high and mixed cell seeding densities.**

	Low						High						Mixed						
FP	Predicted						Predicted						Predicted						
		0ng/mL	1ng/mL	5ng/mL	10ng/mL	Σ		0ng/mL	1ng/mL	5ng/mL	10ng/mL	Σ		0ng/mL	1ng/mL	5ng/mL	10ng/mL	Σ	
	Actual	0ng/mL	84.2 %	10.2 %	3.3 %	2.3 %	1045	0ng/mL	86.3 %	3.2 %	5.9 %	4.6 %	1100	0ng/mL	83.5 %	6.6 %	5.9 %	4.0 %	2140
		1ng/mL	8.8 %	85.2 %	5.0 %	1.0 %	1135	1ng/mL	2.8 %	83.0 %	7.6 %	6.6 %	1075	1ng/mL	6.3 %	80.5 %	7.4 %	5.8 %	2215
		5ng/mL	2.5 %	8.0 %	86.4 %	3.1 %	1210	5ng/mL	2.8 %	6.0 %	88.1 %	3.0 %	1125	5ng/mL	6.5 %	7.8 %	80.1 %	5.6 %	2335
		10ng/mL	3.4 %	2.2 %	1.5 %	92.9 %	1055	10ng/mL	2.8 %	7.5 %	4.4 %	85.4 %	1120	10ng/mL	3.7 %	6.9 %	5.8 %	83.5 %	2175
	Σ	1046	1194	1153	1052	4445	Σ	1042	1079	1187	1112	4420	Σ	2159	2255	2289	2162	8865	
HW	Predicted						Predicted						Predicted						
		0ng/mL	1ng/mL	5ng/mL	10ng/mL	Σ		0ng/mL	1ng/mL	5ng/mL	10ng/mL	Σ		0ng/mL	1ng/mL	5ng/mL	10ng/mL	Σ	
	Actual	0ng/mL	78.5 %	17.5 %	3.1 %	1.0 %	1045	0ng/mL	80.3 %	4.9 %	7.4 %	7.5 %	1100	0ng/mL	75.6 %	13.1 %	5.9 %	5.4 %	2140
		1ng/mL	13.2 %	73.3 %	9.8 %	3.7 %	1135	1ng/mL	3.3 %	80.5 %	4.1 %	12.1 %	1075	1ng/mL	10.5 %	72.1 %	7.0 %	10.5 %	2215
		5ng/mL	3.1 %	8.5 %	82.7 %	5.7 %	1210	5ng/mL	2.8 %	4.8 %	85.2 %	7.2 %	1125	5ng/mL	2.4 %	6.4 %	82.1 %	9.1 %	2335
		10ng/mL	4.4 %	3.8 %	4.1 %	87.8 %	1055	10ng/mL	3.7 %	11.3 %	7.0 %	78.0 %	1120	10ng/mL	4.9 %	11.0 %	9.3 %	74.9 %	2175
	Σ	1053	1158	1187	1047	4445	Σ	991	1100	1162	1167	4420	Σ	2012	2265	2399	2189	8865	

**Table 18: Confidence tables for 70:30 neural network modelling of low, high and mixed cell seeding densities.**

	Low						High						Mixed								
FP	Predicted						Predicted						Predicted								
		0ng/mL	1ng/mL	5ng/mL	10ng/mL	Σ		0ng/mL	1ng/mL	5ng/mL	10ng/mL	Σ		0ng/mL	1ng/mL	5ng/mL	10ng/mL	Σ			
	Actual	0ng/mL	87.1 %	7.9 %	2.7 %	2.2 %	630	Actual	0ng/mL	92.6 %	2.7 %	2.7 %	2.0 %	660	Actual	0ng/mL	86.3 %	6.1 %	4.7 %	2.9 %	1285
		1ng/mL	5.1 %	88.7 %	5.4 %	0.7 %	680		1ng/mL	2.0 %	89.1 %	4.2 %	4.7 %	645		1ng/mL	4.2 %	84.1 %	5.8 %	5.9 %	1330
		5ng/mL	1.8 %	7.6 %	88.1 %	2.5 %	725		5ng/mL	3.3 %	4.1 %	89.5 %	3.1 %	675		5ng/mL	5.3 %	7.5 %	82.3 %	4.9 %	1400
		10ng/mL	2.8 %	1.1 %	0.5 %	95.6 %	635		10ng/mL	2.5 %	6.4 %	4.0 %	87.1 %	675		10ng/mL	3.8 %	6.6 %	4.8 %	84.8 %	1305
	Σ	615	715	696	644	2670	Σ	663	664	676	652	2655	Σ	1289	1389	1352	1290	5320			
HW	Predicted						Predicted						Predicted								
		0ng/mL	1ng/mL	5ng/mL	10ng/mL	Σ		0ng/mL	1ng/mL	5ng/mL	10ng/mL	Σ		0ng/mL	1ng/mL	5ng/mL	10ng/mL	Σ			
	Actual	0ng/mL	72.2 %	22.9 %	3.2 %	1.7 %	630	Actual	0ng/mL	85.0 %	4.5 %	3.9 %	6.5 %	660	Actual	0ng/mL	80.3 %	9.7 %	4.9 %	5.1 %	1285
		1ng/mL	10.0 %	75.9 %	10.1 %	4.0 %	680		1ng/mL	2.2 %	84.8 %	2.9 %	10.1 %	645		1ng/mL	11.6 %	72.0 %	5.3 %	11.2 %	1330
		5ng/mL	2.2 %	7.7 %	84.3 %	5.8 %	725		5ng/mL	3.6 %	4.7 %	82.1 %	9.6 %	675		5ng/mL	2.9 %	6.7 %	83.0 %	7.4 %	1400
		10ng/mL	3.0 %	2.2 %	3.6 %	91.2 %	635		10ng/mL	5.8 %	10.8 %	5.2 %	78.2 %	675		10ng/mL	4.4 %	10.0 %	7.0 %	78.6 %	1305
	Σ	558	730	723	659	2670	Σ	638	682	634	701	2655	Σ	1284	1306	1386	1344	5320			

In contrast to the supernatant data in the benchtop examinations, FTIR of dosed cells (Fig. 99) demonstrates visible variation in absorbance across dosage conditions and stronger signals overall. A greater contrast between the intensity of signals in the fingerprint and high wavenumber regions is also observed, with the fingerprint region showing a greater proportional absorbance. This is assumed to be due to the presence of cells both healthy and inflamed, as opposed to the supernatant sampling conducted in benchtop examinations.

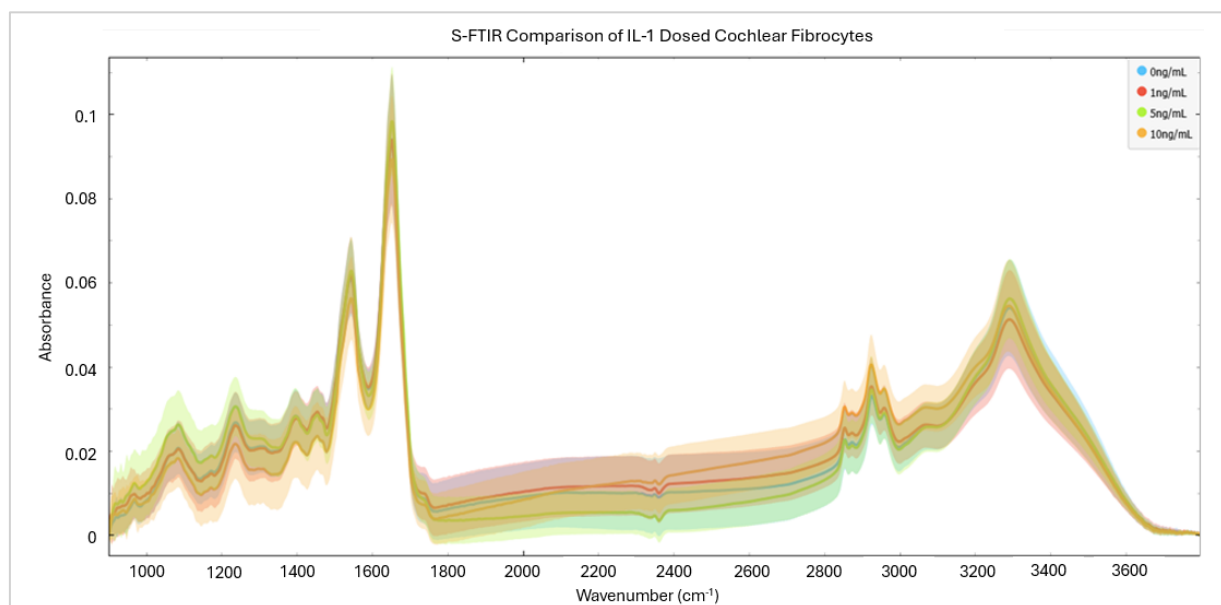


**Figure 99: Average S-FTIR spectra of dosed and undosed cochlear fibrocytes.**

**Average S-FTIR spectra of ~2000 (per dosage condition) cochlear fibrocytes cytopun on  $\text{CaF}_2$ .**

**Cells cytopun and fixed at maximum P8. Spectra collected at Diamond Light Source, Oxford.**

To enable better visualisation of spectral variations, average S-FTIR spectra are presented offset in figure 100. Though spectra demonstrate similar features, consistent with the findings of previous chapters, variations in intensity may be seen across sample conditions in both fingerprint and high wavenumber regions. Interestingly, though noise in this spectral region may affect data, the wavenumber region below  $1100\text{cm}^{-1}$  appears to demonstrate small variations in peak resolution. This area is indicative of bond vibrations in nucleic acids, carbohydrates and phospholipids, which were similarly highlighted in hyperspectral Raman investigations. As seen in previous chapters, there does

not seem to be a notable dose-response gradient arising across conditions, with spectral variations appearing most distinct between dosed and undosed cells more generally.

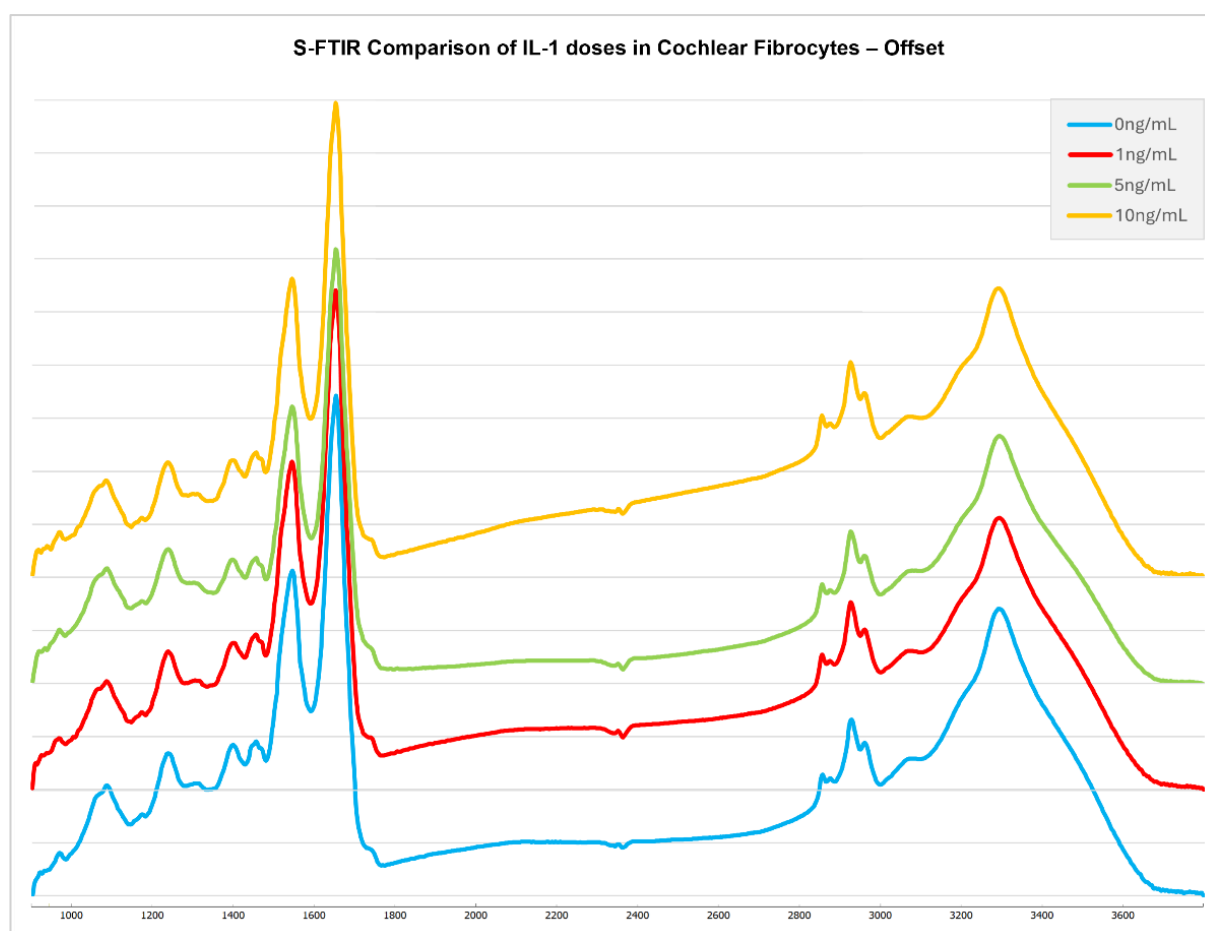


**Figure 100: Offset average S-FTIR spectra of dosed and undosed cochlear fibrocytes.**  
**Average S-FTIR spectra of ~2000 (per dosage condition) cochlear fibrocytes cytopspun on CaF<sub>2</sub>.**  
**Cells cytopspun and fixed at maximum P8. Spectra collected at Diamond Light Source, Oxford.**

By applying the second derivative and cutting spectra to regions of interest, further variations across conditions are made visible in the fingerprint (Fig. 101) and high wavenumber (Fig. 102) regions. In the fingerprint region, spectral differences are once again noted below 1000cm<sup>-1</sup>. Additionally, variation is noted at ~1527cm<sup>-1</sup>, a region typically associated with N-H bending of proteins. This variation was not noted in benchtop media-only samples or supernatant samples, suggesting that the visible difference seen arises from alterations to proteins within cells. A smaller level of distinction

may also be seen between dosed and undosed cells in the region 1115-1130 $\text{cm}^{-1}$ , a region likely attributable to C-O stretching and C-OH antisymmetric stretching in nucleic acids.

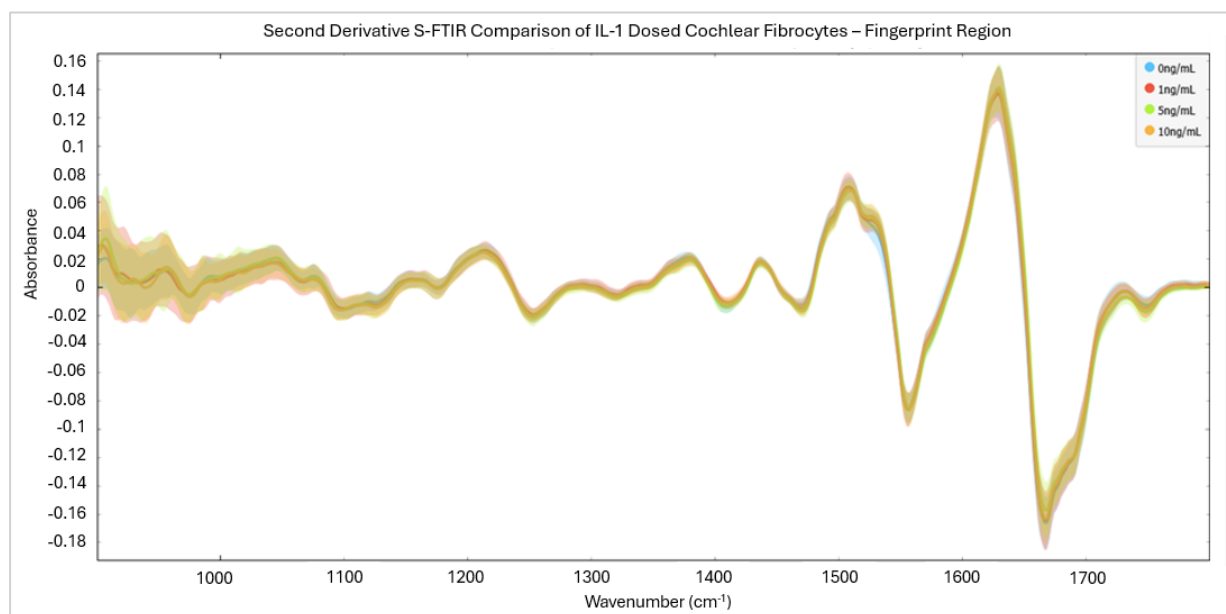


**Figure 101: Second derivative S-FTIR spectral fingerprint region of dosed and undosed cochlear fibrocytes.**

**Second derivative average S-FTIR spectra (fingerprint region) of ~2000 (per dosage condition) cochlear fibrocytes cytopun on  $\text{CaF}_2$ . Cells cytopun and fixed at maximum P8. Spectra collected at Diamond Light Source, Oxford.**

In the high wavenumber region (Fig. 102) variations between dosed and undosed cells are visible at several spectral regions, mostly below 3100 $\text{cm}^{-1}$ . Variations in this region may be attributed to  $\text{CH}_2$  stretching,  $\text{CH}_3$  stretching,  $=\text{CH}$  stretching and amide B vibrations of proteins and lipids.

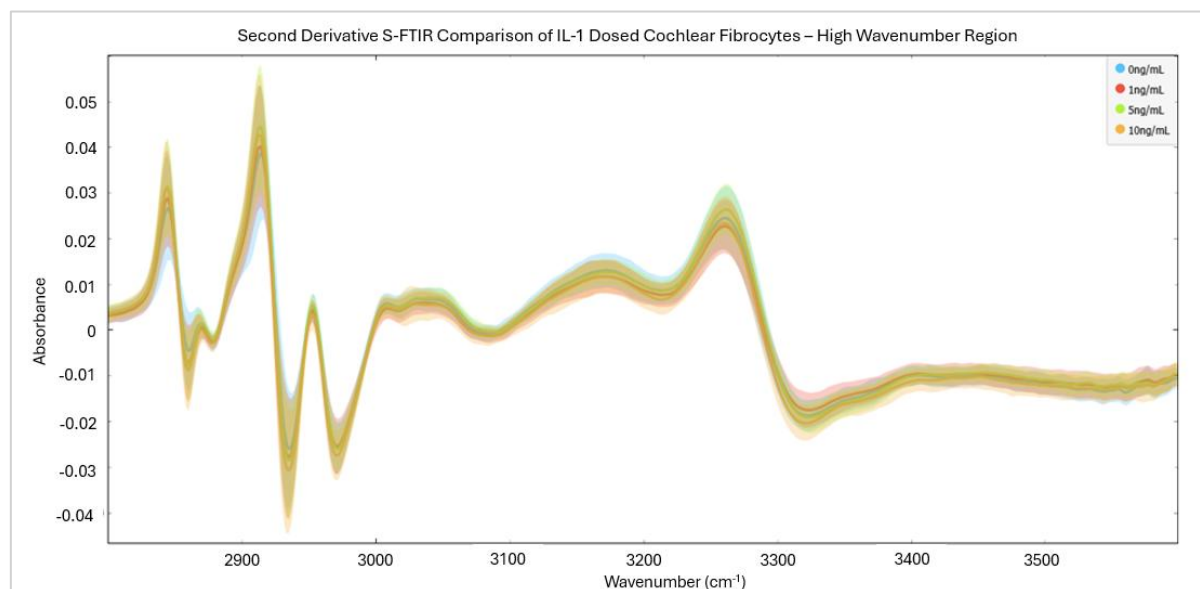


**Figure 102: Second derivative S-FTIR spectral high wavenumber region of dosed and undosed cochlear fibrocytes.**

**Second derivative average S-FTIR spectra (high wavenumber region) of ~2000 (per dosage condition) cochlear fibrocytes cytospun on CaF<sub>2</sub>. Cells cytospun and fixed at maximum P8.**

**Spectra collected at Diamond Light Source, Oxford.**

Conducting PCA on S-FTIR average spectra reveals some grouping between dosage samples and, through the employment of lines of best fit, evidences differences between conditions. PCA of the fingerprint region reveals 85% of variance accounted for in three principal components. Viewing scatter plots of PCs 1-3, some clustering is evident though data is difficult to visualise due to significant overlap between sample points (Fig. 103a, 103b). In this instance, lines of best fit are consulted to infer sample variations. Overlap of sample points is believed to be largely due to the high data volume (over 850 points per condition), with the influence of individual cellular differences (e.g. cell cycle phase) further reducing clarity. Nonetheless, the loadings plot of fingerprint region PCA (Fig. 98c) indicates variance arising between samples below 1000cm<sup>-1</sup>, and in protein associated bands such as 1550cm<sup>-1</sup>.

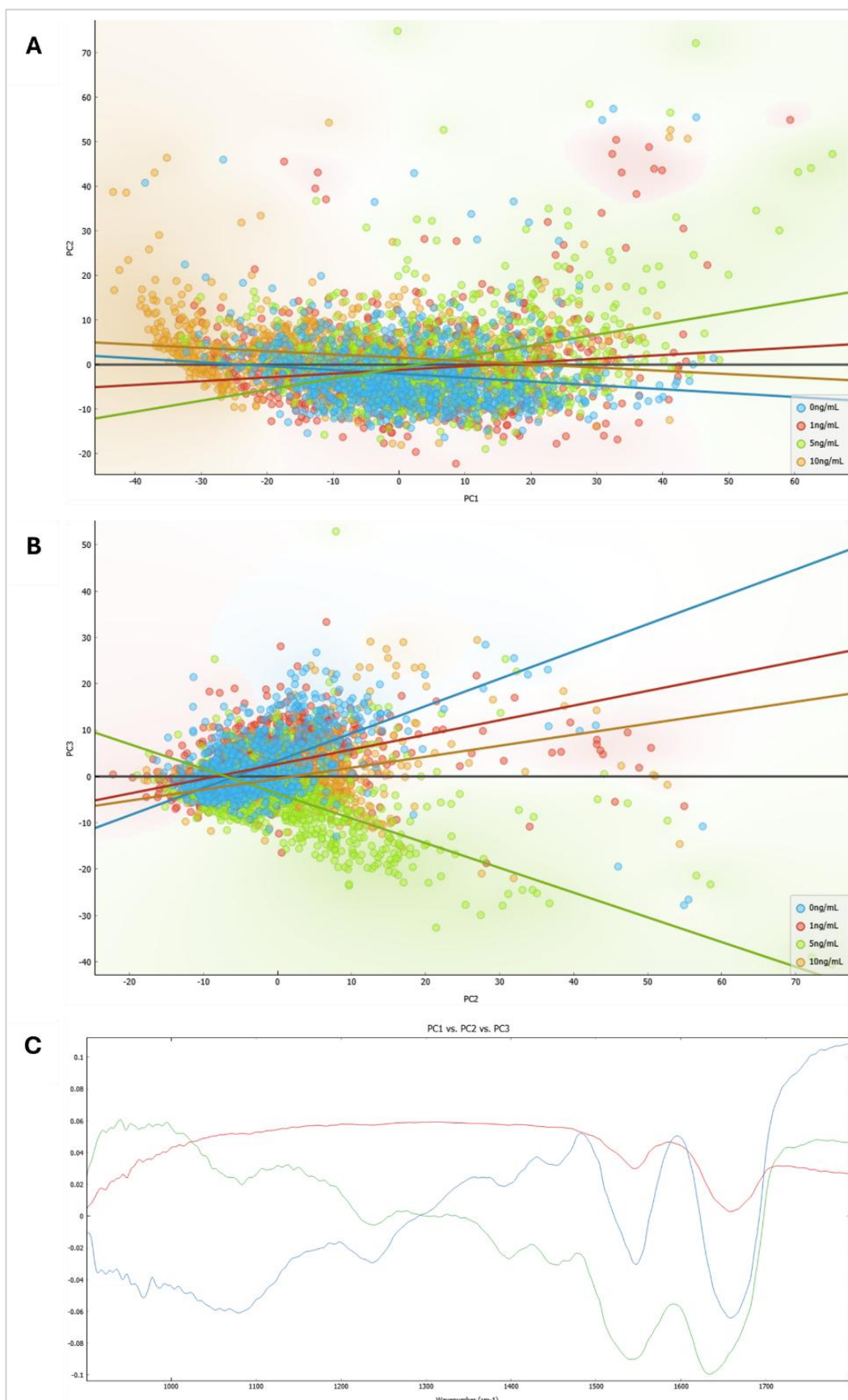


**Figure 103: PCA of the fingerprint region of IL-dosed cochlear fibrocyte S-FTIR.**  
 From average S-FTIR spectra (fingerprint region) of ~2000 (per condition) cells  
 cytopun on CaF<sub>2</sub>. A) Plot of PC1 (58%) vs PC2. (17.1%) B) Plot of PC2 (17.1%) vs PC3  
 (10.4%). C) Loadings plot of PC1 (red) vs PC2 (green) vs PC3 (blue).

PCA of the high wavenumber region reveals 97% of variance explained in three principal components. Scatter plots (Fig. 104a, 104b) similar to those for the fingerprint region demonstrate clustering, though this is tricky to visualise due to overlap. Viewing the plot of PC1 vs PC2 (Fig. 104a), lines of best fit show a clear difference between dosed and undosed samples. Loadings plots (Fig. 104c) indicate that this variation arises primarily below  $3100\text{cm}^{-1}$  in the spectral region associated with  $\text{CH}_2$  stretching,  $\text{CH}_3$  stretching,  $=\text{CH}$  stretching, and amide B vibrations of proteins and lipids.

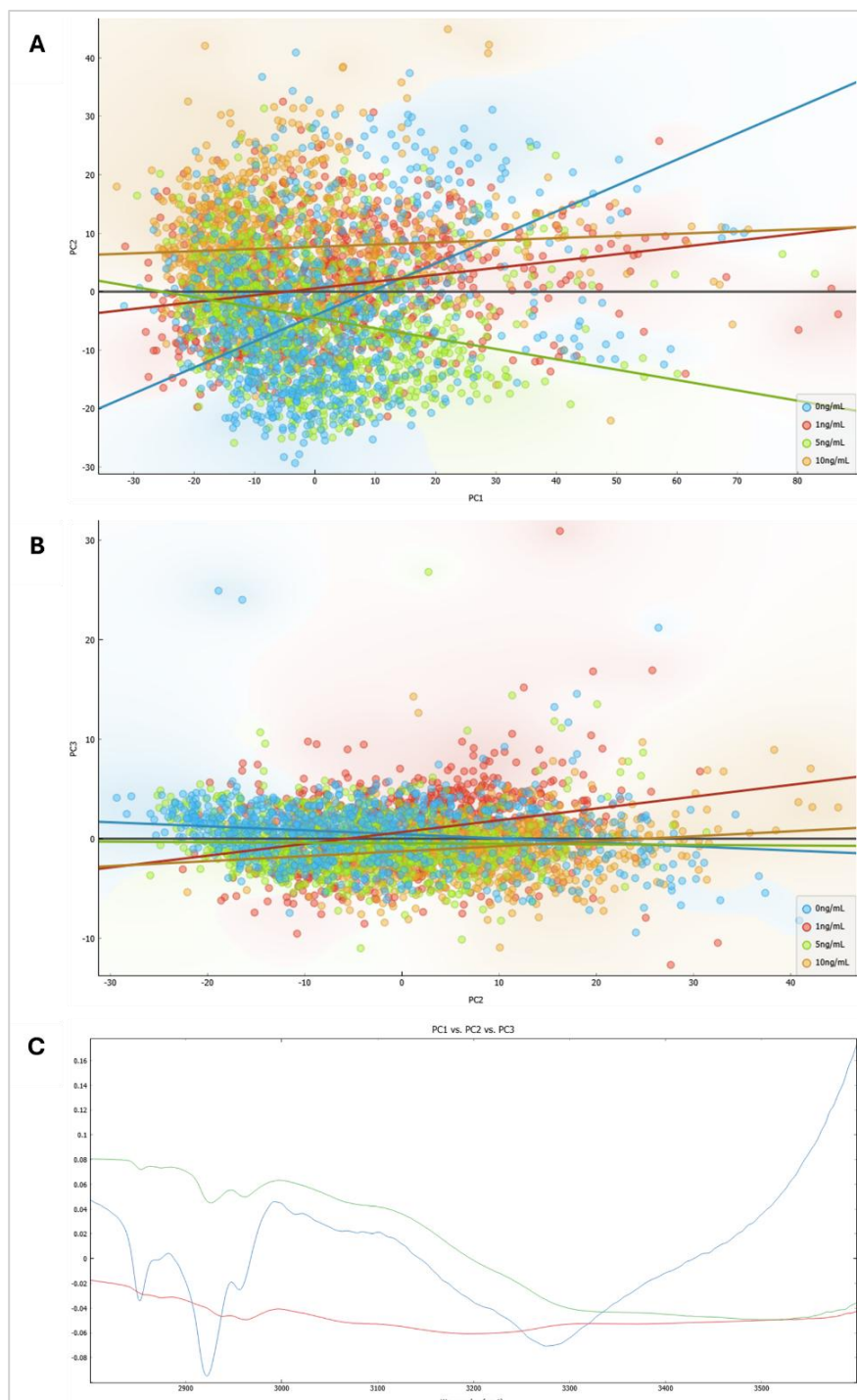


**Figure 104: PCA of the high wavenumber region of IL-dosed cochlear fibrocyte S-FTIR.**

From average S-FTIR spectra (fingerprint region) of ~2000 (per condition) cells cytopun on  $\text{CaF}_2$ . A) Scatter plot of PC1 (63%) vs PC2 (32.2%). B) Scatter plot of PC2 (32.2%) vs PC3 (2.4%). C) Loadings plot of PC1 (red) vs PC2 (green) vs PC3 (blue).

In seeking to corroborate findings of Raman analyses, the hypothesised membrane-related spectral region noted in Raman data ( $<600\text{cm}^{-1}$ ) was not viable for analysis in this section of research due to noise. Nonetheless, variations in proteins, lipids and nucleic acids are still evident. These findings are consistent with expectations of inflamed cells <sup>[215]</sup>.

To better visualise variations on a dose-by-dose basis, pairwise comparisons are conducted for 0ng/mL and each dosage condition. Beginning with 0ng/mL vs 1ng/mL, spectra do not appear to reveal substantial variation between conditions in the fingerprint region (Fig. 105). Some variation is suggested in the region below  $1000\text{cm}^{-1}$ , likely attributable to nucleic acid variations similar to those noted in Raman analysis.

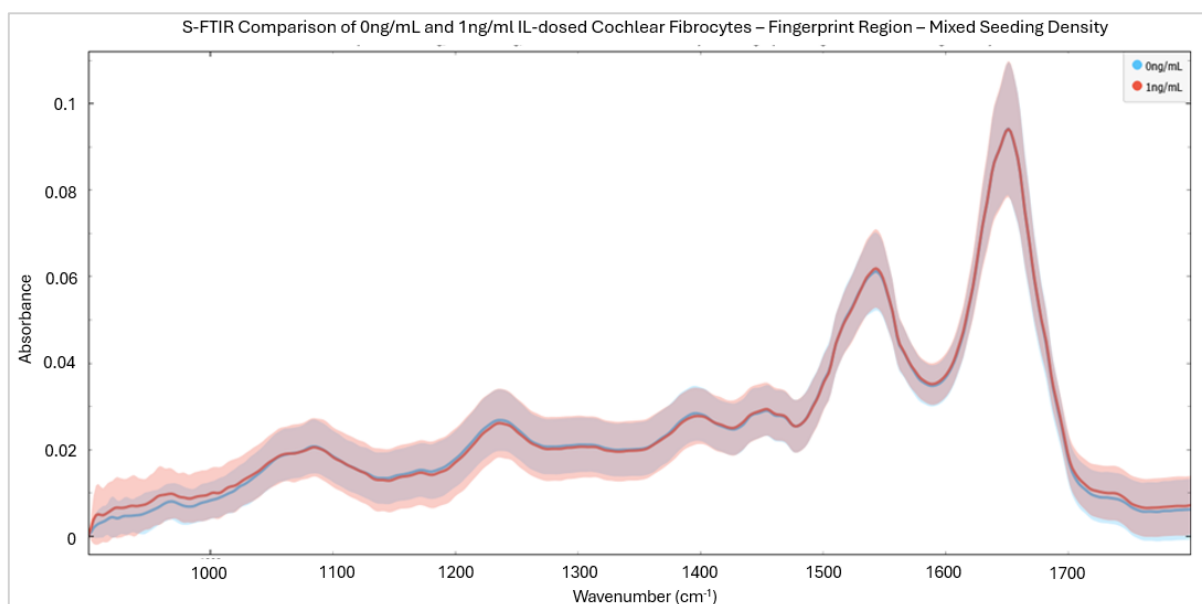


**Figure 105: Average S-FTIR fingerprint region spectra of 0ng/mL and 1ng/mL IL-dosed cochlear fibrocytes.**

**Average S-FTIR spectra (fingerprint region) of ~2000 IL-dosed vs ~2000 undosed cochlear fibrocytes cytospun on  $\text{CaF}_2$ . Cells cytospun and fixed at maximum P8. Spectra collected at Diamond Light Source, Oxford, UK.**

Applying the second derivative, a notable variation is revealed (Fig. 106). As seen in comparisons of all dosages together, second derivative spectra demonstrate a notable difference at  $1527\text{cm}^{-1}$ . This is attributed to N-H bending of proteins and may be indicative of cytokine presence in cells.

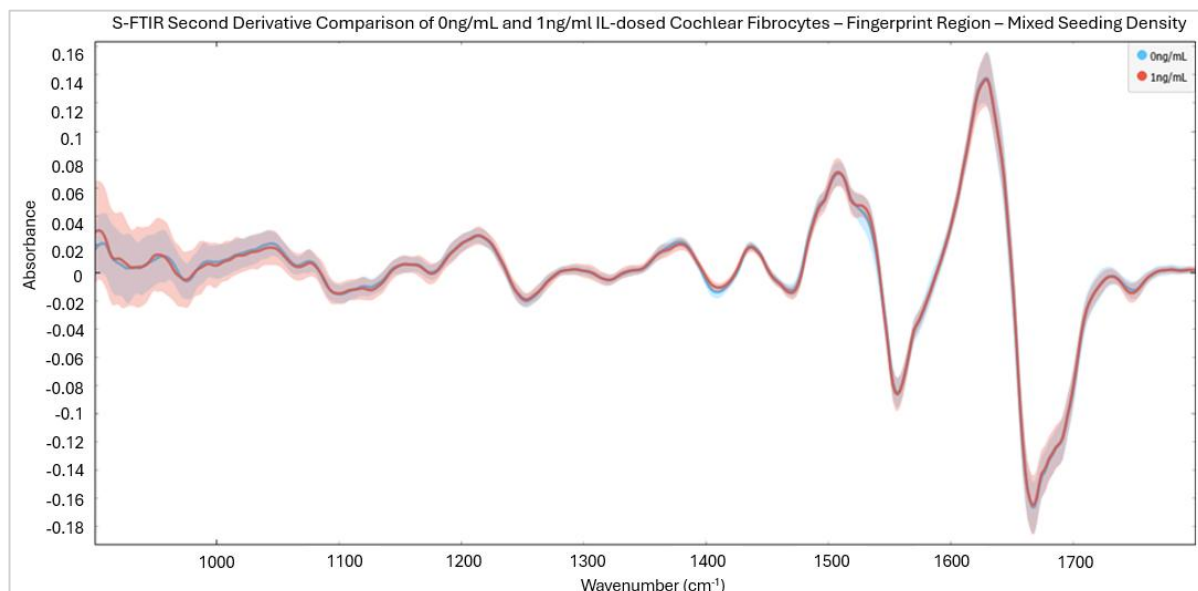


**Figure 106: Second derivative fingerprint region S-FTIR spectra of 0ng/mL and 1ng/mL IL-dosed cochlear fibrocytes.**

Second derivative average S-FTIR spectra (high wavenumber region) of ~2000 IL-dosed vs ~2000 undosed cochlear fibrocytes cytopun on CaF<sub>2</sub>. Cells cytopun and fixed at maximum P8. Spectra collected at Diamond Light Source, Oxford, UK.

Conducting PCA on 0ng/mL and 1ng/mL data confirms that there is limited distinction to be made between samples (Fig. 107). Some clustering can be seen in scatter plots, however, there is substantial overlap. This is believed to occur as 1ng/mL is the lowest dosage applied to cells and is expected to have the least effect. Thus some cells in the 1ng/mL dosed population may respond as if they are healthy. In this analysis, 85% of variance was accounted for in 3 principal components.

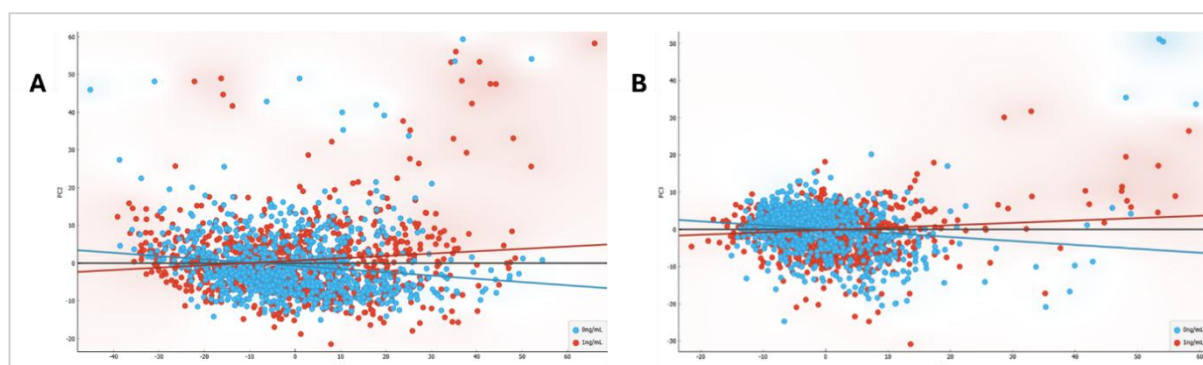


**Figure 107: PCA scatter plots of the fingerprint region of IL-dosed cochlear fibrocyte S-FTIR.**  
From average S-FTIR spectra (fingerprint region) of ~2000 IL-dosed vs ~2000 undosed cochlear fibrocytes cytopun on CaF<sub>2</sub>. Cells cytopun and fixed at maximum P8. PC1 = 58%, PC2 = 18.7%, PC3 = 8.3%.

Though conditions cannot be distinguished by eye from PCA plots, 1ng/mL-dosed cells are still distinguishable from undosed cells by neural network, discussed in section 2.4.3.

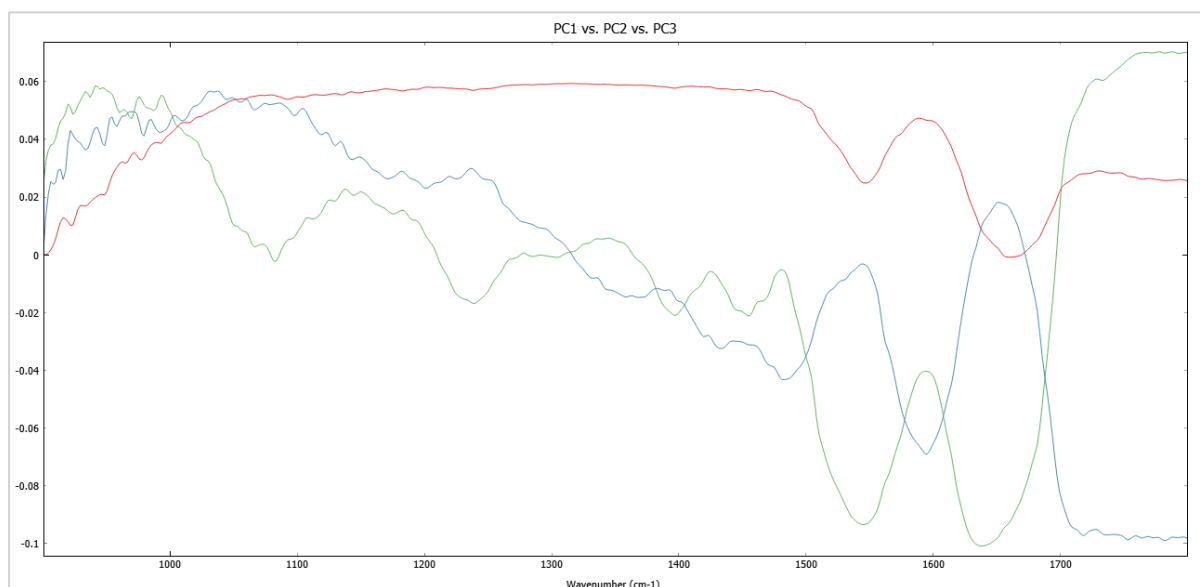


**Figure 108: PCA loadings plot of the fingerprint region of IL-dosed cochlear fibrocyte S-FTIR. From average S-FTIR spectra (fingerprint region) of ~2000 IL-dosed vs ~2000 undosed cochlear fibrocytes cytopun on CaF<sub>2</sub>. Cells cytopun and fixed at maximum P8. PC1 (red) vs PC2 (green) vs PC3 (blue).**

The loadings plot of PC1-3 reveals sources of variation between 0ng/mL and 1ng/mL dosed cells (Fig. 108). As anticipated from second derivative spectral results, the majority of variation appears to arise in protein associated regions.

\Examining the high wavenumber region of 0ng/mL and 1ng/mL spectra, further differences may be seen (Fig. 109). In this region, differences between examined dosage conditions are more apparent. The 0ng/mL condition demonstrates lower signal intensity than the 1ng/mL condition below

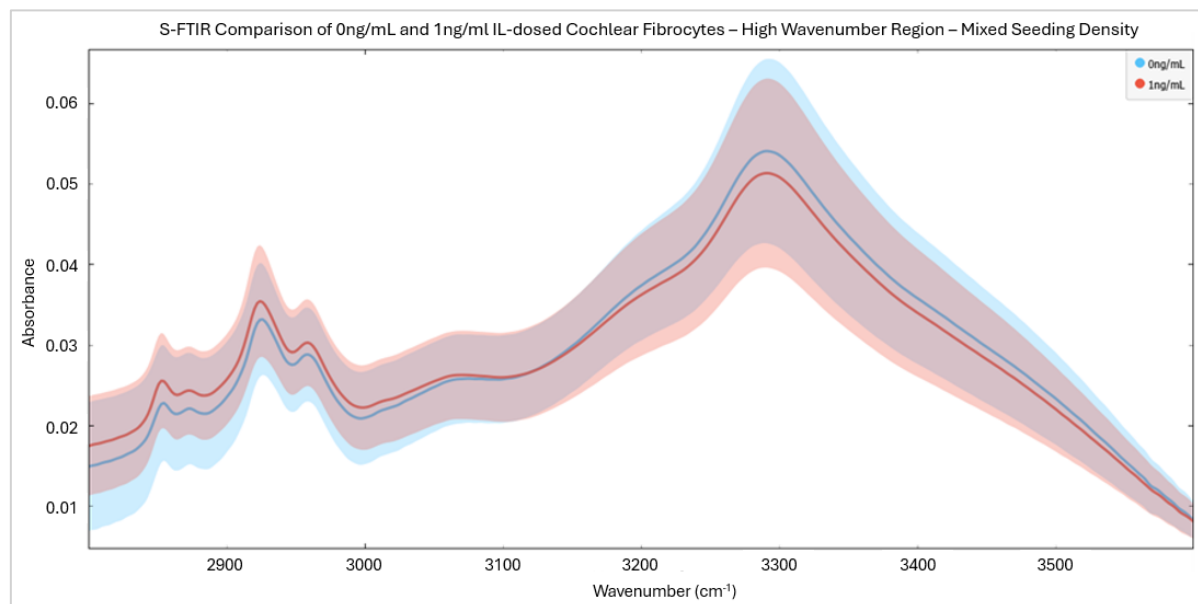


**Figure 110: Average S-FTIR high wavenumber region spectra of 0ng/mL and 1ng/mL IL-dosed cochlear fibrocytes.**

**Average S-FTIR spectra (high wavenumber region) of ~2000 IL-dosed vs ~2000 undosed cochlear fibrocytes cytopun on CaF<sub>2</sub>. Cells cytopun and fixed at maximum P8. Spectra collected at Diamond Light Source, Oxford, UK.**

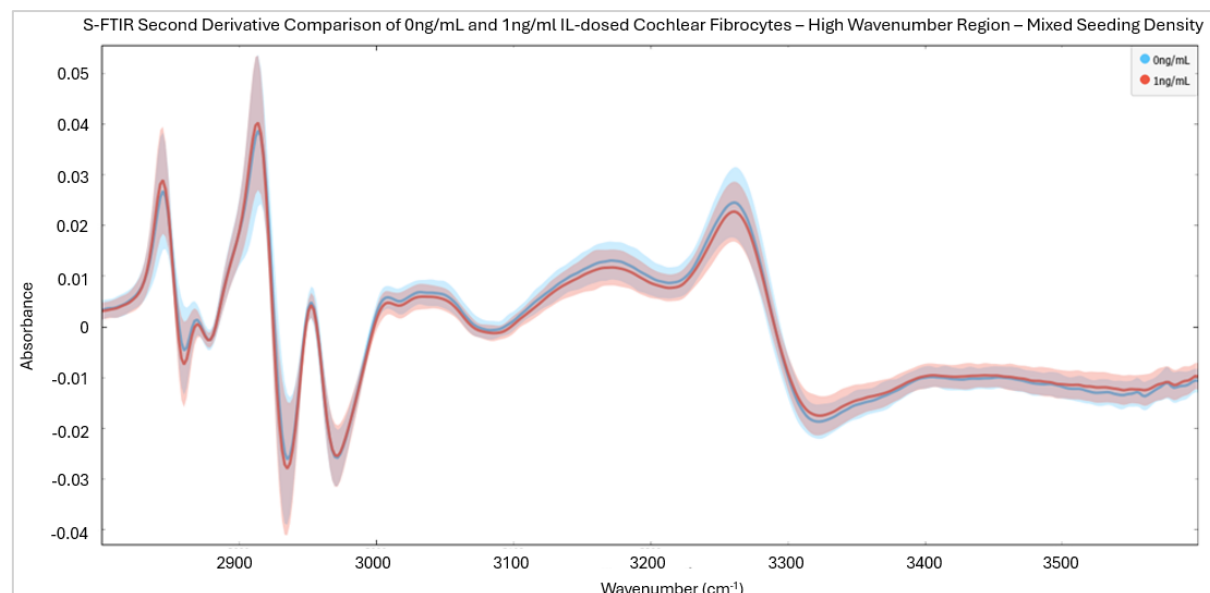


**Figure 109: Second derivative S-FTIR high wavenumber region spectra of 0ng/mL and 1ng/mL IL-dosed cochlear fibrocytes.**

**Second derivative average S-FTIR spectra (high wavenumber region) of ~2000 IL-dosed vs ~2000 undosed cochlear fibrocytes cytopun on CaF<sub>2</sub>. Cells cytopun and fixed at maximum P8. Spectra collected at Diamond Light Source, Oxford, UK.**

3100cm<sup>-1</sup> and higher signal intensity above, further suggesting protein-based alterations as well as some lipid-based changes.

Applying the second derivative to this region reveals variations at regions including 2845cm<sup>-1</sup>, 2861cm<sup>-1</sup> and 2935cm<sup>-1</sup> (Fig. 110). These regions are typically associated with bond vibrations of proteins/lipids including CH<sub>2</sub> stretching, CH<sub>3</sub> stretching, =CH stretching and amide B.

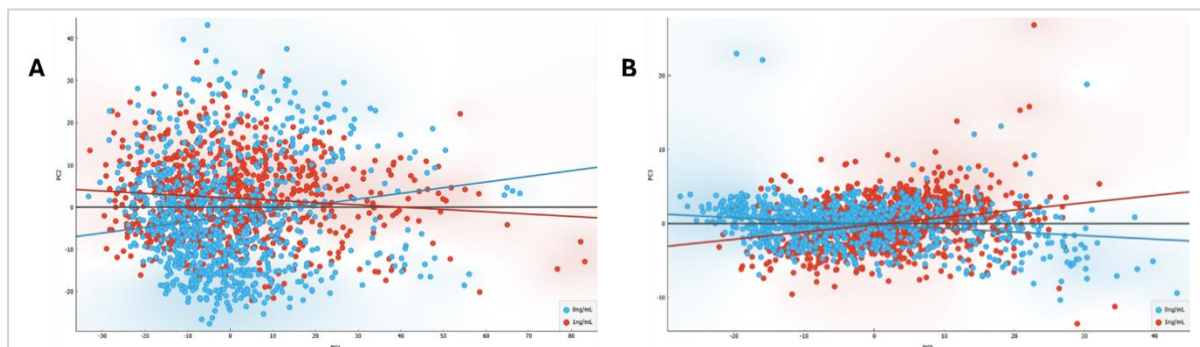


**Figure 111: PCA scatter plots of the high wavenumber region of 0ng/mL and 1ng/mL IL-dosed cochlear fibrocyte S-FTIR.**

**From average S-FTIR spectra (high wavenumber region) of ~2000 IL-dosed vs ~2000 undosed cochlear fibrocytes cytopspun on CaF<sub>2</sub>. Cells cytopspun and fixed at maximum P8. PC1 = 62.5%, PC2 = 32.7%, PC3 = 2.5%.**

PCA of high wavenumber region data is similar to that of the fingerprint region, with some clustering suggested, but little visible grouping difference between 0ng/mL and 1ng/mL-dosed cell populations (Fig. 111). In this analysis, 97% of variance was accounted for in 3 principal components.

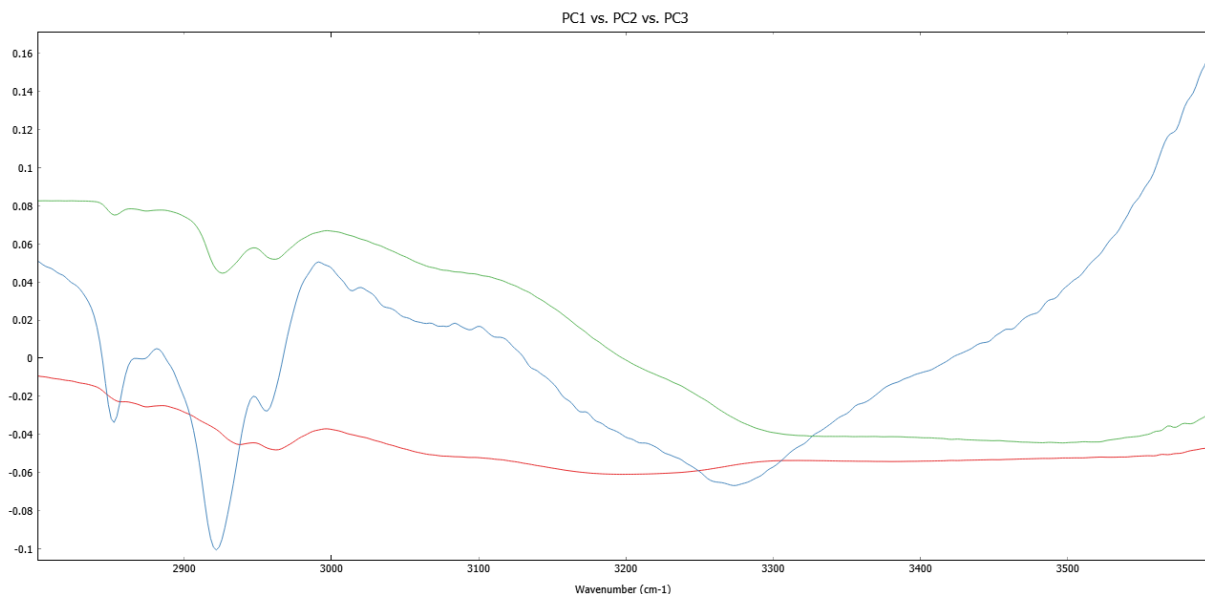


**Figure 112: PCA loadings plot of the high wavenumber region of 0ng/mL and 1ng/mL IL-dosed cochlear fibrocyte S-FTIR.**

**From average S-FTIR spectra (high wavenumber region) of ~2000 IL-dosed vs ~2000 undosed cochlear fibrocytes cytopspun on CaF<sub>2</sub>. Cells cytopspun and fixed at maximum P8. PC1 (red) vs PC2 (green) vs PC3 (blue).**

The corresponding loadings plot reveals sources of variation between doses (Fig. 112). As identified from spectra, most variation appears to arise in protein/lipid associated regions below  $3100\text{cm}^{-1}$ .

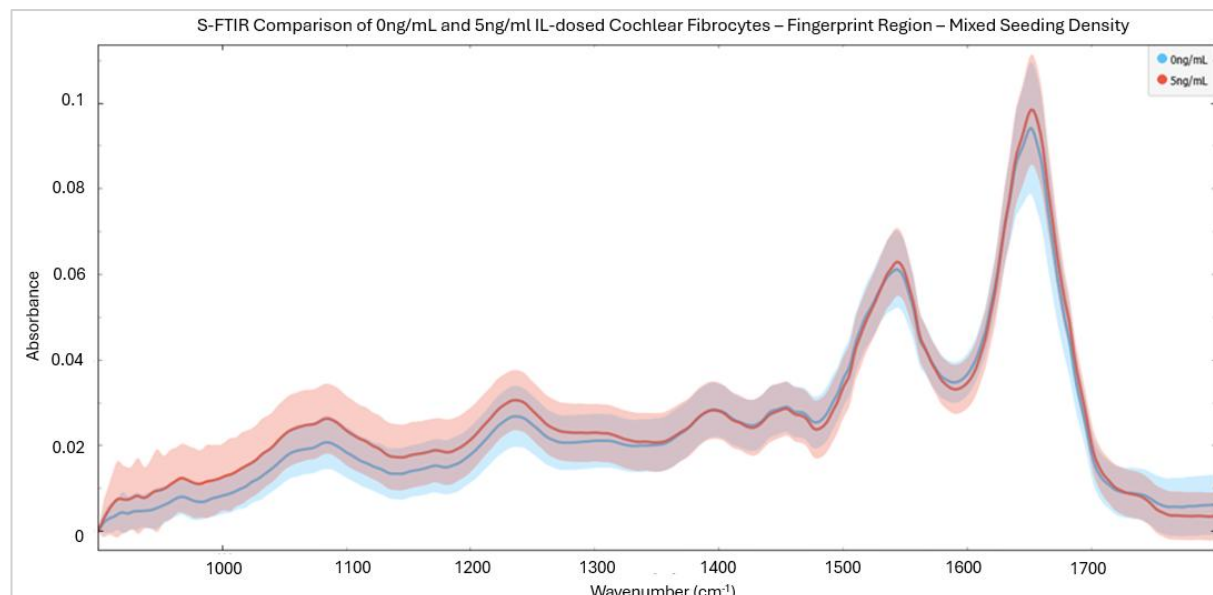


**Figure 113: Average S-FTIR fingerprint region spectra of 0ng/mL and 5ng/mL IL-dosed cochlear fibrocytes.**

**Average S-FTIR spectra (fingerprint region) of ~2000 IL-dosed vs ~2000 undosed cochlear fibrocytes cytospun on  $\text{CaF}_2$ . Cells cytospun and fixed at maximum P8. Spectra collected at Diamond Light Source, Oxford, UK.**

Moving on to 0ng/mL vs 5ng/mL, spectra demonstrate visibly greater difference between conditions in the fingerprint region than that seen in 0ng/mL and 1ng/mL comparisons (Fig. 113). Variations arise in regions such as  $<1350\text{cm}^{-1}$ ,  $1545\text{cm}^{-1}$ ,  $1650\text{cm}^{-1}$ , and  $>1700\text{cm}^{-1}$ . Such regions are

attributed to proteins and nucleic acids, amide II, amide I and lipids respectively. This suggests a more substantial cell response as a result of increased dosage.

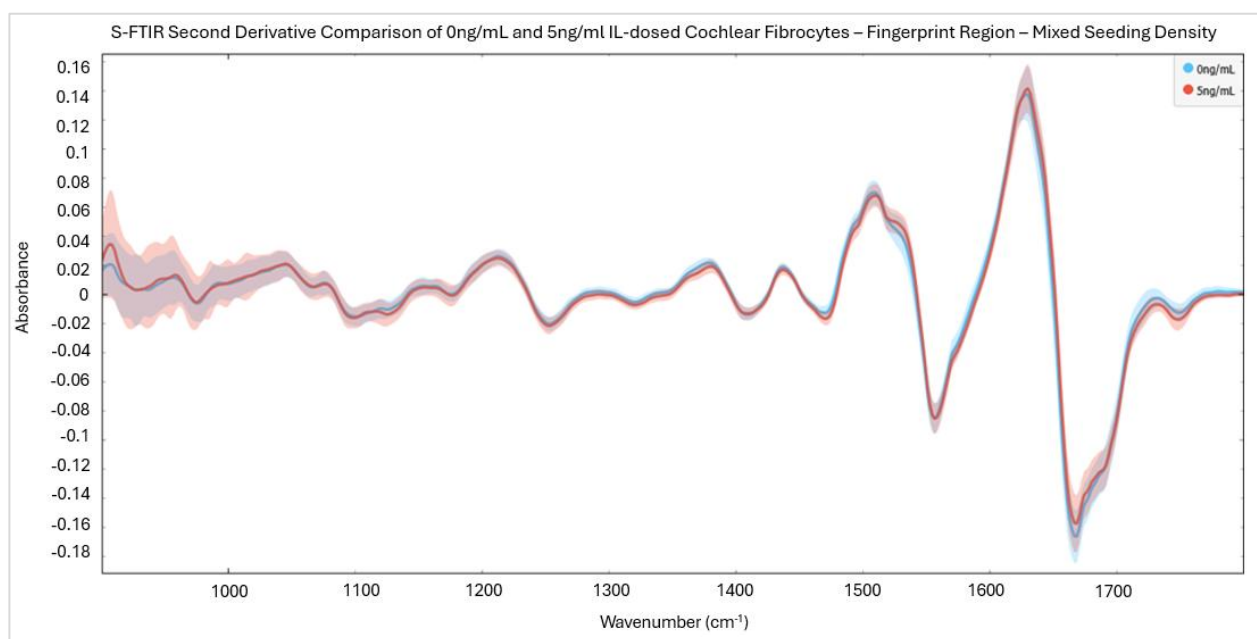


**Figure 114: Second derivative S-FTIR fingerprint region spectra of 0ng/mL and 5ng/mL IL-dosed cochlear fibrocytes.**

**Second derivative average S-FTIR spectra (fingerprint region) of ~2000 IL-dosed vs ~2000 undosed cochlear fibrocytes cytospun on CaF<sub>2</sub>. Cells cytospun and fixed at maximum P8. Spectra collected at Diamond Light Source, Oxford, UK.**

Second derivative spectra further illustrate sites of variation (Fig 114). As seen in 0ng/mL and 1ng/mL comparisons, a notable difference at 1527cm<sup>-1</sup> as well as variation below 1000cm<sup>-1</sup> is seen. Some intensity difference at 1650cm<sup>-1</sup> may also be seen.

PCA of 0ng/mL and 5ng/mL fingerprint region data, as anticipated, shows clearer grouping than lower dosage conditions (Fig. 115). Such grouping is particularly visible in the scatter plot of PC2 vs PC3. In this analysis, as in the previous, 85% of variance was accounted for in 3 principal components.

The accompanying loadings plot demonstrates sources of variation between 0ng/mL and 5ng/mL dosed cells (Fig. 116). As noted from spectra, variations arise from <1350cm<sup>-1</sup>, 1545cm<sup>-1</sup>,

1650 $\text{cm}^{-1}$ , and >1700 $\text{cm}^{-1}$ . Compared to 1ng/mL, greater variation arising from the lower end of the spectrum can be seen.

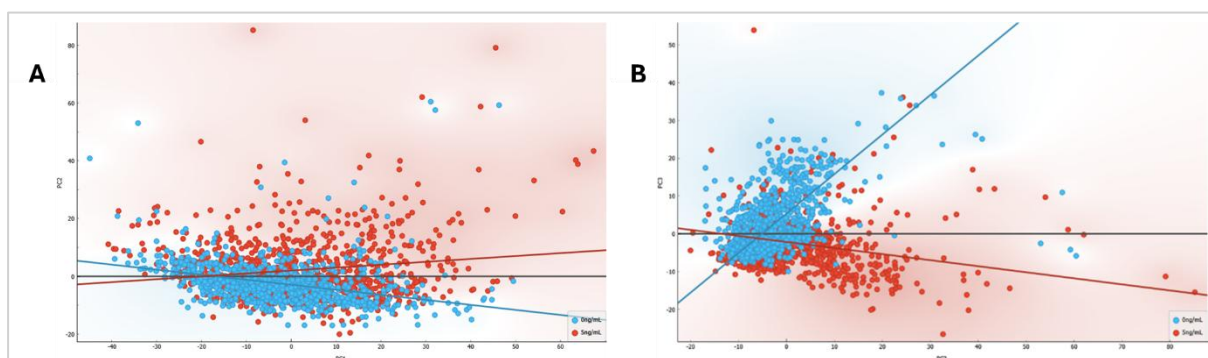


**Figure 116: PCA scatter plots of the fingerprint region of 0ng/mL and 5ng/mL IL-dosed cochlear fibrocyte S-FTIR.**

From average S-FTIR spectra (fingerprint region) of ~2000 IL-dosed vs ~2000 undosed cochlear fibrocytes cytospun on  $\text{CaF}_2$ . Cells cytospun and fixed at maximum P8. Spectra collected at Diamond Light Source, Oxford, UK. PC1= 52.9%, PC2 = 20%, PC3 = 12.7%.

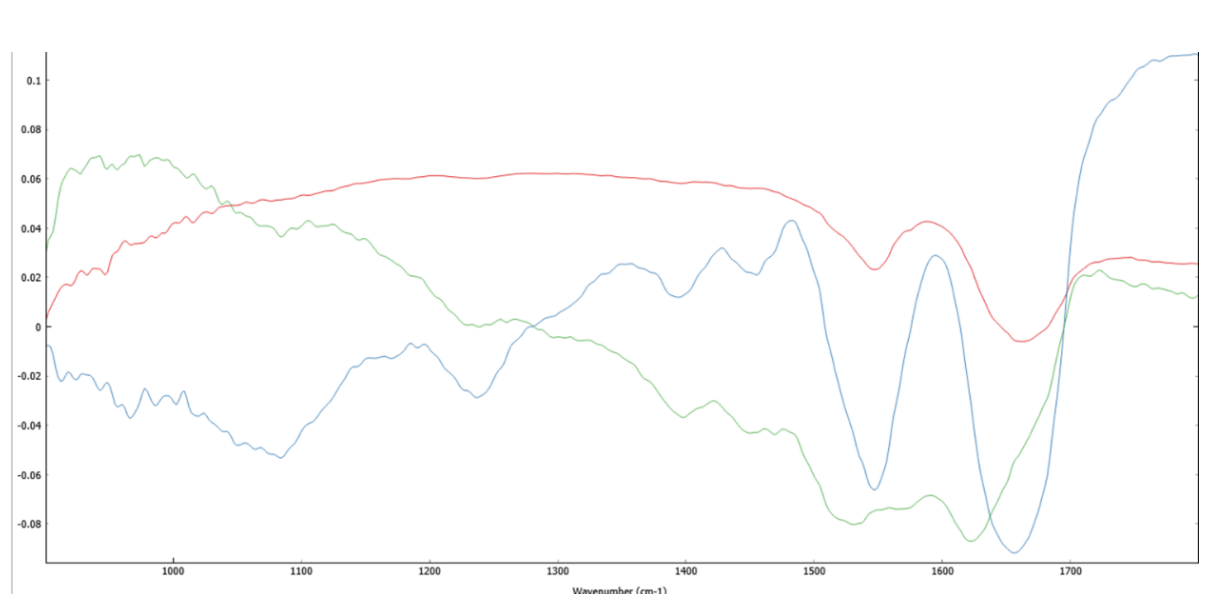


**Figure 115: PCA loadings plot of the fingerprint region of 0ng/mL and 5ng/mL IL-dosed cochlear fibrocyte S-FTIR.**

From average S-FTIR spectra (fingerprint region) of ~2000 IL-dosed vs ~2000 undosed cochlear fibrocytes cytospun on  $\text{CaF}_2$ . Cells cytospun and fixed at maximum P8. Spectra collected at Diamond Light Source, Oxford, UK. PC1 (red) vs PC2 (green) vs PC3 (blue).

The high wavenumber region of 0ng/mL and 5ng/mL spectra, reveal differing results to those of 0ng/mL and 1ng/mL comparison (Fig. 117). Unlike 1ng/mL-dosed cells, 5ng/mL-dosed cells show greater spectral intensity than undosed cells above 3100cm<sup>-1</sup>.

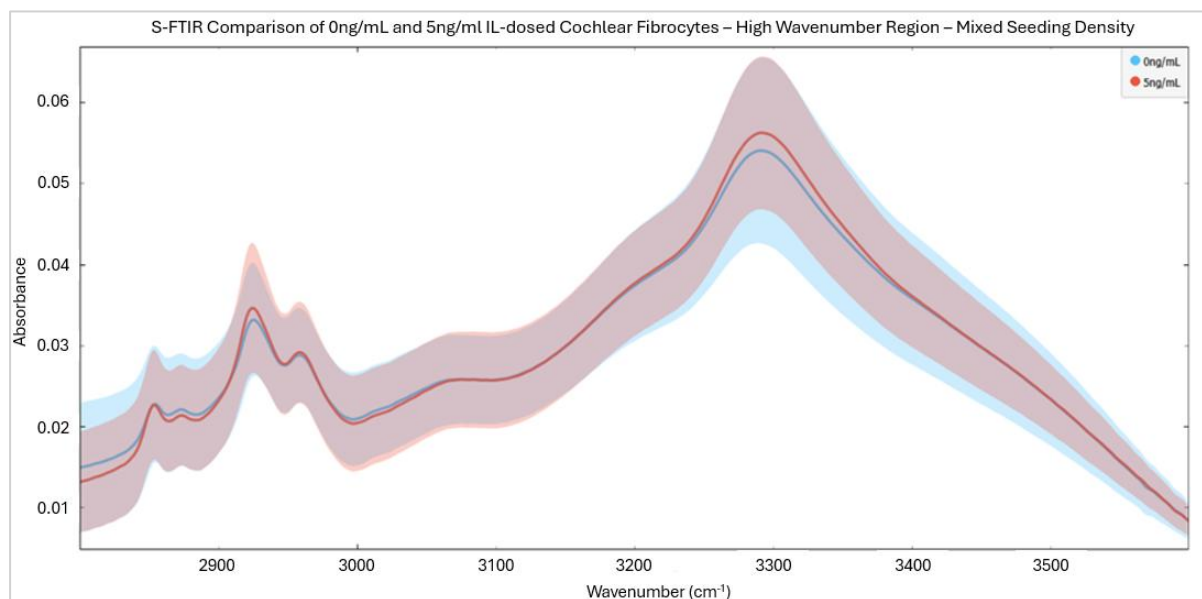


**Figure 117: Average S-FTIR high wavenumber region spectra of 0ng/mL and 5ng/mL IL-dosed cochlear fibrocytes.**

**Average S-FTIR spectra (high wavenumber region) of ~2000 IL-dosed vs ~2000 undosed cochlear fibrocytes cytopspun on CaF<sub>2</sub>. Cells cytopspun and fixed at maximum P8. Spectra collected at Diamond Light Source, Oxford, UK.**

Second derivative spectra of 0ng/mL and 5ng/mL-dosed cells in the high wavenumber region show variations (of greater intensity than those between 0ng/mL and 1ng/mL) at regions including 2845cm<sup>-1</sup>, 2861cm<sup>-1</sup> and 2935cm<sup>-1</sup>. Variation is additionally visible at 2915cm<sup>-1</sup> (Fig. 118). At 3260cm<sup>-1</sup>

<sup>1</sup>, where undosed cell signal intensity was previously higher than dosed cells, intensity is now lower than dosed cells.

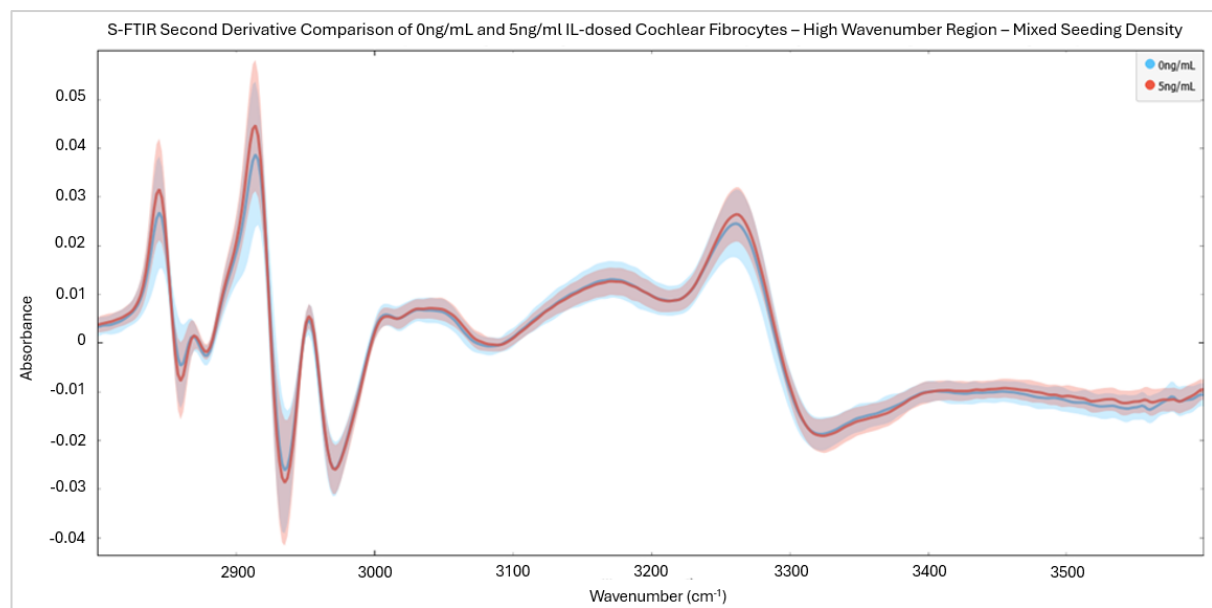


**Figure 118: Second derivative S-FTIR high wavenumber region spectra of 0ng/mL and 5ng/mL IL-dosed cochlear fibrocytes.**

Second derivative average S-FTIR spectra (high wavenumber region) of ~2000 IL-dosed vs ~2000 undosed cochlear fibrocytes cytopspun on CaF<sub>2</sub>. Cells cytopspun and fixed at maximum P8.

Spectra collected at Diamond Light Source, Oxford, UK.

As seen in 0ng/mL vs 1ng/mL, PCA of 0ng/mL and 5ng/mL high wavenumber regions demonstrates some clustering, though this is tricky to visualize due to overlap (Fig. 119). In this analysis, as for 0 vs 1ng/mL, 97% of variance was accounted for in 3 principal components.

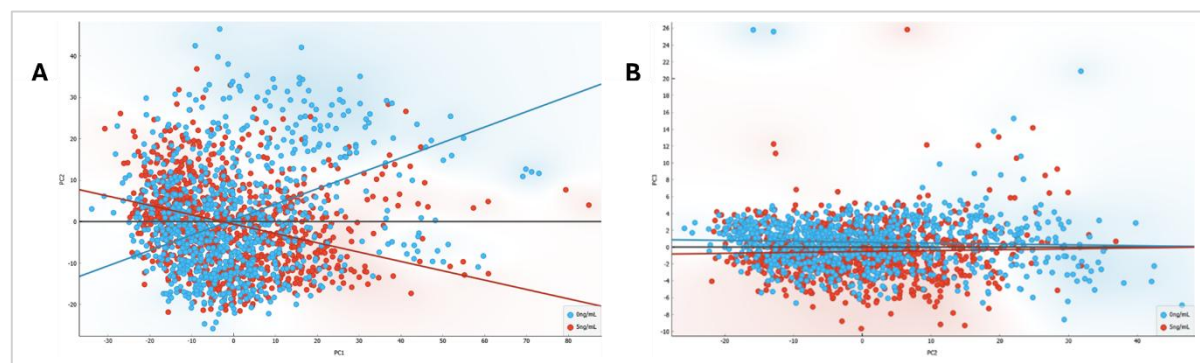


**Figure 119: PCA scatter plots of the high wavenumber region of 0ng/mL and 5ng/mL IL-dosed cochlear fibrocyte S-FTIR.**

From average S-FTIR spectra (high wavenumber region) of ~2000 IL-dosed vs ~2000 undosed cochlear fibrocytes cytopspun on CaF<sub>2</sub>. Cells cytopspun and fixed at maximum P8. Spectra collected at Diamond Light Source, Oxford, UK. PC1 = 60%, PC2 = 34.6%, PC3 = 2.3%.

The corresponding loadings plot demonstrates sources of variation between 0ng/mL and 5ng/mL dosed cells (Fig. 120). Little difference is seen from the loadings plot generated by 0 vs 1ng/mL high wavenumber PCA.

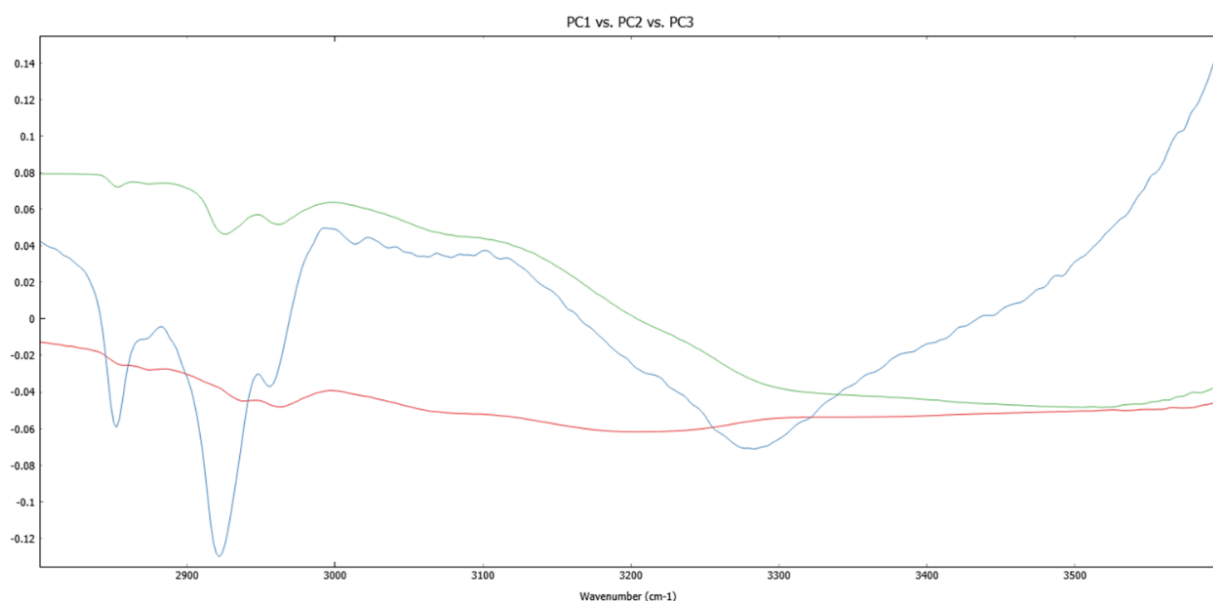


**Figure 120: PCA loadings plot of the high wavenumber region of 0ng/mL and 5ng/mL IL-dosed cochlear fibrocyte S-FTIR.**

**From average S-FTIR spectra (high wavenumber region) of ~2000 IL-dosed vs ~2000 undosed cochlear fibrocytes cytospun on CaF<sub>2</sub>. Cells cytospun and fixed at maximum P8. Spectra collected at Diamond Light Source, Oxford, UK. PC1 (red) vs PC2 (green) vs PC3 (blue).**

Finally, comparing 0ng/mL and 10ng/mL spectra, 10ng/mL-dosed cells appear to show the greatest spectral difference from undosed cells (Fig. 121). This is as expected for the highest dosage

condition trialled. In general, spectral intensity is higher in all fingerprint region wavenumbers for 0ng/mL, apart from below 500cm<sup>-1</sup>.

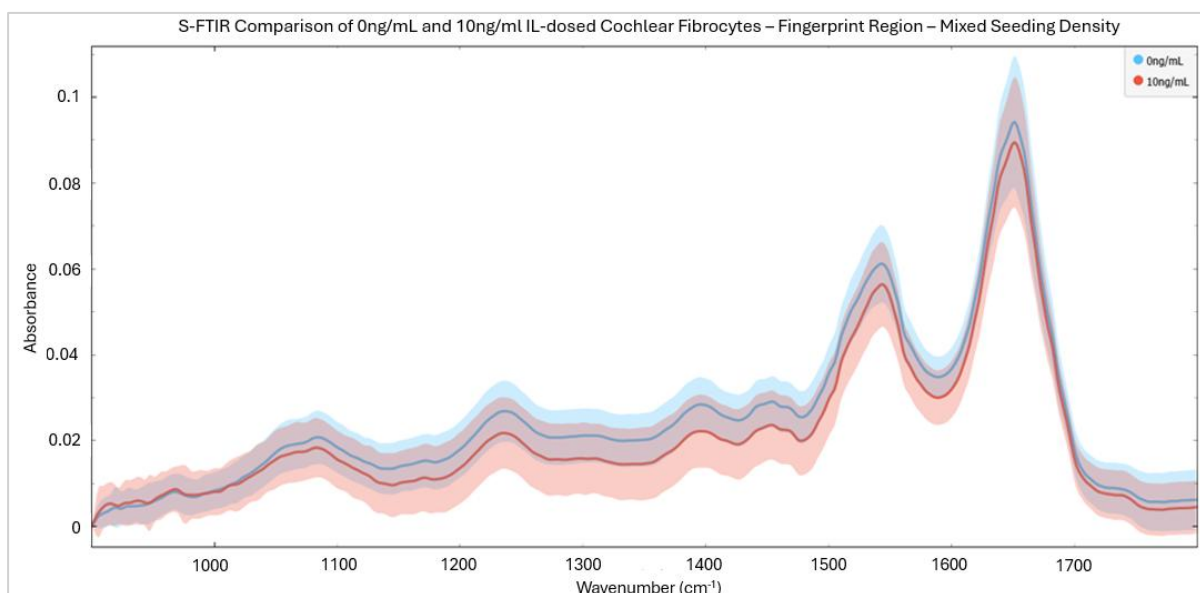


**Figure 122: Average S-FTIR fingerprint region spectra of 0ng/mL and 10ng/mL IL-dosed cochlear fibrocytes.**

**Average S-FTIR spectra (fingerprint region) of ~2000 IL-dosed vs ~2000 undosed cochlear fibrocytes cytospun on CaF<sub>2</sub>. Cells cytospun and fixed at maximum P8. Spectra collected at Diamond Light Source, Oxford, UK.**

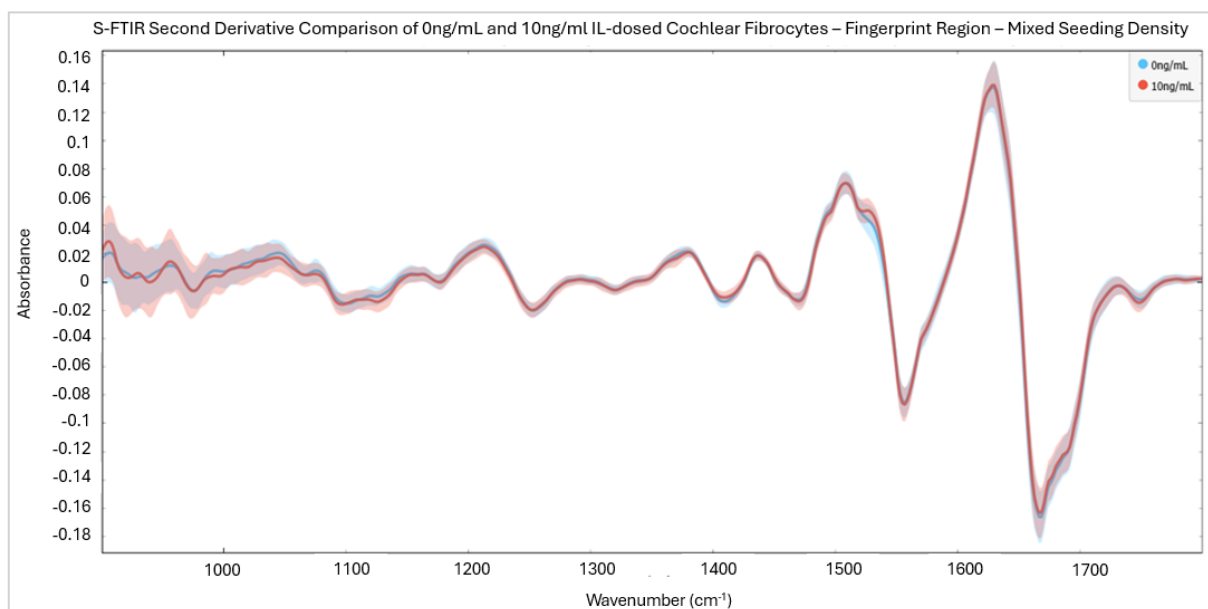


**Figure 121: Second derivative S-FTIR fingerprint region spectra of 0ng/mL and 10ng/mL IL-dosed cochlear fibrocytes.**

**Second derivative average S-FTIR spectra (fingerprint region) of ~2000 IL-dosed vs ~2000 undosed cochlear fibrocytes cytospun on CaF<sub>2</sub>. Cells cytospun and fixed at maximum P8. Spectra collected at Diamond Light Source, Oxford, UK.**

As in previous comparisons, second derivative spectra demonstrate a notable difference at  $1527\text{cm}^{-1}$  as well as variations in nucleic acid associated regions below  $1000\text{cm}^{-1}$  and between  $1120\text{--}1140\text{cm}^{-1}$  (Fig.122). A small variation is noted at  $1408\text{cm}^{-1}$ , attributable to  $\text{COO}^-$  symmetric stretching (amino acids/fatty acids). Variation at  $1650\text{cm}^{-1}$  may also be seen.

As spectral data would suggest, comparison of  $0\text{ng/mL}$  and  $10\text{ng/mL}$ -dosed cell populations by PCA yields the most distinct group clustering (Fig.123). Some overlap is still seen, likely due to the overall similar shape of spectra despite notable intensity differences. In this analysis, once again, 85% of variance was accounted for in 3 principal components.

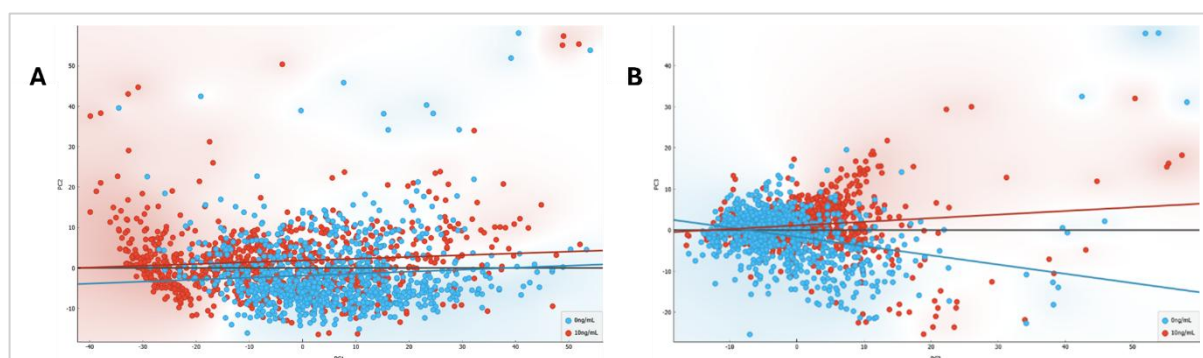


**Figure 123: PCA scatter plots of the fingerprint region of  $0\text{ng/mL}$  and  $10\text{ng/mL}$  IL-dosed cochlear fibrocyte S-FTIR.**

**From average S-FTIR spectra (fingerprint region) of  $\sim 2000$  IL-dosed vs  $\sim 2000$  undosed cochlear fibrocytes cytospun on  $\text{CaF}_2$ . Cells cytospun and fixed at maximum P8. Spectra collected at Diamond Light Source, Oxford, UK. PC1 = 61%, PC2 = 15.6%, PC3 = 8.7%.**

The corresponding loadings plot appears similar to previous comparisons, confirming that variations arise from similar spectral regions but to different extents (Fig. 124). This is a logical outcome given that the same cytokine is applied in all conditions, simply to different levels.

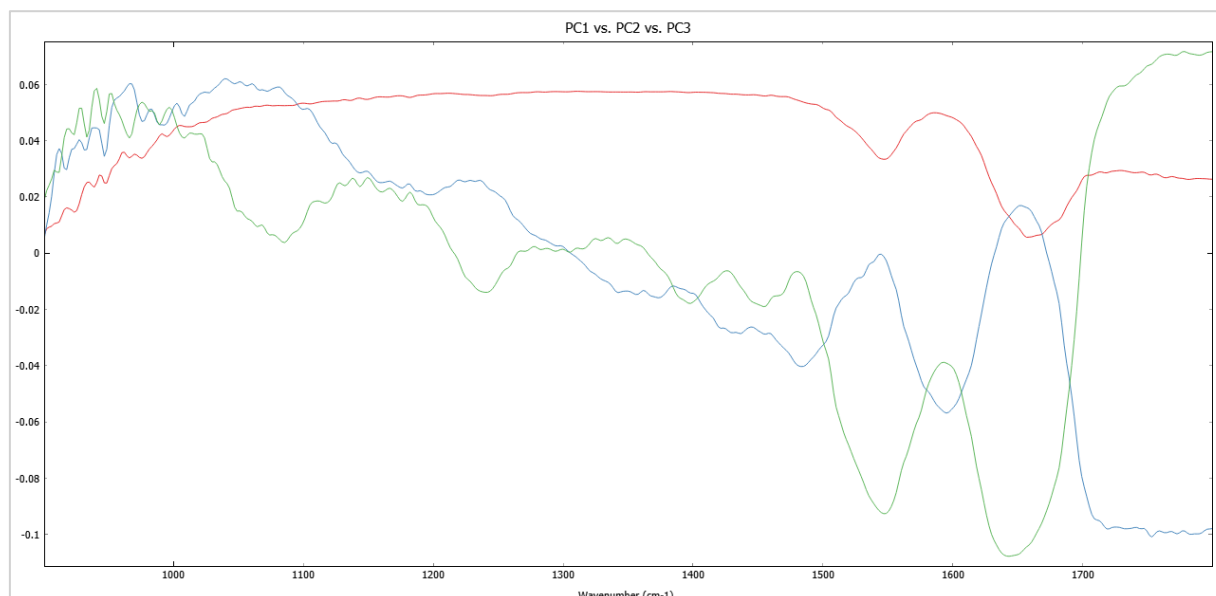


**Figure 124: PCA loadings plot of the fingerprint region of 0ng/mL and 10ng/mL IL-dosed cochlear fibrocyte S-FTIR.**

**From average S-FTIR spectra (fingerprint region) of ~2000 IL-dosed vs ~2000 undosed cochlear fibrocytes cytopun on CaF<sub>2</sub>. Cells cytopun and fixed at maximum P8. Spectra collected at Diamond Light Source, Oxford, UK. PC1 (red) vs PC2 (green) vs PC3 (blue).**

As anticipated, high wavenumber examination shows that 10ng/mL-dosed cells show the greatest spectral variation from undosed cells, particularly below 3200cm<sup>-1</sup> (Fig.125).

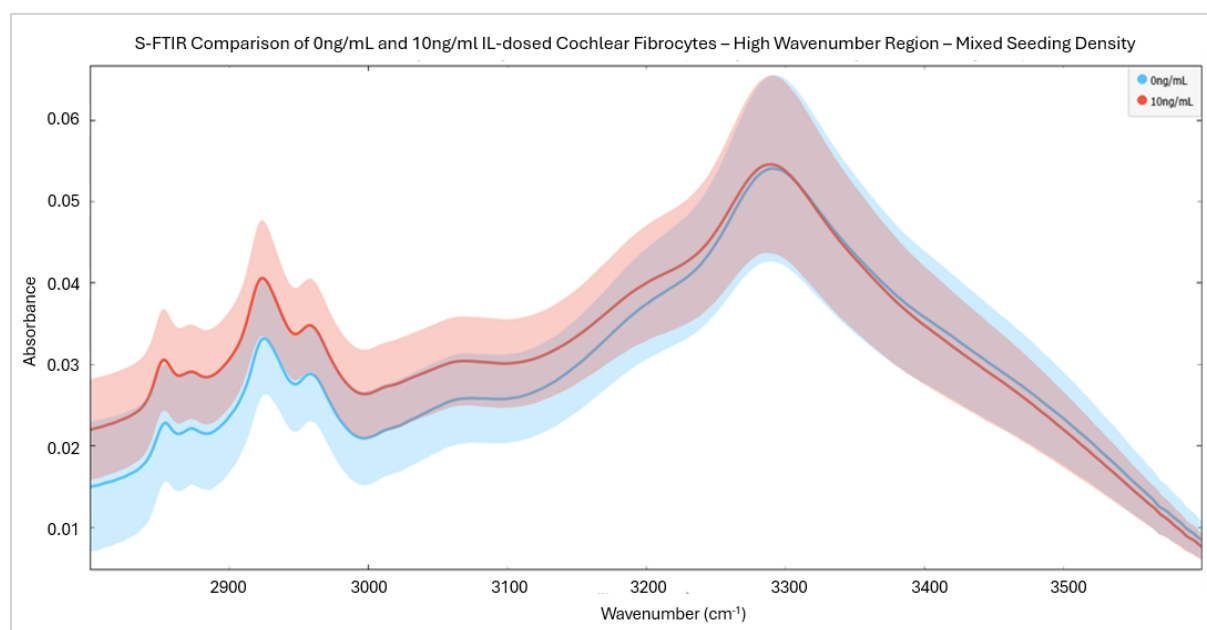


**Figure 125: Average S-FTIR high wavenumber region spectra of 0ng/mL and 10ng/mL IL-dosed cochlear fibrocytes.**

Average S-FTIR spectra (high wavenumber region) of ~2000 IL-dosed vs ~2000 undosed cochlear fibrocytes cytospun on CaF<sub>2</sub>. Cells cytospun and fixed at maximum P8. Spectra collected at Diamond Light Source, Oxford, UK.

As noted in 0ng/mL vs 5ng/mL comparisons, cells in the high wavenumber region show variations at regions including 2845cm<sup>-1</sup>, 2861cm<sup>-1</sup>, 2915cm<sup>-1</sup>, and 2935cm<sup>-1</sup> (Fig. 126). Variation is additionally visible at 2972cm<sup>-1</sup>, as well as more generally throughout spectra.

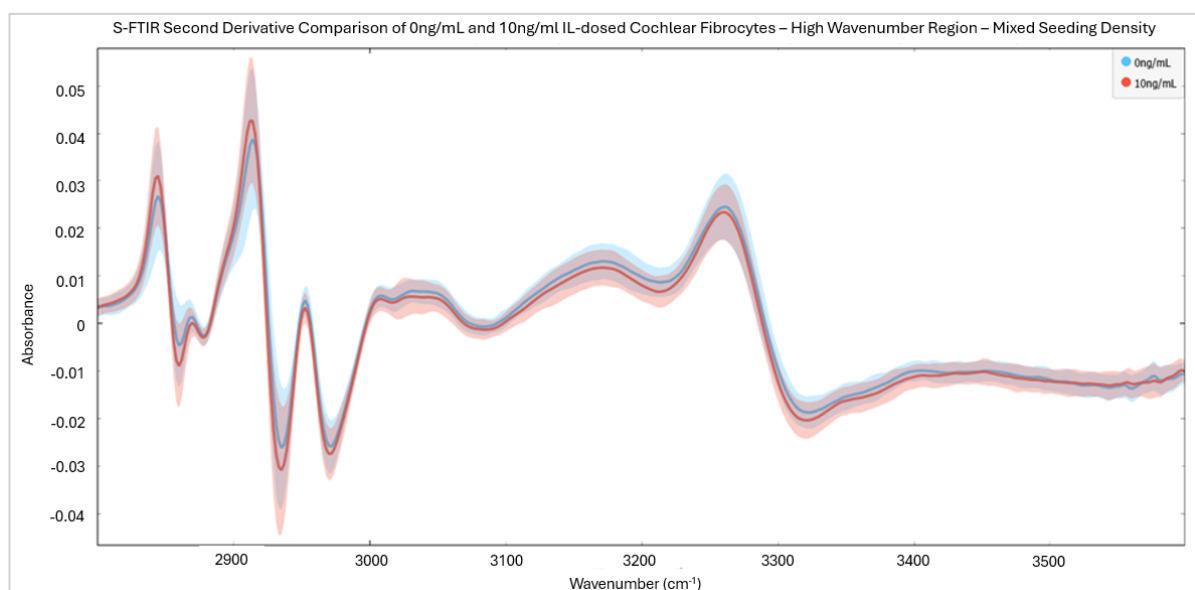


**Figure 126: Second derivative S-FTIR high wavenumber region spectra of 0ng/mL and 10ng/mL IL-dosed cochlear fibrocytes.**

Second derivative average S-FTIR spectra (high wavenumber region) of ~2000 IL-dosed vs ~2000 undosed cochlear fibrocytes cytospun on CaF<sub>2</sub>. Cells cytospun and fixed at maximum P8. Spectra collected at Diamond Light Source, Oxford, UK.

Once again, as anticipated from spectra, PCA of 0ng/mL vs 10ng/mL-dosed cells reveals the most apparent grouping of samples for the high wavenumber region (Fig. 127). In this analysis 98% of variance was accounted for in 3 principal components.

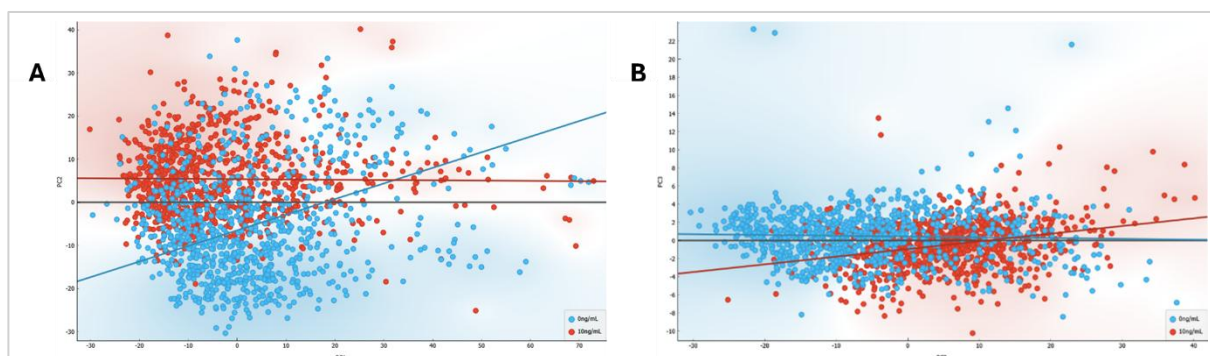


**Figure 128: PCA scatter plots of the high wavenumber region of 0ng/mL and 10ng/mL IL-dosed cochlear fibrocyte S-FTIR.**

From average S-FTIR spectra (high wavenumber region) of ~2000 IL-dosed vs ~2000 undosed cochlear fibrocytes cytopspun on CaF<sub>2</sub>. Cells cytopspun and fixed at maximum P8. Spectra collected at Diamond Light Source, Oxford, UK. PC1 = 60%, PC2 = 36.3%, PC3 = 1.9%.

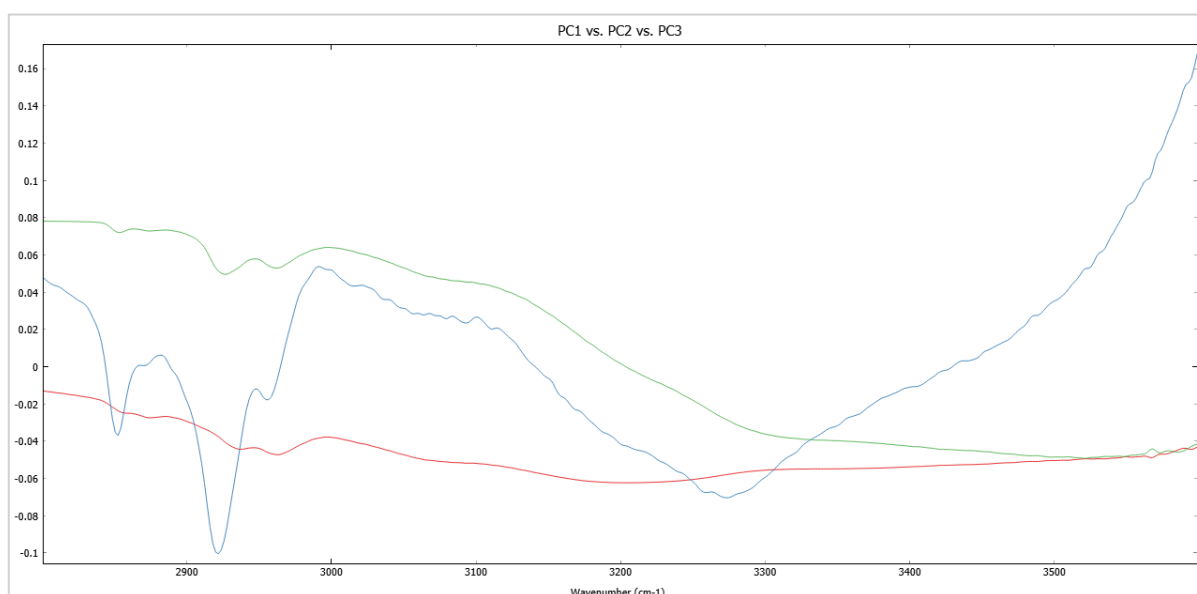


**Figure 127: PCA loadings plot of the high wavenumber region of 0ng/mL and 10ng/mL IL-dosed cochlear fibrocyte S-FTIR.**

Average S-FTIR spectra (fingerprint region) of ~2000 IL-dosed vs ~2000 undosed cochlear fibrocytes cytopspun on CaF<sub>2</sub>. Cells cytopspun and fixed at maximum P8. Spectra collected at Diamond Light Source, Oxford, UK. PC1 (red) vs PC2 (green) vs PC3 (blue).

Little difference is seen from the loadings plot generated by other high wavenumber PCA comparisons, again confirming that variations arise from similar spectral regions, just to different extents (Fig. 128).

With these results in mind, there is a clear implication that dosed and undosed cells can be successfully distinguished based upon spectral variation, with variation appearing to increase with dosage. Though low and high seeding density conditions demonstrate some differences, dosage distinction is not impeded greatly when mixing seeding densities. Mixing seeding densities, as done presently, is arguably of greater physiological and translational relevance than observing densities separately.

The use of spectral data in distinguishing healthy and inflamed cells is explored further using mathematical modelling techniques. This is discussed in section 4.4.3 below.

#### 4.4.3. FTIR – Generation of the Non-linear Model

Building on observations from spectral analysis and PCAs, a non-linear predictive model was employed to further elucidate variation between conditions on a level that may not be visible through PCA. By employing a neural network to predict conditions, it becomes clear that there are distinct variations present between interleukin dosage conditions implying that, while present, important differences in spectral profile may be too subtle to detect through PCA and manual peak assignment alone.

In using PCA as a first step to reduce data dimensionality (employing 6 PCs accounting for 93.5% of variance), a neural network is able to successfully predict dosage condition with accuracy in around 80% of cases on average (Fig. 129). This is particularly impressive when considering that a 50:50 test to train split was used in forming the model, meaning that from presentation of condition labels for half of the data at random (around 425 samples per condition) the model was able to predict the correct dosage condition of the unseen half with high accuracy. This performance is further validated through the use of a 5-fold method, wherein data was re-randomised and independently tested 5-times with presented accuracy formed from an average across all folds.

		Predicted					
		0ng/mL	1ng/mL	5ng/mL	10ng/mL	Σ	
A	Actual	0ng/mL	83.5 %	6.6 %	5.9 %	4.0 %	2140
		1ng/mL	6.3 %	80.5 %	7.4 %	5.8 %	2215
		5ng/mL	6.5 %	7.8 %	80.1 %	5.6 %	2335
		10ng/mL	3.7 %	6.9 %	5.8 %	83.5 %	2175
		Σ	2159	2255	2289	2162	8865

		Predicted					
		0ng/mL	1ng/mL	5ng/mL	10ng/mL	Σ	
B	Actual	0ng/mL	75.8 %	14.4 %	5.0 %	4.8 %	2140
		1ng/mL	11.5 %	71.3 %	10.2 %	6.9 %	2215
		5ng/mL	6.0 %	8.3 %	75.8 %	9.9 %	2335
		10ng/mL	5.3 %	15.6 %	6.8 %	72.3 %	2175
		Σ	2135	2423	2249	2058	8865

Figure 129: Confidence tables from 50:50 train to test neural network model showing predicted condition as a proportion of actual condition.

From S-FTIR spectra IL-dosed vs undosed cochlear fibrocytes cytopun on CaF<sub>2</sub>. Cells cytopun and fixed at maximum P8. Spectra collected at Diamond Light Source, Oxford, UK. A) Fingerprint region. B) High wavenumber region.

Employing a more conventional 70:30 train to test split, accuracy is improved for fingerprint region-based classification as would be expected, with improved performance facilitated by allowing the model access to a greater proportion of data on which to train. This is demonstrated in confidence tables wherein the updated neural network demonstrates an increase in accuracy of 3% (Fig. 130a). This is likely to be improved by further by increasing the proportion of training data, though this approach risks limiting the model's statistical relevance by reducing the number of test data points.

The high wavenumber region, contrastingly, demonstrates a reduction in model accuracy with the provision of increased training data. This is likely due to noise in the sampled data. If this approach were to be pursued in further investigations, it is advised that an increase in folds is employed or, preferably, more data points on which to train and test are gathered to ensure maximum data accuracy.

		Predicted				
		0ng/mL	1ng/mL	5ng/mL	10ng/mL	Σ
Actual	0ng/mL	86.3 %	6.1 %	4.7 %	2.9 %	1285
	1ng/mL	4.2 %	84.1 %	5.8 %	5.9 %	1330
	5ng/mL	5.3 %	7.5 %	82.3 %	4.9 %	1400
	10ng/mL	3.8 %	6.6 %	4.8 %	84.8 %	1305
	Σ	1289	1389	1352	1290	5320

		Predicted				
		0ng/mL	1ng/mL	5ng/mL	10ng/mL	Σ
Actual	0ng/mL	73.7 %	13.6 %	7.4 %	5.3 %	1285
	1ng/mL	9.8 %	69.8 %	10.6 %	9.8 %	1330
	5ng/mL	4.3 %	9.6 %	77.6 %	8.4 %	1400
	10ng/mL	3.8 %	14.4 %	8.0 %	73.8 %	1305
	Σ	1187	1426	1427	1280	5320

**Figure 130: Confidence tables from 70:30 train to test neural network model showing predicted condition as a proportion of actual condition.**

**From S-FTIR spectra IL-dosed vs undosed cochlear fibrocytes cytopun on CaF<sub>2</sub>. Cells cytopun and fixed at maximum P8. Spectra collected at Diamond Light Source, Oxford, UK. A) Fingerprint region. B) High wavenumber region.**

Nonetheless, with a good prediction accuracy rate, particularly when considering the variability of biological samples, the demonstrated model shows promise in classifying interleukin dose/inflammation level in *in vitro* cochlear fibrocytes, particularly in the distinction of dosed from undosed samples.

In aims to classify interleukin dose/inflammation level in *in vitro* cochlear fibrocytes, it is evident from the presented confidence tables that the model's ability to distinguish dosage conditions varies depending upon the sample region examined. Analysis of the fingerprint region yields a model which demonstrates its greatest accuracy in the distinction of undosed from dosed cells. Analysis of the high wavenumber region alone yields a model which demonstrates its greatest accuracy in the distinction of 5ng/mL dosed samples. It is recommended based upon this that when seeking to continue in the present line of research, the focus of the model be adjusted to reflect the goal outcome. That is, where distinction of healthy vs inflamed cells in general is required, a fingerprint focus is recommended.

Generating a model based on recommended parameters (neural network, 70:30 train to test, fingerprint region focus) capacity to distinguish undosed from dosed cells more generally can be evaluated (Fig. 131). The confidence table, in contrast to the findings of separated dosage classification models, demonstrates greater accuracy in the classification of dosed cells than undosed. That is, the false negative prediction rate (classified as undosed when actually dosed) is substantially lower than the false positive rate (classified as dosed when actually undosed). Though improvement of the model through additional sampling is still recommended, whether this error poses a substantial issue moving forward is dependent upon the consequences of related decisions. This is discussed further in section 2.5.

		Predicted		$\Sigma$
		Undosed	Dosed	
Actual	Undosed	68.2 %	31.8 %	660
	Dosed	2.1 %	97.9 %	1995
$\Sigma$		492	2163	2655

**Figure 131: Confidence table from dosed vs undosed neural network trial.**  
**From S-FTIR spectra IL-dosed vs undosed cochlear fibrocytes cytopun on CaF<sub>2</sub>.**  
**Cells cytopun and fixed at maximum P8. Spectra collected at Diamond Light**  
**Source, Oxford, UK.**

In data such as the above, wherein some results demonstrate accuracies nearing 100%, caution must be taken to ensure that over-fitting is not occurring. In the present research, reported accuracies are based on test data, which was held out from the training process in each model. As such, the models were not exposed to this data during training, mitigating the risk of overfitting. In addition, models were trained multiple times with different random data splits (70:30 and 50:50 as noted), which helps to ensure that the performance is not biased due to a particular data partition. As accuracy and confidence remained consistent across these repeated runs, stability in model performance is suggested. For further validation, steps such as cross validation may be considered. Though not demonstrated in this report, 5-fold cross-validation was investigated for the data shown and yielded outcomes of negligible difference from those presented, indicating that the presented data are not overfit.

## 4.5. Discussion

Overall, data gathered from Diamond Light Source, B22 supports the findings of previous chapters, refines modelling requirements, and further elucidates the pathology of IL-induced inflammation in cochlear fibrocytes. Both hyperspectral Raman data and synchrotron S-FTIR data provide insight into the process of cochlear fibrocyte inflammation via interleukin 1- $\beta$  and thus add value to the field.

Hyperspectral Raman results demonstrate data predominantly consistent with previous chapters' findings, with variations in molecular and distribution evident of inflammation-related structural changes that may extend beyond those originally hypothesised. Such changes are suggested to arise from changes to intercellular transport, membrane integrity/content, biosynthesis in cytoplasm, and molecular accumulation within cells in response to inflammation. Comparison of undosed and dosed cell pairs is of particular interest, as in native tissue cochlear fibrocytes are densely packed and likely to be in contact with neighbours. Thus, findings arising from cells in contact are likely of greater physiological relevance than findings arising from isolated cells.

From such comparison, well-documented inflammatory responses may be seen in dosed cells. These include signs of metabolic dysfunction such as reduced coenzyme A (927 $\text{cm}^{-1}$  and 950 $\text{cm}^{-1}$ ), accumulation of lipids (1447 $\text{cm}^{-1}$ ) consistent with apoptosis progression, the presence of compounds

indicative of ROS ( $962\text{cm}^{-1}$ ), and potential alterations in protein/lipid membrane assemblies ( $1658\text{cm}^{-1}$ )<sup>[257]</sup>. Such variations indicate metabolic dysfunction and ROS accumulation, known hallmarks of the inflamed cell state and noted causes of cochlear fibrocyte loss<sup>[4, 5, 48-52]</sup>. This is consistent with findings noted in previous chapters and provides further insight into the mechanisms of inflammatory damage in cochlear fibrocytes.

Interestingly, cells in contact are shown to undergo substantial variations in spectral regions where membrane/intersection localisation is seen ( $<600\text{cm}^{-1}$ ,  $>1712\text{cm}^{-1}$ ) when subject to interleukin dosage. This is hypothesised presently to indicate decreased intercellular communication, with signs of protein structural changes marking membrane protein alteration/degradation as a possible cause. This is of particular interest when the role of cochlear fibrocytes *in vivo* is considered. That is, if membrane and protein alterations limit ion transport during inflammation, endocochlear potential reduction may originate from such alterations, as well as from cell respiration failure as previously noted<sup>[50]</sup>. This suggestion, unfortunately, cannot be verified at present, with literature to date seemingly note no similar phenomena. As such, further research into this is recommended.

Though data relating to it are uncertain, the presence of the examined granulated dosed cell and others like it evidences variations in level of cell inflammation within dosage samples. This is assumed to be a result of cell-cycle-based fluctuations in cytokine uptake, consistent with cell metabolism variation and similar to those seen in nanoparticle studies<sup>[248, 249]</sup>. Though, as mentioned previously, reliable conclusions cannot be drawn from the granular cell data presented at this stage, examination of such cells is vital in elucidating the full breadth of inflammatory impacts on cochlear fibrocytes and other such cells. Thus, it is recommended that future studies conduct further hyperspectral Raman analysis in order to clarify the true nature of the presented results.

Turning to S-FTIR, variations supporting previously outlined hypotheses of protein alteration, lipid accumulation and membrane integrity changes are seen. In particular, variations are noted in spectra at wavenumber regions corresponding to vibrations in nucleic acids ( $<110\text{cm}^{-1}$ ,  $1115\text{-}1130\text{cm}^{-1}$ ), carbohydrates ( $<110\text{cm}^{-1}$ ), phospholipids ( $<110\text{cm}^{-1}$ ), proteins ( $1527\text{cm}^{-1}$ ,  $2800\text{-}3100\text{cm}^{-1}$ ) and lipids ( $2800\text{-}3100\text{cm}^{-1}$ ). Phospholipid and carbohydrate vibrational changes likely indicate variations in membrane structure and biosynthesis. Protein vibrational changes are, as noted from previous

data, potentially indicative of alteration in protein structure. Lipid vibrational changes may indicate lipid accumulation, commonly seen in inflamed cells. Considering the findings of Dunkhunthod *et al.* (2020)<sup>[215]</sup>, the present S-FTIR data may warrant consideration of a fibrocyte activation state similar to that seen in macrophages. With this in mind, further study in this area is recommended to lend clarity in distinguishing whether this is the case. This may include the conduction of single cell gel electrophoresis to assess DNA damage, ROS assays to monitor potential sources of such damage, proteomics-based analyses to examine protein expression, and lipid metabolism assays to quantify glycerol and cholesterol etc.

Regarding the use of a neural network in the classification of inflamed (dosed) and non-inflamed (undosed) cells, the present trials show promise. In seeking to reliably distinguish between dosed and undosed cells from the fingerprint regions of spectra, it is notable that the employed model demonstrates a substantially lower false negative prediction rate (classified as undosed when actually dosed) than false positive rate (classified as dosed when actually undosed). As stated, whether this error poses a substantial issue moving forward is dependent upon the consequences of related decisions.

In a diagnostic context, though FTIR spectroscopy of cells is unlikely to be employed due to the invasive and high-risk nature of cell retrieval, a high false positive rate is preferable to a high false negative rate. In this instance, it is hoped that patients receiving a positive result would be subject to further verification of disease state, potentially through the other methods discussed in the present thesis. Improvement of the model to reduce error in both positive and negative result assignment is recommended regardless. Ideally, model improvements would take the form of confidence ratings, wherein the model may assign a suggested classification and a percentage confidence for its selection. This would facilitate re-testing of patients who receive low confidence results. However, in order to achieve this, a more complex model (e.g. a Bayesian neural network) is recommended. Such modelling is beyond the scope of the present research.

In a monitoring context (i.e. where observing cells' health prior to therapeutic application) the same may be stated, as false negative results may lead to the use of unsuitable cells in the treatment of patients- a clearly unacceptable therapeutic outcome. However, a higher false positive rate may

lead to the untimely disposal of cell populations, an outcome which would cost laboratories both time and money to recover. With this in mind, the employment of additional testing methods and improvements to modelling suggested above are reaffirmed.

## 4.6. Concluding Remarks

To conclude, this section of research meets the aims outlined within section 2.2.

Aim 1 was met through the successful use of hyperspectral Raman spectroscopy to examine the effects of IL-1 $\beta$  in cultured cells. This included examinations of molecular distribution within viewed cells.

Aim 2 was met through the successful use of S-FTIR in the distinction of IL-dosed fibrocyte cultures, with evidence of inflammation-induced changes consistent with literature noted.

Aim 3 was met through the successful employment of a neural network in the accurate distinction of inflamed cells and the classification of cells by dosage level.

With this in mind, it is clear that the techniques demonstrated are of interest for further investigation with the hope of future application to ARHL diagnostics and treatment. In pursuit of diagnostic use, further study is particularly recommended to elucidate whether cell membrane integrity and protein alterations play a key role in the decrease of the endocochlear potential under inflamed conditions. Where treatment is concerned, such techniques may already be viable in the monitoring of cells for reimplantation (etc.) *in vitro* thanks to success in the distinction of healthy cells from those inflamed. When considering diagnostic potential, a suitable biofluid for non-invasive diagnosis must be identified in order to facilitate application of research findings.

## 5. Towards Translation- Exploring the Potential of SIFT-MS and Cerumen Sampling in Non-Invasive ARHL Diagnoses

---

### 5.1. Introduction

#### 5.1.1. Headspace Analysis for Non-invasive Cell Profiling

Despite the capacity to distinguish inflammation of cochlear fibrocytes demonstrated by Raman and FTIR spectroscopies, these methods are less than ideal where translation to diagnostic and therapeutic purposes is concerned. In a diagnostic context, the necessity for cell or liquid samples means that patients would likely require invasive sample collection procedures which may be both off-putting and potentially dangerous <sup>[123]</sup>. In a therapeutic context, these techniques are better applied, with vibrational spectroscopic analysis alongside CI implantation <sup>[111]</sup> as well as monitoring of potential replacement cells *in vitro* feasible. However, a truly non-invasive procedure is undoubtedly more desirable.

With this in mind, cell headspace analysis is trialled in this section of research. For patients, successful application of headspace analysis methods may mean diagnosis and monitoring of therapies at greater speed and with reduced discomfort. In the context of cell culture monitoring, headspace analysis would limit disturbances to cultures such as cell and liquid removal for sampling.

As discussed in section 1.7.5, this research employed SIFT-MS in examining the gas headspace of cochlear fibrocytes *in vitro*. This method allows real-time identification of compounds within gaseous samples, with minimal preparation required ahead of sampling. To date, it would appear that there have been no studies involving the examination of cochlear fibrocytes via SIFT-MS.

Arguably the closest research has come yet to examining cochlear fibrocytes and their inflammation via gas analysis is in the 2017 study by Zhang *et al.* <sup>[139]</sup> wherein depletion of the H<sup>+</sup> Transporter SLC4A11 was observed by GC-MS. Though this research is conducted in the context of corneal endothelium rather than the inner ear, it remains of some relevance to the present study due the presence and function of SLC4A11 in cochlear fibrocytes <sup>[140]</sup>. However, despite relevance, this

study does not provide any clues as to what can be expected from fibrocytes in the context of the present study.

### 5.1.2. ARHL Investigation- Considering the Cerumen Approach

In seeking to apply headspace analysis methods to ARHL diagnosis and treatment, translational considerations must begin with the selection of an appropriate biofluid for sampling. Regarding investigations of hearing, the most accessible and patient-friendly sample type which could potentially hold insight into hearing status is ear wax (cerumen). This sample type has recently been employed in identification of cancer biomarkers and may offer valuable tool in diagnosis <sup>[127]</sup>.

This study, and others like it, demonstrate the potential of cerumen to offer far greater diagnostic value than that for which it is currently employed in the clinic. It is known that cerumen can be used to accurately identify a range of patient features, including ethnicity, gender and even diet <sup>[182]</sup>. More recently, investigators are growing to appreciate the potential benefits of cerumen as a tool in diagnoses <sup>[183]</sup>. In the first study of its kind, the investigation by Prokop-Prigge *et al.* <sup>[182]</sup> used GC-MS (with SPME (solid phase micro-extraction)) to identify the VOC profile of human cerumen.

In their pilot study, Shokry *et al.* <sup>[184]</sup>, demonstrated the use of cerumen in volatile metabolite profiling (Using gas chromatography mass spectrometry (GC-MS)) for diabetes mellitus. During this investigation, researchers were able to discriminate healthy individuals from diabetes patients with high accuracy, as well as detecting which type of diabetes was present in sufferers. Biomarkers of note were ethanol, acetone, methoxyacetone, hydrourea, isobutarylaldehyde and acetic acid. Methoxyacetone, in particular, was able to distinguish between the two diabetes subtypes with no data from other volatiles necessary. These findings are supported by the association of diabetes mellitus and risk of bilateral hearing loss development <sup>[31, 185,186]</sup>. Such hearing loss is attributed to diabetic neuropathy <sup>[187]</sup> and would suggest manifestation primarily in the form of sensorineural hearing loss. These studies bolster the premise that cerumen may be used as an effective diagnostic sample type for a variety of health conditions, additionally highlighting the benefits of cerumen as a patient-friendly, non-invasive method of sample collection, and noting the minimal requirement of pre-treatment for samples.

In general, from volatile analysis of cerumen, notable VOCs in normal cerumen profiles are alcohols, ketones, dimethyl disulphide and C2 to C6 acids, though levels of these may vary across individuals <sup>[182, 184]</sup>. The majority of volatile acids, aldehydes and alcohols seen in cerumen are produced via interaction of bacteria with gland secretions <sup>[188]</sup>. Ketones in cerumen profiles are believed to originate from the oxidation of squalene <sup>[189-191]</sup>. Levels of such VOCs may vary significantly across individuals depending upon a range of factors, including natural variation, pathology, and treatment.

Concerning SIFT-MS and cerumen, no studies combining the two have been conducted to date. With the relative speed and ease of use of SIFT-MS compared to GC-MS, it is arguable that, could cerumen based studies be performed via SIFT-MS, this would be a more clinic-friendly diagnosis method than the use of GC-MS. The primary issue in such translation, it would seem, is in transition from the use of SPME with GC-MS to what is effectively direct headspace injection with SIFT-MS. Thus, the capacity for the effective concentration of cerumen samples in order to obtain such a headspace must be reviewed. Additionally, there are a number of factors affecting the production, composition, and retention of cerumen that must be thoroughly considered in order properly assess its suitability for diagnostic use via non-invasive mass spectrometry. These variations are discussed in sections 5.1.3 and 5.1.4 below.

### 5.1.3. Typical Production and Composition of Cerumen

Where considering the potential for clinical translation of the previous chapters' findings to ARHL diagnoses, a viable method of patient sampling must be considered as a priority. Of course, patient fibrocytes themselves cannot reasonably be sampled, nor can cochlear fluids- these strategies would both be unnecessarily invasive and damaging to the cochlear environment. As an alternative, the present research presents cerumen (ear wax) sampling for consideration. Cerumen is a weakly acidic, wax-like substance found in the ear canal of mammals. Its purposes are primarily to trap foreign particles and facilitate cleaning and protection of the ear canal, with studies highlighting its antimicrobial properties <sup>[192]</sup>. It is produced by 1000-2000 modified apocrine sweat glands in the ear canal known as ceruminous glands <sup>[193]</sup>, alongside sebaceous glands. The modification of apocrine

glands to produce cerumen often results in comparison of cerumen to sweat in a research context. In such a context, it is noted that sweat may be used in non-invasive profiling of disease <sup>[194]</sup>. Therefore, cerumen may be used similarly in a relevant context.

General cerumen type is known to vary across individuals, with ethnicity often determining cerumen type. Two distinct cerumen phenotypes have been identified- wet/sticky and dry/brittle- with a single nucleotide polymorphism in the ABCC11 gene thought to determine type expressed <sup>[195, 196]</sup>. Wet type cerumen is primarily found in Caucasian and African American populations and drier type cerumen often found in Asian and Native American populations <sup>[192, 197]</sup>. In European, Middle Eastern, South African, and Pacific Island populations, dry cerumen is of intermediate frequency, with some individuals possessing wet type cerumen <sup>[198, 199]</sup>.

It would appear that wet type cerumen is the dominant phenotype, as the wet type homozygote (WW) phenotype is the same as the heterozygote (Ww) phenotype <sup>[195]</sup>. This genetic variation influences the secretory products of glands in the ear canal, with secretory cells of wet type cerumen demonstrating lipid droplets and pigment granules in their cytoplasm <sup>[199]</sup>. In individuals with dry cerumen, ceruminous glands are comparatively underdeveloped, alongside axillary and breast glands (which are also apocrine glands) <sup>[199]</sup>.

In a GC-MS-based examination, Prokop-Prigge *et al.* <sup>[182]</sup>, demonstrated that, similarly to cerumen appearance, the VOC profile of cerumen differs depending upon patient ethnicity. In general, it would seem that VOCs emitted are the same across ethnicities, but amounts produced vary greatly, with Caucasians generally exhibiting a greater level of VOCs than East Asians. With this in mind, factors such as age and gender may also alter the VOC profile of cerumen. These factors, as well as general phenotype, should be considered in as much detail as possible where uses in diagnoses and treatment are concerned. In particular, level of moisture in cerumen should be considered in detail as the requirements for sample preparation (as well as for accounting for water level when taking measurements) may vary across phenotypes.

Even with general individual differences such as age, race, and gender accounted for in metabolic profiles of cerumen, other variations may still obstruct the clear identification of cochlear cell pathologies. Although not the focus of this review, there are a range of factors which may contribute

to hearing difficulty such as infection, which could impact/challenge the VOC profiling of cerumen and identification of cell death.

The presence of infection is likely to impact a VOC profile of cerumen because changes in body odour are often reported during infection, and cerumen as a bodily secretion is often compared to sweat <sup>[194, 200]</sup>. Other conditions such as <sup>[184]</sup> and cancer <sup>[127]</sup> that may be detected via cerumen must also be accounted for in order to produce clear profiles of ARHL and non-ARHL conditions (as well as specific ARHL subtypes if possible).

#### 5.1.4. Factors Affecting Cerumen Production and Composition

Cerumen production and retention in the ear could also be affected by patient and professional intervention. Alterations to cerumen may occur as a result of treatment for issues directly associated with cerumen itself, or as a side effect of treatments for other conditions. One such issue associated with cerumen is impaction, wherein a build-up of cerumen leads to blockage of the ear canal, pain, and auditory issues such as tinnitus <sup>[201]</sup>. Though it is unclear what effect impaction may produce in metabolite analysis, it is likely that factors involved in treatment may alter VOC profiles. Often, impaction is treated via removal of wax which may make sufficiently sized sampling difficult if cerumen is to be used in diagnosis.

Additional impaction treatments include wax softeners, which allow drainage of wax from the ear canal. Wax softeners are usually available over the counter thus are often self-administered by patients <sup>[202]</sup>. As such, aside from the optimistic assumption that patients will adhere to product instructions and advised dosage, there is little way of regulating the use of such products among impaction patients.

Further treatments for ear-related issues may also present problems in diagnosis, though the lack of research centred on cerumen makes this difficult to verify at present. However, with VOC profiles having previously been used in drug screening, it is possible that any techniques to ascertain VOC profiles in cerumen may pick up drug-based treatments such as antibiotics <sup>[203]</sup>. This factor, additionally, would unlikely be limited to treatments for ear issues (e.g. otitis), with cerumen VOC

profiles potentially displaying markers of treatments administered for any condition. Nonetheless, like non-ear pathologies discussed previously, as long as these markers may be distinguished from those of ARHL, effective diagnosis is unlikely to be affected significantly.

## 5.2. Chapter Aims

The aims of this section of research are as follows:

1. Establish a headspace profile of healthy cochlear fibrocytes using SIFT-MS.
2. Establish a headspace profile of TNF- $\alpha$  -dosed cochlear fibrocytes and distinguish between healthy and inflamed cells using SIFT-MS.
3. Establish a headspace profile of IL-1 $\beta$ -dosed cochlear fibrocytes and distinguish between healthy and inflamed cells using SIFT-MS.
4. Conduct preliminary investigations of the spectral and VOC profiles of human cerumen samples using Raman spectroscopy, ATR-FTIR spectroscopy and SIFT-MS.

## 5.3. Materials and methods

### 5.3.1. Cochlear Fibrocyte Cultures

As outlined in section 2.1, murine cochlear fibrocytes were retrieved from CD/1 mice using methods adapted from the gerbil dissection protocol of Gratton *et al.* <sup>[89]</sup>. All cochlear fibrocyte cell culture was conducted under sterile conditions in a class 2 BSC. Cells were grown in a 37°C (5% CO<sub>2</sub>) incubator with media changes every other day. Cells were passaged and stored as outlined in section 2.1.3.

Ahead of SIFT-MS sampling, cochlear fibrocyte and associated control media samples were created in triplicate in 150ml bottles with black rubber septum lids. Sample conditions in healthy cell investigations were media only controls, 15,000 cells and 100,000 cells per sample. Samples were seeded, air purged using dry compressed air, and incubated at 37°C for approximately 16 hours before measurement. Where additional processing (e.g. incubation of inflammatory agents) was required, 16-hour incubation time was factored into this (see section 5.3.2).

### 5.3.2. Induction of Inflammation in Cochlear Fibrocytes

Following confirmation of successful inflammation-like state induction by TNF- $\alpha$  and IL-1 $\beta$ , cells were inflamed via the addition of TNF- $\alpha$  or IL-1 $\beta$  to culture media. To do this, standard cochlear fibrocyte culture media was dosed with 1ng/mL, 5ng/mL and 10ng/mL of cytokine (TNF- $\alpha$  or IL-1 $\beta$ ) solution to produce conditions. Cells were then incubated (37°C, 5% CO<sub>2</sub>) for 24 hours in this media, with air purge at 16 hours as outlined in section 5.3.1.

### 5.3.3. Headspace Analysis of Cochlear Fibrocyte Cultures Using SIFT-MS

During measurement, samples were heated in a 37°C water bath and normalised to a water vapour level of 4% using in-software flow rate adjustment. Measures of VOCs in sample headspace were conducted using Transpectra Software, Transpectra UK, with observations across H<sub>3</sub>O<sup>+</sup> and NO<sup>+</sup> precursors for compounds of m/z 1-180. Multi-ion monitor mode samples were taken using the uploaded kinetic library for 40 seconds in each bottle for both reagent ions. Average scans (each scan= average of 3 20 second scans) of each sample were also taken for both reagent ions. Headspace in bottles was topped up using a purge bag containing dry compressed air between each measurement.

### 5.3.4. Human Cerumen Samples

All human cerumen samples employed in this research were commercially sourced via Caltag Medsystems (Buckingham). As samples were purchased through a commercial supplier and no patients were directly involved in the research, no patient-focused ethical clearance was necessitated. Nonetheless, ethical clearance for use of the biofluid was obtained via Keele University's Faculty of Medicine and Health Sciences Research Ethics Committee.

Due to the potential for tissue presence in cerumen samples and the resulting classification as a 'relevant material' (point 54, Human Tissue Act, 2004), all samples were handled, stored, transported and disposed of according to the Human Tissue Act (2004).

### 5.3.5. Raman Spectroscopy of Cerumen

For the purposes of Raman spectroscopy, a single cerumen sample was transferred from the cotton swab upon which it arrived to a  $\text{CaF}_2$  substrate. No fixation or further treatment was applied. Sampling was conducted using a Thermofisher DXR 3 Raman spectrometer (532nm laser, full range grating) as outlined in section 2.2.1. A 120 second acquisition time was used for each sample point, with 3 scans per sample and 4 scans of background. A series of 'blank' spectra were taken from cerumen free substrate regions. Prior to sample spectrum collection, samples were photobleached for 30 seconds to mitigate sample fluorescence and improve the contrast of Raman bands in spectra. A high cosmic ray threshold was employed.

### 5.3.6. ATR-FTIR Spectroscopy of Cerumen

In preparation for ATR-FTIR, cerumen swabs trialled in both wet and 'processed' states. Dry wax was not subjected to any preparation, it was transferred to sample slides. 'Processed' wax was submerged in 200 $\mu\text{L}$   $\text{dH}_2\text{O}$  and heated to 37°C for 10 minutes. Vials of  $\text{dH}_2\text{O}$  containing cerumen were then centrifuged at 1200RPM for 3 minutes. Supernatants were discarded and samples vortexed for 10 seconds followed by thorough mixing. Mixed samples were pipetted onto Dxcovers® sample slides (6 $\mu\text{L}$  per silicon wafer) and air dried.

ATR-FTIR measurements were taken using a Thermo Scientific iS50 spectrometer coupled with the Specac Quest ATR accessory onto which a Dxcovers® autosampler was positioned. Dxcovers® Sample Slides were loaded into the Dxcovers® auto sampler for measurement as outlined in section 2.3.2. Spectral parameters were set as follows: 128 co-added scans per spectrum with a resolution of 4 $\text{cm}^{-1}$  across a 4000-400 $\text{cm}^{-1}$  range.

### 5.3.7. Headspace Analysis of Cerumen Using SIFT-MS

Cerumen samples on swabs were placed into 150mL glass bottles as used in cellular investigations, with swab stems trimmed to allow sealing of bottles. Samples were air purged with dry compressed air 16 hours prior to sampling to remove laboratory air and to allow VOC accumulation. Samples were then incubated for 16 hours at 37°C.

Following incubation, measures of VOCs in sample headspace were taken as outlined in section 5.3.3. Water correction was conducted at 2% rather than 4% to account for the use of dry samples.

### 5.3.8. Data Processing and Analysis

SIFT-MS sampling was conducted either in the form of a 40 second duration continuous abundance/time profile (MUI) or an average scan (3 scans of 20 seconds) of abundance per sample in counts/second (FS). SIFT-MS acquired profiles were handled in either SIFT time profile viewer or SIFT mass spectra software (for MUI and FS data respectively). MUI data samples were normalized via water value correction to 4% (wet samples) or 2% (dry samples). Statistical testing of MUI data was conducted via Mann Whitney U test or Kruskal Wallace H test (depending upon condition numbers), performed in SPSS data analysis software to a  $p \leq 0.05$  significance level. Bar charts presenting MUI data were generated in Microsoft Excel 2016. FS data were automatically normalized and averaged, before exporting into Microsoft Excel 2016 for compilation and formatting. For  $\text{H}_3\text{O}^+$  FS data,  $m/z$  17-180 were presented, with precursor isotopologues removed:  $m/z$ s 19, 20, 21, 30, 32, 34, 37, 38, 39, 48, 55, 56, 57, 66, 73, 74, 75, 91.  $\text{NO}^+$  data were treated similarly, with removal of  $m/z$  30. FS heat maps were generated using Quasar software. Where relevant, bar charts of compounds were generated in Microsoft Excel.

Raman data processing and analysis was conducted in Orange (Quasar) software as detailed in chapter 2.4.2. Spectra were cut for noise, baseline corrected (rubber band), smoothed (Savitsky-Golay), normalised (vector normalisation) and cut to areas of interest. An average of obtained spectra is presented.

ATR-FTIR samples were processed using Orange (Quasar) software. Spectra were cut for noise, baseline corrected (rubber band), smoothed (Savitsky-Golay), normalised (vector normalisation) and cut to areas of interest. Graphs of average spectra were created in Microsoft Excel to enable offsetting. Manual peak identification was performed on average spectra. vibrations and potential molecules through literature consultation.

## 5.4. Results and Interpretation

### 5.4.1. SIFT-MS of Healthy Cochlear Fibrocytes

In general, SIFT-MS analysis of healthy cochlear fibrocytes demonstrates distinct and detectable differences between cultures containing cochlear fibrocytes and media-only controls at both high (100,000 cells per sample) and low, biologically relevant (15,000 cells per sample) cell numbers.

Examining the FS profiles of healthy cells under both  $\text{H}_3\text{O}^+$  and  $\text{NO}^+$  precursors, it becomes clear that  $\text{H}_3\text{O}^+$  yields far richer signal than  $\text{NO}^+$  (Fig.132). With this in mind, the majority of SIFT-MS observations in the present research are made under the  $\text{H}_3\text{O}^+$  precursor.



**Figure 132: FS heat maps demonstrating compound visualisation across  $\text{H}_3\text{O}^+$  and  $\text{NO}^+$  conditions for cellular samples.**

**A)  $\text{H}_3\text{O}^+$  B)  $\text{NO}^+$**

Looking into  $\text{H}_3\text{O}^+$  FS data more closely, differences between cells and media controls may be seen, with several m/z arising that appear to be unique to the cellular profile (Fig. 133). Possible compounds identified have likely origins in cells (pyrrole- cytoplasm, hexyl acetate and menthone- membranes) and highlight SIFT-MS detectable profiles for cochlear fibrocytes. Additionally, variations in compounds associated with cellular respiration such as acetaldehyde and pyruvic acid.

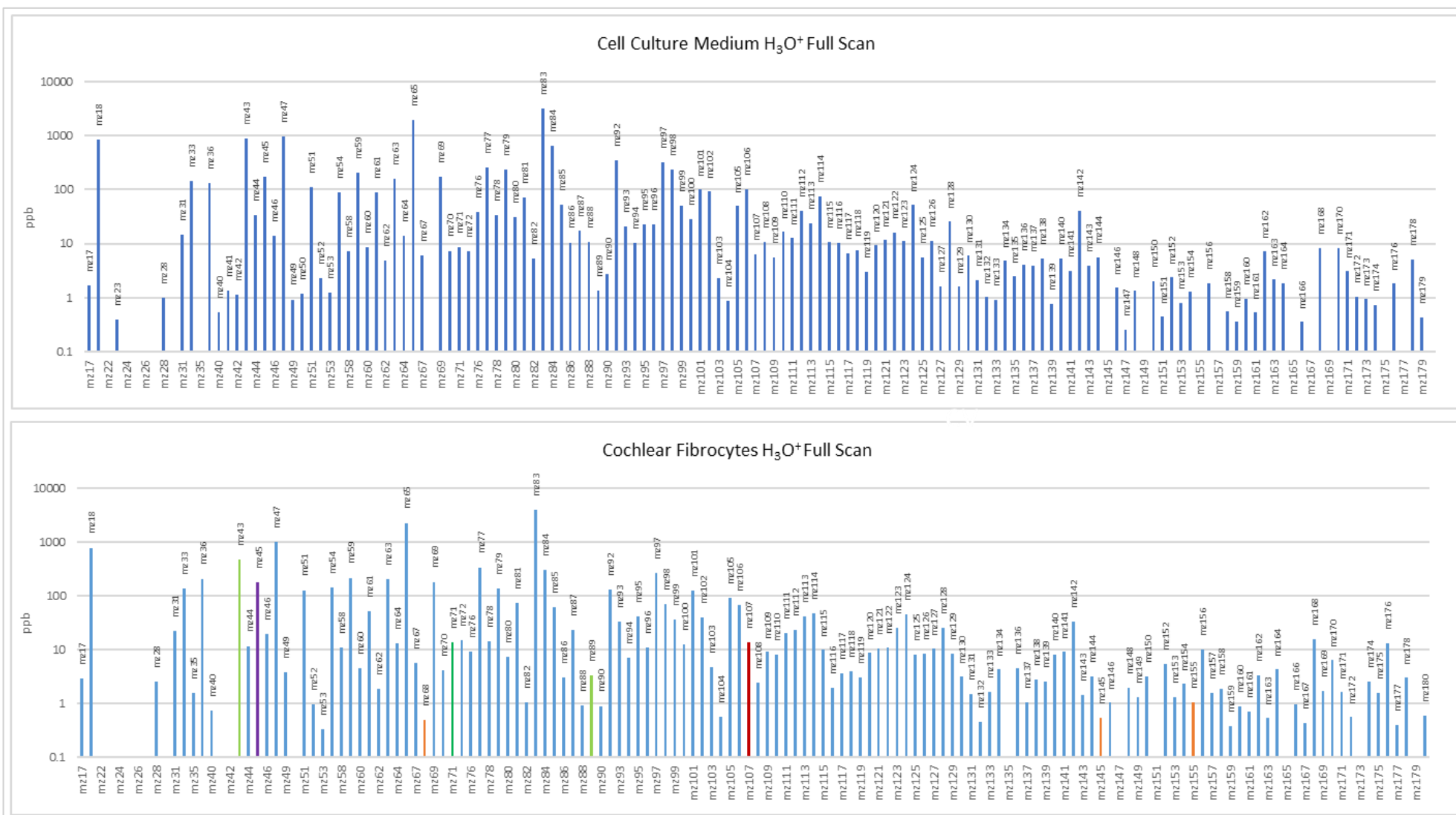


**Figure 133: Full scan mode H<sub>3</sub>O<sup>+</sup> data for cell culture media and cochlear fibrocyte samples.**

Compounds of interest including pyruvic and butyric acid (green), acetaldehyde (purple) and benzaldehyde (red) are highlighted in the cellular profile. Unique to cell compounds (pyrrole, hexyl acetate, menthone) are also identified.

Based upon the findings of FS, multi-ion monitor  $\text{H}_3\text{O}^+$  data was examined for variations in cell-associated compounds.  $\text{H}_3\text{O}^+$  MUI analysis of cells and media controls showed significant differences in acetaldehyde ( $U(N_{\text{media}}=N_{15000}=3)=2$ ,  $z=-2.193$ ,  $p<0.05$ ), butyric acid ( $U(N_{\text{media}}=N_{15000}=3)=2$ ,  $z=-2.193$ ,  $p<0.05$ ), benzaldehyde ( $U(N_{\text{media}}=N_{15000}=3)=0$ ,  $z=-2.611$ ,  $p<0.05$ ) and pyruvic acid ( $U(N_{\text{media}}=N_{15000}=3)=0$ ,  $z=-2.611$ ,  $p<0.05$ ) between media and fibrocyte samples (Fig. 134). These compounds are commonly noted in various mammalian biofluids and predominantly vary as a result of processes such as glucose metabolism and cellular respiration.

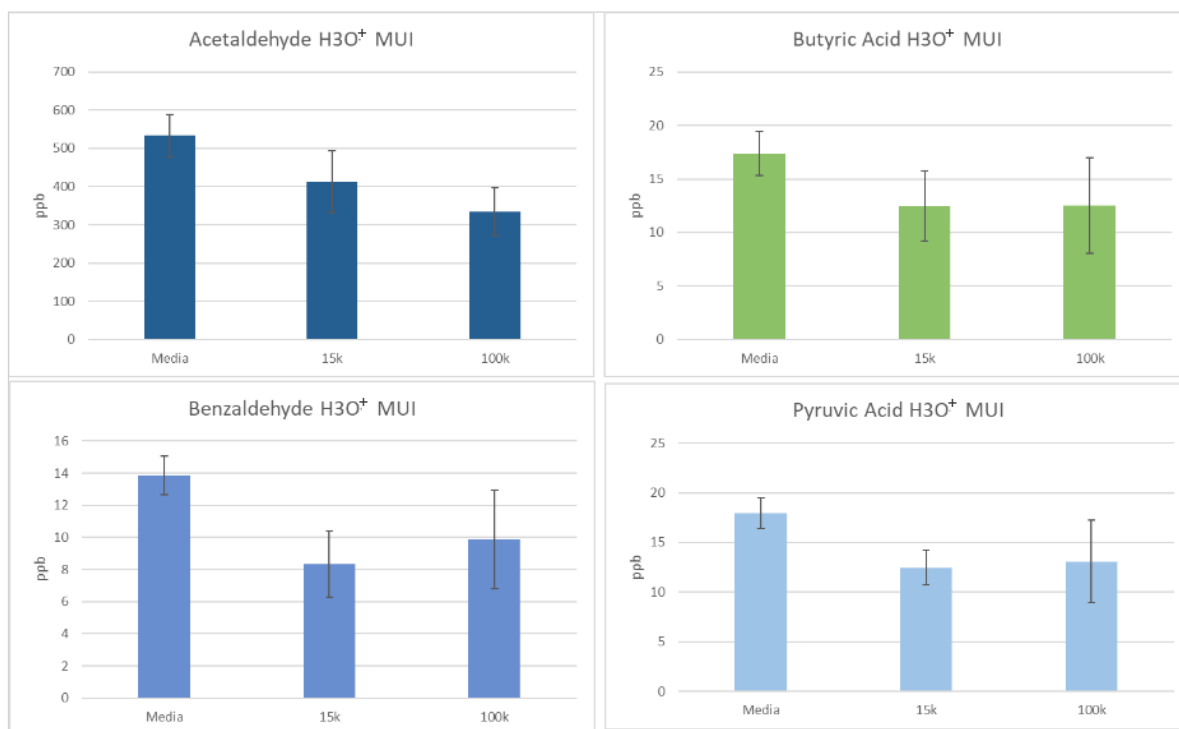


**Figure 134: MUI  $\text{H}_3\text{O}^+$  data demonstrating statistically significant compound differences between cell culture media and cochlear fibrocyte samples. PPB = parts per billion.**

Based upon examined significance, it would appear that acetaldehyde and pyruvic acid are the most consistently reliable indicators of cell presence in fibrocyte samples when compared with media only controls. In the case of acetaldehyde (though no statistically significant difference is seen between 15,000 and 100,000 cell conditions) the overall decreasing trend as cell number increases suggests a consumption of the compound by cells, though this does not appear proportional to cell number – potentially due to cells reaching a consumption limit/becoming saturated. In any case, the significant differences shown indicate that cochlear fibrocyte metabolic action may be visualised

through SIFT-MS examination even at small cell numbers, a vital step in moving towards inflammation examination.

#### 5.4.2. SIFT-MS of TNF- $\alpha$ -dosed Cochlear Fibrocyte Culture Headspace

Ahead of the examination of SIFT-MS results, it is important to note that some issues in culture were noted at this stage of research. Though seemingly healthy and dosed with antibiotics, cells did not adhere well to the culture surface prior to conduction of experiments. This is assumed to be due to the possible semi-thawing of cells at a point during storage due to storage system failure.

As in healthy cell analysis,  $\text{H}_3\text{O}^+$  FS results appear to demonstrate richer signals than those in  $\text{NO}^+$ , with more scope for exploration of variation across conditions apparent (Fig 135). Thus,  $\text{H}_3\text{O}^+$  results are prioritised in MUI analysis.

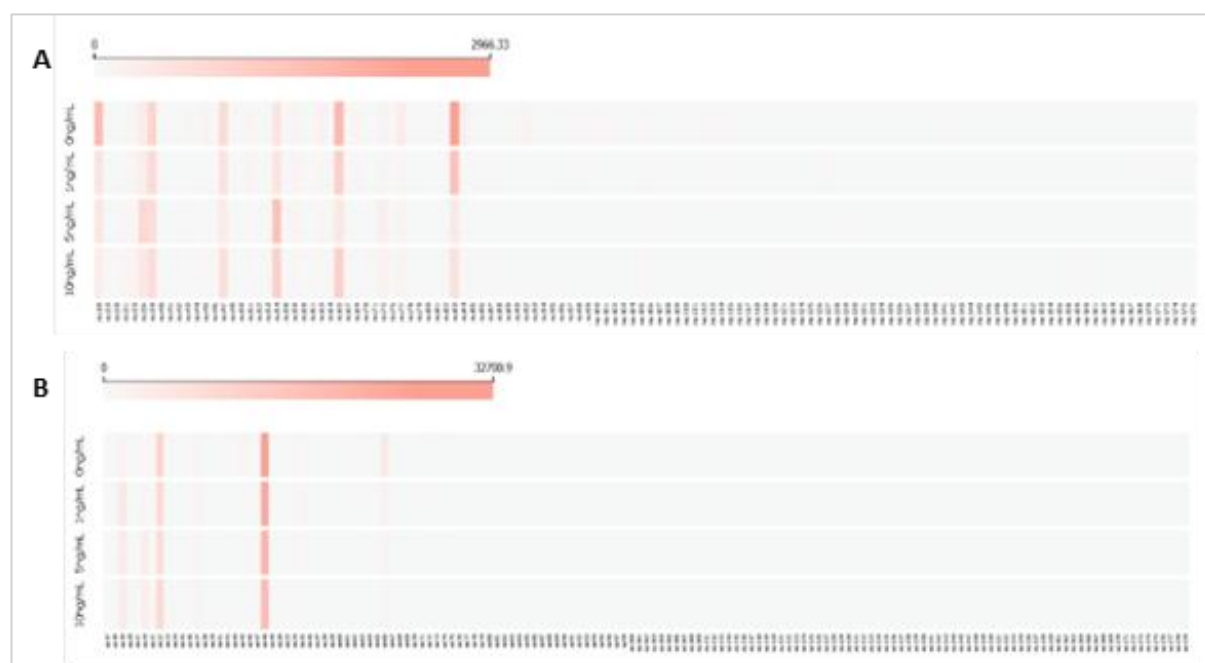


**Figure 135: FS heat maps demonstrating compound visualisation across  $\text{H}_3\text{O}^+$  and  $\text{NO}^+$  conditions for TNF-dosed cellular samples.**

**A)  $\text{H}_3\text{O}^+$  B)  $\text{NO}^+$**

In SIFT-MS investigations of TNF-dosed cochlear fibrocyte cultures, several variations in headspace across dosage are visible. Conducting a Kruskal-Wallis H test of  $\text{H}_3\text{O}^+$  MUI data showed statistically significant differences ( $p < 0.05$ ) in the levels of several compounds between dosage conditions: acetaldehyde ( $H(3)=16.734$ ,  $p = < 0.001$ ), propanol ( $H(3)=12.606$ ,  $p = 0.006$ ), acetic acid

(H(3)=14.023, p=0.003), DMS/ethanthiol (H(3)=18.544, p=<0.001), pentene (H(3)=9.895, p=0.19), putresceine (H(3)=11.492, p=0.009), terpenes (H(3)=11.422, p=0.10), benzene (H(3)=13.763, p=0.003), and DMSO (H(3)=16.457, p=<0.001). Based upon literature and the findings of chapter 3, acetaldehyde variation is particularly of interest.

Though there does not appear to be a distinct dosage response across conditions, H<sub>3</sub>O<sup>+</sup> MUI data (Fig. 136) shows acetaldehyde level in cell headspace is significantly decreased in the presence of TNF- $\alpha$ . This variation strongly suggests a reduction in cell metabolic capacity, likely as a result of inflammation induced cellular damage.

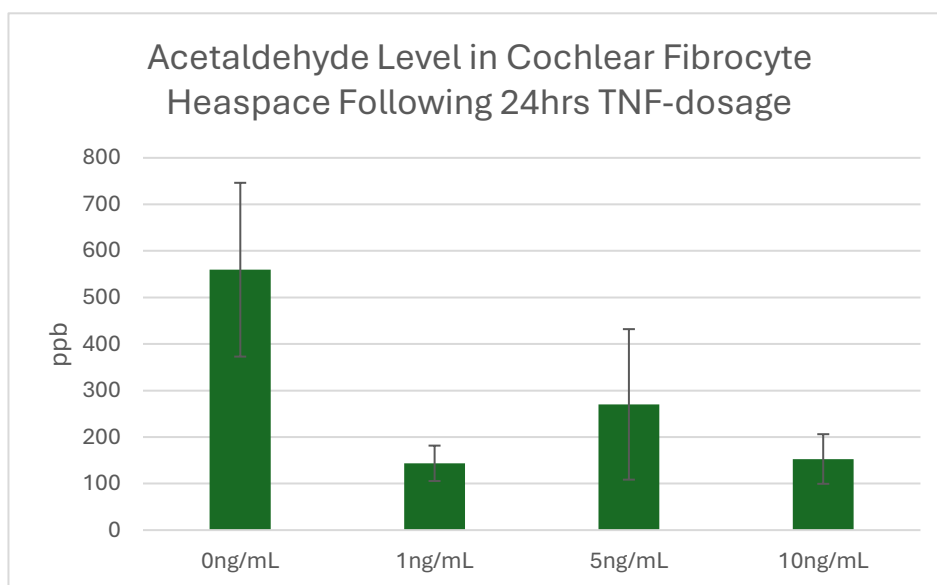


**Figure 136: SIFT-MS MUI H<sub>3</sub>O<sup>+</sup> data demonstrating significant differences across acetaldehyde levels in TNF-dosed cochlear fibrocytes. PPB = parts per billion.**

Though no statistically significant difference was found across dosage conditions, it is of note that pyruvic acid level (Fig. 137) is shown to be far greater in both the 1ng/mL and 10ng/mL TNF dosage condition compared to controls, though this is not reflected in 5ng/mL. (Such lack of consistency is believed to originate from the issues in culture noted prior.) Though inconsistent, increase in pyruvic acid level strongly implies inflammation-induced alterations in cellular respiration. Arguably with greater sample numbers and more fortunate culture outcomes, significant differences in this metabolite may be seen across dosages.

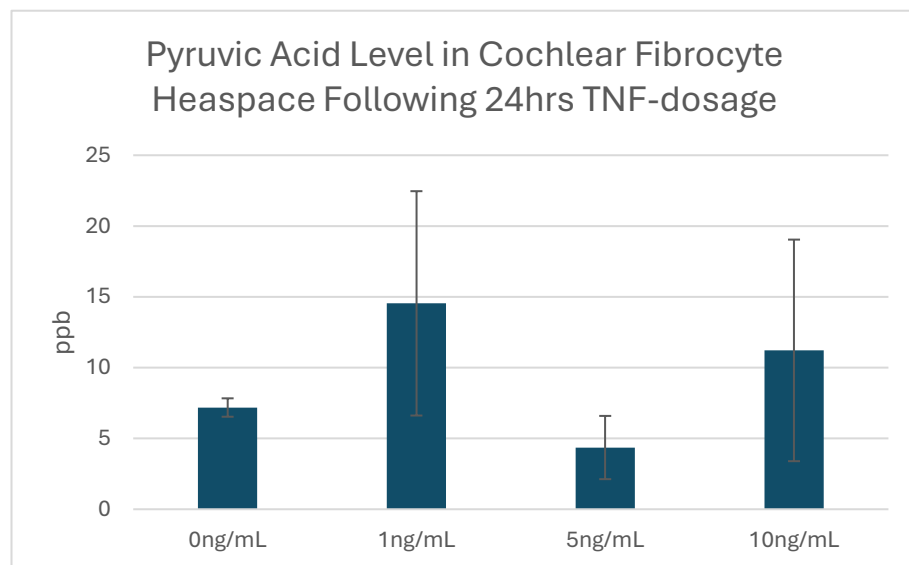


**Figure 137: SIFT-MS MUI  $\text{H}_3\text{O}^+$  data demonstrating significant differences across pyruvic acid levels in TNF-dosed cochlear fibrocytes. PPB = parts per billion.**

#### 5.4.3. SIFT-MS of IL-1 $\beta$ -dosed Cochlear Fibrocyte Culture Headspace

In investigating the VOC profiles of IL-1 $\beta$  cochlear fibrocytes, several compounds are of interest based upon the changes to cells noted in previous chapters and vibrational spectroscopy analysis. In particular, acetaldehyde and pyruvic acid are deemed of note in the present research context.

Beginning again with FS data (Fig. 138), it is clear that  $\text{H}_3\text{O}^+$  precursor scans demonstrate far richer and more concentrated signal. This is ideal for the present purposes, hence  $\text{H}_3\text{O}^+$  MUI examination was prioritised. It should also be noted that  $\text{H}_3\text{O}^+$ , unlike other precursors, cannot cause fractionation of samples, yielding a far more direct, reliable sample analysis than  $\text{NO}^+$  and  $\text{O}_2^+$ .



**Figure 138: FS heat maps demonstrating compound visualisation across  $H_3O^+$  and  $NO^+$  conditions for IL-dosed cellular samples.**

**A)  $H_3O^+$  B)  $NO^+$**

Continuing to MUI data, a Kruskal-Wallis H test of  $H_3O^+$  MUI data showed a statistically significant difference ( $p < 0.05$ ) in acetaldehyde level between IL- $1\beta$  dosage conditions for ( $H(3) = 7.937$ ,  $p = 0.047$ ).

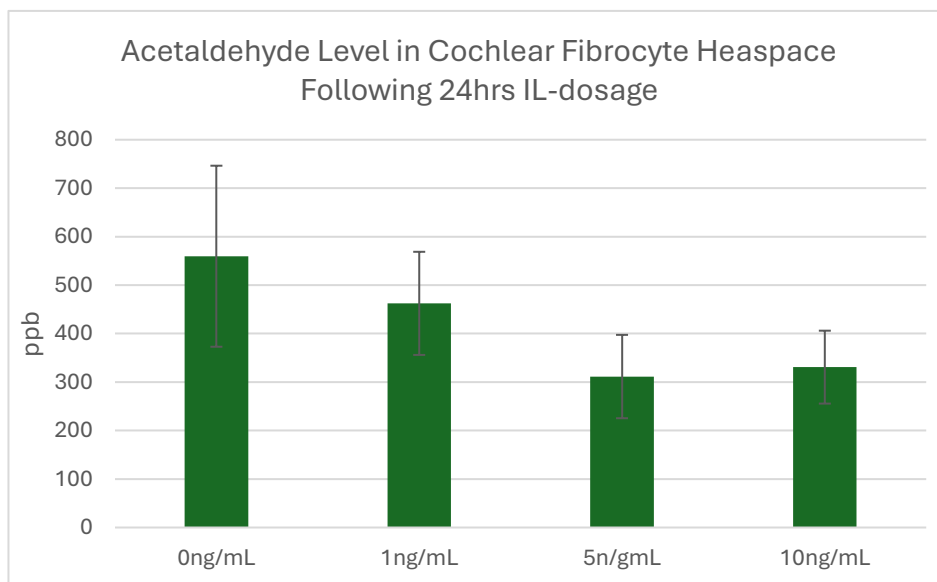


**Figure 139: SIFT-MS MUI  $H_3O^+$  data demonstrating significant differences across acetaldehyde levels in IL-dosed cochlear fibrocytes. PPB = parts per billion.**

Viewing these results graphically (Fig. 139), acetaldehyde level in cell headspace appears to decrease as IL-1 $\beta$  dosage increases, though there is a small increase in the 10ng/mL dosage condition. This general decrease in headspace acetaldehyde across dosage conditions implies a reduction in cellular metabolic processes such as respiration as dosage increases and the effects of inflammation become more pronounced.

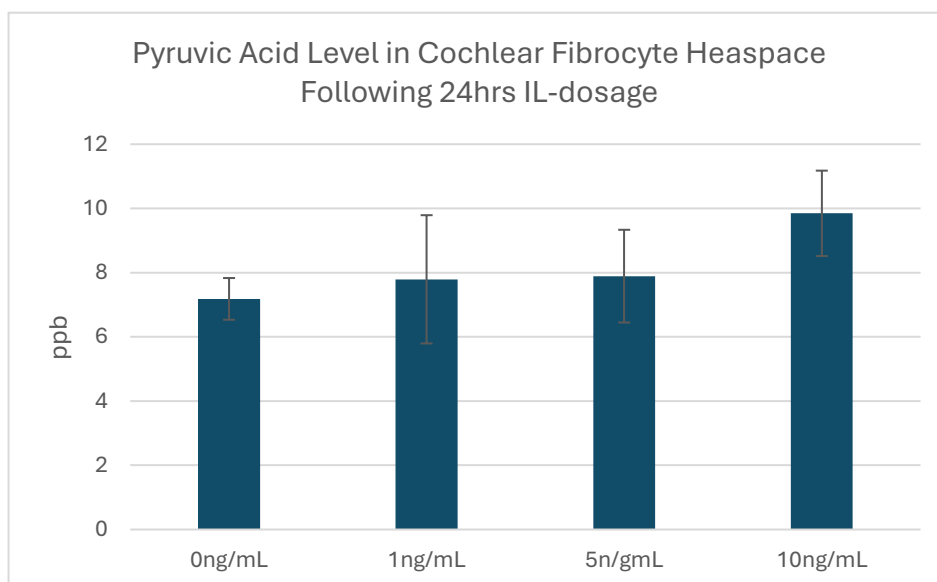


**Figure 140: SIFT-MS MUI H<sub>3</sub>O<sup>+</sup> data demonstrating significant differences across pyruvic acid levels in IL-dosed cochlear fibrocytes. PPB = parts per billion.**

Pyruvic acid level, in contrast, appears to demonstrate a generally increasing trend across dosage conditions (Fig. 140). Though statistical significance is limited by the low sample number trialled, it may be stated that this increasing trend is as expected. That is, an increase in pyruvic acid level strongly implies inflammation-induced alterations in cellular respiration, particularly in the stages which follow glycolysis (citric acid cycle etc.). Such alterations may, in turn, imply mitochondrial dysfunction- an expected consequence of such inflammation.

Based upon these findings, and considering those in previous sections, it is suggested that IL-1 $\beta$  application yields similar inflammatory effects to TNF- $\alpha$ , with similar changes in cell metabolism arising as a result of dosage. Whether this similarity indicates upregulation of each cytokine by the other in the present context is unclear. Exploration of this through immunocytochemistry and other means is recommended in future study.

#### 5.4.4. Raman Spectroscopy of Human Cerumen

When examining Raman spectra of cerumen samples, it should first be noted that signals demonstrate far greater clarity and intensity than those of cells as examined in previous chapters (Fig. 141). Signal clarity is likely improved in this case due to homogeneity of the sample employed- that is, point samples were conducted across a single wax sample and considerations typical of cellular samples (e.g. variations in cell cycle) are not in effect.

It should also be noted that there appears to be an overall shift in signal towards the high wavenumber end, potentially arising as a result of the irregular topography and density of the wax sample. This is taken into consideration when assigning sample bands.

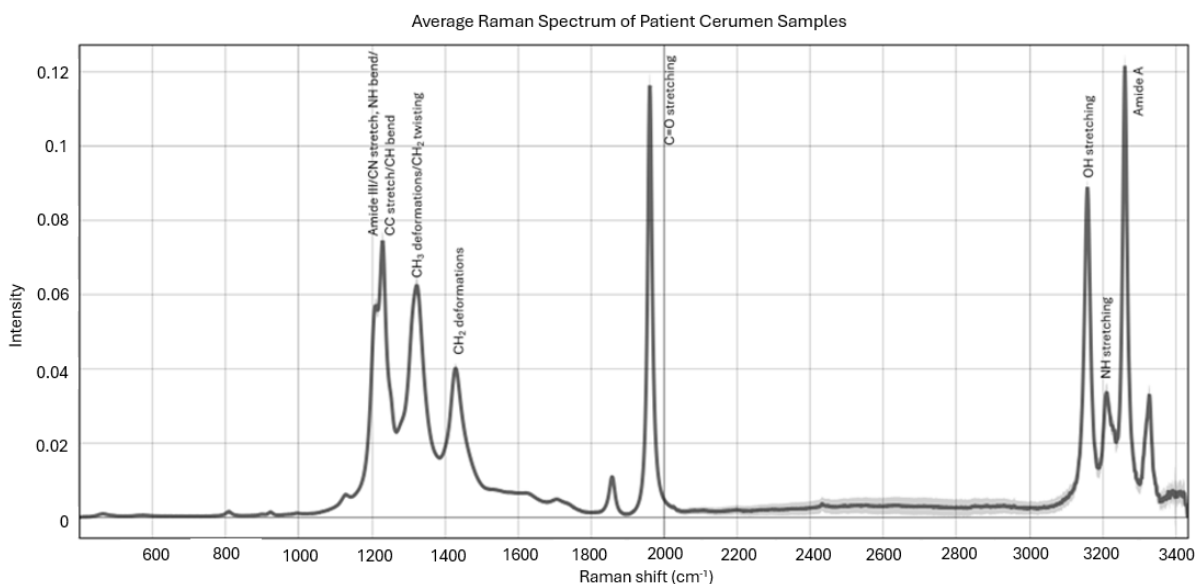


**Figure 141: Average Raman spectrum of human cerumen samples from patients.**

Examining the average spectrum gathered, it would appear that there is very little signal below  $1000\text{cm}^{-1}$ , with only negligible peaks arising in the regions associated with glycogen, proteins and carbohydrates in this section of spectrum. Considering the potential use of cerumen as a carrier of cell signals, it is observed that many areas of interest highlighted in cell investigations (see previous chapters) do not demonstrate signal in cerumen samples.

Despite this, very clear signal is present in regions associated with  $\text{CH}_2$  deformation ( $1200\text{--}1600\text{cm}^{-1}$ ) and  $\text{C=O}$  stretching of lipids ( $1800\text{--}2000\text{cm}^{-1}$ ) with visible signal, though seemingly shifted, somewhat resembling other waxes examined via Raman spectroscopy (e.g. paraffin wax) <sup>[204]</sup>. The high

wavenumber region, additionally, shows signals of far greater complexity than those seen in cell samples and consistent with a lipid-based sample such as cerumen.

Bands are tentatively assigned in Figure 141 above, with presence of noted vibrational modes believed to arise from constituent components of ear wax such as keratin and squalene. Evidence of both saturated and unsaturated fatty acids can be seen, though spectra lack the distinct C=C band expected in the  $1650\text{cm}^{-1}$  wavenumber region for unsaturated fatty acids.

#### 5.4.5. ATR-FTIR Spectroscopy of Human Cerumen

In the sample optimisation stage, both dry and 'processed' wax conditions were trialled as detailed in section 5.3.6. Differences between dry and processed wax are clear even before spectral preprocessing (Fig. 142), with dry wax samples yielding signal & baseline. 'Processed' wax, in contrast, demonstrates clearer signal in both the fingerprint and high wavenumber regions. This indicates the necessity for processing steps in sample preparation if using dry wax and stored samples such as those from commercial sources.

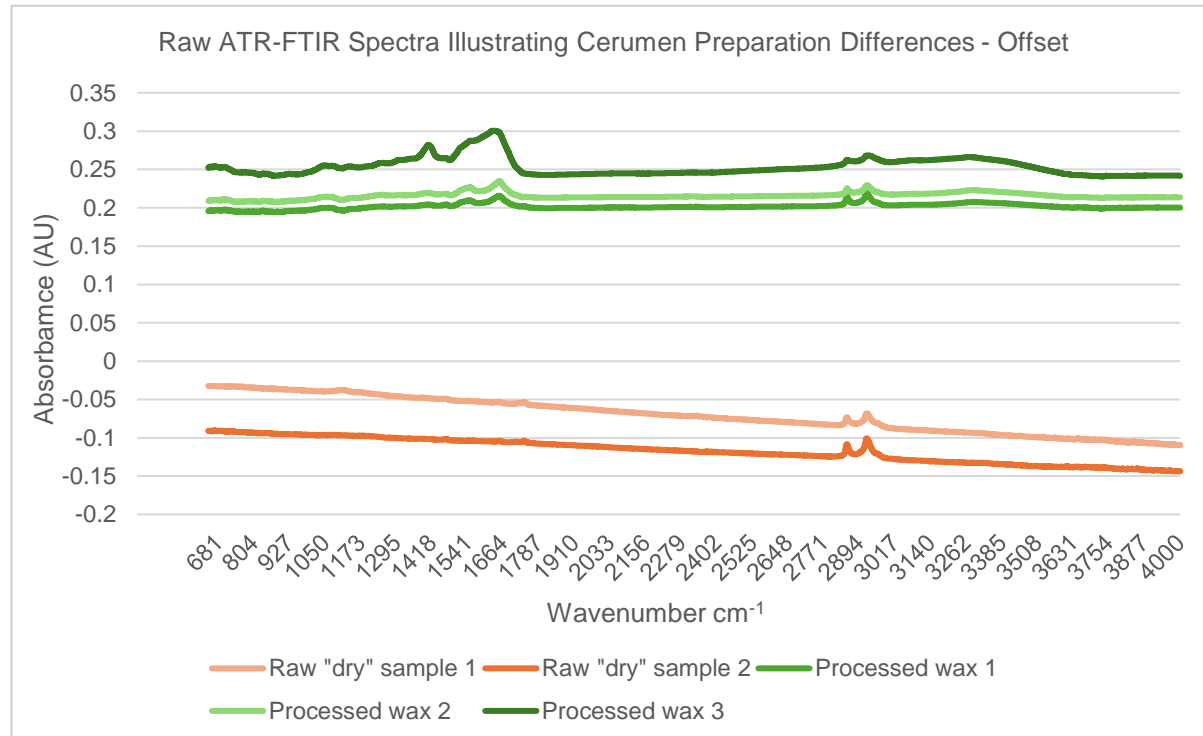


**Figure 142: Raw ATR-FTIR spectra of human cerumen samples in dry and processed states.**

Following spectral pre-processing, average spectra of each patient sample were analysed in order to explore variation across individuals (Fig. 143). Recurring bands across all sample spectra arose at locations such as  $1650\text{cm}^{-1}$  and  $2918\text{cm}^{-1}$ , attributable to protein and lipid presence in samples.

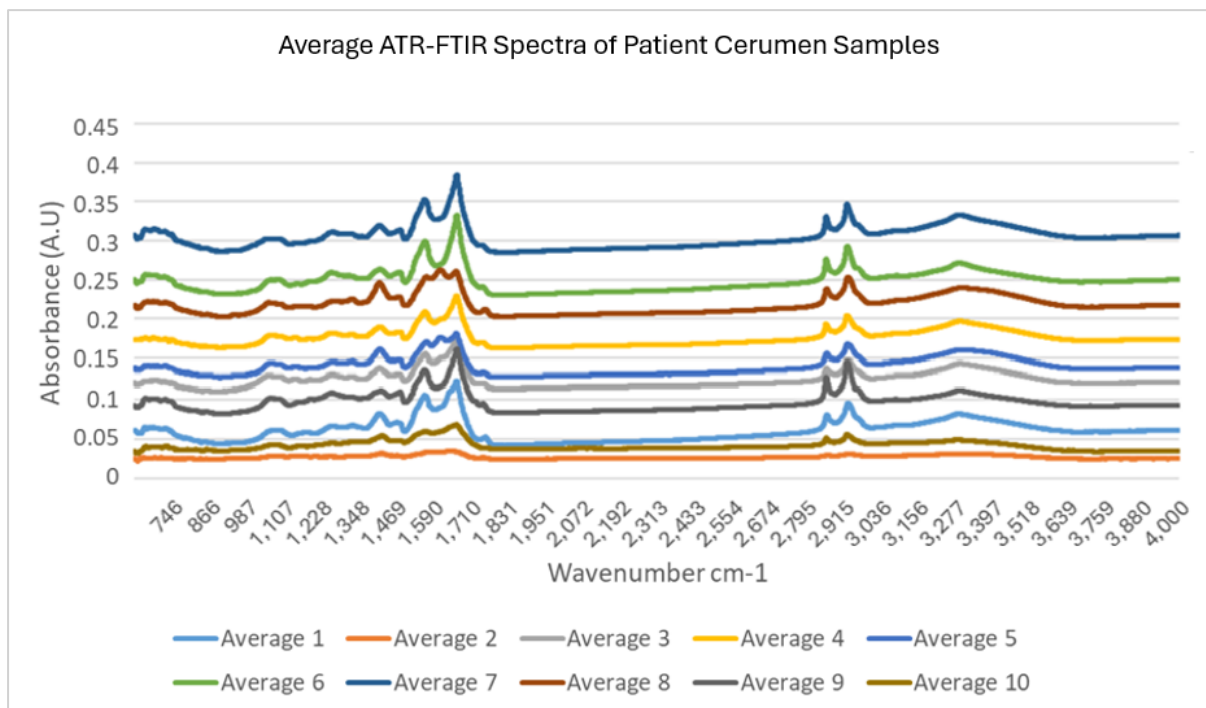


**Figure 143: Average ATR-FTIR spectra of human cerumen samples.**

Though bands are not as clear as those seen in direct Raman spectroscopic analysis, signal is still present in regions associated with  $\text{CH}_2$  deformation of lipids ( $\sim 1340\text{cm}^{-1}$ ),  $\text{COO}^-$  symmetric stretching of fatty acids ( $\sim 1400\text{cm}^{-1}$ ) and  $\text{C=O}$  stretching of lipids ( $\sim 1710\text{cm}^{-1}$ ,  $2900\text{--}3000\text{cm}^{-1}$ ). Though, unlike in Raman spectra, the presence of unsaturated lipids is not clear in IR observations, there is some evidence of  $\text{C=C}$  stretching in the  $1640\text{--}1650\text{ cm}^{-1}$  range. Further indicators of unsaturated lipids such as methylene deformation (noted above) are also present in spectra. This is indicative of unsaturated lipid presence, with lack of clarity in spectra believed to arise due to IR spectroscopy's limited sensitivity to unsaturated bonds compared with Raman and the general presence of broader, less distinct bonds in the spectral fingerprint region.

As in the Raman spectrum, there is very little signal below  $1000\text{cm}^{-1}$ . This region is recommended for explorations of cell signals in fresh cerumen samples in the future. The wax signal

shown by ATR-FTIR, like in Raman analyses, resembles other waxes examined using similar techniques such as beeswax [264].

Despite the lack of cell-related signals in observations, this trial has nonetheless optimised a sample preparation method for cerumen utilising the Dxcover® Infrared Platform with ATR-FTIR technology. Coupled with improvements in sampling (i.e. the use of fresh patient samples to optimise signal potential), this research marks the first step towards creating a non-destructive, rapid cerumen sampling approach using ATR-FTIR.

5.4.6. SIFT-MS of Cerumen Sample Headspace

Investigating the VOC profiles of human cerumen samples, it would appear that there is very little distinction to be made between wax samples and blank swabs. H<sub>3</sub>O<sup>+</sup> MUI of blank swabs vs cerumen shows no significant differences when subjected to Mann Whitney U test. Similarly, NO<sup>+</sup> MUI of blank swabs vs cerumen shows no significant differences when subjected to Mann Whitney U test. As no significant differences are seen, graphical data is not presented for MUI.

Examining full scan data, it is once again made apparent that there is little difference to be found between swabs with and without cerumen (Fig. 144). In contrast to the findings of Raman spectroscopy investigations, it may also be seen from FS results that cerumen demonstrates a far weaker VOC signal than cellular samples, with an almost ten-fold reduction in signal intensity.

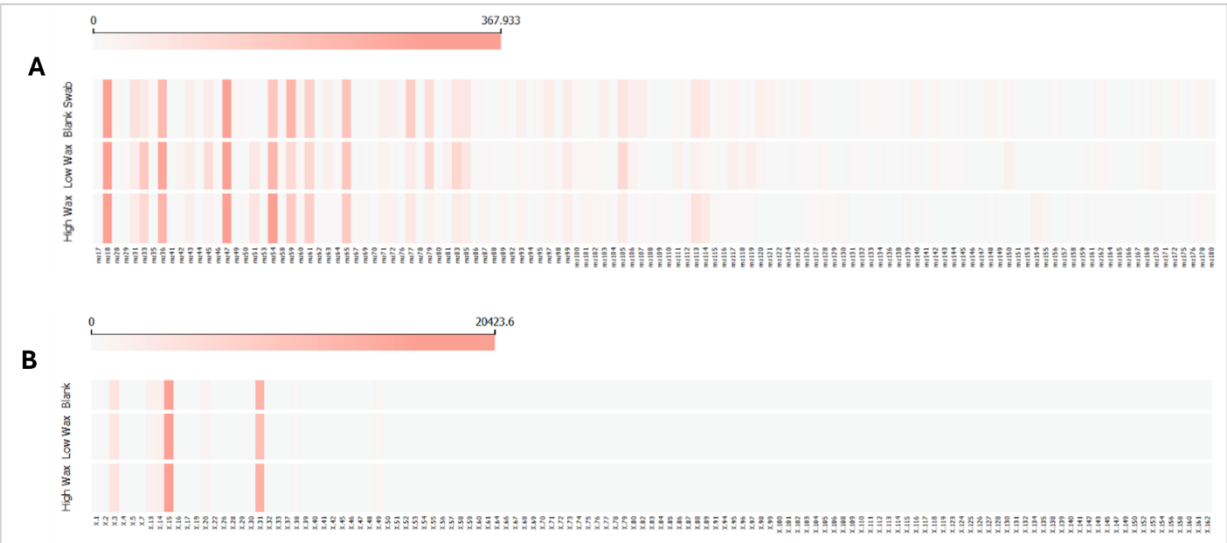


Figure 144: FS heat maps demonstrating compound visualisation across H<sub>3</sub>O<sup>+</sup> and NO<sup>+</sup> conditions for human cerumen samples.

A) H<sub>3</sub>O<sup>+</sup> B) NO<sup>+</sup>

It is clear from the data gathered that there is little distinction to be made between human cerumen samples and the blank swab controls used for comparison. Several factors may be implicated in consideration of why this is the case, including sample wax volume and the potential of blank swab signals overpowering those of wax itself.

In consideration of wax samples, it should be noted that the samples provided were not of consistent wax volume or mass. In fact, many of the provided samples did not contain solid cerumen masses, rather small smudges upon swabs. Where no larger cerumen sample was available for comparison, the possibility that wax signal was simply too weak for detection against swabs cannot be ruled out.

## 5.5. Discussion

In general, this section of research demonstrates advancements in the earliest stages of SIFT-MS employment in non-invasive ear health analyses. A VOC profile of cochlear fibrocytes is established, with cellular inflammation seemingly detectable through SIFT-MS analysis. With a view to future translation of this finding, human cerumen sampling methods are trialled using Raman spectroscopy, ATR-FTIR and SIFT-MS.

SIFT-MS results demonstrated clear differences between cellular and media only conditions, with significant differences arising in compounds attributable to the metabolic functioning of cells in culture. The presence of acetaldehyde is of particular interest as this compound is well correlated with cell presence, and metabolic activity <sup>[128, 130]</sup>. The significant reduction in pyruvic acid seen between media controls and cell-containing samples indicates cellular respiration, wherein pyruvic acid (also referred to as pyruvate) is a key metabolite employed in the formation of acetyl-CoA and subsequently ATP through the citric acid cycle in typical aerobic conditions. Aerobic conditions are to be expected in the native spiral ligament due to proximity with the highly vascularised *stria vascularis*. The apparent consumption of pyruvic acid seen in SIFT-MS results hence implies healthy cellular respiration at work.

It is notable that, while acetaldehyde levels are known to correlate with cell presence and metabolic activity, they are not taken as a direct indicator of cell viability in the present research. Instead, these levels are believed to reflect metabolic function and the cellular response to inflammation (under dosed conditions), with the observed trends in acetaldehyde concentration across different conditions indicative of its role as a metabolic marker rather than a definitive measure of cell viability. Future investigations may wish to conduct direct viability assays to establish a clearer link between metabolic shifts and cell survival. As such, regarding the absence of a statistically significant difference in acetaldehyde levels between 15,000 and 100,000 cell conditions, a potential saturation effect is considered. Though lack of significance here could be a product of low sample number and resultant error, it may also indicate that cochlear fibrocytes either metabolize or produce acetaldehyde up to a threshold, beyond which further increases in cell number do not lead to proportional changes in VOC levels. Additional research investigating metabolic flux and enzyme activity in this cell type at varying densities may be of interest.

VOC profiles of TNF-dosed cochlear fibrocytes indicate several significant differences across conditions. However, considering the culture issues noted at this stage of research, it is unclear whether such changes may be attributed to inflammation effects rather than poor cell health from culture difficulties. Again, future investigations may wish to conduct viability assays to investigate. Nonetheless, when considering compounds of interest (acetaldehyde and pyruvic acid), and the results of vibrational spectroscopy work, some conclusions of value may be drawn.

In particular, the statistically significant decrease in acetaldehyde in dosed cells indicates issues in cell metabolism of ethanol and other such compounds. Combined with the increase of pyruvic acid seen in VOC profiles, evidence of mitochondrial changes noted in Raman spectroscopy, and the changes to the histidine-associated region noted in FTIR- based analyses, inflammatory pathology through mitochondrial dysfunction is suggested.

It is believed, based on the findings of complementary research conducted, that the significant reduction in acetaldehyde levels observed in TNF- $\alpha$ -dosed samples reflects inflammation-induced metabolic alterations rather than a simple reduction in viability. TNF- $\alpha$  is known to influence

mitochondrial function and metabolic pathways, potentially leading to shifts in ethanol metabolism and in the processing and clearance of acetaldehyde. The observed trend in pyruvic acid levels further supports this, with findings suggesting that TNF- $\alpha$  impacts cellular metabolism beyond viability alone, reinforcing the importance of metabolic profiling in understanding inflammatory responses.

While direct viability assays were not conducted in this study, the observed metabolic shifts in acetaldehyde and pyruvate levels provide insight into cellular function under different conditions. Future research could incorporate viability testing, such as MTT or live/dead staining assays, with SIFT-MS analyses to complement VOC assessment and provide a more comprehensive understanding of cellular health in response to inflammatory stimuli.

Referring again to Johnson *et al.* <sup>[153]</sup>, histidine and other amino acid variations noted in vibrational spectroscopy work may indicate a change in citrate synthase. Such a change would likely yield mitochondrial dysfunction in the conduction of the citric acid cycle. A change of this nature is evidenced by the accumulation of pyruvate in TNF-dosed cells (indicating that glycolysis is occurring), with acetaldehyde reduction indicating a general limitation in cell metabolism and respiration. However, TNF-dosed cells do not clearly demonstrate this effect, with the 5ng/mL dosage condition demonstrating unexpected results compared with 1ng/mL and 10ng/mL dosages. This is believed to be due to the culture issues previously noted.

Despite evidence of varying modes of action from vibrational spectroscopy data, analysis of IL-1 $\beta$ -inflamed cells further support the histidine hypothesis, with reductions in acetaldehyde production significantly correlated to increased IL dosage. This, combined with the general increase seen in pyruvate (indicative of continuing glycolysis), once again implies a histidine-based change to the working of the citric acid cycle. Though this cannot be confirmed through the investigations conducted, it is clear from the VOC data obtained that IL dosage has a tangible effect on cellular respiration, with inflammation-related mitochondrial dysfunction a likely cause. While these results generally align with those observed in TNF- $\alpha$ -treated cells, further investigation is recommended to determine whether IL-1 $\beta$  and TNF- $\alpha$  truly induce distinct metabolic responses or act through overlapping pathways.

Turning to cerumen investigations, at this stage of research it does not appear that cerumen is a viable biofluid for the diagnosis of ARHL. However, this does not rule out its use in future investigations with appropriate refinements. Though little evidence of cerumen acting as a carrier for cell signals was established, it's potential cannot be ruled out. Thus it is recommended that research be conducted into the ability of cerumen to carry cell headspace signals in the future.

Raman analysis of cerumen demonstrated little signal below  $1000\text{cm}^{-1}$ . This may indicate cerumen's potential as a cell signal carrier as various cell-related spectral bands arise in this region. With this in mind, it is recommended that fresh cerumen samples be used wherever possible in future investigation. In general, Raman spectroscopy of cerumen shows signals resembling other waxes examined such as paraffin <sup>[204]</sup>.

ATR-FTIR analysis, unlike Raman spectroscopy, enables non-destructive sampling of cerumen. Additionally, the sample preparation methods illustrated enable the homogenisation of cerumen samples, accounting for topographic variability in spectra. Though, once again, no cell signal was observed in cerumen samples analysed, this work provides insight into preparation methods needed to begin larger scale, clinically relevant studies employing cerumen as a carrier for cochlear fibrocyte VOCs. Such research, wherein cerumen is employed as an intermediate step in cultured cell VOC sampling, was planned for the present thesis. However, time constraints and limitations to sample availability meant that this was not feasible at this stage of investigation.

Concerning volatile analysis, it is unlikely based upon previous research such as that by Prokop-Prigge *et al.* <sup>[182]</sup>, that cerumen does not yield a significant base VOC signal to be detectable via SIFT-MS. Thus, it is concluded that poor signal visibility above swabs occurs due to a necessity for improved sample methods, with substantial alterations to methods required in order to observe any variations in the headspace of cerumen samples.

Particularly, it is noted that distinctions between wax samples and blank swabs would likely be better made between blanks and larger volume wax samples than those obtained. Based upon this it is strongly recommended that cerumen samples be collected by researchers or collaborating clinicians in future studies, rather than purchased from commercial sources. This would not only

enable greater wax collection capacity but would minimise wait times within research that would otherwise be spent awaiting the third-party collection and arrival of commercial samples.

In addition to increased speed and greater experimental, research group-based sample collection would enable the consideration of other sampling methods. Such sampling methods may be employed to negate the necessity for cotton swabs, allowing larger volume wax-only samples to be gathered from patients. The use of alternative methods would also likely reduce risks associated with cotton swab use such as infection caused by fibre retention <sup>[16]</sup>. Possible removal options include curette use (particularly helpful where cerumen is hardened) and microsuction, which is already employed in patient care <sup>[205]</sup>. Where curette use is considered, perforation risk must be kept in mind when assessing procedure safety <sup>[15]</sup>.

In addition to sample collection method changes, refinement of the SIFT-MS methods with cerumen samples in mind is a necessity when pursuing future study. That is, SIFT-MS techniques employed are not presently optimised for the use of wax samples. In order to gain better results, it is recommended that future studies focus efforts on the concentration of sample signal- perhaps by allowing longer VOC accumulation periods and adjusting incubation temperatures to better suit the release of VOCs from wax. It should be noted that in previous volatile studies using GC-MS, solvent extraction is commonly used in order to prepare cerumen samples and, though not ideal, may be useful to consider during refinement stages <sup>[206]</sup>.

## 5.6. Concluding Remarks

Despite no significant differences arising between cerumen samples and carrier swabs in SIFT-MS investigation, it may be stated that the present section of research fulfils its aims.

Aim 1 was met through the use of SIFT-MS in establishing a VOC profile of cultured cochlear fibrocyte headspace. Cell signals were detectable even at low, physiologically relevant cell numbers, with compounds attributable to cell metabolism identified.

Aim 2 was met through the establishment of headspace profile of TNF- $\alpha$ -dosed cochlear fibrocytes and the distinction between healthy and inflamed cells using SIFT-MS. Several statistically

significant differences were identified between healthy and inflamed cells, with alterations to acetaldehyde and pyruvate levels of particular interest.

Aim 3 was met through the use of SIFT-MS to establish a headspace profile of IL-1 $\beta$ -dosed cochlear fibrocytes and the successful distinction between healthy and inflamed cells using this method. Reduction in acetaldehyde and increase in pyruvic acid level with increased cytokine dosage strongly suggests alterations to cell respiration as a result of inflammation.

Aim 4 was met through the conduction of preliminary investigations to establish spectral and VOC profiles of human cerumen samples. Vibrational spectroscopy methods illustrated refinements made in sample preparation methods and produced signals similar to that of other wax types. SIFT-MS results highlighted future optimisation steps required for further progress in cerumen use.

From this section of research, it is clear that VOC analyses have a place in the non-invasive examination of cochlear fibrocyte health and that, with appropriate method refinement, cerumen may be used as a biofluid for cell monitoring. From this, further study centred on method refinement as well as large-scale categorisation of patient wax samples in the context of hearing status is recommended.

## 6. Conclusions and Future Work

---

### 6.1. Addressing the Necessity- ARHL Revisited

As discussed in depth in chapter 1, ARHL is a debilitating, highly prevalent condition which significantly affects quality of life in the elderly. With over half of all people over 75 affected by ARHL, it is clear that the condition is a global-scale issue and that improvements to diagnosis and treatment technologies is of substantial value in the improvement of healthcare for those above a certain age [1-5].

As stated, the present research focused on highlighting the diagnostic potential of spiral ligament fibrocytes, as well as the potential for application of the present methods in monitoring of cells *in vitro* for therapeutics. Such therapeutics have shown promise in animal studies and are a useful target in progressing ARHL therapeutics in the future [94, 95].

Thus, in the first research of its kind, this thesis presents spectral and VOC profiles of cultured murine cochlear fibrocytes both in untreated and inflamed states, providing proof of concept for the use of the trialled methods in further inner ear-focused study. From this early research, it is hoped that methods facilitating the minimally invasive monitoring of cochlear fibrocyte health may be established. This is applicable both to a diagnostic and treatment context, with the findings of value both in the assessment of patient cells and in the monitoring of potential cell replacement therapies both *in vitro* and following implantation.

### 6.2. Study Findings

The first experimental chapter (chapter 3) of this research focused upon the establishment of cochlear fibrocyte spectral profiles using benchtop Raman spectroscopy and ATR-FTIR spectroscopy methods. Spectral profiles of healthy cells (and supernatant) as well as those inflamed using TNF- $\alpha$  and IL-1 $\beta$  were explored.

Raman spectroscopic profiles of healthy cochlear fibrocytes were consistent with expectations for cellular samples and provided a control with which inflamed-state spectra could be compared. Raman spectroscopy of TNF-inflamed cochlear fibrocytes, though spectra proved difficult

to distinguish by eye, demonstrated clear differences between dosage conditions, with spectral variations indicative of inflammation-induced changes to proteins of interest, nucleic acids and cellular respiration. Both distinction between undosed and dosed cells as well as specific dosage conditions was demonstrated and verified using multivariate analysis and non-linear predictive modelling. This is of great promise in the potential monitoring of cochlear fibrocyte health. In contrast to sensory cells, which do not experience damage from TNF- $\alpha$  unless present in extremely high concentrations <sup>[157-159]</sup>, cochlear fibrocytes demonstrated TNF-induced alterations at even 1ng/mL. Though, it should be noted that some overlap was seen between undosed and 1ng/mL conditions suggesting that inflammation by TNF- $\alpha$  may have to reach a certain level before confident detection via Raman may occur.

Raman spectroscopy of IL-dosed cochlear fibrocytes further demonstrated detectable differences between dosed and undosed cells at all dosage levels with successful distinction of dosage conditions verified by both multivariate analysis and neural network model. Comparison of IL-dosed and undosed spectra demonstrated differences arising in regions attributed to nucleic acids and polysaccharides in addition to those relating to lipids and proteins noted from TNF analyses (consistent with expectations of damage to cells undergoing inflammation <sup>[215]</sup>). Differences seen between IL-dosed and healthy cells often directly contrasted with observed differences in TNF-dosed and undosed cells, illustrating the different signalling pathways of inflammatory action in the two cytokines examined. This is similarly encouraging in the pursuit of potential cochlear fibrocyte health monitoring methods.

ATR-FTIR of healthy cochlear fibrocytes supported the findings of Raman spectroscopy, with cell supernatant spectra evidencing cell presence. FTIR findings also served to confirm the successful distinction of cell supernatant from control media, with signals demonstrating visible differences and distinction confirmed through multivariate analysis. Average supernatant profiles gathered in this stage of research provided a control with which supernatant samples from inflamed cells could be compared.

ATR-FTIR of TNF-dosed cell supernatant demonstrated clear differences between dosage conditions. As in Raman spectroscopic analysis, distinction between undosed and dosed cells as well

as specific dosage conditions was demonstrated using multivariate analysis. In particular, the peak attributed to histidine (a key amino acid in citrate synthase) was noted as demonstrating correlative variation across dosage conditions. This was confirmed via PCA, where changes in the associated peak were shown to be responsible for a large portion of sample variance.

ATR-FTIR analysis of IL-1-dosed supernatant, similarly to TNF analysis, revealed distinguishable differences between dosage conditions. This, again, was demonstrated using multivariate analysis. Differences between dosed and undosed supernatant conditions were shown to arise predominantly in regions associated with nucleic acids, amino acids and proteins, with variation once again noted at  $1590\text{cm}^{-1}$ , potentially indicative of alterations to histidine.

This study successfully fulfilled its aims through the examination and distinction of healthy, TNF-dosed and IL-1-dosed cochlear fibrocyte samples through Raman spectroscopy and ATR-FTIR spectroscopy. Such success presents excellent progress towards furthering the understanding of cochlear fibrocyte inflammatory pathology. Chapter 3 also illustrates the potential for vibrational spectroscopy applications in cochlear fibrocyte health analysis moving forward.

The second experimental chapter (chapter 4) of this research focused upon the in-depth analysis of IL-1 $\beta$  dosage effects on cochlear fibrocytes using hyperspectral Raman and S-FTIR techniques at Diamond Light Source synchrotron facility (Oxford, UK). Spectral profiles of healthy cells (and supernatant) as well as those inflamed using 1ng/mL, 5ng/mL and 10ng/mL of IL-1 $\beta$  were explored.

Hyperspectral Raman spectroscopy of cells demonstrated results mainly consistent with the findings of previous chapters, with protein changes visible between dosed and undosed conditions. Variations in peak intensity and molecular distribution within cells are consistent with literature findings and suggest structural changes to cells arising as a result of IL-1 dosage. Changes are suggested to arise as a result of functional alterations to membranes, biosynthesis, molecular accumulation and intercellular transport. In general, noted variations indicate metabolic dysfunction and ROS accumulation, known hallmarks of the inflamed cell state and noted causes of cochlear fibrocyte loss [4, 5, 48-52]. Interestingly, it is noted that dosed cells in contact more closely resemble single undosed cells than those in contact, suggesting that alterations to cellular communication are

a key process in inflammation by IL-1. Such alterations are hypothesised to arise as a result of alterations to membrane proteins- a potential key mechanism in metabolic ARHL pathology and the reduction of the endocochlear potential.

Similarly, S-FTIR data gathered at the Diamond Light Source synchrotron facility support previous chapters' findings of protein alteration, lipid accumulation and membrane integrity changes in response to cytokine dosage. Variations between conditions are once again distinguishable through the employment of a neural network model. In particular, variations are noted in spectra at wavenumber regions corresponding to vibrations in nucleic acids ( $<600\text{cm}^{-1}$ ,  $1115\text{-}1130\text{cm}^{-1}$ ), carbohydrates ( $<600\text{cm}^{-1}$ ), phospholipids ( $<600\text{cm}^{-1}$ ), proteins ( $1527\text{cm}^{-1}$ ,  $2800\text{-}3100\text{cm}^{-1}$ ) and lipids ( $2800\text{-}3100\text{cm}^{-1}$ ). A potential fibrocyte activation state similar to that seen in macrophages is noted as a point for further investigation.

This study successfully fulfilled its aims through the successful use of hyperspectral Raman spectroscopy to examine the effects of IL-1 $\beta$  in cultured cells, the successful use of S-FTIR in the distinction of IL-dosed fibrocyte cultures, and the successful employment of a neural network in the accurate distinction of inflamed cells and the classification of cells by dosage level.

The final experimental chapter of this research (chapter 5) provided early preliminary investigation of the use of SIFT-MS in evaluating the health of cochlear fibrocytes *in vitro*. This chapter also explored the potential of human cerumen as a biofluid for clinical translation of ear cell health testing.

SIFT-MS of healthy cochlear fibrocytes confirmed, similarly to FTIR, distinction between cells and media. Through this, the technique demonstrated the capacity to distinguish cells at low, physiologically relevant cell numbers through headspace samples. Average cell headspace profiles formed a control with which inflamed cell headspace could be compared, with results at this stage used to identify optimal precursor ions and compounds of interest for inflammation studies.

SIFT-MS of TNF-dosed cells demonstrated detectable variation across the dosages examined, with significant differences in levels of acetaldehyde, propanol, acetic acid, DMS/ethanethiol, pentene, putrescine, terpenes, benzene and DMSO found between conditions. Of most relevance is arguably

the variation in acetaldehyde, the significant decline of which in dosed conditions indicates a reduction in cell metabolism.

Similarly to TNF-dosed results, SIFT-MS of IL-dosed cell headspace demonstrated detectable variation across the dosages examined, with significant differences arising in acetaldehyde level. Further examination indicated that acetaldehyde level appeared to decrease in cell headspace as dosage increased, strongly implying a reduction in cellular respiration and consistent with the findings indicative of mitochondrial damage from Raman spectroscopy. In contrast, though no significant difference was seen, pyruvic acid level in headspace was shown to increase with IL-dosage, further verifying that alterations to respiration are likely a result of mitochondrial changes through the indication that glycolysis (occurring in cell cytoplasm) is still active where further processes (taking place in mitochondria) may not be.

Though little insight into cerumen was found, likely due to the limited nature of the samples themselves, this research presents the first venture of its kind into the examination of human cerumen by the present methods. It is hoped that with improvements to sample quality, such methods will be applicable in the detection of metabolic changes through cerumen, as seen in previous studies focused on GC-MS and other methods.

This study successfully fulfilled its aims through the non-invasive examination and distinction of healthy and inflamed cochlear fibrocytes via SIFT-MS and through the preliminary evaluation of cerumen as a biofluid for use in patient-based investigations.

## 6.3.Future Work

### 6.3.1. Improving the Model

Though the present research shows promise in the distinction of inflamed and healthy cochlear fibrocytes and is of undeniable value in the monitoring of such cells *in vitro*, it may be debated as to whether culture conditions are of great enough physiological relevance to draw conclusions for diagnostic purposes. In order to further the physiological relevance of examined models, it is recommended that future studies focus efforts towards the analysis of cells in 3D culture.

For such cultures, it is recommended that researchers consult the paper by Osborn *et al.* <sup>[207]</sup> who successfully cultured cochlear fibrocytes resembling those of native tissue in *in vitro* 3D cultures.

Of course, where improving translatability of the model is concerned, one must also consider examining alternatives to murine cochlear fibrocytes. Naturally, where modelling of a condition for human treatment is concerned, there is no better origin species for cells than humans. However, human cochlear fibrocytes cannot be safely, ethically or easily obtained from living patients or the deceased. With this in mind, it is recommended that the methods employed in the present research be trialled using human MSCs in future research.

### 6.3.2. Next Experimental Steps – Investigating the Citric Acid Cycle

Though no firm conclusions can be drawn regarding the precise pathway of mitochondrial dysfunction arising in inflamed cochlear fibrocytes, this research points to alterations in the citric acid cycle as a contributing factor. This is particularly apparent in IL-1 $\beta$  inflammation investigations.

In VOC analysis, increased pyruvic acid levels in inflamed cells strongly suggested accumulation of pyruvate as a result of inflammation. This indicates that glycolysis continues as normal in inflamed cells at the dosages observed. In contrast, decreases in acetaldehyde level in inflamed conditions point to failures in normal cellular respiration, implying that faults in the process occur after glycolysis has successfully taken place.

In vibrational spectroscopy analyses, inflamed cells demonstrated variations from healthy cells consistent with various elements of inflammation including mitochondrial dysfunction. Benchtop analyses demonstrated, among other markers of inflammation, alterations in an amino acid-related spectral region potentially attributable to histidine. This region, regardless of specific attribution, may indicate inflammation induced changes to the structure and function of essential proteins such as respiration-associated enzymes (e.g. citrate synthase). Synchrotron-based analysis, alongside validating the inflammatory pathways seen in benchtop examinations, provided further insight into potential mitochondrial dysfunction players. Such investigations hinted at coenzyme-A accumulation in cytosol, potentially indicating a dysfunction in its conversion to acetyl-coenzyme-A.

With this in mind, it is recommended that the next stage of research into improving the understanding of inflammation in cochlear fibrocytes begin with the conduction of enzymatic assays under different inflammatory conditions. In particular, assays of the abundance and function of citrate synthase, acetyl CoA synthetase and pyruvate dehydrogenase in cochlear fibrocytes (both healthy and inflamed) are recommended.

Following such assays, the next logical step in understanding CF inflammatory pathology (should assays demonstrate dysfunction), is to conduct protein structure examinations such as NMR-based studies. NMR may be used to map the structural properties of small molecules such as enzymes and enables the detection of alterations potentially induced by inflammation.

Should an amino acid such as histidine or, on a larger scale, an enzyme such as citrate synthase be shown to be dysfunctional, efforts may then focus on prevention of damage/functional recovery. Such efforts may include (for example) supplementation of histidine in efforts to protect fibrocyte function ahead of inflammaging-based damage<sup>[260,261]</sup>.

If changes to a supplemental amino acid such as histidine are definitively shown to be a key player in CF inflammation, clinical studies may be explored. It is recommended that such studies conduct longitudinal examinations of histidine supplementation on hearing status and general health in those over 55.

### 6.3.3. Towards Clinical Translation- Bioreactors and the Application of Automation

Though it is clear from chapters 4, 5 and 6 that there are distinctions to be made between inflamed and healthy cells through all methods trialled, it may be argued that the methods used to examine cell supernatant and headspace are limited by the hands on nature of the techniques employed (benchtop FTIR, SIFT-MS). That is, these methods required extensive manual sampling which limited the number of samples that could be taken in the present research. For example, where the present SIFT-MS setup is concerned, due to the lengthy preparation of samples as well as the necessity for manual sampling and data processing, only 9 samples per condition could be trialled. This is in contrast with Raman spectroscopy and Synchrotron FTIR samples, where hundreds of data

points were collected per sample, enabling the employment of non-linear modelling to distinguish conditions.

It is with this in mind that the application of automation is recommended wherever possible in the pursuit of further research of this nature. In the case of SIFT-MS for instance, this may include the use of an autosampler to collect sample headspace, minimising the necessity for researcher intervention and enabling round-the-clock sampling. Such methods are particularly advised in the translation of the present methods to the monitoring of cells for potential therapeutic applications, wherein bioreactors may be favoured to further minimise researcher intervention in culture.

Concerning sample preparation, it is arguable that this will pose less of an issue in scale-up of the demonstrated techniques, as a single-researcher benchtop approach is unlikely to persist if pursued on a larger scale. For example, if employing SIFT-MS methods in the monitoring of bioreactor-cultured cells it is likely that samples will consist only of extracted headspace from cultures as opposed to individual samples of cells in bottles.

With such measures taken, it is highly possible that the techniques not presently employable in the generation of predictive models may become so due to the capacity for greater sample collection. Thus, if possible, it is recommended that larger scale investigations into the use of SIFT-MS in the detection of inflammation in cochlear cells be conducted.

#### 6.3.4. Towards Clinical Translation- Alternatives to Biofluids

Turning to the potential for clinical translation of the research to diagnostic purposes, it is evident from chapter 5 that the use of cerumen in inflammation detection via the current methods is a work in progress. With this in mind, alternate routes must be deliberated in order to apply the techniques presently demonstrated for inflammation detection, particularly SIFT-MS.

Concerning the liquid sampling potential demonstrated in benchtop ATR-FTIR investigations presently, direct sampling of cochlear fluids seems an ideal approach at first glance, with endolymph and perilymph both accessible via incision to the tympanic membrane. Though this method is shown to be relatively safe in rodents <sup>[256]</sup>, it would require invasive methods of extraction and may result in

damage to the ear. This damage is likely to occur both by the manual disruption of cochlear tissues and by alteration to the delicate pressure gradients within the cochlear chambers. With this in mind, such a sampling method is unlikely to be considered viable for patient examination. However, it will be interesting to monitor the progress of Höhl *et al.* (2019) with a view to applying the present methods to perilymph sampling in the future.

Turning to the successful use of Raman spectroscopy in the distinction of inflamed cells- though unlikely to be applicable in early stage diagnosis due to its invasive nature, literature has demonstrated the use of Raman technology via microendoscopy<sup>[208]</sup>. Though this technology, to date, appears to employ only CARS and SRS Raman techniques, it is not beyond possibility that the present research findings be applied in order to enable Raman analysis of the inner ear via CI route in severe hearing loss cases.

## 6.4. Final Conclusions

In conclusion, the presented thesis the research aims set out within its chapters. Where aims are not wholly met, potential methods to rectify this in future research are clearly outlined.

In addition, an overall direction for future work is highlighted, with a particular emphasis on the progression of research findings towards a more clinically relevant and potentially translatable path. This includes highlighting the importance of automation, as manual sampling and resultant human error are believed to have played a substantial role in the limitations of the present research.

With this in mind, this thesis has provided the very first step in proof of concept for a clinical path which, to date, appears yet unexplored. That is, through the use of relevant biofluids and significant refinement of the techniques outlined, SIFT-MS may be employed as a tool to non-invasively detect inflammation in cochlear fibrocytes, and as such, be employed in diagnosis, monitoring and treatment of ARHL. SIFT-MS inflammation detection in particular, if successfully translated to patient samples, may facilitate the timely application of fibrocyte repair/replacement strategies and potentially delay or prevent further hearing damage.

Additionally, the benefits of Raman spectroscopy and ATR-FTIR as complementary or standalone techniques in the detection of fibrocyte inflammation are highlighted. These techniques, too, are applicable in the development of diagnostic techniques and the facilitation of novel ARHL treatments. However, where diagnoses are concerned, they are limited by the necessity for invasive sampling, extensive sample preparation and lack of real time sampling capacity.

Overall, it is confidently surmised that this thesis has made a tangible contribution to the understanding of cochlear fibrocyte metabolism and inflammation, has examined several previously unexplored techniques in the field, and presents a potential method by which lateral wall inflammation may be observed non-invasively and potentially before ARHL symptoms arise.

## References

---

1. Gates, G., and Mills, J. (2005). Presbycusis. *The Lancet*, 366(9491), pp. 1111-1120.
2. Oshima, K., Suchert, S., Blevins, N., and Heller, S. (2010). Curing hearing loss: Patient expectations, health care practitioners, and basic science. *Journal of Communication Disorders*, 43(4), 311-318.
3. Stevens, G., Flaxman, S., Brunskill, E., Mascarenhas, M., Mathers, C. and Finucane, M. (2011). Global and regional hearing impairment prevalence: an analysis of 42 studies in 29 countries. *European Journal of Public Health*, 23(1), pp.146-152.
4. Sánchez-Rodríguez, C., Martín-Sanz, E., Cuadrado, E., Granizo, J., and Sanz-Fernández, R. (2016). Protective effect of polyphenols on presbycusis via oxidative/nitrosative stress suppression in rats. *Experimental Gerontology*, 83, pp. 31-36.
5. Watson, N., Ding, B., Zhu, X., and Frisina, R. (2017). Chronic inflammation –inflammaging – in the ageing cochlea: A novel target for future presbycusis therapy. *Ageing Research Reviews*, 40, 142-148.
6. Brink, P. and Stones, M. (2007). Examination of the relationship among hearing impairment, linguistic communication, mood, and social engagement of residents in complex continuing care facilities. *Gerontologist*, 47, pp. 633–641.
7. Dillon, C., Gu, Q., Hoffman, H. and Ko, C (2010) Vision, hearing, balance, and sensory impairment in Americans aged 70 years and over. *NCHS Data Brief*, Apr(31), pp. 1-8.
8. Mick, P., Kawachi, I. and Lin, F. (2014). The association between hearing loss and social isolation in older adults. *Otolaryngol Head Neck Surg*, 150, pp. 378–384.
9. Ciorba, A., Hatzopoulos, S., Bianchini, C., Aimoni, C., Skarzynski, H., and Skarzynski, P. (2015). Genetics of presbycusis and presbystasis. *International Journal of Immunopathology and Pharmacology*, 28(1), 29-35.

10. Pichora-Fuller, M., Mick, P. and Reed, M. (2015). Hearing, cognition, and healthy aging: social and public health implications of the links between age-related declines in hearing and cognition. *Semin Hear*, 36, pp. 122–139.
11. Sheffield, A. and Smith, R. (2018). The Epidemiology of Deafness. *Cold Spring Harbor Perspectives in Medicine*, 9(9), p.a033258.
12. World Health Organization (2018). *Global Health Estimates 2016: Disease burden by Cause, Age, Sex, by Country and by Region, 2000–2016*.
13. Pacala, J. and Yueh, B. (2012). Hearing Deficits in the Older Patient. *JAMA*, 307(11), p.1185.
14. Subha, S. and Raman, R. (2006). Role of Impacted Cerumen in Hearing Loss. *Ear, Nose & Throat Journal*, 85(10), pp.650-653.
15. Hempel, J., Becker, A., Müller, J., Krause, E., Berghaus, A. and Braun, T. (2012). Traumatic Tympanic Membrane Perforations. *Otology & Neurotology*, 33(8), pp.1357-1362.
16. Charlton, A., Janjua, N. and Rejali, D. (2019). Cotton bud in external ear canal causing necrotising otitis externa and subdural abscess. *BMJ Case Reports*, 12(3), p.e227971.
17. Collins, J. (1997). Prevalence of selected chronic conditions: United States 1990–1992. *Vital Health Stat* 10, 194, pp. 1–89.
18. Chisolm, T., Willott, J. and Lister, J. (2003). The aging auditory system: anatomic and physiologic changes and implications for rehabilitation. *International Journal of Audiology*, 42(sup2), pp.3-10.
19. Kamil, R., Betz, J., Powers, B., *et al.* (2016). Association of hearing impairment with incident frailty and falls in older adults. *J Aging Health*, 28, pp. 644–660.
20. Lin, F., Metter, E., O’Brien, R., *et al.* (2011). Hearing loss and incident dementia. *Arch Neurol*, 68, pp. 214–220.
21. Lin, F., Yaffe, K., Xia, J., *et al.* (2013). Hearing loss and cognitive decline in older adults. *JAMA Intern Med*, 173, pp. 293–299.

22. Dubno, J., Eckert, M., Lee, F., Matthews, L., and Schmiedt, R. (2013). Classifying Human Audiometric Phenotypes of Age-Related Hearing Loss from Animal Models. *Journal of the Association for Research in Otolaryngology*, 14(5), pp. 687-701.
23. Schuknecht, H., and Gacek, M. (1993). Cochlear Pathology in Presbycusis. *Annals of Otology, Rhinology & Laryngology*, 102, pp. 1-16.
24. Schuknecht, H. (1964). Further Observations on the Pathology of Presbycusis. *Archives of Otolaryngology-Head and Neck Surgery*, 80(4), pp. 369-382.
25. Schuknecht, H., Watanuki, K., Takahashi, T., Belal, A., Kimura, R., Jones, D., and Ota, C. (1974). ATROPHY OF THE STRIA VASCULARIS, A COMMON CAUSE FOR HEARING LOSS. *The Laryngoscope*, 84(10), pp. 1777-1821.
26. Wang, B., Chen, H., Shen, J., Zhong, W., Zheng, Y., Lou, M., Tong, L., and Yuan, C. (2023). Multiple Sensory Impairments in Relation to Cognitive Function: Two Nationwide Cross-sectional Studies. *Current Alzheimers Research*, [Advance online publication].
27. Edmiston, R. and Mitchell, C. (2013). Hearing loss in adults. *BMJ*, 346(apr25 2), pp.f2496-f2496.
28. Uy, J., and Forciea, M.(2013). In the clinic. Hearing loss. *Ann Intern Med.*, 158(7), pp. ITC4-ITC1.
29. Li, Y., Watanabe, K., Fujioka, M. and Ogawa, K. (2017). Characterization of slow-cycling cells in the mouse cochlear lateral wall. *PLOS ONE*, 12(6), p.e0179293.
30. Kim, M. (2017). Diabetes mellitus and the incidence of hearing loss: a cohort study. *International Journal of Epidemiology*, p.dyw342.
31. McKee, M., Stransky, M. and Reichard, A. (2018). Hearing loss and associated medical conditions among individuals 65 years and older. *Disability and Health Journal*, 11(1), pp.122-125.
32. Gupta, S., Eavey, R., Wang, M., Curhan, S. and Curhan, G. (2018). Type 2 diabetes and the risk of incident hearing loss. *Diabetologia*, 62(2), pp.281-285.

33. Michels, T., Duffy, M. and Rogers, D. (2019). Hearing Loss in Adults: Differential Diagnosis and Treatment. *Am Fam Physician*, 100(2), pp.98-108.
34. Edmiston, R. and Mitchell, C. (2013). Hearing loss in adults. *BMJ*, 346(apr25 2), pp.f2496-f2496.
35. Vaden, K. I., Jr, Eckert, M. A., Matthews, L. J., Schmiedt, R. A., and Dubno, J. R. (2022). Metabolic and Sensory Components of Age-Related Hearing Loss. *Journal of the Association for Research in Otolaryngology*, 23(2), 253–272.
36. Stachler, R., Chandrasekhar, S., Archer, S., *et al.* (2012) American Academy of Otolaryngology-Head and Neck Surgery. Clinical practice guideline: sudden hearing loss. *Otolaryngol Head Neck Surg.*, 146(sup3), pp. S1-S35.
37. Zhao, H. (2017). Hypothesis of K<sup>+</sup>-Recycling Defect Is Not a Primary Deafness Mechanism for Cx26 (GJB2) Deficiency. *Frontiers in Molecular Neuroscience*, 10.
38. Weber, P., Cunningham, C., and Schulte, B. (2001). Potassium Recycling Pathways in the Human Cochlea. *The Laryngoscope*, 111(7), pp. 1156-1165.
39. Henson, M., and Henson, O. (1988). Tension fibroblasts and the connective tissue matrix of the spiral ligament. *Hearing Research*, 35(2-3), pp. 237-258.
40. Mahendrasingam, S., Bebb, C., Shepard, E., and Furness, D. (2011). Subcellular Distribution and Relative Expression of Fibrocyte Markers in the CD/1 Mouse Cochlea Assessed by Semiquantitative Immunogold Electron Microscopy. *Journal of Histochemistry & Cytochemistry*, 59(11), pp. 984-1000.
41. Adachi, N., Yoshida, T., Nin, F., Ogata, G., Yamaguchi, S., Suzuki, T., Komune, S., Hisa, Y., Hibino, H., and Kurachi, Y. (2013). The mechanism underlying maintenance of the EP by the K<sup>+</sup> transport system in fibrocytes of the inner ear. *The Journal of Physiology*, 591(18), pp. 4459-4472
42. Liu, W., Schrott-Fischer, A., Glueckert, R., Benav, H., and Rask-Andersen, H. (2017). The Human “Cochlear Battery” – Claudin-11 Barrier and Ion Transport Proteins in the Lateral Wall of the Cochlea. *Frontiers in Molecular Neuroscience*, 10.

43. Lang, H., Schulte, B., and Schmiedt, R. (2003). Effects of Chronic Furosemide Treatment and Age on Cell Division in the Adult Gerbil Inner Ear. *JARO - Journal of the Association for Research in Otolaryngology*, 4(2), 164-175.
44. Spicer, S., and Schulte, B. (1991). Differentiation of inner ear fibrocytes according to their ion transport-related activity. *Hearing Research*, 56(1-2), pp. 53-64.
45. Spicer, S., and Schulte, B. (1996). The fine structure of spiral ligament cells relates to ion return to the stria and varies with place-frequency. *Hearing Research*, 100(1-2), pp. 80- 100.
46. Furness, D., 2019. Forgotten Fibrocytes: A Neglected, Supporting Cell Type of the Cochlea With the Potential to be an Alternative Therapeutic Target in Hearing Loss. *Frontiers in Cellular Neuroscience*, 13.
47. Hequembourg, S., and Liberman, M. (2001). Spiral Ligament Pathology: A Major Aspect of Age Related Cochlear Degeneration in C57BL/6 Mice. *Journal of the Association for Research in Otolaryngology*, 2(2), pp. 118-129.
48. Mahendrasingam, S., MacDonald, J., and Furness, D.N. (2011). Relative Time Course of Degeneration of Different Cochlear Structures in the CD/1 Mouse Model of Accelerated Aging. *Journal of the Association for Research in Otolaryngology*, 12(4), pp. 437-453.
49. Someya, S., Xu, J., Kondo, K., Ding, D., Salvi, R., Yamasoba, T., Rabinovitch, P., Weindruch, R., Leeuwenburgh, C., Tanokura, M., and Prolla, T. (2009). Age related hearing loss in C57BL/6Jmice is mediated by Bak-dependent mitochondrial apoptosis. *Proceedings of the National Academy of Sciences*, 106(46), pp. 19432-19437.
50. Miwa, T., Katsuno, T., Wei, F. Y., & Tomizawa, K. (2023). Mitochondrial alterations in the cochlea of Cdk5rap1-knockout mice with age-related hearing loss. *FEBS open bio*, 13(7), 1365–1374.
51. Minowa, O., Ikeda, K., Sugitani, Y., Oshima, T., Nakai, S., Katori, Y., Suzuki, M., Furukawa, M., Kawase, T., and Zheng, Y. (1999). Altered cochlear fibrocytes in a mouse model of DFN3 nonsyndromic deafness. *Science*, 285, pp. 1408–1411.

52. Wu, T., and Marcus, D.C. (2003). Age-related changes in cochlear endolymphatic potassium and potential in CD/1 and CBA/CaJ mice. *Journal of the Association for Research in Otolaryngology*, 4, pp. 353–362.
53. Franceschi, C., Garagnani, P., Parini, P. *et al.* (2018). Inflammaging: a new immune–metabolic viewpoint for age-related diseases. *Nat Rev Endocrinol* 14, 576–590.
54. Fujioka, M., Okano, H., and Ogawa K. (2014). Inflammatory and immune responses in the cochlea: potential therapeutic targets for sensorineural hearing loss. *Frontiers in Pharmacology*, 5.
55. Gates, G. A., Cobb, J. L., D'Agostino, R. B., & Wolf, P. A. (1993). The relation of hearing in the elderly to the presence of cardiovascular disease and cardiovascular risk factors. *Archives of otolaryngology--head & neck surgery*, 119(2), 156–161.
56. Frisina, S. T., Mapes, F., Kim, S., Frisina, D. R., & Frisina, R. D. (2006). Characterization of hearing loss in aged type II diabetics. *Hearing research*, 211(1-2), 103–113.
57. Verschuur, C., Agyemang-Prempeh, A. and Newman, T.A. (2014) Inflammation is associated with a worsening of presbycusis: Evidence from the MRC national study of hearing, *International Journal of Audiology*, 53:7, 469-475
58. Fetoni, A., Picciotti, P., Paludetti, G., and Troiani, D. (2011). Pathogenesis of presbycusis in animal models: A review. *Experimental Gerontology*, 46(6), pp. 413-425.
59. Seicol, B.J., Lin, S. and Xie, R. (2022). Age-related hearing loss is accompanied by chronic inflammation in the cochlea and the cochlear nucleus. *Front. Aging Neurosci.*, 14, Article 846804
60. Ito, T., Kurata, N., & Fukunaga, Y. (2022). Tissue-Resident Macrophages in the Stria Vascularis. *Frontiers in neurology*, 13, 818395.
61. Cominetti, M. R., Pott, H., Zúñiga, R. G., & Romero-Ortuno, R. (2023). Protecting cognitive function in older adults with age-related hearing loss: Insights from The Irish Longitudinal Study on Ageing (TILDA) and the role of hearing aids. *Archives of gerontology and geriatrics*, 112, 105043.

62. Bishop, C., Hamadain, E., Galster, J., Johnson, M., Spankovich, C. and Windmill, I. (2017). Outcomes of Hearing Aid Use by Individuals with Unilateral Sensorineural Hearing Loss (USNHL). *Journal of the American Academy of Audiology*, 28(10), pp.941-949.
63. Kates, J., Arehart, K., Anderson, M., Kumar Muralimanohar, R. and Harvey, L. (2018). Using Objective Metrics to Measure Hearing Aid Performance. *Ear and Hearing*, 39(6), pp.1165-1175.
64. Kwak, M., Kang, Y., Kim, D., An, Y. and Shim, H. (2018). Further Beneficial Effect of Hearing Aids on Speech Recognition Performance Besides Amplification. *Otology & Neurotology*, 39(8), pp.e618-e626.
65. Mondelli, F., Souza, P. (2012). Quality of life in elderly adults before and after hearing aid fitting. *Braz J Otorhinolaryngol*, 78, pp. 49–56
66. Gopinath, B., Schneider, J., Hartley, D., Teber, E., McMahon, C., Leeder, S. and Mitchell, P. (2011). Incidence and Predictors of Hearing Aid Use and Ownership Among Older Adults With Hearing Loss. *Annals of Epidemiology*, 21(7), pp.497-506.
67. Simpson, A., Matthews, L., Cassarly, C. and Dubno, J. (2019). Time From Hearing Aid Candidacy to Hearing Aid Adoption. *Ear and Hearing*, 40(3), pp.468-476.
68. Kochkin, S., and Rogin, C. (2000) Quantifying the obvious: the impact of hearing instruments on quality of life. *Hear Rev*, 7, pp. 8-34.
69. McCormack, A. and Fortnum, H. (2013). Why do people fitted with hearing aids not wear them? *International Journal of Audiology*, 52(5), pp.360-368.
70. Otavio, A., Coradini, P. and Teixeira, A. (2015). Self-Assessment of Hearing and Purchase of Hearing Aids by Middle-Aged and Elderly Adults. *International Archives of Otorhinolaryngology*, 20(01), pp.048-053.
71. Vuorialho, A., Karinen, P. and Sorri, M. (2006). Effect of hearing aids on hearing disability and quality of life in the elderly. *International Journal of Audiology*, 45(7), pp.400-405.
72. Kitterick, P. and Ferguson, M. (2018). Hearing Aids and Health-Related Quality of Life in Adults With Hearing Loss. *JAMA*, 319(21), p.2225.

73. Giroud, N., Lemke, U., Reich, P., Matthes, K. and Meyer, M. (2017). The impact of hearing aids and age-related hearing loss on auditory plasticity across three months – An electrical neuroimaging study. *Hearing Research*, 353, pp.162-175.
74. Uchida, Y., Sugiura, S., Nishita, Y., Saji, N., Sone, M. and Ueda, H. (2019). Age-related hearing loss and cognitive decline — The potential mechanisms linking the two. *Auris Nasus Larynx*, 46(1), pp.1-9.
75. Clark, J., Yeagle, J., Arbaje, A., Lin, F., Niparko, J. and Francis, H. (2012). Cochlear Implant Rehabilitation in Older Adults: Literature Review and Proposal of a Conceptual Framework. *Journal of the American Geriatrics Society*, 60(10), pp.1936-1945.
76. Yueh, B., Souza, P., McDowell, J., Collins, M., Loovis, C., Hedrick, S., Ramsey, S. and Deyo, R. (2001). Randomized Trial of Amplification Strategies. *Archives of Otolaryngology–Head & Neck Surgery*, 127(10), p.1197.
77. Francis, H., Chee, N., Yeagle, J., Cheng, A. and Niparko, J. (2002). Impact of Cochlear Implants on the Functional Health Status of Older Adults. *The Laryngoscope*, 112(8), pp.1482-1488.
78. Vermeire, K., Brokx, J., Wuyts, F., Cochet, E., Hofkens, A. and Van de Heyning, P. (2005). Quality-of Life Benefit from Cochlear Implantation in the Elderly. *Otology & Neurotology*, 26(2), pp.188-195.
79. Takiguchi, Y., Sun, G., Ogawa, K., and Matsunaga, T. (2013). Long-lasting changes in the cochlear K<sup>+</sup> recycling structures after acute energy failure. *Neuroscience Research*, 77(1-2), 33-41.
80. Mizutari, K. (2014). Spontaneous recovery of cochlear fibrocytes after severe degeneration caused by acute energy failure. *Frontiers in Pharmacology*, 5.
81. Li, Y., Watanabe, K., Fujioka, M. and Ogawa, K. (2017). Characterization of slow-cycling cells in the mouse cochlear lateral wall. *PLOS ONE*, 12(6), p.e0179293.
82. Moriyama, M., Yoshida, K., Ichimiya, I. and Suzuki, M. (2007). Nitric oxide production from cultured spiral ligament fibrocytes: effects of corticosteroids. *Acta Oto-Laryngologica*, 127(7), pp.676-681.

83. Nakanishi, H., Yamada, S., Kita, J., Shinmura, D., Hosokawa, K., Sahara, S., & Misawa, K. (2022). Auditory and Vestibular Characteristics of NLRP3 Inflammasome Related Autoinflammatory Disorders: Monogenic Hearing Loss Can Be Improved by Anti-interleukin-1 Therapy. *Frontiers in neurology*, 13, 865763.
84. Nakanishi H, Prakash P, Ito T, Kim HJ, Brewer CC, Harrow D, *et al.* (2020). Genetic hearing loss associated with autoinflammation. *Front Neurol*. 11:141.
85. Komeda, M., Roessler, B. J., & Raphael, Y. (1999). The influence of interleukin-1 receptor antagonist transgene on spiral ganglion neurons. *Hearing research*, 131(1-2), 1–10.
86. Yamahara, K., Yamamoto, N., Nakagawa, T., & Ito, J. (2015). Insulin-like growth factor 1: A novel treatment for the protection or regeneration of cochlear hair cells. *Hearing research*, 330(Pt A), 2–9.
87. Oh S., Woo J. I., Lim D. J., and Moon S. K. (2012). ERK2-dependent activation of c-Jun is required for nontypeable *Haemophilus influenzae*-induced CXCL2 upregulation in inner ear fibrocytes. *J. Immunol*. 188, pp. 3496–3505.
88. Zhuo, X. L., Wang, Y., Zhuo, W. L., Zhang, Y. S., Wei, Y. J., & Zhang, X. Y. (2008). Adenoviral-mediated up-regulation of *Otos*, a novel specific cochlear gene, decreases cisplatin-induced apoptosis of cultured spiral ligament fibrocytes via MAPK/mitochondrial pathway. *Toxicology*, 248(1), 33–38.
89. Gratton M. A., Schulte B. A., Hazen-Martin D. J. (1996). Characterization and development of an inner ear type I fibrocyte cell culture. *Hear. Res.* 99, pp. 71–78.
90. Suko T., Ichimiya I., Yoshida K., Suzuki M., Mogi G. (2000). Classification and culture of spiral ligament fibrocytes from mice. *Hear. Res.* 140, pp. 137–144.
91. Ichimiya, I., Suzuki, M., Yoshida, K. and Mogi, G. (2003). Expression of Adhesion Molecules by Cultured Spiral Ligament Fibrocytes Stimulated with Proinflammatory Cytokines. *Annals of Otolology, Rhinology & Laryngology*, 112(8), pp.722-728

92. Regmi, S., Pathak, S., Kim, J., Yong, C. and Jeong, J. (2019). Mesenchymal stem cell therapy for the treatment of inflammatory diseases: Challenges, opportunities, and future perspectives. *European Journal of Cell Biology*, 98(5-8), p.151041.
93. Sun, G., Fujii, M. and Matsunaga, T. (2012). Functional interaction between mesenchymal stem cells and spiral ligament fibrocytes. *Journal of Neuroscience Research*, 90(9), pp.1713-1722
94. Kamiya K., Fujinami Y., Hoya N., Okamoto Y., Kouike H., Komatsuzaki R., *et al.* . (2007). Mesenchymal stem cell transplantation accelerates hearing recovery through the repair of injured cochlear fibrocytes. *Am. J. Pathol*, 171, pp. 214–226.
95. Ma, Y., Guo, W., Yi, H., Ren, L., Zhao, L., Zhang, Y., Yuan, S., Liu, R., Xu, L., Cong, T., Ek, O., Zhai, S., & Yang, S. (2016). Transplantation of human umbilical cord mesenchymal stem cells in cochlea to repair sensorineural hearing. *American journal of translational research*, 8(12), 5235–5245.
96. Jiang, W., & Xu, J. (2020). Immune modulation by mesenchymal stem cells. *Cell proliferation*, 53(1), e12712.
97. Maharajan, N., Cho, G. W., & Jang, C. H. (2021). Therapeutic Application of Mesenchymal Stem Cells for Cochlear Regeneration. *In vivo (Athens, Greece)*, 35(1), 13–22.
98. Adamczyk, A., Matuszyk, E., Radwan, B., Rocchetti, S., Chlopicki, S. and Baranska, M. (2021). Toward Raman Subcellular Imaging of Endothelial Dysfunction. *Journal of Medicinal Chemistry*, 64 (8), 4396-4409
99. Guerrini L, Alvarez-Puebla RA. (2019). Surface-Enhanced Raman Spectroscopy in Cancer Diagnosis, Prognosis and Monitoring. *Cancers*, 11(6):748.
100. Ryzhikova, E., Ralbovsky, N.M., Sikirzhytski, V., Kazakov, O., Halamkova, L., Quinn, J., Zimmerman, E.A. and Lednev, I.K. (2021). Raman spectroscopy and machine learning for biomedical applications: Alzheimer's disease diagnosis based on the analysis of cerebrospinal fluid. *Spectrochimica Acta Part A: Molecular and Biomolecular Spectroscopy*, 248, 119188

101. Kashif, M., Majeed, M.I., Hanif, M.A., and Ur Rehman, A. (2020). Surface Enhanced Raman Spectroscopy of the serum samples for the diagnosis of Hepatitis C and prediction of the viral loads. *Spectrochimica Acta Part A: Molecular and Biomolecular Spectroscopy*, 242, 118729
102. Jadhav, S.A., Biji, P., Panthalingal, M.K., Krishna, C.M., Rajkumar, S., Joshi, D.S., and Sundaram, N. (2021). Development of integrated microfluidic platform coupled with Surface-enhanced Raman Spectroscopy for diagnosis of COVID-19. *Medical Hypotheses*, 146, 110356
103. Griffiths, P.R. and Haseth, J.A.D., 2007. *Fourier Transform Infrared Spectrometry* 2nd edn. Hoboken, New Jersey: Wiley & Sons.
104. Roy, S., Perez-Guaita, D., Bowden, S., Heraud, P., and Wood, B.R. (2019). Spectroscopy goes viral: Diagnosis of hepatitis B and C virus infection from human sera using ATR-FTIR spectroscopy, *Clinical Spectroscopy*, 1, 100001
105. Rodrigues, R. P., Aguiar, E. M., Cardoso-Sousa, L., Caixeta, D. C., Guedes, C. C., Siqueira, W. L., Maia, Y. C. P., Cardoso, S. V., & Sabino-Silva, R.. (2019). Differential Molecular Signature of Human Saliva Using ATR-FTIR Spectroscopy for Chronic Kidney Disease Diagnosis. *Brazilian Dental Journal*, 30(5), 437–445.
106. Giamougiannis, P., Morais, C.L.M., Rodriguez, B. *et al.* (2021). Detection of ovarian cancer ( $\pm$  neo-adjuvant chemotherapy effects) via ATR-FTIR spectroscopy: comparative analysis of blood and urine biofluids in a large patient cohort. *Anal Bioanal Chem* 413, 5095–5107
107. Singh, S.P. *et al.* (2019). Identification of early inflammatory changes in the tympanic membrane with Raman spectroscopy. *The Analyst*, 144(22), pp. 6721–6728.
108. Zhou, Z., Pandey, R., Valdez, T.A. (2024). Label-Free Optical Technologies for Middle-Ear Diseases. *Bioengineering*, 11, pp. 104.
109. Cozma, V., Rosca, I., Radulescu, L., Martu, C., Nastasa, V., Varganici, C.-D., Ursu, E.-L., Doroftei, F., Pinteala, M., Racles, C. (2021). Antibacterial Polysiloxane Polymers and Coatings for Cochlear Implants. *Molecules*, 26, pp. 4892.

110. Höhl, M., Meinhardt-Wollweber, M., Schmitt, H., Lenarz, T., and Morgner, U. (2016). UV-resonance Raman spectroscopy of amino acids. *Proc. SPIE 9704, Biomedical Vibrational Spectroscopy 2016: Advances in Research and Industry*, 970404 (7 March 2016).
111. Höhl, M., Zeilinger, C., Roth, B., Meinhardt-Wollweber, M., Morgner, U. (2019). Multivariate discrimination of heat shock proteins using a fiber optic Raman setup for in situ analysis of human perilymph. *Rev. Sci. Instrum.*, 90 (4), pp. 043110.
112. Heat Shock Protein-Based Therapies, 1st ed., Heat Shock Proteins, Vol. 9, edited by A. Asea, N. N. Almasoud, S. Krishnan, and P. Kaur (Springer International Publishing, Cham, 2015).
113. Chippendale, T., Španěl, P., Smith, D. and El Haj, A. (2014). Counting cell number in situ by quantification of dimethyl sulphide in culture headspace. *Analyst*, 139(19), pp.4903-07.
114. Smith, D. and Španěl, P. (2005). Selected ion flow tube mass spectrometry (SIFT-MS) for on-line trace gas analysis. *Mass Spectrometry Reviews*, 24(5), pp.661-700.
115. Smith, D., Sovová, K., Dryahina, K., Doušová, T., Dřevínek, P. and Španěl, P. (2016). Breath concentration of acetic acid vapour is elevated in patients with cystic fibrosis. *Journal of Breath Research*, 10(2), p.021002.
116. Demirjian, S., Paschke, K., Wang, X., Grove, D., Heyka, R. and Dweik, R. (2017). Molecular breath analysis identifies the breathprint of renal failure. *Journal of Breath Research*, 11(2), p.026009.
117. Dryahina, K., Smith, D., Bortlík, M., Machková, N., Lukáš, M. and Španěl, P. (2017). Pentane and other volatile organic compounds, including carboxylic acids, in the exhaled breath of patients with Crohn's disease and ulcerative colitis. *Journal of Breath Research*, 12(1), p.016002.
118. Chandran, D., Ooi, E., Watson, D., Kholmurodova, F., Jaenisch, S. and Yazbeck, R. (2019). The Use of Selected Ion Flow Tube-Mass Spectrometry Technology to Identify Breath Volatile Organic Compounds for the Detection of Head and Neck Squamous Cell Carcinoma: A Pilot Study. *Medicina*, 55(6), p.306

119. Miolo, G., Basile, D., Carretta, A., Santeufemia, D., Steffan, A. and Corona, G. (2019). The metabolomic scent of cancer disease progression in soft tissue sarcoma: A case report. *The International Journal of Biological Markers*, 34(2), pp.205-09.
120. Španěl, P. and Smith, D. (2008). Quantification of trace levels of the potential cancer biomarker formaldehyde, acetaldehyde and propanol in breath by SIFT-MS. *Journal of Breath Research*, 2(4), p.046003.
121. Ross, B.M., Puukila, S., Malik, I., Babay, S., Lecours, M., Agostino, A., Wondimu, T., and Khaper, N. (2013). The Use of SIFT-MS to Investigate Headspace Aldehydes as Markers of Lipid Peroxidation. *Current Analytical Chemistry*, 9 (4), pp, 600-613.
122. Hastie, C., Thompson, A., Perkins, M., Langford, V. S., Eddleston, M., and Homer, N. Z. (2021). Selected Ion Flow Tube-Mass Spectrometry (SIFT-MS) as an Alternative to Gas Chromatography/Mass Spectrometry (GC/MS) for the Analysis of Cyclohexanone and Cyclohexanol in Plasma. *ACS omega*, 6(48), pp. 32818–32822.
123. Alsbrooks, K., and Hoerauf, K. (2022). Prevalence, causes, impacts, and management of needle phobia: An international survey of a general adult population. *PLOS ONE*, 17(11), pp. e0276814.
124. Hasegawa, S., Ichiyama, T., Sonaka, I. *et al.* (2012). Cysteine, histidine and glycine exhibit anti-inflammatory effects in human coronary arterial endothelial cells. *Clinical and Experimental Immunology*, 167 (2), pp. 269–274,
125. Borek-Dorosz, A., Pieczara, A., Orleanska, J. *et al.* (2024). Raman microscopy reveals how cell inflammation activates glucose and lipid metabolism. *Biochimica et Biophysica Acta (BBA) - Molecular Cell Research*, 1871 (1), pp. 119575.
126. Liu, L., Chen, M., Zhang, J., *et al.* (2024). Oriented polyaniline/poly-L-lactic acid/gelatin nanofiber scaffolds promote outgrowth of spiral ganglion neurons. *J Biomed Mater Res.*, 112(5), pp.700-709.

127. Barbosa, J., Pereira, N., David, L., de Oliveira, C., Soares, M., Avelino, M., de Oliveira, A., Shokry, E. and Filho, N. (2019). Cerumenogram: a new frontier in cancer diagnosis in humans. *Scientific Reports*, 9(1).
128. Rutter, A., Chippendale, T., Yang, Y., Španěl, P., Smith, D., Sulé-Suso, J. (2013). Quantification by SIFT-MS of acetaldehyde released by lung cells in a 3D model. *Analyst*, 138(1), pp. 91-5.
129. Le, T., & Priefer, R. (2023). Detection technologies of volatile organic compounds in the breath for cancer diagnoses. *Talanta*, 265, 124767.
130. Sulé-Suso, J., Pysanenko, A., Španěl, P. and Smith, D. (2009). Quantification of acetaldehyde and carbon dioxide in the headspace of malignant and non-malignant lung cells in vitro by SIFT-MS. *The Analyst*, 134(12), p.2419
131. Rask-Andersen, H., Liu, W., Erixon, E., Kinnefors, A., Pfaller, K., Schrott-Fischer, A., and Glueckert, R. (2012). Human Cochlea: Anatomical Characteristics and their Relevance for Cochlear Implantation. *The Anatomical Record: Advances in Integrative Anatomy and Evolutionary Biology*, 295(11), 1791-1811.
132. Beurg, M., Barlow, A., Furness, D. and Fettiplace, R. (2019). A Tmc1 mutation reduces calcium permeability and expression of mechanoelectrical transduction channels in cochlear hair cells. *Proceedings of the National Academy of Sciences*, 116(41), pp.20743-20749.
133. Furness, D., Lawton, D., Mahendrasingam, S., Hodierne, L., and Jagger, D. (2009). Quantitative analysis of the expression of the glutamate-aspartate transporter and identification of functional glutamate uptake reveal a role for cochlear fibrocytes in glutamate homeostasis. *Neuroscience*, 162(4), pp. 1307-1321
134. Nordang, Leif & Cestreicher, E & Arnold, Wolfgang & Anniko, M. (2000). Glutamate is the afferent neurotransmitter in the human cochlea. *Acta oto-laryngologica*. 120. 359-62.
135. Hibino, H., Nin, F., Tsuzuki, C., and Kurachi, Y. (2009). How is the highly positive EP formed? The specific architecture of the stria vascularis and the roles of the ion transport apparatus. *Pflügers Archiv - European Journal of Physiology*, 459(4), pp. 521-533.

136. Kelly, J., Forge, A., and Jagger, D. (2012). Contractility in Type III Cochlear Fibrocytes Is Dependent on Non-muscle Myosin II and Intercellular Gap Junctional Coupling. *Journal of the Association for Research in Otolaryngology*, 13(4), pp. 473-484.
137. Adams, J. (2009). Immunocytochemical Traits of Type IV Fibrocytes and Their Possible Relations to Cochlear Function and Pathology. *Journal of the Association for Research in Otolaryngology*, 10(3), pp. 369-382.
138. Qu C, Liang F, Smythe NM, Schulte BA. 2007. Identification of ClC-2 and ClC-K2 chloride channels in cultured rat type IV spiral ligament fibrocytes. *J Assoc Res Otolaryngol*. 8:205–219
139. Zhang, W., Ogando, D.G., Kim, E.T., Choi, M.J., Li, H., Tenessen, J.M., and Bonanno, J.A. (2017) Conditionally Immortal Slc4a11<sup>-/-</sup> Mouse Corneal Endothelial Cell Line Recapitulates Disrupted Glutaminolysis Seen in Slc4a11<sup>-/-</sup> Mouse Model. *Invest. Ophthalmol. Vis. Sci.*, 58(9):3723-3731.
140. Bonanno, J. A., Shyam, R., Choi, M., & Ogando, D. G. (2022). The H<sup>+</sup> Transporter SLC4A11: Roles in Metabolism, Oxidative Stress and Mitochondrial Uncoupling. *Cells*, 11(2), 197.
141. Sawada, S., Takeda, T., Kitano, H., Takeuchi, S., Okada, T., Ando, M., Suzuki, M., and Kakigi, A. (2003). Aquaporin-1 (AQP1) is expressed in the stria vascularis of rat cochlea. *Hearing Research*, 181(1–2), 15-19.
142. Nottingher I, Verrier S, Haque S, Polak JM, Hench LL. (2003). *Biopolymers (Biospectroscopy)*. 72:230–40.
143. Short, KW, Carpenter S, Freyer JP, Mourant JR. (2005). *Biophys J*. 88:4274–88.
144. Verrier S, Nottingher I, Polak JM, Hench LL. (2004). *Biopolymers.*, 74:157–62.
145. Owens CA, Nottingher I, Hill R, Stevens M, Hench LL. (2006). *J Mat Sci Mat Med.*, 17:1019–23.
146. Boyd, A. R., Burke, G. A., and Meenan, B. J. (2010). Monitoring cellular behaviour using Raman spectroscopy for tissue engineering and regenerative medicine applications. *J Mater Sci: Mater Med*, 21:2317–2324

147. Pogostin, B. H., Malmendal, A., Londergan, C. H., & Åkerfeldt, K. S. (2019). pKa Determination of a Histidine Residue in a Short Peptide Using Raman Spectroscopy. *Molecules*, 24(3), 405.
148. Sabbatini, S. *et al.* (2017). 'Infrared Spectroscopy as a New Tool for Studying Single Living Cells: Is There a Niche?' *Biomedical Spectroscopy and Imaging*. 6. 85-99.
149. Venyaminov SYu, Kalnin NN. (1990) Quantitative IR spectrophotometry of peptide compounds in water (H<sub>2</sub>O) solutions. I. Spectral parameters of amino acid residue absorption bands. *Biopolymers*, 30(13-14):1243-57.
150. Resendes BL, Kuo SF, Robertson NG, Giersch AB, Honrubia D, Ohara O, Adams JC, Morton CC. (2004). Isolation from cochlea of a novel human intronless gene with predominant fetal expression. *J Assoc Res Otolaryngol*. 5(2):185-202.
151. Abe, S., Usami, Si. & Nakamura, Y. (2003). Mutations in the gene encoding KIAA1199 protein, an inner-ear protein expressed in Deiters' cells and the fibrocytes, as the cause of nonsyndromic hearing loss. *J Hum Genet* 48, 564–570
152. Riva C, Donadieu E, Magnan J, Lavieille JP. (2007). Age-related hearing loss in CD/1 mice is associated to ROS formation and HIF target proteins up-regulation in the cochlea. *Exp Gerontol*. 42(4):327-36.
153. Johnson, K.R., Gagnon, L.H., Longo-Guess, C., and Kane, K.L.(2012) Association of a citrate synthase missense mutation with age-related hearing loss in A/J mice, *Neurobiology of Aging*, 33(8), 1720-1729
154. Verschuur, C.A. *et al.* (2012) Markers of inflammatory status are associated with hearing threshold in older people: findings from the Hertfordshire Ageing Study. *Ageing*, 41, 92-97
155. Michaud, M., Balardy, L., Moulis, G., Gaudin, C., Peyrot, C., Vellas, B., Cesari, M., and Nourhashemi, F. (2013). Proinflammatory Cytokines, Aging, and Age-Related Diseases, *Journal of the American Medical Directors Association*, 14, 12, 877-882.

156. Fujioka, M., Kanzaki, S., Okano, H.J., Masuda, M., Ogawa, K. and Okano, H. (2006). Proinflammatory cytokines expression in noise-induced damaged cochlea. *J. Neurosci. Res.*, 83: 575-583.
157. Dinh CT, Haake S, Chen S, *et al.* (2008). Dexamethasone protects organ of corti explants against tumor necrosis factor- $\alpha$ -induced loss of auditory hair cells and alters the expression levels of apoptosis-related genes. *Neuroscience*. 157(2), 405-413.
158. Keithley EM, Wang X, Barkdull GC. (2008). Tumor necrosis factor  $\alpha$  can induce recruitment of inflammatory cells to the cochlea. *Otol Neurotol*. 29(6):854-859.
159. Moon, S. K., Woo, J. I., & Lim, D. J. (2019). Involvement of TNF- $\alpha$  and IFN- $\gamma$  in Inflammation-Mediated Cochlear Injury. *The Annals of otology, rhinology, and laryngology*, 128(6\_suppl), 8S–15S.
160. Davis, R. H., Fisher, J. S., and McGowan, L. (1968). Local Antiphlogistic Activity of L-Phenylalanine and L-Tryptophane. *Journal of Endocrinology*, 41(4), 603-604.
161. Wade, A.M., and Tucker, H.N. (1998). Antioxidant characteristics of L-histidine. *The Journal of Nutritional Biochemistry*, 9(6), 308-315
162. Hashimoto, S., Billings, P., Harris, J.P., Firestein, G.S., and Keithley, E.M. (2005) Innate immunity contributes to cochlear adaptive immune responses. *Audiol Neurotol*, 10(1), 35–43.
163. Mangan, M.S.J. *et al.* (2018). Targeting the NLRP3 inflammasome in inflammatory diseases. *Nat. Rev. Drug Discov.*, 17, 588-606
164. Seoane, P.I. *et al.* (2020). The NLRP3-inflammasome as a sensor of organelle dysfunction. *J. Cell Biol.*, 219, Article e202006194
165. Martinon, F., Burns, K., and Tschopp, J. (2002) The inflammasome: a molecular platform triggering activation of inflammatory caspases and processing of proIL- $\beta$ . *Mol Cell*, 10, 417–26.
166. Broz, P., and Dixit, V.M. (2016). Inflammasomes: mechanism of assembly, regulation and signalling. *Nat Rev Immunol*, 16, 407–20

167. Guo, H., Callaway, J.B., and Ting, J.P. (2015). Inflammasomes: mechanism of action, role in disease, and therapeutics. *Nat Med.*, 21, 677–87
168. Menu, P. and Vince, J.E. (2011). The NLRP3 inflammasome in health and disease: the good, the bad and the ugly. *Clin Exp Immunol.*, 166, 1–15
169. Nakanishi, H., Prakash, P., Ito, T., Kim, H.J., Brewer, C.C., Harrow, D., *et al.* (2020). Genetic hearing loss associated with autoinflammation. *Front Neurol.*, 11, 141.
170. Okano, T., Nakagawa, T., Kita, T., Kada, S., Yoshimoto, M., Nakahata, T., *et al.* (2008). Bone marrow-derived cells expressing Iba1 are constitutively present as resident tissue macrophages in the mouse cochlea. *J Neurosci Res.*, 86(8), 1758-67.
171. Du, X., Choi, C.H., Chen, K., Cheng, W., Floyd, R.A., and Kopke, R.D. (2011). Reduced formation of oxidative stress biomarkers and migration of mononuclear phagocytes in the cochleae of chinchilla after antioxidant treatment in acute acoustic trauma. *Int J Otolaryngol*, 612690.
172. Hirose, K., Discolo, C.M., Keasler, J.R., and Ransohoff, R. (2005) Mononuclear phagocytes migrate into the murine cochlea after acoustic trauma. *J Comp Neurol.*, 489(2), 180-94.
173. Tornabene, S.V., Sato, K., Pham, L., Billings, P., and Keithley, E.M. (2006). Immune cell recruitment following acoustic trauma. *Hear Res.*, 222(1-2), 115-24.
174. Hu, B.H., Zhang, C., and Frye, M.D. (2018). Immune cells and non-immune cells with immune function in mammalian cochleae. *Hear Res.*, 362, 14-24.
175. Miyao, M., Firestein, and G.S., Keithley, E.M. (2008) Acoustic trauma augments the cochlear immune response to antigen. *Laryngoscope*, 118(10), 1801-8.
176. Bae, S.H. *et al.* (2021). Three-Dimensional Distribution of Cochlear Macrophages in the Lateral Wall of Cleared Cochlea. *Clinical and Experimental Otorhinolaryngology*, 14(2), 179-184
177. Youm, Y.H. *et al.* (2013). Canonical Nlrp3 inflammasome links systemic low-grade inflammation to functional decline in aging. *Cell Metab.*, 18, 519-532

178. Carr, G.L., (1999). High-resolution microspectroscopy and sub-nanosecond time-resolved spectroscopy with the synchrotron infrared source. *Vibrational Spectroscopy*, 19(1), 53-60.
179. Miller, L.M. and Smith, R.J., (2005). Synchrotrons versus globars, point-detectors versus focal plane arrays: Selecting the best source and detector for specific infrared microspectroscopy and imaging applications. *Vibrational Spectroscopy*, 38(1–2), 237-240.
180. Pelletier, J., Bellot, G., Gounon, P., Lacas-Gervais, S., Pouysségur, J., and (2012). Mazure, N.M. Glycogen Synthesis is Induced in Hypoxia by the Hypoxia-Inducible Factor and Promotes Cancer Cell Survival. *Front Oncol.* 2:18.
181. Matthews, Q., Isabelle, M., Harder, S.J., Smazynski, J., Beckham, W., Brolo, A.G., Jirasek, A., and Lum, J.J. (2015). Radiation-Induced Glycogen Accumulation Detected by Single Cell Raman Spectroscopy Is Associated with Radioresistance that Can Be Reversed by Metformin. *PLoS One.* 10(8), e0135356.
182. Prokop-Prigge, K., Thaler, E., Wysocki, C. and Preti, G. (2014). Identification of volatile organic compounds in human cerumen. *Journal of Chromatography B*, 953-954, pp.48-52.
183. Feig, M.A., Hammer, E., Völker, U., and Jehmlich, N. (2013) In-depth proteomic analysis of the human cerumen—A potential novel diagnostically relevant biofluid, *Journal of Proteomics*, 83, 119-129
184. Shokry, E., de Oliveira, A., Avelino, M., de Deus, M. and Filho, N. (2017). Earwax: A neglected body secretion or a step ahead in clinical diagnosis? A pilot study. *Journal of Proteomics*, 159, pp.92-101
185. Kim, M. (2017). Diabetes mellitus and the incidence of hearing loss: a cohort study. *International Journal of Epidemiology*, p.dyw342
186. Gupta, S., Eavey, R., Wang, M., Curhan, S. and Curhan, G. (2018). Type 2 diabetes and the risk of incident hearing loss. *Diabetologia*, 62(2), pp.281-285

187. Ren, H., Wang, Z., Mao, Z., Zhang, P., Wang, C., Liu, A. and Yuan, G. (2017). Hearing Loss in Type 2 Diabetes in Association with Diabetic Neuropathy. *Archives of Medical Research*, 48(7), pp.631-637.
188. Bernier, U., Kline, D., Barnard, D., Schreck, C. and Yost, R. (2000). Analysis of Human Skin Emanations by Gas Chromatography/Mass Spectrometry. 2. Identification of Volatile Compounds That Are Candidate Attractants for the Yellow Fever Mosquito (*Aedes aegypti*). *Analytical Chemistry*, 72(4), pp.747-756
189. Coleman, B., Destailats, H., Hodgson, A. and Nazaroff, W. (2008). Ozone consumption and volatile byproduct formation from surface reactions with aircraft cabin materials and clothing fabrics. *Atmospheric Environment*, 42(4), pp.642-654.
190. Ikeguchi, N., Nihira, T., Kishimoto, A. and Yamada, Y. (1988). Oxidative Pathway from Squalene to Geranylacetone in *Arthrobacter* sp. Strain Y-11. *Applied and Environmental Microbiology*, 54(2), pp.381-385.
191. Wells, J., Morrison, G., Coleman, B., Spicer, C. and Dean, S. (2008). Kinetics and Reaction Products of Ozone and Surface-Bound Squalene. *Journal of ASTM International*, 5(7), p.101629.
192. Schwaab, M., Gurr, A., Neumann, A., Dazert, S. and Minovi, A. (2011). Human antimicrobial proteins in ear wax. *European Journal of Clinical Microbiology & Infectious Diseases*, 30(8), pp.997-1004
193. Shelley, W., Perry, E. (1956). The physiology of the apocrine (ceruminous gland) of the human ear canal. *J Invest Dermatol*, 26 (1), pp. 13–22
194. Mal, M. (2016) Noninvasive metabolic profiling for painless diagnosis of human diseases and disorders, *Future Science* 2, 2
195. Tomita, H., Yamada, K., Ghadami, M., Ogura, T., Yanai, Y., Nakatomi, K., Sadamatsu, M., Masui, A., Kato, N. and Niikawa, N. (2002). Mapping of the wet/dry earwax locus to the pericentromeric region of chromosome 16. *The Lancet*, 359(9322), pp.2000-2002.

196. Yoshimura, K., Kinoshita, A., Ishida, T., Ninokata, A., Ishikawa, T., *et al.* (2006). A SNP in the ABCC11 gene is the determinant of human earwax type. *Nature Genetics*, 38(3), pp.324-330.
197. Chai, T. and Chai, T. (1980). Bactericidal activity of cerumen. *Antimicrobial Agents and Chemotherapy*, 18(4), pp.638-641.
198. Ibraimov, A. (1991). Brief communication: Cerumen phenotypes in certain populations of Eurasia and Africa. *American Journal of Physical Anthropology*, 84(2), pp.209-211.
199. Matsunaga, E. (1962). The dimorphism in human normal cerumen. *Annals of Human Genetics*, 25(4), pp.273-286
200. Prugnotte, F., Lefèvre, T., Renaud, F., Møller, A., Missé, D. and Thomas, F. (2009). Infection and body odours: Evolutionary and medical perspectives. *Infection, Genetics and Evolution*, 9(5), pp.1006-1009.
201. Olusanya, B. (2003). Hearing impairment in children with impacted cerumen. *Annals of Tropical Paediatrics*, 23(2), pp.121-128.
202. Grossan, M. (1998). Cerumen Removal — Current Challenges. *Ear, Nose & Throat Journal*, 77(7), pp.541-548.
203. Ramoo, B., Funke, M., Frazee, C. and Garg, U. (2016). Comprehensive Urine Drug Screen by Gas Chromatography/Mass Spectrometry (GC/MS). *Methods Mol Biol*, 1383, pp.125-131.
204. Vrabie, V., Huez, R., Gobinet, C., Piot, O., Tfayli, A., and Manfait, M. (2006). ON THE MODELING OF PARAFFIN THROUGH RAMAN SPECTROSCOPY, *IFAC Proceedings Volumes*, 39(18)
205. Munro, K.J., Giles, T.C., Smith-Howell, C. and Nazareth, I. (2023) Ear wax management in primary care: what the busy GP needs to know. *British Journal of General Practice*, 73 (727), 90-92.
206. Shokry, E., & Filho, N. R. A. (2017). Insights into cerumen and application in diagnostics: past, present and future prospective. *Biochemia medica*, 27(3), 030503.

207. Osborn, A., Caruana, D., Furness, D. N., & Evans, M. G. (2022). Electrical and Immunohistochemical Properties of Cochlear Fibrocytes in 3D Cell Culture and in the Excised Spiral Ligament of Mice. *Journal of the Association for Research in Otolaryngology : JARO*, 23(2), 183–193.
208. Brustlein, S. *et al.* (2011). Double-clad hollow core photonic crystal fiber for coherent Raman endoscope. *Optics Express*, 19(13)
209. Peng, H., & Herzog, E. L. (2012). Fibrocytes: emerging effector cells in chronic inflammation. *Current opinion in pharmacology*, 12(4), pp. 491–496.
210. Reinhardt, J.W., Breuer, C.K. (2021). Fibrocytes: A Critical Review and Practical Guide. *Frontiers in Immunology*, 12.
211. Becker L., Lu, C., Montes-Mojarro, I.A. *et al.* (2023). Raman microspectroscopy identifies fibrotic tissues in collagen-related disorders via deconvoluted collagen type I spectra. *Acta Biomaterialia*, 162, pp. 278-291
212. Bellisola, G., Della Peruta, M., Vezzalini, M. *et al.* (2010). Tracking infrared signatures of drugs in cancer cells by Fourier transform microspectroscopy. *Analyst*, 135(12), pp. 3077-3086.
213. Whelan, D.R., Bambery, K.R., Puskar, L. *et al.* (2013). Synchrotron Fourier transform infrared ( FTIR ) analysis of single living cells progressing through the cell cycle. *Analyst*, 14.
214. Lipiec, E., Birarda, G., Kowalska, J. *et al.* (2013). A new approach to studying the effects of ionising radiation on single cells using FTIR synchrotron microspectroscopy. *Radiation Physics and Chemistry*, 93, pp.135-141
215. Dunkhunthod, B., Talabnin, C., Murphy, M.F., Thumanu, K., Sittisart, P., Hengpratom, T., & Eumkeb, G. (2020). Intracellular ROS Scavenging and Anti-Inflammatory Activities of *Oroxylum indicum* Kurz (L.) Extract in LPS plus IFN- $\gamma$ -Activated RAW264.7 Macrophages. *Evidence-based Complementary and Alternative Medicine : eCAM*, 2020.
216. Pezzotti, G. (2021). Raman spectroscopy in cell biology and microbiology. *Journal of Raman Spectroscopy*, 52(12), pp. 2348-2443

217. De Gelder, J., De Gussem, K., Vandenabeele, P. *et al.* (2007). Reference database of Raman spectra of biological molecules. *Journal of Raman Spectroscopy*, 38, pp. 1133-1147.
218. Dazzoni, R., Grélard, A., Morvan, E. *et al.* (2020). The unprecedented membrane deformation of the human nuclear envelope, in a magnetic field, indicates formation of nuclear membrane invaginations. *Sci Rep* 10, 5147.
219. Ledeen, R. and Wu, G. (2009). Nuclear Lipids and Their Metabolic and Signaling Properties. In: Lajtha, A., Tettamanti, G., Goracci, G. (eds) *Handbook of Neurochemistry and Molecular Neurobiology*. Springer, Boston, MA.
220. Gunasekaran, S. (2010). Experimental and semi-empirical computations of the vibrational spectra of methionine, homocysteine and cysteine. *Archives of Physics Research*, 1(1), pp. 12-26.
221. Fontecave, M., Atta, M., and Mulliez, E. (2004). S-adenosylmethionine: nothing goes to waste. *Trends in biochemical sciences*, 29(5), pp. 243–249.
222. Pezzotti, G. (2019). Silicon Nitride: A Bioceramic with a Gift. *ACS applied materials & interfaces*, 11(30), pp. 26619–26636.
223. Brauchle, E., Thude, S., Brucker, S. Y., and Schenke-Layland, K. (2014). Cell death stages in single apoptotic and necrotic cells monitored by Raman microspectroscopy. *Scientific reports*, 4, pp. 4698.
224. Kneipp, K., Haka, A.S., Kneipp, H. *et al.* (2002). Surface-Enhanced Raman Spectroscopy in Single Living Cells Using Gold Nanoparticles. *Applied Spectroscopy*, 56(2), pp. 150-154.
225. Kubryk, P., Niessner, R. and Ivleva, N.P. (2016). The origin of the band at around 730 cm<sup>-1</sup> in the SERS spectra of bacteria: a stable isotope approach. *Analyst*, 10.
226. Shalabaeva, V., Lovato, L., La Rocca, R. *et al.* (2017). Time resolved and label free monitoring of extracellular metabolites by surface enhanced Raman spectroscopy. *PloS ONE*, 12(4), pp. e0175581.

227. Neugebauer, U., Schmid, U., Baumann, K. *et al.* (2006). Towards a Detailed Understanding of Bacterial Metabolism—Spectroscopic Characterization of *Staphylococcus Epidermidis*. *ChemPhysChem*, 8(1), pp. 124-137.
228. Olszynska, S., Dupuy, N., Vrielynck, L. and Komorowska, M. (2006). Water Evaporation Analysis of L-Phenylalanine from Initial Aqueous Solutions to Powder State by Vibrational Spectroscopy. *Applied Spectroscopy*, 60(9), pp. 1040-1053.
229. Wiercigroch, E. (2017). Raman and infrared spectroscopy of carbohydrates: A review. *Spectrochimica Acta, Part A: Molecular and Biomolecular Spectroscopy*, 185, pp. 317-335.
230. Guanyong, Z. (2011). Raman spectra of amino acids and their aqueous solutions. *Spectrochimica Acta, Part A: Molecular and Biomolecular Spectroscopy*, 78A(3), pp. 1187-1195.
231. Olszynska, S. (2006). Water evaporation analysis of L-phenylalanine from initial aqueous solutions to powder state by vibrational spectroscopy. *Applied Spectroscopy*, 60(9), pp. 1040-1053.
232. Alberts, B., Johnson, A., Lewis, J. *et al.* *Molecular Biology of the Cell*. 4th edition. New York: Garland Science; 2002. The Transport of Molecules between the Nucleus and the Cytosol.
233. Guicheteau, J., Argue, L., Hyre, A., Jacobson, M. and Christesen, S.D. (2006). “Raman and surface-enhanced Raman spectroscopy of amino acids and nucleotide bases for target bacterial vibrational mode identification.” *Proc. SPIE 6218, Chemical and Biological Sensing VII*, 62180O (19 May 2006)
234. Ramirez-Guerrero, S., Guardo-Maya, S., Medina-Rincón, G.J. *et al.* (2022). Taurine and Astrocytes: A Homeostatic and Neuroprotective Relationship. *Front. Mol. Neurosci.*, 15.
235. Krafft, C., Neudert, L., Simat, T. and Salzer, R. (2005). Near infrared Raman spectra of human brain lipids. *Spectrochimica Acta, Part A: Molecular and Biomolecular Spectroscopy*, 61(7), pp. 1529-1535.
236. Shetty, G., Kendall, C., Shepherd, N. *et al.* (2006). Raman spectroscopy: elucidation of biochemical changes in carcinogenesis of oesophagus. *Br J Cancer* 94, pp. 1460–1464.

237. Cockcroft, S. (2021). Mammalian lipids: structure, synthesis and function. *Essays Biochem.*, 65(5), pp. 813-845.
238. Mandair, G. S. and Morris, M. D. (2015). Contributions of Raman spectroscopy to the understanding of bone strength. *Bonekey Reports*, 4, pp. 620.
239. Balla, T. (2013). Phosphoinositides: tiny lipids with giant impact on cell regulation. *Physiological reviews*, 93(3), pp. 1019–1137.
240. Kay, J.G. and Fairn, G.D. (2019). Distribution, dynamics and functional roles of phosphatidylserine within the cell. *Cell Communication and Signaling*, 17, pp. 126.
241. Calzada, E., Onguka, O. and Claypool, S. M. (2016). Phosphatidylethanolamine Metabolism in Health and Disease. *International review of cell and molecular biology*, 321, pp. 29–88.
242. Schie, I. and Huser, T.R. (2013). Methods and applications of Raman microspectroscopy to single-cell analysis. *Applied Spectroscopy*, 67(8), pp. 813-828.
243. Grove, R.Q. and Karpowicz, S.J. (2017). Reaction of hypotaurine or taurine with superoxide produces the organic peroxysulfonic acid peroxytaurine. *Free Radical Biology and Medicine*, 2018, pp. 575-584.
244. Mittal, M., Siddiqui, M.R., Tran, K. *et al.* (2014). Reactive Oxygen Species in Inflammation and Tissue Injury. *Antioxid. Redox Signal.*, 20(7), pp. 1126-1167.
245. Zhang, Q., Chen, S., Guo, Y. *et al.* (2023). Phenylalanine diminishes M1 macrophage inflammation. *Sci. China Life Sci.* 66, pp. 2862–2876.
246. Pansarasa, O., Mimmi, M.C., Davin, A. *et al.* (2022). Inflammation and cell-to-cell communication, two related aspects in frailty. *Immun. Ageing*, 19, pp. 49.
247. Yoshida, K., Ichimiya, I., Suzuki, M. and Mogi, G. (1999). Effect of proinflammatory cytokines on cultured spiral ligament fibrocytes. *Hearing Research*, 137, pp. 155-159.
248. Kim, J.A., Åberg, C., Salvati, A. and Dawson, K.A. (2012). Role of cell cycle on the cellular uptake and dilution of nanoparticles in a cell population. *Nature Nanotechnology*, 7, pp. 62-68.

249. Kalucka, J., Missiaen, R., Georgiadou, M., Schoors, S., Lange, C., De Bock, K., Dewerchin, M., & Carmeliet, P. (2015). Metabolic control of the cell cycle. *Cell Cycle*, 14(21), pp. 3379–3388.
250. Ohnishi K., Semi K., Yamamoto T., Shimizu M., Tanaka A., Mitsunaga K., Okita K., Osafune K., Arioka Y., Maeda T., *et al.* (2014). Premature termination of reprogramming in vivo leads to cancer development through altered epigenetic regulation. *Cell*. 156. 663–677. doi: 10.1016/j.cell.2014.01.005.
251. Schnabel L.V., Abratte C.M., Schimenti J.C., Felipe M.J., Cassano J.M., Southard T.L., Cross J.A., and Fortier L.A. (2014). Induced pluripotent stem cells have similar immunogenic and more potent immunomodulatory properties compared with bone marrow-derived stromal cells in vitro. *Regen. Med.* 9. 621–635. doi: 10.2217/rme.14.29.
252. Jeon SJ, Oshima K, Heller S, and Edge AS. (2007). Bone marrow mesenchymal stem cells are progenitors in vitro for inner ear hair cells. *Molecular and Cellular Neurosciences*. 34(1). 59-68. doi: 10.1016/j.mcn.2006.10.003. PMID: 17113786; PMCID: PMC3136105.
- 253.** Kada S., Hamaguchi K., Ito J., Omori K., and Nakagawa T. (2020). Bone Marrow Stromal Cells Accelerate Hearing Recovery via Regeneration or Maintenance of Cochlear Fibrocytes in Mouse Spiral Ligaments. *Anat. Rec.* 303. 478–486. doi: 10.1002/ar.24063.
- 254.** Kada S, Nakagawa T, and Ito J. (2009). A mouse model for degeneration of the spiral ligament. *J Assoc Res Otolaryngol.* 10(2). 161-72. doi: 10.1007/s10162-008-0147-6
255. Lee H.S., Kim W.J., Gong J.S., and Park K.H. (2017). Clinical Safety and Efficacy of Autologous Bone Marrow-Derived Mesenchymal Stem Cell Transplantation in Sensorineural Hearing Loss Patients. *J. Audiol. Otol.* 22. 105–109. doi: 10.7874/jao.2017.00150.
256. Eshraghi A.A., Ocak E., Zhu A., Mittal J., Davies C., Shahal D., Bulut E., Sinha R., Shah V., Perdomo M.M., *et al.* (2020). Biocompatibility of Bone Marrow-Derived Mesenchymal Stem Cells in the Rat Inner Ear following Trans-Tympanic Administration. *J. Clin. Med.* 9. 1711. doi: 10.3390/jcm9061711.

257. Yang B, Oo TN, Rizzo V. Lipid rafts mediate H<sub>2</sub>O<sub>2</sub> prosurvival effects in cultured endothelial cells. *FASEB J.* 2006 Jul;20(9):1501-3. doi: 10.1096/fj.05-5359fje. Epub 2006 Jun 5. PMID: 16754746.
258. Byrne, H., Bonnier, F., McIntyre, J., and Parachalil, D.R. (2020). Quantitative analysis of human blood serum using vibrational spectroscopy. *Clinical Spectroscopy*. 2.
259. Sabouni Tabari, R., Chen, Y., Thummavichai, K., Zhang, Y., Saadi, Z., Neves, A.I.S., Xia, Y., and Zhu, Y. (2022). Piezoelectric Property of Electrospun PVDF Nanofibers as Linking Tips of Artificial-Hair-Cell Structures in Cochlea. *Nanomaterials*, 12, pp. 1466.
260. Vera-Aviles, M., Vantana, E., Kardinasari, E., Koh, N. L. and Latunde-Dada, G. O. (2018). Protective Role of Histidine Supplementation Against Oxidative Stress Damage in the Management of Anemia of Chronic Kidney Disease. *Pharmaceuticals*, 11(4), pp. 111.
261. Thalacker-Mercer, A. E. and Gheller, M. E. (2020). Benefits and Adverse Effects of Histidine Supplementation. *The Journal of nutrition*, 150(Suppl 1), pp. 2588S–2592S.
262. Kendall, C. et al. (2009) Vibrational Spectroscopy: A clinical tool for cancer diagnostics, *The Analyst*, 134(6), p. 1029.
263. Schie, I. and Huser, T.R. (2013). Methods and applications of Raman microspectroscopy to single-cell analysis. *Applied Spectroscopy*, 67(8), pp. 813-828.
264. Baglioni, M. et al. (2018). A Triton X-100-Based Microemulsion for the Removal of Hydrophobic Materials from Works of Art: SAXS Characterization and Application. *Materials*, 11(7), p.1114.
265. Borek-Dorosz, A. et al. (2024). Raman microscopy reveals how cell inflammation activates glucose and lipid metabolism. *Biochimica et Biophysica Acta (BBA)*, 1871(1), p. 119575.
266. Czamara, K. et al. (2017). Unsaturated lipid bodies as a hallmark of inflammation studied by Raman 2D and 3D microscopy. *Scientific Reports*, 7, p. 40889.
267. Tamosaityte, S. et al. (2016). Inflammation-related alterations of lipids after spinal cord injury revealed by Raman spectroscopy. *Journal of Biomedical Optics*, 21(6), p. 061008.

268. Tian, P. et al. (2015). Intraoperative diagnosis of benign and malignant breast tissues by fourier transform infrared spectroscopy and support vector machine classification. *Int J Clin Exp Med*, 8(1), pp. 972-981.
269. Theophilou, G. et al. (2016). ATR-FTIR spectroscopy coupled with chemometric analysis discriminates normal, borderline and malignant ovarian tissue: classifying subtypes of human cancer. *Analyst*, 2.
270. Rodrigues, L.M. et al. (2017). Evaluation of inflammatory processes by FTIR spectroscopy. *Journal of Medical Engineering & Technology*, 42(3), pp. 228-235.
271. Vethanayagam, R.R. et al. (2016). Toll-like receptor 4 modulates the cochlear immune response to acoustic injury. *Cell Death & Disease*, 7.
272. Ji, D. et al. (2020). Effects of inflammatory and anti-inflammatory environments on the macrophage mitochondrial function. *Scientific Reports*, 10.
273. Choi, H. M. et al. (2010). Differential effect of IL-1 $\beta$  and TNF $\alpha$  on the production of IL-6, IL-8 and PGE2 in fibroblast-like synoviocytes and THP-1 macrophages. *Rheumatology international*, 30(8), pp. 1025–1033.
274. Quan, T. E., Cowper, S. E., and Bucala, R. (2006). The role of circulating fibrocytes in fibrosis. *Curr. Rheumatol. Rep.* 8, pp. 145–150.
275. Stanley, A. C., and Lacy, P. (2010). Pathways for cytokine secretion. *Physiology*, 25(4), pp. 218–229.
276. Flanagan, A.R., and Glavin, F.G. (2023). A Comparative Analysis of Data Synthesis Techniques to Improve Classification Accuracy of Raman Spectroscopy Data. *Journal of Chemical Information and Modeling*, 64(7).

# Appendix A – Authorisation for Animal Use



16th November 2020

Dear Sir/Madam,

I am writing as the Named Animal Care and Welfare Officer for Keele University. Please accept this letter as confirmation that authorization was sought, and approved, for the supply and use of mouse tissues by Amy Worrall, for her project conducted under the supervision of Dr Abigail Rutter, in collaboration with and under the guidance of Professor David Furness. Animals were bred and maintained according to the Code of Practice for the housing and care of animals bred, supplied or used for scientific purposes, and in accordance with the Establishment Licence held by Keele University. Animals were culled humanely using approved Schedule 1 methods, by trained personnel.

Best wishes,

Stefanie

---

Stefanie Jones PhD NACWO/NTCO

Life Sciences

Keele University

ST5 5BG

s.m.jones@keele.ac.uk

School of Life Sciences, Huxley Building, Keele University, Keele, Staffordshire, ST5 5BG.  
Telephone: +44 (0)1782 734414, Fax +44 (0)1782 733516

## Appendix B – Kinetic Library for SIFT-MS Analysis

water <sub>1.7</sub> (H <sub>3</sub> O <sup>+</sup> )	37 2.5e-9 1.0	acetone(H <sub>3</sub> O <sup>+</sup> )
1 precursor	55 2.3e-9 1.0	4 precursors
19 1.7e-11 1.0	73 2.1e-9 1.0	19 3.9e-9 1.0
3 products	3 products	37 3.3e-9 1.0
37 1.0	18 1.0	55 2.5e-9 1.0
55 1.0	36 1.0	73 2.4e-9 1.0
73 1.0	54 1.0	3 products
water(NO <sup>+</sup> )	ammonia <sub>18_only</sub> (H <sub>3</sub> O <sup>+</sup> )	59 1.0
1 precursor	4 precursors	77 1.0
30 0.2e-11 1.0	19 2.6e-9 1.0	95 1.0
2 products	37 2.5e-9 0.54	acetone <sub>dry_air</sub> (NO <sup>+</sup> )
48 1.0	55 2.3e-9 0.43	3 precursor
66 1.0	73 2.1e-9 0.2	30 1.8e-9 1.0
water(O <sub>2</sub> <sup>+</sup> )	1 products	48 1.5e-9 1.0
1 precursor	18 1.0	66 1.4e-9 1.0
32 0.2e-11 1.0	ammonia(O <sub>2</sub> <sup>+</sup> )	1 product
1 products	1 precursor	88 1.0
73 1.0	32 2.4e-9 1.0	acetone <sub>breath</sub> (NO <sup>+</sup> )
ammonia(H <sub>3</sub> O <sup>+</sup> )	2 products	3 precursor
4 precursors	17 1.0	30 2.1e-9 1.0
19 2.6e-9 1.0	35 1.0	48 2.0e-9 1.0

66 1.8e-9 1.0	30 2.5e-9 1.0	37 3.4e-15 1.0
1 product	1 product	55 3.4e-15 1.0
88 1.0	130 1.0	73 3.4e-15 1.0
acetone(O2+)	heptanone(NO+,all_isomers)	3 products
1 precursor		63 1.0
32 3.1e-9 1.0	1 precursors	45 -0.576
2 products	30 2.5e-9 1.0	81 -0.831
43 1.0	1 product	co2_corrDMS_AA(H3O+)
58 1.0	144 1.0	4 precursors
butanone(NO+,all_isomers)	octanone(NO+,all_isomers)	19 3e-15 1.0
1 precursors	1 precursors	37 3e-15 1.0
30 2.5e-9 1.0	30 2.5e-9 1.0	55 3e-15 1.0
1 product	1 product	73 3e-15 1.0
102 1.0	158 1.0	3 products
pentanone(NO+,all_isomers)	nonanone(NO+,all_isomers)	63 1.0
	)	45 1.5
1 precursors	1 precursors	81 -6
30 2.5e-9 1.0	30 2.5e-9 1.0	CO2(NO+)
1 product	1 product	3 precursors
116 1.0	172 1.0	30 1.5e-15 1.0
hexanone(NO+,all_isomers)	co2(H3O+,Capno)	48 1.5e-15 1.0
1 precursors	4 precursors	66 1.5e-15 1.0
	19 3.4e-15 1.0	

3 products	acetaldehyde(H <sub>3</sub> O <sup>+</sup> ,BAMO	acetaldehyde(NO <sup>+</sup> )
74 1.0	D)	1 precursor
73 -0.0029	5 precursors	30 0.6e-9 1.0
43 -0.33	19 3.7e-9 1.0	1 products
CO <sub>2</sub> nopowerlaw(NO <sup>+</sup> )	37 3.0e-9 1.0	43 1.0
3 precursors	55 2.7e-9 1.0	acetaldehydeC <sub>88</sub> (NO <sup>+</sup> )
30 2e-15 1.0	73 2.6e-9 1.0	4 precursors
48 2e-15 1.0	32 3.7e-9 1.0	30 3.4e-9 1.0
66 2e-15 1.0	3 products	48 3.0e-9 -1.0
3 products	45 1.576	64 2.7e-9 0.0
74 1.0	81 1.831	32 3.7e-9 1.0
43 -0.33	83 -100.5	2 products
73 -0.0029	acetaldehyde <sub>3245</sub> (H <sub>3</sub> O <sup>+</sup> )	43 1.44
formaledhydeBAMOD(H <sub>3</sub> O	5 precursors	88 -100.9
+,corr.EtOH MeOH)	19 3.7e-9 1.0	propanal(NO <sup>+</sup> )
2 precursor	37 3.0e-9 -1.0	4 precursors
19 2.7e-9 1.0	55 2.7e-9 0.0	30 2.0e-9 1.0
32 2.7e-9 1.0	73 2.6e-9 0.0	48 5.0e-10 1.0
3 product	32 3.7e-9 1.0	64 5.0e-10 1.0
31 1.0	2 products	32 3.7e-9 1.0
33 -100.4	45 1.1	2 products
83 -100.9	83 -100.5	55 -0.006

57 1.0	37 1.9e-9 -0.12	1 products
acetaldehydeC58(NO+)	55 1.9e-9 -0.34	83 1.0
3 precursors	73 1e-11 -0.48	ethanol(NO+)
30 3.4e-9 1.0	2 products	3 precursors
48 3.0e-9 -1.0	33 0.81	30 1.9e-9 1.0
64 2.7e-9 0.0	51 1.13	48 2.1e-9 1.0
2 products	ethanol(H3O+)	66 1.9e-9 1.0
43 1.44	4 precursors	3 products
58 -0.6	19 2.7e-9 1.0	45 1.0
methanol(H3O+)	37 2.3e-9 1.0	63 1.0
4 precursors	55 2.1e-9 1.0	81 1.0
19 2.4e-9 1.0	73 1e-11 1.0	propanol(H3O+,all_isomers
37 1.9e-9 1.0	3 products	)
55 1.9e-9 1.0	47 1.0	4 precursors
73 1e-11 1.0	65 1.0	19 2.7e-9 1.0
3 products	83 1.0	37 2.3e-9 1.0
33 1.0	ethanol83(H3O+)	55 2.2e-9 1.0
51 1.0	4 precursors	73 2.1e-9 1.0
69 1.0	19 2.7e-9 0	4 products
methanol33_51(H3O+)	37 2.3e-9 0.8	43 1.0
4 precursors	55 2.1e-9 2.5	61 1.0
19 2.4e-9 1.0	73 1e-11 2.5	79 1.0

97 1.0	37 2.2e-9 1.0	4 precursors
propanol43(H3O+,BAMOD)	55 1.9e-9 1.0	19 2.6e-9 1.0
4 precursors	73 1.8e-9 1.0	37 1.9e-9 1.0
19 2.7e-9 1.0	5 products	55 1.9e-9 1.0
37 2.3e-9 -0.1	57 1.0	73 1.8e-9 1.0
55 2.2e-9 -0.1	55 -0.006	3 products
73 2.1e-9 -0.1	75 1.0	61 1.0
1 products	73 -0.008	79 1.0
43 1.0	93 1.0	97 1.0
propanol(NO+,all_isomers)	pentanol(H3O+,all_isomers )	acetic_acid(NO+)
3 precursors	4 precursors	3 precursors
30 2.4e-9 1.0	19 2.8e-9 1.0	30 1.5e-9 1.0
48 2.0e-9 1.0	37 2.2e-9 1.0	48 5e-10 1.0
66 1.9e-9 1.0	55 1.9e-9 1.0	66 5e-10 1.0
4 products	73 1.8e-9 1.0	2 products
59 1.0	4 products	90 1.0
77 1.0	71 1.0	108 1.0
95 1.0	89 1.0	acetic_acid90(NO+)
113 1.0	107 1.0	3 precursors
butanol(H3O+,all_isomers)	125 1.0	30 1.5e-9 1.0
4 precursors	acetic_acid(H3O+)	48 5e-10 1.0
19 2.8e-9 1.0		66 5e-10 1.0

1 products	4 precursors	94 1.0
90 1.67	19 2.5e-9 1.0	h2s(H3O+)
isoprene(NO+)	37 1.8e-9 1.0	4 precursors
3 precursors	55 1.8e-9 1.0	19 2e-9 1.0
30 1.7e-9 1.0	73 1.8e-9 1.0	37 1e-11 0.15
48 1e-12 1.0	1 products	55 1e-11 0.15
66 1e-12 1.0	63 1.04	73 1e-11 0.15
2 products	DMS(NO+)	1 product
66 -0.004	1 precursor	35 1.0
68 1.0	30 2.2e-9 1.0	methanthiol_nominal
isoprene(O2+)	1 products	(H3O+)
1 precursor	62 1.04	4 precursors
32 1.7e-9 1.0	DMS_64incl(NO+)	19 2.5e-9 1.0
2 products	1 precursor	37 1.8e-9 1.0
67 1.05	30 2.2e-9 1.0	55 1.8e-9 1.0
68 1.05	2 products	73 1.8e-9 1.0
isoprene_67only(O2+)	62 1.0	3 products
1 precursor	64 1.0	49 1.0
32 1.7e-9 1.0	DMDS(NO+)	67 1.0
1 products	1 precursor	85 1.0
67 2.1	30 2.4e-9 1.0	methanthiol78(NO+)
DMS+ethanthiol(H3O+)	1 products	2 precursors

30 0.5e-9 1.0	4 precursors	37 1.9e-9 1.0
48 0.4e-9 1.0	19 3.7e-9 1.0	55 1.9e-9 1.0
1 product	37 3.2e-9 1.0	73 1.9e-9 1.0
78 1.0	55 2.8e-9 1.0	4 products
HCN(H <sub>3</sub> O <sup>+</sup> )	73 2.6e-9 1.0	73 -0.008
4 precursors	3 products	75 1.0
19 3.8e-9 1.0	101 1.0	93 1.0
37 1e-11 -0.037	119 1.0	111 1.0
55 1e-11 -0.037	137 1.0	butyric_acid(H <sub>3</sub> O <sup>+</sup> ,all_isom
73 1e-11 -0.037	benzaldehyde (H <sub>3</sub> O <sup>+</sup> )	ers)
1 product	4 precursors	4 precursors
28 1.0	19 3.7e-9 1.0	19 2.9e-9 1.0
3-methylbutanal(H <sub>3</sub> O <sup>+</sup> )	37 3.2e-9 1.0	37 1.9e-9 1.0
4 precursors	55 2.8e-9 1.0	55 1.9e-9 1.0
19 3.8e-9 1.0	73 2.6e-9 1.0	73 1.9e-9 1.0
37 3.2e-9 1.0	3 products	3 products
55 2.8e-9 1.0	107 1.0	89 1.0
73 2.6e-9 1.0	125 1.0	107 1.0
2 products	143 1.0	125 1.0
87 1.0	propanoic_acid(H <sub>3</sub> O <sup>+</sup> )	pentanoic_acid(H <sub>3</sub> O <sup>+</sup> ,all_is
105 1.0	4 precursors	omers)
hexanal (H <sub>3</sub> O <sup>+</sup> )	19 2.7e-9 1.0	4 precursors
		19 2.4e-9 1.0

37 1.9e-9 1.0	55 2.3e-9 1.0	2 products
55 1.9e-9 1.0	73 2.1e-9 1.0	100 1.0
73 1.7e-9 1.0	3 products	118 1.0
3 products	105 1.0	methylisothiocyanate(NO+)
103 1.0	123 1.0	3 precursors
121 1.0	141 1.0	30 2.2e-9 1.0
139 1.0	3-HBAcid(NO+)	48 2.0e-9 -1.0
hexanoic_acid(H3O+,all_isomers)	3 precursors	64 1.9e-9 0.0
4 precursors	30 2.9e-9 1.0	3 products
19 2.4e-9 1.0	48 2.4e-9 1.0	99 1.0
37 1.9e-9 1.0	66 2.2e-9 1.0	117 1.0
55 1.9e-9 1.0	3 products	129 1.0
73 1.7e-9 1.0	104 1.0	pentene(H3O+)
3 products	116 1.0	4 precursors
117 1.0	134 1.0	19 2.5e-9 1.0
135 1.0	methylisothiocyanate(H3O+)	37 1.8e-9 1.0
153 1.0	4 precursors	55 1.8e-9 1.0
3-HBAcid(H3O+)	19 2.4e-9 1.0	73 1.8e-9 1.0
4 precursors	37 1.9e-9 1.0	1 product
19 3.5e-9 1.0	55 1.9e-9 1.0	71 1.0
37 2.7e-9 1.0	73 1e-11 1.0	diethyl_ether(H3O+)
		4 precursors

19 2e-9 1.0	55 1.2e-9 1.0	pyrolle(H3O+)
37 1.8e-9 1.0	73 5e-10 1.0	4 precursors
55 1.7e-9 1.0	2 products	19 2.5e-9 1.0
73 1.6e-9 1.0	123 1.0	37 1.9e-9 1.0
4 products	141 1.0	55 1.9e-9 1.0
73 -0.008	putresceine(H3O+)	73 1.9e-9 1.0
75 1.0	4 precursors	2 products
93 1.0	19 2.3e-9 1.0	68 1.0
111 1.0	37 1.8e-9 1.0	86 1.0
methyl_phenol(H3O+)	55 1.6e-9 1.0	terpenes(H3O+,total)
4 precursors	73 1.4e-9 1.0	4 precursors
19 2.8e-9 1.0	1 product	19 2.6e-9 1.0
37 1.7e-9 1.0	89 2	37 1e-9 1.0
55 1.2e-9 1.0	cadaverine(H3O+)	55 1e-11 1.0
73 5e-10 1.0	4 precursors	73 1e-11 1.0
2 products	19 2.3e-9 1.0	2 products
109 1.0	37 1.7e-9 1.0	81 1.06
127 1.0	55 1.5e-9 1.0	137 1.1
ethyl_phenol(H3O+)	73 1.4e-9 1.0	carvone(H3O+,total)
4 precursors	2 products	4 precursors
19 2.8e-9 1.0	86 1.2	19 3e-9 1.0
37 1.7e-9 1.0	103 1.5	37 2e-9 1.0

55 2e-9 1.0	4 precursors	55 1e-11 1.0
73 2e-9 1.0	73.9 1e-9 1.0	73 1e-11 1.0
2 products	74.0 1e-9 1.0	1 product
151 1.1	74.1 1e-9 1.0	93 1.0
169 1.1	74.2 1e-9 1.0	xylene(H3O+,all_isomers)
menthol(H3O+)	4 products	4 precursors
4 precursors	74.9 1.0	19 2.3e-9 1.0
19 3.1e-9 1.0	75.0 1.0	37 1e-11 1.0
37 2.1e-9 1.0	75.1 1.0	55 1e-11 1.0
55 2.1e-9 1.0	75.2 1.0	73 1e-11 1.0
73 2.1e-9 1.0	benzene(H3O+)	1 product
1 products	4 precursors	107 1.0
139 1.1	19 2e-9 1.0	indole(H3O+)
menthone(H3O+)	37 1e-11 1.0	4 precursors
4 precursors	55 1e-11 1.0	19 3.3e-9 1.0
19 3.4e-9 1.0	73 1e-11 1.0	37 2.5e-9 1.0
37 2.4e-9 1.0	1 product	55 2.2e-9 1.0
55 2.4e-9 1.0	79 1.0	73 2.0e-9 1.0
73 2.4e-9 1.0	toluene(H3O+)	2 products
1 products	4 precursors	118 1.0
155 1.1	19 2.1e-9 1.0	136 1.0
HDO(H3O+)	37 1e-11 1.0	methyldole(H3O+)

4 precursors	37 1e-9 1.0	99 1.0
19 3.3e-9 1.0	55 1e-9 1.0	benzaldehyde(NO+)
37 2.5e-9 1.0	73 1e-9 1.0	1 precursor
55 2.1e-9 1.0	4 products	30 2.8e-9 1.0
73 2.0e-9 1.0	81 -4.8	1 product
2 products	137 1.1	105 1.0
132 1.0	155 1.1	trans-2-pentene(NO+)
150 1.0	173 1.1	3 precursors
pyruvic acid (H3O+)	butanal(NO+)	30 1.8e-9 1.0
4 precursors	1 precursor	48 1.4e-9 1.0
19 3.3e-9 1.0	30 3.3e-9 1.0	66 1.3e-9 1.0
37 2.5e-9 1.0	1 product	2 products
55 2.2e-9 1.0	71 1.0	69 1.0
73 2.0e-9 1.0	3-methylbutanal(NO+)	70 1.0
4 products	1 precursor	propionic_acid(NO+)
89 1.0	30 3.2e-9 1.0	3 precursors
107 1.0	1 product	30 1.5e-9 1.0
125 1.0	85 1.0	48 5e-10 1.0
143 1.0	hexanal(NO+)	66 5e-10 1.0
eucalyptol(H3O+)	1 precursors	4 products
4 precursors	30 2.5e-9 1.0	104 1.0
19 2.6e-9 1.0	1 product	122 1.0

57 1.0	66 8.1e-10 1.0	30 2.3e-9 1.0
55 -0.006	2 products	48 1.6e-9 1.0
butyric_acid(NO+)	86 1.0	66 1.3e-9 1.0
3 precursors	116 1.0	2 products
30 1.9e-9 1.0	methyl_phenol(NO+)	122 1.0
48 7e-10 1.0	3 precursors	140 1.0
66 7e-10 1.0	30 2.2e-9 1.0	terpenes(NO+,total)
3 products	48 1.6e-9 1.0	3 precursors
118 1.0	66 1.3e-9 1.0	30 2.0e-9 1.0
136 1.0	2 products	48 1e-9 1.0
71 1.0	108 1.0	66 1e-9 1.0
acetoin (NO+)	126 1.0	1 products
3 precursors	phenol(NO+)	136 1.2
30 2.97e-9 1.0	3 precursors	menthone+eucalyptol(NO+, inspect ratio)
48 2.59e-9 1.0	30 2.2e-9 1.0	3 precursors
66 2.35e-9 1.0	48 1.6e-9 1.0	30 2.8e-9 1.0
1 products	66 1.3e-9 1.0	48 2.3e-9 1.0
118 1.25	2 products	64 2.3e-9 1.0
diacetyl (NO+)	94 1.0	2 products
3 precursors	112 1.0	154 1.1
30 1.36e-9 1.0	ethyl_phenol(NO+)	184 1.1
48 9.71e-10 1.0	3 precursors	

benzene(NO+)	117 1.0	2 precursors
3 precursor	xylene(NO+,all_isomers)	32 0.8e-9 1.0
30 1.5e-9 1.0	3 precursors	55 0.8e-9 -5.0
48 0.01e-9 1.0	30 1.4e-9 1.0	2 products
66 0.01e-9 1.0	48 1e-11 1.0	42 2.0
2 products	66 1e-11 1.0	72 2.0
78 1.0	1 product	pentane42only(O2+)
108 1.0	106 1.0	2 precursors
toluene(NO+)	pyruvic acid (NO+)	32 0.8e-9 1.0
1 precursor	3 precursors	55 0.8e-9 -5.0
30 1.7e-9 1.0	30 2.1e-9 1.0	1 products
1 product	48 1.5e-9 1.0	42 4.0
92 1.0	66 1.3e-9 1.0	pentane72only(O2+)
methyldole(NO+)	2 products	2 precursors
1 precursor	118 1.0	32 0.8e-9 1.0
30 2.5e-9 1.0	136 1.0	55 0.8e-9 -5.0
1 product	methane(O2+)	1 products
131 1.0	1 precursor	72 4.0
indole(NO+)	32 5.5e-12 1.0	DMS(O2+)
1 precursor	1 products	1 precursor
30 2.8e-9 1.0	47 1.0	32 2.2e-9 1.0
1 product	pentane(O2+)	2 products

62 1.0	1 product	1 precursor
80 1.0	30 1.05	32 1.6e-9 1.0
DMDS(O2+)	diacetyl (O2+)	1 product
1 precursor	1 precursors	78 1.0
32 2.3e-9 1.0	32 1.5e-9 1.0	tolulene(O2+)
1 product	1 products	1 precursor
94 1.25	86 3.0	32 1.4e-9 1.0
methanthiol(O2+)	methyl_phenol(O2+)	1 product
1 precursor	1 precursor	92 1.0
32 2.2e-9 1.0	32 2.2e-9 1.0	xylene(O2+,all_isomers)
2 products	2 products	1 precursors
47 1.0	108 1.0	32 1.4e-9 1.0
48 1.0	126 1.0	1 products
carbon_disulphide(O2+,no_78)	ethyl_phenol(O2+)	106 1.0
1 precursor	1 precursor	indole(O2+)
32 7e-10 1.0	32 2.2e-9 1.0	1 precursor
1 product	4 products	32 2.8e-9 1.0
76 1.04	107 1.0	1 product
nitric_oxide(O2+)	122 1.0	117 1.0
1 precursor	125 1.0	methyindole(O2+)
32 5.5e-10 1.0	140 1.0	1 precursor
	benzene(O2+)	32 2.4e-9 1.0

3 products	66 1.8e-9 1.0
131 1.0	2 products
130 1.0	78 1.0
117 1.0	108 1.0
OCS_nominal(O2+)	DMSO_nominal(O2+)
1 precursor	1 precursor
32 1.46e-9 1.0	32 3.1e-9 1.0
1 product	1 product
60 1.0	78 1.0
DMSO_nominal(H3O+)	NOISE(H3O+)
4 precursors	4 precursors
19 3.9e-9 1.0	19 2.6e-9 1.0
37 3.3e-11 1.0	37 2.5e-9 1.0
55 2.5e-11 1.0	55 2.3e-9 1.0
73 2.4e-11 1.0	73 2.1e-9 1.0
2 products	1 products
79 1.0	10 1.0
97 1.0	NOISE(NO+)
DMSO_nominal(NO+)	1 precursors
3 precursor	30 2.5e-9 1.0
30 2.4e-9 1.0	1 product
48 2.0e-9 1.0	10 1.0

## Appendix C – FMHS FREC Approval for Cerumen Use

Keele University FMHS Faculty Research Ethics Committee  
[health.ethics@keele.ac.uk](mailto:health.ethics@keele.ac.uk)



18 March 2020

Dear Abigail

<b>Project Title:</b>	Establishing a volatile organic compound (VOCs) profile of human ear wax using selected ion flow tube mass spectrometry
<b>REC Project Reference:</b>	MH-200116
<b>Type of Application</b>	Main application

Keele University's Faculty of Medicine and Health Sciences Research Ethics Committee (FMHS FREC) reviewed the above project application

### **Favourable Ethical opinion**

The members of the Committee gave a favourable ethical opinion of the above research on the basis described in the application form, protocol and supporting documentation, subject to the conditions specified below.

### **Conditions of the favourable opinion**

The favourable opinion is subject to the following conditions being met prior to the start of the project.

1.	None
----	------

### **Reporting requirements**

The University's standard operating procedures give detailed guidance on reporting requirements for studies with a favourable opinion including:

- Notifying substantial amendments
- Notifying issues which may have an impact upon ethical opinion of the study
- Progress reports
- Notifying the end of the study

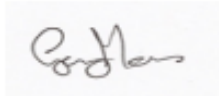
### **Approved documents**

The documents reviewed and approved are:

Document	Version	Date
FREC Application Commercial Ear Wax Abigail Rutter V1 - Abigail Rutter.pdf	1	07.02.2020

---

Yours sincerely,

A handwritten signature in black ink, appearing to read "Dr. Gary Moss", enclosed within a light gray rectangular border.

**Dr Gary Moss**  
**Chair**